



I. R. IRAN

ISSN: 1728-1431

e-ISSN: 1735-9244



**International Journal of Engineering**

Journal Homepage: [www.ije.ir](http://www.ije.ir)



**TRANSACTIONS A: BASICS**

Volume 36, Number 01, January 2023

*Materials and Energy Research Center*

---

---

**INTERNATIONAL JOURNAL OF ENGINEERING**  
**Transactions A: Basics**

---

---

**DIRECTOR-IN-CHARGE**

A. R. Khavandi

**EDITOR-IN-CHIEF**

G. D. Najafpour

**ASSOCIATE EDITOR**

A. Haerian

**EDITORIAL BOARD**

- |      |                                                                                |       |                                                                         |
|------|--------------------------------------------------------------------------------|-------|-------------------------------------------------------------------------|
| S.B. | Adeloju, Charles Sturt University, Wagga, Australia                            | A.    | Mahmoudi, Bu-Ali Sina University, Hamedan, Iran                         |
| K.   | Badie, Iran Telecomm. Research Center, Tehran, Iran                            | O.P.  | Malik, University of Calgary, Alberta, Canada                           |
| M.   | Balaban, Massachusetts Ins. of Technology (MIT), USA                           | G.D.  | Najafpour, Babol Noshirvani Univ. of Tech., Babol, Iran                 |
| M.   | Bodaghi, Nottingham Trent University, Nottingham, UK                           | F.    | Nateghi-A, Int. Ins. Earthquake Eng. Seis., Tehran, Iran                |
| E.   | Clausen, Univ. of Arkansas, North Carolina, USA                                | S. E. | Oh, Kangwon National University, Korea                                  |
| W.R. | Daud, University Kebangsaan Malaysia, Selangor, Malaysia                       | M.    | Osanloo, Amirkabir Univ. of Tech., Tehran, Iran                         |
| M.   | Ehsan, Sharif University of Technology, Tehran, Iran                           | M.    | Pazouki, Material and Energy Research Center, Meshkindasht, Karaj, Iran |
| J.   | Faiz, Univ. of Tehran, Tehran, Iran                                            | J.    | Rashed-Mohassel, Univ. of Tehran, Tehran, Iran                          |
| H.   | Farrahi, Sharif University of Technology, Tehran, Iran                         | S. K. | Sadrnezhaad, Sharif Univ. of Tech, Tehran, Iran                         |
| K.   | Firoozbakhsh, Sharif Univ. of Technology, Tehran, Iran                         | R.    | Sahraeian, Shahed University, Tehran, Iran                              |
| A.   | Haerian, Sajad Univ., Mashhad, Iran                                            | A.    | Shokuhfar, K. N. Toosi Univ. of Tech., Tehran, Iran                     |
| H.   | Hassanpour, Shahrood Univ. of Tech., Shahrood, Iran                            | R.    | Tavakkoli-Moghaddam, Univ. of Tehran, Tehran, Iran                      |
| W.   | Hogland, Linnaeus Univ, Kalmar Sweden                                          | T.    | Teng, Univ. Sains Malaysia, Gelugor, Malaysia                           |
| A.F. | Ismail, Univ. Tech. Malaysia, Skudai, Malaysia                                 | L. J. | Thibodeaux, Louisiana State Univ, Baton Rouge, U.S.A                    |
| M.   | Jain, University of Nebraska Medical Center, Omaha, USA                        | P.    | Tiong, Nanyang Technological University, Singapore                      |
| M.   | Keyanpour rad, Materials and Energy Research Center, Meshkindasht, Karaj, Iran | X.    | Wang, Deakin University, Geelong VIC 3217, Australia                    |
| A.   | Khavandi, Iran Univ. of Science and Tech., Tehran, Iran                        |       |                                                                         |

**EDITORIAL ADVISORY BOARD**

- |       |                                                                          |       |                                                                        |
|-------|--------------------------------------------------------------------------|-------|------------------------------------------------------------------------|
| S. T. | Akhavan-Niaki, Sharif Univ. of Tech., Tehran, Iran                       | A.    | Kheyroddin, Semnan Univ., Semnan, Iran                                 |
| M.    | Amidpour, K. N. Toosi Univ of Tech., Tehran, Iran                        | N.    | Latifi, Mississippi State Univ., Mississippi State, USA                |
| M.    | Azadi, Semnan university, Semnan, Iran                                   | H.    | Oraee, Sharif Univ. of Tech., Tehran, Iran                             |
| M.    | Azadi, Semnan University, Semnan, Iran                                   | S. M. | Seyed-Hosseini, Iran Univ. of Sc. & Tech., Tehran, Iran                |
| F.    | Behnamfar, Isfahan University of Technology, Isfahan                     | M. T. | Shervani-Tabar, Tabriz Univ., Tabriz, Iran                             |
| R.    | Dutta, Sharda University, India                                          | E.    | Shirani, Isfahan Univ. of Tech., Isfahan, Iran                         |
| M.    | Eslami, Amirkabir Univ. of Technology, Tehran, Iran                      | A.    | Siadat, Arts et Métiers, France                                        |
| H.    | Hamidi, K.N.Toosi Univ. of Technology, Tehran, Iran                      | C.    | Triki, Hamad Bin Khalifa Univ., Doha, Qatar                            |
| S.    | Jafarmadar, Urmia Univ., Urmia, Iran                                     | S.    | Hajati, Material and Energy Research Center, Meshkindasht, Karaj, Iran |
| S.    | Hesaraki, Material and Energy Research Center, Meshkindasht, Karaj, Iran |       |                                                                        |

**TECHNICAL STAFF**

M. Khavarpour; M. Mohammadi; V. H. Bazzaz, R. Esfandiar; T. Ebadi

**DISCLAIMER**

The publication of papers in International Journal of Engineering does not imply that the editorial board, reviewers or publisher accept, approve or endorse the data and conclusions of authors.

## CONTENTS

## Transactions A: Basics

<b>A. Pourafzal; A. Fereidunian; K. Safarihamid</b>	Chaotic Time Series Recognition: A Deep Learning Model Inspired by Complex Systems Characteristics	1-9
<b>E. Eswanto; H. Hasan; Z. M. Razlan</b>	An Analysis on Performance of Pico-hydro with Archimedes Screw Model Viewed from Turbine Shaft Angle	10-18
<b>M. Tamjidi; K. Danesh Narooei</b>	Investigating the Effect of Considering Different Cross Section Design in Friction Stir Welded Joint Line of Dissimilar Aluminum Alloys	19-27
<b>A. Chandiwala; S. Vasanwala</b>	Experimental Study of Lateral Loading on Piled Raft Foundations on Sandy Soil	28-34
<b>F. Marchione</b>	Shear Stress Distribution in Double-lap Adhesive Joints Reinforced with Nylon Fabric: Numerical Investigation	35-40
<b>A. Kharbat Shadhar; B. Basheer Mahmood; M. Hashim Al Quraishi</b>	A Novel Methodology for Predicting Roadway Deterioration in Iraq	41-49
<b>D. Pangemanan; R. Usman Latief; S. Hamzah; R. Arifuddin</b>	Study on the Application of Sustainable Construction in the Development of the Likupang Special Economic Zone	50-59
<b>P. Lap-Arparat; K. Tuchinda</b>	Computational Study of Excitation Controlling Parameters Effect on Uniform Beam Deformation under Vibration	60-70
<b>P. B. Shah; C. R. Patel</b>	Integration of Remote Sensing and Big Data to Study Spatial Distribution of Urban Heat Island for Cities with Different Terrain	71-77
<b>A. Albarghooth; A. Ramiar; R. Ramyar</b>	Earth-to-air Heat Exchanger for Cooling Applications in a Hot and Dry Climate: Numerical and Experimental Study	78-89
<b>G. R. Einy-Sarkalleh; R. Tavakkoli-Moghaddam; A. Hafezalkotob; S. E. Najafi</b>	Developing a Fuzzy Measurement of Alternatives and Ranking Compromise Solution Method for Determining Essential Barriers in Iranian Car Industry	90-97
<b>S. N. Abdulmadjid; B. S. Hartadi; R. Mitaphonna; M. Iqhrammullah</b>	Discrimination of Plastic Waste using Laser-induced Breakdown Spectroscopy-principal Component Analysis: Highlighting Molecular LIBS	98-107
<b>E. Sadeghi; E. Ebrahimi</b>	Ultra Low Power Temperature Compensated Complementary Metal Oxide Semiconductor Ring Oscillator in Subthreshold	108-118

<b>N. Mohseni; H. Nematzadeh; E. Akbarib; H. Motameni</b>	Outlier Detection in Test Samples using Standard Deviation and Unsupervised Training Set Selection	119-129
<b>G. Spoorthy; S. G. Sanjeevi</b>	Multi-criteria– Recommendations using Autoencoder and Deep Neural Networks with Weight Optimization using Firefly Algorithm	130-138
<b>B. Alipenhani; H. Bakhshandeh Amnieh; A. Majdi</b>	Application of Finite Element Method for Simulation of Rock Mass Caving Processes in Block Caving Method	139-151
<b>A. Krishna; S. Palanivelu</b>	Energy Harvesting from Vibrating Cantilever Structure of Different Base Materials using Piezoelectric Material: Theoretical and Experimental Approach	152-162
<b>V. Janani; P. T. Ravichandran</b>	Recent Trends in Stabilization of Expansive Soil using Calcined Clay	163-170
<b>P. Pasha; F. Taghinia; F. Nadalinia Chari; B. Jalili; P. Jalili; D. Domiri Ganji</b>	Chemical Reaction-Diffusion Model Around a Vessel for Studying Temperature and Concentration of Three Chemical Species by Finite Element Method	171-181
<b>V. Kadam; A. Deshmukh; S. Bhosale</b>	Hybrid Beamforming for Dual Functioning Multi-input Multi-output Radar using Dimension Reduced-baseband Piecewise Successive Approximation	182-190





## Chaotic Time Series Recognition: A Deep Learning Model Inspired by Complex Systems Characteristics

A. Pourafzal<sup>a</sup>, A. Fereidunian<sup>\*a</sup>, K. Safarihamid<sup>b</sup>

<sup>a</sup> Faculty of Electrical Engineering, K. N. Toosi University of Technology, Tehran, Iran

<sup>b</sup> School of Electrical Engineering, Iran University of Science and Technology, Tehran, Iran

### PAPER INFO

#### Paper history:

Received 07 November 2021

Received in revised form 01 October 2022

Accepted 07 October 2022

#### Keywords:

Chaotic Behavior

Time Series Classification

Deep Learning Models

Fully Convolutional Network

Complex Systems

Lorenz System

### ABSTRACT

A deep learning method is developed for chaotic time series classification. We investigate the chaotic state of a dynamical system, based on the output of the system. One of the main obstacles in time series classification is mapping a high-dimensional vector into a scalar value. To reduce the dimensions, it is common to use an average pooling layer block after feature extraction block. This blind process results in models with high computational complexity and potent to overfitting. One alternative is to extract the features manually, then apply shallow learning models to classify the time series. In fact, since complexity lies between the chaos and order, it is a sound idea to refer to complex systems characteristics to explore the chaotic region entrance. Therefore, chaotic state of a dynamical system can be recognized solely based on these characteristics. Inspired by this concept, we conclude that there is a feature space in which the output vector can be sparsified. Thus, we propose a deep learning method which the feature space dimensions successively are reduced in the feature extraction process. Specifically, we employ a fully convolutional network and add on two maximum pooling layers to the relevant feature extraction block. To validate the proposed model, the Lorenz system is employed which exhibits chaotic/non-chaotic states. We generate a labeled dataset containing 10000 samples each with 20000 features of the output of Lorenz system. The proposed model achieves 99.45 percent accuracy over 2000 unseen samples, higher than all the other competitor methods.

doi: 10.5829/ije.2023.36.01a.01

## 1. INTRODUCTION

A chaotic state is basically referred to a state of a system, in which no order is observed. In other words, a chaotic system cannot be described with a linear or predictable behavior. However, it complies with the deterministic laws of a nonlinear dynamism. Accordingly, identification of chaotic signals from random ones is a difficult task [1]. In modern science literature, many natural and human-made signals have been recognized as chaotic systems. Hence, the necessity of proficient knowledge on chaos detection becomes quite evident.

Chaos detection in time-series has been of great interest as many real-world problems including human-made or natural systems have chaotic behavior. As some examples of time-series classification applications, rotor analysis in electric machines [2], controlling cardiac

chaos [1], load demand forecasting [3], seismographic applications [4], weather forecasting and wind speed prediction [5], forecasting cryptocurrency prices [6] and even the pandemic outbreak [7], can be considered noteworthy.

One of the major challenges in chaotic time series detection is to distinguish between different states of the system. In fact, depending on the parameters of the differential equations, the system experiences different states, having different equilibrium points. Thus, the state of a chaotic system is fully explained by its parameters. Nonetheless, due to the substantial influence of initial values on the output, behavior of the system is unpredictable, and estimation of the parameters solely based on the outputs is rather difficult [8].

To address this issue, several studies have been conducted, which can be categorized into two main

\*Corresponding Author Institutional Email: [fereidunian@kntu.ac.ir](mailto:fereidunian@kntu.ac.ir)  
(A. Fereidunian)

groups, namely, model-based approaches and data-driven approaches.

Within model-based approaches, Barahona and Poon [9] have suggested a method based on the prediction feature. Later, Kodba et al. [10] presented Lyapunov exponent was as a powerful feature. Thereafter, Wernecke et al. [11] suggested a modification of this method with higher performance. However, the error and computational complexity of all these model-based methods depend vastly on how well the chosen model has been fitted.

Data-driven approaches are more comprehensible compared to model-based approaches; we believed. Gottwald and Melbourne [12] have introduced first the correlation test which performs well for noise-free scenarios and seeks for chaotic behavior in a given deterministic dynamical system. Then the regression test was introduced to reduce the noise. Tempelman and Khasawneh [13] have recommended a framework in which both correlation and regression tests were utilized. Also, Bhattacharya and Ray [14] utilized Hidden Markov Models (HMM) classification to identify chaos within the time-series of different attractors. Khosravi and Gholipour [15] estimated the Lorenz system parameters through metaheuristic algorithms. Kirichenko et al. [16] utilized the Hurst exponent as a feature to be fed into Random Forest and neural network methods to detect fractals.

Moreover, approaches by Pourafzal and Fereidunian [17] and Safarihamid et al. [18] took advantages of the link between complex systems and chaotic systems. According to Poincaré, the unpredictable behaviour of non-linear dynamical systems can be interpreted as an extreme point of complexity instead of disorder [19]. Thus, in this group of approaches, complex system features are utilized to detect chaotic time series. Pourafzal and Fereidunian [17] stated the most important features of complex systems as emergence, self-organization, predictability, and complexity. Then, information theoretic definitions of such characteristics were investigated and employed for chaos recognition.

Additionally, Safarihamid et al. [18] reviewed the definitions of characteristics and they substituted with measured-theoretic entropies (based on Kolmogorov complexity). Specifically, it is shown that emergence is indeed the violation of regularities in a time-series, whereas self-organization can be defined as the expectation of limited outcomes in a system. Then, they utilized these properties to develop a joint-entropy time series classifier with better performance compared to single entropy classifiers.

Deep learning models are considered as another member of data-driven approaches. These models provide an end-to-end framework which avoids a lot of heavy pre-processing and feature extractions [20]. Architectures like Long Short-Term Memory (LSTM)

network [21], Deep multilayer perceptron (MLP) [22], Residual Networks (ResNet) [22], Multi Scale Convolutional Neural Networks (MCNN) [23] and Fully Convolutional Networks (FCN) [22] are among the most important models which could achieve desired performance without any prior feature extraction.

MLP constitutes one of the most common architectures, where all the neurons in the current layer are fully connected to the former one. The main issue with such networks is that each neuron will be associated with a specific time stamp in the time series and thus the temporal correlations between datapoints would be ignored [22]. CNNs are usually employed in 2D classifications, such as image classification applications. However, this structure could act as a moving average filter in one dimensional domain, following by a proper activation function [22]. The architecture of ResNet is the deepest one (with 11 layers), among all these candidates. It leverages from a residual block as a shortcut, which avoids vanishing gradient by connecting the shallow layers to the output [22]. Theoretically, MCNN could reach to the best performance among all the models [24]. However, the large extraction of hyper-parameters in such models makes it almost impossible to find the best solution.

### 1. 1. Motivation

We realize that the number of trainable parameters in deep learning models (number of filters, kernels, and depth of the network) are chosen based on a trial-and-error process. However, as suggested by Pourafzal and Fereidunian [17] and Safarihamid et al. [18], regardless of observation length of chaotic time series, they can be classified using a few features of the complex system [17, 18]. This gives us the intuition that there is a feature space in which the given chaotic time series can be sparsified. Thus, we employed the Fully Convolutional Networks (FCN) proposed by Boullé et al. [25] and utilize two Max Pooling layers in the feature extraction block. By this mean, we prune all the redundant insignificant features in the feature extraction block, resulting in reducing the signal dimensions. The proposed deep model can be observed as the deep counterpart of the proposed shallow learning model by Pourafzal and Fereidunian [17]. Supported by the simulations, it is shown that the proposed deep model can reach to 99.45 percent accuracy over unseen test data, higher than other state-of-the-art methods compared in the text.

The rest of this paper is organized as follows. In Section 2, chaos recognition with complex system theory will be explained and some of the most important features of a complex system will be mentioned. In section 3, the proposed deep learning model is developed. In section 4, implementation of each method as well as the time series generation will be explored. In section 5, the simulation results and performance of the proposed method in

comparison with other methods is stated. We conclude the paper in section 6.

## 2. CHAOS RECOGNITION USING COMPLEX SYSTEMS CHARACTERISTICS

In this section, we briefly discuss the intuition behind the proposed deep learning model. In the following, we discussed the utilized model as well as the features used to detect chaos in a given time series.

**2.1. Lorenz System** We employed Lorenz system as a well-known chaotic system, to generate a chaotic time-series. The Lorenz system is defined in three-dimensional space by three parameters of  $\rho$ ,  $\sigma$  and  $\beta$  [26]. The parameter  $\rho$  which is proportional to Rayleigh number [26], can specify the state of the system alone. Based on Hopf bifurcation, we have the following condition [27]

$$\rho < \sigma \frac{\sigma + \beta + 3}{\sigma - \beta - 1}. \quad (1)$$

With violation of the Hopf bifurcation condition, the system loses the stability of equilibrium point which results in chaotic behavior [26].

**2.2. Feature Extraction** In data-driven approaches, each state is classified based on the time-series itself, rather than estimating the parameters. On average these approaches result in better performance compared to model-based approaches. However, the dimensions of the feature space are the identical to the input time series, which could be a burden on the time and space capacity of the system.

To reduce these complexities, proper feature-space reduction preprocessing units are beneficial. In feature engineering, having a prior knowledge about the number of features helps us avoiding the overfitting problem. Also, a model with less features to train is much lower time and space complexity.

Motivated by Pourafzal and Fereidunian [17], we investigate the dimensions of features in a chaotic time series employing complex system features. For a complex system, different number of features are mentioned in the literature. For instance, Grus et al. [28] have studied up to 13 different attributes related to complex systems. Here, the same as Pourafzal and Fereidunian [17], we investigate Emergence, Complexity, Predictability, Self-organization and Sensitivity to initial conditions [8] as the most cited features of a complex system.

**2.2.1. Unpredictability** As one of the main characteristics of complex systems, unpredictability is defined as being incapable of calculating the future

samples of the system according to the past observations, without precise information about its initial conditions.

Different methods have been suggested to measure unpredictability. Diebold and Kilian [29] proposed a measure based on the precision of forecasting future samples. Another well-known measure is the Hurst exponent, which is fully discussed by Hurst [30], and takes a value in the range of [0,1]. This value categorizes the system based on its behavior, into three different states, indicating the long-term tendency of the signal to follow its current trends.

**2.2.2. Emergence** According to the systems theory, the components of a system which do not have a certain attribute, may show that behavior when working as a whole system. For instance, the color of an element is cannot be observed in the atoms of that element [31]. In the information theoretical literature, emergence can be seen as the difference between the output and input information of the system, which are related to the state of the system and its initial conditions, respectively. This means that the additional produced information has been emerged within the system as a result of the interaction between its inner subsystems. Bearing this in mind, it can be concluded that different entropy levels, could be interpreted as a measure of emergence within the system. Accordingly, the emergence was defined by Gershenson and Fernández [32] stated as follows:

$$E = \frac{H_{output}}{H_{input}} \quad (2)$$

$$H \triangleq - \sum p(X) \log p(X)$$

**2.2.3. Self-organization** A self-organized system is able to find its way through forming a specific structure or pattern without any external effects and only due to the nature of its components [8]. In other words, once a pattern is observed within the system, the internal particles of the system will find their way to form that pattern again, regardless of the external situations of the system. Therefore, linearity in a system can be seen as a completely self-organizing behavior. According to this, it could be claimed that self-organization is inversely proportional to the entropy, as the information production rate.

**2.2.4. Complexity** The above-mentioned features are not capable of identifying chaotic behavior, as emergence fails in the presence of noise, and self-organization identifies linear systems as the most self-organized systems. Hence, Gershenson and Fernández [32] have suggested to define complexity as a combination of these two features, by multiplying them. Alternatively stated, the maximum complexity occurs between the extremes of emergence and self-organization.

**2. 3. Shallow Learning Classification** To assess the strength of these features, we applied them as inputs to four machine learning models, namely support vector machine (SVM), K-Nearest Neighbors (KNN), Multilayer Perceptron (MLP) and Random Forest. Then, we measured the accuracy of classification on a test data.

### 3. PROPOSED DEEP LEARNING MODEL

The main advantage of deep learning methods in time-series classification is that we can feed the raw data without any preprocessing into the machine. This is due to its automatic feature extraction. Nevertheless, aiding the machine to select a subset of features can improve the time complexity and avoid overfitting.

The overall architecture of this network is provided in Figure 1. This network consists of three blocks of feature extraction, pooling, and classification. We assumed that most of the features extracted in the feature extraction block are redundant, and the feature space dimensions could be reduced. Thus, at the feature extraction block, we employed Max Pooling layers between the convolutional layers (CL) to prune the features at each layer.

**3. 1. Feature Extraction Block** In this layer, firstly, three 1-D CL are utilized, each with 10 feature maps, kernel size of three, and stride of one, to learn the feature space, followed by a Batch Normalization (BN) unit to speed up the convergence. Also, to avoid overfitting problem by selecting specific neurons to update at each iteration, Rectified Linear Unit (ReLU) as the activation function is chosen. Then, between the CLs, we take advantage of a Max Pooling layer, which reduces the dimensions step by step. Assuming the input is vector  $\mathbf{x}_0$ , the feature extraction block is described as follows [33]:

$$\begin{aligned} \mathbf{y}_i &= \mathbf{h}_i * \mathbf{x}_{i-1} + \mathbf{b}_i \\ \mathbf{o}_i &= \sigma(f(\mathbf{y}_i)) \\ \mathbf{x}_i &= \mathcal{M}(\mathbf{o}_i, K_i) \\ \forall i &\in \{1,2\} \end{aligned} \quad (3)$$

where  $\mathbf{h}_i$  is the  $i$ -th convolutional layer,  $\mathbf{b}_i$  is bias term,  $f(\cdot)$  is the batch normalization [34],  $\sigma(\cdot)$  is activation layer and  $\mathcal{M}(\cdot, K_i)$  is the max pooling layer with size of  $K_i$ . This procedure assists the model to learn the overall pattern better by dismissing the unimportant features. Although using this architecture the learning curve increases slower than the conventional FCN method, it expresses faster performance in evaluation phase.

**3. 2. Average Pooling Block** Subsequently, the outputs of the feature extraction block are fed into a global average pooling layer prior to the classifier. Pooling layers create a response for each feature map, which reduce the dimensions without overfitting problem of the flattening layer. Traditionally, the global average pooling layer penalize the feature extraction block to dismiss the output features with insignificant values. However, the error fails to propagate properly when the rank of feature matrix is much higher than the pooling layer output.

Here, by employing two Max pooling layer in the feature extraction block, we ensure that the feature matrix is sparse. Thus, there is no need for skip connection.

**3. 3. Classification Block** Finally, in the last block, three fully connected layers with the size of 10, 5 and 2, in addition to a sigmoid activation layer are employed. The output of this layer is evaluated for binary classification.

### 4. IMPLEMENTATION AND RESULTS

**4. 1. Dataset Generation** To train and test the machine learning models, a dataset based on the Lorenz attractor is collected. Specifically, we perform 10000 independent simulation trial with the following specifications. We set the parameters  $\sigma = 10$  and  $\beta = 8/3$ , and the observation time window is 20 seconds for each trial. The parameter  $\rho$  is selected with uniform distribution from the set of  $\{0.1, 0.2, \dots, 44.9\}$ . Moreover, the initial conditions of each trial are standard white Gaussian random vectors  $N(0,1)$  in 3-D space. Finally,

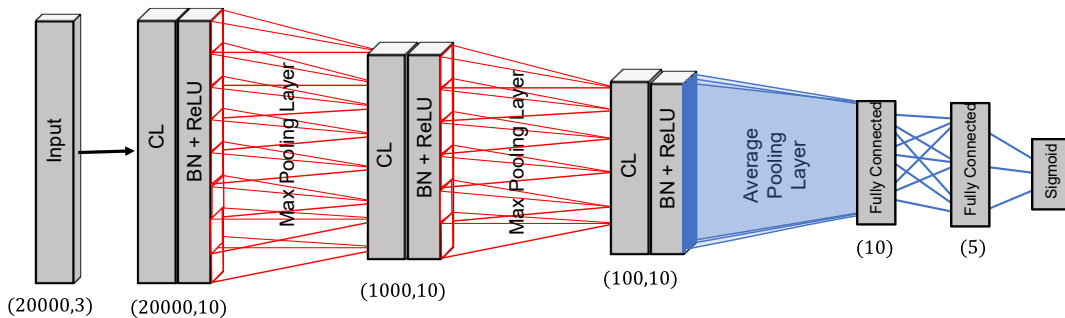


Figure 1. Deep Learning Network Architecture

the numerical method applied on the ordinary differential equations has the step-size of  $10^{-3}$ s.

Chaotic behavior is among the three different phases that Lorenz attractor experiences in which the value  $\rho$  violates the inequality of Equation (1). Likewise, we selected Hopf condition as an ideal candidate for the Target of our binary classification.

$$\begin{aligned} Target &= 1 \\ \rho &\geq 24.7 \\ Target &= 0 \end{aligned} \quad (4)$$

Thus, the final dataset consists of two data frames, an input with the size of (10000, 20000, 3) and the targets with the size of (10000, ), respectively.

The computer for the simulation is a Core-i7 @ 2.70 GHz with 16 GB of RAM for the tasks on CPU setting in addition to 12 GB of GPU on Tesla K80 for deep learning. The dataset is generated and collected in a comma-separated values (CSV) file, with the volume of 5 Giga Byte (GB).

**4. 2. Complex Systems Approach** In the complex system approach discussed in section 2, the features are extracted from the collected dataset and then, they are fed into the shallow learning models.

We extract the predictability with Hurst exponent [17] with 20 lags, self-organization with Disequilibrium [17] with  $K = 10$  and emergence using distribution entropy with 10 frequency bins [18]. In addition, complexity is the product of emergence and self-organization.

The candidates for shallow learning classifiers are as follows. In SVM models, the applied hyper parameters are linear, polynomial, and radial basis function (RBF),  $C = \{1, 10, 100, 200\}$  for different penalty parameters, and the value of Gamma is chosen within the set of  $\{10^{-3}, 10^{-4}\}$ . For the KNN classifier, the numbers of neighbours are selected within the range of  $\{3, 4, \dots, 30\}$ , as the distance metric of this classifier. We also utilized MLP with Adam solver as a posterior to our work [35]. The hyper-parameters in this model are chosen as 50 and 100 as different numbers of hidden layers, {sigmoid, ReLU} as activation functions, and  $1 \times 10^{-3}$  and  $5 \times 10^{-2}$  as different regularization terms (L2 penalty). We also adopted different learning rate schedules of constant and adaptive. In Random Forest, different combinations of decision trees are utilized to find the highest performance. The investigated hyper parameters are the total number of internal classifiers in the set of  $\{100, 150, 200, 250\}$  and maximum depth of each tree in the set of  $\{5, 10, 15, 20, 30\}$ .

The dataset is shuffled and separated into train/test subsets with proportion of 80%, 20%, respectively.

The classification report using shallow learning methods, as well as the details about the best hyper-parameters, are depicted in Table 1. As it is apparent the

shallow learning models provide good performance in either precision or recall. This is due to the loss of information between feature extraction and classification. In fact, as we calculate the features manually, accumulation over all the available samples without proper weighting factor will cause a uniform importance which cause destroying the information.

The consumed time in a simulation run is averaged over 5000 time series. Each Hurst exponent requires  $1.43 \times 10^{-3}$  seconds to perform, as well as  $2.11 \times 10^{-2}$  for emergence and  $4.7 \times 10^{-4}$  for the self-organization measure. In training phase, on average, SVM takes  $5.5 \times 10^{-1}$  [s], KNN requires  $2.3 \times 10^{-3}$ ,  $9.8 \times 10^{-1}$  for Random Forest as well as  $1.6 \times 10^{-1}$  for MLP. Also in prediction phase, average times are  $2.5 \times 10^{-4}$ ,  $5.7 \times 10^{-4}$ ,  $6 \times 10^{-3}$  and  $9.06 \times 10^{-5}$ , respectively.

**4. 3. Feature Importance** In this section, we obtain the importance of extracted features utilizing the Mutual Information (MI) [36] between features well as the Mean Decrease in Impurity (MDI) of Random Forest classifier.

Specifically, we calculate the two metrics (MI and MDI) for the features of predictability (Hurst), self-organization (Disequilibrium), emergence (Entropy), complexity and initial condition for each axis (x, y, z) of the dataset.

The bar plots of feature importance are given in Figure 2. Overall, all features except for initial condition seem to be crucial for the classification as none of them were declined in these results. However, emergence stands at higher level in both metrics, followed by predictability and Self-organization, just about 25 percent each. Moreover, x-axis and y-axis contain more information compared to z-axis. This is important for low-complexity applications due to high-volume of each axis in computation and memory allocation. It is worth mentioning that emergence and self-organization are among the most important characteristics of complex systems supporting the idea of using these characteristics in chaos recognition [17].

**4. 4. Proposed Deep Learning Model Implementation**

Here instead of train/test split, we split the shuffled dataset into three subsets of train (60%), validation (20%) and test (20%). The dataset contains 60000 features to classify the data, while there are only 10000 samples of different time-series available. This well-known data-dimensionality problem as it is mentioned in section 3.

We train the proposed deep model using the train set for 100 epochs. For validating the model at each epoch, we use the validation set. For both, the batch size is set to 750 with Adam optimizer introduced by Kingma and Ba [37].

**TABLE 1.** Performance of Conventional Machine Learning methods + Feature Extraction

Model	Selected Hyper Parameters	Performance				
		Accuracy	Precision		Recall	
			0	1	0	1
SVM	$C = 100$ $Kernel = Linear$ $\gamma = 10^{-3}$	0.75	0.97	0.54	0.16	0.99
KNN	27 Neighbors	0.77	0.55	0.98	1	0.18
MLP	Activation: ReLU, layers = 100, alpha = $10^{-3}$ learning rate = adaptive	0.74	0.95	0.54	0.16	0.99
Random Forest	Max depth = 30 Estimators = 200	0.75	0.96	0.54	0.16	0.99

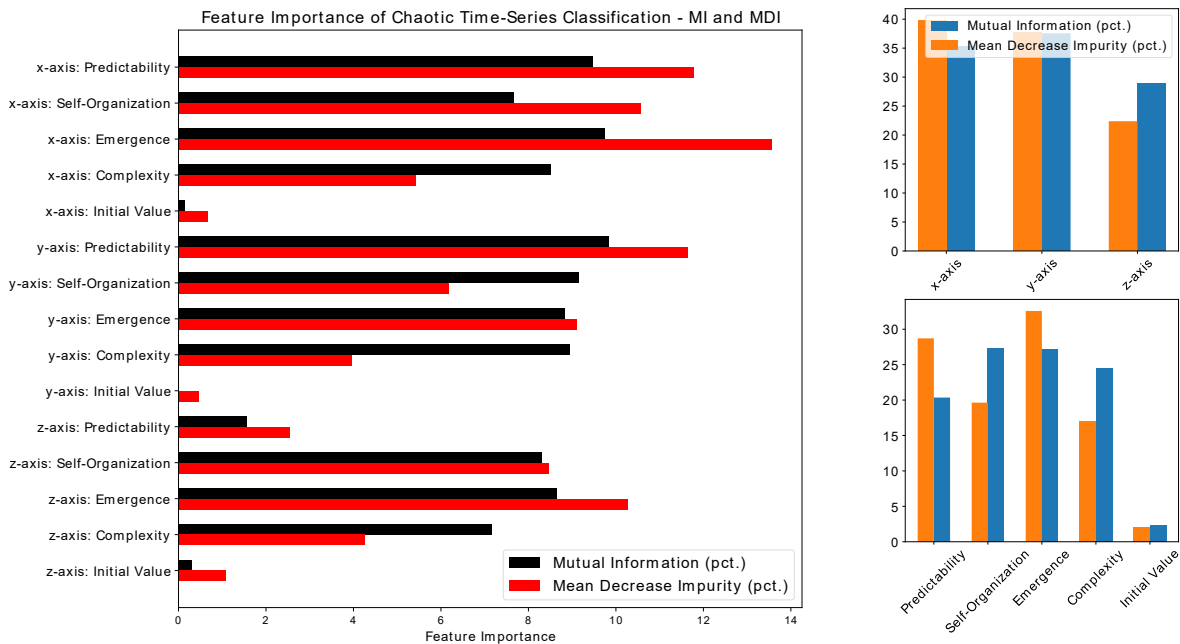
We tune the model using two hyper parameters of  $K_1$  and  $K_2$ , the pool size of first and second max pooling layer in the feature extraction block, respectively. In addition, we optimal value of learning rate is explored in 100 points linearly spaced the range of  $(10^{-4}, 1)$ .

Dimensions of the output of feature extraction block as well as the final performance of model associated with each pool size are shown as pairs, respectively, in Table 2. It can be observed that by reducing the dimensions from 10000 to 50 the performance degrades up to 10 percent accuracy, which supports the redundancy of input features. In addition, the performance degrades more when we reduce the dimensions in later stages. Indeed,

employing only one global averaging (as used by Boullé et al. [25]) at the output of feature extraction block can be interpreted as the worst-case scenario of this experiment. Based on this table, we choose  $K_1 = 20, K_2 = 10$  to set a trade-off between performance and dimensions.

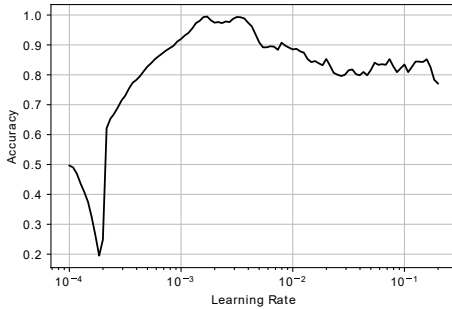
Figure 3 illustrates the dependency of performance on the learning rate for the selected pool sizes. Based on this figure, we select  $2 \times 10^{-3}$  as the optimal value of learning rate.

To evaluate the time-complexity improvement when the Max pooling layer is employed, we compare the consumed time of proposed deep model against FCN proposed by Boullé et al. [25]. For both deep learning models, there are an overall of 957 trainable parameters.

**Figure 2.** Feature importance of extracted complex system features

**TABLE 2.** Parameter selection of Max Pooling Layer for the proposed method

	$K_2 = 2$	$K_2 = 4$	$K_2 = 10$	$K_2 = 20$
$K_1 = 2$	(5000, 0.79)	(2500, 0.75)	(1000, 0.77)	(500, 0.78)
$K_1 = 4$	(2500, 0.79)	(1250, 0.78)	(500, 0.78)	(250, 0.74)
$K_1 = 10$	(1000, 0.78)	(500, 0.8)	(200, 0.8)	(100, 0.74)
$K_1 = 20$	(500, 0.79)	(250, 0.78)	(100, 0.78)	(50, 0.72)

**Figure 3.** Dependency of Accuracy on Learning rate

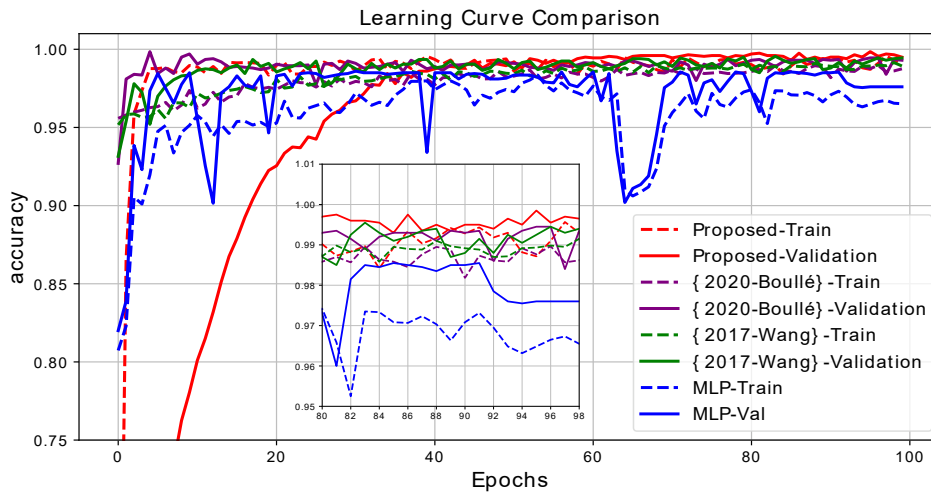
By enabling the GPU in the simulations, approximately  $7 \times 10^{-3}$  [s] is required for each batch in the training phase given by Boullé et al. [25]. While this value is  $6 \times 10^{-3}$  [s] for the proposed model. In addition, the classification could be performed by  $3 \times 10^{-3}$  [s] in evaluation phase. To make a fair comparison with shallow learning methods, we also provide the consumed time when only CPU is available. In these setting, each batch of data in training model by Boullé et al. [25] requires  $1.02 \times 10^{-1}$  [s], as well as 19 [s] for an epoch. On the contrary, when we utilize Max Pooling, these values are reduced to  $4 \times 10^{-2}$  [s] and 8 [s], respectively. Moreover, in the evaluation of these models in the same

setting,  $6.2 \times 10^{-3}$  [s] is required for the average of a classification task using FCN [25], while it requires  $5.2 \times 10^{-3}$  [s] for the proposed deep model.

Finally, we compared our proposed deep learning model with FCN proposed by Boullé et al. [25], the FCN network proposed by Wang et al. [22] and deep MLP also by Wang et al. [22]. For fair comparison with Boullé et al. [25], we select the same parameters as the proposed network, while the only difference is max pooling layer. For Wang et al. [22], we employ three CL layers with {32,64,32} filters each with {8,5,3} kernels. Also, for the MLP we choose three fully connected layer with the size of {200,200,1} and two dropout layers with fractions of {0.1, 0.1}.

In Figure 4, the learning curves of different models are illustrated. As expected, the proposed model (red solid line) requires more epochs to learn the data. However, it converges to a value higher than other deep network.

Finally, to evaluate the performance of proposed deep network, we give the 2000 test observation as the input to all the trained networks and validate the output labels against the actual ones. In Table 3, number of correct labels as well as the accuracy are reported. The proposed network outperforms other networks with 1989 correct labels, which indicates the strength of model in classification.

**Figure 4.** Comparison between the learning curves of Different Deep Learning models

**TABLE 3.** Performance of Deep Models on Unseen Test Data

	Number of correct labels (from 2000)	Accuracy
Proposed	1989	0.9945
FCN [25]	1984	0.992
FCN [22]	1987	0.9935
MLP [22]	1945	0.9725

## 5. CONCLUSIONS

Recognition of chaotic time series plays an important role in engineering and science as a lot of real-world signals (e.g., earthquakes, biomedical signals, and climatic data) could be modeled within this certain group. Complex systems as one of the well-known essentials in systems theory, share some considerable similarities with the chaotic models. Specifically, a lot of chaotic events can be explained based on only four features of a complex system, namely, prediction, emergence, self-organization, and complexity.

This similarity inspired us to seek the characteristic of a complex system in a chaotic time series. Therefore, we developed a network in which instead of blind feature extractions, we gradually reduce the dimensions of features. This is in fact similar to manual feature extraction done by complex system-based time series classifications yet is more efficient in computational complexity and accuracy. The simulation results indicate an overall performance of 99.45 percent accuracy for the proposed deep network, which is higher compared to all the other methods discussed in this paper.

## 6. REFERENCES

- Lorenz, E.N. and Haman, K., "The essence of chaos", *Pure and Applied Geophysics*, Vol. 147, No. 3, (1996), 598-599.
- Moadesahmadi, S., Ghazavi, M. and Sheikhzad Saravani, M., "Dynamic analysis of a rotor supported on ball bearings with waviness and centralizing springs and squeeze film dampers", *International Journal of Engineering, Transactions C: Aspects*, Vol. 28, No. 9, (2015), 1351-1358. doi: 10.5829/idosi.ije.2015.28.09c.13
- Al-ani, B. and Erkan, E., "A study of load demand forecasting models in electricity using artificial neural networks and fuzzy logic model", *International Journal of Engineering, Transactions C: Aspects*, Vol. 35, No. 6, (2022), 1111-1118. doi: 10.5829/ije.2022.35.06c.02
- Sparrow, C., "The Lorenz equations: Bifurcations, chaos, and strange attractors, Springer Science & Business Media, Vol. 41, (2012). doi: 10.1002/zamm.19840640122
- Chinforoush, N. and Latif Shabgahi, G., "A novel method for forecasting surface wind speed using wind-direction based on hierarchical markov model", *International Journal of Engineering, Transactions B: Applications*, Vol. 34, No. 2, (2021), 414-426. doi: 10.5829/ije.2021.34.02b.13
- Derbentsev, V., Babenko, V., Khrustalev, K., Obruch, H. and Khrustalova, S., "Comparative performance of machine learning ensemble algorithms for forecasting cryptocurrency prices", *International Journal of Engineering, Transactions A: Basics*, Vol. 34, No. 1, (2021), 140-148. doi: 10.5829/ije.2021.34.01a.16
- Babaei, A., Jafari, H., Banihashemi, S. and Ahmadi, M., "Mathematical analysis of a stochastic model for spread of coronavirus", *Chaos, Solitons & Fractals*, Vol. 145, (2021), 110788. doi: 10.1016/j.chaos.2021.110788
- Fereidunian, A., Lesani, H., Zamani, M.A., Kolarijani, M.A.S., Hassanpour, N. and Mansouri, S.S., "A complex adaptive system of systems approach to human-automation interaction in smart grid", *Contemporary Issues in Systems Science and Engineering*, (2015), 425-500. doi: 10.1002/9781119036821.ch12
- Barahona, M. and Poon, C.-S., "Detection of nonlinear dynamics in short, noisy time series", *Nature*, Vol. 381, No. 6579, (1996), 215-217. doi: 10.1038/381215a0
- Kodba, S., Perc, M. and Marhl, M., "Detecting chaos from a time series", *European Journal of Physics*, Vol. 26, No. 1, (2004), 205. doi: 10.1088/0143-0807/26/1/021
- Wernecke, H., Sándor, B. and Gros, C., "How to test for partially predictable chaos", *Scientific reports*, Vol. 7, No. 1, (2017), 1-12. doi: 10.1038/s41598-017-01083-x
- Gottwald, G.A. and Melbourne, I., "On the implementation of the 0-1 test for chaos", *SIAM Journal on Applied Dynamical Systems*, Vol. 8, No. 1, (2009), 129-145. doi: 10.1137/080718851
- Tempelman, J.R. and Khasawneh, F.A., "A look into chaos detection through topological data analysis", *Physica D: Nonlinear Phenomena*, Vol. 406, (2020), 132446. doi: 10.1016/j.physd.2020.132446
- Bhattacharya, C. and Ray, A., "Data-driven detection and classification of regimes in chaotic systems via hidden markov modeling", *ASME Letters in Dynamic Systems and Control*, Vol. 1, No. 2, (2021). doi: 10.1115/1.4047817
- Khosravi, A. and Gholipour, R., "Parameter estimation of Lorenz chaotic dynamic system using bees algorithm", *International Journal of Engineering, Transactions C: Aspects*, Vol. 26, No. 3, (2013), 257-262. doi: 10.5829/idosi.ije.2013.26.03c.05
- Kirichenko, L., Radivilova, T. and Bulakh, V., "Binary classification of fractal time series by machine learning methods", in International Scientific Conference "Intellectual Systems of Decision Making and Problem of Computational Intelligence", Springer. (2019), 701-711. doi: 10.1007/978-3-030-26474-1\_49
- Pourafzal, A. and Fereidunian, A., "A complex systems approach to feature extraction for chaotic behavior recognition", in 2020 6th Iranian Conference on Signal Processing and Intelligent Systems (ICSPIS), IEEE. (2020), 1-6. doi: 10.1109/ICSPIS51611.2020.9349551
- Safarihamid, K., Pourafzal, A. and Fereidunian, A., "A joint-entropy approach to time-series classification", in 2021 7th International Conference on Signal Processing and Intelligent Systems (ICSPIS), IEEE. (2021), 1-7. doi: 10.1109/ICSPIS54653.2021.9729371
- Hayles, N.K., "Chaos bound: Orderly disorder in contemporary literature and science, Cornell University Press, (2018).
- Ismail Fawaz, H., Forestier, G., Weber, J., Idoumghar, L. and Muller, P.-A., "Deep learning for time series classification: A review", *Data Mining and Knowledge Discovery*, Vol. 33, No. 4, (2019), 917-963. doi: 10.1007/s10618-019-00619-1
- Zhou, T., Chu, C., Xu, C., Liu, W. and Yu, H., "Detecting predictable segments of chaotic financial time series via neural

- network", *Electronics*, Vol. 9, No. 5, (2020), 823. doi: 10.3390/electronics9050823
22. Wang, Z., Yan, W. and Oates, T., "Time series classification from scratch with deep neural networks: A strong baseline", in 2017 International joint conference on neural networks (IJCNN), IEEE. (2017), 1578-1585. doi: 10.1109/IJCNN.2017.7966039
  23. Pei, S.-C. and Tseng, C.-C., "Complex adaptive iir notch filter algorithm and its applications", *IEEE Transactions on Circuits and Systems II: Analog and Digital Signal Processing*, Vol. 41, No. 2, (1994), 158-163. doi: 10.1109/82.281849
  24. Cui, Z., Chen, W. and Chen, Y., "Multi-scale convolutional neural networks for time series classification", arXiv preprint arXiv:1603.06995, (2016). doi: 10.48550/arXiv.1603.06995
  25. Boullé, N., Dallas, V., Nakatsukasa, Y. and Samaddar, D., "Classification of chaotic time series with deep learning", *Physica D: Nonlinear Phenomena*, Vol. 403, (2020), 132261. doi: 10.1016/j.physd.2019.132261
  26. Lorenz, E.N., "Simplified dynamic equations applied to the rotating-basin experiments", *Journal of the Atmospheric Sciences*, Vol. 19, No. 1, (1962), 39-51. doi: 10.1175/1520-0469(1962)019<0039:SDEATT>2.0.CO;2
  27. Marsden, J.E. and McCracken, M., "The hopf bifurcation and its applications, Springer Science & Business Media, Vol. 19, (2012). doi: 10.1007/978-1-4612-6374-6
  28. Grus, L., Crompvoets, J. and Bregt, A.K., "Spatial data infrastructures as complex adaptive systems", *International Journal of Geographical Information Science*, Vol. 24, No. 3, (2010), 439-463. doi: 10.1080/13658810802687319
  29. Diebold, F.X. and Kilian, L., "Measuring predictability: Theory and macroeconomic applications", *Journal of Applied Econometrics*, Vol. 16, No. 6, (2001), 657-669. doi: 10.1002/jae.619
  30. Hurst, H.E., "Long-term storage capacity of reservoirs", *Transactions of the American Society of Civil Engineers*, Vol. 116, No. 1, (1951), 770-799. doi: 10.1061/TACEAT.0006518
  31. Anderson, P.W., "More is different: Broken symmetry and the nature of the hierarchical structure of science", *Science*, Vol. 177, No. 4047, (1972), 393-396. doi: 10.1126/science.177.4047.393
  32. Gershenson, C. and Fernández, N., "Complexity and information: Measuring emergence, self-organization, and homeostasis at multiple scales", *Complexity*, Vol. 18, No. 2, (2012), 29-44. doi: 10.1002/cplx.21424
  33. Chollet, F., "Deep learning with python, Simon and Schuster, (2021).
  34. Ioffe, S. and Szegedy, C., "Batch normalization: Accelerating deep network training by reducing internal covariate shift", in International conference on machine learning, PMLR., (2015), 448-456.
  35. Lucas, C., Lesani, H. and Fereidunian, A., "Distribution systems reconfiguration using pattern recognizer neural networks", *International Journal of Engineering*, Vol. 15, No. 2, (2002), 135-144.
  36. Torkkola, K., "Feature extraction by non-parametric mutual information maximization", *Journal of Machine Learning Research*, Vol. 3, No. Mar, (2003), 1415-1438.
  37. Kingma, D.P. and Ba, J., "Adam: A method for stochastic optimization", arXiv preprint arXiv:1412.6980, (2014). doi: 10.48550/arXiv.1412.6980

---

### Persian Abstract

#### چکیده

آشکارسازی سیگنال‌های آشوبی با توجه به کاربرد آن‌ها در علوم مختلف یکی از مسائل مورد توجه در دهه های اخیر بوده است. امروزه با گسترش فناوری، سیستم‌های مبتنی بر یادگیری ماشین قادرند تا این سیگنال‌ها را با دقت بالایی دسته بندی کنند. در این مقاله، یک روش مبتنی بر یادگیری عمیق به منظور طبقه بندی این سیگنال‌ها ارائه شده است. طبقه بندی سری های زمانی تنها با بهره گیری از شبکه‌های عمیق و بدون توجه به ساختار تنک داده موجب بالا رفتن بار محاسباتی سیستم می‌شود. از این رو به منظور کاهش بار محاسباتی و با توجه به ارتباط تنگاتنگ آشوب و سیستم‌های پیچیده به این موضوع پی بردیم که می‌توان ورودی را در یک فضای تنک ترسیم کرد. ما یک شبکه عمیق جدید ارائه کردیم که در بلوک استخراج ویژگی آن، ابعاد ماتریس ورودی را با کمک لایه‌ی Max Pooling در چند مرحله کاهش می‌دهیم. سپس با تولید یک سری زمانی از سیستم لورنز، روش ارائه شده را به بوته آزمایش گذارديم. شبیه سازی‌ها نشان می‌دهد روش ما برتر از دیگر روش‌ها قابلیت طبقه بندی سری‌های زمانی را تا دقت ۹۹.۶۵ درصد داراست.

---



## An Analysis on Performance of Pico-hydro with Archimedes Screw Model Viewed from Turbine Shaft Angle

E. Eswanto<sup>\*a</sup>, H. Hasan<sup>b</sup>, Z. M. Razlan<sup>c</sup>

<sup>a</sup> Mechanical Engineering, Universitas Negeri Medan, Jl. Willem Iskandar/Pasar V, Medan, Indonesia

<sup>b</sup> Engineering Automotiv Education, Universitas Negeri Medan, Jl. Willem Iskandar/Pasar V, Medan, Indonesia

<sup>c</sup> School of Mechatronic Engineering, University Malaysia Perlis, Pauh Putra Campus, Arau, Perlis, Malaysia

### PAPER INFO

#### Paper history:

Received 17 April 2022

Received in revised form 13 September 2022.

Accepted 27 September 2022.

#### Keywords:

Pico Hydro

Screw Turbine

Shaft Angle

Efficiency

Renewable Energy

### ABSTRACT

The use of energy, especially for daily needs, is important. Pico hydro is an environmentally friendly power plant model that can take advantage of low flow rates and generate electricity below 1 kW. The purpose of this research is to obtain the best performance of pico hydro with a screw-shaped turbine model or what is called Archimedes Screw Turbine. The research method was carried out experimentally by adjusting the angle of the Archimedes screw turbine shaft, namely 30°, 45° and 60°. Observations at a discharge of 15 m<sup>3</sup>/h with an angle of 30° provide information that the screw turbine power obtained is 111.4 W with an efficiency of 57%. For an angle of 45° the power is 165.7 W and an efficiency of 77% while at an angle of 60° it produces 186 W of power with an efficiency of 87%. The results of this analysis prove that the pico-hydro model with a screw turbine by adjusting the angle variation on the turbine shaft gives the conclusion that the greater the given angle is, the greater the obtained performance will be, in terms of power and efficiency.

doi: 10.5829/ije.2023.36.01a.02

### NOMENCLATURE

$P_{Hydraulic}$	The hydraulic power of the screw turbine (W)	A	Cross-sectional area (m <sup>2</sup> )
$P_{Turbine}$	Turbine power (W)	V	Flow velocity (m/s)
Q	Water discharge (m <sup>3</sup> /s)	<b>Greek Symbols</b>	
R	Turbine Radius	$\rho$	Density of water (kg/m <sup>3</sup> )
F	Force (N)	$\tau$	Torque (Nm)
U	circumferential speed of screw	$\Omega$	Angular velocity (rad/s)
$F_R$	the resultant force on the blade	$\eta$	Efficiency
H	Height of water falling (m)	<b>Subscripts</b>	
g	Gravity (m/s <sup>2</sup> )	P	Power

## 1. INTRODUCTION

Power plants using renewable energy sources by utilizing water energy can be made on a large or small scale. This depends on the water source that will be used to drive water turbines and waterwheels. Currently, several types of hydropower plants have been made by many people independently, in groups, or at the company level. The types of existing hydropower plants as sources of

renewable energy are micro-hydropower plants and large-hydropower plants that produce above 1 MW electricity. Making large-hydro power plants requires great investment and detailed procedure, as mentioned by Phrakonkham et al. [1]. The power plant with a pico-hydro model that is currently starting to be developed is a hydroelectric power plant that utilizes small-scale flows. These power plants use hydropower as their driving force, such as irrigation channels for rice fields,

\*Corresponding Author Institutional Email: [eswanto@unimed.ac.id](mailto:eswanto@unimed.ac.id)  
(E. Eswanto)

rivers around the house, or natural waterfalls by utilizing the height of the falls (head), and the amount of water discharge [2, 3]. One of the most important components in a pico-hydro power plant is the turbine serving as the drive for the generator shaft or alternator. Therefore, the researchers conducted measurable research in this study which focused on the angle of the turbine shaft in the form of a screw. This screw turbine is very important because it can provide a lighter kinetic effect in rotating the water turbine blades, as stated by Julien et al. [4], Rosly et al. [5] and Noori et al. [6].

A pico-hydro power plant is a type of power generation system that uses hydropower on a small scale with a capacity of under 5 kW, as confirmed by Williamson et al. [7] and Kaunda et al. [8]. A pico-hydro power plant intended to be built should meet several requirements, such as a good flow of river water and a place that meets the criteria to be used as a pico-hydro location. The situation based on the requirements can be seen from the slope of the corner of the water channel [9, 10]. One of the studies that became a basis of in this research was a study that has been carried out by Adam et al. [11] and Assari et al. [12]. They revealed that a water block using a bulb turbine on a pico-hydro had higher efficiency compared to other types of pico-hydro turbines but is constrained by backflow in the bulb blades. This problem causes disturbances, such as unstable power and the output that becomes smaller and also affects the performance results on other properties, as underlined by Kozyn and Lubitz [13]. Gianluca et al. [14] and Shahverdi et al. [15] conducted studies by comparing the results of experiments in the laboratory and the results of simulations using software on a computer, in which the most important component that is examined is the slope of the support shaft. Their findings focused section on the slope of the shaft had an effect on the maximum efficiency of the generator with low discharge. In other words, the more inclined the shaft was, the more optimum the results would be obtained [14-16].

A study conducted by Ihfazhet et al. [17] concerning a method of implementing a pico-hydro power plant using a TC 60 open flume propeller turbine revealed that the obtained results were 71 W of electrical power with the highest voltage of 5.5% from 220 volt, a decrease in voltage to -13.3% from 220 volts, and a decrease in frequency to -19% from 90 Hz. In certain geometric parts of an Archimedes screw, it is determined by several external parameters, namely the radius of the outermost tip, the length of the thread, and the slope which is adjusted to the desired condition, as explained by Guilhem et al. [18].

Other affecting parameters were internal parameters (i.e., the radius measured at the deepest part, the number of blades, and the blade pitch) and external parameters (i.e., the location of the Archimedes thread placement

and how much water would be lifted or pushed by each screw) [19]. Meanwhile, Pallavet et al. [20] and Muhammad et al. [21] argued that the importance of internal parameters which was independently determined to optimize the performance of the thread. On the other hand, the Archimedean screw pump is the oldest type of pump, invented since people paid attention to fluid transfer. Currently, this type of pump is still widely used because of having several advantages. This pump can work optimally at an installation angle of  $30^\circ$  to  $40^\circ$  [20, 21].

The working principle of the Archimedean hydrodynamic screw turbine is the reversal of the Archimedean pump in which this turbine utilizes water flow energy to be mechanical energy. The power output range is from 1 to 250 kW, the flow rate is from 100 to 5000 l/s, and the slope is from  $22^\circ$  to  $36^\circ$  [22]. Because the impact of the water-energy converted by the turbine becomes larger, the gear type that must be chosen is the first-level transmission. It is because the first-level shaft with a small rotation will make the torque value larger. Furthermore, by taking into account the aesthetic dimensional factor due to the low turbine rotation and intention to get the turbine dimensions as compact as possible, the pulley-and-belt transmission system should not be used, as revealed in studies conducted by Budiarsa et al. [23, 24]. If the pulley-and-belt transmission system is used, the dimensions will be very large because of using type C pulleys with more than two lanes, as illustrated by Joel and Bakthavastsalam [25] and Scott et al. [26].

In this research, the problems that arise are related to the power and performance produced by the pico-hydro power plant which is less than optimal, most of the research results obtained efficiency below 50%, so further research required to get an idea of what or which parts of pico-hydro power plant can improve the plant performance. Therefore, we conducted this research by choosing to examine the angle of the turbine shaft. In determination of the shaft angles of  $30^\circ$ ,  $45^\circ$  and  $60^\circ$  were carried out to find the best angle position in the pico-hydro power plant application.

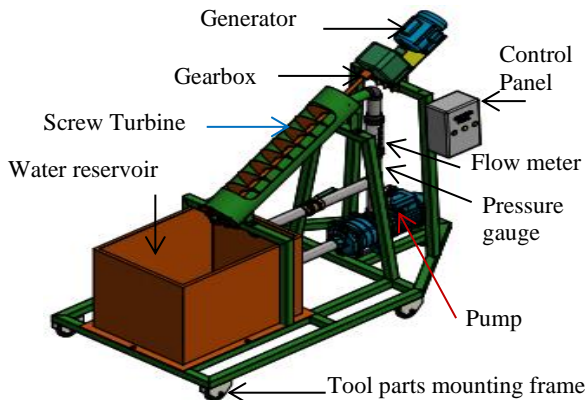
## 2. METHODS

In this study, the researchers employed an applied experimental method on a prototype basis before being tested industrially to be applied to the actual system conditions. In addition, at the end of this study, the researchers correlated the results obtained with the results of previous studies, especially those that applied a similar theory. Furthermore, the researchers also analyzed the prototype made in the relation to usable or applicable standards concerning optimal pico-hydro performance. In general, the main stages in this study

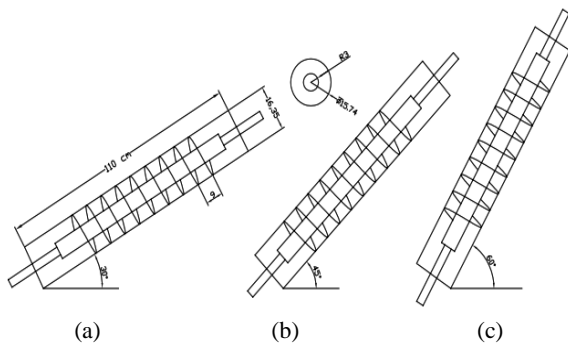
were preparation, implementation, analysis, and report writing. All of those stages are carried out by the research team.

Figure 1 demonstrates the installation of the tools used in this study, all components were installed according to their functions starting from the main equipment, supporting tools to measuring instruments for data collection. In general, the way it works is that after the pump is turned on, the water from the water reservoir will flow through the distribution pipe to the water flow meter, after the valve is opened according to the desired opening, the water will go to the screw turbine to turn the screw which in turn rotates the turbine shaft. The rotation is forwarded to the gearbox to regulate its stability so that the rotation of the turbine shaft will drive an electric generator, the cycle occurs repeatedly in operational conditions.

Figure 2 is an illustration related to the condition and position of the turbine screw shaft angle variation model, where this screw model was made to ensure the latest in pico hydro power research, where some existing references are micro hydro power plants. The turbine shaft is made permanently attached to the screw blades, this condition ensures that the construction is installed



**Figure 1.** Complete installation of test equipment of pico hydro screw turbine



**Figure 2.** Model of shaft angle variation of screw turbine: (a) 30°, (b) 45°, and (c) 60°

and can operate perfectly. The water fluid enters through the bottom side of the screw, where the acting force starts at the tip pressure to strike the first screw surface. Furthermore, the water pushes the sides of the screw to rotate all parts of the screw blade starting from the first part to the end of the screw, so that the water pushes each part of the screw which eventually turns the turbine shaft.

The theoretical concepts and equations used in this study are as follows.

- Determine turbine power

The performance of the turbine is the mechanical power generated from a turbine. To get the value of turbine power, the data needed are angular velocity ( $\omega$ ) and torque ( $\tau$ ) as stated by Arismunandar and Susumuku [27], using Euler equation:

$$P_{Turbine} = \tau \cdot \omega \quad (1)$$

where:  $P_{Turbine}$  = Power (Watt);  $\tau$  = Torque (Nm);  $\omega$  = Angular velocity (rad/s). In addition, concerning hydraulic power, it can be calculated using the following formula, Euler equation:

$$P_{Hydraulic} = \rho \cdot g \cdot h \cdot Q \quad (2)$$

where:  $P_{Hydraulic}$  = The hydraulic power of the screw turbine (Watt);  $\rho$  = The density of water ( $\text{kg/m}^3$ );  $h$  = Height of water falling (m);  $Q$  = Water discharge ( $\text{m}^3/\text{s}$ ). For turbine efficiency, it can be calculated using the following formula Euler:

$$\eta = \frac{P_{Turbine}}{P_{Hydraulic}} = \frac{\tau \cdot \omega}{\rho \cdot g \cdot h \cdot Q} \quad (3)$$

where:  $\eta$  = Efficiency;  $P_{Turbine}$  = Turbine power (Watt);  $P_{Hydraulic}$  = Hydraulic power (Watt)

- Torque

The following is the formula to calculate torque ( $\tau$ ).

$$\tau = F \times r \quad (4)$$

where:  $F$  = Force (N) and  $r$  = Turbine radius

- The force acting on the screw

To calculate this force, using the rule of movement force with the formula is.

$$F = Q \times \rho \times U \quad (5)$$

where:  $F$  = Force (N);  $Q$  = Water flow rate ( $\text{m}^3/\text{s}$ );  $\rho$  = Density of water ( $\text{kg/m}^3$ ); and  $U$  = Circumferential speed of screw. For the mass rate of flowing water, it is calculated using the following formula.

$$m = Q \times \rho \quad (6)$$

where:  $m$  = Mass flow rate of water ( $\text{kg/s}$ );  $Q$  = Water flow rate ( $\text{m}^3/\text{s}$ );  $\rho$  = The density of water ( $\text{kg/m}^3$ ). Forces that occur on the inlet side can be observed in Figure 3.

For the resultant force on the blade, it is calculated using the following formula.

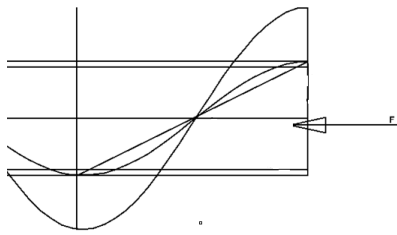


Figure 3. Water inlet side on the screw

$$F_R = \sqrt{F_s^2 + F_c^2 + 2 \cdot F_c \cdot F_s \cos \alpha} \quad (7)$$

where:  $F_R$  = Resultant force (N);  $F_s$  = Force on screw turbine blade (N);  $F_c$  = Critical force on blade surface (N).

▪ Determine flow rate

To calculate the flow rate of water, it uses the following formula Continuity equation.

$$Q = AxV \quad (8)$$

where:  $Q$  = Water discharge ( $m^3/s$ );  $A$  = Cross-sectional area ( $m^2$ );  $V$  = Flow velocity ( $m/s$ )

▪ Determine flow velocity

The flow velocity in open flow is calculated using Manning's equation, as follows.

$$V = \left(\frac{1}{n}\right) m^{2/3} \sqrt{i} \quad (9)$$

where:  $n$  = Manning's roughness constant;  $i$  = The slope of the energy line;  $m$  = Hydraulic mean depth. Moreover, the formula to calculate the hydraulic mean depth is as follows.

$$m = \frac{(into\ the\ water)xA}{(into\ the\ water)x\pi D + 0,8 D} \quad (10)$$

### 3. RESULTS AND DISCUSSION

#### 3. 1. Making the Prototype of Screw Turbine

The preparation of the prototype design is carried out using technical drawings with predetermined dimensions and taking into account manufacturing standards when assembling all pico-hydro components. In the manufacturing process, it is made on a small scale (laboratory scale) while still paying attention to the scale and approaching the actual conditions. This is to facilitate the retrieval or collection of the desired data if, one day later, it is applied to the actual water flow in the field. The shape and dimensions of the prototype of the screw turbine can be seen in Figure 4. The prototype of the screw turbine made in this study is a small-scale screw turbine, in which the tilt angle of the screw turbine shaft varies, namely  $30^\circ$ ,  $45^\circ$ , and  $60^\circ$ .

This research is based on pico-hydro scale generators, for efficiency and better power already exist, but for micro hydro power plants at an angle of  $40^\circ$  as has been studied by Phrakonkham et al. [1] and Kaunda et al. [8] by explaining that for micro hydro power plants the angle should be turbine shaft is made above  $40^\circ$ .

The selection of angles of  $30^\circ$ ,  $45^\circ$  and  $60^\circ$  in this study was carried out to find the characteristics of the best angle position resulting from the three choices for pico-hydro power plant applications, because some references as stated by Shahverdi et al. [15, 22] that the angle of inclination  $22^\circ$  the efficiency obtained is below 50%, so it is very important to do research to determine the best turbine shaft tilt angle for pico-hydro power plants.

#### 3. 2. Selection of Turbine Materials

In the turbine material section, it is very important to choose the type of material used. This is to provide the right effect when the pico-hydro operation is running. For example, the condition of being not too heavy and or not too light in getting the impetus from the water will push the screw turbine blades. In other conditions, mass also has an important impact on the material selection process. Therefore, because the number of pitch screws is 9 pieces, the total mass, if calculated, becomes as follows:  $9 \times 0.10 \text{ kg} = 0.9 \text{ kg}$ .

▪ The following is the calculation in finding out the average radius ( $R_m$ ).

$$\text{Thread depth, } \frac{t}{2} = \frac{102}{2} = 51 \text{ mm}$$

Then :

$$R_m = \frac{147\text{mm} - 51\text{mm}}{2} = 48 \text{ mm}$$

In this study, in the initial planning for the manufacture of test equipment, a comprehensive selection of construction materials was carried out following the applicable standards in design and material selection, such as the selection of shafts. The diameter of the shaft is the most important part in supporting this study. The diameter of the shaft used to support a bearing is 20 mm. This condition has been adjusted to the standard nominal diameter following ASME standards and ASTM materials. Therefore, the shaft used is safe to

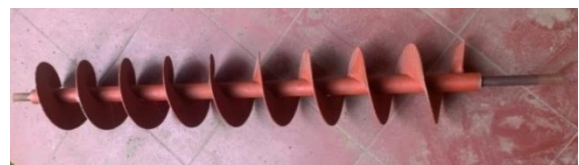


Figure 4. The models of the screw turbines

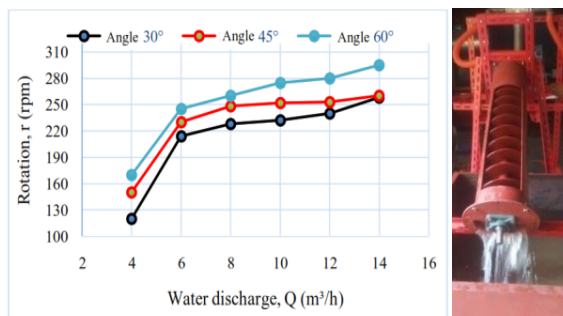


Figure 5. Screw turbine shaft

apply because the allowable diameter is smaller than the diameter used (13 mm < 20 mm). For this reason, according to the textbook, the shaft used in this screw turbine is declared safe in its use. Safety in determining these parts will be very useful when the operational conditions of pico-hydro are on running. Because the Reynolds number obtained from this study is larger (10604.65 > 2000), then the flow is considered to be turbulent ( $Re > 2000$ ) [28], which greatly affects the performance of the system.

**3. 3. Testing the Rotation of the Screw Turbine without Load** In this section, after installing the screw turbine on the housing and engine frame that has been made in such a way, further testing is carried out to obtain experimentally measured data by first testing the pico-hydro condition without giving a load, meaning that the load is made zero. To find out the rotation produced by the turbine before being given a load, a test is carried out with a predetermined angle of laying the turbine shaft ( $\alpha$ ) and discharge (Q).

Figure 6 presents the results obtained by the no-load test. In this figure, it can be seen that the relationship between the given flow rate and the rotation produced by the pico-hydro. If considering the color of the line graph, we can see the dominance of the blue color. In this study, it is the largest angle, namely 60°. This situation is caused by the variation of the opening of the tilt angle. In other words, the greater the flow of water is, the heavier and tighter the pressure will be. Consequently, it increases the thrust of the water that presses the blades of the screw turbine. From the graphic shown in Figure 6 above, we can see the difference in rotation produced at each different angle with a discharge from 4 m<sup>3</sup>/h to 14 m<sup>3</sup>/h, in which the largest rotation is at an angle of 60° with the resulting rotation of 295 rpm at a discharge (Q) of 14 m<sup>3</sup>/h. Meanwhile, the smallest rotation is at an angle of 30° with the resulting rotation of 120 rpm at a discharge (Q) of 4 m<sup>3</sup>/h. This condition is highly precise with the principle that occurs in a flow at a certain height and angle.



**Figure 6.** Graph of the relationship between flow rate (Q) and turbine rotation (r) at various variations of the turbine shaft angle

**3. 4. Turbine Power and Water Power Used** In this discussion, before describing in detail related to the power generated in this study, we firstly review the fluid flow capacity which determines the power obtained during this study. This condition is indirectly closely related to the angle of the screw turbine shaft which is the single object in the observation process. Determination of the screw tilt angle will have a significant impact on the system being served, namely the screw. The screw model which is used as a single model by varying the angle of the turbine shaft will have a lot of effects if the capacity, of the water fluid flow used as a source of energy to drive the turbine blades, increases.

In the pico-hydro model, the head is needed as an implementation of falling-water height and also flowing discharge to produce power, which is useful as a system in changing power that works by absorbing energy from the flow and altitude of the water. After that, it channels energy in the form of power. This statement is in line with what was conveyed by Edwin et al. [29] Cobb and Sharp [30]. and Eswanto et al. [31] that friction, heat, sound, and others are forms of energy lost due to changes in energy that cannot be transferred as much as has been received or absorbed.

Figures 7, 8, and 9 are graphs of the relationship between flow discharge variations and the power obtained. The test conditions of a slope angle are 30°, 45°, and 60°. Here, the power is the water propulsion power or water power, and the turbine power working on certain normal operating conditions. In Figure 7 with a slope angle of 30°, the red line shows the maximum turbine power reaching 111.4 Watt at a discharge of 15 m<sup>3</sup>/h. On the other hand, the black line shows the greater increase in water power, namely 240 Watt at a discharge of 10 m<sup>3</sup>/h. This is certainly different from the discharge conditions compared to the turbine power. In general, the power generated from the test results describes the actual measured conditions. Under certain conditions, the water power in Figure 7 first experienced an increase in succession to a peak of 10 Watt. This is because the water impetus that hit the turbine blades continues to move

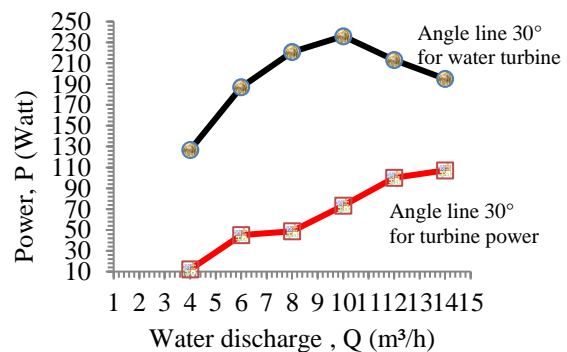


**Figure 7.** Graph of water power (P<sub>water</sub>) and turbine power (P<sub>turbine</sub>) influenced by water discharge (Q) at an angle of 30°

normally due to the steady flow of water. However, a decrease is seen in the discharge to 15 m<sup>3</sup>/h. This condition is due to the water flow experiencing a decrease in water flow rate.

Tests and measurements are carried out appropriately with the installation of measuring instruments based on planned needs in the research being carried out. Figure 8 is a graph of the results of data processing after measurements have been carried out in the form of the relationship between water discharge and power at the angle of the second test model, namely the shaft angle of 45°. Similar to the previous tests, the given water discharge is carried out in variations so that measurable results are obtained. Figure 8 shows that the two graph lines of water power and turbine power increase regularly. However, an increase in experienced by water power is slightly different, namely, after an increase from the initial flow of 4 m<sup>3</sup>/h. After that, it decreases. This condition is probably due to water flow which is very heavy pushing the blade of the screw turbine because the angle opening is larger than previously. In this study, at an angle of 45°, the researchers obtain the maximum power of 141.7 Watt (water power) which occurs at the discharge opening of 10 m<sup>3</sup>/h. The results obtained, if observed, are certainly greater than those obtained at a slope angle of 30° with the difference in power as a performance, namely 30.1 Watt. In another discussion which is also still in the schematic of Figure 8, the green line or turbine power shows a trend that continues to increase massively from the start of the first opening water discharge to the discharge point of 8 m<sup>3</sup>/h. After that, it decreases to the normal limit. This means that it is not too far from the initial maximum increase in the turbine performance line. In line with that, it can also be clearly seen that another increase continues to move without a decrease after the discharge of 10 m<sup>3</sup>/h at the turbine power of 68 Watt. In this study, the nozzle used is designed with one jet hole placed at the end of the inlet to enter the water flow to the screw turbine blades so that the thrust that occurs can maximally provide energy in one direction of the water jet. This makes the turbine blade rotation stable.

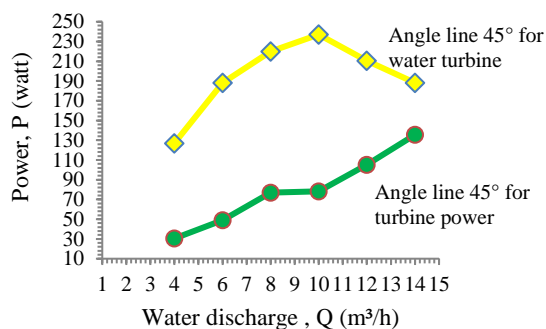


**Figure 8.** Graph of water power ( $P_{\text{water}}$ ) and turbine power ( $P_{\text{turbine}}$ ) influenced by water discharge ( $Q$ ) at an angle of 45°

The next presented analysis results and their comments are concerning the data presented in Figure 9 in which the phenomena that occur are similar to the 30° and 45° angle models. The difference is seen in the turbine power graph line, namely the position of the water discharge from 6 m<sup>3</sup>/h to 8 m<sup>3</sup>/h. It reoccurs at the position of the water discharge from 10 m<sup>3</sup>/h to 12 m<sup>3</sup>/h. However, after that, there is an increase in back to normal. This phenomenon must be of particular concern because it will have an impact on the final results of this study in obtaining optimum performance results.

Figure 9 provides information on actual conditions based on experimental analysis in which the greater the flow of water used is, the greater the turbine power produced will be. Meanwhile, the actual water power that occurs does not affect the turbine power. This can be seen at the discharge of 12 m<sup>3</sup>/h and 15 m<sup>3</sup>/h, in which there is a decrease in water power due to the lowest head. In this study, the greatest turbine power is obtained at an angle of 60° with a discharge of 15 m<sup>3</sup>/h and the power generated of 186 Watt.

If viewed from all the events that have an impact on the performance of pico-hydro by using various variations of the given shaft angle, the water flow is certainly one of the main determinants of orbiting the size of the performance. The larger the water flow opening is (in this case: the discharge), the higher the impact of the obtained turbine power will be. This condition also occurs if the opposite thing is carried out. The water that flows towards the turbine blades will first pass through the nozzle as the tip of the thrust shot which converts the energy in the water into kinetic energy. The phenomenon occurs due to the reduction of the cross-sectional area of the pipe to the nozzle. Therefore, the impact of the amount of kinetic energy given is the increasing velocity of the jet of water. The next analysis is when the water spray comes out of the nozzle which then definitely hits the center of the screw turbine blade due to the collision between the water spray and the blade so that the turbine rotates continuously following the given water flow. Therefore, the greater the water flow that is inserted to push the turbine blades is, the greater the turbine

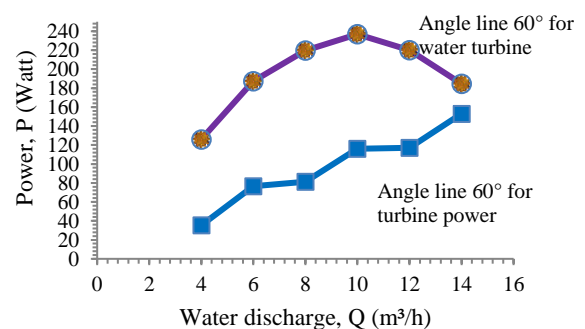


**Figure 9.** Graph of water power ( $P_{\text{water}}$ ) and turbine power ( $P_{\text{turbine}}$ ) influenced by water discharge ( $Q$ ) at angle of 60°

performance on the pico-hydro will be. This is also in line with what has been conveyed by Aggidis and Židonis [32], that if the water flow is increased, greater rotation will be generated. Therefore, the output of power, electrical energy, and overall performance will also improve on a prototype scale. Likewise, the opposite law applies. It means that the less the given water is, the smaller the turbine rotation, the electrical energy, and the electrical performance will be.

The optimization is carried out using the response surface method with a model comparing three variations of the turbine shaft angle. The results of the optimization of experimental data are processed and calculated numerically to obtain the characteristics of the overall pico-hydro performance. Furthermore, an analysis of each test and operational conditions is carried out on each of the tested shaft angle blade models.

In the analysis of the electrical performance, as shown in Figure 10, it can be seen that the efficiency generated in the pico-hydro made in this study is increased. This condition is generated by an increase in water flow and rotation produced by the turbine. The performance of pico-hydro, which in this case is represented by efficiency, which is presented in Figure 10, in which the greatest efficiency is obtained at an angle of  $60^\circ$  with a rotation of 295 rpm and the yielded efficiency of 87%. Meanwhile, the smallest efficiency is obtained at an angle of  $30^\circ$  with a rotation of 120 rpm and the yielded efficiency of 57%. An increase in efficiency, generally, is obtained in the three variations of the screw turbine shaft angle. It is because the angle of the given opening is getting greater, which increases the height of the falling water, meaning that the angle position is getting straighter and closer to  $90^\circ$ , resulting in increased efficiency. The basic reason for this statement has also been explained from Zhou's reference and Irwansyah's research which states that an angle position that is greater or closer to  $90^\circ$  can reduce the flow resistance and facilitate the flow of water falling where the falling water force, pressure and velocity are free of obstacles. The turbine screw blades that rotate as a result of the impetus of water at an angle position close to straight make it

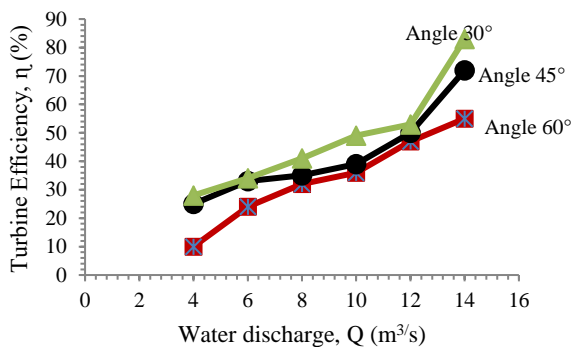


Figure 10. Effect of water discharge on efficiency

easier to move one blade to the blade in front of it, so that performance in the form of efficiency increases along with system operations that run smoothly, this condition will certainly be more efficient difficult to rotate if the blade angle is smaller or below  $30^\circ$ . When compared with the three variations of the shaft angle used, the best performance is obtained at the largest angle. Meanwhile, the decrease in thrust due to the size of the water flow discharge opening gives different responses in each test model. These results of the analysis are also close to what has been reported by Zhou et al. [33] and Irwansyah et al. [34] regarding the optimization of the screw turbine. However, their studies are carried out numerically. Their studies revealed that the water discharge opening on the flowmeter will have a very large impact on changes in all components of the generator, especially the final performance that will be obtained. Therefore, determining the initial design is very important in produced optimal performance.

#### 4. CONCLUSION

From the results and discussion, there is a correlation between the initial planning and the results obtained. In this study, the measurements are carried out on the amount of water discharge produced, the rotation of the turbine blades, the rotation of the transmission, the rotation of the alternator, and the power generated. Furthermore, the variations in the angle of the screw shaft used in this study are  $30^\circ$ ,  $45^\circ$ , and  $60^\circ$  on the screw turbine part which is traversed by the flow of water. The obtained data are processed in the performance analysis on each test model. The results of the measurement indicate that the magnitude of the turbine shaft angle and the flow rate used will affect the performance of pico-hydro verbally. Observations at the discharge of  $15 \text{ m}^3/\text{h}$  with an angle of  $30^\circ$  provide information that the obtained screw turbine power is 111.4 Watt with an efficiency of 60%. For an angle of  $45^\circ$ , the produced power is 141.7 Watt and an efficiency of 77%. Meanwhile, at an angle of  $60^\circ$ , the produced power is 165.5 Watt and an efficiency of 87%. The results of this analysis proved that the pico-hydro model with a screw turbine by adjusting the angle variation on the turbine shaft gives the conclusion that the greater the given angle is greater the obtained performance will be, in terms of power and efficiency.

#### 5. ACKNOWLEDGMENT

We the research team, would like to thank those who have assisted in the smooth running of this research activity, most importantly, the Universitas Negeri Medan as the institution providing funds for this research from

the beginning to the end of these activities. In addition, we also thank the leadership and staff of the Unimed mechanical engineering department for supporting the process of making tools and testing at the Unimed mechanical engineering manufacturing workshop.

## 6. REFERENCES

- Phrakonkham, S., Remy, G., Diallo, D. and Marchand, C., "Pico vs micro hydro based optimized sizing of a centralized ac coupled hybrid source for villages in laos", *Energy Procedia*, Vol. 14, (2012), 1087-1092. <http://dx.doi.org/10.1016/j.egypro.2011.12.1059>
- Lahimer, A., Alghoul, M., Sopian, K., Amin, N., Asim, N. and Fadhel, M., "Research and development aspects of pico-hydro power", *Renewable and Sustainable Energy Reviews*, Vol. 16, No. 8, (2012), 5861-5878. <http://dx.doi.org/10.1016/j.rser.2012.05.001>
- Lashofer, A., Hawle, W. and Pelikan, B., "State of technology and design guidelines for the archimedes screw turbine", *Proceedings of the Hydro*, (2012).
- Rohmer, J., Knittel, D., Sturtzer, G., Flieller, D. and Renaud, J., "Modeling and experimental results of an archimedes screw turbine", *Renewable Energy*, Vol. 94, (2016), 136-146. <https://doi.org/10.1016/j.renene.2016.03.044>
- Rosly, C.Z., Jamaludin, U.K., Azahari, N.S., Mu'tasim, M.A.N., Oumer, A.N. and Rao, N., "Parametric study on efficiency of archimedes screw turbine", *ARPJ Journal of Engineering and Applied Sciences*, Vol. 11, No. 18, (2016), 10904-10908.
- Noori, Y., Teymourash, A.R. and Zafarmand, B., "Use of random vortex method in simulating non-newtonian fluid flow in a t-junction for various reynolds numbers and power-law indexes", *International Journal of Engineering, Transaction B : Applications*, Vol. 35, No. 5, (2022), 954-966. doi: 10.5829/ije.2022.35.05b.11.
- Williamson, S.J., Stark, B.H. and Booker, J.D., "Low head pico hydro turbine selection using a multi-criteria analysis", *Renewable Energy*, Vol. 61, (2014), 43-50. <http://dx.doi.org/10.1016/j.renene.2012.06.020>
- Kaunda, C.S., Kimambo, C.Z. and Nielsen, T.K., "A technical discussion on microhydropower technology and its turbines", *Renewable and Sustainable Energy Reviews*, Vol. 35, (2014), 445-459. <https://doi.org/10.1016/j.rser.2014.04.035>
- Nuramal, A., Bismantolo, P., Date, A., Akbarzadeh, A., Mainil, A.K. and Suryono, A.F., "Experimental study of screw turbine performance based on different angle of inclination", *Energy Procedia*, Vol. 110, (2017), 8-13. <http://dx.doi.org/10.1016/j.egypro.2017.03.094>
- Ghadimi, A., Razavi, F. and Mohammadian, B., "Determining optimum location and capacity for micro hydropower plants in lorestan province in iran", *Renewable and Sustainable Energy Reviews*, Vol. 15, No. 8, (2011), 4125-4131. <https://doi.org/10.1016/j.rser.2011.07.003>
- Piper, A.T., Rosewarne, P.J., Wright, R.M. and Kemp, P.S., "The impact of an archimedes screw hydropower turbine on fish migration in a lowland river", *Ecological Engineering*, Vol. 118, (2018), 31-42. <https://doi.org/10.1016/j.ecoleng.2018.04.009>
- Assari, M.R., Basirat Tabrizi, H., Jafar Gholi Beik, A. and Shamesri, K., "Numerical study of water-air ejector using mixture and two-phase models", *International Journal of Engineering, Transaction B : Applications*, Vol. 35, No. 2, (2022), 307-318. doi: 10.5829/ije.2022.35.02b.06.
- Kozyn, A. and Lubitz, W.D., "A power loss model for archimedes screw generators", *Renewable Energy*, Vol. 108, (2017), 260-273. <https://doi.org/10.1016/j.renene.2017.02.062>
- Zitti, G., Fattore, F., Brunori, A., Brunori, B. and Brocchini, M., "Efficiency evaluation of a ductless archimedes turbine: Laboratory experiments and numerical simulations", *Renewable Energy*, Vol. 146, (2020), 867-879. <https://doi.org/10.1016/j.renene.2019.06.174>
- Shahverdi, K., Loni, R., Ghobadian, B., Gohari, S., Marofi, S. and Bellos, E., "Numerical optimization study of archimedes screw turbine (ast): A case study", *Renewable Energy*, Vol. 145, (2020), 2130-2143. <https://doi.org/10.1016/j.renene.2019.07.124>
- Vatani, M. and Domiri-Ganji, D., "Experimental examination of gas-liquid two-phase flow patterns in an inclined rectangular channel with 90 bend for various vertical lengths", *International Journal of Engineering, Transaction A : Basics*, Vol. 35, No. 4, (2022), 685-691. doi: 10.5829/ije.2022.35.04a.07.
- Nugraha, I.N.E., Waluyo, W. and Syahrial, S., "Penerapan dan analisis pembangkit listrik tenaga pikohidro dengan turbin propeller open flume tc 60 dan generator sinkron satu fasa 100 va di upi bandung", *Reka Elkomika*, Vol. 1, No. 4, (2013).
- Dellinger, G., Simmons, S., Lubitz, W.D., Garambois, P.-A. and Dellinger, N., "Effect of slope and number of blades on archimedes screw generator power output", *Renewable Energy*, Vol. 136, (2019), 896-908. <https://doi.org/10.1016/j.renene.2019.01.060>
- Erinofiard, P.G., Date, A., Akbarzadeh, A., Bismantolo, P., Suryono, A., Mainil, A. and Nuramal, A., "A review on micro hydropower in indonesia", *Energy Procedia*, Vol. 110, (2017), 316-321. <http://dx.doi.org/10.1016/j.egypro.2017.03.146>
- Gogoi, P., Handique, M., Purkayastha, S. and Newar, K., "Potential of archimedes screw turbine in rural india electrification: A review", *ADB Journal of Electrical and Electronics Engineering (AJEEE)*, Vol. 2, No. 1, (2018), 30-35. <https://journals.dbuniversity.ac.in/ojs/index.php/AJEEE/article/view/554>
- Maulana, M.I. and Putra, G.S., "Performance of single screw archimedes turbine using transmission", in *IOP Conference Series: Materials Science and Engineering*, IOP Publishing. Vol. 536, (2019), 012022.
- Shahverdi, K., Loni, R., Ghobadian, B., Monem, M., Gohari, S., Marofi, S. and Najafi, G., "Energy harvesting using solar orc system and archimedes screw turbine (ast) combination with different refrigerant working fluids", *Energy Conversion and Management*, Vol. 187, (2019), 205-220. <https://doi.org/10.1016/j.enconman.2019.01.057>
- Budiarso, W., Lubis, M.N. and Adanta, D., "Performance of a low cost spoon-based turgo turbine for pico hydro installation", *Energy Procedia*, Vol. 156, (2019), 447-451. <https://doi.org/10.1016/j.egypro.2018.11.087>
- Budiarso, D.F., Febriansyah, D. and Adanta, D., "The effect of wheel and nozzle diameter ratio on the performance of a turgo turbine with pico scale", *Energy Reports*, Vol. 6, (2020), 601-605. <https://doi.org/10.1016/j.egypro.2019.11.125>
- Titus, J. and Ayalur, B., "Design and fabrication of in-line turbine for pico hydro energy recovery in treated sewage water distribution line", *Energy Procedia*, Vol. 156, (2019), 133-138. <https://doi.org/10.1016/j.egypro.2018.11.117>
- Gladstone, S., Tersigni, V., Francfort, K. and Haldeman, J.A., "Implementing pico-hydropower sites in rural rwanda", *Procedia Engineering*, Vol. 78, (2014), 279-286. <http://dx.doi.org/10.1016/j.proeng.2014.07.068>
- Arismunandar, A. and Kuwahara, S., "Teknik tenaga listrik pembangkitan dengan tenaga air", *Jakarta: Pradaya Paramitha*, (2004).

28. Sheng, W., "Wave energy conversion and hydrodynamics modelling technologies: A review", *Renewable and Sustainable Energy Reviews*, Vol. 109, (2019), 482-498. doi. <https://doi.org/10.1016/j.rser.2019.04.030>
29. Gallego, E., Rubio-Clemente, A., Pineda, J., Velásquez, L. and Chica, E., "Experimental analysis on the performance of a pico-hydro turgo turbine", *Journal of King Saud University-Engineering Sciences*, Vol. 33, No. 4, (2021), 266-275. <https://doi.org/10.1016/j.jksues.2020.04.011>
30. Cobb, B.R. and Sharp, K.V., "Impulse (turgo and pelton) turbine performance characteristics and their impact on pico-hydro installations", *Renewable Energy*, Vol. 50, (2013), 959-964. <http://dx.doi.org/10.1016/j.renene.2012.08.010>
31. Eswanto, S.J., Sitompul, T.S. and Iwan Gunawan, A., "Aplikasi pltmh penghasil energi listrik di sungai lawang desa simbang jaya kecamatan bahorok", *Dinamika: Jurnal Ilmiah Teknik Mesin*, Vol. 11, No. 2, (2020), 56-64. <https://doi.org/10.33772/djitm.v11i2.11678>
32. Aggidis, G.A. and Židonis, A., "Hydro turbine prototype testing and generation of performance curves: Fully automated approach", *Renewable Energy*, Vol. 71, (2014), 433-441. <https://doi.org/10.1016/j.renene.2014.05.043>
33. Zhou, D., Gui, J., Deng, Z.D., Chen, H., Yu, Y., Yu, A. and Yang, C., "Development of an ultra-low head siphon hydro turbine using computational fluid dynamics", *Energy*, Vol. 181, (2019), 43-50. <https://doi.org/10.1016/j.energy.2019.05.060>
34. Irwansyah, R., Rusli, C.C. and Nasution, S.B., "Analysing hydraulic efficiency of water vortex pico-hydro turbine using numerical method", *Journal of Advanced Research in Fluid Mechanics and Thermal Sciences*, Vol. 77, No. 2, (2021), 91-101. <https://doi.org/10.37934/arfmts.77.2.91101>

---

### Persian Abstract

---

#### چکیده

استفاده از انرژی، به ویژه برای نیازهای روزانه، مهم است. پیکو هیدرو یک مدل نیروگاه سازگار با محیط زیست است که می تواند از نرخ جریان پایین بهره برده و برق کمتر از 1 کیلو وات تولید کند. هدف از این تحقیق به دست آوردن بهترین عملکرد پیکو هیدرو با مدل توربین پیچی شکل یا آنچه که توربین پیچی ارشمیدس نامیده می شود می باشد. روش تحقیق به صورت تجربی با تنظیم زاویه محور توربین پیچی ارشمیدس یعنی 30 درجه، 45 درجه و 60 درجه انجام شد. مشاهدات در دبی 15 متر مکعب در ساعت با زاویه 30 درجه اطلاعاتی را ارائه می دهد که توان توربین پیچی به دست آمده 111.4 وات با بازده 57 درصد است. برای زاویه 45 درجه قدرت 165.7 وات و بازده 77 درصد است در حالی که در زاویه 60 درجه 186 وات توان با بازده 87 درصد تولید می کند. نتایج این تحلیل ثابت می کند که مدل پیکو هیدرو با توربین پیچی با تنظیم تغییرات زاویه روی شفت توربین به این نتیجه می رسد که هر چه زاویه داده شده بیشتر باشد، عملکرد به دست آمده از نظر قدرت و بازده بیشتر خواهد بود.

---



## Investigating the Effect of Considering Different Cross Section Design in Friction Stir Welded Joint Line of Dissimilar Aluminum Alloys

M. Tamjidi<sup>\*a</sup>, K. Danesh Narooei<sup>b</sup>

<sup>a</sup> Department of Industrial Engineering, Velayat University, Iranshahr, Iran

<sup>b</sup> Department of Industrial Engineering, Faculty of Industry and Mine Khash, University of Sistan and Baluchestan, Zahedan, Iran

### PAPER INFO

#### Paper history:

Received 28 June 2022

Received in revised form 13 September 2022

Accepted 18 September 2022

#### Keywords:

Friction Stir Welding

Cross Section in Joint Line

Tensile Properties

### ABSTRACT

Using friction heat, welded joints of the Friction stir welding (FSW) process are made that are utilized to forge metal components together. Since there is no parent metal melting, several advantages are obtained by the FSW process over fusion welding. The alloys AA6XXX and AA7XXX Al are two sets of the most extensively utilized structural materials in rail transportation, automotive, and aerospace industries. The objective of present study was to investigate the effects of novel cross-sections in joint lines and further analyze the improvement in mechanical features. Due to the importance of the weld zone properties, many researchers seek to improve the mechanical behavior of the weld zone. For this, friction stir welded joint under four different new design in cross section named E1, E2, E3, E4 and one conventional cross section, E5 were conducted. Better outcomes are obtained by joints made utilizing this method based on joint quality and strength. The very good tensile features are displayed by the fabricated joints with Ultimate Tensile Strength (UTS) > 254 MPa and elongation > 7%. The highest UTS value which is occurred in E3 condition (Downward step) is 24.7% higher than required for FSW of AA6061 alloy at T6 condition in the American Welding Society (AWS) standard (186 MPa).

doi: 10.5829/ije.2023.36.01a.03

## 1. INTRODUCTION

The Welding Institute (TWI) developed friction stir welding (FSW) in 1991, which is employed successfully to weld aluminum alloys, mainly 2XXX or 7XXX series aluminum alloys. Welding these alloys is difficult through conventional thermal welding approaches [1, 2].

FSW is an emergent solid-state joining procedure where the welding material is not melted and recast, rather it can be arranged as the butt weld (Figure 1). The lower cost reduced weight by joining light-weight metals with metallurgical features, and a reduced requirement for skilled people make FSW an attractive welding technique [3]. Moreover, the higher energy efficiency and eco-friendliness make FSW a "green" procedure [4]. Utilizing this welding technique, it becomes possible to decrease energy consumption by 99% and installation cost by 40% compared to resistance spot welding [5].

Moreover, FSW is a hot-shear solid-state joining process using a non-consumable rotational instrument for producing frictional heat at the welding location with no material melting. It forms a smaller temperature gradient and defect-free joints than the conventional arc procedure [6].

The cost and quality of the completed weld can be affected by the joint design. Determining the most suitable joint design for a welding need special attention. Each of weld joint designs for a job requires to be compromised. For instance, this compromise can be between strength and cost, equipment available and welded skill, or between any two, three or more factors. Thus, an appropriate joint design requires experience. Even having experience, trial welds are necessary before selecting the final joint configuration and welding parameters [7]. The term weld joint design can be defined as the way that two pieces of metal are put together or

\*Corresponding Author Institutional Email: [m.tamjidi@velayat.ac.ir](mailto:m.tamjidi@velayat.ac.ir)  
(M. Tamjidi)

aligned with each other. The five basic weld joint designs are butt joints, lap joints, tee joints, outside corner joints, and edge joints [8].

The joint has reasonably higher strength. However, its use is not proposed when the metals are under impact loads or fatigue. This joint is simply prepared since it only requires matching the plates' edges together [6]. Though, correct fitting is important for the joint's total length as with any other joint.

In soldering, braze welding, and brazing, the finished part's tensile strength is highly affected by the space between the joining parts greatly. By heating the parts, the initial space may decrease or increase, based on the joint fixturing and design. Increasing the area being joined can increment the strength of a butt joint. The parts with the thickness of 1/4 in. (6 mm) need to be not considered for soldering or brazing when another process will successfully work. There are three basic joint designs in brazing including lap, butt and scarf (Figure 1). It is worth noting that a scarf joint is a type of butt joint where an increased area of bond is presented without incrementing the bond's thickness [9]. The area of a bond is based on the scarf angle cut for the joint.

In addition to the above-mentioned joint design, there is a method known as splice joint where two members are joined end to end in woodworking. The splice joint is utilized when no required length of the material being joined exists. It is a substitution for other joints like the scarf joint and butt joint. Splice joints are more robust than unenforced butt joints. They are potentially stronger than a scarf joint [10]. Three main kinds of splice joints were considered including bevel lap, half lap, and tabled splice joint (Figure 2). The half-lap splice is the most prevalent type of the splice joint.

As previously stated, the FSW process is solid state welding process in which an inconsumable rotation pin is inserted into the adjoining edges of the metals to be welded with a proper tilt angle and then moved all along the joint. The pin generates frictional and plastic deformation heating in the welding zone [11]. Thus, tool movement parameters and tool geometry which can be controlled by operators are among the key factors that

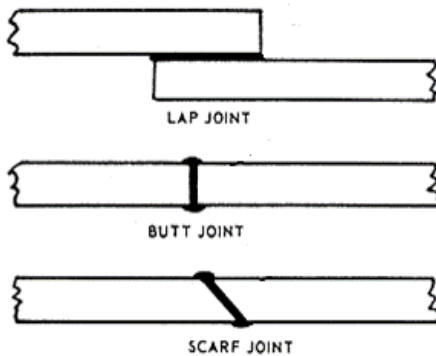


Figure 1. Three types of common joint designs for brazing

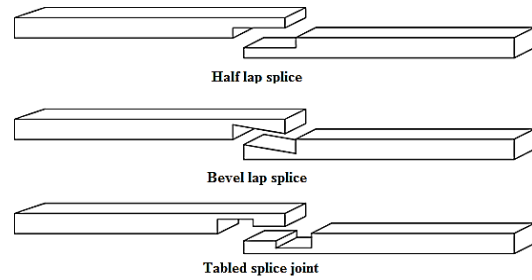


Figure 2. Three main types of splice joints

affect the quality of the fabricated joint and welding properties [12]. The terminology as described in Figure 3 is based on the international standard for FSW of aluminum (ISO 25239) [13]. Parameters which apply to FSW and are not mentioned in this standard, are previously explained in other standards such as the international standard for friction welding (ISO 15620) [14]. Other factors like work-piece thickness, material placement, machine characteristics and control mechanisms will also affect the weld quality [15].

Mechanical properties of FSW are paramount to industry, and is a very attractive field. The main particular areas of focus have been on tensile strength, yield strength, hardness/microhardness and percentage of elongation. Hardness tests can be used to not only ascertain an approximate strength of a material, but also see how strength varies from one part of a FSW to another. In butt welds tensile tests can be performed horizontally and vertically, where the nugget is either tested in the traverse direction or the longitudinal direction. Many studies relating to the dissimilar welding of aluminum alloys have been performed and reported in the literature. Table 1 classifies the previous works based on the mechanical properties of dissimilar FSW Al alloys. Also Table 2 lists the tool geometries, tool materials and welding variables used for FSW of dissimilar Al alloys in the literature.

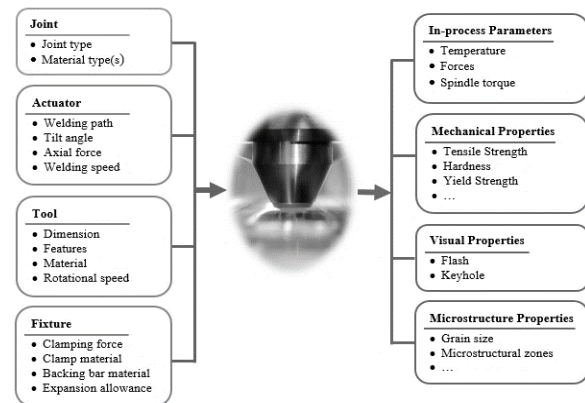


Figure 3. Input parameter influence FSW process (left) and the resulting output parameters (right) and welding properties

**TABLE 1.** Classification of pervious work on mechanical properties of dissimilar FSW Al alloys

Reference	Mechanical Properties		
	UTS	H	E
Azeez, et al. [16]	×	×	
Avinash et al. [17]	×	×	
Cole et al. [12]	×		
Haribalaji et al. [18]	×		
Prasanth and Raj [19]	×		×
Guo et al. [20]	×	×	
Kasman and Yenier [3]	×	×	
Kesharwani et al. [21]	×		×
Peng, et al. [22]	×	×	
RajKumar et al. [23]	×	×	
Heidarzadeh et al. [24]	×	×	×
Azeez et al. [25]	×		×
Venkateswarlu et al. [26]	×		×

This research is challenging since it needs to take into account the effects of various cross-sections in joint line (joint line design) for improving the mechanical features in dissimilar FSW of AA7075-T6 and AA6061-T6 aluminum alloys joints. This innovative technique can assist to present practical solutions to applications with difficulties in welding dissimilar alloys. Such applications are prone to the creation of harmful intermetallic compounds.

Therefore, the aim of this study is to investigate the effects of novel cross-sections in joint lines. Friction stir welded joint, In two different joint designs, called scarf joint and half lap splice joint, under four different new design in cross section named E1, E2, E3, E4 and one conventional cross section, E5 were conducted. Ultimate tensile strength (UTS), yield strength (YS), elongation (E) and minimum hardness (HV) of dissimilar FSW of AA6061-T6 and AA7075-T6 joints under process parameters found in the previous studies which are tool rotational speed of 1040 rpm, tool traversing speed 135 mm/min and tilt angle 2°. Rest of this paper is organized as follows: section 2 describes the experimental details,

**TABLE 2.** Literature review on tool material, profiles and welding parameters used for dissimilar Al alloys FSW

Reference	Workpiece material	Tool material	Tool shape and size	Operating parameters
Ahmad M. Z. et al. [27]	AA2024-T4 / (4 mm Thickness) AA7075-T6, (5 mm thickness)	H13	SD: 20 mm; PS: Threaded cylindrical; PD: 3.8 mm	RS: 400,600,800 rpm TS: 50 mm min <sup>-1</sup>
Avinash et al. [17]	AA2024, (5 mm) / AA7075, (6 mm)	H13	SD: 25 mm; PS: Square; PD: 5 mm; PL: 4.8 mm	RS: 710, 1000, 1400 rpm; TS: 80, 120 mm min <sup>-1</sup> TO: 1 mm towards AA2024
Cole et al. [12]	AA6061-T6 / AA7075-T6, (4.76 mm)	H13	SD: 15 mm; PS: Threaded conical; PD: 7 to 5.2 mm; PL: 4.7 mm	RS: 700-1450 rpm TS: 100 mm min <sup>-1</sup> MP: 6061-7075, 7075-6061 TO: -2 to 2 mm
Torzewski et al. [28]	AA7020-T651 / AA5038-H111, (5mm)	HSS	SD: 15 mm; PS: Cylindrical; PD: 5 mm; PL: 2.6 mm	RS: 400, 800, 1200 rpm TS: 100,200,300 mm min <sup>-1</sup> AF: 17 kN, TA: 2° RS: 1200 rpm
Guo et al. [20]	AA6061-T6 / AA7075-T6, (6.3 mm)	-	SD: 15 mm; PS: Threaded conical; PD: 5 mm	TS: 120,180, 300 mm min <sup>-1</sup> AF: 6-7 kN, TA: 2.5° MP: 6061-7075, 7075-6061
Kasman and Yenier [3]	AA5754-H111 / AA7075-T651, (5 mm)	H13	SD: 18-20-22 mm; PS: Threaded cylindrical ; PD: 6 mm; PL: 4.8 mm	RS: 1000-1200 rpm TS: 80-125 mm min <sup>-1</sup> TA: 3°, DT: 30 s
Kesharwani et al. [21]	AA5052-H32 / AA5754-H22, (2 mm)	SS-316	SD: 12-15-20 mm; PS: Circular, triangular, square; PD: 1/3 SD for circular pin; PL: 1.8 mm	RS: 1120, 1400, 1800 rpm TS: 50, 125, 200 mm min <sup>-1</sup>
Koilraj et al. [29]	AA2219-T87 / AA5038-H321, (6 mm)	H13	SD: 1.5- 3 (D/d ratio); PS: Straight and tapered cylindrical, cylindrical and tapered threaded; PD: 6 mm; PL: 5.7 mm	RS: 400-800 rpm TS: 15-60 mm min <sup>-1</sup>
RajKumar et al. [23]	AA5052 / AA6061	H13	SD:18 mm; PS: Threaded cylindrical ; PD: 6 mm; PL: 4.8 mm	RS: 710 rpm TS: 20, 28 mm min <sup>-1</sup>

Shojaeefard et al. [30]	AA7075-O / AA5083-O, (6 mm)	-	SD:20 mm; PS: Tapered ; PD: 10 mm to 5 mm; PL: 5.85 mm	RS: 500-1600 rpm TS: 30-90 mm min <sup>-1</sup>
Kumar et al. [31]	AA5083 / AA6061	HSS	PS: Tapered cylindrical, Tapered square, Tapered Hexagon, Paddle shape, Straight cylinder	RS: 800-1600 rpm TS: 40-80 mm min <sup>-1</sup> AF: 15-35 kN
Venkateswarlu et al. [26]	AA2219/ AA7039, (6 mm)		SD: 19 mm; PS: Threaded with three different shoulder surface PD: 7 mm; PL: 4.7 mm	RS: 500-1000 rpm TS: 20-40 mm min <sup>-1</sup> AF: 5-8 kN

SD: Shoulder Diameter; PS: Pin Shape; PD: Pin Diameter; PL: Pin Length; RS: Rotational Speed; TS: Traverse Speed; TO: Tool Offset; MP: Material Placement; DT: Dwell Time; TA: Tilt Angle; AF: Axial Force

section 3 presents the weld joint cross section design, section 4 results and discussion, and section 5 provides the final conclusion.

## 2. EXPERIMENTAL WORKS

Dissimilar aluminum alloys were chosen in this study such as AA7075 and AA6061 in the T6 temper circumstances for butt scarf welding by FSW procedure. Both plates with a thickness of 6 mm were cut before welding to a length of 100 mm and a width of 50 mm. The FSW weld direction is vertical to the plates' rolling direction. Before implementing the experiments, the mechanical features of base aluminum alloys, AA6061 and AA7075 were measured. AA6061 and AA7075 have the ultimate tensile strength of 310.MPa and 524.MPa, and the elongation of the 12% and 11 %, respectively.

The experiments were performed using an instrument made of AISI H13 hot work steel with a square pin profile. To increment its wear resistance, it used to be heat-treated to a hardness of 52 HRC after machining (see Figure 4).

The ASTM E8M guidelines were followed in order to preparing the specimens for obtaining the real mechanical properties and fracture location of FSW welded joints for the sub size specimen. At slightest three examples were extracted from each FSWed joint following GOST ISO 25239-4-2020. The arrangement and measurement of each transverse tensile example device balanced position as shown in Figure 5.

## 3. WELD JOINT CROSS SECTION DESIGN

After validation of results conducted on the FSW butt joint configuration, the final step in this study is to consider the effect of different weld joint designs on the mechanical properties in order to improve the joint efficiency. In this study two joint designs, called scarf joint and half lap splice joint, were investigated from mechanical point of view using the experimental parameters found in the previous studies which are tool

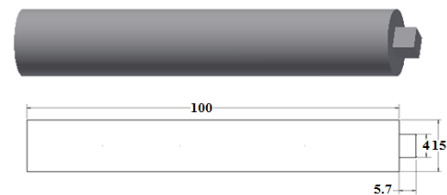


Figure 4. Geometry of tool design

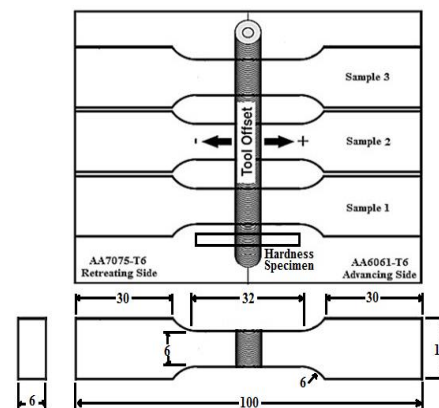


Figure 5. Arrangement and measurement of each tensile example device balanced position

rotational speed of 1040rpm, tool traversing speed 135 mm/min and tilt angle 2°. Figure 6 and Figure 7 illustrate the scarf and half lap splice joint design, respectively.

Figure 6(a) demonstrates a downward scarf joint cross section which represents the inclination from advancing side to retreating side and Figure 6(b) shows the upward scarf joint cross section in which the slope is expanded up from advancing side to retreating side.

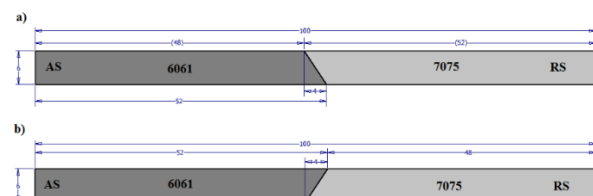


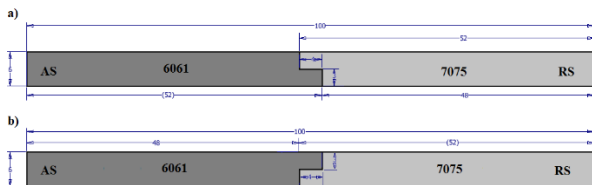
Figure 6. Interface design in weld line: a) downward scarf and b) upward scarf

Figure 7(a) demonstrates a downward half lap splice cross section design which represents the downward step from advancing side to retreating side and Figure 7(b) shows the upward step half lap splice cross section in which the step is expanded up from advancing side to retreating side.

In order to investigate the effect of different welding joint design on mechanical properties of the FSW joints, five experiments were performed using the optimal level of process parameters found in previous section. The detailed experimental conditions with their cross section are listed in Table 3. Dissimilar FSW joints were produced along the longitudinal direction of five plates of AA6061 and five plates of AA7075 were cut into measurements measuring 100 mm long and 52 mm wide (rolling direction) employing a Jonford milling machine as shown in Figure 8. The tensile testing of the FSW joints is conducted in exact Universal Testing Machine Instron 3382 and their ultimate tensile strength (UTS), YS, E are measured. A maximum of 31 measurements were taken on each sample spaced every 1 mm in the weld region and every 8 mm outside of the tools footprint. The microhardness plots will also highlight the differing weld regions.

#### 4. RESULTS AND DISCUSSION

Table 4 shows the mechanical properties of the base AA6061 and the various cross-sectional structural



**Figure 7.** Interface design in weld line: a) downward half lap splice and b) upward half lap splice

**TABLE 3.** Experimental conditions and cross section design

Condition	Weld cross section	Cross section appearance
E1	Downward scarf	AS 6061 / 7075 RS
E2	Upward scarf	AS 6061 / 7075 RS
E3	Downward half lap splice	AS 6061 / 7075 RS
E4	Upward half lap splice	AS 6061 / 7075 RS
E5	Butt joint	AS 6061 / 7075 RS



**Figure 8.** The Johnford vertical milling machine

connections between the AA6061 and AA7075. The mechanical properties of AA6061 are listed in this table. This is because all joints on the AA6061 side were damaged at the location of the HAZ region where the minimum hardness is shown in Figure 9. As detailed already in different FSW of other Al alloys, the friction stir welded joints ordinarily fractured at areas in HAZ on the weaker fabric side [15,25]. Furthermore it may, those researchers did not consider the impact of cross-section design on the mechanical properties. The disappointment areas in HAZ shows consistent holding has been accomplished between disparate AA6061 and AA7075 alloys beneath all examined welding conditions. According to Table 4, very exact tensile residences are represented by all the joints with UTS > 254 MPa and elongation > 7%. The maximum UTS value occurring in the E3 condition (Downward step) is 24.7% larger than the value needed for the FSW of AA6061 alloy at the T6 condition in the American Welding Society (AWS) standard (186 MPa): AWS D17.3/ D17.3M:200X.

The Vicker’s microhardness profiles of the cross-section for the dissimilar joints made under various conditions (E1–E5) are shown in Figure 8. Generally, both AA7075 and AA6061 alloys represented definite microhardness reduction in the weld in comparison with their equivalent base metals (the two materials in T6 temper conditions).

The main reason is the dissolution, coarsening, and precipitation of strengthening precipitates resulting from FSW thermal cycles. However, there are some minor contributions associated with grain structure refinement. In the HAZ, coarsening of strengthening precipitates and the disappearance of Guinier–Preston (G.P.) zones cause a slightly lower hardness the same as an over-aging procedure. Further severe coarsening and probably complete dissolution of precipitates happened in the TMAZ, owing to the similar effects of treating the solution. In the nugget, some precipitation may occur after complete dissolution owing to the higher temperature for the material in this area. The transition of

microhardness is more gradual in the nugget from AA6061 to AA7075.

In all the cases (the marked arrows in Figure 8), irrespective of the applied process parameters or the relative materials' position, the hardness minima are observed in the HAZ on the AA6061 side. Indeed, in HAZ regions, all joints had a failure on the AA6061 side near the TMAZ in tensile testing, in which the minimum hardness is placed. The reduced microhardness in HAZ is caused by the disappearance of G.P. zones and coarsening of the strengthening precipitates which it can be seen in Figure 9. Therefore, in the HAZ of the joints made with less heat input, less severe precipitate coarsening could happen. Thus, the highest minimum value is obtained by the hardness profile of the joints made with the least heat input (condition E3) (Figure 8).

Figure 10 represents the tensile tested samples' fractured surfaces under SEM for circumstances E3 and E5. Fractographic analysis was performed using these two circumstances since UTS is the key objective

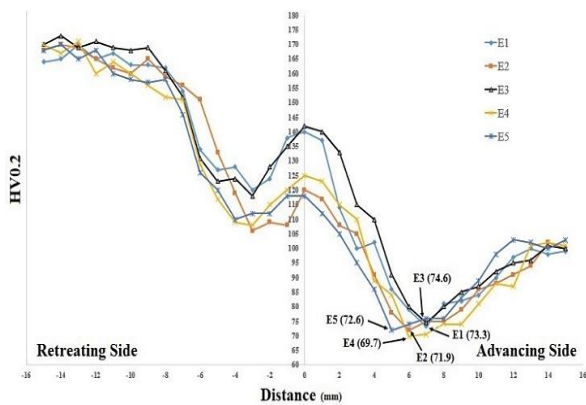


**Figure 9.** Vicker's microhardness profile of different cross-section joints

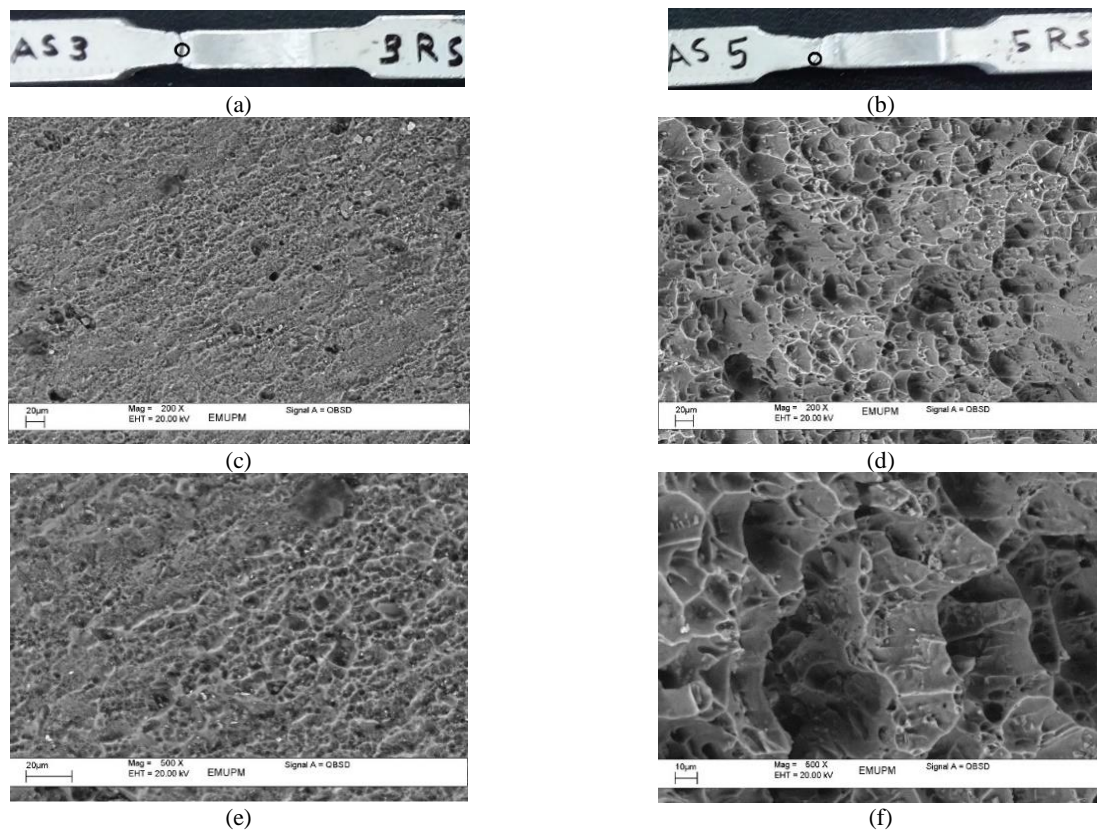
associated with the joints' tensile behavior and the different UTS between these two circumstances is the most marginal. The fractured surfaces have characteristically a higher quantity of almost equal dimples with different sizes (Figure 10 (c) and 10(d)). The fractured surface of the joints made under condition E3 represents shallower dimples in comparison with condition E5. It is also indicated that the joint E3 has further higher hardness compared to E5 as can be seen in the Figure 8 and Table 4. In such a dimple rupture mode, the fracture is mainly caused by the overload and microvoids direct the failure through coalescence. Nucleation of the microvoids may occur near second phase particles, grain boundaries, inclusions, and dislocation pileups.

Figure 10(b) illustrates higher distorted grain characterization in HAZ and TMAZ zone of transverse section. Moreover, relevant sign of distorted grain size is observed, indicating the deformation of material before fracture. It shows more elongation compare to condition E3 (Figure 10(a)), as summarized in Table 4.

Therefore, the microvoids grow and coalesce, thus forming a continuous fracture surface by increasing the strain during tensile testing. Hence, the shallower dimples are formed in condition E3 probably owing to further severe precipitate coarsening occurring during FSW. Hence, in the HAZ of the joints produced under condition E5, less closely spaced Mg<sub>2</sub>Si phase particles are created. During the fracture process, nucleation sites are effectively provided by the second phase particles such as incoherent Mg<sub>2</sub>Si phase and different Al-Fe-Si intermetallic in AA6061 alloy for microvoids. Nevertheless, it is unrealistic to quantitatively measure the quantity of such second-phase particles because the particles are mostly concealed at the bottom of the dimples and possess a color similar to the nearby Al matrix on fractured surfaces under SEM.

**TABLE 4.** Mechanical properties of the dissimilar FSWed in different cross-section

Condition	Mechanical properties				Joint efficiency (%)	Refs.
	UTS (MPa)	YS (MPa)	E (%)	Min H (HV)		
AA6061-T6	310	275	12	110	-	-
Butt joint	245	177	6	-	79	[25]
Butt joint	257.9	-	1.1	78	83	[32]
E1	261.4	179.2	8.1	73.3	84.3	This study
E2	254.7	178.7	8.6	71.9	82.1	This study
E3	262.7	178.6	7.9	74.6	84.7	This study
E4	254.4	176.7	8.4	69.7	82	This study
E5	254.2	177.1	8.2	72.1	82	This study



**Figure 10.** The tensile fractured surfaces under SEM in different conditions E3 and E5: a, c and e) condition E3 and b, d and f) condition E5

## 5. CONCLUSION

In order to improve mechanical properties of dissimilar FSW of AA6061-T6 and AA7075-T6, a new design in cross section of weld joint is presented. The proposed design in cross-section of joint line is a new method to improve the mechanical properties. This study reveal that the different cross-section in joint line has critical effect on the joint efficiency, which is plays an important role in different industries such as automotive, aerospace, electronics and shipbuilding. Friction stir welded joint under four different new design in cross section named E1, E2, E3, E4 and one conventional cross section, E5 were conducted. The mechanical test comes about uncover that the joints welded in all the conditions display exceptionally great ductile properties with UTS higher than 254 MPa and elongation higher than 7%. The highest UTS value which is occurred in E3 condition (Downward step) is 24.7% higher than required for FSW of AA6061 alloy at T6 condition in the American Welding Society (AWS) standard (186 MPa). In addition E3 condition has the best tensile strength which is 2.77 % more than the E5 condition. The weld joint efficiency of the E3 condition (characterized as the proportion of the quality of the weld joint to that of the base metal) accomplished 84.7% of the base metal.

## 6. REFERENCES

1. Fu, B., Qin, G., Li, F., Meng, X., Zhang, J. and Wu, C., "Friction stir welding process of dissimilar metals of 6061-t6 aluminum alloy to az31b magnesium alloy", *Journal of Materials Processing Technology*, Vol. 218, (2015), 38-47. doi: 10.1016/j.jmatprotec.2014.11.039.
2. Rafiee, A., Nickabadi, S., Nobarian, M., Tagimalek, H. and Khatami, H., "Experimental investigation joining al 5083 and high-density polyethylen by protrusion friction stir spot welding containing nanoparticles using taguchi method", *International Journal of Engineering, Transactions C: Aspects*, Vol. 35, No. 6, (2022), 1144-1153. doi: 10.5829/IJE.2022.35.06C.06.
3. Kasman, Ş. and Yenier, Z., "Analyzing dissimilar friction stir welding of aa5754/aa7075", *The International Journal of Advanced Manufacturing Technology*, Vol. 70, No. 1, (2014), 145-156. doi: 10.1007/s00170-013-5256-7.
4. Tiwan, H., Ilman, M. and Kusmono, K., "Effect of pin geometry and tool rotational speed on microstructure and mechanical properties of friction stir spot welded joints in aa2024-o aluminum alloy", *International Journal of Engineering, Transactions B: Applications*, Vol. 34, No. 8, (2021), 1949-1960. doi: 10.5829/IJE.2021.34.08B.16.
5. Mishra, R.S. and Ma, Z., "Friction stir welding and processing", *Materials science and engineering: R: reports*, Vol. 50, No. 1-2, (2005), 1-78. doi: 10.1016/j.msre.2005.07.001.
6. Khatami, H., Azdast, T., Mojaver, M., Hasanzadeh, R. and Rafiei, A., "Study of friction stir spot welding of aluminum/copper dissimilar sheets using taguchi approach", *International Journal*

- of Engineering, Transactions B: Applications*, Vol. 34, No. 5, (2021), 1329-1135. doi: 10.5829/IJE.2021.34.05B.28.
7. Ethiraj, N., Sivabalan, T., Sivakumar, B., Vignesh Amar, S., Vengadeswaran, N. and Vetrivel, K., "Effect of tool rotational speed on the tensile and microstructural properties of friction stir welded different grades of stainless steel joints", *International Journal of Engineering, Transactions A: Basics*, Vol. 33, No. 1, (2020), 141-147. doi: 10.5829/IJE.2020.33.01A.16.
  8. Gibson, B.T., Lammlein, D., Prater, T., Longhurst, W., Cox, C., Ballun, M., Dharmaraj, K., Cook, G. and Strauss, A., "Friction stir welding: Process, automation, and control", *Journal of Manufacturing Processes*, Vol. 16, No. 1, (2014), 56-73. doi: 10.1016/j.jmapro.2013.04.002.
  9. Singh, R., Rizvi, S.A. and Tewari, S., "Effect of friction stir welding on the tensile properties of aa6063 under different conditions", *International Journal of Engineering, Transactions A: Basics*, Vol. 30, No. 4, (2017), 597-603. doi: 10.5829/idosi.ije.2017.30.04a.19.
  10. Torres, E., Graciano-Urbe, J. and Santos, T., "Control of steel detachment and metal flow on aluminum-steel friction stir welding of thin joints", *International Journal of Engineering, Transactions A: Basics*, Vol. 34, No. 4, (2021), 1024-1034. doi: 10.5829/IJE.2021.34.04A.29.
  11. Salah, A.N., Mehdi, H., Mehmood, A., Hashmi, A.W., Malla, C. and Kumar, R., "Optimization of process parameters of friction stir welded joints of dissimilar aluminum alloys aa3003 and aa6061 by rsm", *Materials Today: Proceedings*, Vol. 56, (2022), 1675-1683. doi: 10.1016/j.matpr.2021.10.288.
  12. Cole, E., Fehrenbacher, A., Duffie, N., Zinn, M., Pfeifferkorn, F. and Ferrier, N., "Weld temperature effects during friction stir welding of dissimilar aluminum alloys 6061-t6 and 7075-t6", *The International Journal of Advanced Manufacturing Technology*, Vol. 71, No. 1, (2014), 643-652. doi: 10.1007/s00170-013-5485-9.
  13. Verbičiči, V., Cojocaru, R., Bojilă, L.N., Ciucă, C. and Perianu, I.A., "Considerations on the ultimate tensile strength of butt welds of the en aw 5754 aluminium alloy, made by friction stir welding (FSW)", in *Advanced Materials Research, Trans Tech Publ.* Vol. 1157, (2020), 38-46.
  14. Huang, C., Lu, J., Zhu, M., Xu, Y., Li, B., Zhou, Y. and Huang, J., "Oxidation behaviors of the rotary friction welded joints of ht700 superalloy in saturated water steam at 700° c", *Corrosion Communications*, (2022). doi: 10.1016/j.corcom.2021.11.008.
  15. El-Sayed, M.M., Shash, A., Abd-Rabou, M. and ElSherbiny, M.G., "Welding and processing of metallic materials by using friction stir technique: A review", *Journal of Advanced Joining Processes*, Vol. 3, (2021), 100059. doi: 10.1016/j.jajp.2021.100059.
  16. Azeez, S. and Akinlabi, E., "Effect of processing parameters on microhardness and microstructure of a double-sided dissimilar friction stir welded aa6082-t6 and aa7075-t6 aluminum alloy", *Materials Today: Proceedings*, Vol. 5, No. 9, (2018), 18315-18324. doi: 10.1016/j.matpr.2018.06.170.
  17. Avinash, P., Manikandan, M., Arivazhagan, N., Ramkumar, K.D. and Narayanan, S., "Friction stir welded butt joints of aa2024 t3 and aa7075 t6 aluminum alloys", *Procedia Engineering*, Vol. 75, (2014), 98-102. doi: 10.1016/j.proeng.2013.11.020.
  18. Haribalaji, V., Boopathi, S. and Asif, M.M., "Optimization of friction stir welding process to join dissimilar aa2014 and aa7075 aluminum alloys", *Materials Today: Proceedings*, Vol. 50, No., (2022), 2227-2234. doi: 10.1016/j.matpr.2021.09.499.
  19. Prasanth, R. and Hans Raj, K., "Determination of optimal process parameters of friction stir welding to join dissimilar aluminum alloys using artificial bee colony algorithm", *Transactions of the Indian Institute of Metals*, Vol. 71, No. 2, (2018), 453-462. doi: 10.1007/s12666-017-1176-9.
  20. Guo, J., Chen, H., Sun, C., Bi, G., Sun, Z. and Wei, J., "Friction stir welding of dissimilar materials between aa6061 and aa7075 al alloys effects of process parameters", *Materials & Design (1980-2015)*, Vol. 56, (2014), 185-192. doi: 10.1016/j.matdes.2013.10.082.
  21. Kesharwani, R., Panda, S. and Pal, S., "Multi objective optimization of friction stir welding parameters for joining of two dissimilar thin aluminum sheets", *Procedia Materials Science*, Vol. 6, No., (2014), 178-187. doi: 10.1016/j.mspro.2014.07.022.
  22. Peng, G., Ma, Y., Hu, J., Jiang, W., Huan, Y., Chen, Z. and Zhang, T., "Nanoindentation hardness distribution and strain field and fracture evolution in dissimilar friction stir-welded aa 6061-aa 5a06 aluminum alloy joints", *Advances in Materials Science and Engineering*, Vol. 2018, (2018). doi: 10.1155/2018/4873571.
  23. RajKumar, V., VenkateshKannan, M., Sadeesh, P., Arivazhagan, N. and Ramkumar, K.D., "Studies on effect of tool design and welding parameters on the friction stir welding of dissimilar aluminium alloys aa 5052-aa 6061", *Procedia Engineering*, Vol. 75, No., (2014), 93-97. doi: 10.1016/j.proeng.2013.11.019.
  24. Heidarzadeh, A., Javidani, M., Mofarreh, M., Farzaneh, A. and Chen, X.-G., "Submerged dissimilar friction stir welding of aa6061 and aa7075 aluminum alloys: Microstructure characterization and mechanical property", *Metals*, Vol. 11, No. 10, (2021), 1592. doi: 10.3390/met11101592.
  25. Azeez, S., Akinlabi, E., Kailas, S. and Brandi, S., "Microstructural properties of a dissimilar friction stir welded thick aluminum aa6082-t6 and aa7075-t6 alloy", *Materials Today: Proceedings*, Vol. 5, No. 9, (2018), 18297-18306. doi: 10.1016/j.matpr.2018.06.168.
  26. Venkateswarlu, D., Mahapatra, M., Harsha, S.P. and Mandal, N., "Processing and optimization of dissimilar friction stir welding of aa 2219 and aa 7039 alloys", *Journal of Materials Engineering and Performance*, Vol. 24, No. 12, (2015), 4809-4824. doi: 10.1007/s11665-015-1779-4.
  27. Ahmed, M.M., El-Sayed Seleman, M.M., Zidan, Z.A., Ramadan, R.M., Ataya, S. and Alsaleh, N.A., "Microstructure and mechanical properties of dissimilar friction stir welded aa2024-t4/aa7075-t6 t-butt joints", *Metals*, Vol. 11, No. 1, (2021), 128. doi: 10.3390/met11010128.
  28. Torzewski, J., Łazińska, M., Grzelak, K., Szachogłuchowicz, I. and Mierzyński, J., "Microstructure and mechanical properties of dissimilar friction stir welded joint aa7020/aa5083 with different joining parameters", *Materials*, Vol. 15, No. 5, (2022), 1910. doi: 10.3390/ma15051910.
  29. Koilraj, M., Sundareswaran, V., Vijayan, S. and Rao, S.K., "Friction stir welding of dissimilar aluminum alloys aa2219 to aa5083-optimization of process parameters using taguchi technique", *Materials & Design*, Vol. 42, (2012), 1-7. doi: 10.1016/j.matdes.2012.02.016.
  30. Shojaefard, M.H., Akbari, M., Khalkhali, A., Asadi, P. and Parivar, A.H., "Optimization of microstructural and mechanical properties of friction stir welding using the cellular automaton and taguchi method", *Materials & Design*, Vol. 64, (2014), 660-666. doi: 10.1016/j.matdes.2014.08.014.
  31. Kumar, K.K., Kumar, A. and Satyanarayana, M., "Effect of friction stir welding parameters on the material flow, mechanical properties and corrosion behavior of dissimilar aa5083-aa6061 joints", *Proceedings of the Institution of Mechanical Engineers, Part C: Journal of Mechanical Engineering Science*, Vol. 236, No. 6, (2022), 2901-2917. doi: 10.1177/09544062211036102.
  32. İpekoğlu, G. and Çam, G., "Effects of initial temper condition and postweld heat treatment on the properties of dissimilar friction-stir-welded joints between aa7075 and aa6061 aluminum alloys", *Metallurgical and Materials Transactions A*, Vol. 45, No. 7, (2014), 3074-3087. doi: 10.1007/s11661-014-2248-7.

---

**Persian Abstract**

---

**چکیده**

اتصالات جوشی در فرآیند جوشکاری اصطکاکی اغتشاشی (FSW) توسط گرمای اصطکاکی بوجود آمده جهت اتصال اجزای فلزی جهت ساخت قطعات مورد استفاده قرار می‌گیرد. به دلیل عدم وجود ذوب فاز اصلی، فرآیند FSW چندین مزیت را نسبت به جوشکاری ذوبی ارائه می‌دهد. آلیاژهای AA6XXX و 7XXX AI دو سری از پرکاربردترین مواد ساختاری در صنایع خودروسازی، حمل و نقل ریلی و هوافضا هستند. هدف از این مطالعه بررسی اثر مقطع جدید در خط اتصال و تجزیه و تحلیل جزئیات برای بهبود بیشتر خواص مکانیکی بوده است. اتصال جوشی اصطکاکی اغتشاشی تحت چهار طرح جدید مختلف در مقاطع به نام های E1، E2، E3، E4 و یک مقطع معمولی E5 انجام شده است. اتصالات ساخته شده با استفاده از این روش منجر به نتایج بهتر از نظر استحکام و کیفیت مفصل می‌شود. اتصالات ساخته شده دارای خواص کششی بسیار خوبی با استحکام کششی نهایی (UTS) بالاتر از ۲۵۴ مگاپاسکال و ازدیاد طول بیشتر از ۷٪ است. بالاترین مقدار UTS که در شرایط E3 (گام رو به پایین) رخ داده است، ۲۴۷٪ بیشتر از مقدار مورد نیاز برای FSW آلیاژ AA6061 در شرایط T6 در استاندارد انجمن جوشکاری آمریکا (AWS) (۱۸۶ مگاپاسکال) می‌باشد.

---



## Experimental Study of Lateral Loading on Piled Raft Foundations on Sandy Soil

A. Chandiwala\*, S. Vasanwala

Department of Civil Engineering, Sardar Vallabhbhai National Institute of Technology, Surat, Gujarat, India

### PAPER INFO

#### Paper history:

Received 16 July 2022

Received in revised form 25 September 2022

Accepted 09 October 2022

#### Keywords:

Pile Raft Foundation

Soil-Structure Interaction

Settlement

Portable Travelling Pluviator

Bearing Pressure Enhancement

### ABSTRACT

A Shallow foundation on cohesionless soil cannot support greater weights; piled raft foundations are recommended because they combine the load-bearing qualities of piles and raft. Combined Piled Raft Foundations (CRPF) are efficient for tall buildings because they account for both vertical and lateral loads. In a pile raft foundation, the raft's load-resistance is disregarded due to soil-structure interaction. Simplification may lead to an uneconomical design. While study on raft's vertical resistance is extensive, its horizontal resistance is limited. In the present study, 160 mm x 160 mm pile-raft model with different pile spacing and pile length was tested. Studies showed that pile length and spacing of pile improve bearing capacity and reduce settlement of raft. The pile raft system rests 65 percentage of the lateral load, depending on pile spacing and its length. Pile spacing and pile length lessen the raft's lateral load contribution. Furthermore, as increasing in pile spacing reduces raft overturning by 60 percentage. Upgrade pile raft system design may make a cheaper and more efficient option for skyscrapers and make this foundation system more economical design.

doi: 10.5829/ije.2023.36.01a.04

## 1. INTRODUCTION

In circumstances where a raft foundation alone doesn't meet design criteria, adding piles can improve a raft's performance [1]. Piled raft foundations (PRFs) were first proposed by Poulos and Davis [2]. In a later study, Burland et al. [1] suggested employing the pile group to lessen the effects of settlement. Several studies have analyzed the piles' and the raft's load-carrying capacities to develop better design strategies for Piled raft Foundation Systems (PRFs). The PRFs' behavior and load carrying capability can be analyzed using a variety of simplified approaches [3], semi-analytical methods [4], and numerical methods [5]. In typical pile-raft design, the raft's contribution to vertical and lateral load resistance is often overlooked [6]. Recent experiments employing small and large-scale models have examined the raft's vertical load contribution [7]. In the modern context, designers integrate not only vertical load, but also lateral load contribution, which has an impact on soil bearing capacity, pile length, and spacing [8]. The raft in Combined piled raft foundation (CPRF) reduces the cost

of tall building foundations. Its lateral load contribution is rarely studied. Very little research has been done on pile rafts under lateral loads like earthquakes, retaining wall pressure, and wind. Laterally loaded piled raft response is governed by pile-head rigidity, relative stiffness, pile spacing, pile-soil, pile-pile, and raft-pile interactions [9]. The complex behavior of piled raft foundations subjected to horizontal loads is poorly understood [10]. A seismic design concept for piled raft foundations is needed in highly seismic places like Kutch, Gujarat (India) [11]. Pile-raft foundations have been used in India; however, most seismic designs ignore piles [12]. Considering the trend toward performance-based design in geotechnical engineering, the behavior of piled raft foundations subjected to horizontal loads must be justified [13]. This study employed centrifuge modeling to analyze piled raft foundations. Centrifuge modeling helps analyze pile-raft interactions in sandy soils [14]. This paper presents the results of horizontal loading testing on piled raft models and rafts alone. To keep structures from settling, the primary goal of piles in a piled raft is to reduce settlement and avoid overturning

\*Corresponding Author Email: [chandiwaanuj@gmail.com](mailto:chandiwaanuj@gmail.com)  
(A. Chandiwala)

the raft [15, 16]. This study explores the influence of pile length and pile spacing of a pile raft model on loose sandy soil. Underneath this piled raft, nine settlement-reducing piles were tested. Pile-supported raft foundations should be examined for settlement and bearing capacity (such as pile length, and pile spacing). Pile-raft foundations affect performance.

**2. PILED RAFT FOUNDATION**

Design engineers should understand how loads are carried from the raft to piles and soil media so they can predict raft performance like settlement, bearing pressure enhancement, and borrowing capacity rate, as well as pile behavior like displacement and load sharing across piles [17-19]. Pile skin friction in a piled raft foundation helps carry the superstructure's weight. In Figure 1, the raft carries the remaining weight via soil contact.  $Q_P$  is the pile weight,  $Q_R$  is the raft weight, and  $Q$  is the applied horizontal load on a piled raft foundation. The pile-soil-pile interaction is caused by pile spacing and installation style, like free-standing piles [20].

**3. TEST SETUP**

**3.1. Soil Properties** Narmada river dry sand has been used for this research work. The sandy soil's physical properties were tested using Indian standards (IS). Table 1 shows the characteristic of soil. Table 2 represents the geotechnical properties of soil. Figure 2 shows the sand gradation curve.

**3.2. Model Piled Raft and Tank** The steel tank measured 1000 mm long, in height and width. Each side

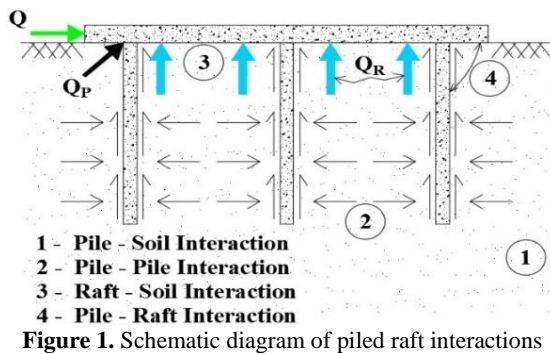


**TABLE 1. Soil characteristics**

$D_{10}$	$D_{30}$	$D_{60}$	$G_s$	$\gamma_{min}$ ( $kN/m^3$ )	$\gamma_{max}$ ( $kN/m^3$ )	$\phi$
0.2	0.5	0.7	2.63	14.80	17.65	37°

**TABLE 2. Geotechnical Properties of Soil**

Geotechnical Properties	Values	Units
Specific Gravity (G)	2.63	-
Maximum dry density	17.65	$kN/m^3$
Minimum dry density	14.80	$kN/m^3$
Relative Density at 20%	15.49	$kN/m^3$

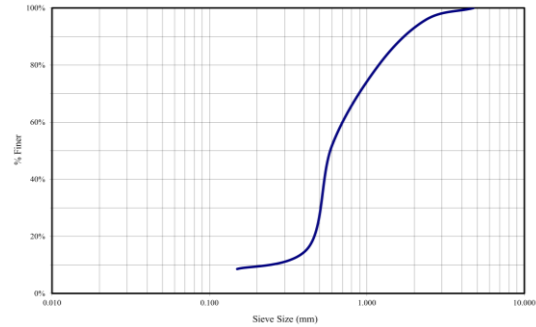


**Figure 2. Particle size distribution curve for sand**

includes two 2.5-meter-tall columns and two 1.5-meter-tall horizontal beams. Figure 3 shows a schematic view of the model test setup. A mild steel square model raft was made to imitate a narrow structure with horizontal loads. 160 × 160 mm and 10 mm thick, the model raft. The model raft contains holes for vertically-spaced pilings. Each piling was supplied with a 6-mm-diameter, 20-mm-long bolt. Model rafts and piles have  $1.8 \times 10^5$  MPa elasticity. The piles were 10, 15, and 20 cm long with slenderness ratios of 10, 15, and 20. Model-piled rafts prevent anxiety at the tank's edge. To avoid stiff tank foundations from affecting pile behavior. The model raft's settling was measured by Linear Variable Differential Transformer (LVDT).

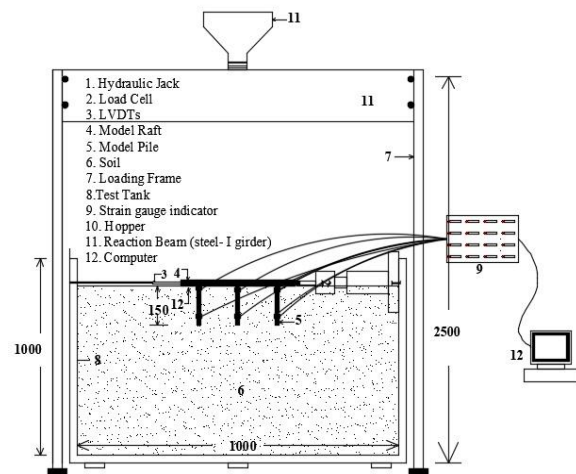


**Figure 3. Schematic view of the model test setup**

As shown in Figure 4, the diffuser sieves were angled to reduce sand flow. Vertically pluviating the tube increased sand dispersion. The sand was redirected using sieves. Thin horizontal layers of sand were pluviated using a stiff vertical tube. Regulating flow generated a steady, uniform sand rain. Flow management prevented sand from collecting on diffuser sheets, ensuring consistent sand rain.

**3. 3. Test Procedure**

The portable traveling pluviator (PTP) [21] has a 20-kilogram fixed hopper and a 100-centimeter rigid tube for uniform, reproducible packing. Several model experiments were done to study a horizontally loaded raft on the sand. Figure 5 shows different piles' designs. Installation of non-displacement piles is as follows. First, a Portable Traveling pluviator (PTP) [22, 23] deposited sand, then non-displacement piles needed 28 cm of sand from the tank's bottom. To ensure adequate seating, 20 cm piles with 10 mm penetration were set vertically in the sand. The mounds will remain as long as the tank isn't complete. The model raft was then nuted to each pile. The failure occurred at 0.1 kN/min. LVDT measured raft displacement. Deposition strength, fall height, sand rain uniformity, and particle characteristics determine air pluviation's relative density (Rd) [24]. Structural piles were instrumented with 350 Ω strain gauges at their uppermost portion, below the raft's level. The load in the piles at the strain gauge's plane is calculated from the recorded strain and predicted using the equation:

$$Q = \epsilon \times A_p \times E_p \tag{1}$$

where Q is load (kN), ε denotes the measured strain (microstrain), A<sub>p</sub> indicates the c/s Area of the pile (m<sup>2</sup>), and E<sub>p</sub> is the Modulus of elasticity of pile (kN/m<sup>2</sup>).

Twenty-channel strain gauges were used to measure pile stresses. The locally-made strain indicator provides precise, high-resolution strain measurements. The tape protected and sealed the strain gauge. Mild steel rafts and piles had elasticity moduli of 1.8 x 10<sup>5</sup> MPa and 0.2, respectively. Table 3 shows the experimental program of the raft and piled raft to study pile length (L), spacing (P), and pattern. Figure 6 illustrates three piled raft models with different piling designs. The pattern I had nine 10

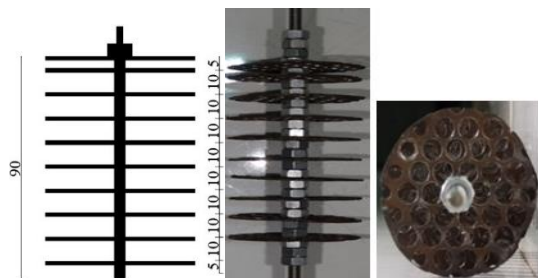


**Figure 4.** Experimental diffuser arrangement

cm piles, Pattern II had nine 15 cm piles, and Pattern III had nine 20 cm piles (Pattern III). All trials used nine piles. Figure 7 shows the pile spacing employed in the study: 3d (Arrangement 1), 4d (Arrangement 2), and 5d (Arrangement 3) for a 160 mm x 160 mm piled-raft system. Repeatability and consistency were tested. Load-settlement patterns differed by only 2.5% in maximum

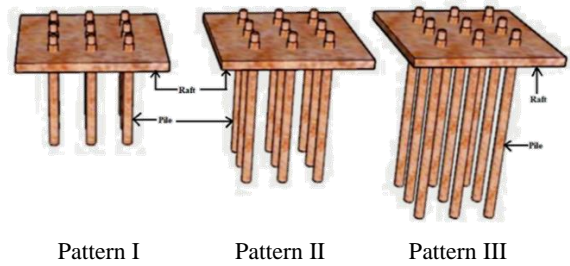


**Figure 5.** Pile arrangement configuration of 160 mm x 160 mm piled raft

**TABLE 3.** Experimental Test Programme

Series	Constant Parameters	Spacing of piles	No. of Piles
1	Unpiled Raft		
3	Piled raft; L/d = 10	3d,4d,5d	9
4	Piled raft; L/d = 15	3d,4d,5d	9
5	Piled raft; L/d = 20	3d,4d,5d	9

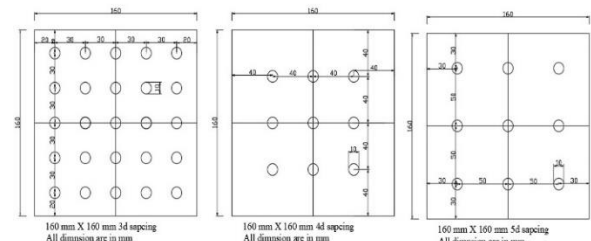


**Figure 6.** Various pile spacing for 160 mm x 160 mm piled raft



**Figure 7.** Horizontal load applied on model piled raft foundation

settlement values. The difference was ignored. Figure 7 shows the horizontal load applied on the model pile raft foundation. The following steps were part of the test methodology: Sand was placed using the Portable Traveling Pluviator (PTP) rainfall method [25]. The tank's bottom required to be 28 cm above the non-displacement piles in height. 20 cm long piles with a 10 mm penetration were placed vertically in the sand to ensure proper sitting. The heaps will stay put so long as the tank isn't finished. The model raft was then screwed onto each pile following that. A loading platform was used to load the model raft. The load was applied at 0.1 kN/min till failure. The maximum load capacity of a raft is frequently calculated as the settlement equal to 10% of the width [26-28]. The raft was loaded as a result until it settled at least 10% of B, or 16 mm.

**4. RESULTS AND DISCUSSION**

Over 20 model tests on prototype rafts for cohesionless soil are shown. The horizontal load behavior of rafts supported by varied pile arrangement patterns was studied. The influence of  $A_{GPR}$  on raft settlement, bearing pressure enhancement, and raft tilt are examined.

**4. 1. Influence of Pile Length** The settlement was measured for 0.1 percent of width of raft. Figure 8 shows typical changes in ultimate load versus raft center settling at 16 mm settlement for different L/d ratio. Raft horizontal load, Figure 8 shows that rigid piles increase load-carrying capacity with less settlement.

The graph indicates that a rigid pile affects a raft's load-carrying capacity when horizontally loaded. Pile length boosts a raft's load-carrying capacity. Figure 9 shows that the unpiled raft's load-carrying capacity (2.03 kN) increased to 3.94, 4.47, and 4.98 kN for

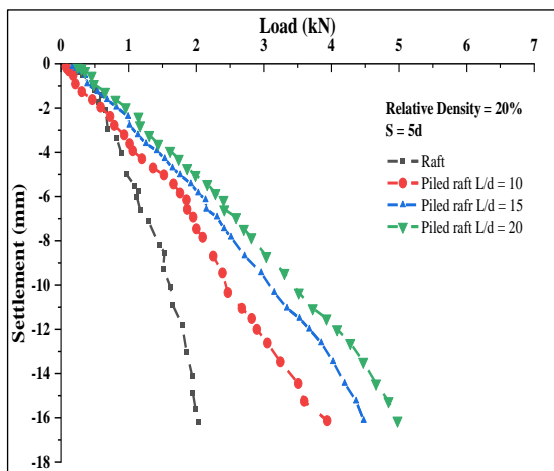


**Figure 8.** The behavior of raft and piled raft for various pile length

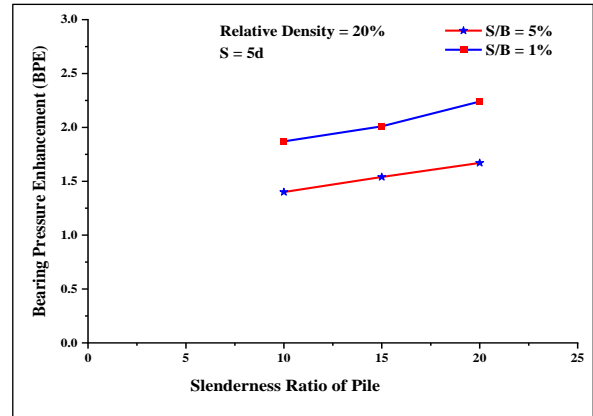


**Figure 9.** Effect of L/d ratio on BPE with respect to various S/B ratio

L/d = 10, 15, and 20, respectively. As the pile length increases, skin friction increases, boosting the raft's load-carrying capability.

Figure 9 shows how the S/B ratio (1 percent and 5 percent) affects raft bearing pressure with different L/d ratios. L/d ratios for both S/B ratios boost the raft's maximum load-bearing capability. As pile length rises, rigidity reduces [12]. Long piles may be better than short ones for reducing horizontal raft settling. However, increasing pile length improves the stiffness of the piling raft system.

**4. 2. Impact of Pile to Raft Area Ratio**

The influence of pile arrangement on model raft footing performance on loose sand under horizontal loads was tested using three pile slenderness ratios. As in Figure 6, Figure 10 shows the model raft's load settlement behavior. The 5d spacing configuration offers a more significant area proportion of the pile to the raft. As a result, it indicates higher stiffness and load-carrying capacity than the 3d and 4d spacing configurations for

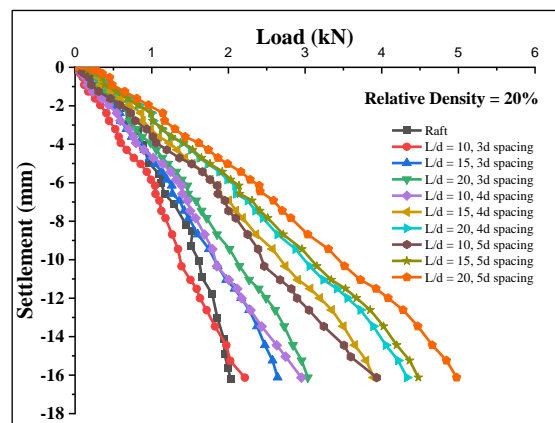


**Figure 10.** Ultimate load variation with maximum settlement for various  $A_{GPR}$

horizontal loading. This is because the 5d spacing configuration gives a more significant area proportion of the pile to the raft. Nine 5d-spaced piles are stiffer and resist tilting better. This model illustrates minimum differential settlement due to a larger pile-to-raft ratio. 3d and 4d pile arrangement patterns concentrate more in the raft's center, reducing rigidity. Other researchers [13] have noted that piles are concentrated in the plate's center, and that settlement is lower in the middle but higher on the outside.

**4. 3. Influence of Model Raft's Tilt** Figure 11 illustrated the settlements along the center line portions of the model rafts when they were loaded with horizontal load applied along the width of the raft and kept on loose sand to evaluate the effect that different pile design had on the behavior of the rafts. In Solitary, piles tied to a raft with  $L/d=20$  and raft settlements are plotted. At the same minimum load level (the unpiled raft failure load illustrated in Figure 8), the settlement values for each of the various pile design were calculated and compared to one another [14]. The graph indicates that using a pile layout with a 5d spacing will result in a reduction in the maximum raft settlements and tilt. The maximum settlements decreased from 16.18 millimeters to 10.75 millimeters, 6.68 millimeters, and 2.44 millimeters, respectively, when 3d, 4d, and 5d pile layouts were adopted. In the 5d pile configuration, the  $A_{GPR}$  is increased, and as a consequence of this, the horizontal load resistivity is enhanced. As a result of this, the tilt is decreased in comparison to the 3d and 4d arrangements.

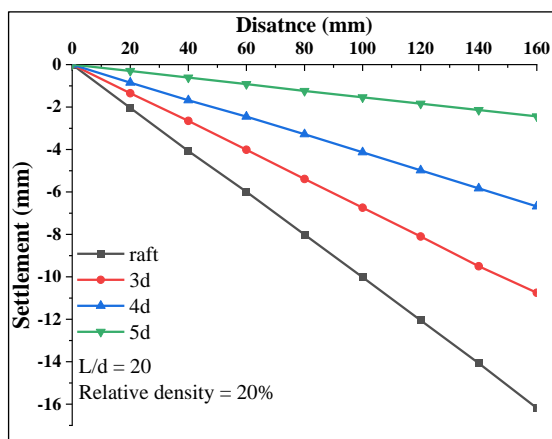


**Figure 11.** Tilt of raft and piled rafts for different pile spacing

## 5. CONCLUSION

The effectiveness of using short vertical piles under a raft with a secure attachment was investigated. A number of different piles spacing and pile length configurations in

loose, cohesionless soils were investigated. Previous settlement research reveals numerous elements that affect the settlement of pile-supported rafts. Under the same loading and soil conditions, the length and spacing of piles reduce total settlement and increase their load-carrying capacity. The following is a list of the most important things that were learned from the laboratory experiments:

- It has been found that when a raft is subjected to a horizontal load for settlement of 0.1% of the raft's width, the load-carrying capacity of the raft is enhanced. When compared to raft foundations, piled rafts with  $L/d$  ratios of 10, 15, and 20 have an improved load carrying capability of 48.33 percent, 54.65 percent, and 59.29 percent, respectively. As the pile length increases, skin friction causes an increase in carrying capacity for the pile.
  - When the  $S/B$  ratio is 1 percent and 5 percent, as well as when the  $L/d$  ratio is 10, 15, and 20, it is noted that the performance to resist bearing pressure has improved. The bearing pressure is increased for all  $L/d$  and  $S/B$  ratios. The  $S/B$  ratio of 1 percent results in a maximum increase in bearing pressure of 14.15 percent, whereas the  $S/B$  ratio of 5 percent results in 19.78 percent. The longer pile's increased ultimate load-bearing capacity allows it to withstand greater bearing pressure.
  - Load-bearing capability of piled raft foundations can be increased significantly by varying pile spacing and the  $L/d$  ratio. Out of 3d, 4d, and 5d spacing arrangements for different  $L/d$  ratios, the 5d arrangement performs better than the other arrangements under horizontal loading. With respect to the raft, the maximum increase in ultimate load-bearing capacity is 49.26%, 52.23%, and 63.29% for 3d, 4d, and 5d spacing, respectively. Increases in pile spacing result in a larger pile group's center core area (CCA). As a result, at 5d spacing, the horizontal load carrying capability rises. Having a larger pile to raft area ratio means that the pile group's Contribution to the raft's overall rigidity is greater than the raft's center section alone. According to a study, the 5d arrangement of piles is also more resistant to an overturning moment when situated near the edge.
  - The tilt of the raft dramatically decreases as the pile spacing increases from 3d to 5d. The tilt of the raft is reduced to 2.44 millimetres for 5d spacing, from 16.18 millimetres for raft only. Tilt edges for a horizontal load diminish as pile spacing increases because a bigger area of the piled raft contributes to the resistance of the overturning moment.
- The present study demonstrates that pile length plays a crucial role in preventing raft foundation settlement. However, pile spacing plays a crucial contribution in increasing the bearing capacity of the foundation and reduce the overturning as a whole. This study focuses

exclusively on soft soil. However, this type of study can also be conducted by modifying the soil type and soil conditions.

## 6. ACKNOWLEDGEMENT

The authors would like to express their gratitude to the Department of Civil Engineering at the Sardar Vallabhbhai National Institute of Technology in Surat, India, for all of the help that was provided in many forms to make this research possible.

## 7. REFERENCES

- Burland, J. B., Broms, B. B., and de Mello, V. F. B. "Behaviour of foundations and structures." *Proceedings of the International Conference on Soil Mechanics and Foundation Engineering, Tokyo, Japan*. July 10-15, 1977, Vol. 2, (1977), 495-536.
- Poulos H. G., I and Davis E. H., "Pile foundation analysis and design." *International Journal of Rock Mechanics and Mining Sciences & Geomechanics*. [https://doi.org/10.1016/0148-9062\(81\)90191-1](https://doi.org/10.1016/0148-9062(81)90191-1)
- Ali, A. H., Abbas, H. O., and Abed-Awn, S. H. "Behavior of Raft Foundation Built on Layered Soil under Different Earthquake Excitation." *International Journal of Engineering, Transactions B: Applications*, Vol. 35, No. 8, (2022), 1509-1515. <https://doi.org/10.5829/IJE.2022.35.08B.07>
- Clancy, P., and Randolph, M. F. "An approximate analysis procedure for piled raft foundations." *International Journal for Numerical and Analytical Methods in Geomechanics*, Vol. 17, (1993), 849-869.
- Horikoshi K., and Randolph M. F., "Centrifuge modeling of piled raft foundation on clay." *Geotechnique*, Vol. 46, No. 4, (1996), 741-752.
- Anthony Chibuzo Ekeleme, Benjamin Nnamdi Ekwueme, and Jonah Chukwuemeka Agunwamba, "Modeling Contaminant Transport of Nitrate in Soil Column." *Emerging Science Journal*, Vol. 5, No. 4, (2021), 471-485. doi: 10.28991/esj-2021-01290.
- Widjojo A. Prakoso and Fred H. Kulhawy. "Contribution to Piled Raft Foundation Design." *Journal of Geotechnical and Geoenvironmental Engineering*, Vol. 127, No. 1, (2001), 17-24. [https://doi.org/10.1061/\(ASCE\)10900241\(2001\)127:1\(17\)](https://doi.org/10.1061/(ASCE)10900241(2001)127:1(17))
- Small J. C., and Zhang H. H., "Behavior of piled raft foundations under lateral and vertical loading." *International Journal of Geomechanics*, Vol. 2, No. 1, (2002), 29-45. <https://doi.org/10.1080/15323640208500171>
- Irfan Jamil, Irshad Ahmad, and Wali Ullah, "Contribution of raft to resist lateral loads in a piled raft foundation-experimental finding." *Earthquakes and Structures*, Vol. 21, No. 3, (2021), 265-276. <https://doi.org/10.12989/eas.2021.21.3.265>
- Hamada J., Tsuchiya T., Tanikawa T., and Yamashita K., "Lateral loading tests on piled rafts and simplified method to evaluate sectional forces of piles.", *Geotechnical Engineering Journal*, Vol. 46, No. 2, (2015), 29-42. <https://doi.org/10.1080/1064119X.2020.1766607>.
- Soumya Roy, and Bikash Chandra Chattopadhyay, "Study on Piled Raft Foundation Subjected to Inclined Compressive Loading Condition." *International Journal of Civil Engineering Research*. Vol. 8, No. 2, (2017), 91-111.
- M. Zarinfar., " Investigating the Effect of Soil Layering on Soil-structure Interaction under Seismic Load.", *International Journal of Engineering, Transactions A: Basics*, Vol. 35 No. 10, (2022), 1989-2006.
- B. Thakur, and A. Desai, " Aspects of Foundation-soil Interaction of Nuclear Structures under Seismic Conditions through the State-of-art Review.", *International Journal of Engineering, Transactions C: Aspects*, Vol. 35, No. 09, (2022) 1716-1722.
- Cao X D., Wong I H., Chang M F., "Behavior of Model Rafts Resting on Pile-Reinforced Sand.", *Journal of Geotechnical and Geoenvironmental Engineering*, Vol. 130, No. 2, (2004), 129-138.
- Xiao-jun Zhu, Kang Fei, and Sheng-wei Wang, "Horizontal Loading Tests on Disconnected Piled Raft and a Simplified Method to Evaluate the Horizontal Bearing Capacity." *Advances in Civil Engineering*, Vol. 2018, (2018), 1-12. <https://doi.org/10.1155/2018/3956509>
- Goudar S., Kamatagi A., "An Experimental Evaluation of Axial Load Bearing Capacity of Belled and Straight Piles Embedded in Sand." *International Journal of Engineering, Transactions B: Applications*, Vol. 35, No. 8, (2022), 1599-1607. doi: 10.5829/ije.2022.35.08b.16
- Marwan Adil Hassan, Mohd Ashraf Mohamad Ismail, and Heyam Hussein Shaalan, "Numerical Modeling for the Effect of Soil Type on Stability of Embankment." *Civil Engineering Journal*, Vol. 7, (2022), 41-57. doi: 10.28991/CEJ-SP2021-07-04
- Divya Krishnan K., Swathi Krishna., and P.T Ravichandran, "Experimental Analysis on Settlement of Piled Raft System in Cohesionless Soil.", *Journal of Advance Research in Dynamical & Control Systems*, Vol. 10, No. 4, (2018), 1231-1236.
- Reul O., and Randolph M. F., "Design strategies for piled rafts subjected to non-uniform vertical loading." *Journal of Geotechnical and Geoenvironmental Engineering*, Vol. 130, No. 1, (2004), 1-13. [https://doi.org/10.1061/\(ASCE\)1090-0241\(2004\)130:1\(1\)](https://doi.org/10.1061/(ASCE)1090-0241(2004)130:1(1))
- Plaban Deb, and Sujit Kumar Pal, "Numerical analysis of piled raft foundation under combined vertical and lateral loading.", *Ocean Engineering*, Vol. 190, (2019), 1-13, <https://doi.org/10.1016/j.oceaneng.2019.106431>
- Vinil Kumar Gade, and S. M. Dasaka, "Assessment of Air Pluviation Using Stationary and Movable Pluviators." *Journal of Materials in Civil Engineering*, Vol. 29, No. 5, (2017), 1-7. [https://doi.org/10.1061/\(ASCE\)MT.1943-5533.0001798](https://doi.org/10.1061/(ASCE)MT.1943-5533.0001798)
- Vinil Kumar Gade, and S. M. Dasaka, "Development of a Mechanized Traveling Pluviator to Prepare Reconstituted Uniform Sand Specimens.", *Journal of Materials in Civil Engineering*, Vol. 28, No. 2, (2016), 1-9. [https://doi.org/10.1061/\(ASCE\)MT.1943-5533.0001396](https://doi.org/10.1061/(ASCE)MT.1943-5533.0001396)
- Gade V. K., Chauhan V. B., and Dasaka S. M., "Assessment of Pluviation Method of Sand Bed Preparation by Miniature Cone Penetration.", *Proceedings of the 50th Indian Geotechnical Conference, Pune, Maharashtra, India, (2015) 1-7.*
- N. B. Umravia; C. H. Solanki, "Numerical Analysis to Study Lateral Behavior of Cement Fly Ash Gravel Piles under the Soft Soil.", *International Journal of Engineering, Transactions B: Applications*, Vol. 35, No. 11, (2022), 2111-2119.
- Trudeep N. Dave, and S.M. Dasaka, "Assessment of Portable Travelling Pluviator to Prepare Reconstituted Sand Specimens.", *Geomechanics and Engineering*, Vol. 4, No. 2, (2012), 79-90. DOI:10.12989/gae.2012.4.2.079
- Lee J, and Salgado R. "Determination of pile base resistance in sands.", *Journal of Geotechnical and Geoenvironmental Engineering*, Vol. 125, No. 8, (1999), 673-683, doi: 10.1061/(ASCE)1090-0241(1999)125:8(673).
- Lee J, and Salgado R. "Estimation of bearing capacity of circular

footings on sands based on cone penetration test.”, *Journal of Geotechnical and Geoenvironmental Engineering*, Vol. 131, No. 4, (2005), 442-452, doi: 10.1061/(ASCE)1090-230241(2005)131:4 (442).

28. Cerato AB, and Lutenegeger AJ. “Bearing capacity of square and circular footings on a finite layer of granular soil underlain by a rigid base.”, *Journal of Geotechnical and Geoenvironmental Engineering*, Vol. 132, No. 11, (2006), 1496-501.

---

### Persian Abstract

---

#### چکیده

یک پی کم عمق روی خاک بدون چسبندگی نمی تواند وزنه های بیشتری را تحمل کند. پایه های شمع قایق توصیه می شود زیرا آنها ویژگی های باربری شمع و قایق را با هم ترکیب می کنند. پایه های شمعی ترکیبی (CRPF) برای ساختمان های بلند کارآمد هستند زیرا هم بارهای عمودی و هم بارهای جانبی را شامل می شوند. در فونداسیون رفت شمعی، به دلیل برهمکنش خاک و سازه، مقاومت در برابر بار رفت نادیده گرفته می شود. ساده سازی ممکن است منجر به طراحی غیراقتصادی شود. در حالی که مطالعه روی مقاومت عمودی قایق گسترده است، مقاومت افقی آن محدود است. در مطالعه حاضر مدل شمع-کلک ۱۶۰ میلی متر در ۱۶۰ میلی متر با فاصله شمع ها و طول شمع های مختلف مورد آزمایش قرار گرفت. مطالعات نشان داد که طول شمع و فاصله شمع باعث بهبود ظرفیت باربری و کاهش نشست قایق می شود. بسته به فاصله شمع ها و طول آن، سیستم قایق شمع ۶۵ درصد از بار جانبی را تحمل می کند. فاصله شمع ها و طول شمع سهم بار جانبی قایق را کاهش می دهد. علاوه بر این، با افزایش فاصله شمع ها، واژگونی قایق تا ۶۰ درصد کاهش می یابد. ارتقاء طراحی سیستم رفت شمع ممکن است گزینه ارزان تر و کارآمدتری برای آسمان خراش ها باشد و این سیستم پایه را طراحی اقتصادی تر کند.

---



# Shear Stress Distribution in Double-lap Adhesive Joints Reinforced with Nylon Fabric: Numerical Investigation

F. Marchione\*

Dipartimento di Ingegneria Civile, Edile e Architettura (DICEA), Università Politecnica delle Marche, via B. Bianche, Ancona, Italy

## PAPER INFO

### Paper history:

Received 29 July 2022

Received in revised form 19 September 2022

Accepted 23 September 2022

### Keywords:

Stress Analysis

Double-lap Adhesive Joints

FE Analysis

Adhesively Bonded Joints

Stress Distribution

## ABSTRACT

Nowadays there are an increasing number of industrial fields in which adhesive technology finds application. The main reason for their growing interest in both science and production is due to the high structural efficiency of this type of joining. Numerous studies have investigated the stress distribution in the adhesive layer under unreinforced conditions. The present work analyzes the elastic shear stress distribution in double-lap adhesive joints between timber and float glass adherends, both in the classical configuration and with an introduction of a nylon reinforcement in the two-component (2K) structural epoxy adhesives layers. In particular, three geometric configurations were investigated: nylon placed on the inner adherend, outer adherend and both. The result showed how the presence of the nylon inclusion changes the stress distribution in the joint. Numerical modelling of the joints was carried out using FE ANSYS®19 software. The greatest reduction in peak adhesive stresses is achieved by placing the reinforcement at both interfaces of the adherends with the adhesives. In general, it can be observed that the insertion of the reinforcement layer leads to a reduction in peak shear stresses, resulting in a potential increase in the ultimate strength of the joint.

doi: 10.5829/ije.2023.36.01a.05

## NOMENCLATURE

EPX1	First epoxy adhesive	$\rho$	Density (kg/m <sup>3</sup> )
EPX2	Second epoxy adhesive	$\nu$	Poisson ratio (-)
URM	Unreinforced model	E	Young Modulus (MPa)
RM-G	Reinforced model with nylon on glass surfaces	RM-GT	Reinforced model with nylon on glass and timber surfaces
RM-T	Reinforced model with nylon on timber surfaces		

## 1. INTRODUCTION

Adhesive joints allow dissimilar materials to be joined together, resulting in structures with high mechanical performance and characterised by lightweight properties [1-3].

In numerous industrial applications (e.g., automotive [4], naval [5] and aerospace [6]), these characteristics are fundamental and therefore adhesive technology takes a preferential role over traditional joining methods, such as bolted or riveted joints [7-9].

Some of the most studied adhesive joints are single-lap (SLJ) and double-lap (DLJ) types [10-12]; both types are used to study adhesive shear joint behaviour [13].

Single-lap joints can join two dissimilar adherends and are usually designed to tensile strength to failure [14]; however, misalignment of the adherends with respect to the line of application of the load leads to the occurrence of bending moments that may cause the joint failure, as demonstrated in literature [15-17].

In contrast, double-lap joints overcome the bending moment problem due to its symmetrical geometry, as noted by Marchione [18]. Therefore, this type of joint is more suitable for studying the distribution of shear stresses.

Gaudenzi et al. [19] conducted an experimental campaign to investigate the presence of delamination induced in plastic-reinforced carbon fibre plates by low-

\*Corresponding Author Institutional Email:  
[f.marchione@pm.univpm.it](mailto:f.marchione@pm.univpm.it) (F. Marchione)

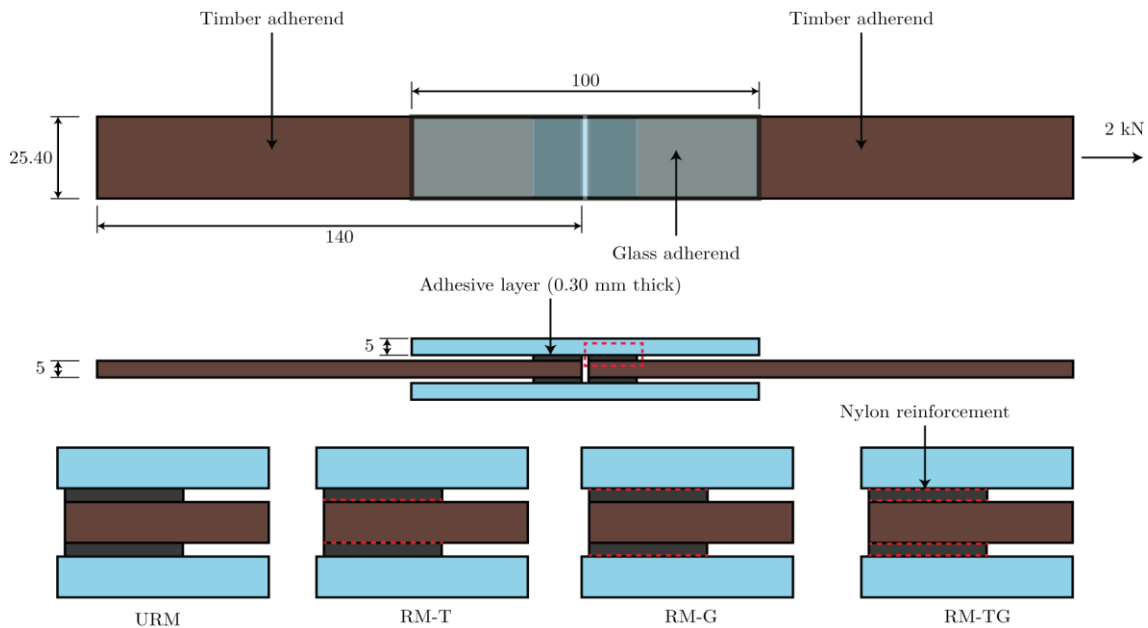


**Figure 1.** Double-lap adhesive joint, plan and section view (measures in mm)

velocity impacts. The results show the effectiveness of the SHM routine developed when a reduced number of sensors is desirable or mandatory.

Hu et al. [20] investigated the effect of non-woven carbon fabric (NWCT) composite adhesive layer on the bond strength and single-lap (SLJ) aluminium alloy joints. Wang et al. [21] investigated a simple method to apply and distribute multi-walled carbon nanotubes on sandblasted steel substrates. Kilik and Davies [22] studied the effect of introducing steel powder particles into the adhesive layer. The introduction of aluminium powder generally resulted in an increase in the static performance of the joints. The dynamic behaviour of the joints was experimentally analyzed and a better performance of copper powder than aluminium powder was observed.

The study of the vibrational behaviour of the double-lap adhesive joint was carried out by Marchione [23]. The influence of the elastic modulus and the density of adherends on the frequency for the various vibration modes was observed. In contrast, the presence of defects does not significantly influence the joint frequency. Further studies by the same author [24-26] have been investigated the potential of structural adhesives through analytical and numerical analyses.

As current research is oriented towards the study of new adhesive joint reinforcement techniques, and as stress measurement technologies often require the insertion of an outer layer into the adhesive joint, this paper analyzes the influence of the interposition of an intermediate adhesive layer. In particular, an FE study is conducted comparing the effect of the introduction of a

P6 nylon layer in double-lap joints between mahogany adherends, further investigating experimental results obtained by the same author [27].

## 2. FINITE ELEMENT ANALYSIS

The present study investigates the stress state of a double-lap adhesive joint. The application of the present study is aimed at the industrial production of building components characterised by adhesive joints between timber and glass adherends. Since in their service life the stresses must remain in the elastic range in such elements, the plastic phase behaviour of the materials is not the subject of this study. The geometry of the joint considered is shown in Figure 1.

The inner clings are made of mahogany and have dimensions of 140 mm × 25.40 mm × 5 mm, representing its length, width and thickness, respectively. The outer adherends are made of transparent float glass and have the same geometric characteristics as the inner adherend. The bonding area has the dimensions of 12.70 mm × 25.40 mm, with a thickness of 0.30 mm.

3D modelling using the commercial software ANSYS©19 was used for the simulation. The model is meshed with PLANE 182, a 4-node structural solid and a base element size of 0.10 mm. The analyzed joints are made of Sapelly mahogany adherends and different adhesives (two epoxies). The same boundary conditions have been applied to all the configurations considered. The surfaces at the ends of fixed adherend are fixed with all DOF constrained ( $U_1=U_2=UR_1 = UR_2 = 0$ ). The

joints were loaded with a constant load of 2 kN on the inner timber adherend which is in the elastic range for the joints considered, as experimented and reported in literature [27].

The results are plotted on the midplane of the adhesive layer. The mechanical and physical characteristics of the adherends and adhesives are shown in Tables 1 and 2, respectively.

### 3. RESULTS AND DISCUSSION

This section reports the results obtained from the numerical analysis of double-lap adhesive joints reinforced with nylon fabric in different configurations. Figure 2 illustrates the stress distribution in unreinforced joints assembled with EPX1 epoxy adhesive. Figure 3 illustrates the stress distribution for unreinforced joints assembled with EPX2 adhesive.

The EPX1 adhesive shows a higher peak tension of 8.18 MPa, located at the end of the joint close to the load application. The higher stress intensity compared to EPX2 adhesive (+18%) is due to the higher stiffness of EPX1 adhesive (3000 MPa).

Figures 4-9 show the stress trends for the different reinforcement configurations, i.e. for the different positions of the nylon fabric in relation to the inner and outer adherends.

The placement of the nylon reinforcement near the interface between the adhesive and the timber adherends results in an intermediate reduction in peak stresses compared to other reinforced configurations.

**TABLE 1.** Adherends characteristics for the FE model

Mahogany timber		
$E_t$ [MPa]	$\rho$ [N/m <sup>3</sup> ]	$\nu$ [-]
11000	7800	0.30
Float glass		
$E_t$ [MPa]	$\rho$ [N/m <sup>3</sup> ]	$\nu$ [-]
75000	24000	0.30

**TABLE 2.** Adhesive's characteristics for the FE model

EPX 1	
E [MPa]	$\nu$ [-]
3.00	0.35
EPX 2	
E [MPa]	$\nu$ [-]
1.50	0.35

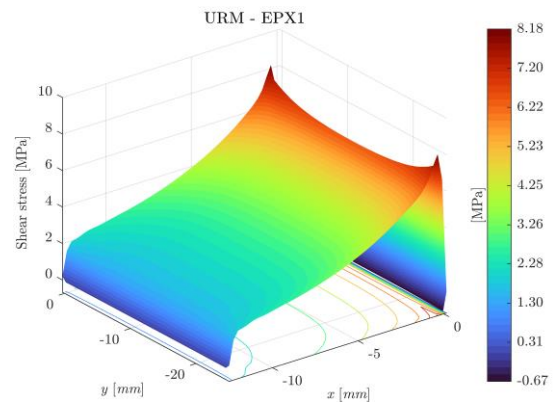


**Figure 2.** Shear stress distribution in the unreinforced joint, assembled with EPX1 adhesive

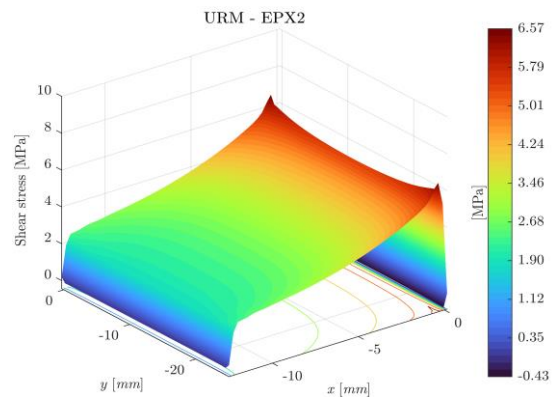


**Figure 3.** Shear stress distribution in the unreinforced joint, assembled with EPX2 adhesive

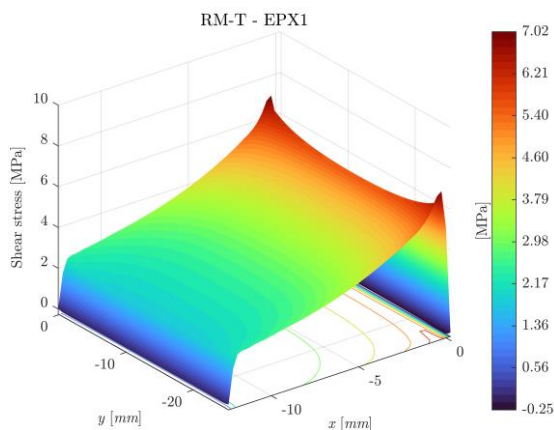


**Figure 4.** Shear stress distribution in the joint reinforced with nylon on timber surfaces, assembled with EPX1 adhesive

The introduction of the reinforcement on the glass surfaces results in a significant reduction in peak tensions, equalising the general trend.

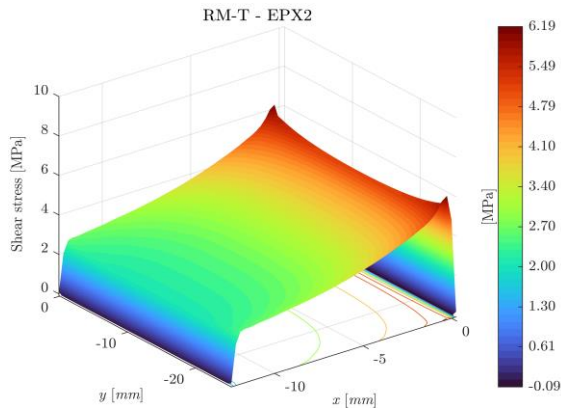


**Figure 5.** Shear stress distribution in the joint reinforced with nylon on timber surfaces, assembled with EPX2 adhesive

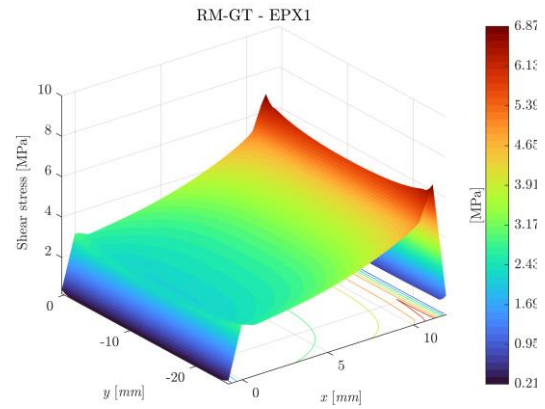


**Figure 8.** Shear stress distribution in the joint reinforced with nylon on both timber and glass surfaces, assembled with EPX1 adhesive

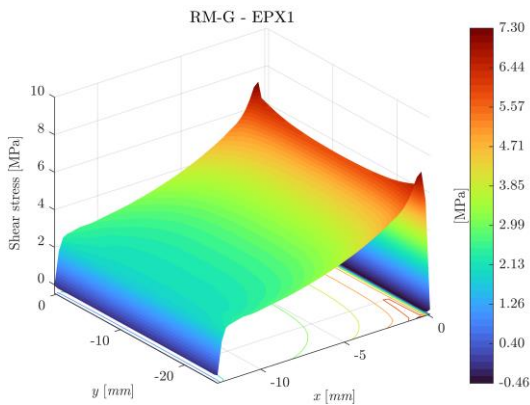


**Figure 6.** Shear stress distribution in the joint reinforced with nylon on glass surfaces, assembled with EPX1 adhesive

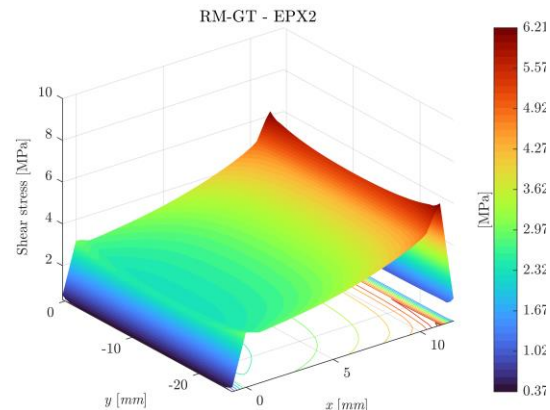


**Figure 9.** Shear stress distribution in the joint reinforced with nylon on both timber and glass surfaces, assembled with EPX2 adhesive

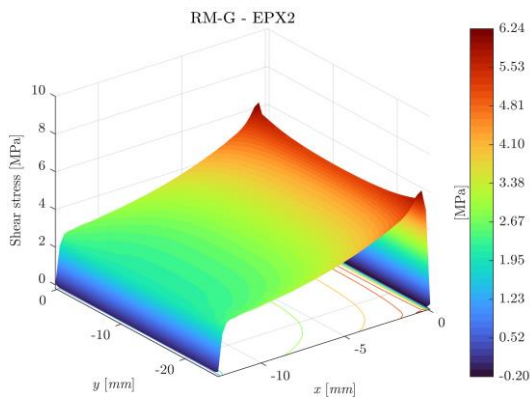


**Figure 7.** Shear stress distribution in the joint reinforced with nylon on glass surfaces, assembled with EPX2 adhesive

The greatest effect is obtained by placing the reinforcement in a double configuration, i.e., on both the glass and the mahogany adhesion. In this case, the tension

peaks are significantly reduced (on average -2 MPa) compared to the unreinforced configuration.

This reinforcement method reduces the internal tension peaks under the same load, potentially increasing the ultimate strength of the adhesive layer. However, this change results in one or more potential new creep and crisis surfaces of the joint. Therefore, there is not always a beneficial effect on the overall behaviour of the joint.

Figure 10 illustrates the peak trends for the various configurations considered.

It is observed that the best effect is obtained by the double reinforcement, with the greatest reduction in stress peaks, due to an increase in deformability of the adhesive layer. Among the single reinforcements (i.e., applied either on the glass or on the mahogany adherends), the greatest reduction is determined by the positioning of the reinforcement on the timber adherend (i.e., the loaded adherend).

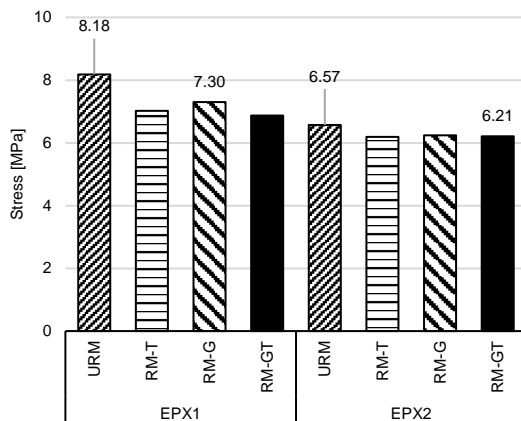


Figure 10. Shear stress peaks in the adhesive layer, for each configuration considered

#### 4. CONCLUSIONS

Adhesive joints allow dissimilar materials to be joined together to create resulting lightweight structures characterized by a more uniform stress distribution than traditional joining technologies.

The present work numerically investigates the shear stress distribution within double-lap adhesive joints between wood and float glass adherends, assembled with two epoxy adhesives characterised by different elastic modulus.

The results showed that:

- The introduction of nylon reinforcement always results in a reduction of stress peaks at the end of the adhesive region, due to the increase in its deformability;
- The reduction in stress intensity potentially leads to an increase in the overall strength of the adhesive joint;
- Of the different reinforcement configurations investigated, the greatest reduction is that resulting from double reinforcement on both adherends; The introduction of the inclusive layer - or layers - into the adhesive may lead to the formation of additional failure interfaces and thus is prone to adhesive failure.

#### 5. REFERENCES

1. Adams, R.D., Adams, R.D., Comyn, J., Wake, W.C. and Wake, W., "Structural adhesive joints in engineering, Springer Science & Business Media, (1997).
2. Da Silva, L.F., Adams, R. and Gibbs, M., "Manufacture of adhesive joints and bulk specimens with high-temperature adhesives", *International Journal of Adhesion and Adhesives*, Vol. 24, No. 1, (2004), 69-83. [https://doi.org/https://doi.org/10.1016/S0143-7496\(03\)00101-5](https://doi.org/https://doi.org/10.1016/S0143-7496(03)00101-5).
3. Yousefsani, S.A., Tahani, M. and Selahi, E., "Analytical solution of stress field in adhesively bonded composite single-lap joints under mechanical loadings", *International Journal of Engineering, Transactions C: Aspects*, Vol. 27, No. 3, (2014), 475-486. <https://doi.org/10.5829/idosi.ije.2014.27.03c.16>
4. Quini, J.G. and Marinucci, G., "Polyurethane structural adhesives applied in automotive composite joints", *Materials Research*, Vol. 15, (2012), 434-439. <https://doi.org/10.1590/S1516-14392012005000042>
5. Parate, B.A., "Propellant actuated device for parachute deployment during seat ejection for an aircraft application", *HighTech and Innovation Journal*, Vol. 1, No. 3, (2020), 112-120. <https://doi.org/10.28991/HIJ-2020-01-03-03>
6. Hadjez, F. and Necib, B., "Experimental characterization and numerical modelling analyses of nano-adhesive-bonded joints", *Frattura ed Integrità Strutturale*, Vol. 12, No. 44, (2018), 94-105. <https://doi.org/10.3221/IGF-ESIS.44.08>
7. da Silva, L.F.M., Öchsner, A. and Adams, R.D., "Handbook of adhesion technology, Springer, Vol. 1, (2011).
8. Mays, G.C. and Hutchinson, A.R., "Adhesives in civil engineering, Cambridge University Press Cambridge, UK., Vol. 32, (1992).
9. Lees, W., "Adhesives in engineering design, Springer, (1984).
10. Ciupack, Y., Pasternak, H., Mette, C., Stammen, E. and Dilger, K., "Adhesive bonding in steel construction-challenge and innovation", *Procedia Engineering*, Vol. 172, (2017), 186-193. <https://doi.org/10.1016/j.proeng.2017.02.048>
11. Stazi, F., Giampaoli, M., Rossi, M. and Munafò, P., "Environmental ageing on gfrp pultruded joints: Comparison between different adhesives", *Composite Structures*, Vol. 133, (2015), 404-414. <https://doi.org/10.1016/j.compstruct.2015.07.067>
12. Tannert, T., Vallée, T. and Hehl, S., "Probabilistic strength prediction of adhesively bonded timber joints", *Wood science and technology*, Vol. 46, No. 1, (2012), 503-513. <https://doi.org/10.1007/s00226-011-0424-0>
13. da Silva, L.F., das Neves, P.J., Adams, R. and Spelt, J., "Analytical models of adhesively bonded joints—part i: Literature survey", *International Journal of Adhesion and Adhesives*, Vol. 29, No. 3, (2009), 319-330. <https://doi.org/10.1016/j.ijadhadh.2008.06.005>
14. Adams, R. and Peppiatt, N., "Stress analysis of adhesive-bonded lap joints", *Journal of Strain Analysis*, Vol. 9, No. 3, (1974), 185-196. <https://doi.org/10.1243/03093247V093185>
15. Marchione, F., "Effect of hollow adherends on stress peak reduction in single-lap adhesive joints: Fe and analytical analysis", *The Journal of Adhesion*, Vol. 98, No. 6, (2022), 656-676. <https://doi.org/10.1080/00218464.2021.1995368>
16. Owens, J.F. and Lee-Sullivan, P., "Stiffness behaviour due to fracture in adhesively bonded composite-to-aluminum joints i. Theoretical model", *International Journal of Adhesion and Adhesives*, Vol. 20, No. 1, (2000), 39-45. [https://doi.org/10.1016/S0143-7496\(99\)00013-5](https://doi.org/10.1016/S0143-7496(99)00013-5)
17. Demir, K., Bayramoglu, S. and Akpinar, S., "The fracture load analysis of different support patches in adhesively bonded single-lap joints", *Theoretical and Applied Fracture Mechanics*, Vol. 108, (2020), 102653. <https://doi.org/10.1016/j.tafmec.2020.102653>
18. Marchione, F., "Stress distribution in double-lap adhesive joints: Effect of adherend reinforcement layer", *International Journal of Adhesion and Adhesives*, Vol. 105, (2021), 102780. <https://doi.org/10.1016/j.ijadhadh.2020.102780>
19. Gaudenzi, P., Nardi, D., Chiappetta, I., Atek, S., Lampani, L., Pasquali, M., Sarasini, F., Tirilló, J. and Valente, T., "Sparse sensing detection of impact-induced delaminations in composite

- laminates", *Composite Structures*, Vol. 133, (2015), 1209-1219. <https://doi.org/10.1016/j.compstruct.2015.08.052>
20. Hu, Z., Kong, H., Tao, L., Qiao, M., Yu, D., Lu, F., Dawelbeit, A. and Yu, M., "Effect of nonwoven carbon tissue-reinforced epoxy resin adhesive layer on the single lap bonding strength of aluminum alloy joints", *ACS omega*, Vol. 6, No. 37, (2021), 23802-23813. <https://doi.org/10.1021/acsomega.1c02635>
  21. Wang, B., Hu, X., Hui, J., Lu, P. and Jiang, B., "Cnt-reinforced adhesive joint between grit-blasted steel substrates fabricated by simple resin pre-coating method", *The Journal of Adhesion*, Vol. 94, No. 7, (2018), 529-540. <https://doi.org/10.1080/00218464.2017.1301255>
  22. Kilik, R. and Davies, R., "Mechanical properties of adhesive filled with metal powders", *International Journal of Adhesion and Adhesives*, Vol. 9, No. 4, (1989), 224-228. [https://doi.org/10.1016/0143-7496\(89\)90065-1](https://doi.org/10.1016/0143-7496(89)90065-1)
  23. Marchione, F., "Investigation of vibration modes of double-lap adhesive joints: Effect of slot", *International Journal of Engineering, Transactions A Basics*, Vol. 33, No. 10, (2020), 1917-1923. <https://doi.org/10.5829/IJE.2020.33.10A.10>
  24. Marchione, F., "Analytical investigation on the stress distribution in structural elements reinforced with laminates subjected to axial loads", *International Journal of Engineering, Transactions A: Basics*, Vol. 35, No. 4, (2022), 692-697. <https://doi.org/10.5829/IJE.2022.35.04A.08>
  25. Marchione, F., "Analytical stress analysis in single-lap adhesive joints under buckling", *International Journal of Engineering, Transactions B: Applications*, Vol. 34, No. 2, (2021), 313-318. <https://doi.org/10.5829/ije.2021.34.02b.02>
  26. Marchione, F., "Enhancement of stiffness in gfrp beams by glass reinforcement", *International Journal of Engineering, Transactions C: Aspects*, Vol. 34, No. 3, (2021), 615-620. <https://doi.org/10.5829/ije.2021.34.03c.04>
  27. Marchione, F. and Munafò, P., "Experimental investigation on timber-glass double-lap adhesive joints reinforced with nylon fabric", *Construction and Building Materials*, Vol. 275, (2021), 122152. <https://doi.org/10.1016/j.conbuildmat.2020.122152>

---

#### Persian Abstract

تا به امروز، بخش های صنعتی که فناوری چسب در آنها کاربرد پیدا می کند، همیشه در حال رشد هستند. دلیل اصلی علاقه روزافزون آنها به هر دو حوزه علمی و تولیدی به دلیل کارایی بالای ساختاری این نوع اتصالات است. مطالعات متعددی به بررسی توزیع تنش ها در لایه چسب در شرایط غیر مسلح پرداخته است. این کار روند تنش های برشی را در اتصالات چسب دولایه بین چسب های چوب و شیشه فلوت، هم در پیکربندی کلاسیک و هم با معرفی یک تقویت کننده نایلونی در لایه چسب اپوکسی ساختاری دو جزئی (2K) تحلیل می کند. به طور خاص، سه پیکربندی هندسی مورد بررسی قرار گرفت: نایلون قرار گرفته بر روی چسبندگی داخلی، خارجی و روی هر دو. نتیجه نشان می دهد که چگونه حضور نایلون باعث تغییر توزیع تنش ها در اتصال می شود. مدل سازی عددی اتصالات با استفاده از نرم افزار © 19 FE ANSYS انجام شد. بیشترین کاهش در کشش پیک چسب با قرار دادن آرماتور در هر دو سطح مشترک چسب با چسب ها به دست می آید. به طور کلی می توان گفت که قرار دادن لایه تقویت کننده منجر به کاهش پیک های تنش برشی و در نتیجه افزایش بالقوه در استحکام نهایی اتصال می شود.

---



## A Novel Methodology for Predicting Roadway Deterioration in Iraq

A. Kharbat Shadhar\*, B. Basheer Mahmood, M. Hashim Al Quraishi

Department of Civil Engineering, College of Engineering, University of Wasit, Iraq

### PAPER INFO

#### Paper history:

Received: 02 August 2022

Received in revised form 07 September 2022

Accepted 23 September 2022

#### Keywords:

Prediction

Deterioration

Infrastructure

Modelling

### ABSTRACT

The accurate prediction of roadway conditions is challenging for infrastructure services, especially when considering an increase in traffic volume. This is the first study conducted in Iraq that focuses on predicting roadway condition deterioration and its relation to yearly traffic volume, using surveying data collected between 2019 and 2021. The main purpose of the conducted study was to inspect the accuracy, reliability, and ability of a combination of predictive techniques, this combination including Markovian Chains (MCs) and Artificial Neural Networks (ANNs), known as (MC-ANN), accurately to forecast mid-term to long-term (yearly) roadway condition. The principal findings of this research are as follows: a) MCs is a powerful method applied to predict future condition depending on previous one; b) ANNs modelling was performed that be able to produce a more reliable model of roadway condition based on selected road traffic volume change, climate circumstances and road age. The study reached a correlation coefficient of 0.94 between inspected and predicted roadway conditions using a valid collected dataset and a slight mean square error of 0.0195.

doi: 10.5829/ije.2023.36.01a.06

### NOMENCLATURE

MCs	Markovian chains	PCR	Pavement condition rating
ANNs	Artificial neural networks	n	Number of road segments
MC-ANN	Markovian chains- artificial neural networks	$P_{ij}$	Probability transition from i to j
RNN	Recurrent Neural Networks	i	Chosen segment number
IRI	International Roughness Index	j	Type of maintenance strategy options
CRI	Condition Rating Index	m	Total number of pavement maintenance options
PSI	Present Service Index	$X_{ij}$	Values between 0 and 1 represent the percent of a segment of the roadway under treatment.
VCI	Visible Condition Index	AI	Artificial intelligence
SVM	Support Vector Machine	ML	Machine learning
M&R	Maintenance and rehabilitation	MSE	Mean square error
MS	Maintenance strategy	MAE	Mean absolute error
DSS	Decision support system	R	Pearson's correlation
SDGs	Sustainable development goals	RMSE	Root mean square error

### 1. INTRODUCTION

The road maintenance management sector faces many obstacles, and the most important of these obstacles are the limited resources and budget. Therefore, developing an appropriate plan for distributing resources, allocating maintenance requirements and choosing the appropriate timing in order to determine the priority of maintenance and rehabilitation (M&R) programs are the most

important success factors. In order to maintain the roads and avoid their deterioration then out of service due to an increase in frequency of traffic load or climatic factors, roads require continuous maintenance work. Especially, in the event that a limited budget is allocated to the road Maintenance and rehabilitation (M&R) works, it has become necessary to use the funding optimally in order to reach an efficient maintenance program that maintains the road as long as possible [1]. The maintenance strategy

\*Corresponding Author Institutional Email: [akhirbat@uowasit.edu.iq](mailto:akhirbat@uowasit.edu.iq)  
(A. Kharbat Shadhar)

represents a plan for the actions or steps of conducting maintenance operations according to available resources at the appropriate time, which depends on defining the actions to be taken such as “identifying pavement defects and their extent and severity, defining the remedial actions for each defect and allocating the necessary resources for those procedures [2].

Based on Shafiee and Sørensen’s [3] study, the maintenance strategy (MS) is defined as the decision support system taken to develop a plan for maintenance activities, in addition to a set of policies and procedures planned to be conducted in order to “maintain” or “restore” the pavement. While another (MS) definition states that it is an integrated administrative system for managing project activities by highlighting the types of maintenance work for each type of defect with its costs and schedule and determining the extent of the impact of these works and procedures on maintenance costs [4]. Maintaining roads within a good or acceptable service level requires an adequate maintenance management system and effective pavement maintenance management plans. While neglecting these measures leads to huge damages that follow by the collapse of the service and high costs of maintenance and rehabilitation alternatives [5].

The process of maintenance management and optimal decision-making requires the provision of integrated data that shows the nature of the infrastructure project understudy and sufficient information about the deterioration curve and the remedial actions taken based on identifying the problem as a key to decision-making. It also requires identifying the most important obstacles that may hinder the preparation of a comprehensive and effective maintenance program for the project under study [6].

In fact, the most important constraint to reaching the project of the effective decision support system (DSS) is identifying the past, current, and future state of the project [7]. Currently, it has become possible to improve the decision-making process by taking advantage of scientific innovation in the field of artificial intelligence and mathematical modeling and integrating them into the field of decision support systems and management sciences. This study will address the use of Markov chains and neural networks as an innovative model for predicting the state of future road projects as a means to help support and make the decision of pavement maintenance management.

## 2. LITERATURE REVIEW

Establishing a system to accurately predict the condition of pavement deterioration is essential and effective for road management. Pavement deterioration progresses continuously but relatively slowly and is caused by various physical and environmental factors, such as track

loads, paving materials and pavement design, total rainfall, and average annual temperature [8, 9]. Most of the previous studies relied on visual inspection data to predict the deterioration of the pavement. The difference between the previous and current amounts of deterioration was compared to find the deterioration speeds [10]. Shin [11] predicted crack deterioration in pavement using a semi-parametric random duration model. Loizos and Karlaftis [12] also developed a model based on the principle of probabilistic duration to predict pavement surface. However, current statistical degradation models suffer from problems and are still in the initial stage [13, 14].

Extensive studies have been conducted using deep learning methodology as well as statistical analysis methods. They can be categorized into studies using Recurrent Neural Networks (RNN) and those using ANN algorithms. Attoh-Okine [15] developed an ANN-type backpropagation algorithm to develop a pavement degradation model. He used explanatory variables to train, such as deformation of track loads, rate of rips, road structure, surface tightness such as patching, and depth of bore in the previous year. A significant improvement was found in the performance of the ANN algorithm for the prediction of degradation when other factors such as life stages of pavement degradation and environmental factors were taken into additional consideration. Attoh-Okine [16] also analyzed the condition of the pavement and developed a degradation model using the ANN back-propagation of the International Roughness Index (IRI). The ANN algorithm and various input variables were used to predict the pit depth, pavement crack depth, Condition Rating Index (CRI), International Roughness Index, Present Service Index (PSI), and Visible Condition Index (VCI) [17]. Furthermore, more studies found that the performance of pavement condition prediction using the ANN algorithm was more accurate and reliable than those models calculated using traditional statistical analysis [18, 19].

In several studies conducted to predict the service life of the platform for analyzing time series data, the RNN algorithm was used, which is suitable for these conditions [20, 21]. Choi and Du [22] reported that prediction using the ANN algorithm improved its performance when overfitting was resolved. Tabatabaee et al. [23] developed a hybrid prediction model for PSI that uses a support vector machine (SVM) as the first stage to classify sections with structural similarity and from other independent variables produced an RNN algorithm to predict PSI in the following year, based on classification results from the first stage. The Minnesota Department of Transportation provided a dataset for a case study that revealed that a hybrid model using the SVM and RNN algorithm was superior, in terms of error rate and prediction performance, to the model that used the RNN algorithm only [23].

In this study, the innovation is to use Markov chains to determine the evolution in pavement degradation as a first stage and then include physical and environmental factors to use the ANN algorithm, to properly deal with time series data. In addition, obtaining an optimal model performance for each by performing an overlapping prediction according to the length of the chronology is a section of the road pavement.

### 3. METHODOLOGY

The proposed methodology is considered new through the combination of a number of techniques, the methodology used, includes:

- 1- Data collection in cooperation with the Wasit Roads and Bridges Directorate, south of Baghdad.
- 2- Markov chains were applied at different time intervals to reduce the error in measuring pavement performance according to weather variables on the time series.
- 3- ANN technique was used to choose the optimal approach to the model inputs.
- 4- The data were divided into three groups (input, training, and output).
- 5- Finally, the new methodology was developed to predict the deterioration of the pavement condition based on weather variables such as rain, temperature, and traffic loads calculated with the lowest error measure. And applying the developed methodology, measuring performance evaluation criteria and the reliability of the results. Figure 1 presents summary of the adopted methodology.

### 4. STUDY AREA DATA SET

A roadway in Iraq located in southern Baghdad city, This road is one of two main roadways that have been used to

connect the capital with the south of Iraq's city. Historical semiannual road condition data of (320) sample variables were collected from the road and bridge department. This data comprised road condition (rating), temperature (°C), traffic load (number of the car), annual rainfall (mm), and road section age (year). Data collected from the road and bridges directorate of Wasit is described in Table 1.

### 5. HYBRID MARKOV CHAINS PREDICTION-ARTIFICIAL NEURAL NETWORK (MC-ANN)

Artificial intelligence (AI) is an important component in the field of civil engineering, especially in the direction of using digital data and intelligence, thus significantly increasing the reliance on automation to improve performance and reliability, in addition to creating efficient communication between physical conditions and digital data of construction [23, 24].

The construction industry can affect national economic sector growth and development [25, 26]. Moreover, governments in most countries around the world are taking more steps toward applying AI in the construction industry to obtain a competitive preference [27].

For example, of government procedure around the world, the U.K. government take serious steps to put the country at the primacy of AI science in order to make its projects creative and more innovative [28, 29]. In a similar way, France plans to spend huge resources on AI developers. Especially, at the national level, such investments can supply the economy with a competitive feature; although, these procedures can cause a negative impact on the globalization of services and production [30, 31]. Companies that fully depend on AI capabilities will not need to take into account outsourcing resources [32-34].

Artificial intelligence can be defined as a means of distribution, statistics, and coding that aims to find solutions by simulating human means through focusing on knowledge and continuous learning, leading to decision-making, and devoting efforts to collect previous data for training and modelling [35-37].

AI can immediately help us make superior improvements toward Sustainable Development Goals (SDGs) [38]. Furthermore, AI offers many opportunities for significant efficiency gains by quickly and accurately

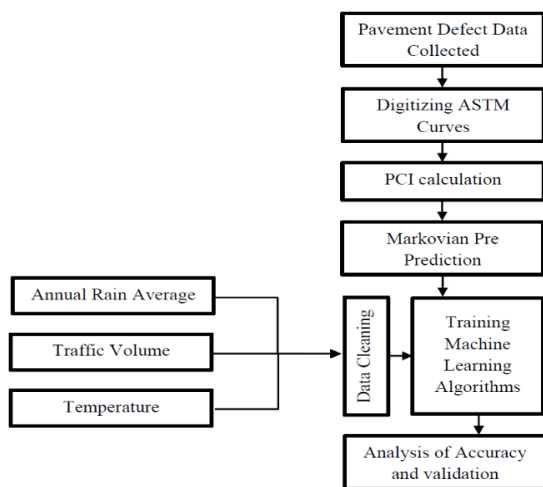


Figure 1. Summary of adopted methodology

TABLE 1. Data set sample

Segment NO.	1	2	3	4	5
PCI	31	61	62	57	36
Rainfall Intensity mm	204	207	198	211	205
Traffic Load	73512	68533	69726	72564	72145
Temperature °c	37	40	36	38	39

analyzing large amounts of data [39]. Moreover, AI systems and technologies can handle complex and non-linear functional problems and, once taught, can make predictions and generalizations at a high rate in digital architecture [40, 41].

Ultimately, AI aroused great interest in a variety of fields, including economics, medical, civil, and mechanical engineering, and especially in the field of forecasting, which attracted the attention of researchers [42, 43].

**5. 1. Markovian Modelling** Markov chain dealt with a series of random factors or variables, that match the state of a confirmed system [44]. In this approach that the pavement condition rating (PCR) at any time depends essentially on its status in a bygone time period [45].

However, if  $X_n = i$ , this shows that the element state is  $i$ , at  $n$  time. The deterioration will transition from state  $i$  to  $j$  and all that shows a constant probability  $P_{ij}$ . In case of the probability of  $P_{ij}$  is not dependent on the time. Therefore, Moreira et al. [46] assume that:

$$P = X_{(n+1)} = i, X_{(n)} = j, X_{(n-1)} = i^{n-1}, \dots X_{(0)} = i^0 \quad (1)$$

Here,  $(i, j, i_{n-1}, i, \dots i_n) \in n$ .

Where,

$P_{ij}$  = the probability transition from  $i$  to  $j$ ;

$X_n$  = PCR for section  $ij$ .

$N_{ij}$  = pavement sections numbers those PCR change from state  $i$  to state  $j$ ;

Noticeably one has [29]:

$$P_{ij} \geq 0, \sum_{i=0}^n P_{ij} = 1, j = 0, 1, \dots \dots \quad (2)$$

where :

$P$  = probability at time  $n$ .

$i, j$  = status at any time, where  $i, j \in n$

In another hand, the transition matrix of probability including  $P_{ij}$ :

$$P_{ij} = \begin{pmatrix} P_{00} & P_{10} & \dots \\ P_{01} & P_{11} & \dots \\ \dots & \dots & \dots \end{pmatrix} \quad (3)$$

It is easy to express the probability matrix as:

$P_{00} = 1 - \alpha, P_{10} = \alpha, P_{11} = 1 - \beta$  and  $P_{01} = \beta$ .

Then the one-next-step (in the next time period) transition matrix of probability as:

$$P = \begin{pmatrix} 1 - \alpha & \beta \\ \alpha & 1 - \beta \end{pmatrix} \quad (4)$$

where  $\alpha$  and  $\beta$  presented are as possible values of probability.

**5. 2. Artificial Neural Network (ANN)** The expression Artificial Intelligence (AI) model denotes one that is obtained from past highway pavement documented data using an artificial intelligence

algorithm. The field of (AI) includes diverse mechanisms that have been utilized in a variety of applications throughout the last past century. There are several models of AI techniques that have been known as influential tools to settle complex problems such as Machine learning (ML) and Artificial neural networks ANNs [47]. The study conducted by Cutore et al. [48] utilized AI tools to develop prediction models for adequacy ratings of bridges using current design, service life, load and density of traffic, and constitutional features. Figure 2 displays the ANN architecture.

MATLAB was used to apply the (MA-ANN) algorithm, Figure 3 shows the ANN model flow chart [49] applied to simplify predict roads deterioration accuracy.

**6. MODEL PERFORMANCE AND RELIABILITY OF MEASUREMENTS**

The assessment process of performance for the proposed model can be reached by utilizing different traditional statistical measures, as shown in Figure 4.

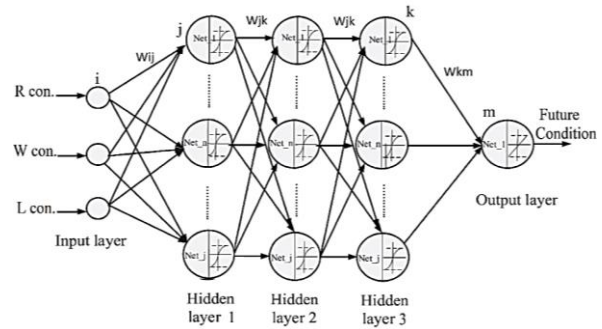


Figure 2. ANN architecture

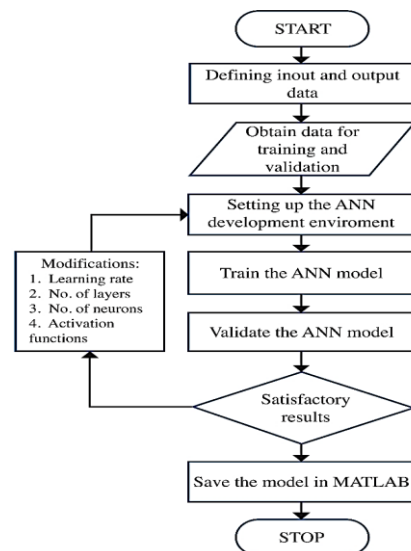


Figure 3. Flow chart of ANN algorithm

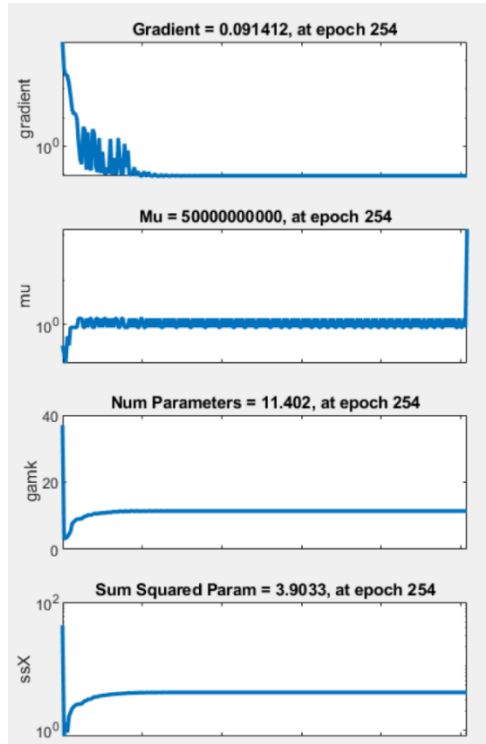


Figure 4. Data assessment

In this study, to examine prediction reliability five standards were used; (MSE) mean square error, (MAE) standard deviation, and (RMSE) root mean square error.

$$MAE = \frac{\sum_{m=1}^N |y_0 - y_p|^2}{N} \tag{5}$$

$$MSE = \frac{\sum_{m=1}^N (y_0 - y_p)^2}{N} \tag{6}$$

$$RMSE = \sqrt{\frac{\sum_{m=1}^N (y_0 - y_p)^2}{N}} \tag{7}$$

$$R = \left[ \frac{\sum_{m=1}^N (y_0 - y_0)(y_p - y_p)}{\sqrt{\sum (y_0 - y_0)^2 - \sum (y_p - y_p)^2}} \right] \tag{8}$$

where  $y_o$ : the observed road condition;  $y_p$ : predicted road condition;  $N$ : population size;  $y_o$ , mean of observed road condition and  $y_p$ , mean of predicted road condition.

## 7. RESULTS AND DISCUSSION

### 7. 1. Development Model Input

It is necessary for normalizing data by applying the normal distribution, the time series data of road conditions rating without noise was obtained by employing the pretreatment signal technique [50].

Pre-processing of collected data increases the correlation coefficients (cc) among independents and dependent variables for a different rating of road conditions, e.g., the cc of raw data of rating increased significantly from 0.72 to 0.94, 0.92, 0.89, and 0.83, respectively, for the three-time series.

Fidell [34] indicated that the relationship between the independent variables and the size sample (N) should be confirmed with Equation (9).

$$N = 50 + 8 m \tag{9}$$

$m$  = predictor variables number.

In this study, the data size needed is 90 less than the case number  $N = 116$ , compliance with the proposition limited by Mardani et al. [34].

### 7. 2. Application of Hybrid Ma-Ann Techniques

After performing data pre-processing methods, data must be divided into three different datasets, training, testing, and validation, as shown in Table 2. This table classifies all datasets into four statistical standards including maximum pavement condition rating (PCRmax), minimum pavement condition rating (PCRmin), mean pavement condition rating (PCRmean), standard deviation (PCRstd), and sample size for each dataset (S). The results present that all sets have the same pattern.

The determination coefficient (R2) was calculated between the observed and predicted road rating for training, testing, and validation sets, to examine the proposed model accuracy for generalization, as shown in Figure 6. The measured pavement condition rating is plotted on the x-axis against the No. of sample on the y-axis. The results were calculated by applying the hybrid(MA-ANN) in comparison with those collected from visual inspection to validate the proposed model.

TABLE 2. Statistical parameters for datasets

Pavement Condition Rating (PCR)	PCRmax	PCRmin	PCRmean	PCRstd	n
Training set	79	61	70	0.055	60
Testing set	80	62	71	0.054	15
Validation set	78	61	70	0.058	15

The resulting deterioration model obtained when applying (MA-ANN), has a small value of root mean square error (RMSE). To explore the performance quality of the proposed prediction methodology for the hybrid model, a regression coefficient (R) was set between the computed and predicted road condition, as shown in Figure 5. The composite model was significant  $R = 0.981$  for the data collected for the road under study, in the validation phase of the results these figures confirm the ability of the hybrid (MA-ANN) technique to forecast precisely road deterioration and indicate its future condition. In addition, various statistical indicators such as CE, MAE, RMSE, and MARE for examining the performance of training, testing, and validation datasets for the (MA-ANN) model, as presented in Table 3.

The error value was calculated to ascertain the reliability of the model. Figure 5 shows scatter plots of the mean square error. In all figures, three significant models of data emerged; The mean square error was very tiny and near to zero, there is no particular tendency for

the distribution pattern and the error intensity distribution for all data is uniform.

Both graphs shown in Figure 6 show the best fit between the actual and expected road conditions, which indicates the ability of this model to accurately simulate time series. Therefore, this proposed model is considered effective by being able to accurately calculate the degradation model of roads in Iraq. Where the outputs represent the results obtained using the hybrid technology, while the goal represents the observed results in the way under study. Figure 5 indicates that the results converged very closely during the training or final production phases.

The impetus for this study was to develop a new methodology to predict the deterioration of roads in Iraq. This methodology consists of two parts: (1) examine the ability of MA-ANN to elicit consistent components and non-consistent components, in addition to the filtering process for different time series from noise, and, (2) verify the reliability of the (hybrid MA-ANN) model to predict the time-series deterioration of roads in Iraq.

**TABLE 3.** performance evaluation and validation

Model	Data Stage	RMSE	MAE	MARE	CE
MA-ANN	Training	0.092	0.0081	0.0058	0.981
	Testing	0.091	0.0079	0.0056	0.987
	Validation	0.094	0.0077	0.0049	0.977

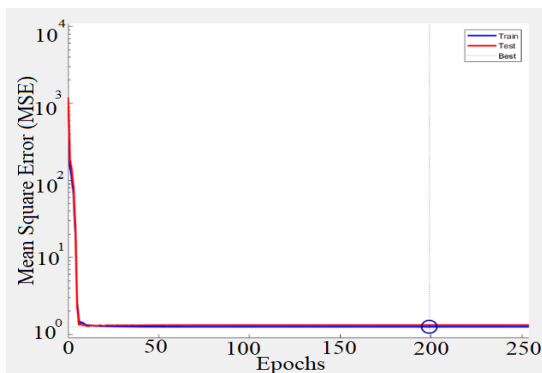


**Figure 5.** Mean square error

The technique of combining Markov chains and ANN was reliable and effective when simulating the road degradation model in Iraq. This paired technique has validation-stage correlation coefficients  $R = 0.981$  for the collected data. This study can be considered as proof in order to encourage road maintenance planning departments to adopt the integrated technology, to accurately predict the degradation model of roads in Iraq.

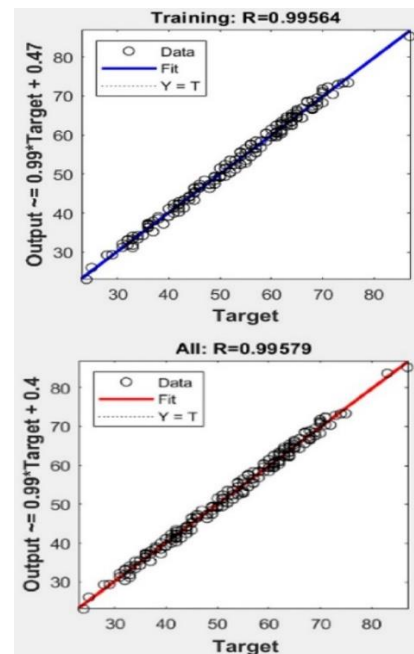


**Figure 6.** Ma-ANN algorithm performance for the validation data

## 8. CONCLUSION

The road management need for planning was the ideal justification for doing this study by finding hybrid techniques that provide accurate forecasting of the road's status during different phases of time, leading to optimal planning for a comprehensive and effective maintenance approach. This study came to meet the requirements of southern Baghdad road to maintenance in order to develop an innovative methodology to predict the road state according to studying various factors.

The output of the (MC-ANN) was highly accurate and yielded an RMSE of 0.02109 and 0.006758 for the data collected for the selected route. Which had more accurate results and better performance than the (ANN) algorithm, which resulted in RMSE of 0.02342 and 0.007657 for the same data, respectively. The technique of combining (ANN) and the Markov chain was reliable and effective when predicting the state of the southern Baghdad road. The developed model (MC-ANN) can be considered a very powerful and flexible tool for highway engineers to be effectively used in planning and budget estimation activities. The developed prioritization model was built based on the current circumstances of Iraq. So, the factors entered into the (MC-ANN) can be changed with regard to the changes in future circumstances.

The study reached that the prediction results of the hybrid approach were compared with the data collected for the chosen road and it was found very close with a slight mean square error of 0.0195, and a correlation coefficient of 0.94 between inspected and predicted road conditions when using a valid collected dataset. That means the reliability of the technique used to give prediction results is very close to reality.

## 9. ACKNOWLEDGMENT

The University of Wasit supported this project. I thank the roads and bridges directorate of Wasit, who provided the information related to the pavement condition rating and all other data of the selected road.

## 10. REFERENCES

1. Velmurugan, R.S. and Dhingra, T., "Maintenance strategy selection and its impact in maintenance function: A conceptual framework", *International Journal of Operations & Production Management*, Vol. 35, No. 12, (2015), 1622-1661. doi: 10.1108/IJOPM-01-2014-0028.
2. Shadhar, A. and Raof Mahjoob, A., "Pavement maintenance management using multi-objective optimization:(case study: Wasit governorate-iraq)", *International Journal of Engineering, Transactions B: Applications*, Vol. 33, No. 11, (2020), 2155-2161. doi: 10.5829/IJE.2020.33.11B.05.
3. Shafiee, M. and Sørensen, J.D., "Maintenance optimization and inspection planning of wind energy assets: Models, methods and strategies", *Reliability Engineering & System Safety*, Vol. 192, (2019), 105993. doi: 10.1016/j.res.2017.10.025.
4. Abd Rani, N.A., Baharum, M.R., Akbar, A.R.N. and Nawawi, A.H., "Perception of maintenance management strategy on healthcare facilities", *Procedia-Social and Behavioral Sciences*, Vol. 170, No., (2015), 272-281. doi: 10.1016/j.sbspro.2015.01.037.
5. Gao, L. and Zhang, Z., "Management of pavement maintenance, rehabilitation, and reconstruction through network partition", *Transportation Research Record*, Vol. 2366, No. 1, (2013), 59-63. <https://doi.org/10.3141/2366-07>
6. Mahjoob, A.R. and Shadhar, A.K., "Roadway deterioration prediction using markov chain modeling (wasit governorate/iraq as a case study)", in 2019 12th International Conference on Developments in eSystems Engineering (DeSE), IEEE., (2019), 326-331.
7. Li, Z. and Sinha, K.C., "Methodology for multicriteria decision making in highway asset management", *Transportation Research Record*, Vol. 1885, No. 1, (2004), 79-87. <https://doi.org/10.3141/1885-12>
8. Prozzi, J. and Madanat, S., "Development of pavement performance models by combining experimental and field data", (2004). doi: <https://doi.org/10.1061>
9. Kim, S.-H. and Kim, N., "Development of performance prediction models in flexible pavement using regression analysis method", *KSCE Journal of Civil Engineering*, Vol. 10, No. 2, (2006), 91-96. doi: 10.1007/BF02823926.
10. Jiang, Y., Saito, M. and Sinha, K.C., "Bridge performance prediction model using the markov chain, (1988).
11. Shin, H.C., "Development of a semi-parametric stochastic model of asphalt pavement crack initiation", *KSCE Journal of Civil Engineering*, Vol. 10, No. 3, (2006), 189-194. <https://doi.org/10.1007/BF02824060>
12. Loizos, A. and Karlaftis, M.G., "Prediction of pavement crack initiation from in-service pavements: A duration model approach", *Transportation research record*, Vol. 1940, No. 1, (2005), 38-42. <https://doi.org/10.1177/0361198105194000105>
13. Kaito, K. and Kobayashi, K., "Bayesian estimation of markov deterioration hazard model", *Journal of Japan Society of Civil Engineers*, Vol. 63, (2007). doi: <https://doi.org/10.2208/jsceja.63.336>
14. Kobayashi, K., Do, M. and Han, D., "Estimation of markovian transition probabilities for pavement deterioration forecasting", *KSCE Journal of Civil Engineering*, Vol. 14, No. 3, (2010), 343-351. doi: 10.1007/s12205-010-0343-x.
15. Attoh-Okine, N.O., "Predicting roughness progression in flexible pavements using artificial neural networks", in Transportation research board conference proceedings. Vol. 1, No. Issue, (1994).
16. Attoh-Okine, N.O., "Analysis of learning rate and momentum term in backpropagation neural network algorithm trained to predict pavement performance", *Advances in Engineering Software*, Vol. 30, No. 4, (1999), 291-302. doi.
17. Owusu-Ababio, S., "Application of neural networks to modeling thick asphalt pavement performance", *Artificial Intelligence and Mathematical Methods in Pavement and Geomechanical Systems*, (1998), 23-30.
18. Lin, J.-D., Yau, J.-T. and Hsiao, L.-H., "Correlation analysis between international roughness index (iri) and pavement distress by neural network", in 82nd Annual Meeting of the Transportation Research Board. Vol. 12, (2003), 1-21.
19. Choi, J.H., Adams, T.M. and Bahia, H.U., "Pavement roughness modeling using back-propagation neural networks", *Computer-Aided Civil and Infrastructure Engineering*, Vol. 19, No. 4, (2004), 295-303. <https://doi.org/10.1111/j.1467-8667.2004.00356.x>

20. Thube, D.T., "Artificial neural network (ANN) based pavement deterioration models for low volume roads in india", *International Journal of Pavement Research and Technology*, Vol. 5, No. 2, (2012), 115. [http://www.ijprt.org.tw/files/sample/V5N2-\(115-120\).pdf](http://www.ijprt.org.tw/files/sample/V5N2-(115-120).pdf)
21. Kırbas, U. and Karasahin, M., "Performance models for hot mix asphalt pavements in urban roads", *Construction and Building Materials*, Vol. 116, (2016), 281-288. <https://doi.org/10.1016/j.conbuildmat.2016.04.118>
22. Choi, S. and Do, M., "Prediction of asphalt pavement service life using deep learning", *International Journal of Highway Engineering*, Vol. 20, No. 2, (2018), 57-65. <https://doi.org/10.7855/IJHE.2018.20.2.057>
23. Tabatabaee, N., Ziyadi, M. and Shafahi, Y., "Two-stage support vector classifier and recurrent neural network predictor for pavement performance modeling", *Journal of Infrastructure Systems*, Vol. 19, No. 3, (2013), 266-274. doi: 10.1061/(ASCE)IS.1943-555X.0000132.
24. Tavana Amlashi, A., Alidoust, P., Pazhouhi, M., Pourrostami Niavol, K., Khabiri, S. and Ghanizadeh, A.R., "AI-based formulation for mechanical and workability properties of eco-friendly concrete made by waste foundry sand", *Journal of Materials in Civil Engineering*, Vol. 33, No. 4, (2021), 04021038. doi: 10.1061/(ASCE)MT.1943-5533.0003645.
25. Luckey, D., Fritz, H., Legatiuk, D., Dragos, K. and Smarsly, K., "Artificial intelligence techniques for smart city applications", in *International Conference on Computing in Civil and Building Engineering*, Springer., (2020), 3-15.
26. Giang, D.T. and Pheng, L.S., "Role of construction in economic development: Review of key concepts in the past 40 years", *Habitat International*, Vol. 35, No. 1, (2011), 118-125. <https://doi.org/10.1016/j.habitatint.2010.06.003>
27. Barbosa, F., Woetzel, J. and Mischke, J., *Reinventing construction: A route of higher productivity*. 2017, McKinsey Global Institute.
28. Donepudi, P.K., Ahmed, A.A.A. and Saha, S., "Emerging market economy (eme) and artificial intelligence (ai): Consequences for the future of jobs", *PalArch's Journal of Archaeology of Egypt/Egyptology*, Vol. 17, No. 6, (2020), 5562-5574. doi: 10.5281/zenodo.5562662.
29. Stojčić, M., Zavadskas, E.K., Pamučar, D., Stević, Ž. and Mardani, A., "Application of mcdm methods in sustainability engineering: A literature review 2008–2018", *Symmetry*, Vol. 11, No. 3, (2019), 350. <https://doi.org/10.3390/sym11030350>
30. Shirowzhan, S., Tan, W. and Sepasgozar, S.M., *Digital twin and cybergis for improving connectivity and measuring the impact of infrastructure construction planning in smart cities*. 2020, MDPI.240.
31. Taeihagh, A., "Governance of artificial intelligence", *Policy and Society*, Vol. 40, No. 2, (2021), 137-157. <https://doi.org/10.1080/14494035-2021.1928377>
32. Pamučar, D., Božanić, D., Lukovac, V. and Komazec, N., "Normalized weighted geometric bonferroni mean operator of interval rough numbers—application in interval rough dematel-copras model", *Facta Universitatis. Series: Mechanical Engineering*, Vol. 16, No. 2, (2018), 171-191. <https://doi.org/10.22190/FUME180503018P>
33. Mardani, A., Streimikiene, D., Zavadskas, E.K., Cavallaro, F., Nilashi, M., Jusoh, A. and Zare, H., "Application of structural equation modeling (SEM) to solve environmental sustainability problems: A comprehensive review and meta-analysis", *Sustainability*, Vol. 9, No. 10, (2017), 1814. <https://doi.org/10.3390/su9101814>
34. Mardani, A., Zavadskas, E.K., Govindan, K., Amat Senin, A. and Jusoh, A., "Vikor technique: A systematic review of the state of the art literature on methodologies and applications", *Sustainability*, Vol. 8, No. 1, (2016), 37. <https://doi.org/10.3390/su8010037>
35. De la Fuente, A., Blanco, A., Armengou, J. and Aguado, A., "Sustainability based-approach to determine the concrete type and reinforcement configuration of tbm tunnels linings. Case study: Extension line to barcelona airport t1", *Tunnelling and Underground Space Technology*, Vol. 61, (2017), 179-188. <https://doi.org/10.1016/j.tust.2016.10.008>
36. Goralski, M.A. and Tan, T.K., "Artificial intelligence and sustainable development", *The International Journal of Management Education*, Vol. 18, No. 1, (2020), 100330. doi: 10.1016/j.ijme.2019.100330.
37. Feroz, A.K., Zo, H. and Chiravuri, A., "Digital transformation and environmental sustainability: A review and research agenda", *Sustainability*, Vol. 13, No. 3, (2021), 1530. <https://doi.org/10.3390/su-13031530>
38. Zubaidi, S.L., Ortega-Martorell, S., Kot, P., Alkhaddar, R.M., Abdellatif, M., Gharghan, S.K., Ahmed, M.S. and Hashim, K., "A method for predicting long-term municipal water demands under climate change", *Water Resources Management*, Vol. 34, No. 3, (2020), 1265-1279. <https://doi.org/10.1007/s11269-020-02500-z>
39. Di Vaio, A., Palladino, R., Hassan, R. and Escobar, O., "Artificial intelligence and business models in the sustainable development goals perspective: A systematic literature review", *Journal of Business Research*, Vol. 121, (2020), 283-314. doi: 10.1016/j.jbusres-2020.08.019.
40. Patrício, D.I. and Rieder, R., "Computer vision and artificial intelligence in precision agriculture for grain crops: A systematic review", *Computers and electronics in agriculture*, Vol. 153, (2018), 69-81. <https://doi.org/10.1016/j.compag.2018.08.001>
41. Wei, Q. and Qingna, L., "Construction of cultural industry development factor model based on factor analysis, artificial intelligence and big data", *Microprocessors and Microsystems*, Vol. 82, (2021), 103880. <https://doi.org/10.1016/j.micpro.2021.103880>
42. Manzoor, B. and Othman, I., Safety management model during construction focusing on building information modeling (bim), in *Advances in civil engineering materials*. 2021, Springer.31-37.
43. Zhu, X., "Research on the reform of higher automotive engineering education under the background of artificial intelligence", in *E3S Web of Conferences*, EDP Sciences. Vol. 245, (2021), 03091.
44. Rezaei, H., Motameni, H. and Barzegar, B., "A hidden markov model for morphology of compound roles in persian text part of tagging", *International Journal of Engineering, Transactions B: Applications*, Vol. 34, No. 11, (2021), 2494-2507. doi: 10.5829/IJE.2021.34.11B.12.
45. Araszkievicz, K., "Digital technologies in facility management—the state of practice and research challenges", *Procedia Engineering*, Vol. 196, (2017), 1034-1042. <https://doi.org/10.1016/j.proeng.2017.08.059>
46. Moreira, I., Pimentel, C., Barros, F.P. and Chaves, D.P., "Modeling fading channels with binary erasure finite-state markov channels", *IEEE Transactions on Vehicular Technology*, Vol. 66, No. 5, (2016), 4429-4434. doi: 10.1109/TVT.2016.2597743.
47. Edirisinghe, R., Setunge, S. and Zhang, G., "Markov model—based building deterioration prediction and iso factor analysis for building management", *Journal of Management in Engineering*, Vol. 31, No. 6, (2015), 04015009. <https://ascelibrary.org/doi/abs/10.1061/%28ASCE%29ME.1943-5479.0000359>
48. Cutore, P., Campisano, A., Kapelan, Z., Modica, C. and Savic, D., "Probabilistic prediction of urban water consumption using the scem-ua algorithm", *Urban Water Journal*, Vol. 5, No. 2, (2008), 125-132. <https://doi.org/10.1080/15730620701754434>

49. Yucel, M., Nigdeli, S.M. and Bekdaş, G., Artificial neural networks (anns) and solution of civil engineering problems: Anns and prediction applications, in Artificial intelligence and machine learning applications in civil, mechanical, and industrial engineering. 2020, IGI Global.13-38.
50. Ansari, R., Banihashemi, S., Taherkhani, R. and Moradi, S., "Decision support system for analyzing key performance indicators in construction projects management", *International Journal of Engineering, Transactions B: Applications*, Vol. 35, No. 5, (2022), 865-874. doi: 10.5829/IJE.2022.35.05B.03.

---

### Persian Abstract

---

#### چکیده

پیش‌بینی دقیق وضعیت جاده‌ها برای خدمات زیرساختی چالش برانگیز است، به‌ویژه زمانی که افزایش حجم ترافیک در نظر گرفته شود. به این ترتیب، این اولین مطالعه انجام شده در عراق است که بر پیش‌بینی وخامت وضعیت جاده‌ها و ارتباط آن با حجم ترافیک سالانه، با استفاده از داده‌های پیمایشی جمع‌آوری‌شده طی دوره بین سال‌های ۲۰۱۹ تا ۲۰۲۱ تمرکز دارد. هدف اصلی مطالعه انجام‌شده، بازرسی دقت بود. قابلیت اطمینان و توانایی ترکیبی از تکنیک‌های پیش‌بینی، این ترکیب شامل زنجیره‌های مارکوفین (MCS) و شبکه‌های عصبی مصنوعی (ANN) با نام (MC-ANN) برای پیش‌بینی دقیق وضعیت راه‌ها میان‌مدت تا بلندمدت (سالانه). یافته‌های اصلی این تحقیق مجدد به شرح زیر است: الف) MCS یک روش قدرتمند است که برای پیش‌بینی شرایط آینده بسته به شرایط قبلی استفاده می‌شود. ب) مدل‌سازی شبکه‌های عصبی مصنوعی که قادر به تولید مدل قابل‌اعتمادتری از وضعیت جاده بر اساس تغییر حجم ترافیک جاده‌ای انتخابی، شرایط آب و هوایی و سن جاده هستند، انجام شد. این مطالعه به ضریب همبستگی ۰.۹۴ بین وضعیت جاده بازرسی شده و پیش‌بینی‌شده هنگام استفاده از مجموعه داده‌های جمع‌آوری‌شده معتبر، و میانگین مجذور خطای جزئی ۰.۱۹۵ رسید.

---



## Study on the Application of Sustainable Construction in the Development of the Likupang Special Economic Zone

D. Pangemanan\*, R. Usman Latief, S. Hamzah, R. Arifuddin

Department of Civil Engineering, Universitas Hasanuddin, Indonesia

### PAPER INFO

#### Paper history:

Received 03 August 2022

Received in revised form 30 September 2022

Accepted 01 October 2022

#### Keywords:

Sustainable Development

Sustainability Construction

Understanding Factors

Special Economic Zone Likupang

Mixed Method

### ABSTRACT

Sustainability construction is starting to become a focus in developing countries such as Indonesia. There are many problems that must be considered in the implementation of sustainable construction. The purpose of this study is to analyze the factors that influence the implementation of sustainable construction in the Likupang SEZ project. The method used is a mixed-method to determine various factors that affect sustainable construction. This research involves various stakeholders such as contractors, consultants, academics, company owners, the government, and the community. The results of this study indicate that the economy and government have a positive and significant influence on sustainable construction. Meanwhile, human resource factors and cultural factors have a positive but not significant effect on sustainable construction. The results of this study also show that environmental, social and investment factors have a negative influence on the implementation of sustainable construction. This study concludes that factors that have a positive and significant impact must be strengthened by prioritizing the role of the government in implementing sustainable construction that has an impact on economic factors, while an adequate strategy is needed to reduce the negative impact of factors that have a negative impact on sustainable construction.

doi: 10.5829/ije.2023.36.01a.07

## 1. INTRODUCTION

Various infrastructures being built today are starting to implement the principles of sustainable construction. This causes many factors to be considered, starting from basic aspects such as technical infrastructure and social infrastructure. Technical infrastructure can be the construction of facilities such as roads, bridges, dams, airports, and ports. While social infrastructures such as the construction of school buildings and hospitals. In its development, environmental issues have become a priority aspect. This is caused by the issue of global warming, which became a central issue in development and the environment. Thus, environmental issues become the basis of the development process. In this context, infrastructure development must take into account the environment, society, and economy to ensure its sustainability. It is in this context that the term

sustainable construction becomes the basis for development. An approach is urgently needed to achieve sustainable development that adopts three main pillars in infrastructure development, such as economic, environmental, and social disparities.

The concept of sustainable construction must have an approach to carrying out the series of activities needed to create a physical facility that meets economic, social, and environmental goals at present and in the future. This concept is a way for the construction industry to realize sustainable development by considering social, economic, environmental, and cultural issues. Sustainable development is a development that seeks to meet the needs of the present without compromising the ability of future generations to meet their own needs. Sustainable construction must meet principles such as common goals, understanding, and action plans, compliance with security, safety, health, and

\*Corresponding Author Institutional Email:

[daisypangemanan79@gmail.com](mailto:daisypangemanan79@gmail.com) (D. Pangemanan)

sustainability standards, reducing the use of resources, whether in the form of land, materials, water, natural resources, and human resources, reducing waste generation. , both physical and non-physical, reuse of resources that have been used previously, use of recycled resources, protection and management of the environment through conservation efforts, risk mitigation of safety, health, climate change, and disasters, orientation to the life cycle, orientation to the achievement of the desired quality, technological innovation for continuous improvement, institutional support, leadership, and management in implementation. In its implementation, it is necessary to have good management and involve various related parties as a form of shared responsibility in maintaining the ecosystem. The implementation of sustainable construction has, in fact, not been fully implemented in accordance with the guidelines contained in the regulation of the Minister of Public Works and Public Housing. The application also varies according to regional conditions, the level of mutual understanding, of sustainable construction by construction project stakeholders, the availability of various existing resources in the form of natural resources (materials and building materials), human resources (construction experts, workers, technicians, laboratory staff, etc.), the availability of other resources such as heavy equipment, implementation methods, as well as adequate financial support.

Massive infrastructure development in Indonesia in the last decade has brought Indonesia to a country that focuses on infrastructure development. This can be seen from the many constructions of toll roads, bridges, airports, dams, ports, and special economic zones in Indonesia. One of the focuses on development is the Special Economic Zone (SEZ). The SEZ was built to become a national area in order to support the industrial, economic, education, and tourism sectors. One of the SEZs built in North Sulawesi is Tanjung Pulisan SEZ, Likupang. This SEZ is expected to become an international gateway in eastern Indonesia. Tanjung Pulisan SEZ is 58.5 km from the capital city of North Sulawesi, Manado, and can be reached by road in approximately 1 hour 47 minutes. This SEZ is also supported by an international export-import port in Bitung City, which is 33.4 km away and can be reached in 1 hour 6 minutes. Some of the main components of infrastructure to be built in Tanjung Pulisan SEZ, namely Hotels, Resorts, and Private Piers which are named the golden triangle dock which include Likupang, Wakatobi, and Raja Ampat.

In practice, sustainable construction requires a model that can be implemented easily and in accordance with the technical, environmental, social, and cultural context of the community. The absence of this has created serious problems in its implementation both at the regional and national levels. Several solutions have been created to try

to solve the problem. The government through the Ministry of Public Works and Public Housing (PUPR) has issued Ministerial Regulation Number 9 of 2021 concerning Guidelines for the Implementation of Sustainable Construction as a guide in the implementation of sustainable construction, but its implementation is still constrained by the diverse context in society which is the subject of this sustainable construction implementation. Another solution that is tried to be studied in several studies is to model sustainable construction well. One of the studies made is the development of a framework in order to achieve sustainable construction [1]. In addition, the human resource factor is tried to be included as a determining factor in the success of sustainable construction management [2]. Human resources also include commitment and performance on various construction projects [3]. Modeling of sustainable construction has been tried by taking into account government, cost, knowledge and information, workforce, and client and market factors. This model has been implemented in Malaysia [4]. Factors that need to be considered are cultural factors as factors that are tried to be included as important factors in environmental sustainability by taking into account the factors of attitudes, company culture, and social responsibility [5]. A holistic solution is needed in building an appropriate model [6]. Sustainable construction is very important to pay attention to local communities as part of the overall model [7]. The absence of a holistic sustainable construction model requires a comprehensive solution by conducting an in-depth study to formulate the right model for implementing sustainable construction. Some of the solutions that have been tried have not been able to solve the problem comprehensively, especially the problems that arise as a result of local wisdom that is not paid attention to in the context of implementing sustainable construction, so it is necessary to conduct an in-depth study to formulate it. Other problems that arise because of this gap, such as government regulations regarding the availability of procurement documents based on sustainable construction are still not consistently implemented during the selection of service providers. In addition, several obstacles need to be overcome by building a model that can be a guide in the implementation of this sustainable construction. These obstacles are in the form of sustainable construction stages, namely aspects of programming, technical planning, construction implementation, utilization, and demolition.

In this study, it is seen that there is a gap that occurs due to the absence of a model due to the many factors that contribute to sustainable construction, so it is very important to conduct a study of these various factors which can later be used as a model of sustainable construction. Several models that have been built

previously are difficult to implement because these factors are not compatible with the local culture in the area. The factors listed in some of these models have several drawbacks such as being too simple and difficult to implement in the field, even though sustainable construction involves many complex factors. On the other hand, in Tanjung Pulisan Likupang SEZ area, cultural factors are a decisive factor, because many local pearls of wisdom are continuously maintained and legalized through village regulations and regional regulations. This causes these models to be difficult to implement. Therefore, it is urgently needed a comprehensive study that contributes to a sustainable construction model that is holistic in nature and becomes a guide for all stakeholders of sustainable construction so that its implementation becomes easier. In this study, a study was conducted on various factors that contributed to the sustainable construction model such as Economic, Social, Environmental, Regulatory, experience, and investment as pre-existing factors. However, these factors have not been holistic, so this study tries to propose a new model that incorporates local cultural/wisdom factors as a new factor in shaping the success of sustainable construction. Thus, it is hoped that a new model of sustainable construction will be formed that is easier to implement.

## 2. METHOD

The research method used is a mixed-method between quantitative and qualitative methods. Mixed Methods Research is a research design based on philosophical assumptions as well as the method of inquiry. Mixed Methods Research is also referred to as a methodology that provides philosophical assumptions in showing directions or giving instructions on how to collect data and analyze data as well as a combination of quantitative and qualitative approaches through several phases of the research process. As a method, mixed methods research focuses on data collection and analysis and combines quantitative data and qualitative data in both a single study and a series study. The central premise that is used as the basis for mixed methods research is to use a combination of quantitative and qualitative approaches to find better research results than using only one approach (for example, with a quantitative approach or a qualitative approach only).

Researchers use this method because mixed method research produces more comprehensive facts in researching research problems. Thus, researchers have the freedom to use all data collection tools according to the type of data needed. The combined method combines quantitative and qualitative research. Researchers choose to conduct research with a qualitative approach first and then proceed with quantitative research, or vice versa. This

is to first see the characteristics of the data in the field, prove the model and justify the results being analyzed. In the quantitative method, the nature of reality is single, classified, concrete, observable and measurable. Then the researcher continued with the qualitative method to analyze the data holistically, dynamically, the results of the construction, and gain understanding to build a strategy according to the research objectives to be achieved (see Figure 1).

For qualitative methods, researchers use to build a strategy to be achieved. The strategy in question is the method chosen so that the achievement of goals can be effective and efficient. This research strategy is related to the acquisition of data in accordance with the indicators of each variable or symptom studied. To be able to prove that the data is an indicator of a variable or a symptom, there are two strategies that can be used, namely by understanding. These two types of strategies each have their own goals.

The first strategy is the measurement strategy, which aims to determine the amount of data that is realized in the form of numbers. All symptoms can be converted into numbers, where this number shows the size or quality of the indicator of the variable. After being measured, then calculated. This process is called the data quantification process, so the resulting data are called quantitative data. While the second strategy is an understanding strategy, namely by seeking deeper information about what is the meaning behind the symptoms that appear from the outside. Researchers are required to understand how research subjects think, behave in accordance with what they do every day in their lives. This is done in-depth and continuously so that the researcher spends time with the subject under study. In this way, the researcher can really understand what is the meaning behind the behavior of the study subject.

To analyze the model and prove the factors that influence the sustainable construction approach, the researcher uses quantitative analysis with SEM models and PLS tools. PLS was chosen to be used by considering the amount of data analyzed, which is less than 100 respondent data. Thus, PLS is the right choice for calculating because it is more suitable and accurate for calculating data that amounts to less than 100 with a high level of accuracy.

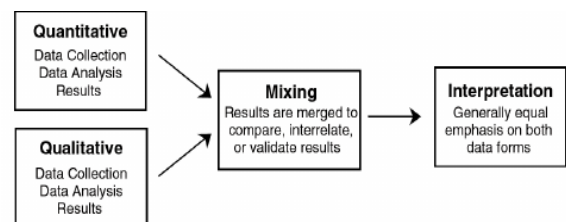


Figure 1. Mix method

### 3. RESULTS AND DISCUSSION

#### 3. 1. Validity and Reliability Calculation Results

The results of the calculation of validity were carried out using the Convergent Validity test (Average Variance Extracted (AVE)). This technique is to measure the Average Variance Extracted value with the measurement value (Average Variance Extracted (AVE)) must meet the value of each variable, which is  $\geq 0.5$ . see Table 1.

The result of calculating the Average Variance Extracted value shows that all the calculated factors have a value greater than 0.5. The results of the Discriminant Validity (Fornell Lacker Criterion) calculation are carried out to determine the value of the Discriminant Validity (Fornell Lacker Criterion) validity, which is the correlation value between the variable itself and variables with other variables, cannot be smaller than other variables. The valid value must be greater between the value of the variable itself and other variables. The results are summarized in Table 2.

The results of the calculations showed that the value of Counting Discriminant Validity (Fornell Lacker Criterion) has fulfilled the requirements of all the calculated variables. The value of validity is also

continued by calculating the value of Discriminant Validity (Cross Loading) which is a validity test between the indicator value that measures the variable itself and the value of other indicator variables. The validity value must be greater than the indicator with other variables. The results of calculating Discriminant Validity (Cross Loading) the correlation between indicators and variables can be seen in Table 3.

**TABLE 1.** Average Variance Extracted

Variabel	Cronbach's Alpha	rho_A	Composite Reliability	AVE
X1 (EK)	0.833	0.838	0.888	0.666
X2 (LI)	0.895	0.918	0.922	0.702
X3 (SO)	0.784	0.702	0.859	0.604
X4 (PE)	0.865	0.883	0.902	0.648
X5 (IN)	0.857	0.874	0.902	0.697
X6 (SDM)	0.927	0.934	0.940	0.662
X7 (BU)	0.791	0.816	0.877	0.704
Y (SC)	0.831	0.832	0.887	0.664

**TABLE 2.** Value of Compute Discriminant Validity (Fornell Larcker Criterion)

Variabel	X1 (EK)	X2 (LI)	X3 (SO)	X4 (PE)	X5 (IN)	X6 (SDM)	X7 (BU)	Y (SC)
X1 (EK)	0.816							
X2 (LI)	0.649	0.838						
X3 (SO)	0.537	0.578	0.777					
X4 (PE)	0.562	0.782	0.605	0.805				
X5 (IN)	0.610	0.663	0.692	0.725	0.835			
X6 (SDM)	0.646	0.757	0.598	0.701	0.698	0.813		
X7 (BU)	0.439	0.526	0.434	0.523	0.482	0.652	0.839	
Y (SC)	0.512	0.481	0.400	0.568	0.444	0.568	0.543	0.815

**TABLE 3.** Value of Discriminant Validity (Cross Loading)

	X1 (Eco)	X2 (Env)	X3 (SOC)	X4 (Gov)	X5 (IN)	X6 (HRM)	X7 (Cul)	Y (SC)
BU3	0,367	0.031	0.349	0.438	0.329	0.492	0.842	0.440
BU4	0.323	0.369	0.392	0.391	0.537	0.507	0.795	0.373
BU5	0.405	0.531	0.361	0.479	0.380	0.628	0.878	0.532
EK1	0.860	0.593	0.429	0.482	0.527	0.499	0.289	0.404
EK2	0.797	0.413	0.345	0.388	0.484	0.460	0.250	0.388
EK3	0.782	0.520	0.503	0.508	0.552	0.600	0.414	0.393
EK4	0.823	0.581	0.469	0.457	0.440	0.547	0.458	0.475
IN1	0.461	0.602	0.584	0.684	0.850	0.593	0.424	0.398
IN2	0.470	0.474	0.535	0.621	0.793	0.499	0.292	0.266

IN3	0.457	0.419	0.598	0.469	0.850	0.534	0.384	0.353
IN4	0.628	0.675	0.589	0.640	0.845	0.672	0.472	0.430
LI1	0.640	0.864	0.611	0.761	0.618	0.704	0.465	0.524
LI2	0.471	0.838	0.335	0.602	0.467	0.569	0.297	0.316
LI3	0.561	0.859	0.401	0.606	0.455	0.587	0.476	0.375
LI4	0.470	0.808	0.561	0.668	0.527	0.617	0.448	0.381
LI5	0.536	0.820	0.443	0.595	0.686	0.665	0.492	0.358
PE1	0.256	0.470	0.347	0.763	0.376	0.438	0.322	0.427
PE2	0.506	0.656	0.476	0.866	0.558	0.631	0.477	0.569
PE3	0.486	0.715	0.584	0.822	0.744	0.631	0.515	0.467
PE4	0.559	0.701	0.497	0.809	0.633	0.576	0.355	0.442
PE5	0.446	0.606	0.559	0.761	0.624	0.527	0.429	0.334
SC1	0.313	0.231	0.146	0.431	0.247	0.361	0.383	0.809
SC2	0.337	0.321	0.247	0.419	0.289	0.375	0.336	0.882
SC3	0.464	0.472	0.425	0.499	0.424	0.477	0.446	0.795
SC4	0.510	0.493	0.434	0.479	0.446	0.587	0.556	0.769
SDM10	0.408	0.553	0.408	0.518	0.477	0.808	0.493	0.403
SDM11	0.499	0.659	0.477	0.578	0.570	0.879	0.580	0.518
SDM2	0.510	0.596	0.522	0.549	0.546	0.797	0.535	0.562
SDM3	0.567	0.633	0.514	0.566	0.575	0.812	0.506	0.382
SDM4	0.539	0.685	0.539	0.650	0.635	0.840	0.573	0.505
SDM5	0.617	0.617	0.512	0.648	0.615	0.828	0.596	0.416
SDM6	0.557	0.544	0.482	0.489	0.529	0.738	0.480	0.405
SDM8	0.524	0.625	0.425	0.555	0.588	0.798	0.465	0.446
SO2	0.519	0.481	0.763	0.453	0.515	0.469	0.270	0.320
SO3	0.482	0.464	0.818	0.567	0.649	0.474	0.336	0.260
SO4	0.292	0.378	0.812	0.396	0.471	0.472	0.365	0.382
SO5	0.417	0.510	0.711	0.514	0.564	0.446	0.388	0.246

The calculation results showed that the discriminant validity (Cross Loading) has met the requirements. The results of Computing Reliability (Composite Reliability and Cronbach's Alpha) are the results of Computing Reliability (Composite Reliability and Cronbach's Alpha) which are defined as the efficacy of the instrument in measuring the indicator value. Reliability Count Value (Composite Reliability and Cronbach's Alpha) must be  $> 0.7$ . the calculation results can be seen in Table 4.

The calculation results have shown that the calculated reliability value (Composite Reliability and Cronbach's Alpha) is greater than 0.7; so it can be said that the instrument is reliable and effective for use in research.

**3. 2. Model Evaluation Results** The results of the model evaluation are carried out by calculating several indicators as follows:

### 3. 2. 1. Model Evaluation Results: Inner Model Test (R-Square)

The value of the Inner Model Test (R-

**TABLE 4.** Value of Compute Reliability (Composite Reliability and Cronbach's Alpha)

Variabel	Cronbach's Alpha	rho_A	Composite Reliability	AVE
X1 (EK)	0.833	0.838	0.888	0.666
X2 (LI)	0.895	0.918	0.922	0.702
X3 (SO)	0.784	0.702	0.859	0.604
X4 (PE)	0.865	0.883	0.902	0.648
X5 (IN)	0.857	0.874	0.902	0.697
X6 (SDM)	0.927	0.934	0.940	0.662
X7 (BU)	0.791	0.816	0.877	0.704
Y (SC)	0.831	0.832	0.887	0.664



**TABLE 7.** Model calculation results: Inner Model Test (Significance T-STATISTIC)

	Original Sample (O)	Sample mean (M)	Standard Deviasi (STDEV)	T Statistics (O/STDEV)	P Values
X1(EK)->Y(SC)	0.256	0.254	0.116	2.203	0.028
X2(LI)->Y(SC)	-0.191	-0.160	0.197	0.972	0.331
X3(SOI)->Y(SC)	-0.008	0.004	0.166	0.047	0.963
X4(PE)->Y(SC)	0.403	0.376	0.199	1.016	0.043
X5[IN]->Y(SCI)	-0.131	-0.130	0.143	0.916	0.360
X6(SDM)->Y(SC)	0.189	0.193	0.175	1.078	0.282
X7(BUI)-> Y(SC)	0.264	0.249	0.139	1.898	0.058
X1(EK)->Y(SC)	0.256	0.254	0.116	2.203	0.028

(culture) has a calculated value of 0.264 which means it has a positive effect on the sustainable construction variable but is not significant on the Y variable because it only has a T-statistic value of 1.898. Thus, human resources and cultural factors do have a positive effect on sustainable construction but do not significantly affect the sustainable construction factor. This means that these two factors must be considered when implementing sustainable construction in Likupang SEZ. The opposite happened to X2 factor, namely the environment. The result of the calculation shows that the environment variable has a negative effect of -0.192 and only has a T-statistical value of 0.972 which means it is smaller than the standard T-statistical significance of 1.96. Thus, environmental factors only have a negative and insignificant effect on sustainable construction. In factor X3, namely social factors, the calculation results show a value of -0.008 which is smaller than 0 so it can be concluded that social variables have a negative effect on sustainable construction. While the T-statistic significance value shows a value of 0.047 which is smaller than the accepted value of 1.96 it is concluded that it is not significant for the sustainable construction variable. The same thing happened to X5 variable, namely investment. The results of the calculation show that X5 value is only -0.131 so it has a negative effect and only has a T-statistic value of 0.916 less than the accepted value of 1.96 so it can be said that it is not significant to the variable Y Sustainable construction. Thus, it can be said that both environmental, social and investment variables only have a negative effect on sustainable construction. This could be because Likupang SEZ development process with a sustainable construction approach still pays attention to the profitability value so that it still does not pay attention to the environment, social and investment.

The results of this study are in line with those stated by El-Mahdy, et al. [8] The use of building construction materials with a sustainable construction approach can reduce production costs so that they become more efficient and make construction materials by utilizing

widely available sand and salt. On the other hand, the model fits with the local wisdom of Egyptian people. The material used is very supportive of climate change because it is environmentally friendly [9]. The findings focus on materials that support sustainable construction that can contribute to economic and environmental factors. Meanwhile, in this study, the researchers focused on a broader issue, namely the sustainable construction model. It is proven that economic and environmental factors have contributed to sustainable construction. The same thing was found by Nasereddin and Andrew [10] that the cost of capital is strongly related to the success of sustainable construction. The capital costs incurred with the sustainable construction approach provide better benefits and reduce operational costs so that costs become cheaper [11]. This model is well received in Jordan. These results are in line with what was found in this study, namely that economic factors in the form of capital have an influence on the implementation of sustainable construction.

In the process of reducing waste, researchers Liu, et al. [12] found that the BIM algorithm can be used to carry out simulations in proactive planning so that it can save materials and provide solutions for sustainable construction. This model can reduce material waste by enabling savings on material cutting for the roof shroud layout. This model can reduce material waste and cost-efficiency. This research provides adequate support for economic and environmental factors in this study. Thus, the economic factor has become one of the key factors in the successful implementation of sustainable construction. Other researchers have also shown that the use of excavated material, which is usually a construction waste, can be used as a construction material by utilizing a stable mixture of soil, aggregate, and water consolidated with high-velocity projections rather than mechanical compaction to obtain structural and non-structural elements [13]. Thus, the material can be utilized in the application of sustainable construction. This proves that the waste indicator is an indicator that contributes to environmental factors which can

contribute to the implementation of sustainable construction.

The results of this study are in line with what was found by He and Chen [14], who found that the success of sustainable construction is closely related to the professionalism and experience of the project management team and a clear definition of responsibility has the highest driving force, which will also increase the likelihood of success and benefit the performance of sustainable construction projects. The findings give consideration that environmental factors are important to consider as one of the success factors of sustainable construction projects. These results strongly support this research because the professionalism factor is also a human resource factor which is the main finding in this study. The more professional HR involved in sustainable construction projects, the greater the chance of success of sustainable construction projects.

Another finding that strongly corroborates this research is that of Muheise and Pavia [15] who found that clay-based materials produce high-quality bricks that can be used in sustainable construction projects and can save more than 4 million euros in economic savings on kiln fuel and fuel. Carbon taxes in 10 years, and will be about half their carbon emissions, substantially reducing the global environmental impact of brick production. This shows that economic and environmental factors play an important role in the successful implementation of sustainable construction projects.

The use of environmentally friendly materials also has an effect on sustainable construction. Hashmi, et al. [16] findings found that a mixture of fly ash concrete made by replacing cement with fly ash in the range of 25% to 60% with an equivalent weight can make concrete that has a fly ash content of 40% have shown satisfactory performance at age. advanced (ie above 28 days) in terms of strength, modulus of elasticity, and deflection. This shows that environmentally friendly materials are a determining factor in sustainable construction which has been proven in this research.

The government factor is one of the findings in this study, this is related to the policies and regulations issued by the government to support the implementation of sustainable construction projects. This is in line with what was found by Nithya, et al. [17] who found that government support in sustainable construction projects in the form of a zero-waste policy has given a high attractiveness to the implementation of sustainable construction projects. The research shows that the Indian government has implemented a zero-waste strategy in the construction sector, which has successfully implemented sustainable construction in construction projects. This shows that the government factor is also a determining factor in the implementation of sustainable construction which is the finding in this study.

These studies show that the factors that influence projects with a sustainable construction approach are proven to have an influence on the success of sustainable construction projects. These factors include economic, environmental, government, and other factors. The results of this study are also in line with many findings from other researchers who also found research results that are in line with this research, especially on the topic of sustainable construction. There are those who research economic factors, environmentally friendly materials, and policies that can be made by the government.

### 3. 2. 4. Inner Model Test Results (Predictive Relevance)

The results of the Inner Model Test (Predictive Relevance) are values to show how well the observations are made. The results of the Inner Model Test Predictive Relevance are calculated using blindfolding in PLS. Inner Model Test Predictive Relevance has an acceptable value of good observation value if  $> 0$  it can be said that the observation is good (see Table 8).

The results of the calculation show that the results of the Inner Model Test Predictive Relevance show the value to be the conclusion of the observation 0.237. This means that the observations that have been made in this study can be said that the observations are good.

### 3. 2. 5. Inner Model Test Result (Model Fit)

The results of this study have produced a model that was built to test whether the model that has been built is good or not. To measure the model, researchers used the Inner Model Test (Model Fit) (see Figure 2).

The Model Inner Model Test (Model Fit) is a value to determine how well the model being studied is. Acceptance value is measured using the value seen in NFI on PLS (see Table 9).

The calculation results show that the Model Fit value is the NFI value = 0.568. This means that the NFI value has shown that the model built has been good. The percentage of the model built is obtained by  $NFI \times 100\%$ ,

**TABLE 8.** Inner Model Test Results (Predictive Relevance)

Variabel	SSO	SSE	Q <sup>2</sup> (=1-SSE/SSO)
X1 (EK)	324.000	324.000	
X2 (LI)	405.000	405.000	
X3 (SO)	324.000	324.000	
X4 (PE)	405.000	405.000	
X5 (IN)	324.000	324.000	
X6 (SDM)	648.000	648.000	
X7 (BU)	243.000	243.000	
Y (SC)	324.000	247.125	0.237

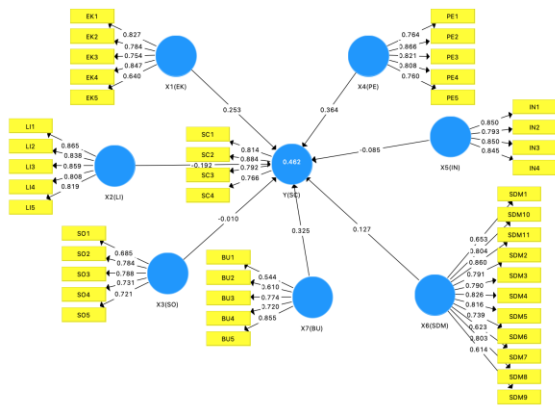


Figure 2. Model fit sustainable construction

TABLE 9. Nilai Inner Model Test (Model Fit)

	Saturated Model	Estimated Model
SRMR	0.092	0.092
d_ULS	5.948	5.948
d_G	3.595	3.595
Chi_Square	1266.411	1266.411
NFI	0.568	0.568

so that the percentage of the model built is obtained by  $NFI = 0.568 \times 100\% = 56.8\%$  Fit model. This means that the sustainable construction model that has been built has 56.8% declared fit and can be implemented in sustainable construction in the Likupang SEZ.

This model is proven to be in line with the results of research put forward by Ristić, et al. [18] who also found that a sustainable construction model with a multi-criteria approach is a good model choice for the development of a sustainable construction model.

The results of this study prove that the model that has been produced can be claimed as a novelty. This novelty can be proven by the results of this study that it has succeeded in building a more holistic model with various factors that make up this sustainable construction model. This model shows that there are 8 (eight) factors that separately contribute to shaping this sustainable construction model. These factors are economic, environmental, social, government, investment, government, human resources, and cultural/local wisdom factors. These factors have been holistically tested with the results of the model fit test of 56.8% and can form a good model. The results of this test indicate that this model can be relied upon in forming a new sustainable construction model. These results can improve the previous model which only consists of 3 factors, namely economic, social and environmental. Thus, the results of this study can claim that improvements in the construction model are sustainable and can be

implemented. The implementation strategy has also been successfully developed by conducting a comprehensive analysis, both internally by taking into account strengths and weaknesses and externally by taking into account current and future opportunities and threats. Thus, the holistic model of sustainable construction that has been produced can be implemented properly.

One of the factors that became interesting findings in this study was the findings on cultural factors/local wisdom. This factor was found to have an influence on the factors of sustainable construction. The successful implementation of sustainable construction must pay attention to cultural factors/local wisdom as an important factor. This finding has improved the previous findings, which only included cultural factors as indicators of social factors. Thus, there has been an improvement in these factors, and can be claimed as a novelty in this study.

The overall results of this study have been carried out with rigorous, valid, and reliable methods and analysis so that the results can be claimed as research findings. The resulting model has been legally proven as a holistic sustainable construction model. This is because the research has used 8 (eight) factors that make up sustainable construction comprehensively. Thus, it can be concluded that this model can be used to update the previous sustainable construction model which only contains 3 factors. The model of the findings of this study is a sustainable construction model that is holistic because it is formed from 8 comprehensive factors as evidenced by valid, valid, and reliable analysis and methods.

#### 4. CONCLUSION

This study concludes that the factors that have been studied can form a model that is produced after fulfilling the requirements as a good model and can be used in the development of sustainable construction. The results of the evidence show that the model produced 56.8% of the model has been good to use. The factors that influence the model have contributed to the development of the model. Several factors have been shown to have a positive and significant effect, such as economic and government factors. While some factors are concluded to have positive factors such as human resource factors and cultural factors. Meanwhile, environmental, social and investment factors have a negative influence on the sustainable construction model in Likupang SEZ. The results of this research conclude that the resulting model can be directly implemented in the development of Likupang SEZ by paying attention to the factors that have a positive influence and stakeholders need to develop a mature strategy in anticipating factors that have a negative influence and maximizing the factors that

contribute positively. so that it is hoped that the implementation of sustainable construction can be successful.

## 5. REFERENCES

- Hammad, A.W., Akbarnezhad, A., Wu, P., Wang, X. and Haddad, A., "Building information modelling-based framework to contrast conventional and modular construction methods through selected sustainability factors", *Journal of Cleaner Production*, Vol. 228, (2019), 1264-1281. <https://doi.org/10.1016/j.jclepro.2019.04.150>
- Sahadi, S. and Wibowo, M.A., "Ketepatan klasifikasi pada pengelompokan manajer proyek konstruksi berdasarkan faktor pengembangan sumber daya manusia menggunakan analisis diskriminan", *Media Komunikasi Teknik Sipil*, Vol. 20, No. 2119-124. <https://doi.org/10.12777/mkts.20.2.119-124>
- Sahadi, S. and Wibowo, M.A., "Pengaruh faktor pengembangan sumber daya manusia terhadap komitmen dan kinerja pada manajer proyek konstruksi", *Media Komunikasi Teknik Sipil*, Vol. 19, No. 167-76. <https://doi.org/10.14710/mkts.v19i1.7836>
- Durdyev, S., Ismail, S., Ihtiyar, A., Bakar, N.F.S.A. and Darko, A., "A partial least squares structural equation modeling (pls-sem) of barriers to sustainable construction in malaysia", *Journal of Cleaner Production*, Vol. 204, (2018), 564-572. <https://doi.org/10.1016/j.jclepro.2018.08.304>
- Ajibike, W., Adeleke, A., Mohamad, F., Bamgbade, J., Nawi, M. and Moshood, T., "An evaluation of environmental sustainability performance via attitudes, social responsibility, and culture: A mediated analysis", *Environmental Challenges*, Vol. 4, (2021), 100161. <https://doi.org/10.1016/j.envc.2021.100161>
- Solaimani, S. and Sedighi, M., "Toward a holistic view on lean sustainable construction: A literature review", *Journal of Cleaner Production*, Vol. 248, (2020), 119213. <https://doi.org/10.1016/j.jclepro.2019.119213>
- Guo, R., Chen, D., Zhou, D., Liu, B., Liu, H., Zhao, Y., Sun, Y. and Fan, J., "The spatial coupling characteristics between the construction of qingzang national park cluster and the sustainable development of local communities", *Geography and Sustainability*, Vol. 2, No. 1, (2021), 1-11. <https://doi.org/10.1016/j.geosus.2021.01.001>
- El-Mahdy, D., Gabr, H.S. and Abdelmohsen, S., "Saltblock as a 3d printed sustainable construction material in hot arid climates", *Journal of Building Engineering*, Vol. 43, (2021), 103134. <https://doi.org/10.1016/j.jobbe.2021.103134>
- Mousavi, S., "Performance of non-fired green brick containing rice husk as sustainable building material", *International Journal of Engineering, Transactions C: Aspects*, Vol. 29, No. 3, (2016), 306-312. <https://doi.org/10.5829/idosi.ije.2016.29.03c.04>
- Nasereddin, M. and Price, A., "Addressing the capital cost barrier to sustainable construction", *Developments in the Built Environment*, Vol. 7, (2021), 100049. <https://doi.org/10.1016/j.dibe.2021.100049>
- Nguyen, D. and Phan, V., "Engineering properties of soil stabilized with cement and fly ash for sustainable road construction", *International Journal of Engineering, Transactions C: Aspects*, Vol. 34, No. 12, (2021), 2665-2671. <https://doi.org/10.5829/IJE.2021.34.12C.12>
- Liu, H., Sydora, C., Altaf, M.S., Han, S. and Al-Hussein, M., "Towards sustainable construction: Bim-enabled design and planning of roof sheathing installation for prefabricated buildings", *Journal of Cleaner Production*, Vol. 235, (2019), 1189-1201. <https://doi.org/10.1016/j.jclepro.2019.07.055>
- Curto, A., Lanzoni, L., Tarantino, A.M. and Viviani, M., "Shot-earth for sustainable constructions", *Construction and Building Materials*, Vol. 239, (2020), 117775. <https://doi.org/10.1016/j.conbuildmat.2019.117775>
- He, Z. and Chen, H., "Critical factors for practicing sustainable construction projects in environmentally fragile regions based on interpretive structural modeling and cross-impact matrix multiplication applied to classification: A case study in china", *Sustainable Cities and Society*, Vol. 74, (2021), 103238. <https://doi.org/10.1016/j.scs.2021.103238>
- Muheise-Araalia, D. and Pavia, S., "Properties of unfired, illitic-clay bricks for sustainable construction", *Construction and Building Materials*, Vol. 268, (2021), 121118. <https://doi.org/10.1016/j.conbuildmat.2020.121118>
- Hashmi, A.F., Shariq, M. and Baqi, A., "An investigation into age-dependent strength, elastic modulus and deflection of low calcium fly ash concrete for sustainable construction", *Construction and Building Materials*, Vol. 283, (2021), 122772. <https://doi.org/10.1016/j.conbuildmat.2021.122772>
- Nithya, M. and Ramasamy, M., "Sustainability in construction industry through zero waste technology in india", *Materials Today: Proceedings*, Vol. 46, (2021), 849-851. <https://doi.org/10.1016/j.matpr.2020.12.851>
- Ristić, V., Maksin, M., Nenković-Riznić, M. and Basarić, J., "Land-use evaluation for sustainable construction in a protected area: A case of sara mountain national park", *Journal of Environmental Management*, Vol. 206, (2018), 430-445. <https://doi.org/10.1016/j.jenvman.2017.09.080>

## Persian Abstract

### چکیده

ساخت و سازه‌های پایدار در حال تبدیل شدن به کانون توجه در کشورهای در حال توسعه مانند اندونزی است. در اجرای ساخت و سازه‌های پایدار مشکلات زیادی وجود دارد که باید مورد توجه قرار گیرد. هدف از این مطالعه تجزیه و تحلیل عواملی است که بر اجرای ساخت و ساز پایدار در پروژه لیکوپانگ SEZ تاثیر می‌گذارد. روش مورد استفاده یک روش ترکیبی برای تعیین عوامل مختلفی است که بر ساخت و ساز پایدار تاثیر می‌گذارد. این تحقیق شامل ذینفعان مختلفی مانند پیمانکاران، مشاوران، دانشگاهیان، صاحبان شرکت‌ها، دولت و جامعه است. نتایج این مطالعه نشان می‌دهد که اقتصاد و دولت بر ساخت و ساز پایدار تاثیر مثبت و معناداری دارند. در این میان، عوامل نیروی انسانی و عوامل فرهنگی بر ساخت و ساز پایدار تاثیر مثبت اما معنادار ندارند. نتایج این مطالعه همچنین نشان می‌دهد که عوامل محیطی، اجتماعی و سرمایه‌گذاری بر اجرای ساخت و سازه‌های پایدار تاثیر منفی دارند. این مطالعه به این نتیجه می‌رسد که عواملی که تاثیر مثبت و معنادار دارند باید با اولویت دادن به نقش دولت در اجرای ساخت و سازه‌های پایدار که بر عوامل اقتصادی تاثیرگذار است، تقویت شوند، در حالی که برای کاهش تاثیر منفی عوامل مؤثر به یک استراتژی کافی نیاز است که تاثیر منفی بر ساخت و ساز پایدار دارد.



## Computational Study of Excitation Controlling Parameters Effect on Uniform Beam Deformation under Vibration

P. Lap-Arparat, K. Tuchinda\*

Material Manufacturing and Surface Engineering Research Center (MaSE), The Sirindhorn International Thai-German Graduate School of Engineering (TGGS), King Mongkut's University of Technology North Bangkok (KMUTNB), Bangkok, Thailand

### PAPER INFO

#### Paper history:

Received 13 August 2022

Received in revised form 30 August 2022

Accepted 18 September 2022

#### Keywords:

Mode Shape Analysis

Geometry Ratio

Structural Response

Shape Deformation

Transverse Vibration

Uniform Beam

### ABSTRACT

Understanding a structure's behavior is necessary for most applications, especially excitation in ultrasonic applications. Currently, ultrasonic devices are used in various fields and have an essential role in nondestructive testing (NDT). The structure's behavior must be concerned with achieving the best practice. The structural vibrational behavior depends on natural frequency and mode shape. This study attempted to determine the effect of influence parameters on shape deformation for designing the adequate excitation condition. In this study, the influence parameters of a uniform beam, including geometry, support condition, and material, were included to investigate their effect on the frequency, mode shape, and structural response. The result showed the significant influence of a structure's length and support condition on the mode frequency, dramatically decreasing mode frequency for extended installation and cantilever support. This study investigated the three common mode shapes revealed that the longitudinal bending shape dominated due to the loading direction. Therefore, the shape deformation of the structure is mainly governed by the external excitation source, and the high structural response is received by applying the excitation near the antinode position of the vibration. Nevertheless, the computational result showed a good agreement with the analytical validation with less than 1 % error. The study leads to understanding the vibration, which can be further used for either the effective sensor attachment or designing the vibration control of ultrasonic applications.

doi: 10.5829/ije.2023.36.01a.08

## 1. INTRODUCTION

Recently, shape deformation due to vibration has been a concern in various contexts, especially structural analysis [1, 2]. A structure's natural frequency ( $\omega_n$ ) is important in structural vibration, showing a less damping force effect [3]. The geometry and material of the structure influence the natural frequency [4-6]. Moreover, the support type also affects the natural frequency. In most cases, the natural frequency is cognizant for a structural study due to the mechanical resonance. The resonant frequency is the frequency of external force that matches the structure's natural frequency and causes a great amplitude of the vibration [7]. Since the incident of Tacoma Narrows Bridge in 1940, when the bridge collapsed due to resonance generated by the wind. The

wind speed was 68 km/h and frequency of 0.2 Hz, nearly close to the bridge's natural frequency (approximately 1 Hz), initiated the vibration of the bridge together with the aeroelastic fluttering. This caused the bridge to oscillate periodically with increasing amplitude in the torsional mode, where the two halves of the bridge twisted in opposite directions before collapsing [8, 9]. The natural frequency and vibrational mode shape of a structure are prime concerns to prevent a recurrence of a similar situation.

Therefore, the vibration study is essential to understand the behavior of the structure. The influence parameters have been investigated for their effect on the vibration. Regarding another researcher's works, many related variables such as boundary conditions [10, 11], stiffness [12], and shape [13] were either experimentally or analytically investigated for their effect on the

\*Corresponding Author Institutional Email: [karuna.t@tggs.kmutnb.ac.th](mailto:karuna.t@tggs.kmutnb.ac.th)  
(K. Tuchinda)

deformation under the vibration. Nevertheless, as reported, those variables influenced the deformation, which should be considered in the vibrational study. Furthermore, some variables were applied to the safety design of the vibration control [14] and structural construction [15-17].

The natural frequency and vibrational mode understanding is currently applied differently for varying applications such as tuning fork and ultrasonic transducer [18, 19]. The design of vibrating devices that are required to operate at resonance to optimize the vibrational amplitude; an example is an ultrasonic transducer. An ultrasonic transducer is a device that converts an electrical signal into a vibration via piezoelectric disks located in between the coupled materials. Generally, the coupled materials have a natural frequency similar to the vibration of the piezoelectric disk; this causes the highest amplitude at the vibrating tip. Furthermore, the mode shape of the vibration is correspondingly designed to perform shape deformation as a targeting purpose, making it operate at a fixed frequency [19]. Nowadays, ultrasonic devices are used in various fields, including medical and industrial [20-22]. Ultrasonic devices have an important role in nondestructive testing (NDT), whether ultrasonic testing or vibrothermography. However, excitation at resonance frequency can cause damage to structures or systems due to the large deformation. Conversely, it can enhance the power of a low-power excitation device.

According to Xu et al. [23], a low-power ultrasonic transducer (5-14 W) was used to apply the excitation for

vibrothermography crack detection. The artificial surface crack was created on a thin beam and clamped on both ends. Under the excitation, the known crack was hardly detected since the power was much lower than the literature, which is up to 2 kW [24]. Although, adjusting the excitation position can improve the detection, which provides a clearer indication of the crack. Consequently, applying an excitation or sensor attachment requires understanding the structural behavior and mode shape to optimize the expected result.

In this study, the structural behavior of the objects was simulated at various frequencies to provide an understanding and the effect of the influenced parameters on a vibrational mode shape. The object's geometry and material were varied, including the support types to provide different degrees of freedom (DOF). The study attempted to understand vibrational behavior to design the effective conditions for excitation based on a laboratory scale of uniform beam excitation. Moreover, steady-state dynamic analysis was applied to investigate each condition's frequency response and structural behavior. The overall research methodology flow is presented as illustrated in Figure 1. This work is the 1st attempt to understand the effect of the geometry ratio including the material and support conditions on vibrational characteristics aiming to develop a computational framework to be used in the design of the excitation controlling system for vibration-based NDT.

## 2. PROCEDURE

### 2.1. Simulation Model Setup

The study of shape deformation and structural behavior was simulated in ABAQUS FEA. In the simulation, a 3-Dimensional model of a rounded rectangular rod was created, as shown in Figure 2. The rectangular rod structure was selected for the study as it is one of the most common structures used for engineering applications. The aspect ratio was applied to differentiate the structure's geometry which has controlled the shape of the structure, as detailed in Table 1. The non-dimensional height of the structure was initially assigned as 10. The scope of the geometry ratio was based on the range of engineering parts used in the industrial automation system which is the main interest of the current work. According to the predefined aspect ratio, 27 models were created and studied under different conditions based on the vibration analysis of a uniform beam. The support conditions were also varied: fixed ends and a cantilever. Moreover, two different metallic materials, i.e., steel and aluminum, were included in the study, and their properties are summarized in Table 2. In total, 108 cases were studied. The 8-node hexahedral elements with reduced integration (C3D8R) were globally applied to optimize the computational time of the simulation model. The work

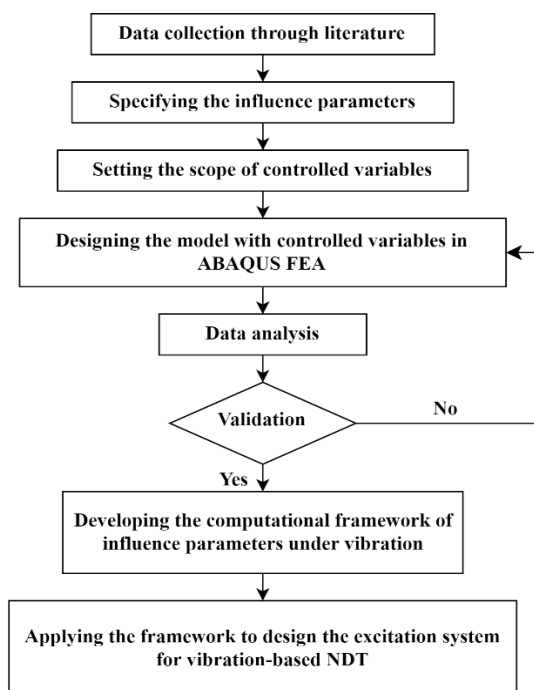


Figure 1. Flowchart of the study

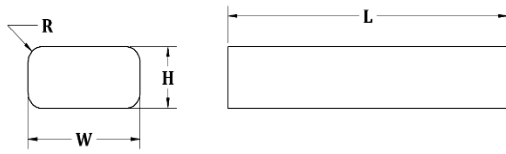


Figure 2. Model shape and dimension

aimed to develop a computational framework to be used in the design of the excitation controlling system for vibration-based NDT from the vibrational characteristic under different conditions of vibration.

**2. 2. Mode Shape Analysis** Frequency analysis of the linear perturbation was applied to investigate the vibrational mode shape of the structure. The effect of the geometry above, including the boundary conditions, on each mode's vibrational frequency, was observed, detailed in section 3. Moreover, the shape and the behavior of deformation were also investigated.

**2. 3. Steady-state Dynamic Analysis** The behavior of the structure under the vibration was studied in the steady-state dynamic modal. A 10 N of harmonic load (P) was applied at different locations of x to investigate the structural behavior, as illustrated in Figure 3.

**3. RESULTS AND DISCUSSION**

The first five modes are taken to show the behavior of the vibration. Three common shapes were included in the first five modes, which were (1) Longitudinal bending, (2) Lateral bending, and (3) Torsional bending (Twist), as shown in Figure 4. The higher order of the mode shape which occurred at higher vibrational frequency provides a more significant number for the antinode vibration, an example of the node and antinode in the structural vibration is illustrated in Figure 5. The effect of the conditions above on mode shape was shown by plotting the vibrational frequency of each mode, as can be seen in Figure 6. From the comparison, the major effect of vibrational frequency was revealed on the length of the structure and the type of support condition. The greater the length significantly decreased the vibrational frequency of each mode, in the same manner as the cantilever support significantly diminished the frequency compared with the fixed ends support. For the corner radius, a minor effect appeared as the larger radius was slightly decreased at the mode shape frequency. Furthermore, the ratio of width to height (W/H) had a complex impact on the frequency, which displayed a noticeable difference in some modes.

However, the ratio dominated the shape deformation; the higher ratio revealed more of the longitudinal bending shape in the first five modes.

**TABLE 1.** Geometry ratio

R/H	W/H	L/H
0	1	10
0.25	2	50
0.5	5	100

**TABLE 2.** Material property

Material	Density (kg/m <sup>3</sup> ) [14]	Elastic modulus (GPa) [14]	Poisson's ratio [15]
Steel	7900	200	0.28
Aluminum	2700	70	0.33

Moreover, the ratio of W/H = 1 has a similar frequency between mode 1 and mode 2 likewise in mode 3 and mode 4. However, the deformation shapes were different, i.e. bending in different directions, as shown in Figure 7. Considering the structure's material, there seemed to be no effect on the vibrational frequency and shape deformation. Lastly, the shapes of each mode are listed in Table 3

Note: the shapes are listed in the following format

X#Y

where X = Bending shape;

B: Longitudinal, LB: Lateral, TB: Torsional

Y = Number of antinodes

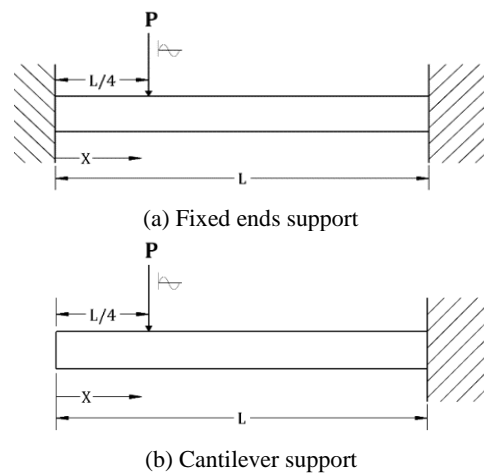


Figure 3. Example model of harmonic load at x = L/4 in steady-state dynamic analysis

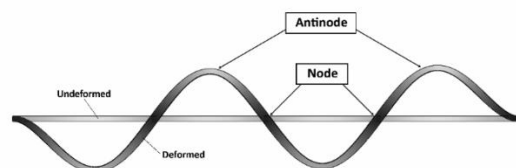
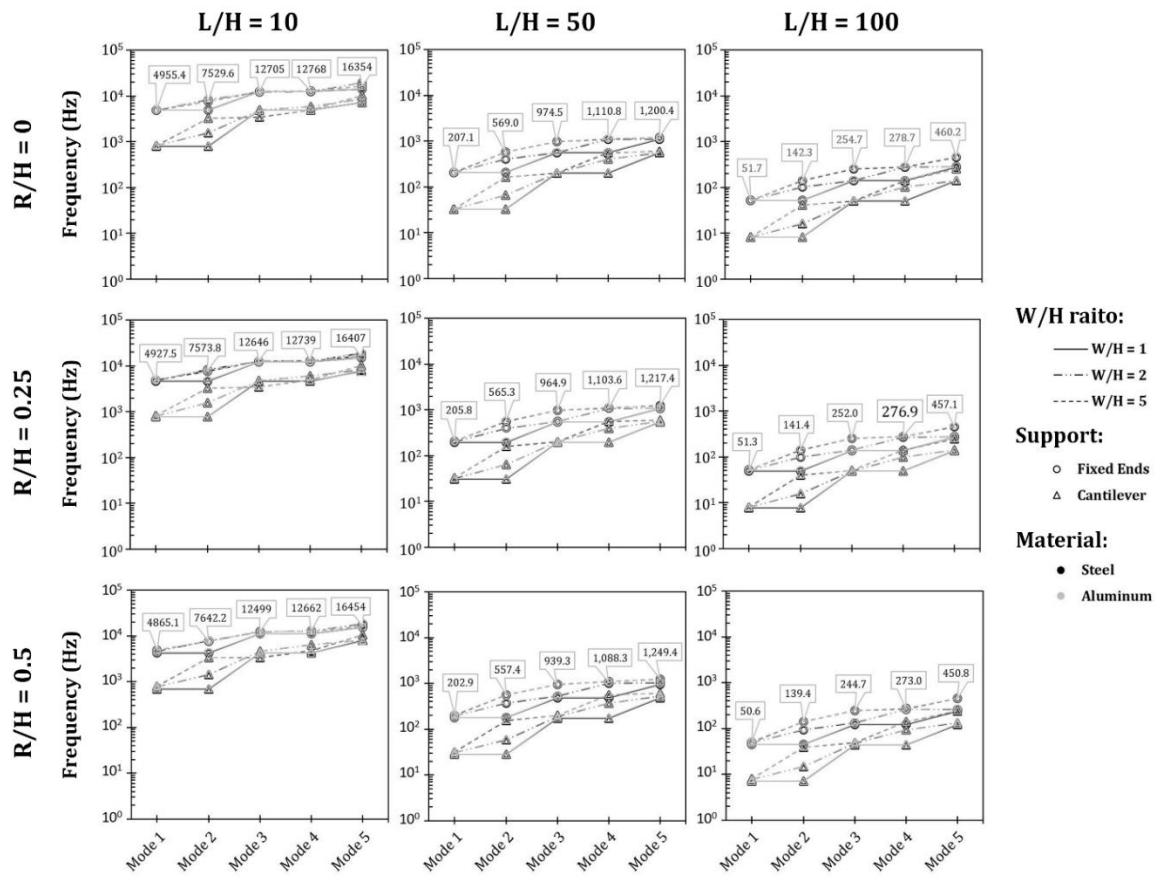
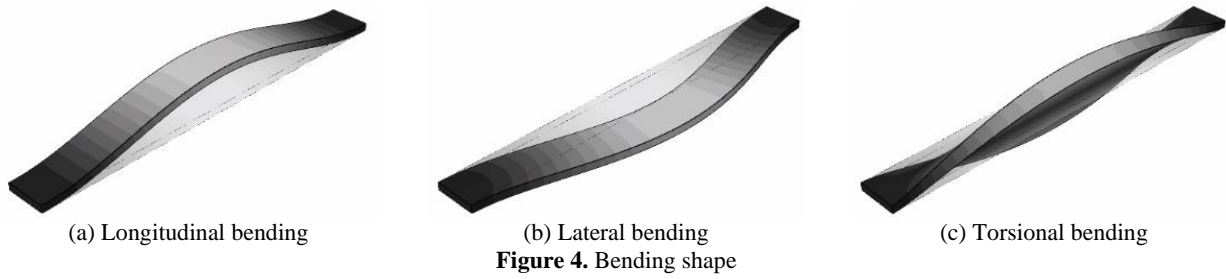
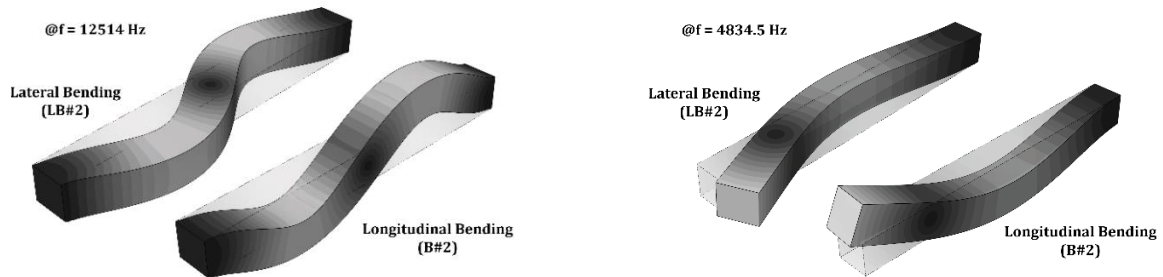


Figure 5. Nodes and antinodes of structural vibration



**Figure 6.** The effect of geometry on the vibrational frequency



(a) Fixed ends support

(b) Cantilever support

**Figure 7.** Example of shape deformation of the geometry ratio  $W/H = 1$  at a similar frequency

**TABLE 3.** List of shape deformation with several antinodes

Support:		Fixed ends					Cantilever				
$R/H = 0$											
W/H	L/H	Mode									
		1	2	3	4	5	1	2	3	4	5
1	10	LB#1	B#1	LB#2	B#2	TB	B#1	LB#1	LB#2	B#2	TB
	50	B#1	LB#1	B#2	LB#2	B#3	B#1	LB#1	B#2	LB#2	B#3
	100	B#1	LB#1	B#2	LB#2	B#3	B#1	LB#1	B#2	LB#2	B#3
2	10	B#1	LB#1	TB	B#2	LB#2	B#1	LB#1	B#2	TB	LB#2
	50	B#1	LB#1	B#2	B#3	LB#2	B#1	LB#1	B#2	LB#2	B#3
	100	B#1	LB#1	B#2	B#3	LB#2	B#1	LB#1	B#2	LB#2	B#3
5	10	B#1	TB	B#2	LB#1	TB	B#1	TB	LB#1	B#2	TB
	50	B#1	B#2	LB#1	B#3	TB	B#1	LB#1	B#2	B#3	TB
	100	B#1	B#2	LB#1	B#3	B#4	B#1	LB#1	B#2	B#3	LB#2
$R/H = 0.25$											
W/H	L/H	Mode									
		1	2	3	4	5	1	2	3	4	5
1	10	LB#1	B#1	LB#2	B#2	TB	LB#1	B#1	LB#2	B#2	TB
	50	LB#1	B#1	LB#2	B#2	LB#3	LB#1	B#1	LB#2	B#2	LB#3
	100	LB#1	B#1	LB#2	B#2	LB#3	LB#1	B#1	LB#2	B#2	LB#3
2	10	B#1	LB#1	B#2	TB	LB#2	B#1	LB#1	B#2	TB	LB#2
	50	B#1	LB#1	B#2	B#3	LB#2	B#1	LB#1	B#2	LB#2	B#3
	100	B#1	LB#1	B#2	B#3	LB#2	B#1	LB#1	B#2	LB#2	B#3
5	10	B#1	TB	B#2	LB#1	TB	B#1	TB	LB#1	B#2	TB
	50	B#1	B#2	LB#1	B#3	TB	B#1	LB#1	B#2	B#3	TB
	100	B#1	B#2	LB#1	B#3	B#4	B#1	LB#1	B#2	B#3	LB#2
$R/H = 0.5$											
W/H	L/H	Mode									
		1	2	3	4	5	1	2	3	4	5
1	10	LB#1	B#1	LB#2	B#2	TB	LB#1	B#1	LB#2	B#2	TB
	50	LB#1	B#1	LB#2	B#2	LB#3	LB#1	B#1	LB#2	B#2	LB#3
	100	LB#1	B#1	LB#2	B#2	LB#3	LB#1	B#1	LB#2	B#2	LB#3
2	10	B#1	LB#1	B#2	TB	LB#2	B#1	LB#1	B#2	TB	LB#2
	50	B#1	LB#1	B#2	LB#2	B#3	B#1	LB#1	B#2	LB#2	B#3
	100	B#1	LB#1	B#2	LB#2	B#3	B#1	LB#1	B#2	LB#2	B#3
5	10	B#1	TB	B#2	LB#1	TB	B#1	TB	LB#1	B#2	TB
	50	B#1	B#2	LB#1	B#3	TB	B#1	LB#1	B#2	B#3	TB
	100	B#1	B#2	LB#1	B#3	B#4	B#1	LB#1	B#2	B#3	LB#2

The steady-state dynamic analysis described the structural response by a log-log scale plot between the normalized deformation magnitude and frequency.

Firstly, the structural response under the harmonic loading at  $L/2$  was observed for the response along the length of the structure. A sharp corner square rod ( $R/H =$

0,  $W/H = 1$ ) with fixed ends support condition was selected in this investigation. The deformation magnitude ratio (minimum/maximum) along the length was plotted as shown in Figure 8.

Figure 8 informs the response from different locations of  $x/L$  under the harmonic loading. The behavior of the responses corresponded with the mode shape, which was noticeably increased at the frequency of the mode shape. The longitudinal bending type only occurred in this investigation. The magnitudes of deformation along the lengths were different. However, the behavior was similar for all locations of  $x/L$ , which increased while approaching the mode frequencies, except for  $x/L$  equal to 0 and 1, which had no responses under loading due to the support condition. To understand the behavior of the structure response, the response at  $x/L = 0.5$  at the different locations of the harmonic load was plotted as shown in Figure 9.

Figure 9 shows the different responses seen in  $L/H = 10$  and  $100$ . Mode 3 was more responsive to the loading at  $L/4$  rather than  $L/2$ . Considering shape deformation, modes 1, 3, and 5 showed the longitudinal bending shape, which has a different number of antinodes. The

deformation shape of the third mode revealed 2 antinodes on the vibration, as shown in Figure 10. According to the loading location,  $L/4$  was located close to the antinode, and  $L/2$  was located close to the node of this vibrational mode. Therefore, the loading at  $L/4$  provided a higher response in mode 3, as shown in Figure 9.

Considering the aspect ratio of the geometry, the response under the harmonic loading at  $L/4$  with fixed ends support was plotted on a stacked log-log chart for a clear display of the geometry effect. The behavior of deformation magnitude at  $x/L = 0.5$  was only concerned in the comparison. The effect of the geometry ratio is shown in Figure 11. Furthermore, the effect of the support-type and structural material was included, as can be seen in Figures 12 and 13, respectively, which were investigated on a sharp corner square rod. Figure 11 shows the difference in the behavior of the structural response from the different geometry. The longitudinal bending only appeared under vibration for the sharp square rod ( $R/H = 0, W/H = 1$ ). Moreover, the higher ratio of  $R/H$  and  $W/H$  revealed a higher chance of lateral and torsional bending. However, longitudinal bending mainly occurred due to the direction of loading. The

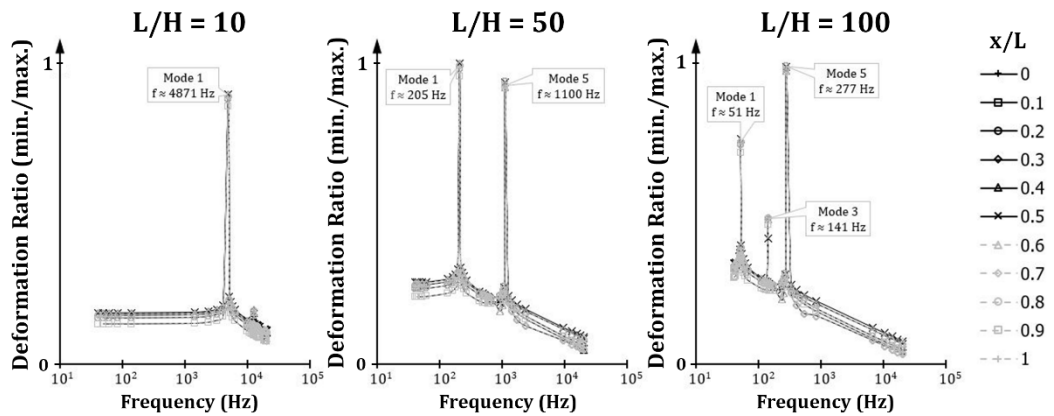


Figure 8. The structural response of the different locations of  $x/L$

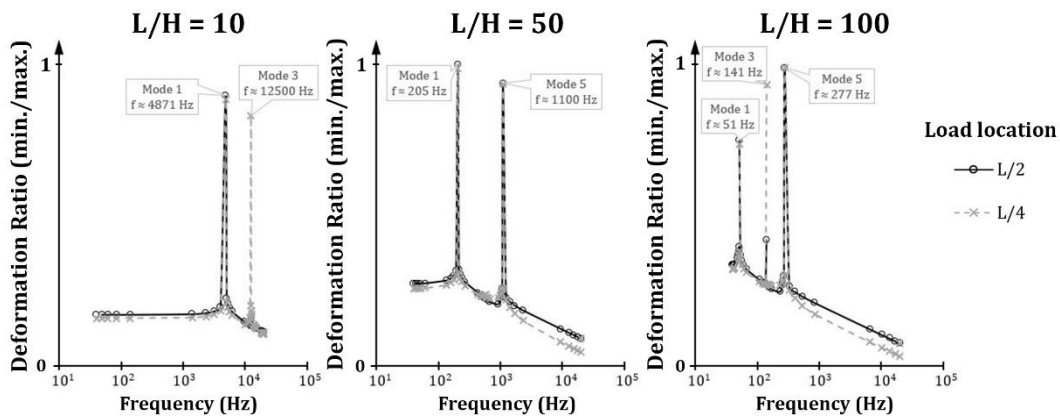


Figure 9. The effect of different loading locations on the structural response

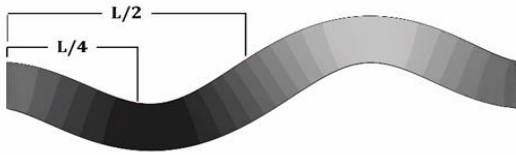


Figure 10. The third mode of sharp corner square rod

cantilever condition for the support condition revealed the torsional bending in the length ratio  $L/H = 10$ ; the rest were longitudinal bending. In contrast, the condition of the fixed ends only revealed longitudinal bending. Furthermore, the effect of structural material in Figure 13. shows a similar trend and shape of the response. In terms of deformation magnitude, a more extended structure had a higher magnitude of deformation, and the mode of longitudinal bending shape was dominant, with the highest response among the deformation shapes. Lastly, aluminum material has a higher response than steel.

The computational results were compared with similar studies, either experimental or computational.

The natural frequency and the structure's response under the vibration could not be compared directly due to the difference in structural geometry. Nonetheless, the small difference in the natural frequency of steel and aluminum was verified in the experimental study of Young et al [25]. Moreover, the shape deformation under transverse vibration of the second structural mode was compared with another experimental study by Hassanpour et al. [26]. Figure 14 shows the shape deformation of a uniform beam with fixed ends. The obtained experimental data roughly provided the shape deformation since only seven measuring points were used in their study. However, the shape deformation along the length had a similar trend. In addition, similar studies correspond well with the current work [27]. In short, the investigation of multi-shape uniform beam revealed the characteristic of the natural frequency at each mode of the structure which was uniquely dependent on boundary conditions and geometry. Under the excitation, the structure vibrated in the direction of the excitation, which governed the shape deformation, i.e., the longitudinal bending occurred from vertical excitation (transverse vibration).

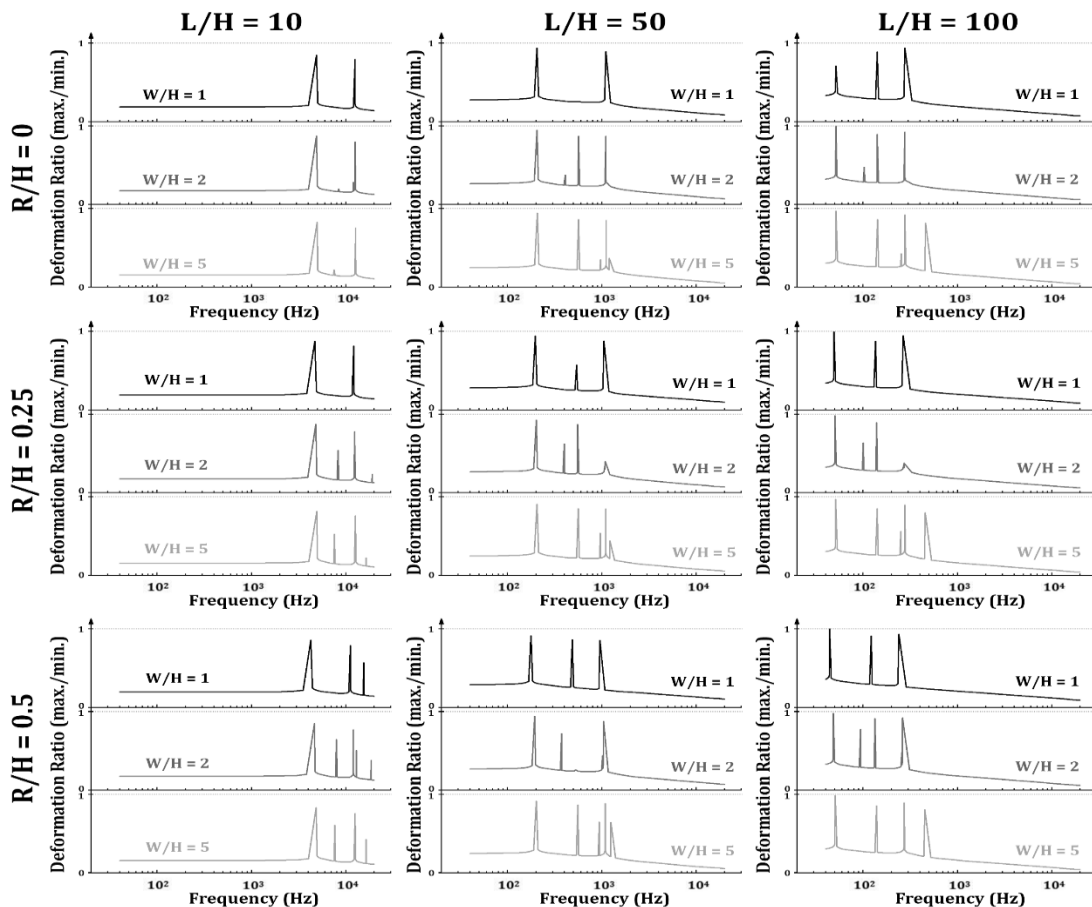


Figure 11. The effect of geometry ratio on the structural response

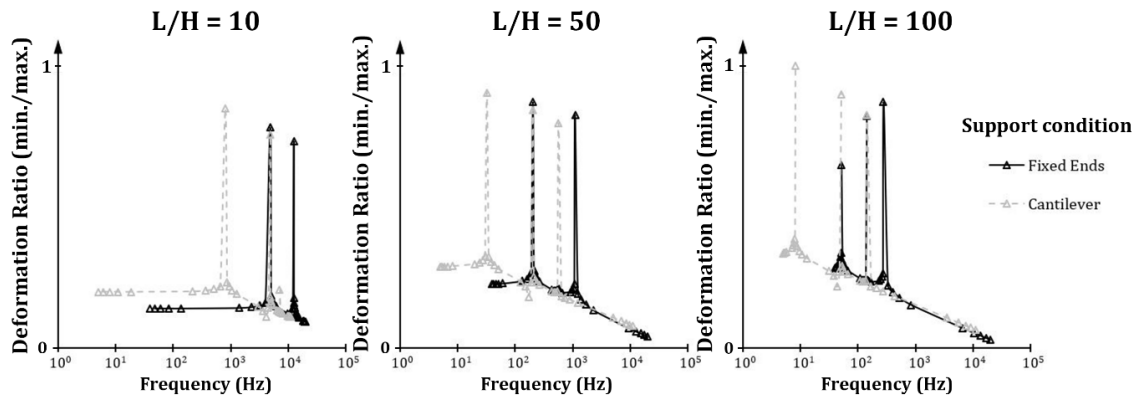


Figure 12. The effect of support conditions on the structural response

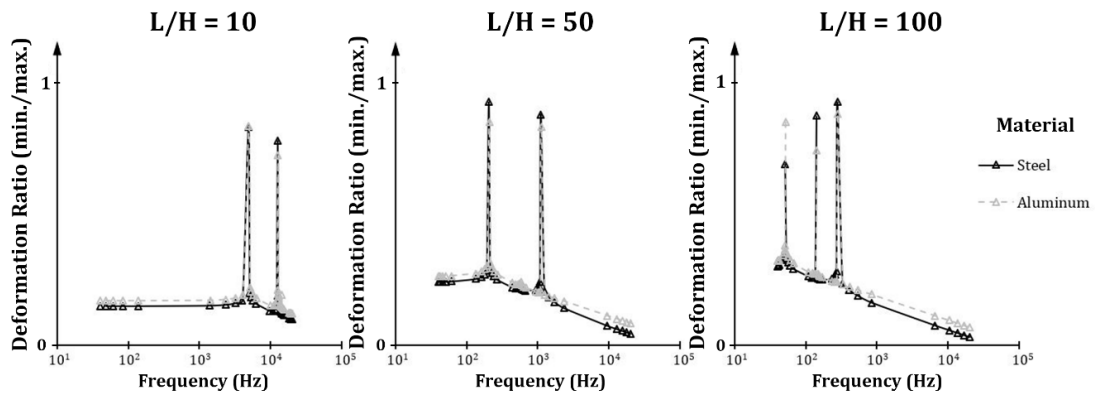


Figure 13. The effect of material on the structural response

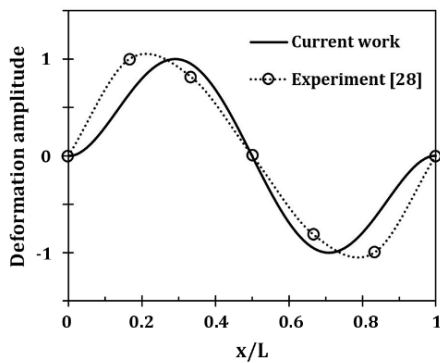


Figure 14. The second mode of the uniform rectangular beam with fixed ends under transverse vibration

Regarding the vibrational mode, the mode of vibration depends on the position and frequency of the excitation. The excitation at the antinode of vibration with a similar mode frequency as the structure would control the occurrence mode of vibration. Nevertheless, the excitation at natural frequency was not recommended for high-power excitation devices, which can cause a failure due to large deformation.

#### 4. ANALYTICAL VALIDATION

According to theoretical calculation, the natural frequency of the uniform beam with both ends fixed can be calculated via the following expression [25, 28]:

$$\omega_n = \frac{K_n}{2\pi} \sqrt{\frac{EI}{\rho AL^4}} \tag{1}$$

- where,  $\omega_n$  = Natural frequency (Hz)
- $E$  = Elastic modulus (Pa)
- $I$  = Area moment of inertia (m<sup>4</sup>)
- $\rho$  = Density (kg/m<sup>3</sup>)
- $A$  = Cross-sectional area (m<sup>2</sup>)
- $L$  = Length (m)
- $K_n$  = Mode constant

Equation (1) was used to validate the FEM results of the sharp corner (R/H = 0) structure with L/H = 100, as detailed in Table 4. The validation was performed on the mode frequency of the longitudinal bending shape under the transverse vibration. The comparison showed a good agreement with an error of less than 1 %.

Moreover, the mode shape (Longitudinal bending) of a uniform beam under the transverse vibration with both

ends fixed conditions was governed by the following equation [29, 30].

$$W_n(x) = C_n \left[ (\sinh \beta_n x - \sin \beta_n x) + \mu (\cosh \beta_n x - \cos \beta_n x) \right]$$

$$\mu = \frac{\sinh \beta_n l - \sin \beta_n l}{\cos \beta_n l - \cosh \beta_n l} \tag{2}$$

where  $\beta_n l$  is the mode parameter which is listed in Table 5 and  $C_n$  is the magnitude constant of vibration. From Equation (2), the nodal position of the vibration is shown in Table 5. To validate the FEM results, four mode shapes of the structural ratio  $R/H = 0$ ,  $W/H = 5$ , and  $L/H = 100$  were plotted, as shown in Figure 15, to compare the position of the node with the analytical data. The nodal

**TABLE 4.** Comparison of the natural frequency for the longitudinal bending mode

W/H = 1				
Mode	$K_n$ [25]	$\omega_{n, Analytic}$ (Hz)	$\omega_{n, FEM}$ (Hz)	Error (%)
1	22.4	51.808	51.470	0.653
2	61.7	142.704	141.760	0.662
3	121	279.857	277.570	0.817
W/H = 1				
Mode	$K_n$ [25]	$\omega_{n, Analytic}$ (Hz)	$\omega_{n, FEM}$ (Hz)	Error (%)
1	22.4	51.808	51.509	0.578
2	61.7	142.704	141.860	0.591
3	121	279.857	277.790	0.739
W/H = 1				
Mode	$K_n$ [25]	$\omega_{n, Analytic}$ (Hz)	$\omega_{n, FEM}$ (Hz)	Error (%)
1	22.4	51.808	51.670	0.267
2	61.7	142.704	142.310	0.276
3	121	279.857	278.700	0.414
4	200	462.574	460.170	0.520

**TABLE 5.** Mode parameters ( $\beta_n l$ ) and nodal position of fixed-fixed uniform beam

Mode	$\beta_n l$ [29]	Nodal position/L [25, 31]
1	4.7300	0.0, 1.00
2	7.8532	0.0, 0.50, 1.00
3	10.9956	0.0, 0.33, 0.67, 1.00
4	14.1372	0.0, 0.25, 0.50, 0.75, 1.00

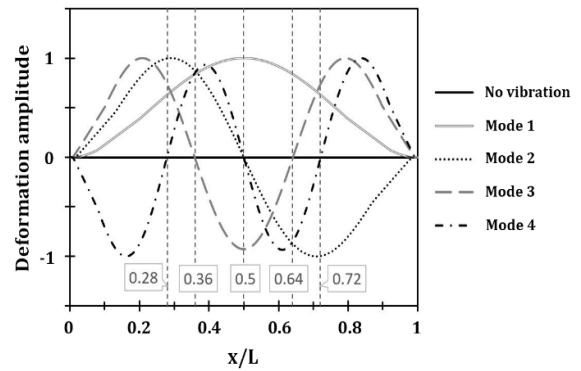


**Figure 15.** Longitudinal mode shape under the transverse vibration of the FEM method

positions of the FEM result were almost identical to the theoretical calculation, which confirmed the correctness of the simulation. Since the behavior of the structural response is governed by natural frequency and mode shape. Consequently, the aforementioned steady-state analysis is undoubtedly certified.

### 5. CONCLUSION

In this study, the influence parameters including geometry, support condition, and material are investigated for their effect on the natural frequency, mode shape, and structural response. Regarding geometry ratio, the structural length had a major effect on the mode frequency of vibration. A more extended structure had a lower natural frequency, and the corner radius of the structure rarely affected the frequency. The width of the structure was dominated by the mode shape, which had a more torsional effect on a larger width. Furthermore, the cantilever support significantly decreased the frequency compared to fixed-fixed conditions, and the material had no significant effect on either mode frequency or mode shape in the investigation. The response of the structure corresponds with the mode shape under vibration. The shape deformation under the vibration is governed by the excitation frequency and loading conditions, including the location and the direction. Consequently, the longitudinal bending mode dominated the structural response due to the applied conditions in this investigation. Moreover, loading at the antinode vibration position provided the maximum magnitude of deformation and lower magnitude for the nodal position. Lastly, the knowledge of the structural behavior under the vibration in this study can be further used for either the effective sensor attachment or controlling the vibration in vibration-based applications.

## 6. ACKNOWLEDGMENT

The research on Computational Analysis of Influence Parameters on Shape Deformation of a Structure under Vibration by King Mongkut's University of Technology North Bangkok received funding support from the National Science, Research and Innovation Fund (NSRF) (KMUTNB-BasicR-64-40).

## 7. REFERENCES

- Hibbeler, R., *Deflections, structural analysis*. 2012, Pearson Prentice Hall, Pearson Education Inc.: Upper Saddle River, NJ, USA.
- Hosseini, O., Malekinejad, M. and Rahgozar, R., "A closed form solution for free vibration analysis of tube-in-tube systems in tall buildings", *International Journal of Engineering, Transactions A: Basics*, Vol. 25, No. 2, (2012), 107-114. doi: 10.5829/idosi.ije.2012.25.02a.01.
- Serway, R.A. and Vuille, C., "College physics, Cengage Learning, (2014).
- Liu, Y. and Chu, F., "Nonlinear vibrations of rotating thin circular cylindrical shell", *Nonlinear Dynamics*, Vol. 67, No. 2, (2012), 1467-1479. <https://doi.org/10.1007/s11071-011-0082-7>
- Baker, C., "Measurements of the natural frequencies of trees", *Journal of Experimental Botany*, Vol. 48, No. 5, (1997), 1125-1132. <https://doi.org/10.1093/jxb/48.5.1125>
- Lashin, M.M., Saleh, W.S. and Alrowais, F., "Determination of different structures' materials natural frequencies using fuzzy logic system", *International Journal of Engineering and Advanced Technology*, Vol. 9, No. 3, (2020), 723-727. doi: 10.35940/ijeat.B3641.029320.
- Halliday, D., Resnick, R. and Walker, J., "Fundamentals of physics, John Wiley & Sons, (2013).
- Billah, K.Y. and Scanlan, R.H., "Resonance, Tacoma narrows bridge failure, and undergraduate physics textbooks", *American Journal of Physics*, Vol. 59, No. 2, (1991), 118-124. <https://doi.org/10.1119/1.16590>
- Griggs Jr, F., "Tacoma narrows bridge failure 1940, galloping gertie part 2", *Structure*, (2022), 60. <https://www.structuremag.org/?p=19995>
- de Macêdo Wahrhaftig, A. and da Fonseca, R.M.L.R., "Representative experimental and computational analysis of the initial resonant frequency of largely deformed cantilevered beams", *International Journal of Solids and Structures*, Vol. 102, (2016), 44-55. <https://doi.org/10.1016/j.ijsolstr.2016.10.018>
- Mondal, S., Ghuku, S. and Saha, K.N., "Effect of clamping torque on large deflection static and dynamic response of a cantilever beam: An experimental study", *International Journal of Engineering and Technologies*, Vol. 15, (2018), 1-16. <https://doi.org/10.18052/www.scipress.com/IJET.15.1>
- Wahrhaftig, A., Brasil, R., Groba, T., Rocha, L., Balthazar, J. and Nascimento, L., "Resonance of a rotary machine support beam considering geometric stiffness", *Journal of Theoretical and Applied Mechanics*, Vol. 58, (2020). doi: 10.15632/jtampl/126681.
- Wahrhaftig, A.d.M., Magalhães, K.M., Silva, M.A., da Fonseca Brasil, R.M. and Banerjee, J.R., "Buckling and free vibration analysis of non-prismatic columns using optimized shape functions and rayleigh method", *European Journal of Mechanics-A/Solids*, Vol. 94, (2022), 104543. <https://doi.org/10.1016/j.euromechsol.2022.104543>
- de Macêdo Wahrhaftig, A., Dantas, J.G.L., da Fonseca Brasil, R.M.L.R. and Kloda, L., "Control of the vibration of simply supported beams using springs with proportional stiffness to the axially applied force", *Journal of Vibration Engineering & Technologies*, (2022), 1-15. <https://doi.org/10.1007/s42417-022-00502-2>
- Wahrhaftig, A.d.M., Silva, M.A.d. and Brasil, R.M., "Analytical determination of the vibration frequencies and buckling loads of slender reinforced concrete towers", *Latin American Journal of Solids and Structures*, Vol. 16, (2019). <https://doi.org/10.1590/1679-78255374>
- Wahrhaftig, A.d.M., Magalhães, K.M., Brasil, R.M. and Murawski, K., "Evaluation of mathematical solutions for the determination of buckling of columns under self-weight", *Journal of Vibration Engineering & Technologies*, Vol. 9, No. 5, (2021), 733-749. <https://doi.org/10.1007/s42417-020-00258-7>
- Ahmed, O.H., Hazem, A.-R. and Shawky, A.A., "Seismic performance of staircases in the 3d analysis of rc building", *Civil Engineering Journal*, Vol. 7, (2022), 114-123. doi: 10.28991/CEJ-SP2021-07-08.
- Ruiter, A.G., Veerman, J.A., Van Der Werf, K.O. and Van Hulst, N.F., "Dynamic behavior of tuning fork shear-force feedback", *Applied Physics Letters*, Vol. 71, No. 1, (1997), 28-30. <https://doi.org/10.1063/1.119482>
- Hansen, H.H., "Optimal design of an ultrasonic transducer", *Structural Optimization*, Vol. 14, No. 2, (1997), 150-157. <https://doi.org/10.1007/BF01812517>
- Gururaja, T., Schulze, W.A., Cross, L.E. and Newnham, R.E., "Piezoelectric composite materials for ultrasonic transducer applications. Part ii: Evaluation of ultrasonic medical applications", *IEEE Transactions on Sonics and Ultrasonics*, Vol. 32, No. 4, (1985), 499-513. doi.
- Krautkrämer, J. and Krautkrämer, H., "Ultrasonic testing of materials, Springer Science & Business Media, (2013).
- Foorginejad, A., Taheri, M. and Mollayi, N., "A non-destructive ultrasonic testing approach for measurement and modelling of tensile strength in rubbers", *International Journal of Engineering, Transactions C: Aspects*, Vol. 33, No. 12, (2020), 2549-2555. doi: 10.5829/IJE.2020.33.12C.16.
- Xu, C., Xie, J., Zhang, W., Kong, Q., Chen, G. and Song, G., "Experimental investigation on the detection of multiple surface cracks using vibrothermography with a low-power piezoceramic actuator", *Sensors*, Vol. 17, No. 12, (2017), 2705. <https://doi.org/10.3390/s17122705>
- Lindgren, E., Forsyth, D., Aldrin, J. and Spencer, F., "Asm handbook, volume 17, nondestructive evaluation of materials", *ASM International*, (2018).
- Young, W.C., Budynas, R.G. and Sadegh, A.M., "Roark's formulas for stress and strain, McGraw-Hill Education, (2012).
- Hassanpour, P.A., Alghemlas, K. and Betancourt, A., "Experimental modal analysis of a fixed-fixed beam under axial force", in ASME International Mechanical Engineering Congress and Exposition, American Society of Mechanical Engineers. Vol. 58370, (2017), V04AT05A053.
- Cafeo, J.A., Trethewey, M.W. and Sommer III, H.J., "Beam element structural dynamics modification using experimental modal rotational data", (1995). doi: 10.1115/1.2874446.
- Zhang, Z. and Zhang, C., "Mechanical properties analysis of bilayer euler-bernoulli beams based on elasticity theory", *International Journal of Engineering, Transactions B: Applications*, Vol. 33, No. 8, (2020), 1662-1667. doi: 10.5829/ije.2020.33.08b.25.
- Rao, S.S., "Vibration of continuous systems: John wiley & sons", *New Jersey*, (2007).

30. Ghazwani, M.H., "Development of an analytical model for beams with two dimples in opposing directions", (2016).
31. Mehdianfar, P., Shabani, Y. and Khorshidi, K., "Natural frequency of sandwich beam structures with two dimensional functionally graded porous layers based on novel formulations", *International Journal of Engineering, Transactions B: Applications*, Vol. 35, No. 11, (2022), 2092-2101. doi: 10.5829/IJE.2022.35.11B.04.

---

### Persian Abstract

---

#### چکیده

درک رفتار یک سازه برای اکثر کاربردها، به ویژه تحریک در کاربردهای اولتراسونیک، ضروری است. در حال حاضر دستگاه های اولتراسونیک در زمینه های مختلف مورد استفاده قرار می گیرند و نقش اساسی در تست های غیر مخرب (NDT) دارند. رفتار ساختار باید با دستیابی به بهترین عملکرد مرتبط باشد. رفتار ارتعاشی ساختاری به فرکانس طبیعی و شکل حالت بستگی دارد. در این مطالعه سعی شده است اثر پارامترهای تاثیر بر تغییر شکل برای طراحی شرایط تحریک مناسب تعیین شود. در این مطالعه، پارامترهای تاثیر یک تیر یکنواخت، شامل هندسه، شرایط تکیه گاه و مواد، برای بررسی تاثیر آنها بر فرکانس، شکل مد و پاسخ سازه گنجانده شد. نتیجه تاثیر قابل توجه طول و شرایط تکیه گاه سازه را بر فرکانس مد، کاهش چشمگیر فرکانس مد برای نصب و پشتیبانی طولانی مدت نشان داد. این مطالعه با بررسی سه شکل حالت رایج نشان داد که شکل خمشی طولی به دلیل جهت بارگذاری غالب است. بنابراین، تغییر شکل ساختار عمدتاً توسط منبع تحریک خارجی کنترل می شود و پاسخ ساختاری بالا با اعمال تحریک در نزدیکی موقعیت آنتی گره ارتعاش دریافت می شود. با این وجود، نتیجه محاسباتی تطابق خوبی با اعتبار سنجی تحلیلی با خطای کمتر از ۱٪ نشان داد. این مطالعه منجر به درک ارتعاش می شود، که می تواند بیشتر برای اتصال موثر حسگر یا طراحی کنترل ارتعاش برنامه های اولتراسونیک مورد استفاده قرار گیرد.

---



## Integration of Remote Sensing and Big Data to Study Spatial Distribution of Urban Heat Island for Cities with Different Terrain

P. B. Shah\*, C. R. Patel

Department of Civil Engineering, Sardar Vallabhbhai National Institute of Technology, Surat, India

### PAPER INFO

#### Paper history:

Received 21 August 2022

Received in revised form 29 September 2022

Accepted 13 October 2022

#### Keywords:

Landsat Surface Temperature

Urban Heat Island

Satellite Dataset

Remote Sensing

Big Data

### ABSTRACT

Urban microclimate has posed a detrimental effect on the life of the urban population. This research drives with an aim of identifying environmentally conscious factor vis-a-vis urban planning which leads to the vicious cycle of urban climate change. The vicious cycle is inclusive of many urban dynamics' parameters, which are complicated to understand. This research emphasizes on using Remote Sensing Big Data on Google Earth Engine as an advancement to study Climate Vulnerability leading to Urban Climate Gentrification. Temporal data of Landsat for the past 30 years has been taken into consideration for the study. Three cities with diverse geographical and terrain characteristics have been selected for the study, to understand the modern decisive planning is in coherence with the Sustainable Development Goals. Understanding spatial and temporal information of Urban hotspots using High-Resolution Satellite data is just not enough to suffice the need to decrease the temperature by 2- 3°C. The present study is a toll on how the reasons for microclimate change vary along with the terrain, spatial location, and urban growth pattern of the city.

doi: 10.5829/ije.2023.36.01a.09

## 1. INTRODUCTION

The current climate issue is wreaking havoc on the world. While growing deforestation and unsustainable industries are easy to criticize; it may come as a shock but the metro cities and urban growth play a significant role and is one of the main causes of the current climate change issue [1]. Nearly, 55% of the world's population resides in urban areas, which is expected to increase vividly and reach 66% worldwide by 2050. The anthropogenic activity in cities is a significant contributor to climate change. These activities are also main source of greenhouse (GHG) emissions [2, 3]. The Climate is fairly different in urban and buildup construction while its different in rural development as a result of the impervious urban fabric, the urban structure and anthropogenic activities [4]. There is a risk of increased depletion of energy and natural resources due to incessant increase in the population in cities. The Urban Heat Island (UHI) effect, which causes cities to be hotter than the nearby rural areas, is a result of this

phenomena. The temperature in a heat island may be 1 to 6 degrees Celsius greater than the surrounding surroundings [5].

Urbanization rate is increasing with an increase in anthropogenic activities, which leads to Land use Landcover (LULC) Change. This rate of change impacts the microclimatic condition of the city and leads to heatwaves and extreme flood events [6-8]. The UHI effect, which makes cities generally warmer than the nearby rural areas, cities are more susceptible to heat waves than rural areas [9]. Climate adaptation and mitigation strategies are more crucial in these developing cities [10]. Developing nations are not yet capable enough to deal with the friction caused by climate change. Climate responsive designs needs to applied at everyday practice for comfortable urban spaces [11]. Characterizing and representing the urban environment has become a crucial element in the steps involved in urban planning and design [12]. The metropolis weather is managed with the aid of using many natural elements, each on the macro-scale and on the meso-scale which

\* Corresponding author email: [poojabshah2512@gmail.com](mailto:poojabshah2512@gmail.com)  
(P. B. Shah)

modulate several natural microclimatic parameters. The different essential elements regulating Urban Micro Climate (UMC) consist of nearby ecosystems together with city parks, vegetation, water bodies and concrete built-up [13]. The trends in UMC varies with different cities.

In the past few years, one of the world's biggest public policy concerns is rising climate change. The Paris Agreement, which came into action in 2015 emphasizes on tackling climate-related activities for developing countries, with a goal of reducing the global temperature by 1.5°C [14]. SDG-11 on sustainable cities and communities requires higher living standards for citizens in every facet while the resilience acts as the pillar. To achieve this global goal and frame policies for mitigating Urban climate (UC) and Urban microclimate (UMC) change it is crucial to understand the Multi-Temporal LULC change and its impact on LST. Several studies have used Remote Sensing and GIS to study LST its impact on UC [15-19]. To carry out Multi Spatio-Temporal study of UMC using Remote Sensing is challenging with the constraints of proprietary software, big data, computer space, and tedious hour of processing data. To address this challenge for large-scale cloud computing, platforms such as Google Earth Engine (GEE) is used for multi-temporal studies, which has extensive archive of open access data from various satellite and sensor.

Recently studies have showcased the potential of GEE for UC studies at city scale. Liang et al. [20] illustrated how GEE can be used to detect spatial and temporal changes in time series of LULC and integrate GEE development tools to post process LULC classification and improve accuracy. Despini et al. [21] investigated the genesis of UHI: Surface Albedo and provided an approach to calculate and improve the albedo for city administrations. Agarwal and Nagendra [22] classified Indian cities using GEE and investigated on how shape of cities plays a role in impacting sustainability outcomes. Ravanelli et al. [23] exploited large scale GEE analysis for US metropolitan area to investigate the temporal variation of UHI. Roy [24] detected urban growth for two decades and estimated LST change with response to that growth [25]. As per Oke [7], there are two major scales to measure UHI (a) Urban Canopy Layer (UCL) and (b) Urban Boundary Layer (UBL) [26]. Intensive studies have been carried out using GEE to combat climate change and understand its relationship with LST at Global and City Scale (UBL). Bherwani et al. [13] in his review, showcased the gaps in research methodology for UMC studies, demonstrated the missing links that besides a lot of progress in UMC research, there are very limited application in the field due to lack of clarity in the targeted outcome and lack of integration between the natural and anthropogenic parameters that affect UMC. Studies carried out at

microscale in developed countries are either done using computational fluid dynamics [27-29], Field data [30, 31] or HRS thermal imagery/ DSM [32, 33]. In developing nation like India, performing CFD and in-situ experiments becomes expensive and cannot be performed at a large scale. Majority of the data are not available on open-source platform to carry out research. To address this challenge this study aims on using Open-Source GEE platform for UMC analysis at a micro level for different cities. However, every city has unique characteristic and terrain which demands for unique climate policy respectively.

This study focuses on understanding the co-relation between LST with variables like climate, population density and land use. For the current study 3 cities Surat, Delhi and Ahmedabad are optimized for the experiment. The unique characteristic of these cities are they have different terrain, different direction of river flowing through the cities, varying land use pattern and population density. The objective of this research is (1) Understanding the heat flux dynamics contemporary to Spatial-Temporal change using GEE for 3 different cities at two scales (i) City Scale and (ii) Micro- Scale; (2) Comparative analysis of LST with city characteristic (i.e. Land use, Population Density) to understand the heat flux; (3) Proposing need of unique climate adaptive policy for each city to meet the Paris Agreement.

## 2. MATERIALS AND METHODS

The study's experimental cities are 1) Surat 2) Ahmedabad and 3) Delhi. These cities have unique geographical condition, population, and socio-economic characteristic. Surat is a coastal city, Ahmedabad and Delhi are landlocked city with river flowing through the city. To understand the influence of cities terrain and land use on land surface temperature, macro level analysis at city scale has been demonstrated and then micro-level analysis for UMC was investigated for the city of Surat, Ahmedabad, and Delhi to understand the effect of land use/ topography on hot spots in the city (see Figure 1).

**2.1. Description of Study Area and Climate** The million plus cities of india as shown in Figure 2 surat, ahmedabad and delhi are investigated for current research. The spatial dynamics, population density, geographical location, terrain, and climate of these cities are studied in correlation to land use to understand the thermal profile of city.

The city of Surat is located at latitude 21°10'N and longitude 72°50'E in the southern state of Gujarat on the west coast of India, with an average elevation of 13 meters. Surat city is located near Tapi river and has tropical savannah (Köppen: Aw) climate. City's wind direction is south-west to north-east, mainly from the sea

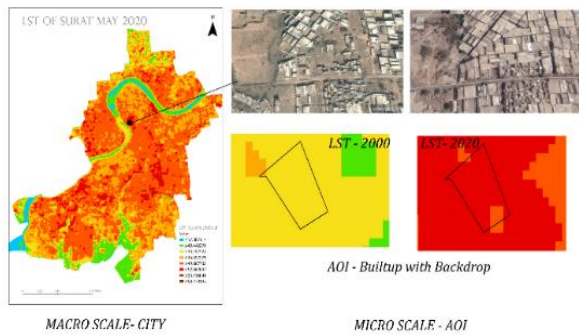


**Figure 1.** Land Surface Temperature at Macro and Micro Scale

towards the capital. Mostly in Indian cities, summer begins in early March and lasts until June. It is observed that April and May are the hottest months, with average highs of 45°C (99°F). It is one of India's most dynamic cities and the fastest growing with immigrants from Gujarat and other Indian states. The population of Diamond City Surat has grown from 2.8 million in 2001 to 4.5 million in 2011, a staggering increase of 58.68%. Surat is ranked the 4th fastest growing city in a global survey of the fastest growing cities conducted by the city mayors' foundation, international urban affairs think tank. In fact, it is the fastest growing Indian city in terms of economic prosperity.

Ahmedabad is strategically located in the heart of Gujarat in the Sabarmati basin. The Sabarmati River, which divides Ahmedabad in half, runs along both city's sides. In western India's landlocked city of Ahmedabad, the climate is hot and semi-arid (Köppen classification: BSh), with somewhat less precipitation than would be needed for a tropical savannah environment. Due to its topography, the city frequently experiences high temperatures. The highest temperature in the city was 50 °C on May 18-19, 2016. In May 2010, a 46.8 °C (heat wave claimed hundreds of lives. The 2011 census, Ahmedabad had a population of 5,633,927, making it her fifth largest city in India. The urban agglomeration centered on Ahmedabad is now the 7th largest urban agglomeration in India with a population of 6,357,693 estimated at 7,650,000. As of 2011, approximately 66% of the population lives in formal housing. Although Ahmedabad's population has grown, the housing stock has remained essentially constant, with both formal and informal housing concentrated and available space being used more economically. Ahmedabad is considered the financial center of Gujarat. The major climate challenge observed in the pockets of city is overburdened and unsustainable planning and increased emissions from industry and vehicles. Which leads to the urban heat island effect. (UHI) in the large cities [34] bordering a hot semi-arid climate (Köppen BSh).

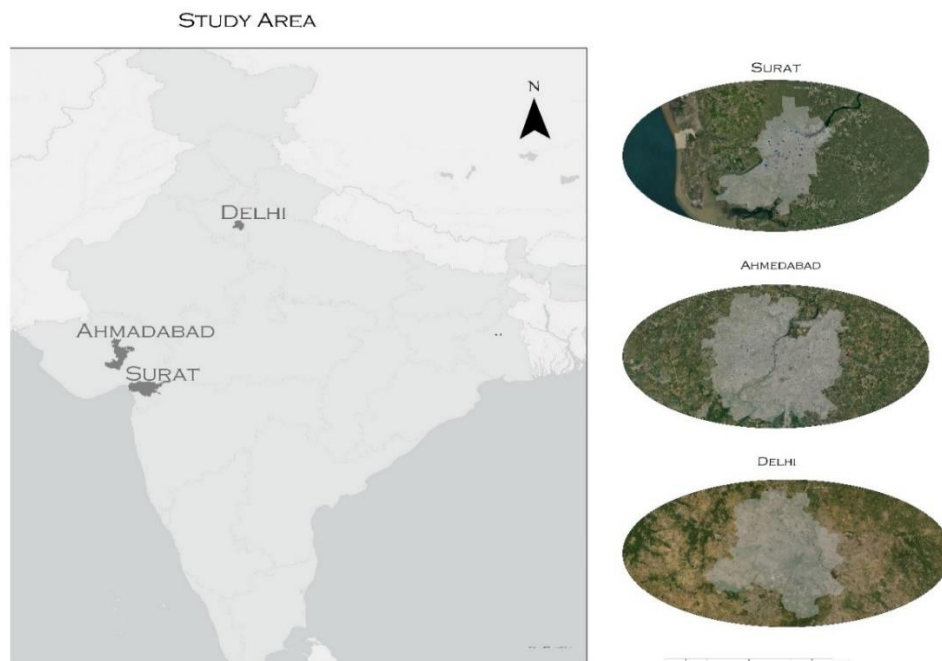


**Figure 2.** Three study area for the present study are selected on the basis of 1) Terrain and 2) City Location and 3) different location of river flowing through the city. The first city is Surat which is a coastal city, Second city Ahmedabad is a landlocked city , third city Delhi is a National capital with mixed weather conditions

India's National Capital is Delhi. Delhi typically experiences a dry-winter humid subtropical climate that is adjacent to a hot semi-arid climate. The temperature is between 2°C and 47 °C. Delhi's geographical setting provided a distinctive environment. It struggles frequently with issues like pollution and environmental deterioration while having a richness and variety of environmental assets, including as the river Yamuna, the Aravalli Ridge, water bodies, forests, etc. [26, 35].

According to India's 2011 census, Delhi has the second-highest population, with 11 million people. One of the urban areas in the world with the quickest growth rates is Delhi, whose GDP is 7.1%. The National Capital Region's economic hub, Delhi, accounts for about 50% of the region's GDP.

## 2.2. Data Used and Pre-Processing

In order to study the dynamics of LST due to anthropogenic activities at defined study area at macro and micro scale, remote sensing dataset were used. To demonstrate the densification and city growth dynamics impacts on LST it is crucial to detect the time series of LST change. A comprehensive thermal imagery dataset of Landsat 5, Landsat 7 and Landsat 8 are retrieved as a primary source from Google Earth Engine [27, 28] and are processed using Ermida [29] algorithm to generate LSTs. In the module "Landsat\_LST" provided by Ermida, the date range provided for the current time series analysis was from 1982- 2020, for the month of April, May, and June. These datasets are retrieved from the Landsat satellite (4, 5, 7, or 8). City Boundaries are uploaded in the asset, as the region of interest to process. NDVI-based correction is applied to emissivity, which loads the respective collections of Top of Atmosphere (TOA), brightness temperatures (BT) and Surface Reflectance (SR). A cloud mask is applied to both using the quality information bands (module cloudmask) and the dataset having cloudcover not more than 10% are selected. Time-series chart is supported in GEE if there are less than 5000 elements in collection. The process is aborted if there are more than 5000 elements, so to prepare the time-series chart date range for 3 years were given as input. The "reducer" function in GEE was used to extract the mosaiced image for the respective timespan, as provided in the input. Temperature obtained from the above collection is mean temperature of the entire city boundary region and measured in kelvin. Temperature conversion from Kelvin to Celsius was performed using python in the pycharm console. These LST datasets are exported in tabular format and time series LST chart is computed for each city.

## 3. RESULTS

In this study, a comparison of land surface temperature of cities with three different geographical terrains have

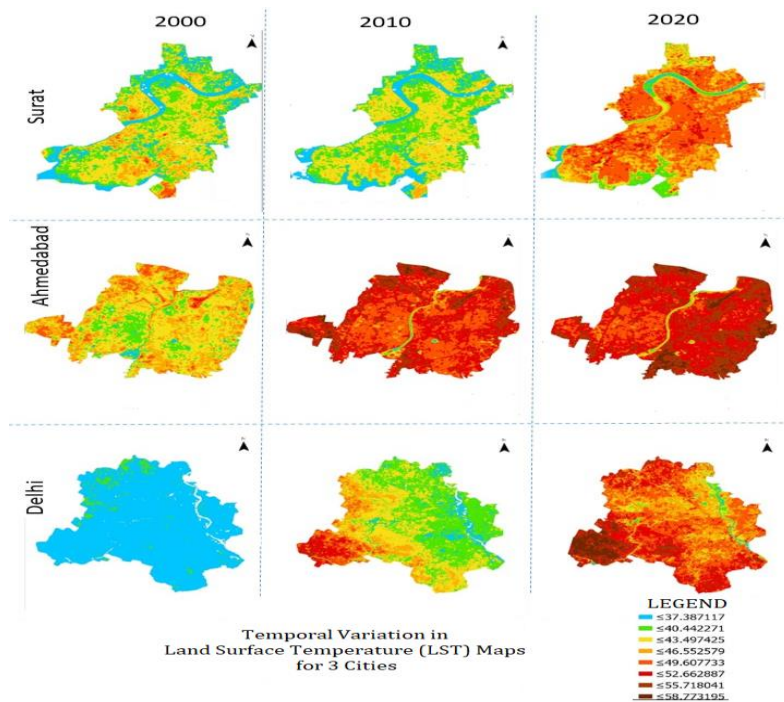
been investigated for 20 years (two decade) to understand the temporal trend of change in LST. Two decadal big data of Landsat 5, 7, and 8 data were processed to understand the Land Surface Temperature variation over the three cities i.e., Surat, Ahmedabad, Delhi. The heat maps were generated using Google Earth Engine and ArcGIS Pro platforms. The heat maps are analyzed to obtain the relationship between the parameters like - increase of air temperature, geographical location of city, water body, terrain of city corresponding to the urban sprawl and density. Urban Heat Maps were prepared using ArcGIS online platform. The different terrain, geographical location spatial and temporal distribution of values of UHI is as shown in Figure 2.

Figure 2 shows LST of three cities Surat, Ahmedabad and Delhi. The rows indicate the different cities and its temporal variation while the columns provide an insight on the comparative values on the LST due to the terrain and geographical location of the cities. The first row shows the temporal and spatial variation in the temperature of Surat city. Surat city is a coastal city and has river Tapi crossing through the NE\_NW of city. The development of city has flourished along the banks of river and then during 2015-2020 Surat city has expanded gradually on the fringes. There is an industrial area which is located on the Southeast side of city. The land use of city of Surat is majorly Residential and Textile Industry on the west side of river. The major commercial activity in Surat city is Diamond Trade and Textiles. There are educational institutes located on the central eastern part of city.

In the second row of Figure 2, city of Ahmedabad is shown. It is a landlocked city with the Sabarmati River flowing through the center of city. On the eastern side of river, the old city of Ahmedabad with very dense urban area is located. The city of Ahmedabad is trade hub of Gujarat state also known as Manchester of Gujarat. It has a lake located on the southeast side. The city of Ahmedabad has observed maximum LST of 51°C.

The direction of wind in India during summers is Southwest while in winters is Northeast. So, there are extreme cold temperature observed in Delhi. While Ahmedabad and Surat observe moderate temperature. Corresponding to it the summers in Ahmedabad are very hot and then in Delhi and Surat. The water body flowing through have different location in all the three cities. In Surat the Tapi river is located on the northwest, The Sabarmati River of Ahmedabad passes through center of city, while in Delhi Yamuna River passes through the northeast of the city which is visually quite evident from Figure 2. The maximum LST that has been observed is 58.8°C in the city of Ahmedabad and Delhi.

The statistical observation of LST from the thematic maps as per Figure 3 is summarized in Table 1. The mean LST temperature for the landlocked cities Ahmedabad and Delhi is more by 2-3°C compared to the coastal city



**Figure 2.** Spatial distribution of Land Surface Temperature (LST) maps of Surat, Ahmedabad, and Delhi City for the year 2000,2010 and 2020. Temporal variation of LST for 20 years of big data is processed using Google Earth Engine for three different city. The maps show a significant rise in temperature from 2010 to 2020 for landlocked city of Delhi and Ahmedabad compared to coastal city of Surat

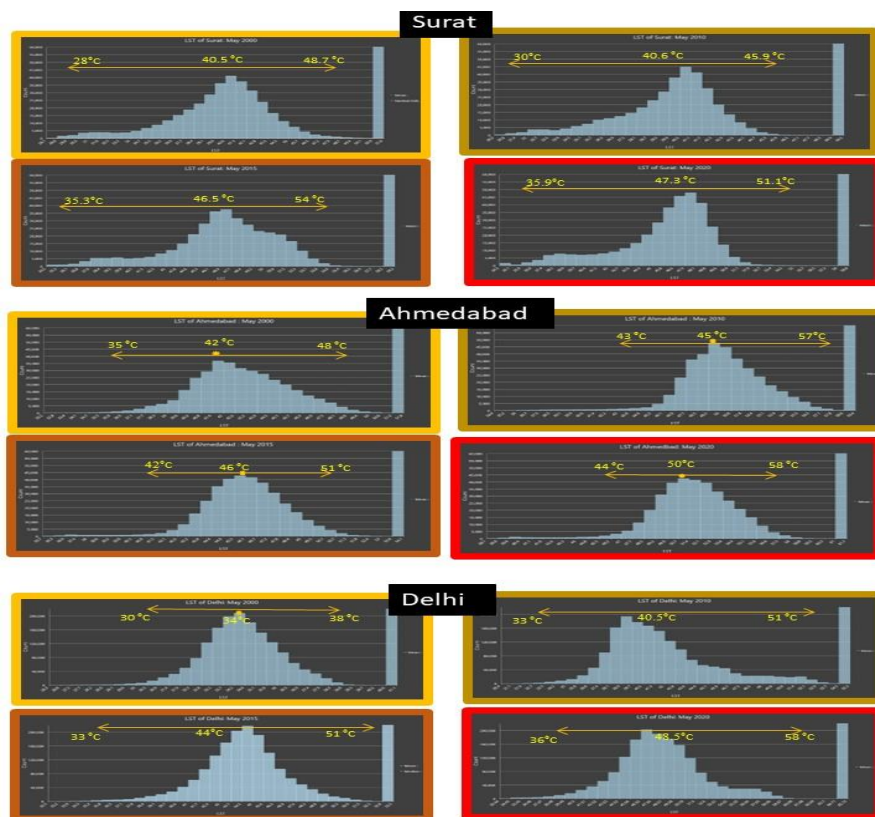


**Figure 3.** Statistical analysis of the LST image of years 2000, 2010, 2015 and 2020 for the cities of Surat, Ahmedabad, Delhi to investigate the change in temperature peak and its intensity

**TABLE 1.** Statistical Data of LST for 3 cities

Year	2000			2010			2015			2020		
	Min	Mean	Max									
Surat	28	40.6	48.7	30	40.6	45.9	35.3	46.9	54.6	35.9	47.3	51.1
Ahmedabad	35	42	49	35	49	57.1	42.1	46.1	50.7	38.9	51.4	58.8
Delhi	30	34.6	38.8	33	40.5	52	35.8	44.3	50.9	36	48	58.8

of Surat. For the year 2010, LST of Ahmedabad shows peak temperature of 49°C, which may be due to some error, and it is considered as outlier.

While investigating the mean vertical profile of Gaussian curves it is observed that, there is a shift in peak LST temperature observed in the Landlocked city of Delhi and Ahmedabad. There is a shift in temperature peak by 8°C in the landlocked city. While the coastal city of Surat observes a shift in LST peak by 6°C [9] in their study mentioned that there is 4.5% increase in mortality rates for 1°C increase in heat wave intensity.

Our results provide strong statistical evidence of significant change in the response of city with coastal and landlocked climate.

#### 4. CONCLUSIONS

In this study, three Indian cities with different terrain were investigated using Landsat dataset to understand the effect of Urban Heat Island. The spatial temporal analysis of the study area indicates that the Landlocked city of Ahmedabad shows higher temperature compared to the coastal city of Surat. The statistical analysis and visually interpreted results confirm strong effect of Urban Heat Island in the different medium-dense built-up pocket of the cities. The impervious surface shows a positive correlation with LST while green space shows negative correlation with LST. The Gaussian analysis of three cities indicates that the landlock city of Ahmedabad experiences extreme temperature for a larger span of time, compared to Surat and Delhi. It is also observed, skewness in the temperature variation compared to the past several years. This inferences out there may be possibility of extreme heat and heatwaves. These events of extreme temperature led to loss of human lives and creating thermal discomfort to the vulnerable group of people. Further, from this study it is found that human anthropogenic activities are playing major role in rising temperature. Invariably this rise in temperature is resulting in climate change. The study can be extended for understanding the factors influencing climate change.

#### 5. REFERENCES

1. "How The Urban Heat Island Effect Is Harming Our Cities." Retrieved March 3, (2022), from <https://hub.beesmart.city/en/solutions/how-the-urban-heat-island-effect-is-harming-our-cities>
2. Hurlimann, A., Moosavi, S., and Browne, G. R. "Urban planning policy must do more to integrate climate change adaptation and mitigation actions." *Land Use Policy*, Vol. 101, (2021), 105188. <https://doi.org/10.1016/j.landusepol.2020.105188>
3. Liu, D., Hu, S., and Liu, J. "Contrasting the performance capabilities of urban radiation field between three microclimate simulation tools." *Building and Environment*, Vol. 175, (2020), 106789. <https://doi.org/10.1016/j.buildenv.2020.106789>
4. Landsberg H.E. *The Urban Climate*. NewYork: The Academic Press, (1981).
5. EPA. "Learn About Heat Islands | Heat Island Effect | US EPA." Retrieved November 18, (2020), from <https://www.epa.gov/heatislands/learn-about-heat-islands>
6. Khordadi, M. J., Alizadeh, A., Mahallati, M. N., Ansari, H., and Sanaeinejad, H. "Climate Change Impact on Precipitation Extreme Events in Uncertainty Situation; Passing from Global Scale to Regional Scale." *International Journal of Engineering, Transactions B: Applications*, Vol. 28, No. 8, (2015), 1140-1144. <https://doi.org/10.5829/idosi.ije.2015.28.08b.05>
7. Oke, T. *Boundary Layer Climates*. Taylor & Francis.
8. Manoli, G., Fatichi, S., Schlöpfer, M., Yu, K., Crowther, T. W., Meili, N., Burlando, P., Katul, G. G., and Bou-Zeid, E. "Magnitude of urban heat islands largely explained by climate and population." *Nature* 2019 573:7772, Vol. 573, No. 7772, (2019), 55-60. <https://doi.org/10.1038/s41586-019-1512-9>
9. Li, D., and Bou-Zeid, E. "Synergistic interactions between urban heat islands and heat waves: The impact in cities is larger than the sum of its parts." *Journal of Applied Meteorology and Climatology*, Vol. 52, No. 9, (2013), 2051-2064. <https://doi.org/10.1175/JAMC-D-13-02.1>
10. Loibl, W., Vuckovic, M., Etminan, G., Ratheiser, M., Tschannett, S., and Österreicher, D. "Effects of densification on urban microclimate—a case study for the city of Vienna." *Atmosphere*, Vol. 12, No. 4, (2021). <https://doi.org/10.3390/atmos12040511>
11. Tavares, S. G., Swaffield, S. R., and Stewart, E. J. "A case-based methodology for investigating urban comfort through interpretive research and microclimate analysis in post-earthquake christchurch, New Zealand." *Environment and Planning B: Urban Analytics and City Science*, Vol. 46, No. 4, (2019), 731-750. <https://doi.org/10.1177/2399808317725318>
12. Touati, N., Gardes, T., and Hidalgo, J. "A GIS plugin to model the near surface air temperature from urban meteorological networks." *Urban Climate*, Vol. 34, (2020), 100692. <https://doi.org/10.1016/j.uclim.2020.100692>
13. Bherwani, H., Singh, A., and Kumar, R. "Assessment methods of urban microclimate and its parameters: A critical review to take the research from lab to land." *Urban Climate*, Vol. 34, (2020), 100690. <https://doi.org/10.1016/j.uclim.2020.100690>
14. United Nation Climate Change. "The Paris Agreement | UNFCCC." Retrieved July 6, (2020), from <https://unfccc.int/process-and-meetings/the-paris-agreement/the-paris-agreement>

15. Roy, B., Bari, E., Nipa, N. J., and Ani, S. A. "Comparison of temporal changes in urban settlements and land surface temperature in Rangpur and Gazipur Sadar, Bangladesh after the establishment of city corporation." *Remote Sensing Applications: Society and Environment*, Vol. 23, (2021), 100587. <https://doi.org/10.1016/j.rsase.2021.100587>
16. Liu, J., and Niyogi, D. "Identification of linkages between urban heat Island magnitude and urban rainfall modification by use of causal discovery algorithms." *Urban Climate*, Vol. 33, (2020), 100659. <https://doi.org/10.1016/j.uclim.2020.100659>
17. Hu, D., Meng, Q., Zhang, L., and Zhang, Y. "Spatial quantitative analysis of the potential driving factors of land surface temperature in different 'Centers' of polycentric cities: A case study in Tianjin, China." *Science of the Total Environment*, Vol. 706, (2020), 135244. <https://doi.org/10.1016/j.scitotenv.2019.135244>
18. Sharma, R., Pradhan, L., Kumari, M., and Bhattacharya, P. "Assessing urban heat islands and thermal comfort in Noida City using geospatial technology." *Urban Climate*, Vol. 35, (2021), 100751. <https://doi.org/10.1016/j.uclim.2020.100751>
19. Ichan Ali, M., Hafid Hasim, A. H. H., and Raiz Abidin, M. "Monitoring the Built-up Area Transformation Using Urban Index and Normalized Difference Built-up Index Analysis." *International Journal of Engineering, Transactions B: Applications*, Vol. 32, No. 5, (2019), 647-653. <https://doi.org/10.5829/ije.2019.32.05b.04>
20. Liang, J., Xie, Y., Sha, Z., and Zhou, A. "Modeling urban growth sustainability in the cloud by augmenting Google Earth Engine (GEE)." *Computers, Environment and Urban Systems*, Vol. 84, (2020), 101542. <https://doi.org/10.1016/j.compenvurbysys.2020.101542>
21. Despini, F., Ferrari, C., Santunione, G., Tommasone, S., Muscio, A., and Teggi, S. "Urban surfaces analysis with remote sensing data for the evaluation of UHI mitigation scenarios." *Urban Climate*, Vol. 35, (2021), 100761. <https://doi.org/10.1016/j.uclim.2020.100761>
22. Agarwal, S., and Nagendra, H. "Classification of Indian cities using Google Earth Engine." *Journal of Land Use Science*. <https://doi.org/10.1080/1747423X.2020.1720842>
23. Ravanelli, R., Nascetti, A., Cirigliano, R. V., Di Rico, C., Monti, P., and Crespi, M. "Monitoring urban heat island through google earth engine: Potentialities and difficulties in different cities of the United States." *International Archives of the Photogrammetry, Remote Sensing and Spatial Information Sciences - ISPRS Archives*, Vol. 42, No. 3, (2018), 1467-1472. <https://doi.org/10.5194/isprs-archives-XLII-3-1467-2018>
24. Roy, B. "Optimum machine learning algorithm selection for forecasting vegetation indices: MODIS NDVI & EVI." *Remote Sensing Applications: Society and Environment*, Vol. 23, (2021), 100582. <https://doi.org/10.1016/j.rsase.2021.100582>
25. Choudhury, D., Das, A., and Das, M. "Investigating thermal behavior pattern (TBP) of local climatic zones (LCZs): A study on industrial cities of Asansol-Durgapur development area (ADDA), eastern India." *Urban Climate*, Vol. 35, (2021), 100727. <https://doi.org/10.1016/j.uclim.2020.100727>
26. Qaid, A., Bin Lamit, H., Ossen, D. R., and Raja Shahminan, R. N. "Urban heat island and thermal comfort conditions at micro-climate scale in a tropical planned city." *Energy and Buildings*, Vol. 133, (2016), 577-595. <https://doi.org/10.1016/j.enbuild.2016.10.006>
27. Xu, M., Bruehlisauer, M., and Berger, M. "Development of a new urban heat island modeling tool: Kent Vale case study." *Procedia Computer Science*, Vol. 108, (2017), 225-234. <https://doi.org/10.1016/j.procs.2017.05.282>
28. Antoniou, N., Montazeri, H., Neophytou, M., and Blocken, B. "CFD simulation of urban microclimate: Validation using high-resolution field measurements." *Science of the Total Environment*, Vol. 695, (2019), 133743. <https://doi.org/10.1016/j.scitotenv.2019.133743>
29. Wong, N. H., He, Y., Nguyen, N. S., Raghavan, S. V., Martin, M., Hii, D. J. C., Yu, Z., and Deng, J. "An integrated multiscale urban microclimate model for the urban thermal environment." *Urban Climate*, Vol. 35, (2021), 100730. <https://doi.org/10.1016/j.uclim.2020.100730>
30. Wang, R., Ren, C., Xu, Y., Lau, K. K. L., and Shi, Y. "Mapping the local climate zones of urban areas by GIS-based and WUDAPT methods: A case study of Hong Kong." *Urban Climate*, Vol. 24, (2018), 567-576. <https://doi.org/10.1016/j.uclim.2017.10.001>
31. Wong, N. H., He, Y., Nguyen, N. S., Raghavan, S. V., Martin, M., Hii, D. J. C., Yu, Z., and Deng, J. "An integrated multiscale urban microclimate model for the urban thermal environment." *Urban Climate*, Vol. 35, (2021), 100730. <https://doi.org/10.1016/j.uclim.2020.100730>
32. Morrison, W., Kotthaus, S., and Grimmond, S. "Urban surface temperature observations from ground-based thermography: intra- and inter-facet variability." *Urban Climate*, Vol. 35, (2021), 100748. <https://doi.org/10.1016/j.uclim.2020.100748>
33. Aleksandrowicz, O., Zur, S., Lebendiger, Y., and Lerman, Y. "Shade maps for prioritizing municipal microclimatic action in hot climates: Learning from Tel Aviv-Yafo." *Sustainable Cities and Society*, Vol. 53, (2020), 101931. <https://doi.org/10.1016/j.scs.2019.101931>
34. Prama, M., Omran, A., Schröder, D., and Abouelmagd, A. "Vulnerability assessment of flash floods in Wadi Dahab Basin, Egypt." *Environmental Earth Sciences*, Vol. 79, No. 5, (2020), 1-17. <https://doi.org/10.1007/s12665-020-8860-5>
35. "Delhi Development Authority." Retrieved November 9, 2021, from [https://dda.org.in/MPD\\_2041.aspx#](https://dda.org.in/MPD_2041.aspx#)

---

### Persian Abstract

#### چکیده

اقلیم خرد شهری تأثیر مخربی بر زندگی جمعیت شهری گذاشته است. این تحقیق با هدف شناسایی عامل آگاه از محیط زیست در مقابل برنامه ریزی شهری که منجر به چرخه معیوب تغییر اقلیم شهری می شود، انجام می شود. چرخه معیوب شامل بسیاری از پارامترهای پویایی شهری است که درک آنها پیچیده است. این تحقیق بر استفاده از داده های بزرگ سنسجش از راه دور در موتور Google Earth به عنوان پیشرفتی برای مطالعه آسیب پذیری آب و هوا که منجر به Gentrification آب و هوای شهری می شود تأکید دارد. داده های زمانی لندست برای ۳۰ سال گذشته برای مطالعه در نظر گرفته شده است. سه شهر با ویژگی های جغرافیایی و زمینی متنوع برای مطالعه انتخاب شده اند تا بفهمیم برنامه ریزی تعیین کننده مدرن در انسجام با اهداف توسعه پایدار است. درک اطلاعات مکانی و زمانی نقاط هات اسپات شهری با استفاده از داده های ماهواره ای با وضوح بالا کافی نیست تا نیاز به کاهش دما بین ۲ تا ۳ درجه سانتیگراد را برآورده کند. مطالعه حاضر نشان می دهد که چگونه دلایل تغییر اقلیم کوچک همراه با زمین، موقعیت مکانی و الگوی رشد شهری شهر متفاوت است.

---



## Earth-to-air Heat Exchanger for Cooling Applications in a Hot and Dry Climate: Numerical and Experimental Study

A. Albarghooth<sup>a</sup>, A. Ramiar<sup>\*b</sup>, R. Ramyar<sup>c</sup>

<sup>a</sup> Mechanical Engineering Department, Microfluidics and MEMS lab, Babol Noshirvani University of Technology, Babol, Iran

<sup>b</sup> Mechanical Engineering Department, Babol Noshirvani University of Technology, Babol, Iran

<sup>c</sup> Principal planner at Prince Williams County, State University of New York, College of Environmental Science and Forestry, United States of America

### PAPER INFO

#### Paper history:

Received 27 August 2022

Received in revised form 08 October 2022

Accepted 09 October 2022

#### Keywords:

Earth-to-air Heat Exchanger

Thermal Performance

Geothermal Energy

CFD Modelling

### ABSTRACT

Shallow geothermal energy, by an earth-to-air heat exchanger (EAHE), is utilized to cool buildings with minimal energy usage. Significant parameters affecting the heat exchanger's performance must be investigated to obtain a suitable design. Shallow geothermal energy, by an earth-to-air heat exchanger (EAHE), is utilized to cool buildings with minimal energy usage. Significant parameters affecting the heat exchanger's performance must be investigated to obtain a suitable design. This article numerically and experimentally investigates the effect of pipe diameter, pipe length, inlet air temperature, soil temperature, airflow velocity, and soil thermal conductivity on the performance of the heat exchanger under hot and dry climate conditions. The soil temperature distribution was measured from the surface to a depth of 7 m in the city of Karbala (center of Iraq) in the summer season. The experimental test for EAHE was carried out in water-saturated soil and ambient air temperatures of 41 °C, 45 °C, and 49.5 °C at four different velocities. The percentage drop in the EAHE outlet air temperature at 9 m/s was 28.3%, 25.5%, and 19.5%, respectively. Also, the three-dimensional model was created, and the simulation results were compared with the experimental results, which were in good agreement. An equation for the outlet air temperature was found as a function of pipe diameter and length, ambient air temperature, soil temperature around the pipe, and soil thermal conductivity. The resulted equation were compared with the current experimental results and experimental results of reported data in literature. As a result, a very good agreement was observed. The results showed that the parameter L (length of the pipe) causes the strongest nonlinear behavior in the equation. For the cases considered, at diameters 75 and 100 mm, an approximate linear behavior for the length required to achieve a specific outlet temperature was observed. It can be concluded from the results that changing the soil type from dry one ( $k=0.5$  W/m K) to saturated one (case of Karbala city,  $k=1.5$  W/m K) resulted about 25% reduction in the length of the pipe. Also, the results showed that at an air velocity of 7m/s, the length required to obtain 26 °C at the outlet of EAHE is 62.1 m which is 55% higher than the case of 29 °C (39.9m).

doi: 10.5829/ije.2023.36.01a.10

## 1. INTRODUCTION

In recent years, humanity has realized the danger of climate change to the continuation of life and that global warming has reached to dangerous levels that threaten environmental disasters. The main reason for climate change is the large consumption of energy, especially the power generated by burning fossil fuels. Most consumption takes place in cities, which is equal to 73%

of the global energy consumption, and the most considerable amount of energy usage is consumption on cooling and heating operations [1]. Using traditional cooling systems in residential areas significantly contributes to increasing the heat in these areas, indirectly through large energy consumption and directly by exposing heat through the condenser to the neighboring regions [2]. Therefore, it is necessary to think of alternative ways to reduce the use of traditional

\* Corresponding author Institutional Email: [aramiar@nit.ac.ir](mailto:aramiar@nit.ac.ir)  
(A. Ramiar)

cooling systems and take advantage of sustainable natural energy sources. Since ancient times, people have benefited from the heat stored in the ground for cooling and heating purposes, as the temperature of the subsurface soil at a depth of between 1-4 m is lower than the ambient air temperature in the summer and higher than the ambient air temperature in the winter [3].

Geothermal energy was used to cool residential buildings and greenhouses, using pipes buried horizontally or vertically under the earth's surface. The heat exchanger can be defined as a device to help the process of heat transfer between various materials without direct mixing [4]. The earth-to-air heat exchanger (EAHE) system is considered adequate and economical in the long run [5]. Unfortunately, its use is still limited due to the relatively high initial cost and the difficulty of digging and burying pipes in residential areas. Because of the human race's significant challenges, all possible natural resources must be used to replace traditional energy with clean, renewable energy, especially in hot areas where residents need to use cooling systems all day throughout the summer. Many parameters affect the operation of the geothermal heat exchanger, including the soil's thermal characteristics and water content. Furthermore, main parameters like the depth of pipe burial, pipe length, pipe diameter, and airflow velocity inside the pipe significantly affect the performance of EAHE.

Many researchers have measured the soil temperature distribution in depths less than 20 meters, e.g., Popiel et al. [6] in Poznan in Poland, and Al-Ajmi et al. [7] in Kuwait. These studies have shown that the temperature distribution of soil depends primarily on geographical location, soil type, outdoor air temperature, ground cover, and measurement time. Also, they showed that temperature increases during the day and decreases at night. It also changes with the change of the months of the year, where the temperature fluctuation is significant at the soil surface and drops to a lower value at a depth of more than 4 meters, beyond which it remains almost constant.

Some researchers investigated the effect of the water content in the soil on the heat transfer to the heat exchanger. Lu et al. [8] developed a numerical model that links thermal conductivity and soil water content. They validated this model using eight soil samples' measured thermal conductivity. The results showed that the thermal conductivity significantly increases with an increase in water content. Song et al. [9] studied the effect of soil density and water content on the thermal conductivity of the soil. They took seven different soil types, made a new mathematical model, and proved that the type of soil and water content significantly affect the magnitude of thermal conductivity. They concluded that heat transfer increases by an increase in the water content in the soil.

The heat transfer in the soil primarily depends on soil thermal conductivity, which is improved by high thermal conductivity near soil for the EAHE system. The thermal conductivity of soil is determined mainly by the soil type, dry density, water saturation level, and particle size [10]. Agrawal et al. [11] made two similar experimental setups of the EAHE system and examined the performance of the dry and wet soil. They noticed that the thermal conductivity of the soil increased when the soil water content increased; which is resulted an enhancement in the thermal efficiency of EAHE.

Many experimental studies have been performed on the heat exchanger's design parameters, including pipe length, diameter, and burial depth. Abbaspour et al. [12], in northeast Iran, conducted 72 practical experiments. The experiment was conducted with two parallel pipes of two different materials (galvanized steel and PVC). They buried pipes at two different depths (2 and 4 m). They used a pipe diameter of 4 inches and three airflow velocities (4, 7, and 10 m/s). The experiments were conducted during the summer and winter at 36.5 °C and 3.8°C, respectively. In summer, the soil temperature was 20 °C and 18 °C at 2 m and 4 m depths. They concluded that all parameters have an important influence on the EAHE system's performance except for the pipe's material. The system performs more effectively with a galvanized pipe at a depth of 4 m and air velocity at 4 m/s.

Bisoniya et al. [13] conducted an experimental study to investigate the effectiveness of the EAHE system in hot weather in Bhopal city (India). They produced 3D models of the EAHE system and validated this model with their experimental results. Modeling and experimental results were in good agreement. They concluded that the lowest outlet air temperature was obtained at the minor diameter and lowest airflow velocity. In Marrakech (Morocco), Khabbaz et al. [14] experimented on a heat exchanger in the summer season, consisting of three parallel horizontal pipes with an inner diameter of 6 inches and a length of 72 m, buried under a depth of (2.2 and 3.2 m). They found that at an ambient air temperature of 44 °C, the cooling capacity was 55 W/m<sup>2</sup>, and the heat exchanger reduced the temperature inside the building to 26 °C.

Serageldin et al. [15] studied the thermal parameters of the (EAHE) system experimentally and numerically in dry and hot weather in Egypt. The study was carried out to investigate the impact of various parameters such as length, diameter, material, pipe thickness, and airflow velocity. They have shown that all parameters have a significant effect, except for pipe materials and thickness, which have a negligible impact. Hasan et al. [16] numerically investigated the performance of the EAHE system in hot regions such as Nasiriyah city (Iraq). They found that when the inlet air temperature was 50 °C,

50 m pipe length, and 3 m burial depth, the EAHE system with a pipe diameter of 150 mm provided the best performance.

Additional research has been conducted in the field of EAHE, mainly to identify the effective parameters of its performance. But it is known that the performance of EAHE depends on some features of the installed location, such as the type of soil, its water content, the vegetation cover, the climate of the region, and the time of the year. The goal of this article is to conduct an experimental and numerical investigation to study the effectiveness of ground cooling systems in a hot and arid area such as Karbala city in central Iraq, which has a temperature of more than 50 °C and an average of more than 45 °C during the summer day. The special condition of the soil in this city is so that at a depth of more than 2 m, the soil is fully saturated (full of water), which has not been reported to be studied in previous articles. Finally, based on experimental and numerical data, a correlation is developed for the air outlet temperature from EAHE as a function of different parameters such as inlet pipe temperature, pipe diameter, air velocity, burial depth, soil thermal conductivity, and pipe length. The equation estimates the effect of designing parameters on the EAHE's performance.

## 2. EXPERIMENTAL SETUP

As previously noted, the EAHE's energy performance mainly depends on climate and soil conditions. As a result, the dynamic thermal behavior of an EAHE is case-sensitive and must be investigated in the context of climate. In this paper, an EAHE system was assembled as a case study in Karbala city, located in the center of Iraq, at 32.37° north latitude and 44.02° east longitude. Karbala has a hot desert climate, with scorching, dry summers, and the average maximum temperature in the summer reaches more than 45 °C and sometimes exceeds 50 °C during July and August. The experimental portion of this study is divided into two parts:

The first stage aimed to measure the ground temperature distribution from the surface to a depth of 7m. Two temperature sensors were used to ensure good measurement accuracy, a K-type thermocouple with 0.5°C accuracy, and the sensors connected to Multi-Channel Data Logger (Fuji phf61b11).

The second type of sensor is a waterproof sensor connected to the Arduino device. The sensors were installed in an open area, clear of vegetation directly exposed to solar radiation, and the water table at depths of 1 m. The measurement was carried out on (15-30) July 2021, the weather was sunny, and the air temperature in the middle of the day was between (45-50) °C. Table 1 summarized the types of sensors used, their depths, the total error rate for each measurement, and a comparison

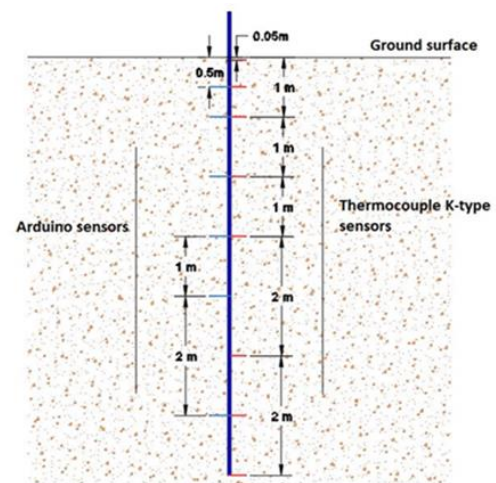
**TABLE 1.** The temperatures along the depth of 7 m

Depth m	Thermometer type	16 July T°C	17 July T°C	19 July T°C	Total error
Ambient	TPM-10	46.5	48	47	
Surface	TPM-10	59	60	59.3	
0.05	Thermocouple	51	52	51.2	1.9
0.5	Arduino	33.1	32.9	33.1	0.6
0.5	Thermocouple	32.9	33.1	33.4	1.5
1	Arduino	30.6	30.8	30.5	1
1	Thermocouple	31	31.1	31.3	0.95
2	Arduino	27.3	27.4	27.7	1.4
2	Thermocouple	27.7	27.6	28.2	2.1
3	Arduino	25.8	25.5	25.6	1.1
3	Thermocouple	25.5	25.4	25.9	1.5
4	Arduino	23.7	24.7	24.9	4.8
5	Thermocouple	23.7	24.2	24.6	3.6
6	Arduino	23.7	24.1	24.2	2
7	Thermocouple	23.7	23.8	24.1	1.6

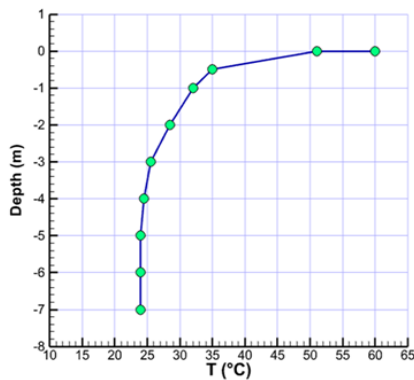
between some measured temperature measurements for three days in July.

Figure 1 shows the distribution of temperature sensors under the ground's surface to a depth of 7 m. It can be observed at a depth of 0.5, 1, 2, and 3 m that two types of Arduino sensors and a thermocouple were installed to compare the measured temperature for both types to obtain the highest measurement accuracy.

Figure 2 shows the temperature distribution of the soil on 17th July 2021 at 14:00, when the ambient temperature was 48°C. A significant increase in surface



**Figure 1.** Distribution of temperature sensors under the ground's surface



**Figure 2.** The ground temperature distribution and sensors on 17th July 2021 at 14:00.

temperature can be observed because of direct exposure of the earth's surface to sunlight. The surface temperature reached 60 °C, dropping dramatically from the surface to a depth of 1m to 32 °C. The temperature drops marginally until it arrives at a depth of 4m. After that, the temperature is almost constant and equal to 24°C.

The second stage is aimed at studying the behavior of the Earth-Air heat exchanger. The experimental EAHE setup consists of a horizontal polyvinyl chloride pipe (PVC) with a diameter of 0.1 m and a total horizontal length of 20 m. The pipe is buried at 2 meters in water-saturated soil on a flat area in Karbala city, as shown in Figure 2. The air is blown through the pipe by a blower driven by a 550-W single-phase electric motor (maximum flow rate of 870 m<sup>3</sup>/h and a maximum velocity of 2820 RPM) with velocity control. The inlet air temperature and the underground air temperature were measured at the pipe center using the temperature sensors, PT100, and a digital thermometer (TPM-10) with 0.5°C accuracy, installed in every 3 meters of the pipe, as shown in Figure 3. The temperature is monitored by the Multi-Channel Data Logger (Fuji phf61b11). The airflow velocity and the air temperature at the outlet EAHE system are measured using an anemometer (RZ8901) hang the range of 0–45 m/s and a thermometer with 3% accuracy. The experiment was carried out on days 6, 8, 13, and 30 Aug 2021, when the temperature ranged between 40 and 50 °C.

### 3. COMPUTATIONAL FLUID DYNAMICS (CFD) MODELING

Computational Fluid Dynamics (CFD) is widely used to solve problems that involve fluid flows. The Navier-Stokes equations are the foundation of practically all CFD issues [17]. Heat transfer affects the soil layer near the EAHE pipe surface. This soil is referred to as thermally disturbed soil, as shown in Figure 4. The

thickness of the disturbed soil layer depends on its thermal properties, the temperature difference between the soil and the air passing through the pipe, the airflow velocity, and the operating time of the heat exchanger [18]. According to some academics, the disturbed soil thickness should be equivalent to the pipe radius [7].

Others suggested that the thickness of the soil layer should be twice [19] or four times the pipe radius [16]. The disturbed soil thickness in this research was assumed to be three times the pipe radius.

3-D fluid flow and conjugate heat transfer analyses under temperature conditions are used to model the heat transfer produced by airflow at various temperatures. The conduction heat transfer occurs in the soil and the pipe

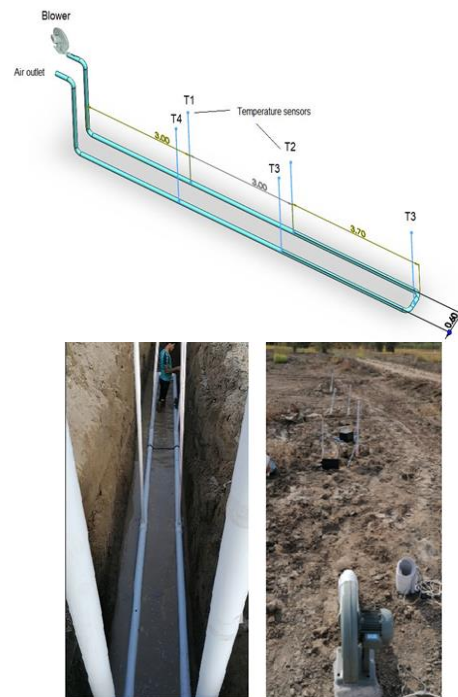


**Figure 3.** EAHE system layout schematic and stages of construction

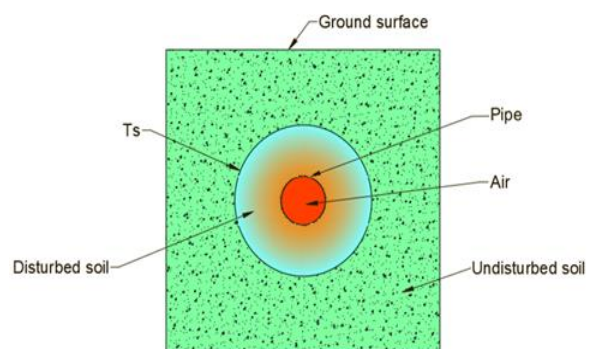


**Figure 4.** Cross-section showing the disturbed and undisturbed soil around the heat exchanger pipe

wall. The heat exchange between the airflow in the pipe and the pipe wall is dominated by convection heat transfer. The k-omega SST turbulence model is chosen to accurately analyze near-wall(s) conditions and boundary layer evolution [20]. The following are the transport equations [21]:

Continuity equation:

$$\frac{\partial}{\partial x_i}(\rho u_i) = 0 \quad (1)$$

Momentum equation:

$$\frac{\partial}{\partial x_i}(\rho u_i u_j) = -\frac{\partial p}{\partial x_i} + \frac{\partial}{\partial x_j} \left( \mu \left( \frac{\partial u_i}{\partial x_j} + \frac{\partial u_j}{\partial x_i} \right) \right) + \frac{\partial}{\partial x_j}(-\rho u_i' u_j') \quad (2)$$

$$\frac{\partial}{\partial x_i}(\rho k u_i) = \frac{\partial}{\partial x_i} \left( \left( \mu + \frac{\mu_t}{\sigma_k} \right) \frac{\partial k}{\partial x_i} \right) + G_k - \rho \beta^* k \omega + S_k \quad (3)$$

$$\frac{\partial}{\partial x_i}(\rho \omega u_i) = \frac{\partial}{\partial x_i} \left( \left( \mu + \frac{\mu_t}{\sigma_\omega} \right) \frac{\partial \omega}{\partial x_i} \right) + \alpha \frac{\omega}{k} G_k - \rho \beta \omega^2 + S_\omega \quad (4)$$

$$\mu_t = \frac{\rho k}{\omega} \quad (5)$$

$$G_k = -\rho u_i' u_j' \frac{\partial u_j}{\partial x_i} \quad (6)$$

where  $k$  is the turbulence kinetic energy,  $\omega$  is the specific dissipation rate,  $\sigma_\omega$  and  $\sigma_k$  are the turbulent Prandtl numbers for  $\omega$  and  $k$ , respectively,  $\mu_t$  is the turbulent viscosity, and  $S_k$  and  $S_\omega$  are introduced source terms. For incompressible flow,  $\beta^* = 0.09$  and  $\beta = 0.075$ . The energy equation for the incompressible and viscous flow of the air, soil, and pipe:

$$U_j \frac{\partial T}{\partial x_j} = \frac{1}{\rho c_p} \frac{\partial}{\partial x_j} \left( k \frac{\partial T}{\partial x_j} - u_j' T' \right) \quad (7)$$

$$\frac{\partial}{\partial x_j} \left( k_p \frac{\partial T}{\partial x_j} \right) = 0 \quad (8)$$

$$\frac{\partial}{\partial x_j} \left( k_s \frac{\partial T}{\partial x_j} \right) = 0 \quad (9)$$

where  $k_p$  and  $k_s$  are the pipe and soil thermal conductivity, respectively. The following equation is used to calculate EAHE's cooling capacity:

$$Q = \dot{m} C_p (T_{in} - T_{out}) \quad (10)$$

$$\dot{m} = \frac{\pi}{4} D^2 \rho V \quad (11)$$

where  $Q$  is the cooling capacity of EAHE;  $\dot{m}$  is the air mass flow rate;  $D$  is pipe diameter;  $\rho$  is air density;  $V$  is airflow velocity;  $C_p$  is the specific heat of air;  $T_{in}$  is the inlet air temperature, and  $T_{out}$  is the outlet air temperature.

#### 4. BOUNDARY CONDITION

In the CFD simulation investigation of the EAHE system, the following boundary conditions were used:

1. Inlet boundary conditions: the constant inlet air velocity and temperature ( $T_{in}$ ) were used. The values of  $T_{in}$  were chosen for the summer season based on the climate conditions of Karbala city in central Iraq.
2. Wall: The conjugate heat transfer model is used to simulate the soil's temperature distribution more realistically in the disturbed region; the temperature  $T_s$  is considered constant on the outer surface and equal to the undisturbed soil temperature at that depth (Figure 4).
3. Outlet boundary conditions: The relative pressure at the outlet was assumed to be constant and equal to 0 atm. The value  $1 \times 10^{-6}$  is used as the convergence criterion for momentum and energy equations.

#### 5. VALIDATION OF THE MODEL

To simulate the process of airflow and heat transfer in the EAHE system, the 3D geometry of both the solid and liquid domains are considered, as shown in Figure 4. A structured grid for soil and the fluid domain reduces the computational time and helps to obtain the most accurate solution. CFD-based analysis was used to calculate the outlet air temperature from EAHE by using ANSYS FLUENT software.

The CFD simulation used the same thermo-physical parameters of the clayey loam soil with high water content as the experiment. Table 2 summarized the thermal properties of air and soil [22]. The soil temperature  $T_s$  is constant at the disturbed soil's outer surface and equals 31.5 °C; it was measured at a depth of 2 m in Karbala city during the summer season. Experimental data was used to validate the numerical model in this research. Because of the high Reynolds number of the flow ( $2.4 \times 10^4$  -  $1.9 \times 10^5$ ), the turbulent model (k- $\omega$  SST) was chosen to compute the temperature and velocity of the airflow inside the pipe and the heat transfer in the soil.

Three types of meshes were tested to obtain a precise solution in the proper time. Figure 5(a) compares the experimental and numerical results of the air temperature

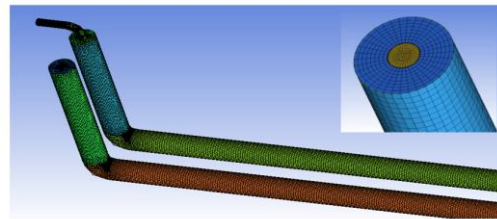


Figure 5. Modeling geometry and mesh of the EAHE

along the EAHE pipe at the air velocity of 5 m/s and the inlet temperature of 49.5 °C. It can be seen that at the mesh size of 850000, a good agreement between the numerical and experimental results is obtained. Table 3 compares the experimental and numerical results for different air velocities. Figure 5(b) represents compare between the results of the present model and the experimental results of Misra et al. [18]. It can be seen that the current numerical model is in good agreement with the experimental results, and the maximum percentage of error was 3.42%. It can investigate the impact of various parameters on the EAHE system's overall performance.

### 6. RESULTS AND DISCUSSION

The numerical analysis was carried out to determine the impact of five essential parameters: pipe length, pipe diameter, airflow velocity, soil thermal conductivity, soil temperature, and inlet air temperature of the EAHE system. Because the average temperature in the summer

is 45°C and the in the winter it is 18°C. The EAHE system has a larger capacity for summer cooling than winter heating under the climatic circumstances of Karbala City [13]. As a result, only summer cooling was considered in the study. The previous heat exchanger design will be studied, but with a 60m pipe length and a distance between the parallel pipes of 1 m. The amount of air exiting the heat exchanger must be sufficient to obtain good cooling capacity in the area at the minimal possible temperature. The EAHE system's performance is improved by increasing the pipes' total surface, which can be enhanced by increasing pipe length and diameter. As a result, the cost rises, so the pipe length should be kept in a proper range. So, we investigate the impact of the previous parameters listed out in Table 4 and the cases to be studied on the outlet air temperature as a function of the pipe length.

Figure 7(a) shows the temperature distribution of air, and adjacent soil layers in the inlet section of the EAHE pipe in the longitudinal plane, with 100 mm pipe diameter, inlet air temperature of 50°C, airflow velocity of 5 m/s, the thermal conductivity coefficient is 1.5 (w/m.k), and soil temperature  $T_s$  is 31.5°C. It can be seen that the temperature of the soil adjacent to the pipe increases due to the heat transfer from the hot air passing inside the pipe. In return, the air temperature decreases gradually in the flow direction. The heat transfer in the first meters is significant due to the temperature difference between the air and the soil, and the heat transfer gradually decreases along the length of the pipe. Figure 7(b) shows the air and soil temperature distribution in a radial direction at pipe lengths of 3 m and 17 m, where the temperature in the center of the pipe was 45 and 36 °C, respectively. It is also noted that the temperature of the soil around the pipe at a length of 3 m increased sharply compared to the soil at a pipe length of 17 m. The temperature drop per unit length can be obtained from the following equation:

$$TD = \frac{\Delta T}{\Delta L} = \frac{T_1 - T_2}{L_2 - L_1} \tag{12}$$

Figure 8 depicts the variation in air temperature along the length for pipe diameters 75, 100, 150, and 200 mm  $V=5\text{m/s}$ ,  $k=1.5 \text{ w/m.K}$ , and  $T_s=25.5^\circ\text{C}$ ). It can be observed that the reduction in air temperature is significant at the first 15m for all pipes diameter. The TD value in the first five meters is high, e.g. (3.34, 2.27, 1.6, 1.07) °C/m for pipe diameters 75, 100, 150, and 200mm, respectively, because the temperature difference between air and soil is significant (24.5°C), which reduces as the length increases. It can also be seen that as the diameter of the pipe increases, the outlet air temperature increases. For a pipe with a diameter of 75 mm, the outlet temperature became 27 °C, and the temperature drop TD was 0.11°C/m at the pipe length of 25 m. The temperature drop can be considered as the criterion for the required length of the EAHE pipe because increasing the length

**TABLE 2.** Thermo-physical properties of air and soil

Material	Density (kg/m <sup>3</sup> )	Specific heat capacity (J/kg K)	Thermal conductivity (W/m-K)
Soil	2050	1840	1.5
Air	1.225	1006.5	0.0242

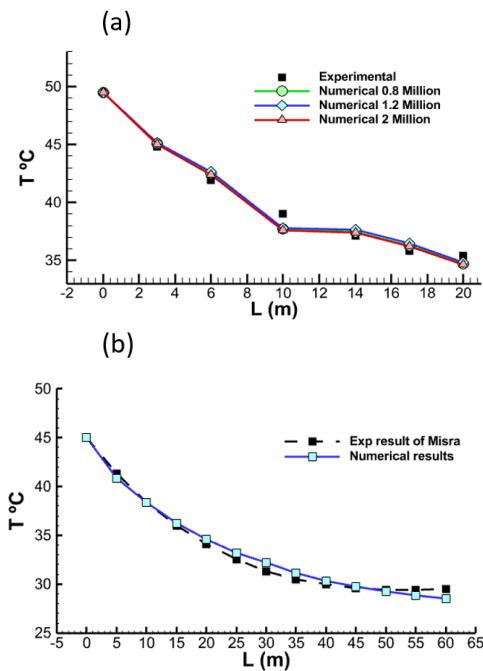


**Figure 6.** Compares the experimental and numerical results for (a) present experimental for different mesh numbers. (b) Experimental result of (Misra et al.) [18]

means increasing the EAHE; the length should be as small as possible; for example, it can be regarded that a temperature drops less than 0.15 °C/m may be sufficient to ensure the efficient operation of EAHE. As shown in Figure 8, for D=100 mm, the length of 30 m can be considered sufficient where  $T_{out} = 27.8^{\circ}\text{C}$  and  $TD=0.15$

°C/m. In other words, to achieve a slight enhancement in outlet temperature from this value ( $27.8^{\circ}\text{C}$ ), a much longer EAHE is needed. For pipe diameters 150 and 200 mm,  $TD < 0.15^{\circ}\text{C/m}$  when the pipe length is 45 m and 55 m, respectively. So, these lengths are recommended for the conditions mentioned above in Karbala.

**TABLE 3.** Comparison between the experimental and numerical results for different air velocities

Location	V=5 m/s			6.5 m/s			9 m/s					
	T <sub>Expe</sub>	T <sub>Num</sub>	T <sub>diff</sub>	T <sub>Expe</sub>	T <sub>Num</sub>	T <sub>diff</sub>	T <sub>Expe</sub>	T <sub>Num</sub>	T <sub>diff</sub>	T <sub>Expe</sub>	T <sub>Num</sub>	T <sub>diff</sub>
T <sub>inlet</sub> °C	49.5	49.5	0	49	49	0	48.5	48.5	0	45	45	0
T1 (3m) °C	44.8	45.1	-0.3	45.1	45.19	-0.09	45.3	45.5	-0.2	43	43.06	-0.06
T2 (6m) °C	41.9	42.49	-0.59	42.8	42.92	-0.12	43.3	43.6	-0.3	41.3	41.87	-0.57
T3 (10m) °C	38.6	37.72	0.88	39.2	38.45	0.75	39.6	39.52	0.08	37.8	39.05	-1.25
T4 (14m) °C	37.1	37.48	-0.38	38.1	38.24	-0.14	38.9	39.37	-0.47	37.1	38.96	-1.86
T5 (17m) °C	35.4	36.29	-0.89	36.6	37.06	-0.46	37.1	38.22	-1.12	35.5	38.1	-2.6
T <sub>out</sub> °C	35.4	34.7	0.7	35.2	35.39	-0.19	35.5	36.5	-1	35	36.73	-1.73

**TABLE 4.** EAHE system variable at different levels

Location	Symbol	Level											
		1	2	3	4	5	6	7	8	9	10	11	12
Diameter of EAHE pipe (mm)	D	75	100	150	200								
Airflow velocity (m/s)	V	5	7.5	10	15								
Thermal conductivity of soil (W/m K)	Ks	0.5	1	1.5									
Inlet air temperature (°C)	T <sub>in</sub>	35	40	45	50								
Soil temperature (°C)	T <sub>s</sub>	25.5	30										
pipe length (m)	L	5	10	15	20	25	30	35	40	45	50	55	60

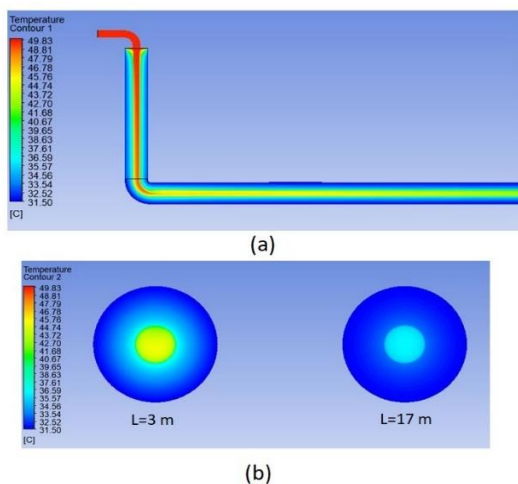


**Figure 7.** Temperature contours of EAHE pipe for air and disturbed e (a) longitudinal plane at the Inlet section (b) Perpendicular plan to the airflow at horizontal lengths 3m and 17m

When the diameter of the pipe increases, the contact surface between the pipe and the soil increases, leading to a rise in the heat transfer between the air and the soil;

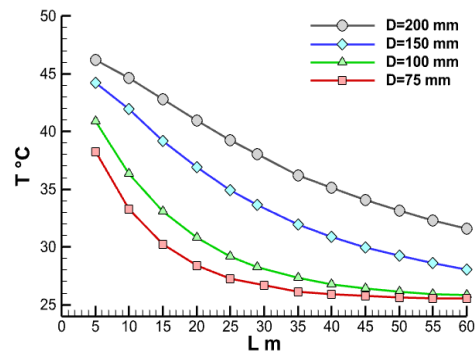


**Figure 8.** The temperature along pipe length for different diameters at 5 m/s airflow velocity and 50 °C inlet air temperature

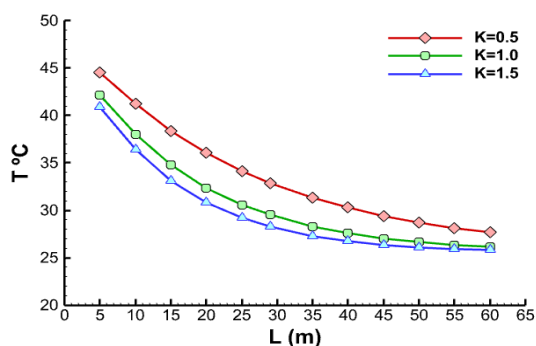
for the same airflow velocity, the volumetric flow rate inside the pipe will be greater, causing a rise in outlet air temperature (Eq. 10). In most cases, the heat transfer through the soil is not fast enough for this amount of air, which causes an increase in the outlet air temperature. Therefore, considering the economic cost, the airflow rate and pipe diameter should be optimized when designing the heat exchanger.

Figure 8 shows the effect of the soil thermal conductivity on the air temperature along the EAHE pipe of 100mm diameter at the inlet air temperature of 50 °C and 5 m/s airflow velocity. It was observed that with increasing the soil thermal conductivity, the outlet air temperature decreases because the heat transfer rate inside the soil increases, leading to improvement in the performance of the heat exchanger. When the thermal conductivity of soil is 1 and 1.5 (W/m K), the outlet air temperature at the length of 35 m is 28.27 and 27.25°C, respectively, and the TD<0.13°C/m; this length can be considered sufficient, but when the thermal conductivity is 0.5 (W/m K), the acceptable pipe length is 45 m where the outlet air temperature is 29.4°C at this length. So changing the soil type from dry one (k=0.5 W/m K) to saturated one (case of Karbala city, k=1.5 W/m K) causes about a 25% reduction in the length of the pipe.

The influence of airflow velocity on the outlet air temperature when  $T_{in}=50\text{ }^{\circ}\text{C}$  and  $k=1.5\text{ W/m K}$  is shown in Figure 9. It can be seen that when the airflow velocity increases, the time that air remains in contact with the soil decreases, causing the outlet air temperature to rise. On the other hand, increased air velocity leads to a higher mass flow rate, leading to increased heat transfer between soil and air, as shown in Equation (10).

It can also be seen in the figure that  $TD<0.15$  when the length of the pipe is 35, 36, 40, and 45 m at the airflow velocity is 5, 7.5, 10, and 15 m/s, respectively, and the outlet air temperature in these cases is 27.3, 28.5, 28.9, and 30°C, respectively.

As a result, it is recommended that the airflow velocity be optimized to get the most out of the EAHE system.



**Figure 9.** Air temperature distribution along the EAHE pipe at 50°C inlet temperature and 5 m/s airflow velocity for three soil thermal conductivity K (0.5,1,1.5) (W/m K)

Many parameters affect soil temperatures ( $T_s$ ), such as soil type, ground surface cover, solar radiation, water content, geographical location, and depth from the ground surface. Figure 10 compares the outlet temperature for two soil temperatures ( $T_s$ ), 25.5 and 30°C, at the 5 m/s airflow velocity with 100 mm pipe diameter and 50°C inlet air temperature. The significant effect of  $T_s$  on the EAHE system's outlet air temperature can be observed. As the soil temperature decreases, the outlet air temperature of the EAHE system decreases. TD is lower than 0.15 at a pipe length of 35 m in both cases, but the outlet air temperature at this length is 27.25°C and 31.5°C when  $T_s$  equal 25.5°C and 30°C, respectively. Therefore, to improve the performance of the heat exchanger,  $T_s$  should be as low as possible.

### 6. 1. Outlet Air Temperature Equation

Previously, the effect of different parameters on the performance of the heat exchanger was discussed; all these parameters can effectively improve the system's performance. In this part of the research, we will try to find an equation that links all these variables shown in Table 4 as a function of the outlet air temperature. The parameters mentioned in the table are considered independent variables of the EAHE system. More than 100 simulated cases were conducted, and 1100 outlet air

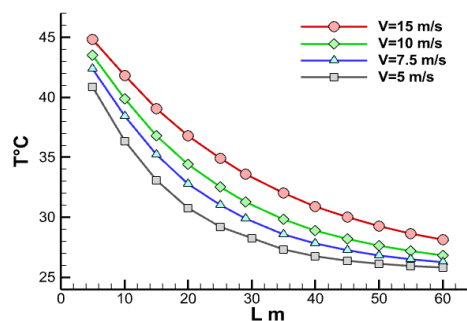


**Figure 10.** Outlet air temperature under the different air velocities with 100 mm pipe diameter, 50°C inlet air temperatures, and soil thermal conductivity is 1.5 (W/m K)

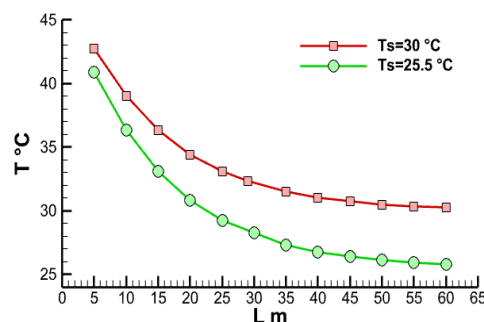


**Figure 11.** Outlet air temperature under the two soil temperatures ( $T_s$ ) 25.5 and 30°C with 100 mm pipe diameter and 50°C inlet air temperatures

temperature values were recorded. Designed experiments type screening was used to find an equation that relates all the variables as a function of the outlet temperature using the Minitab 19 program. Screening designs are the most widely used designs for industrial experimentation. Screening designs typically require fewer trial runs than other designs. It contains three levels per continuous factor to estimate square and linear terms. The temperature equation was obtained as a function of the six variables as follows:

$$T_{out} = 0.93 + 45.2D + .6679T_{in} + 0.3375V - 0.3067L - 1.211K_s + 0.002925L^2 + 0.2862DL - 0.008792T_{in}L - 0.02687LK_s + 0.01217LT_s \quad (13)$$

It should be noted that depending on the influence of the variables, certain parts of the equation have positive and some others have negative impacts; for example, as the length of the pipe increases, the temperature decreases, making its value appear as negative, and so on for the other variables. Also, it can be found that only the parameter L's behavior in the equation is nonlinear. Figure 12 compares the current model with the EAHE outlet air temperature experimental result of Misra et al. [18] (Figure 12(a)) for an air velocity of 5 m/s, 45 °C inlet air temperature, and soil temperature of 27 °C., and also that of Agrawal et al. [11] (Figure 12(b)) for an air velocity of 3.5 m/s, 38.1 °C inlet air temperature and soil temperature of 22 °C, and present experimental result (Figure 12(c)). The results confirm that this equation is valid and can be used to estimate the air temperature outlet of the EAHE system for different cases of similar models.

It is essential in designing the earth-to-air heat exchanger to obtain the lowest temperature and maximum airflow leading to the highest cooling capacity of the outlet ail. The length of the pipe should be as small as possible from the economic and occupying space point of view. So, EES (Engineering Equation Solver) software was used to find where the outlet temperature reaches a specific value. Figure 13(a) shows the length of the pipe to get a suitable outlet air temperature ( $T_{out}$ ) at different airflow velocities ( $V$ ). The relationship between  $L$  and  $V$  for four outlet temperature values 26, 27, 28, and 29°C are displayed, while the  $K_s$ ,  $T_{out}$ ,  $T_s$ , and  $D$  are 1.5 (W/m K), 50°C, 25.5°C, and 0.075m, respectively. As expected, it can be seen that when the  $T_{out}$  decreases, the length of the pipe increases. Curves are approximately linear, and similar behavior is expected to be observed at different velocities. Figure 13(b) represents the relationship between  $V$  and  $L$  under the same conditions as the previous case but at  $D=0.2$  m. Compared to Figure 13(a), it is noticed that the length needed to reach the desired  $T_{out}$  value increases significantly by increasing  $D$ . An asymptotic behavior is seen at higher velocities and lengths. For example, at a velocity of 12.5 m/s, a 60m length of pipe is required to achieve the  $T_{out}$  of 28°C. For  $T_{out}=27$  and 26°C, the equation could not find a length of

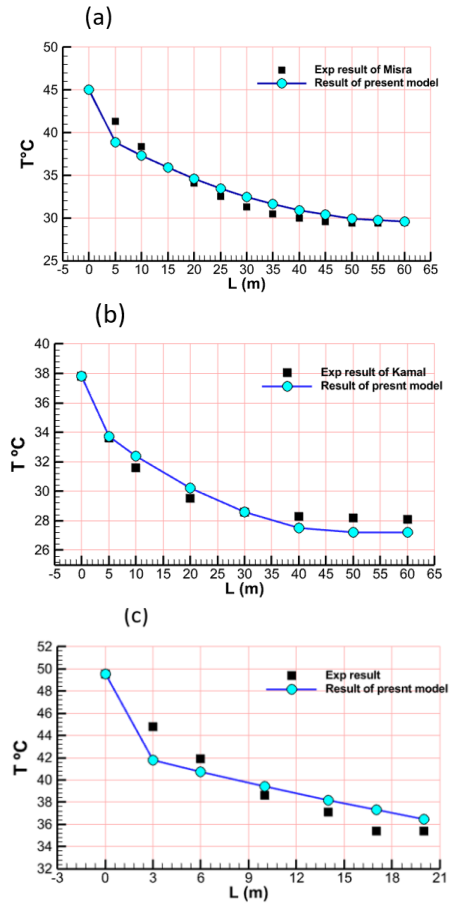


Figure 12. Compares the current model with the experimental result of (a) (Misra et al.) [18]. (b) (Kamal et al.) [11]. (c) The present experimental result

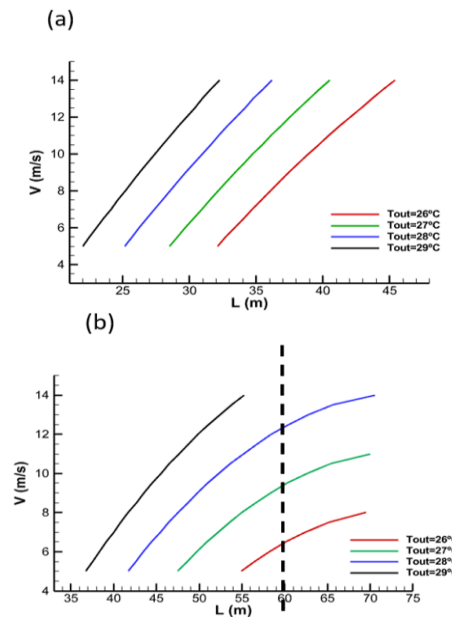


Figure 13. Interaction Plot between airflow velocity  $V$  and pipe length  $L$  when  $T_{out}=26,27,28$  and  $29$  °C for (a) pipe diameter 0.075 m and (b) pipe diameter 0.2 m

the pipe in the desired limit at a velocity higher than 9.5 and 6.5m/s, respectively. For these cases, a pipe longer than 60m is needed to obtain the desired  $T_{out}$ .

The minimum length required for all the considered  $T_{out}$  values in the figure is 23.5 m for  $D=0.075$ m and 36m for  $D=0.2$ m. The length needed to reach 26 °C, 27 °C, 28 °C, and 29 °C at a velocity of 6m/s is 38.2m, 43.3m, 49.9m, and 58.2m, respectively. It means that to decrease the outlet temperature 1°C, 16.6%, 14.7%, and 13.8% increase in the length is required for  $T_{out}$  values of 27 °C, 28 °C, and 29 °C. While these values change to 39.9m, 45.2m, 52m, and 62.1m for the velocity of 7m/s, requiring 19.4%, 15%, and 13.2% increase in the length to achieve 1°C reduction in outlet temperature.

All the  $T_{out}$  values (26 °C, 27 °C, 28 °C, and 29 °C) can be achieved for  $D=0.075$  in lengths lower than 60m, while for  $D=0.2$ , only  $T_{out}=29$  °C can be achieved in a length shorter than 60m, and other  $T_{out}$  values may not be achieved in some higher velocities.

Figure 14(a) shows the relationship between  $T_{in}$  and pipe length for two pipe diameters of 0.1m and 0.15m, when  $T_{out}$ ,  $T_{in}$ ,  $T_s$ ,  $V$ , and  $K_s$  are 28°C, 50 °C, 25.5 °C, 7.5 m/s, and 1.5 (W/m K), respectively. It is noted that when the  $T_{in}$  increases, the length required to obtain a specific  $T_{out}$  value will be increased; for example, to get  $T_{out}=28$  °C at  $T_{in}=50$ °C, the length of the pipe is expected to be 31m at a  $D=0.1$  m, while for the  $D=0.15$  m it will

be 46 m. For the same conditions and at a velocity of 10 m/s, as shown in Figure 14(b), the length required to obtain a  $T_{out}$  of 28 °C increases compared to the previous case, the pipe length of 37 m and 53 m for  $T_{in}$  of 50 °C and a pipe diameter of 0.1 m and 0.15 m is required, respectively. The rate of increase is higher for the diameter of 0.1 m (19%) rather than 0.15m (15%).

## 7. CONCLUSION

Experimental and numerical studies have been conducted to investigate the effect of design parameters (pipe diameter, pipe length, inlet air temperature, soil temperature, airflow velocity, and soil thermal conductivity) on EAHE system performance in hot and dry climates. Since the temperature distribution varies based on the type of soil and the season, it was measured in an open area clear of vegetation in the city of Karbala (Central Iraq) as the first experimental activity. It has been observed that the temperature decreases with increasing depth, the temperature of the soil remaining constant after a depth of about 4 m. An EAHE system was installed in the Karbala, and the effect of different parameters was experimentally investigated. To reduce the cost of study and extend the number of parameters to be considered and their range, a 3D model is created based on the experimental results performed to study the effect of different parameters. The simulation results were compared to experimental results, which were in good agreement. The following conclusions have been drawn based on the numerical and experimental results. With increasing the length of the pipe, the outlet air temperature of the EAHE system decreases, and the heat transfer grows to a certain length beyond which the change is very slight (asymptotic behavior). For example, for a pipe diameter of 100 mm at a depth of 3 m and thermal conductivity of 1.5 (W/m K), the pipe length of 35 m was sufficient when using an air velocity of less than 10 m/s.

The heat transfer rate rises, and the outlet air temperature grows with the increase in air velocity. An airflow velocity of less than 7m/s can be used to cool enclosed and small spaces when a small mass flow rate of air at a relatively low temperature is required and vice versa. Using an air velocity higher than 15m/s is not recommended because the outlet air temperature does not drop much, especially when using a relatively large pipe diameter. For example, at a pipe diameter of 0.2m, airflow velocity of 15m/s, and inlet air temperature of 50 °C, the outlet air temperature at a length of 60m was as high as 38 °C.

The outlet air temperature decreases with decreased pipe diameter. According to the results of this study, it is preferable to use a pipe diameter of 0.1 m to cool closed areas in the city of Karbala since it was able to prepare air with a temperature of less than 29 °C at a velocity of

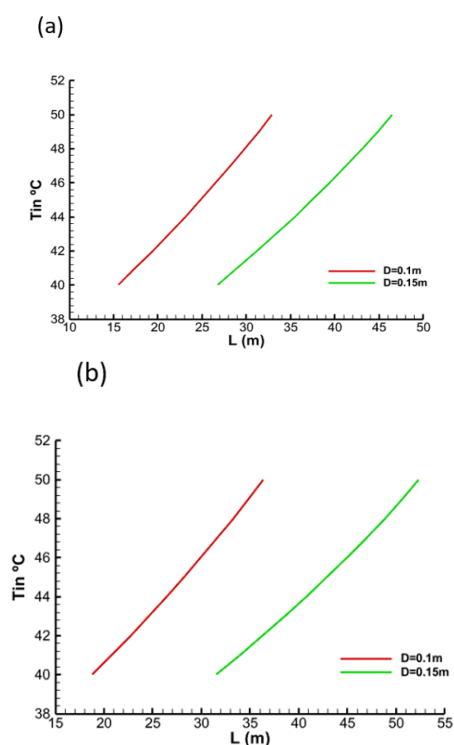


**Figure 14.** Interaction Plot between inlet temperature  $T_{in}$  and pipe length  $L$  when  $T_{out}=28$  °C and pipe diameter  $D=0.1$  and  $0.15$  m at (a) airflow velocity  $V=7.5$  m/s and (b) airflow velocity  $V=10$  m/s

10m/s, a pipe length of 40 m, and an ambient temperature of 50 °C.

The heat transfer is enhanced, and the outlet air temperature decreases when the soil is fully saturated since its thermal conductivity increases with water content. The soil temperature dramatically affects the performance of the heat exchanger, which depends mainly on the depth of pipe burial. The heat transfer increases when the soil temperature decreases.

Based on the experimental and numerical results, an approximate equation was constructed to evaluate the EAHE system outlet air temperature as a function of the pipe diameter, pipe length, inlet air temperature, soil temperature, airflow velocity, and soil thermal conductivity ( $T_{out} = f(T_{in}, D, L, K_s, T_s)$ ). Also, a code is written in EES (Engineering Equation Solver) to find the location at which the air temperature reaches a certain value.

Using the obtained equation, it was found that although all considered  $T_{out}$  values can be achieved for lower diameters of the pipe (such as 0.075 m) in the desired lengths (lower than 60m), for higher diameters (such as 0.2 m), some lower  $T_{out}$  values (26 °C and 27 °C) may not be achieved in velocities more than 10 m/s. The heat EAHE can be used in places with a high temperature of 50 °C for cooling purposes and to obtain air at a temperature of 27 °C. It is proposed as future work to investigate the possibility of using the EAHE to ventilate and cool open areas.

## 8. REFERENCES

1. IEA, I. "World energy outlook 2011." *International Energy Agency*, Vol. 666, (2011).
2. Chen, H., Ooka, R., Huang, H., and Tsuchiya, T. "Study on mitigation measures for outdoor thermal environment on present urban blocks in Tokyo using coupled simulation." *Building and Environment*, Vol. 44, No. 11, (2009), 2290-2299.
3. Ben Jmaa Derbel, H., and Kanoun, O. "Investigation of the ground thermal potential in tunisia focused towards heating and cooling applications." *Applied Thermal Engineering*, Vol. 30, No. 10, (2010), 1091-1100. <https://doi.org/10.1016/j.applthermaleng.2010.01.022>
4. Alrwashdeh, S. S., Ammari, H., Madanat, M. A., and Al-Falahat, A. M. "The effect of heat exchanger design on heat transfer rate and temperature distribution." *Emerging Science Journal*, Vol. 6, No. 1, (2022), 128-137.
5. Mostafaeipour, A., Goudarzi, H., Khanmohammadi, M., Jahangiri, M., Sedaghat, A., Norouziyanpour, H., Chowdhury, S., Techato, K., Issakhov, A., Almutairi, K., and Hosseini Dehshiri, S. J. "Techno-economic analysis and energy performance of a geothermal earth-to-air heat exchanger (EAHE) system in residential buildings: A case study." *Energy Science and Engineering*, Vol. 9, No. 10, (2021), 1807-1825. <https://doi.org/10.1002/ese3.952>
6. Popiel, C. O., Wojtkowiak, J., and Biernacka, B. "Measurements of temperature distribution in ground." *Experimental thermal and fluid science*, Vol. 25, No. 5, (2001), 301-309.
7. Al-Ajmi, F., Loveday, D. L., and Hanby, V. I. "The cooling potential of earth-air heat exchangers for domestic buildings in a desert climate." *Building and Environment*. <https://doi.org/10.1016/j.buildenv.2005.01.027>
8. Lu, S., Ren, T., Gong, Y., and Horton, R. "An Improved Model for Predicting Soil Thermal Conductivity from Water Content at Room Temperature." *Soil Science Society of America Journal*, Vol. 71, No. 1, (2007), 8-14. <https://doi.org/10.2136/sssaj2006.0041>
9. Song, Y., Yao, Y., and Na, W. "Impacts of Soil and Pipe Thermal Conductivity on Performance of Horizontal Pipe in a Ground-source Heat Pump." *China Renewable Energy Resources and a Greener Future*, Vol. 8, No. 2, (2006), 2-7. Retrieved from <https://core.ac.uk/download/pdf/79624551.pdf>
10. Omer, A. "Soil thermal properties: Effects of density, moisture, salt concentration and organic matter." *Advances in Science, Technology and Innovation*, (2018), 113-114. [https://doi.org/10.1007/978-3-319-70548-4\\_39](https://doi.org/10.1007/978-3-319-70548-4_39)
11. Agrawal, K. K., Misra, R., Yadav, T., Agrawal, G. Das, and Jamuwa, D. K. "Experimental study to investigate the effect of water impregnation on thermal performance of earth air tunnel heat exchanger for summer cooling in hot and arid climate." *Renewable Energy*, Vol. 120, (2018), 255-265. <https://doi.org/10.1016/j.renene.2017.12.070>
12. Abbaspour-Fard, M. H., Gholami, A., and Khojastehpour, M. "Evaluation of an earth-to-air heat exchanger for the north-east of Iran with semi-arid climate." *International Journal of Green Energy*, Vol. 8, No. 4, (2011), 499-510. <https://doi.org/10.1080/15435075.2011.576289>
13. Singh Bisoniya, T., Kumar, A., and Baredar, P. "Parametric Analysis of Earth-Air Heat Exchanger System Based on CFD Modelling," Vol. 1, (2014).
14. Khabbaz, M., Benhamou, B., Limam, K., Hollmuller, P., Hamdi, H., and Bennouna, A. "Experimental and numerical study of an earth-to-air heat exchanger for air cooling in a residential building in hot semi-arid climate." *Energy and Buildings*, Vol. 125, (2016), 109-121. <https://doi.org/10.1016/j.enbuild.2016.04.071>
15. Serageldin, A. A., Abdelrahman, A. K., and Ookawara, S. "Earth-Air Heat Exchanger thermal performance in Egyptian conditions: Experimental results, mathematical model, and Computational Fluid Dynamics simulation." *Energy Conversion and Management*, Vol. 122, (2016), 25-38. <https://doi.org/10.1016/j.enconman.2016.05.053>
16. Hasan, M. I., Noori, S. W., and Shkarah, A. J. "Parametric study on the performance of the earth-to-air heat exchanger for cooling and heating applications." *Heat Transfer - Asian Research*, Vol. 48, No. 5, (2019), 1805-1829. <https://doi.org/10.1002/htj.21458>
17. Yamini, O. A., Mousavi, S. H., Kavianpour, M. R., and Ghaleh, R. S. "Hydrodynamic Performance and Cavitation Analysis in Bottom Outlets of Dam Using CFD Modelling." *Advances in Civil Engineering*, Vol. 2021, (2021). <https://doi.org/10.1155/2021/5529792>
18. Misra, R., Aseri, T. K., and Bansal, V. "Cfd analysis of thermal influence zone of earth air tunnel heat exchanger under transient conditions." 14th International Conference of IBPSA - Building Simulation 2015, BS 2015, Conference Proceedings, No. 1991, (2015), 1655-1662.
19. Gauthier, C., Lacroix, M., and Bernier, H. "Numerical simulation of soil heat exchanger-storage systems for greenhouses." *Solar Energy*, Vol. 60, No. 6, (1997), 333-346. [https://doi.org/10.1016/S0038-092X\(97\)00022-4](https://doi.org/10.1016/S0038-092X(97)00022-4)
20. Wilcox, D. C. "Formulation of the k- $\omega$  turbulence model revisited." *AIAA Journal*, Vol. 46, No. 11, (2008), 2823-2838. <https://doi.org/10.2514/1.36541>
21. Yamini, O. A., Movahedi, A., Mousavi, S. H., Kavianpour, M. R., and Kyriakopoulos, G. L. "Hydraulic Performance of Seawater Intake System Using CFD Modeling." *Journal of Marine*

*Science and Engineering*, Vol. 10, No. 7, (2022).  
<https://doi.org/10.3390/jmse10070988>

22. Lu, Y., Lu, S., Horton, R., and Ren, T. "An Empirical Model for

Estimating Soil Thermal Conductivity from Texture, Water Content, and Bulk Density." *Soil Science Society of America Journal*, Vol. 78, No. 6, (2014), 1859-1868.  
<https://doi.org/10.2136/sssaj2014.05.0218>

---

### Persian Abstract

---

#### چکیده

انرژی زمین گرمایی کم عمق، توسط مبدل حرارتی زمین به هوا (EAHE)، برای خنک کردن ساختمان‌ها با حداقل مصرف انرژی استفاده می‌شود. پارامترهای مهمی که بر عملکرد مبدل حرارتی تأثیر می‌گذارند باید بررسی شوند تا طراحی مناسبی به دست آید. انرژی زمین گرمایی کم عمق، توسط مبدل حرارتی زمین به هوا (EAHE)، برای خنک کردن ساختمان‌ها با حداقل مصرف انرژی استفاده می‌شود. پارامترهای مهمی که بر عملکرد مبدل حرارتی تأثیر می‌گذارند باید بررسی شوند تا طراحی مناسبی به دست آید. این مقاله به صورت عددی و تجربی تأثیر قطر لوله، طول لوله، دمای هوای ورودی، دمای خاک، سرعت جریان هوا و هدایت حرارتی خاک را بر عملکرد مبدل حرارتی در شرایط آب و هوایی گرم و خشک بررسی می‌کند. توزیع دمای خاک از سطح زمین تا عمق ۷ متری در شهر کربلا (مرکز عراق) در فصل تابستان اندازه‌گیری شد. آزمایش تجربی برای EAHE در خاک اشباع شده از آب و دمای هوای محیط ۴۱ درجه سانتیگراد، ۴۵ درجه سانتیگراد و ۴۹.۵ درجه سانتیگراد با چهار سرعت مختلف انجام شد. درصد کاهش در دمای هوای خروجی EAHE در ۹ متر بر ثانیه به ترتیب ۲۸.۳٪، ۲۵.۵٪ و ۱۹.۵٪ بود. همچنین مدل سه بعدی ایجاد شد و نتایج شبیه‌سازی با نتایج تجربی که تطابق خوبی داشتند مقایسه شد. معادله ای برای دمای هوای خروجی به عنوان تابعی از قطر و طول لوله، دمای هوای محیط، دمای خاک اطراف لوله و هدایت حرارتی خاک پیدا شد. معادله به دست آمده با نتایج تجربی فعلی و نتایج تجربی متون داده‌های گزارش شده مقایسه شد. در نتیجه توافق بسیار خوبی مشاهده شد. نتایج نشان داد که پارامتر  $L$  طول لوله قوی‌ترین رفتار غیرخطی را در معادله ایجاد می‌کند. برای موارد در نظر گرفته شده، در قطرهای ۷۵ و ۱۰۰ میلی‌متر، یک رفتار خطی تقریبی برای طول مورد نیاز برای دستیابی به دمای خروجی خاص مشاهده شد. از نتایج به دست آمده می‌توان نتیجه گرفت که تغییر نوع خاک از خشک ( $k=0.5 \text{ W/m K}$ ) به خاک اشباع مورد شهر کربلا، ( $k=1.5 \text{ W/m K}$ ) باعث کاهش حدود ۲۵ درصدی طول خاک شد. لوله. همچنین، نتایج نشان داد که در سرعت هوای ۷ متر بر ثانیه، طول مورد نیاز برای به دست آوردن ۲۶ درجه سانتی‌گراد در خروجی EAHE 1/62 متر است که ۵۵ درصد بیشتر از حالت ۲۹ درجه سانتی‌گراد (۳۹/۹ متر) است.

---



## Developing a Fuzzy Measurement of Alternatives and Ranking Compromise Solution Method for Determining Essential Barriers in Iranian Car Industry

G. R. Einy-Sarkalleh<sup>a</sup>, R. Tavakkoli-Moghaddam<sup>\*b</sup>, A. Hafezalkotob<sup>c</sup>, S. E. Najafi<sup>a</sup>

<sup>a</sup> Department of Industrial Engineering, Science and Research Branch, Islamic Azad University, Tehran, Iran

<sup>b</sup> School of Industrial Engineering, College of Engineering, University of Tehran, Tehran, Iran

<sup>c</sup> School of Industrial Engineering, South Tehran Branch, Islamic Azad University Tehran, Iran

### PAPER INFO

#### Paper history:

Received 11 August 2022

Received in revised form 14 October 2022

Accepted 24 October 2022

#### Keywords:

Supply Chain Management

Lateral Contract

Alliance

Coordination

Multi-criteria Decision-making

### ABSTRACT

In some lateral alliances, firms coordinate their interactions in Supply Chain Management (SCM) via contracts. Successful implementation of contracts in lateral alliances remains challenging in practice because of the incomplete identification of implementation barriers by firms involved in the alliance. This paper investigates the implementation issues of lateral contracts. To identify the barriers, the literature and interview experts on the subject matter are reviewed. By adopting the novel Fuzzy Measurement of Alternatives and Ranking according to the Compromise Solution (FMARCOS) prioritization method, we evaluate the main barriers that firms face in the successful implementation of contracts discovered in our identification phase. A sensitivity analysis is conducted to demonstrate the stability and robustness of our proposed method. To check the reliability of the proposed model, a case study is solved with three methods of Multi-Criteria Decision-Making (MCDM) methods. The results show that they do not differ much from each other, which indicates the validity of this model. To validate the findings, a list of barriers is applied to assess a set of firms in the Iranian car industry, and more prepared firms are located as future partners of potential lateral alliances. The results are consistent with the common intuition toward these sample firms in the case study. The main contributions of this work include the application of the FMARCOS method in the study of the bidirectional implementation barriers, the consideration of novel aspects of implementation barriers unaddressed in the extant literature, and a real-case study in the Iranian car industry.

doi: 10.5829/ije.2023.36.01a.11

## 1. INTRODUCTION

Coordination in Supply Chain Management (SCM) comprises four common mechanisms: information technology, information sharing, concerted decision making, and coordination contracts [1]. In implementing coordination mechanisms, firms face barriers of various types such as technological, financial, social, and knowledge and support dimensions [2]. Firms in the supply chain experience challenging relations if these barriers are not sufficiently scrutinized, and therefore, left ignored. To address these challenges, a recent lateral contract has been employed in various industries, in which firms simultaneously increase their share of product manufacturing capacity - capacity expansion and

their efficiency- cost reduction by designing and following cost reduction programs. The pursuit of these two goals poses different kinds of challenges by creating managerial issues [3]. For example, the uncertain nature of demand for the products that are newly presented to the market makes the prediction of capacity for future demand a difficult task. As another example, investment in capacity has a lumpy nature and cannot be made in "bits and pieces", which necessitates over-investment in capacity. Therefore, these firms are likely to use their capacity in an underutilized manner.

The underutilized capacity may be used for other firms, which are interested in establishing an outsourcing relationship. There are various methods to carry out this type of relationship, in which lateral contracts are

\*Corresponding Author Institutional Email: [tavakoli@ut.ac.ir](mailto:tavakoli@ut.ac.ir)  
(R. Tavakkoli-Moghaddam)

approached. We illustrate this approach with some examples. In the United States, Nestle and Ocean Spray have established a long-term relationship to share their capacity interchangeably. This means that Ocean Spray provides its extra production capacity to its partner in exchange for Nestlé's extra distribution capacity. In this partnership, Ocean Spray is responsible for filling the bottles needed in the final product and Nestle is in charge of supply and distribution. Therefore, firms can exploit their capacity fully based on the capacity strength point. In India, Fiat and Tata have formed a long-term partnership such that Fiat uses its extra capacity to produce cars for Tata and Tata shares its dealership network and marketing capacity with Fiat. This type of partnership is not limited to these cases and has a rising trend in other industries and geographic places.

Although this type of contract tries to alleviate the issues related to sharing capacity in co-manufacturing and co-distribution alliances, the incomplete identification of implementation barriers by partners of the alliance can critically damage the outcome. These days managers face challenging problems to provide the necessary resources that their company needs to fulfill its mission. Various economic, political, social, technological, and even environmental conditions constrain firms in their access to resources. These factors often necessitate firms to prioritize the implementation barriers and allocate the scarce resources most properly to guarantee the successful implementation of lateral contracts. This has been made possible solely by removing the most important obstacles to these implementation practices.

## 2. LITERATURE REVIEW

The barriers to the implementation of contracts common in the supply chain have extensively been studied in the literature. we provide some examples of these studies [4]: (1) examining the barriers to the implementation of green SCM in the construction industry. Their study has outlined nine essential barriers to contract implementation [5], (2) analyzing the interaction between barriers to implementing sustainable SCM. Their study has resulted in outlining 13 barriers to contract implementation in the context of sustainable SCM [6], (3) examining the barriers to the implementation of SCM, which is a case study of small- and medium-sized contracts in Turkey [7], (4) identifying the barriers of SCM (in manufacturing organizations based on a systematic literature review and identified the most critical barriers hindering the performance of the supply chain. They found 23 key SCM barriers, which help industrial practitioners and academic experts implement SCM [8], (5) investigating the building blocks of GSCM and developing a structure of GSCM

implementation for the manufacturing industry. Their research results in a framework with five concepts, 22 dimensions, and 82 elements [9], (6) advancing perception of international similarities and dissimilarities in SCM prospects and practices, by scrutinizing the inherent differences between supply chain managers both in Scandinavia and America. They considered the definition of SCM as well as facilitators of and obstacles to SCM implementation. Their investigation leads to the understanding that SCM implementation is slower and more difficult than expected from the managers' viewpoint both in Scandinavian and American supply chains [10], (7) scrutinizing possible barriers to IT applications in the supply chain system of the Indian sugar industry and rank these barriers in terms of their severity [11], and (8) developing a conceptual framework by reviewing the pertinent GSCM literature and identifying the main barriers to GSCM implementation. They classified these barriers into five main classes, namely knowledge, technology, finances, outsourcing, and management. They also found that commitment of top management; changes in technologies and existing policies; improving the awareness of environmental issues; training and education; and waste management systems and implementation of efficient materials are among the best strategies to improve GSCM practices [12].

MCDM methods have widely been applied in the literature. In the manufacturing industry, these methods have been applied to solve problems of selection of FMS and industrial robots [13], suppliers of digital stores are ranked and evaluated based on Analytical Hierarchy Process (AHP) and TOPKOR methods [14], a method is proposed to propose based on a combination of fuzzy versions of the SWARA and MARCOS methods to select green suppliers [15], a method is proposed to choose the best online food delivery using a Pythagorean Fuzzy TOPSIS method [16], and a method is designed based on the MOORA method to select the best blanking die materials [17].

In this paper, we investigate whether there exists a tool to help managers find the most important barriers to implementing lateral contracts. We propose a decision-theoretic model, which enables firms to prioritize the implementation barriers. Our model belongs to the class of multi-attribute decision-making problems and is based on the FMARCOS method [18]. We first identify the barriers that are involved in the implementation of lateral contracts (i.e., list of barriers and review the pertinent literature to uni-directional alliances to identify the thirty most relevant barriers). Then, we scrutinize this list to filter out or add in the unrelated and related barriers by consulting with fifteen experts with a considerable background in industrial alliances. This provides the final list of barriers for lateral alliances to finalize our investigation for a proper list of barriers. Also, we

validate the final list of barriers to demonstrate the applicability of our tool in real-life conditions. We find more prepared firms as future partners of potential lateral alliances by applying our list of barriers to assess a set of firms in the Iranian car industry. The results follow the common sense toward these selected firms and show the validity of our method.

As mentioned in the research literature, considerable research has been done on the types of coordination and the types of contracts in the supply chain with the provision of mathematical models. Identification and evaluation of supply chain barriers have also been done with a variety of multi-criteria decision-making (MCDM) methods. However, there has not been much research on bi-direction contracts in general. The barriers to implementing bi-directional contracts in the supply chain have not been much studied, especially based on MCDM methods. Bi-directional contracts are a sharing of resources and surplus capacity, while the one-way contract is a form of outsourcing - that is, outsourcing part of the firm's demand fulfillment mission to another firm. However, in the case of bi-directional contracts, this is not the case. In fact, in these contracts, the actions of each of the parties affect the other, so the issues of game theory are raised, which is beyond the scope of our discussion in this paper. This paper aims to review and analyze the barriers to implementing bi-directional contracts in the supply chain based on the FMARCOS method.

**3. PROBLEM STATEMENT**

This paper considers the Iranian car industry as a case study. In this industry, there are many challenges, which may be categorized as internal and external issues. External issues mainly deal with macro-economic parameters (e.g., currency rate and inflation) under the main impact of economic sanctions. On the other hand, internal issues are chiefly related to productivity and efficiency problems throughout the car supply chain requiring a better level of coordination and integration between the supply chain players. In this regard, the proper contract design plays an important role currently under the consideration of managers of Iranian car manufacturing firms. However, implementing these contracts in the car industry, especially bidirectional contracts, face various barriers with a multidimensional nature. This necessitates a multi-criteria decision making (MCDM) method for the problem. The experts interviewed in this method include experts from the Iranian car industry and related logistics and supply chain players.

**3. 1. Fuzzy Number** A fuzzy number  $\tilde{A}$  is said to be a TFN on  $R$  provided that its membership function  $\mu_{\tilde{A}}(X) = R \rightarrow [0,1]$  is equivalent to [15]:

$$\mu_{\tilde{A}}(X) = \begin{cases} \frac{x-l}{m-l} & l \leq x \leq m \\ \frac{u-x}{u-m} & m \leq x \leq u \\ 0 & \text{Otherwise} \end{cases} \quad (1)$$

where  $l$  and  $u$  denote the lower and upper limits of fuzzy number  $\tilde{A}$ , respectively, and  $m$  represents the modal value.

The TFN can be marked as  $\tilde{A} = (l, m, u)$

$$\tilde{A}(ID) = \max_i \tilde{x}_{ij} \text{ if } J \in B \text{ and } \min_i \tilde{x}_{ij} \text{ if } J \in C \quad (2)$$

The operation of TFN  $\tilde{A}_1 = (l_1, m_1, u_1)$  and  $\tilde{A}_2 = (l_2, m_2, u_2)$  are as follows:

Addition:  $\tilde{A}_1 = (l_1, m_1, u_1)$

$$\tilde{A}_1 \oplus \tilde{A}_2 = (l_1, m_1, u_1) \oplus (l_2, m_2, u_2) = (l_1 + l_2, m_1 + m_2, u_1 + u_2) \quad (3)$$

$$\tilde{A}_1 \otimes \tilde{A}_2 = (l_1, m_1, u_1) \otimes (l_2, m_2, u_2) = (l_1 \times l_2, m_1 \times m_2, u_1 \times u_2) \quad (4)$$

Subtraction:

$$\tilde{A}_1 - \tilde{A}_2 = (l_1, m_1, u_1) - (l_2, m_2, u_2) = (l_1 - l_2, m_1 - m_2, u_1 - u_2) \quad (5)$$

Division:

$$\frac{\tilde{A}_1}{\tilde{A}_2} = \frac{(l_1, m_1, u_1)}{(l_2, m_2, u_2)} = \left( \frac{l_1}{u_2}, \frac{m_1}{m_2}, \frac{u_1}{l_2} \right) \quad (6)$$

Reciprocal:

$$\tilde{A}^{-1} = (l_1, m_1, u_1)^{-1} = \left( \frac{1}{u_1}, \frac{1}{m_1}, \frac{1}{l_1} \right) \quad (7)$$

**3. 2. Fuzzy MARCOS<sup>1</sup>** The new fuzzy MARCOS method encompasses the following steps:

1) In this step, an elementary two-dimensional fuzzy matrix is constructed with decision alternatives as its rows and decision-making criteria as its columns.

2) Here, two generated alternatives are added to our matrix. The first one is defined as the worst fuzzy ideal alternative (AAI) and the second one as the best fuzzy ideal alternative (AI) [18]:

$$X^{\%} = \begin{matrix} & \begin{matrix} \mathcal{C}_1^{\%} & \mathcal{C}_2^{\%} & \dots & \mathcal{C}_n^{\%} \end{matrix} \\ \begin{matrix} A^{\%}(AI) \\ A_1^{\%} \\ A_2^{\%} \\ \vdots \\ \vdots \\ A_M^{\%} \\ A^{\%}(ID) \end{matrix} & \begin{bmatrix} \mathcal{A}_{11}^{\%} & \mathcal{A}_{12}^{\%} & \dots & \mathcal{A}_{1n}^{\%} \\ \mathcal{A}_{21}^{\%} & \mathcal{A}_{22}^{\%} & \dots & \mathcal{A}_{2n}^{\%} \\ \vdots & \vdots & \ddots & \vdots \\ \mathcal{A}_{M1}^{\%} & \mathcal{A}_{M2}^{\%} & \dots & \mathcal{A}_{Mn}^{\%} \\ \mathcal{A}_{ID1}^{\%} & \mathcal{A}_{ID1}^{\%} & \dots & \mathcal{A}_{IDn}^{\%} \end{bmatrix} \end{matrix} \quad (8)$$

<sup>1</sup> Measurement Alternatives and Ranking according to Compromise Solution

The desirable criteria are categorized in set  $B$  and the undesirable criteria in set  $C$  [18,13]:

$$\tilde{A}(A_i) = \min_j \tilde{x}_{ij} \text{ if } j \in B \text{ and } \max_j \tilde{x}_{ij} \text{ if } j \in C \quad (9)$$

3) Matrix  $\tilde{N} = [\tilde{n}_{ij}]_{m \times n}$  is needed to normalize our matrix in which  $n_{ij}$  is defined as follows:

$$\tilde{n}_{ij} = (n_{ij}^l, n_{ij}^m, n_{ij}^u) = \left[ \frac{x_{ij}^l}{x_{ij}^u}, \frac{x_{id}^m}{x_{ij}^m}, \frac{x_{id}^u}{x_{ij}^u} \right] \text{ if } j \in C \quad (10)$$

$$\tilde{n}_{ij} = (n_{ij}^l, n_{ij}^m, n_{ij}^u) = \left[ \frac{x_{ij}^l}{x_{ij}^u}, \frac{x_{id}^l}{x_{ij}^m}, \frac{x_{id}^l}{x_{ij}^u} \right] \text{ if } j \in B \quad (11)$$

where elements  $x_{ij}^l, x_{ij}^m, x_{ij}^u$  and  $x_{id}^l, x_{id}^m, x_{id}^u$  denote the elements of the matrix  $X$ .

4)  $\tilde{V} = [\tilde{v}_{ij}]_{m \times n}$  is used to provide a weighted version of our matrix whose elements are defined as follows:

$$\tilde{v}_{ij} = (v_{ij}^l, v_{ij}^m, v_{ij}^u) = (\tilde{n}_{ij} \otimes \tilde{w}_{ij}) \\ = (n_{ij}^l \otimes w_j^l, n_{ij}^m \otimes w_j^m, n_{ij}^u \otimes w_j^u) \quad (12)$$

5) Let  $\tilde{S}_i$  denote the aggregation of fuzzy matrix  $\tilde{V}$  as the summation of its elements; i.e. [13]

$$\tilde{S}_i = \sum_{j=1}^n \tilde{v}_{ij} \quad (13)$$

6) The following equations are applied to calculate the degree of utility relevant to alternative  $i$ :

$$K_i^- = \frac{S_i}{s_{ai}} = \left( \frac{s_i^l}{s_{ai}^u}, \frac{s_i^m}{s_{ai}^m}, \frac{s_i^u}{s_{ai}^l} \right) \quad (14)$$

$$K_i^+ = \frac{S_i}{s_{id}} = \left( \frac{s_i^l}{s_{id}^u}, \frac{s_i^m}{s_{id}^m}, \frac{s_i^u}{s_{id}^l} \right) \quad (15)$$

7) Computation of fuzzy matrix  $T_i^{\%}$  based on Equation (16).

$$\tilde{T}_i = \tilde{t}_i = (t_i^l, t_i^m, t_i^u) = k_i^- \otimes k_i^+ = (k_i^{-l} + k_i^{+l}, k_i^{-m} + k_i^{+m}, k_i^{-u} + k_i^{+u}) \quad (16)$$

Then, it is required that define a new fuzzy number  $\tilde{D}$  is defined by:

$$\tilde{D} = (d^l, d^m, d^u) = \max_i \tilde{t}_{ij} \quad (17)$$

Afterward, it is required to defuzzy the number  $\tilde{D}$  by applying the expression  $df_{crisp} = \frac{1+4m+u}{6}$  to obtain the  $df_{crisp}$  number [15].

8) The utility functions based on the worst and best ideal alternatives are denoted by  $f(\tilde{k}_i^-)$  and  $f(\tilde{k}_i^+)$ , respectively.

Based on the best ideal alternative and the worst ideal alternative, utility functions are calculated by the following equations:

$$f(\tilde{k}_i^-) = \frac{\tilde{k}_i^-}{df_{crisp}} = \left( \frac{k_i^{-l}}{df_{crisp}}, \frac{k_i^{-m}}{df_{crisp}}, \frac{k_i^{-u}}{df_{crisp}} \right) \quad (18)$$

$$f(\tilde{k}_i^+) = \frac{\tilde{k}_i^+}{df_{crisp}} = \left( \frac{k_i^{+l}}{df_{crisp}}, \frac{k_i^{+m}}{df_{crisp}}, \frac{k_i^{+u}}{df_{crisp}} \right) \quad (19)$$

9) We are now ready to calculate the utility function of alternative  $i$  by the following equation:

$$f(k_i) = \frac{k_i^+ + k_i^-}{1 + \frac{1-f(k_i^+)}{f(k_i^+)} + \frac{1-f(k_i^-)}{f(k_i^-)}} \quad (20)$$

10) Finally, the alternatives are sorted to create a ranked list of alternatives.

Besides the design of the fuzzy MARCOS method, a novel linguistic size for comparing alternatives has been defined, which is demonstrated in Table 1. Here, an aggregate of nine linguistic terms and their TFN is determined [18].

#### 4. RESEARCH METHODOLOGY

In this research, we first extract 30 criteria related to the implementation of uni-directional contracts by reviewing the pertinent literature. Then, we discussed these criteria with 15 experts in SCM and logistics to investigate the suitability of the criteria for lateral contracts. Our effort lead to the confirmation of six criteria for lateral contracts as summarized in Table 2.

Therefore, in this study, it is assumed that the barriers to implementing bilateral contracts include; lack of training for employees, the poor commitment by top management and employee, lack of motivation and employee involvement, fear of failure, unwillingness to change, and lack of corporate social responsibility. Previous studies of bilateral contracts have failed to consider the training, commitment, motivation, and responsibility aspects of bidirectional contracts [1, 33, 34]. Ignorance of these humanistic aspects has limited the existing literature.

**TABLE 1.** A newly determined size for evaluating potential solutions

Linguistic Term	Mark	TFN
Extremely poor	EP	(1,1,1)
Very poor	VP	(1,1,3)
Poor	P	(1,3,3)
Medium poor	MP	(3,3,5)
Medium	M	(3,5,5)
Medium good	MG	(5,5,7)
Good	G	(5,7,7)
Very good	VG	(7,7,9)
Extremely good	EG	(7,9,9)

**5. NUMERICAL STUDY**

Here, a numerical illustration of the results is provided in the context of the Iranian car industry. The necessary readiness for eight Iranian car manufacturing companies to implement lateral contracts is ranked based on nine criteria resulting from experts' opinions. First, the weight of each criterion is determined based on the average of three experts' opinions. Then, the companies are ranked using an MCDM method, named fuzzy MARCOS. After the first step where we construct the MADM model with eight alternatives and nine criteria. In the second step, we define two solutions, namely, fuzzy anti-ideal  $\tilde{A}$  (AI) and

fuzzy ideal  $\tilde{A}$  (ID) based on Equation (8) and Equation (9) to extend the fuzzy initial matrix. This matrix is formed using linguistics ratings in which values are quantified by triangular fuzzy numbers. The ranking of the results is shown in Table 3.

**6. SENSITIVITY ANALYSIS AND COMPARISON WITH OTHER METHODS**

We show the stability and robustness of our method in this section. To demonstrate the stability of our method, we generate 10 sets of weights based on the simulation as illustrated in Figure 1 [35]. The order of alternatives based on these scenarios is depicted in Figure 2. As it is clear from this figure, ignoring the small change in  $A_2$  and  $A_3$ , the order of alternatives is considerably stable in all scenarios.

The addition or removal of an alternative to the decision matrix may change the ranking of alternatives, which is an important weakness point present in the classic MCDM method [36, 37]. To check the robustness of our method, we first eliminate the worst alternative (i.e.,  $A_5$ ).

The simulated weights for 8 scenarios are shown in Figure 2.

We notice that the order of the remaining alternatives remains fixed and repeat the elimination process with  $A_8$  as the second worst alternative. The order is the same as the pre-elimination step. We continue the elimination process in the same trend based on the scenarios listed in Table 4. It is evident that the order of alternatives ( $A_1 > A_6 > A_2 > A_7 > A_3 > A_4 > A_8 > A_5$ ) is not affected by eliminating the alternatives, which shows the robustness of our proposed method.

In this paper, we compared the fuzzy MARCOS model with three other MCDM models; namely, FSAW, FTOPSIS, and FMULTIMOORA. As shown in Figure 3, company 1 tops the ranking list in all three models due to its suitable infrastructure to implement lateral contracts. As can be seen, the results of the four models are so close

**TABLE 2.** Categories of the issue

Item	Barriers	References	Description
1	Lack of training for employee	[7, 12-17]	Education and training are necessary for any organization to learn new concepts and apply them effectively.
2	Poor commitment by top Management and employee	[6, 13, 14, 18, 20]	Extreme barrier is poor commitment by the top management.
3	Lack of motivation and employee involvement	[13, 19, 20-24]	Optimistic behavioral elements include confidence, passion, and self-image, which must be improved. Negative behavioral elements include sarcasm, destructive criticism, status consciousness, and fear of estimation which must be minimized.
4	Fear of Failure	[1, 18, 30]	Companies must allow workers to do jobs without fear of failure and ensure that they will not lose their job.
5	Unwillingness to change	[1, 2, 6, 13, 19, 25, 26, 27, 28, 31]	Previous failure experience, lack of standard training and education, and inadequate level of resources are among the main factors which lead to resistance to change. These must be properly dealt with to overcome the unwillingness to change.
6	Lack of corporate social responsibility	[13, 16, 29, 32]	The concept of commitment and economic development and enhancing the quality of life of employees and their families and the general public.

**TABLE 3.** Ranking the obtained results

Alternatives	$K_i$	RANK
A1	0.86	1
A2	0.63	3
A3	0.57	5
A4	0.54	6
A5	0.10	8
A6	0.76	2
A7	0.60	4
A8	0.21	7

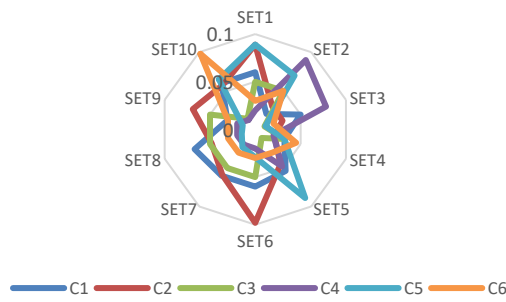


Figure 1. Simulated weights for scenarios

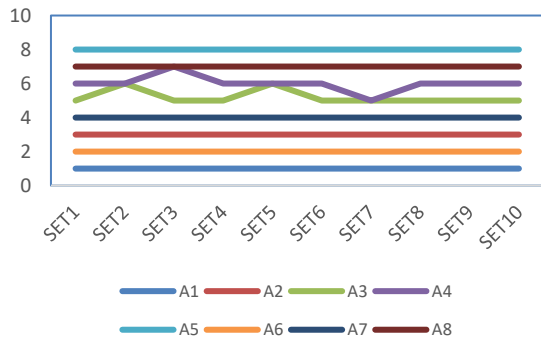


Figure 2. Ranking of airlines under different scenarios

TABLE 4. Rank reversal effect in the application

Alternative	Initial Rank	Scenario1	Scenario2	Scenario2
A1	1	1	1	1
A2	3	3	3	3
A3	5	5	5	5
A4	6	6	6	0
A5	8	0	0	0
A6	2	2	2	2
A7	4	4	4	4
A8	7	7	0	0

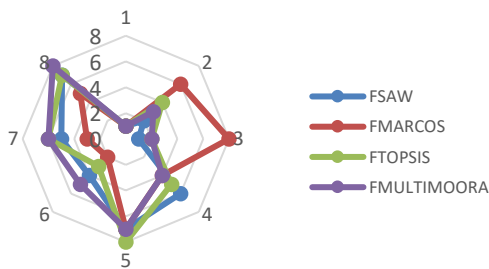


Figure 3. Comparison of the fuzzy TOPSIS, fuzzy SAW, and fuzzy MULTIMOORA methods

to each other. The application of the fuzzy method has enabled the experts to enhance the way they express their opinion about the companies.

### 7. MANAGERIAL INSIGHTS

As the results of the previous section indicate the company related to alternative number 1 ranks first regardless of the solution technique chosen to solve the ranking problem.

There is no surprise in such performance for alternative 1 since it has a significant background in critical success factors of a company. The company has improved the motivation of its employees by providing proper training and mentorship [38]. While adjusting the scope of its intended improvement at specific and broad levels of organizational enhancement [39]. This has both direct and indirect impacts on the performance of employees leading to the success of the company [40]. Since the company is highly active in Industry 4.0 projects, it has provided a sufficient level of management support, training, and external expert involvement as important success factors for such projects [41]. The company has also constantly been successful in escaping from business failure situations because it has been able to “operate as a sustainable entity” and avoid stopping operations and firing employees [42] by avoiding environmental mismatch and internal misalignment failure factors [43].

Based on these findings and considering the nature of automaking industries, the managers of car manufacturing firms should consider their employees as the core of bidirectional contracts implementation, hence, require to focus on their motivation, training, and mentorship issues. They need to concentrate on the sustainability of their firms in terms of social, economic, and environmental factors to guarantee the long-term operation of their manufacturing activities by avoiding both internal and external failure contexts.

### 8. CONCLUSION AND FUTURE STUDIES

Coordination in supply chain management is carried out based on various tools among which contracts are well-known for their impressive effect on coordinating relations of partners involved in the supply chain. In this paper, lateral contracts are investigated as they are understudied in the extant literature. We first extracted 30 criteria related to the implementation of uni-directional contracts by reviewing the pertinent literature. Then, we discussed these criteria with 15 experts in SCM and logistics to investigate the suitability of the criteria for lateral contracts. Our effort led to the confirmation of 6 criteria for lateral contracts. Subsequently, we identified

the weights of these criteria using the expert method. Finally, we validated our method by solving the problem based on multi-criteria decision-making methods (MCDM), namely FMARCOS, FSAW, FTOPSIS, and FMULTIMOORA. This analysis resulted in the same ranking of put top sample firms (i.e., sample firms one and two). Based on our interview with experts, the background of the firm, its highly experienced experts in designing and forming contracts, and its administrative organization are among the reasons for these firms to top the list ranking. These results validated our method and showed its fitness for real-life applications.

This paper may be extended in several directions. For example, instead of using the fixed weights for criteria of lateral contracts implantation, novel methods (i.e., FARAS<sup>1</sup>, FSWARA<sup>2</sup>, and FIDOCRIW<sup>3</sup>) of comparison in MADM may be applied to the model. Also, an extension of the MARCOS method based on such theories as grey theory and neutrosophic, single-valued intuitionistic fuzzy numbers is recommended.

## 9. REFERENCES

- Govindan, K., Kaliyana, M., Kannan, D. and Haq A.N., "Barriers analysis for green supply chain management implementation in Indian industries using analytic hierarchy process", *International Journal of Production Economics*, Vol. 147, (2014), 555-568. doi:10.1016/j.ijpe.2013.08.018
- Moktadir, M. A., Ali, S. M., Rajesh, R. and Paul, S. K., "Modeling the interrelationships among barriers to sustainable supply chain management in leather industry", *Journal of Cleaner Production*, Vol. 181, (2018), 631-651. doi: 10.1016/j.jclepro.2018.01.245
- Li, Q. and Liu, Z., "Supply chain coordination via a two-part tariff contract with price and sales effort dependent demand", *Decision Science Letters*, Vol. 4, No. 1, (2015), 27-34. doi: 10.5267/j.dsl.2014.9.003
- Ojo, E., Mbowe, C. and Akinlabi, E. T., "Barriers in implementing green supply chain management in construction industry", The Proceedings of the International Conference on Industrial Engineering and Operations Management, Bali, Indonesia, (2014).
- Al Zaabi, S., Al Dhaheri, N. and Diabat, A., "Analysis of interaction between the barriers for the implementation of sustainable supply chain management", *The International Journal of Advanced Manufacturing Technology*, Vol. 68, Nos. 1-4, (2013), 895-905. doi: 10.1007/s00170-013-4951-8
- Salami, E., Aydinli, S. and Oral, E. L., "Barriers to the implementation of supply chain management-case of small to medium sized contractors in turkey", *International Journal of Science and Research*, Vol. 14, No. 9, (2013), 2319-7064. doi: 10.21275/ART20161582
- Parmer, V. and Shah, H. G., "A literature review on supply chain management barriers in manufacturing organisation", *International Journal of Engineering Development and Research*, Vol. 4, No. 1, (2016), 26-42.
- Wibowo, M. A., Handayani, N. U. and Mustikasari, A., "Factors for implementing green supply chain management in the construction industry", *Journal of Industrial Engineering and Management*, Vol. 11, No. 4, (2018), 651-679. doi: 10.3926/jiem.2637
- Halldórsson, Á., Larson, P. D. and Poist, R. F., "Supply chain management: a comparison of Scandinavian and American perspectives", *International Journal of Physical Distribution & Logistics Management*, Vol. 38, No. 2, (2008), 126-142. doi: 10.1108/09600030810861206
- Kumar, R. and Kansara, S., "Information technology barriers in Indian sugar supply chain: an AHP and fuzzy AHP approach", *Benchmarking: An International Journal*, Vol. 25, No. 7, (2018), 1978-1991. doi: 10.1016/j.inpa.2020.09.005
- Wyawahare, A. and Udawatta, N., "A framework for successful implementation of green supply chain management (GSCM) in construction organisations", *EPiC Series in Education Science*, 1, (2017), 402-410, doi: 10.29007/jx4z
- Rouibah, K., Hamdy, H. I. and Al-Enezi, M. Z., "Effect of management support, training, and user involvement on system usage and satisfaction in Kuwait", *Industrial Management & Data Systems*, Vol. 109, No. 3, (2009), 338-356. doi: 10.1108/02635570910939371
- Biswas, T.K. and Chaki, S., Applications of modified simple additive weighting method in manufacturing environment. *International Journal of Engineering, Transactions A: Basics*, Vol. 35, No. 4, (2022), 830-836, doi: 10.5829/ije.2022.35.04A.23
- Beheshtinia, M.A., Falsafi, P., Qorbani, A. and Jalinouzade, H., "Evaluating and ranking digital stores' suppliers using TOPKOR method" *International Journal of Engineering, Transactions B: Applications*, Vol. 35, No. 11, (2022), 2130-2138. doi: 10.5829/ije.2022.35.11b.10
- Ayşegül, T. U. Ş. and Adali, E. A., "Green supplier selection based on the combination of fuzzy SWARA (SWARA-F) and fuzzy MARCOS (MARCOS-F) Methods. *Gazi University Journal of Science*, Vol. 35, No. 4, (2022), 1535-1554. doi: 10.35378/gujs.978997
- Arora, H.D., Naithani, A. and Gupta, S., "Distance measures of Pythagorean fuzzy TOPSIS approach for online food delivery apps" *International Journal of Engineering, Transactions A: Basics*, Vol. 35, No. 10, 1877-1886. doi: 10.5829/ije.2022.35.10a.07, 2022.
- Patel, S.S. and Prajapati, J.M., Multi-criteria decision-making approach: Selection of blanking die material. *International Journal of Engineering, Transactions B: Applications*, Vol. 30, No. 5, (2017), 800-806. https://doi: 10.5829/idosi.ije.2017.30.05b.21
- Bakır, M. and Atalık, Ö., "Application of fuzzy AHP and fuzzy MARCOS approach for the evaluation of e-service quality in the airline industry". *Decision Making: Applications in Management and Engineering*, Vol. 4, No. 1, (2021), 127-152. doi: 10.31181/dmame2104127b
- Gorane, S. J. and Kant, R., "Modelling the SCM implementation barriers", *Journal of Modelling in Management*, Vol. 10, No. 2, (2015), 158-178.
- Gill, S. S. and Pabla, B. S. "Critical review of performance measurement frameworks in supply chain management. *International Journal of Engineering Research & Technology*, Vol. 2, No. 10, (2013), 2464-2471.
- Wickramasinghe, V. and Gamage, A. "High-involvement work practices, quality results, and the role of HR function", *The TQM Journal*, Vol. 23, No. 5, (2011), 516-530. doi: 10.1108/17542731111157626
- Archer, N., Wang, S. and Kang, C. "Barriers to the adoption of online supply chain solutions in small and medium enterprises",

<sup>1</sup> Fuzzy Additive Ratio Assessment method

<sup>2</sup> Fuzzy Step-wise Weight Assessment Ratio Analysis

<sup>3</sup> Fuzzy Integrated Determination of Objective Criteria Weights

- Supply Chain Management: An International Journal*, Vol. 13, No. 1, (2008), 73-82.
23. Manzouri, M., Rahman, M. N. A., Arshad, H. and Ismail, A. R., "Barriers of supply chain management implementation in manufacturing companies: a comparison between Iranian and Malaysian companies", *Journal of the Chinese Institute of Industrial Engineers*, Vol. 27, No. 6, (2010), 456-472. doi: 10.1080/10170669.2010.526379
  24. Abu, N. H., Huat, K. K. and Mansor, M. F., "Implementation of green new product development among SMEs: Barriers and critical success factors", In: MATEC Web of Conferences, 530, (2018), 500-533. EDP Sciences. doi: 10.1051/mateconf/201815005038
  25. Van Donk, D.P. "Challenges in relating supply chain management and information and communication technology", *International Journal of Operations & Production Management*, Vol. 28, (2008), 308-312. doi: 10.1051/mateconf/201815005038
  26. Lee, Y. C., Chu, P. Y. and Tseng, H. L. Corporate performance of ICT-enabled business process re-engineering. *Industrial Management & Data Systems*, Vol. 111, (2011), 735-754. doi: 10.1108/02635571111137287
  27. Mafini, C., "Barriers to public supply chain management strategy implementation: an exploratory diagnosis", *Problems and Perspectives in Management*, Vol. 14, (2016), 256-265. doi: 10.21511/ppm.14(3-1).2016.12
  28. Tsinopoulos, C. and Bell, K., "Supply chain integration systems by small engineering to order companies. *Journal of Manufacturing Technology Management*, Vol. 21, No. 1, (2010), 50-62. doi: 10.1108/17410381011011489
  29. Sadi, M. A. and Al-Dubaisi, A. H., "Barriers to organizational creativity", *Journal of Management Development*, Vol. 27, (2008), 574-599. doi: 10.1108/02621710810877839
  30. Ikram, M., Sroufe, R. and Zhang, Q., "Prioritizing and overcoming barriers to integrated management system (IMS) implementation using AHP and G-TOPSIS", *Journal of Cleaner Production*, Vol. 254, (2020), 120121. doi: 10.1016/j.jclepro.2020.120121
  31. Amaral, P. and Sousa, R., "Barriers to internal benchmarking initiatives: an empirical investigation", *Benchmarking: An International Journal*, Vol. 16, No. 4, (2009), 523-542. doi: 10.1108/14635770910972441
  32. Luthra, S. and Haleem, A., "Hurdles in implementing sustainable supply chain management: An analysis of Indian automobile sector", *Procedia-Social and Behavioral Sciences*, Vol. 189, No. 1, (2015), 175-183. https://doi.org/10.1016/j.sbspro.2015.03.212
  33. Katunzi, T.M., "Obstacles to process integration along the supply chain: manufacturing firms' perspective". *International Journal of Business and Management*, Vol. 6, No. 5, (2015), 105-113. doi: 10.5539/ijbm.v6n5p105
  34. Khan, S.A.R., Zkik, K., Belhadi, A. and Kamble, S.S., "Evaluating barriers and solutions for social sustainability adoption in multi-tier supply chains", *International Journal of Production Research*, Vol. 59, No. 11, (2021), 3378-3397. doi: 10.1080/00207543.2021.1876271
  35. Ghorabae, M. K., Amiri, M., Zavadskas, E. K. and Antucheviciene, J., "A new hybrid fuzzy MCDM approach for evaluation of construction equipment with sustainability considerations", *Archives of Civil and Mechanical Engineering*, Vol. 18, No. 1, (2018), 32-49. doi: 10.1016/j.acme.2017.04.011
  36. Stanković, M., Stević, Ž., Das, D.K., Subotić, M. and Pamučar, D., "A new fuzzy MARCOS method for road traffic risk analysis", *Mathematics*, Vol. 8, No. 3, (2020), 457. doi: 10.3390/math8030457
  37. Yazdani, M., Chatterjee, P., Pamucar, D. and Abad, M. D., "A risk-based integrated decision-making model for green supplier selection", Vol. 49, No. 4, (2019), 1229-1252. doi: 10.1108/K-09-2018-0509
  38. Kulathunga, D. and Fernando, M. K. "User satisfaction factors of ERP systems: The case of a manufacturing company in Sri Lanka", *European Journal of Business and Management*, Vol. 11, No. 33, (2019), 105-114. doi: 10.7176/EJBM/11-33-12
  39. Lo, C. Y. and Lai, W. H. "An investigation of corporate social responsibility in the high-tech industry. *Review of Integrative Business and Economics Research*, Vol. 9, No. 2, (2020), 46-62.
  40. Ozkeser, B., "Impact of training on employee motivation in human resources management", *Procedia Computer Science*, 158, (2019), 802-810. doi: 10.1016/j.procs.2019.09.117
  41. Van Assen, M. F., "Empowering leadership and contextual ambidexterity - The mediating role of committed leadership for continuous improvement", *European Management Journal*, Vol. 38, No. 3, (2020), 435-449. doi: 10.1016/j.emj.2019.12.002
  42. Luo, Z., Ma, M. and Li, E., "Driving frontline employees' performance through mentorship, training, and interpersonal helping: The case of upscale hotels in China", *International Journal of Tourism Research*, Vol. 23, No. 5, (2021), 846-857. doi: 10.1002/jtr.2447
  43. Eskedal, V. and Gullsmoedmoen Indrebø, L., "Critical success factors and barriers affecting the successful implementation of the general data protection regulation: A multiple case study of three companies operating in the banking and insurance industry", Thesis, Master of Science Business, Leadership and Change, BI Norwegian Business School - Campus Oslo. Sweden, (2019).

---

### Persian Abstract

#### چکیده

هماهنگ می کنند. اگرچه چنین رویکرد قراردادی در مدیریت زنجیره تامین هم در صنعت و هم در دانشگاه رایج است، اجرای موفقیت آمیز قراردادها در اتحادهای دو طرفه به دلیل شناسایی ناقص موانع اجرایی توسط شرکت های درگیر در اتحاد، در عمل چالش برانگیز است. این مقاله به بررسی مسائل اجرای قراردادهای دوطرفه می پردازد. برای شناسایی موانع، با استفاده از مرور ادبیات و مصاحبه کارشناسان مرتبط با موضوع مورد بررسی قرار گرفت و در نهایت معیارهای اصلی موانع پیاده سازی قراردادهای دو طرفه استخراج گردید. در این تحقیق از روش تصمیم گیری جدیدی به نام روش ماکوس فازی جهت رتبه بندی شرکت ها مورد استفاده قرار گرفت بدین صورت که میزان آمادگی ۸ شرکت های خودروسازی در ایران جهت پیاده سازی قراردادهای دو طرفه مورد تحلیل قرار گرفت و میزان آمادگی این شرکت ها بر اساس معیارهای استخراج شده مورد ارزیابی و اولویت بندی قرار گرفت.

---



## Discrimination of Plastic Waste using Laser-induced Breakdown Spectroscopy-principal Component Analysis: Highlighting Molecular LIBS

S. N. Abdulmajid<sup>\*a</sup>, B. S. Hartadi<sup>a</sup>, R. Mitaphonna<sup>b</sup>, M. Iqhrammullah<sup>b</sup>

<sup>a</sup> Department of Physics, Faculty of Mathematics and Natural Sciences Universitas Syiah Kuala, Banda Aceh, Indonesia

<sup>b</sup> Graduate School of Mathematics and Applied Sciences, Universitas Syiah Kuala, Banda Aceh, Indonesia

### PAPER INFO

#### Paper history:

Received 24 May 2022

Received in revised form 09 September 2022

Accepted 11 October 2022

#### Keywords:

Molecular Laser-induced Breakdown

Spectroscopy

Plastic Waste

Polyethylene Terephthalate

Polypropylene

Principal Component Analysis

### ABSTRACT

Growing plastic waste emission as a planetary threat urges the development of a rapid and efficient recycling process, especially during the classification process. Herein, we aimed to solve the problem by employing laser-induced breakdown spectroscopy (LIBS) in combination with principal component analysis (PCA) as means for automated plastic waste classification. Samples used in the study were plastic wastes derived from beverage, food, and stationery products of different brands. The Nd:YAG laser was shot to the sample surface without a pre-treatment and under an open-air system (laser energy= 54 mJ; time delay= 1-2  $\mu$ s). The spectral profile of each plastic waste revealed the presence of metal components such as those indicated by Ca II 396.85 nm, Al I 395.92 nm, Mg I 383.83 nm, and Fe I 404.85 emission lines. Peak intensities of organic material-related emission lines (C I 247.86 nm, O II 777.32 nm, O I 844.48 nm, H I 666.22 nm, N II 818.83 nm, and N II 821.62 nm) were revealed fluctuating, suggesting that a mere LIBS spectral analysis could not discriminate the plastic waste. PCA analysis revealed that C<sub>2</sub> molecular band 490–520 nm had the most discriminative properties against polyethylene terephthalate (PET) and polypropylene (PP). The molecular band was generated differently between PET and PP because of their contrast thermal behavior. In conclusion, molecular LIBS-PCA could be used to distinguish PET and PP in a simple and rapid way.

doi: 10.5829/IJE.2023.36.01a.12

### NOMENCLATURE

LIBS	Laser-induced breakdown spectroscopy	PC	Principal component
PCA	Principal component analysis	ICP-MS	Inductively coupled plasma-mass spectrometry
PET	Polyethylene terephthalate	ICP-OES	Inductively coupled plasma-atomic emission spectroscopy
PP	Polypropylene	ICCD	Intensified charge-coupled device
LDPE	Low density polyethylene	DDG	Digital delay generator

### 1. INTRODUCTION

Plastics are notorious solid waste that contribute to the increased risk of human health and climate change through ‘chain reactions’ [1]. With the current state of plastic generation, plastic waste emission is predicted to reach 35.8-90.0 Mt [2]. This number exceeds the mitigation efforts [2], suggesting the need of efficient plastic waste management. Of which, recycling is

considered to play a key role in saving the world from plastic waste disaster [3, 4]. One of the examples of the recycled plastic use is in asphalt mixture [5, 6], which requires certain type of plastics to achieve optimum durability. Prior to recycling process, an important step needs carried out is classifying the plastic waste based on its type [3]. Moreover, plastic waste should be classified further based on the contents of impurities and contaminants [3]. With our experience in previous researches of analyzing organic [7-9] or inorganic materials [10-13], we believed laser-induced breakdown spectroscopy (LIBS) could be the right technology to be applied to discriminate the plastic waste.

\*Corresponding Author Email: [syahrin\\_madjid@unsyiah.ac.id](mailto:syahrin_madjid@unsyiah.ac.id)  
(S.N. Abdulmajid)

LIBS is a versatile tool utilizing spectroscopical analysis on laser-ablated sample for multiple kinds of samples [14, 15]. Unlike complex inductively coupled plasma-mass spectrometry or -atomic emission spectroscopy (ICP-MS or -OES), LIBS uses a simple set up where the analysis is directly carried out on the plasma generated after the ablation. Interestingly, LIBS is capable of analyzing all elements in a single run without requiring sample pre-treatment [14]. Moreover, due to its simplicity, LIBS could be coupled with a machine allowing the automation of plastic separation [16]. In the case of plastic waste management, LIBS itself has been studied for its utilization to analyze hazardous impurities in plastics [17, 18]. Several previous reports have even suggested the discriminative ability of LIBS against various types of plastics or polymers [19, 20].

For discriminating plastic waste using LIBS, some studies were coupled LIBS with other analytical methods such as machine learning [19] and chemometrics [21, 22]. Indeed the grouping of plastics could be conducted based on simple analysis on the spectral intensities [23]. However, the investigation was only carried out on pure plastics [23], hence could not be used for plastic wastes that contain different kinds of additives or contaminants. Herein, we offer a simple chemometric technique namely principal component analysis (PCA). The technique reduces the dimensionality of large data sets [24], which is useful for LIBS spectral data with wide wavelength range. The objective of our study was to investigate the feasibility of LIBS-PCA for plastic waste discrimination. As a novelty of our research, we analyzed the plastic waste acquired from different products and brands. Moreover, the emergence of molecular band in the LIBS spectra was elucidated, contributing to more insights towards molecular LIBS.

## 2. MATERIALS AND METHODS

**2. 1. Materials and Study Design** All plastic wastes used in this study were collected around Universitas Syiah Kuala (Banda Aceh, Indonesia) in June 2021. Based on the label, the plastic wastes consisted of several plastic types, namely polyethylene terephthalate (PET), polypropylene (PP), low density polyethylene (LDPE), and Teflon which were produced and used by different industries. PET was produced by PT. Coca Cola Indonesia (Jakarta, Indonesia) and PT Reckitt Benckiser Indonesia (Jakarta, Indonesia), PP – Zhejiang Xiulong Packaging Materials Co., Ltd. (Jiaying, China), PT. Unilever Indonesia (Jakarta, Indonesia), and Jenia (Tangerang, Indonesia), LDPE – PT. Sinergi Inti Plastindo (Jakarta, Indonesia), and teflon – PT. Unilever Indonesia (Jakarta, Indonesia).

Labels in the packaging were checked for the main polymeric components (PET, PP, LDPE, and teflon). Types or percentages of the additives in the packaging were not known to the researchers. Samples were directly shot using Nd-YAG laser without any pretreatment in an open-air system, where spectral data were then analyzed to discriminate the plastic wastes based on their respective type. All laser analyses were performed in triplicate to ensure the spectral stability.

**2. 2. LIBS Set Up and Experiment** A Q-switched Nd:YAG laser (Quanta-Ray, LAB 130-10, USA) was used for the study. The laser was operated at 1064 nm with 8-ns pulse width and 10-Hz pulse duration to generate an ablation and plasma on a sample surface. The laser energy was set constant at 54 mJ. Prior of reaching the sample surface, the beam was focused using a lens with 150-mm focal length. The signals from the plasma were captured using an optical fiber (numerical aperture=0.22), distanced 6 cm from a sample. The signals were sent to a spectrometer coupled with an intensified charge-coupled device (ICCD) camera (Andor iStar' intensified CCD 1,024 x 256 pixels, UK). To trigger the laser and ICCD camera, a digital delay generator (DDG 535, Stanford Research System, USA) was employed. The gate width was of the ICCD was made constant at 30  $\mu$ s with variation of time delays (1, 1.5, and 2  $\mu$ s). The spectra were produced by 10 shots accumulation.

**2. 1. Data Analysis** Principal component analysis (PCA) was carried out on spectra produced with 2- $\mu$ s time delay using OriginLab version 9.6.5.169 (Northampton, USA), where data were extracted into 2 components. Spectral widths were obtained from a peak analysis carried out on the same OriginLab with constant baseline setting.

## 3. RESULTS AND DISCUSSION

**3. 1. LIBS Spectral Profiles of Plastic Waste** Firstly, we conducted a spectral analysis on the whole wavelength to observe the differences between sample with wavelength range of 200 to 900 nm. The data are presented in Figure 1, depicting LIBS spectral profile for PET (1-4), PP (1-3), LDPE, and Teflon. Except in PP 1 and LDPE, CN (0,0) 388.3 nm bands appear significant in all samples. Discussion on CN band in details would be provided in the later part of this manuscript. Other than organic materials-related emission lines (C, H, O, and N), several metals could be observed in the spectra. Of which, Ca II 396.85 nm line is the most commonly appear. Interestingly, the emission line was significantly resolved at later delay time, assigned to the disappearance of ionic species in

the plasma [25]. Furthermore, Al I 395.92 nm and Mg I 383.83 nm emission lines are also present in several samples. Those metals could be associated to the presence of additives in the plastic packaging. Ca, in a form of  $\text{CaCO}_3$ , is the most popular additives in plastic [26, 27]. Al and Mg, or their combination (Al-Mg), are also added by the plastic producer to improve the material resistance [28]. It is worth mentioning that LDPE sample in this study had crowded spectral profile. Moreover, Fe I 404.85 line was uniquely found in the LDPE. There are reports where Fe, in its salt form, is added to the plastic matrix to produce more durable composite. These metals were also found in plastics waste from other countries [20].

Plastics, like other organic materials, mostly consist of carbon (C) and followed by hydrogen (H) and oxygen (O) [9, 29]. Hence, we present the data of C I 247.86 nm emission line of all collected samples in Figure 2. The spectral line could be observed even after

the 2- $\mu\text{s}$  time delay. In the spectrum of PET 4, the Mg II 280.23 line was attenuated significantly at later delay time, suggesting its decaying from the plasma. Though at longer delay time the atomic emission has a tendency to decay, several peaks were observed higher [30]. This is probably due to the discrimination between the emission line and continuum noise.

CN bands are common in carbon-containing material, especially when the ablation is carried out in an open-air [9, 12]. To observe the CN bands, LIBS spectra of each plastic waste focusing on the wavelength range between 300 nm and 400 nm are presented (Figure 3). The CN molecules could be deriving from the ablated C atom from the material and recombined with N from the material or from the ambient air [29]. Increase of CN band intensity is dependent on the delay time, ascribing to its formation during plasma cool down [31].

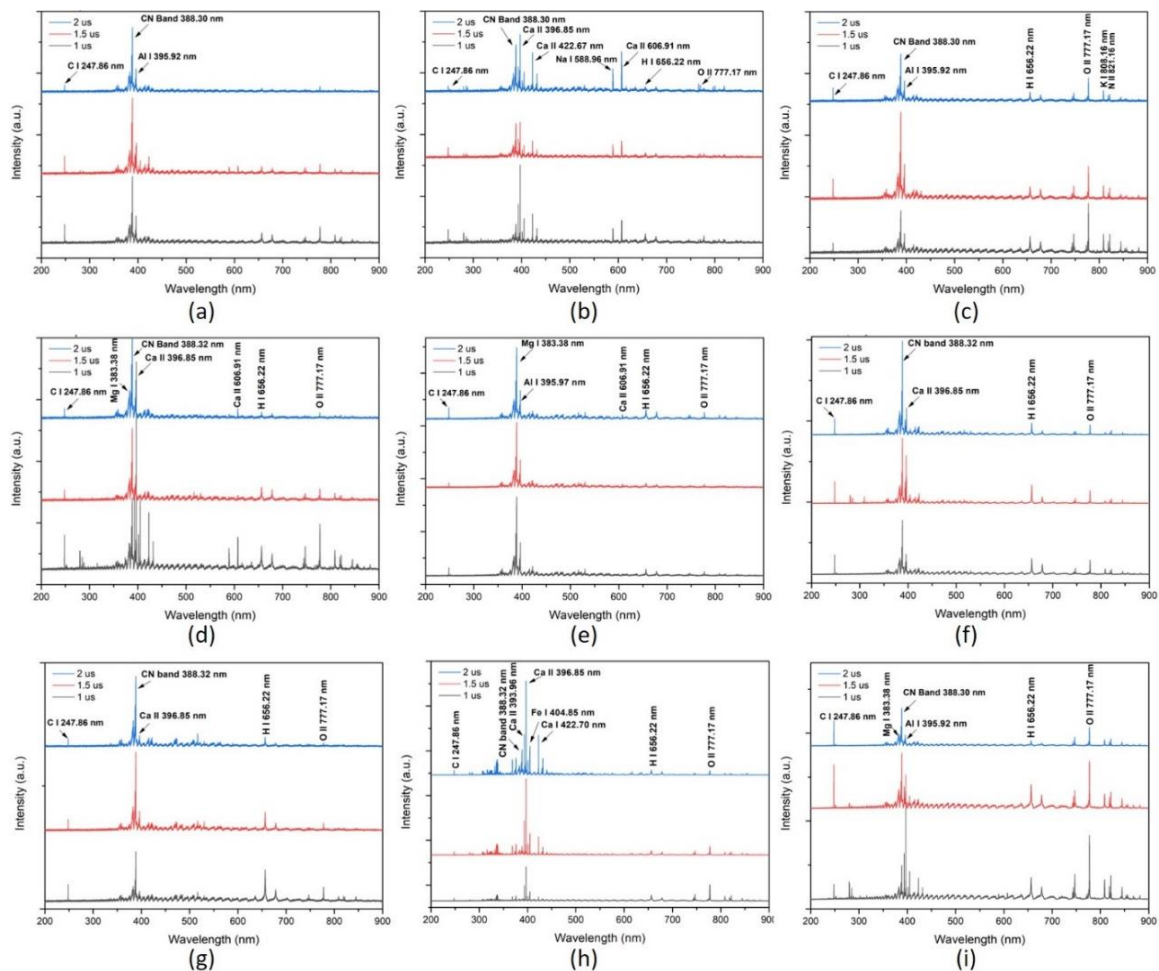


**Figure 1.** LIBS spectra of PET 1 (a), PET 2 (b), PET 3 (c), PET 4 (d), PP 1 (e), PP 2 (f), PP 3 (g), LDPE (h), and Teflon (i). Observed with delay time variation (1, 1.5, and 2  $\mu\text{s}$ ) at full wavelength (200–900 nm)

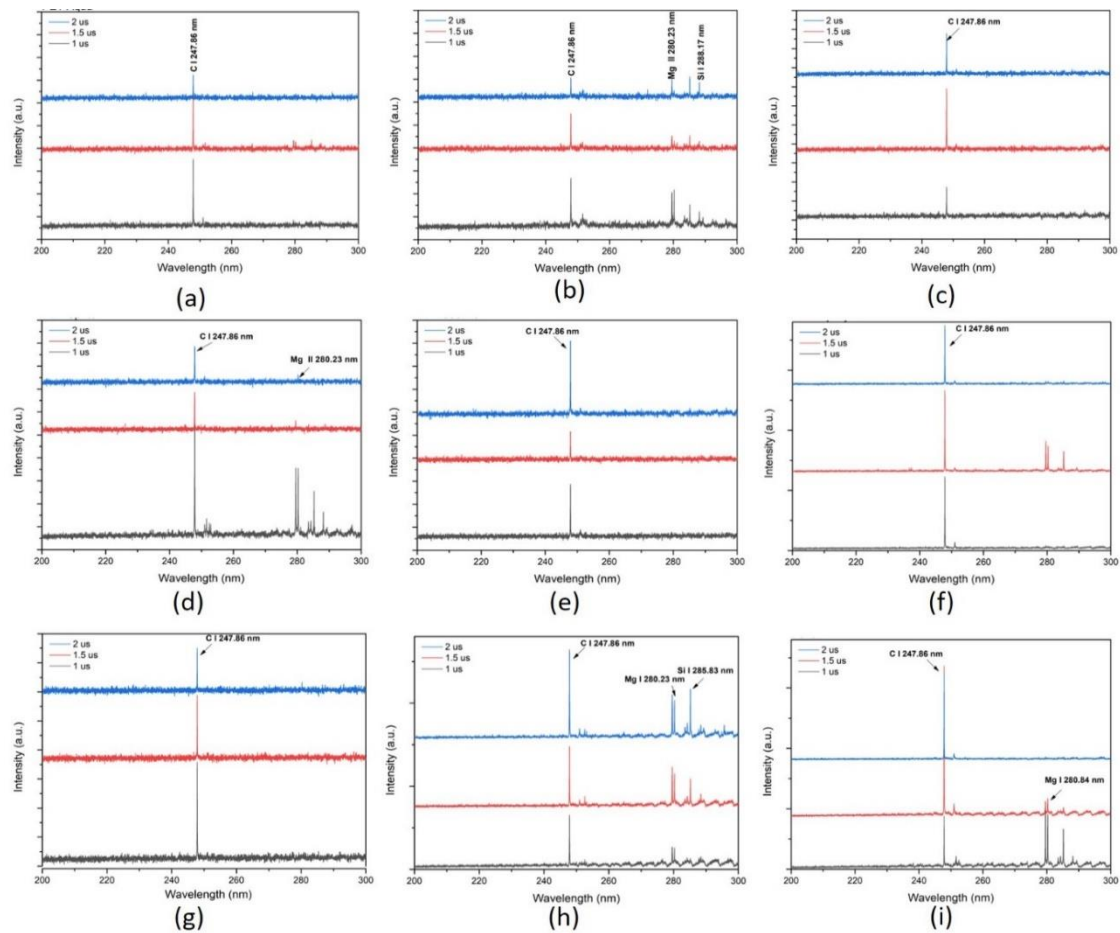


**Figure 2.** LIBS spectra of PET 1 (a), PET 2 (b), PET 3 (c), PET 4 (d), PP 1 (e), PP 2 (f), PP 3 (g), LDPE (h), and Teflon (i). Observed with delay time variation (1, 1.5, and 2  $\mu$ s) at 200–300 nm

Within the wavelength range of 300–400 nm, several emission lines of metallic elements could be observed such as Mg I 383.32 nm, Al 394.75 nm, Al 395.92 nm, Ca II 393.36 nm, and Ca II 396.85 nm. Uniquely, multiple emission lines corresponding to Ti was present in LIBS spectra of LDPE. The presence of Ti in the plastic could be derived from  $\text{TiO}_2$ , a common coloring additive in plastics [32]. The presence of these metal could be an indication of plastic recyclability, where the presence of impurities might lower the quality grade of the recycled plastic [3].

O is also an interesting atom to be analyzed when it comes to organic sample. LIBS spectra ranged from 750 to 900 nm of all samples are presented in Figure 4, where typical emission lines for oxygen (O II 777.32 nm and O I 844.48 nm) could be observed. Except in PET 2, those aforementioned lines could be seen clearly even after 2  $\mu$ s delay. In PET 2, the emission of O II 777.32 nm and O I 844.48 nm could be observed clearly only when the delay time was set at 1  $\mu$ s, where their intensities reduced over time. Similar to carbon, oxygen

is also a light atom, capable of escaping the plasma during the early time of plasma generation [33]. Our data show interesting fact, despite its absence in several samples (PP, LDPE, and teflon), the presence of oxygen was captured in all spectra. It suggests that the oxygen is deriving from the ambient air, since its presence occupies around 21% of the total air; second most dominant after nitrogen (78%).

In this study, the presence of hazardous metals such as Pb, Cr or Hg was not found in the all plastics waste. Previously, LIBS was reported capable of identifying those aforementioned toxic elements in PP mixture [18]. Our suspicion regarding the toxic elements is based on the fact that heavy metals could form a surface chemical interaction with the binding sites available on the plastic [34, 35]. Therefore, even though the manufacturer does not add toxic metals to the plastic, it still capable of adsorbing the heavy metal from the environment. Based on these facts, plastics waste investigated herein are safe because of the absence of toxic heavy metals either originating from the producer or environment.

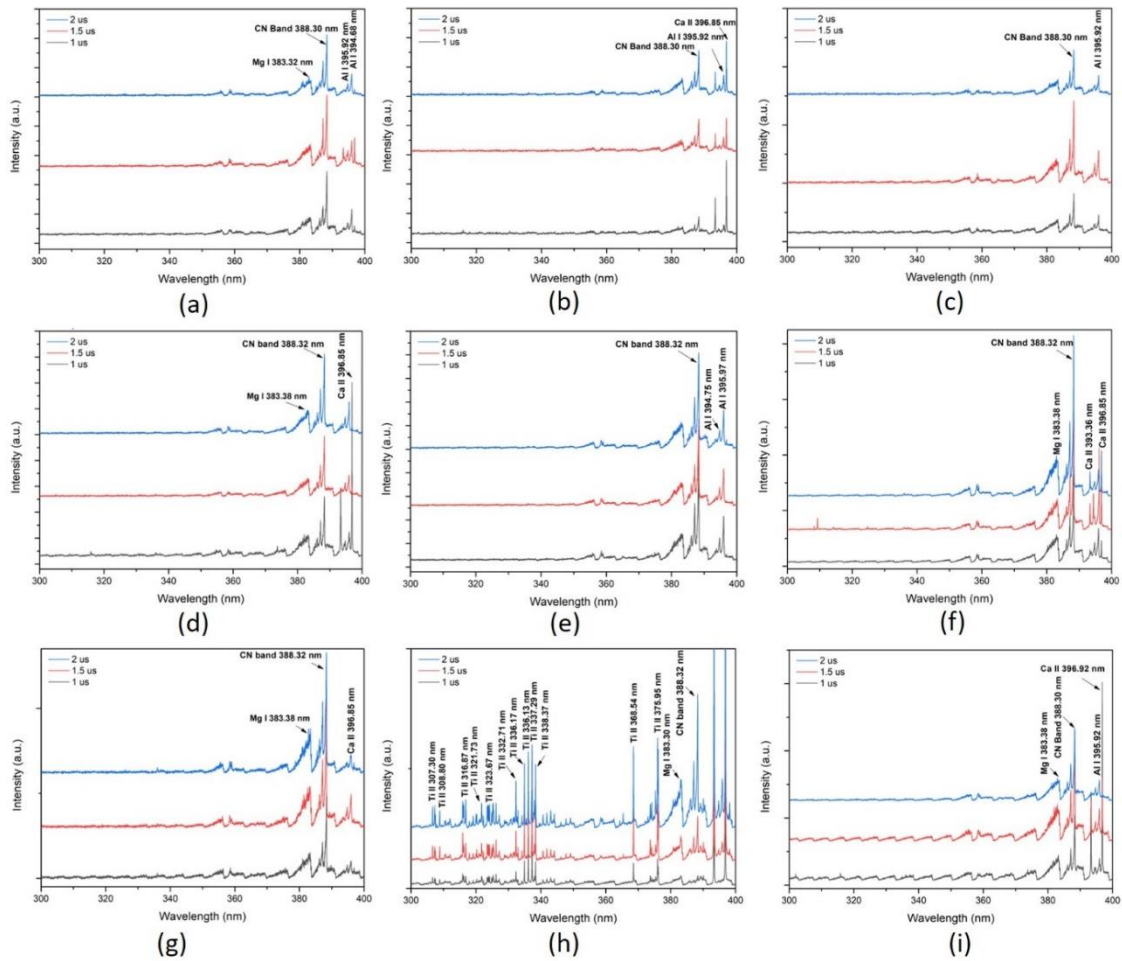


**Figure 3.** LIBS spectra of PET 1 (a), PET 2 (b), PET 3 (c), PET 4 (d), PP 1 (e), PP 2 (f), PP 3 (g), LDPE (h), and Teflon (i). Observed with delay time variation (1, 1.5, and 2  $\mu$ s) at 300–400 nm.

Taken together, the spectral profile of each sample shows a variety of element components depending on the additives used by the producer. Even when we eliminate the mineral spectral lines and focus only to the organic spectral lines, the variation could be found. Not necessarily because of the open-air set up, but also because of the mineral additives are used as salts which commonly contains O and C (such as  $\text{CaCO}_3$  or  $\text{TiO}_2$ ). These differences suggest that LIBS could be used to inspect the origin of the plastic waste (brand or product). In regard of plastic waste management, we do not only expect to differentiate, but also to group the plastic based on its type. Therefore, in the following analysis, we wish to reveal the ability of LIBS to discriminate the plastic waste based on its type. To do that, we employed the data from PET and PP since their availability is more than 1.

### 3. 2. Discrimination of PET and PP Plastic Waste

To understand the underlying differences between PET

and PP, we have provided their chemical structure in Figure 5. PET has a cyclic carbon with ester, carboxylate, and alcohol functional groups. Meanwhile, PP has an aliphatic structure, with repeating C-C and one primary alkyl present along its chain. One may suspect that the presence of O in its structure could be the key in differentiating it with PP. Nonetheless, when it comes to commercial packaging O could also be found in PP deriving from the additives, as discussed previously. We ourselves have conducted the principal component analysis for LIBS spectra with wavelength ranges of 200–300, 300–400, and 750–900 nm. However, the analysis could not discriminate PET from PP (data not displayed).

To continue our efforts of discriminating PET from PP using LIBS-PCA, we focused on the  $\text{C}_2$  molecular band at 464–474 nm (Figure 6a) and 490–520 nm (Figure 6b). It could be seen that the PP has higher intensities of  $\text{C}_2$  molecular bands than that of PET in both observed wavelength ranges. Nonetheless, it is

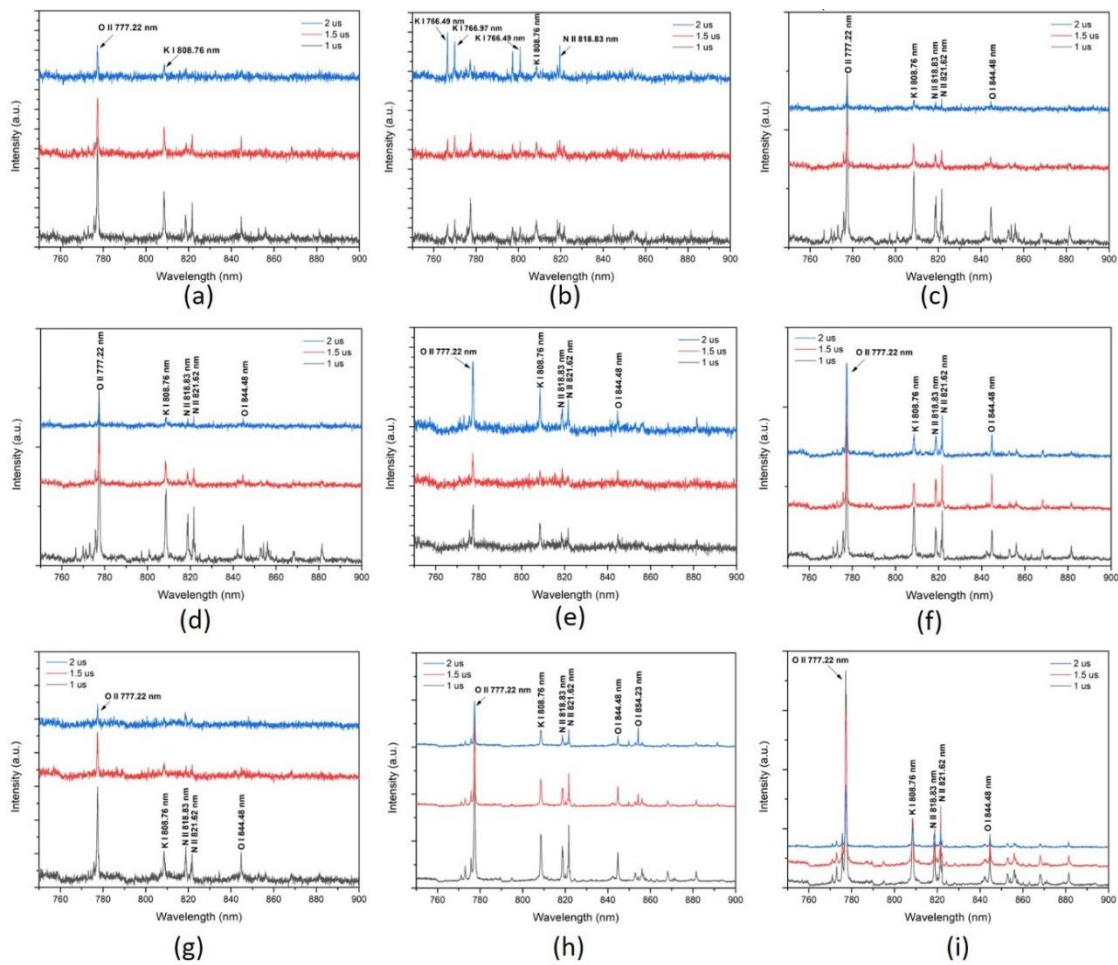


**Figure 4.** LIBS spectra of PET 1 (a), PET 2 (b), PET 3 (c), PET 4 (d), PP 1 (e), PP 2 (f), PP 3 (g), LDPE (h), and Teflon (i). Observed with delay time variation (1, 1.5, and 2  $\mu$ s) at 750–900 nm.

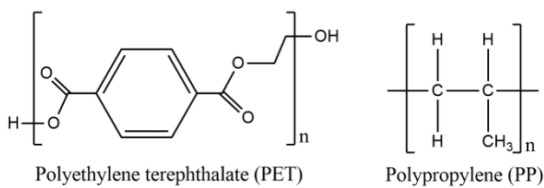


**Figure 5.** Chemical structures of PET and PP

impossible to discriminate the plastic waste based on this slight difference with human naked-eye. The PCA analysis using such wavelength ranges yielded satisfying results, where the data are presented in Figures 6b and 6c. It could be seen that the PET and PP could form their own group in the PCA plots. However, PET group at  $C_2$  band at 464–474 nm is overlapping with that of PP. By observing the  $C_2$  band at other wavelength range, the plastic waste could be grouped without overlapping one another (Figure 6d). Several studies have reported that the  $C_2$  band at the range of

490–520 nm appears stronger than that of at other ranges [36, 37]. Taken altogether,  $C_2$  molecular band at 490–520 nm could be used to distinguish PET from PP in an open-air system. In this study, there is no data pre-processing (such as smoothing) and only spectral data from wavelength range of 490–520 nm used. In comparison with other studies [38], this is a novel approach of employing LIBS-PCA that allows shorter time to complete the data processing due to less numbers of step and data used.

Correlation analysis using a combined data from PET (1-4) and PP (1-3) was shown to exhibit a positive correlation. Where increasing C I 247.8 nm spectral area could contribute to higher spectral area of the  $C_2$  molecular band (Figure 7a). The Pearson's correlation coefficient ( $r$ ) was obtained 0.862 with slope statistically significant than 0 according to ANOVA ( $p < 0.05$ ). The emission from C atoms contribute to the formation of the molecular band of  $C_2$  as high as 74.34%. Hence, ablation of carbon from the material

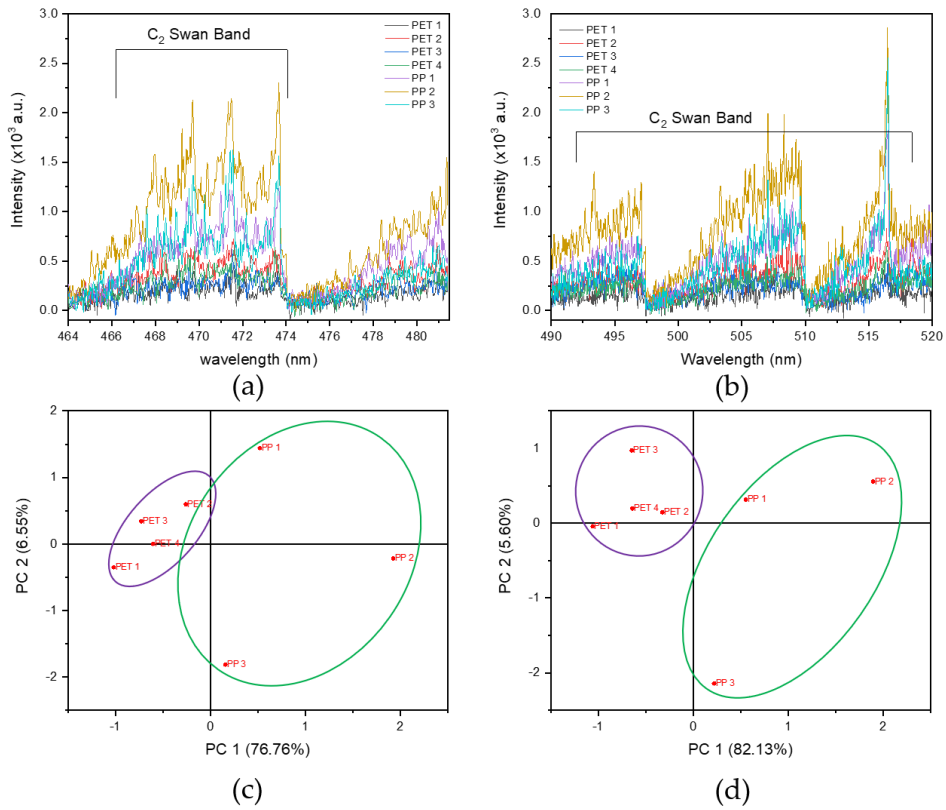


**Figure 6.** LIBS C<sub>2</sub> molecular band of PET (1-4) and PP (1-3), observed at 464—483 nm (a) and 490—520 nm (b). PCA plots obtained from LIBS spectra with wavelength ranges of 464—483 nm (c) and 490—520 nm (d). PC represents principal component.

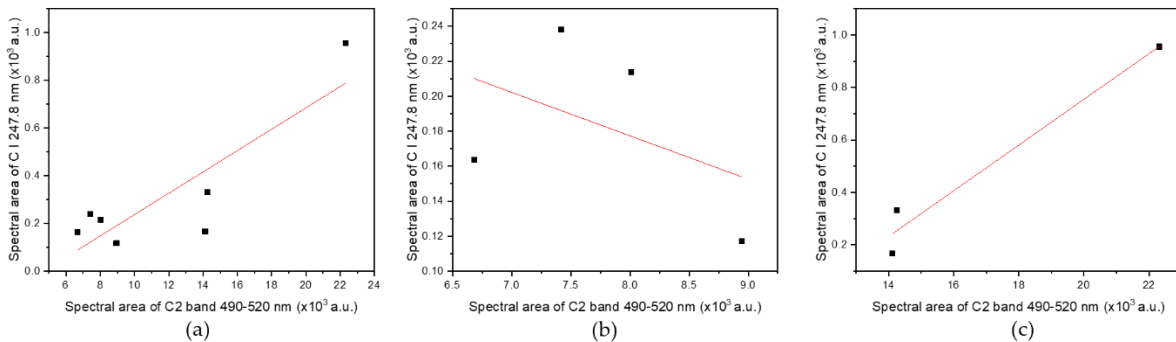


**Figure 7.** Linear correlation between the spectral area of C I 247.8 nm and spectral area of C<sub>2</sub> band 490-520 nm.

persists as the underlying factor that is responsible for the discrimination between PET and PP.

When further analyzed using the data from each plastic type, the correlation was obtained poor for PET (Figure 7b), where negative *r* value is negative (*r* = -0.441) and correlation percentage is small (19%). On contrary, spectral data from PP generated a better correlation with *r* value and correlation percentage

reaching 0.982 and 96.6%, respectively. It could mean that each type of plastic may have different origins of its molecular band in the LIBS spectra. Herein, the molecular band of C<sub>2</sub> captured in the LIBS spectra of PET could not be explained by the recombination of atomized C. We suspect that the C<sub>2</sub> molecules occupying the plasma are originated from the existing C—C bound.

Previous reports suggest that PET had better thermal stability than PP [39, 40], where thermal degradation of PET involved several binding cleavages [40]. In contrast, PP could be thermally degraded in a single step [39]. C<sub>2</sub> molecular band in the PET spectra possibly related to the thermal phenomena, allowing the C—C species to occupy the plasma. Consequently, the molecular band of C<sub>2</sub> in PET sample could not be explained solely by the ablated C variable. Nonetheless, to reach a better conclusion, more samples are required for the analysis

#### 4. CONCLUSIONS

Plastics obtained from different products or brands have distinctive spectral profile, depending on the additives incorporated in the plastic. Thus, a mere spectral analysis LIBS is only capable of differentiating the plastic according to its producers. To discriminate the plastic wastes based on their types or chemical structures, employing the molecular band spectra was found to be strategic. Herein, we had successfully discriminated the PET and PP plastic wastes through PCA analysis on the spectral wavelength range of C<sub>2</sub> molecular band. The molecular bands of PET and PP were speculated to be dependent on the thermal degradation mechanism of PET and PP, which could be associated to their structure differences. Further investigation with higher number of samples and more plastic types is warranted.

#### 5. FUNDING

This research was funded by Universitas Syiah Kuala through Penelitian Professor Scheme No. 166/UN11/SPK/PNBP/2021.

#### 6. REFERENCES

- Rochman, C.M., Browne, M.A., Halpern, B.S., Hentschel, B.T., Hoh, E., Karapanagioti, H.K., Rios-Mendoza, L.M., Takada, H., Teh, S. and Thompson, R.C., "Policy: Classify plastic waste as hazardous", *Nature*, Vol. 494, No. 7436, (2013), 169-171. doi: /10.1038/494169a
- Borrelle, S.B., Ringma, J., Law, K.L., Monnahan, C.C., Lebreton, L., McGivern, A., Murphy, E., Jambeck, J., Leonard, G.H., Hilleary, M.A., Eriksen, M., Possingham, H.P., De Frond, H., Gerber, L.R., Polidoro, B., Tahir, A., Bernard, M., Mallos, N., Barnes, M. and Rochman, C.M., "Predicted growth in plastic waste exceeds efforts to mitigate plastic pollution", *Science*, Vol. 369, No. 6510, (2020), 1515-1518. doi: 10.1126/science.aba3656
- Faraca, G. and Astrup, T., "Plastic waste from recycling centres: Characterisation and evaluation of plastic recyclability", *Waste Management*, Vol. 95, (2019), 388-398. doi: 10.1016/j.wasman.2019.06.038
- Vollmer, I., Jenks, M.J.F., Roelands, M.C.P., White, R.J., van Harmelen, T., de Wild, P., van der Laan, G.P., Meirer, F., Keurentjes, J.T.F. and Weckhuysen, B.M., "Beyond mechanical recycling: Giving new life to plastic waste", *Angewandte Chemie International Edition*, Vol. 59, No. 36, (2020), 15402-15423. doi: 10.1002/anie.201915651
- Al-Haydari, I.S., Al-Haidari, H.S., Mohammed-Noor Khudhur, H., Waleed Jummah, N. and Abd Al-Hamza, M., "Durability and aging characteristics of sustainable paving mixture", *International Journal of Engineering, Transactions B: Applications*, Vol. 34, No. 8, (2021), 1865-1873. doi: 10.5829/IJE.2021.34.08B.07
- Mosa, A.M., Jawad, I.T. and Salem, L.A., "Modification of the properties of warm mix asphalt using recycled plastic bottles", *International Journal of Engineering, Transactions C: Aspects*, Vol. 31, No. 9, (2018), 1514-1520. doi: 10.5829/IJE.2022.31.9C.06
- Marpaung, A.M., Abdulmadjid, S.N., Ramli, M., Idris, N., Khumaeni, A., Budi, W.S., Suyanto, H., Suliyanti, M.M., Karnadi, I., Tanra, I., Pardede, M., Jobiliong, E., Hedwig, R., Lie, Z.S., Kurniawan, K.H. and Kagawa, K., "Emission spectrochemical analysis of soft samples including raw fish by employing laser-induced breakdown spectroscopy with a subtarget at low-pressure helium gas", *ACS Omega*, Vol. 5, No. 27, (2020), 16811-16818. doi: 10.1021/acsomega.0c01904
- Iqbal, J., Pardede, M., Jobiliong, E., Hedwig, R., Ramli, M., Khumaeni, A., Budi, W.S., Idris, N., Abdulmadjid, S.N., Lahna, K., Marpaung, M.A., Karnadi, I., Lie, Z.S., Suyanto, H., Kurniawan, D.P., Lie, T.J., Kurniawan, K.H., Kagawa, K. and Tjia, M.O., "Shock wave plasma generation in low pressure ambient gas from powder sample using subtarget supported micro mesh as a sample holder and its potential applications for sensitive analysis of powder samples", *Microchemical Journal*, Vol. 142, (2018), 108-116. doi: 10.1016/j.microc.2018.06.022
- Abdulmadjid, S.N., Meilina, H., Hedwig, R. and Kurniawan, K.H., "Elemental detection of arabica and robusta green bean coffee using laser-induced plasma spectroscopy", in The 6<sup>th</sup> International Conference on Theoretical and Applied Physics (The 6<sup>th</sup> ICTAP), Makassar, Indonesia. Vol. 1801, (2017), 050001. doi: 10.1063/1.4973099
- Iqhrammullah, M., Marlina, Hedwig, R., Karnadi, I., Kurniawan, K.H., Olaiya, N.G., Mohamad Haafiz, M.K., Abdul Khalil, H.P.S. and Abdulmadjid, S.N., "Filler-modified castor oil-based polyurethane foam for the removal of aqueous heavy metals detected using laser-induced breakdown spectroscopy (libs) technique", *Polymers (Basel)*, Vol. 12, No. 4, (2020), 903. doi: 10.3390/polym12040903
- Iqhrammullah, M., Marlina, M., Khalil, H., Kurniawan, K.H., Suyanto, H., Hedwig, R., Karnadi, I., Olaiya, N.G., Abdullah, C.K. and Abdulmadjid, S.N., "Characterization and performance evaluation of cellulose acetate-polyurethane film for lead ii ion removal", *Polymers (Basel)*, Vol. 12, No. 6, (2020). doi: 10.3390/polym12061317
- Iqhrammullah, M., Suyanto, H., Rahmi, Pardede, M., Karnadi, I., Kurniawan, K.H., Chiari, W. and Abdulmadjid, S.N., "Cellulose acetate-polyurethane film adsorbent with analyte enrichment for in-situ detection and analysis of aqueous Pb using laser-induced breakdown spectroscopy (LIBS)", *Environmental Nanotechnology, Monitoring & Management*, Vol. 16, (2021). doi: 10.1016/j.enmm.2021.100516
- Pardede, M., Karnadi, I., Hedwig, R., Tanra, I., Iqbal, J., Marpaung, M.A., Suliyanti, M.M., Jobiliong, E., Abdulmadjid, S.N., Idris, N., Khumaeni, A., Shiddiq, M., Rhizma, M.G.A., Lie, Z.S., Bilal, M., Kurniawan, D.P., Lie, T.J., Kurniawan, K.H. and Kagawa, K., "High sensitivity hydrogen analysis in zircaloy-4 using helium-assisted excitation laser-induced breakdown spectroscopy", *Scientific Reports*, Vol. 11, No. 1, (2021), 21999. doi: 10.1038/s41598-021-01601-y

14. Hussain Shah, S.K., Iqbal, J., Ahmad, P., Khandaker, M.U., Haq, S. and Naeem, M., "Laser induced breakdown spectroscopy methods and applications: A comprehensive review", *Radiation Physics and Chemistry*, Vol. 170, (2020), 108666. doi: 10.1016/j.radphyschem.2019.108666
15. Iqhrammullah, M., Abdulmadjid, S.N., Suyanto, H., Rahmi, Marlina and Kemala, P., "A review of membrane-facilitated liquid-solid conversion: Adding laser-induced breakdown spectroscopy (LIBS) multi-applicability for metal analysis", *Journal of Physics: Conference Series*, Vol. 1951, No. 1, (2021). doi: 10.1088/1742-6596/1951/1/012044
16. Palanco, S. and Laserna, J.J., "Full automation of a laser-induced breakdown spectrometer for quality assessment in the steel industry with sample handling, surface preparation and quantitative analysis capabilities", *Journal of Analytical Atomic Spectrometry*, Vol. 15, No. 10, (2000), 1321-1327. doi: 10.1039/B003632N
17. Ladic, V., Filella, M. and Turner, A., "Determination of antimony concentrations in widely used plastic objects by laser induced breakdown spectroscopy (LIBS)", *Journal of Analytical Atomic Spectrometry*, Vol. 33, No. 11, (2018), 1917-1924. DOI: 10.1039/C8JA00181B
18. Liu, K., Tian, D., Xu, H., Wang, H. and Yang, G., "Quantitative analysis of toxic elements in polypropylene (PP) via laser-induced breakdown spectroscopy (LIBS) coupled with random forest regression based on variable importance (VI-RFR)", *Analytical Methods*, Vol. 11, No. 37, (2019), 4769-4774. doi: 10.1039/C9AY01796H
19. Yan, B., Liang, R., Li, B., Tao, J., Chen, G., Cheng, Z., Zhu, Z. and Li, X., "Fast identification and characterization of residual wastes via laser-induced breakdown spectroscopy and machine learning", *Resources, Conservation and Recycling*, Vol. 174, (2021). doi: 10.1016/j.resconrec.2021.105851
20. Liu, K., Tian, D., Li, C., Li, Y., Yang, G. and Ding, Y., "A review of laser-induced breakdown spectroscopy for plastic analysis", *TrAC Trends in Analytical Chemistry*, Vol. 110, (2019), 327-334. doi: 10.1016/j.trac.2018.11.025
21. Costa, V.C., Aquino, F.W.B., Paranhos, C.M. and Pereira-Filho, E.R., "Identification and classification of polymer e-waste using laser-induced breakdown spectroscopy (LIBS) and chemometric tools", *Polymer Testing*, Vol. 59, (2017), 390-395. doi: 10.1016/j.polymertesting.2017.02.017
22. Liu, K., Tian, D., Wang, H. and Yang, G., "Rapid classification of plastics by laser-induced breakdown spectroscopy (LIBS) coupled with partial least squares discrimination analysis based on variable importance (VI-PLS-DA)", *Analytical Methods*, Vol. 11, No. 9, (2019), 1174-1179. doi: 10.1039/C8AY02755B
23. Gondal, M.A. and Siddiqui, M.N., "Identification of different kinds of plastics using laser-induced breakdown spectroscopy for waste management", *Journal of Environmental Science and Health Part A*, Vol. 42, No. 13, (2007), 1989-1997. doi: 10.1080/10934520701628973
24. Jolliffe, I.T. and Cadima, J., "Principal component analysis: A review and recent developments", *Philosophical Transactions of the Royal Society A: Mathematical, Physical and Engineering Sciences*, Vol. 374, No. 2065, (2016), 20150202. doi: 10.1098/rsta.2015.0202
25. Pardede, M., Jobiliong, E., Lahna, K., Idroes, R., Suyanto, H., Marpaung, A.M., Abdulmadjid, S.N., Idris, N., Ramli, M., Hedwig, R., Lie, Z.S., Lie, T.J., Karnadi, I., Tanra, I., Kwaria, D., Suliyanti, M.M., Khumaeni, A., Setia Budi, W., Kurniawan, K.H., Kagawa, K. and Tjia, M.O., "Underlying physical process for the unusual spectral quality of double pulse laser spectroscopy in He gas", *Analytical Chemistry*, Vol. 91, No. 12, (2019), 7864-7870. doi: 10.1021/acs.analchem.9b01618
26. Zhang, Q., Li, Y., Wen, J., Yuan, S. and Zhu, Z., "The effects of CaCO<sub>3</sub> on the properties of pcl wood-plastic composites", *IOP Conference Series: Earth and Environmental Science*, Vol. 233, (2019), 022004. doi: 10.1088/1755-1315/233/2/022004
27. Luo, S. and Pan, S., "Numerical study on the effect of caco3 ratio on the mechanical properties of CaCO<sub>3</sub>/PVC composites", *Journal of Physics: Conference Series*, Vol. 1820, No. 1, (2021), 012140. doi: 10.1088/1742-6596/1820/1/012140
28. Bill, A., Haarman, A., Gasser, M., Böni, H., Rösslein, M. and Wäger, P.A., "Characterizing plastics from large household appliances: Brominated flame retardants, other additives and density profiles", *Resources, Conservation and Recycling*, Vol. 177, (2022), 105956. doi: 10.1016/j.resconrec.2021.105956
29. Moros, J. and Laserna, J., "Laser-induced breakdown spectroscopy (LIBS) of organic compounds: A review", *Applied Spectroscopy*, Vol. 73, No. 9, (2019), 963-1011. DOI: 10.1177/0003702819853252
30. Yi, R., Yang, X., Lin, F. and Ren, S., "Improving the spectral qualities of major elements in soil by controlling the ambient pressure in time-resolved laser-induced breakdown spectroscopy", *Applied Optics*, Vol. 58, No. 32, (2019), 8824-8828. doi: 10.1364/AO.58.008824
31. Hemalaxmi, R., Vasa, N.J. and Seshadri, S., "Understanding the mechanism of molecular carbon emissions using time-resolved LIBS during online coal characterization", in 14th Pacific Rim Conference on Lasers and Electro-Optics (CLEO PR 2020), Sydney, Optical Society of America., (2020), P3\_19. doi: 10.1364/CLEOPR.2020.P3\_19
32. George, G., "The structural and optical studies of titanium doped rare earth pigments and coloring applications", *Dyes and Pigments*, Vol. 112, (2015), 81-85. doi: 10.1016/j.dyepig.2014.06.013
33. Washburn, K.E., "Rapid geochemical and mineralogical characterization of shale by laser-induced breakdown spectroscopy", *Organic Geochemistry*, Vol. 83-84, (2015), 114-117. doi: 10.1016/j.orggeochem.2015.03.004
34. Rahmi, Lubis, S., Az-Zahra, N., Puspita, K. and Iqhrammullah, M., "Synergetic photocatalytic and adsorptive removals of metanil yellow using TiO<sub>2</sub>/grass-derived cellulose/chitosan (TiO<sub>2</sub>/GC/Ch) film composite", *International Journal of Engineering, Transactions B: Applications*, Vol. 34, No. 8, (2021), 1827-1836. doi: 10.5829/IJE.2021.34.08B.03
35. Rahmi, Julinawati, Nina, M., Fathana, H. and Iqhrammullah, M., "Preparation and characterization of new magnetic chitosan-glycine-pegde (Fe<sub>3</sub>O<sub>4</sub>/Ch-G-P) beads for aqueous Cd(II) removal", *Journal of Water Process Engineering*, Vol. 45, (2022), 102493. doi: 10.1016/j.jwpe.2021.102493
36. Mousavi, S.J., Hemati Farsani, M., Darbani, S.M.R., Asadorian, N., Soltanolkotabi, M. and Eslami Majd, A., "Identification of atomic lines and molecular bands of benzene and carbon disulfide liquids by using LIBS", *Applied Optics*, Vol. 54, No. 7, (2015), 1713. doi: 10.1364/AO.54.001713
37. Rao, E.N., Mathi, P., Kalam, S.A., Sreedhar, S., Singh, A.K., Jagatap, B.N. and Rao, S.V., "Femtosecond and nanosecond LIBS studies of nitroimidazoles: Correlation between molecular structure and LIBS data", *Journal of Analytical Atomic Spectrometry*, Vol. 31, No. 3, (2016), 737-750. doi: 10.1039/C5JA00445D
38. Unnikrishnan, V.K., Choudhari, K.S., Kulkarni, S.D., Nayak, R., Kartha, V.B. and Santhosh, C., "Analytical predictive capabilities of laser induced breakdown spectroscopy (LIBS) with principal component analysis (PCA) for plastic classification", *RSC Advances*, Vol. 3, No. 48, (2013), 25872. doi: 10.1039/C3RA44946G

39. Esmizadeh, E., Tzoganakis, C. and Mekonnen, T.H., "Degradation behavior of polypropylene during reprocessing and its biocomposites: Thermal and oxidative degradation kinetics", *Polymers (Basel)*, Vol. 12, No. 8, (2020), 1627. doi: 10.3390/polym12081627
40. Das, P. and Tiwari, P., "Thermal degradation study of waste polyethylene terephthalate (PET) under inert and oxidative environments", *Thermochimica Acta*, Vol. 679, (2019), 178340. doi: 10.1016/j.tca.2019.178340

---

### Persian Abstract

---

#### چکیده

انتشار زباله های پلاستیکی در حال رشد به عنوان یک تهدید سیاره ای، توسعه یک فرآیند بازیافت سریع و کارآمد، به ویژه در طول فرآیند طبقه بندی را ضروری می کند. در اینجا، هدف ما حل مشکل با استفاده از طیف سنجی شکست ناشی از لیزر (LIBS) در ترکیب با تجزیه و تحلیل اجزای اصلی (PCA) به عنوان ابزاری برای طبقه بندی خودکار زباله های پلاستیکی است. نمونه های مورد استفاده در این تحقیق، ضایعات پلاستیکی مشتق شده از محصولات نوشیدنی، مواد غذایی و لوازم التحریر با برندهای مختلف بود. لیزر Nd:YAG بدون پیش تیمار و تحت یک سیستم هوای آزاد به سطح نمونه شلیک شد (انرژی لیزر = ۵۴ mJ؛ تاخیر زمانی = ۱-۲ میکرو ثانیه). مشخصات طیفی هر زباله پلاستیکی وجود اجزای فلزی مانند مواردی که توسط خطوط انتشار Ca II 396.85 نانومتر، Al I 395.92 نانومتر، Mg I 383.83 نانومتر، و Fe I 404.85 نشان داده شده است را نشان داد. اوج شدت خطوط انتشار مرتبط با مواد آلی (C I 247.86 نانومتر، O II 777.32 نانومتر، O I 844.48 نانومتر، H I 666.22 نانومتر، N II 818.83 نانومتر، و N II 821.62 نانومتر نشان می دهد که می تواند 821.62 nm را نشان دهد) برای زباله های پلاستیکی تبعیض قائل نشود. تجزیه و تحلیل PCA نشان داد که باند مولکولی C2 490-520 نانومتر دارای بیشترین خواص متمایزکننده در برابر پلی اتیلن ترفتالات (PET) و پلی پروپیلن (PP) است. نوار مولکولی به دلیل رفتار حرارتی کنتراست آنها بین PET و PP متفاوت ایجاد شد. در نتیجه، LIBS-PCA مولکولی می تواند برای تشخیص PET و PP به روشی ساده و سریع استفاده شود.

---



# Ultra Low Power Temperature Compensated Complementary Metal Oxide Semiconductor Ring Oscillator in Subthreshold

E. Sadeghi<sup>a,b</sup>, E. Ebrahimi<sup>\*a</sup>

<sup>a</sup> IC Design Research Laboratory, Electrical & Robotic Engineering Department, Shahrood University of Technology, Shahrood, Iran

<sup>b</sup> Department of Medical Physics and Biomedical Engineering, Faculty of Medicine, Tehran University of Medical Sciences, Tehran, Iran

## PAPER INFO

### Paper history:

Received 15 July 2022

Received in revised form 25 September 2022

Accepted 30 October 2022

### Keywords:

Complementary to Absolute Temperature

Current Reference Ring Oscillator

Subthreshold

Thermal Compensation

## ABSTRACT

Low power consumption, low chip area and fabrication in the standard complementary metal oxide semiconductor (CMOS) process are vital requirements for oscillators used in low-cost bio-implantable and wearable devices. Conventional ring oscillators (ROs) are good candidates for using in biomedical applications. However, their oscillation frequency strongly depends on the temperature. In this study, a temperature compensated ring oscillator with low power consumption is proposed. The transistors of the proposed ring oscillator operate in the subthreshold region to achieve a low power and low voltage performance. Since, in the subthreshold region, the oscillation frequency of a conventional ring oscillator increases with increase in the temperature, two current sources are used to power the proposed subthreshold ring oscillator: a temperature independent current source and a complementary to absolute temperature (CTAT) current source. In the proposed circuit, the CTAT current forms a small part of the total supplied current and its duty is to compensate for the oscillation frequency deviation. Two prototypes of the subthreshold ring oscillator were designed and simulated for a target frequency of 1MHz using commercially available 0.18 $\mu$ m RF-CMOS technology. The thermal coefficient (TC) of the uncompensated ring oscillator was 2400 ppm/ $^{\circ}$ C from -40 $^{\circ}$ C to 85 $^{\circ}$ C, though applying the proposed technique reduces the TC of the ring oscillator to 80.4 ppm/ $^{\circ}$ C with total power consumption as low as 14.5 $\mu$ W.

doi: 10.5829/ije.2023.36.01a.13

## 1. INTRODUCTION

Synthesizing a stabilized clock signal is essential for different analog and digital systems such as RFID and wireless sensor networks (WSNs). The most usual clock references are based on quartz crystal oscillators [1]. Despite excellent stability of crystal oscillators against temperature and process variation, crystal resonators cannot be integrated on a chip by using standard CMOS process; that increases the area and cost of the system. Hence, CMOS oscillators are appropriate candidates for producing clock in various low power and low cost applications such as implantable and wearable biomedical devices, cubic millimetre WSN applications [2] and FRID tags [3]. Different types of CMOS oscillators include LC oscillators, RC relaxation, and ring

oscillators (ROs). The oscillation frequency in CMOS oscillators suffers from poor thermal stability. The thermal instability of the oscillation frequency in CMOS oscillators is due to the dependency of different parameters, such as electron/hole mobility ( $\mu$ ) and threshold voltage ( $V_{TH}$ ) to the temperature and process variations. So, in order to achieve desirable frequency stability, using compensation techniques [4, 5] is mandatory. Thus, several researches have been devoted to effective compensation of the CMOS oscillators [4, 6-13]. Considering the type of application that oscillator is designed for, the appropriate compensation technique is developed. For example, as reported by Katebi et al. [10] the main challenges in the military fields are the precision of the oscillation frequency as well as its thermal stability. To combat these challenges a hybrid cross-

\*Corresponding Author Institutional Email:

[ebrahimi@shahroodut.ac.ir](mailto:ebrahimi@shahroodut.ac.ir) (E. Ebrahimi)

coupled Colpitts VCO is presented by Katebi et al. [10], in which the varactors are driven by CTAT voltages. Although the temperature coefficient (TC) of the VCO and its phase noise are acceptable, its high-power consumption and chip area (due to use of inductors) are not appropriate for biomedical devices. An LC VCO used in an RFID system is also thermally compensated with using an auxiliary varactor loop in a PLL configuration [11]. The proposed method provides adequate frequency stability, but occupies more area because of using several inductors.

Using a frequency to voltage (FV) converter in a feedback loop the TC of a current-reused stacked ring oscillator has been improved by Rodrigues et al. [12]; however, the circuit suffers from the high complexity and nonlinearity of the FV. In order to reduce the TC nonlinearity of an RC oscillator in a wired-communication system a frequency locked loop (FLL) is used by Park et al. [13] that locks the period of the oscillator to a reference time constant. The accuracy of the output frequency of this oscillator over temperature variation is largely depends on the behaviour of the reference resistor used in this configuration; however, this technique provides a low power RC oscillator with moderate TC.

In biomedical and RFID applications, some problems such as low power consumption, low chip area and cost, are the main design considerations [14, 15]. Among different types of the CMOS oscillators, the ring oscillators has the capability of high integration that makes them as an area efficient option for clock generation. However, the main drawback of the ring oscillators is the dependency of their oscillation frequency on the temperature and process variations.

Oscillation frequency in the relaxation oscillators is determined by the RC time constant. The most important result of this dependency is that the frequency of oscillation is affected by the high thermal coefficient of a typical resistance. A technique to compensate the frequency fluctuations in a relaxation oscillator is combination of two polysilicon resistors with positive and negative thermal coefficients in parallel and series. Ueno et al. [6], used two polysilicon resistors with positive and negative thermal coefficients, the frequency temperature coefficient of a relaxation oscillator is reduced to 90 ppm/°C in a temperature range of -20°C to 100°C. This method provides a suitable temperature coefficient and reduces the phase noise by filtering the noise. However, the capacitors and resistors used in this design increase the die area significantly, and the circuit suffers from leakage current of the capacitors in high frequencies. A current mode relaxation oscillator is presented by Chiang and Liu [16] in which a proportional to absolute temperature (PTAT) and a CTAT current source are combined to supply the oscillator with a temperature independent current reference. The main

privilege of the proposed technique is the frequency variations as low as 64 ppm/°C with low power consumption and low chip area. Operation of the transistors in subthreshold can supply a reliable margin for power consumption in long life applications. However, the main drawback of this design is the need for special features like trimming for implementation of precise resistors.

Another technique that improves the stability of the oscillation frequency in a ring oscillator has been proposed by Wang et al. [17]. In this method, the Brokaw's voltage reference with transistors operating in the subthreshold region generate a PTAT voltage source. Since the temperature coefficient of the gate-source voltage of transistors in the ring oscillator is negative [18] (i.e. CTAT), using the PTAT voltage reference provides a temperature independent bias current for the ring oscillator. The main advantages of the method presented by Wang et al. [17] are low jitter and wide temperature operation range with small temperature drift. The main drawback of the circuit introduced by Wang et al. [17] is its high-power consumption and the need for high supply voltage.

Due to the diversity of the thermal compensation techniques, only a conceptual diagram is shown in Figure 1 to demonstrate the idea behind of all thermally compensated ROs.

Chang and Liu. [8] proposed a method to compensate thermal dependency of a bandgap reference (BGR) which is used for analog feature extraction of ECG signals in the sub-blocks of an RFID tag. The PTAT and CTAT voltage generators of the proposed BGR use a cascode structure to reduce frequency dependency on the supply voltage and temperature. However, due to the stack of transistors, this technique is not suitable for low voltage designs.

As reported by Tang and Tang [9], providing a stable bias voltage for a ring VCO can mitigate the frequency instability caused by the process and temperature variations. Tang and Tang [9] stated that the bias voltage which was produced by an external off-chip LDO (Figure 2) along with a compensation circuit; that has provided a reference voltage for the ring oscillator. Using off-chip

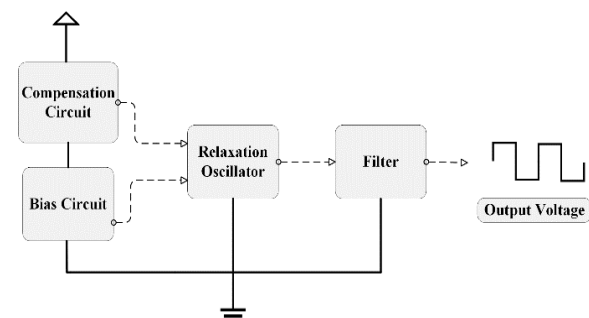
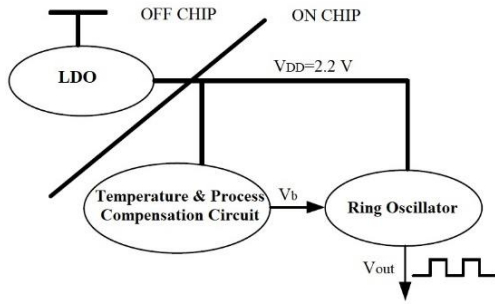


Figure 1. Conceptual model of compensation technique



**Figure 2.** Use of off-chip LDO and compensation circuit in [9]

components can be an obstacle for building an area-efficient biomedical system. Besides, using an LDO increase the power consumption and results in higher total power dissipation and lower battery life in the mobile applications. It is worth mentioning that the frequency variation of the circuit reported by Tang and Tang [9] is 2% while the power consumption is as high as  $200\mu\text{W}$ .

A modified RC network has been proposed by Huang and Wentzloff [19] for frequency compensation of a relaxation oscillator. The RC network adds an additional zero to the transfer function of the oscillator that enables temperature compensation of the step response of the oscillator. Due to the temperature dependency of the oscillator time constant (i.e. RC), two different polysilicon and diffusion resistors are used for temperature compensation. In fact, the use of two resistors with negative and positive TC neutralizes the effect of temperature variation on the oscillation frequency. Although very low power consumption and small chip area are achieved by the aforesaid method, its temperature coefficient is not very low.

While different compensated oscillators are introduced in prior works, our work aims to present a new compensation technique for a low power and area efficient ring oscillator operating in the subthreshold region. The rest of the paper organized as follows. The proposed compensation techniques and behaviour of the ring oscillator in the subthreshold region are described in section 2. In section 3, the simulation results are presented, and finally, the conclusion is defined in section 4.

## 2. PROPOSED TECHNIQUE AND CIRCUIT

### 2. 1. Thermal Behavior of a MOSFET in Subthreshold

In the low power circuits, MOS devices usually are biased in weak inversion (subthreshold). A MOS transistor can operate in weak inversion with very low supply voltage and low power consumption. The drain current  $I_D$  of a transistor in

subthreshold is an exponential function of the gate-source voltage ( $V_{GS}$ ) and drain-source voltage ( $V_{DS}$ ) given by Equation (1) [20]:

$$I_D = kI_0 \exp\left(\frac{V_{GS}-V_{TH}}{\eta V_T}\right) \times \left(1 - \exp\left(-\frac{V_{DS}}{V_T}\right)\right) \quad (1)$$

in which  $I_0 = \mu_0 C_{ox} (\eta-1) V_T^2$ ,  $k$  is the aspect ratio of the transistor,  $\mu$  is the carrier mobility,  $C_{ox}$  is the gate oxide capacitance,  $V_T$  is the thermal voltage,  $V_{TH}$  is the threshold voltage of the MOSFET and  $\eta$  is the subthreshold slope factor. For  $V_{DS} > 0.1\text{V}$  the current  $I_D$  is almost independent of  $V_{DS}$  and is given by Equation (2) [21]:

$$I_D = k\mu_0 C_{ox} (\eta-1) V_T \exp\left(\frac{V_{GS}-V_{TH}}{\eta V_T}\right) \quad (2)$$

The carrier mobility, thermal and threshold voltages in Equation (2) are the parameters that depend on the temperature. Therefore, Equation (2) shows that the drain current of a MOS device in subthreshold region extremely depends on the temperature. As discussed by Tajalli and Leblebici [22], the subthreshold current  $I_D$  is proportional to the temperature, and an increase in temperature results in an increase in drain current [23].

### 2. 2. CMOS Ring Oscillator in Subthreshold

A conventional ring oscillator is comprised of an odd number of inverters in a loop. Figure 3 demonstrates a typical ring oscillator with five stages.

Each stage includes a CMOS inverter operating as a delay element and is shown in Figure 4. While ring oscillators occupy very small chip area, their high power consumption and temperature dependency of oscillation frequency are the main issues addressed by prior works [17].

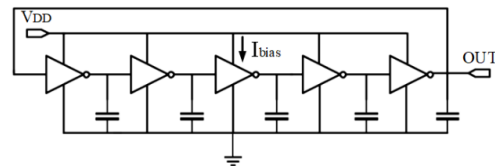


**Figure 3.** Structure of a five-stage conventional ring oscillator

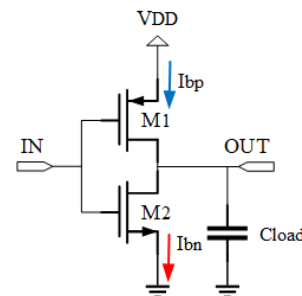


**Figure 4.** Single-stage inverter

In a single stage inverter, the low to high ( $T_{PLH}$ ) and high to low ( $T_{PHL}$ ) propagation delays are controlled by the bias currents of transistors and are given as below:

$$\begin{cases} T_{PHL} = C_{eff}(V_{DD} - V_{tp})/I_{bn} \\ T_{PLH} = C_{eff}V_{tp}/I_{bp} \end{cases} \quad (3)$$

in which  $I_{bp}$  is the source current through PMOS transistor,  $I_{bn}$  is the sink current through NMOS transistor,  $C_{eff}$  is the effective load capacitance of each inverter, and  $V_{tp}$  is the inverter trip voltage. The oscillation frequency of a ring oscillator with N stage is given by Equation (4).

$$f_{osc} = 1/(N(T_{PHL} + T_{PLH})) \quad (4)$$

So the number of inverters (N) and their propagation delays ( $T_{PHL}$  and  $T_{PLH}$ ) define the oscillation frequency of a ring oscillator [24]. According to Equations (3) and (4), the oscillation frequency of a ring oscillator is a function of the bias current, the supply voltage, and  $V_{tp}$ . Since the threshold voltage and carrier mobility of a transistor are modulated by the temperature, the bias current and  $V_{tp}$  are also varied by the temperature. In the design of an inverter the source ( $I_{bp}$ ) and sink ( $I_{bn}$ ) currents are typically chosen identical by proper sizing of the inverters' PMOS and NMOS transistors. Thus, supposing  $I_{bn} = I_{bp} = I_{bias}$  and replacing  $T_{PHL}$  and  $T_{PLH}$  from Equation (3) to Equation (4), the oscillation frequency can be written as Equation (5). Apparently, Equation (5) indicates that the oscillation frequency of the RO is linearly controlled by the NMOS and PMOS drain currents.

$$f_{osc} = I_{bias}/(N(C_{eff}V_{DD})) \quad (5)$$

The transistors of an inverter in a ring oscillator can be designed to operate in subthreshold (weak inversion) or above threshold (strong inversion). In the strong inversion region, the current of each inverter decreases with an increase in the temperature, that results in reduction of the oscillation frequency [25]. On the other hand, due to the diffusion nature of the subthreshold current in MOS transistors, an increase in temperature results in increase in the transistor current and, according to Equation (5), leads to an increase in the oscillation frequency in subthreshold region [18, 20]. Thus, the temperature behaviour of an RO in subthreshold region is the opposite of that of in the above threshold.

In this study, a conventional 5-stage ring oscillator with 1 MHz oscillation frequency is designed in the subthreshold region with 1.44  $\mu$ W power consumption (without bias circuitry). The variation of the oscillation frequency of the oscillator with temperature is simulated and depicted in Figure 5. As shown in this figure, the uncompensated oscillator has 2400 ppm/ $^{\circ}$ C frequency variation (about 30% frequency deviation) in the temperature range of -40  $^{\circ}$ C to 85  $^{\circ}$ C. In order to use such

a low-power subthreshold ring oscillator as a reference frequency in an area efficient application such as RFIDs and biomedical devices, using some compensation techniques are mandatory. Therefore, a new compensation technique for the ring oscillators that operate in weak inversion is presented as follows.

### 2. 3. Concept of the Proposed Compensation Technique

As discussed above and illustrated in Figure 5, the oscillation frequency of a subthreshold RO is almost proportional to the absolute temperature (PTAT). To alleviate this issue a conceptual model of the proposed compensation technique is illustrated in Figure 6. In this technique, a constant current source as well as a CTAT current source are used to supply the ring oscillator. The constant current source provides the main portion of the required current and the CTAT current source only compensate the PTAT behaviour of the frequency variation. In other word, while the frequency of the subthreshold oscillator increases with the temperature, the CTAT current source reduces supplied current source in such a way that a minimum frequency variation is achieved. The exact value of the CTAT current can be obtained through simulations.

**2. 3. 1. CTAT and Constant Current Sources** To verify the proposed concept, two prototypes of the low-power thermally compensated ring oscillators with different CTAT current sources were designed and

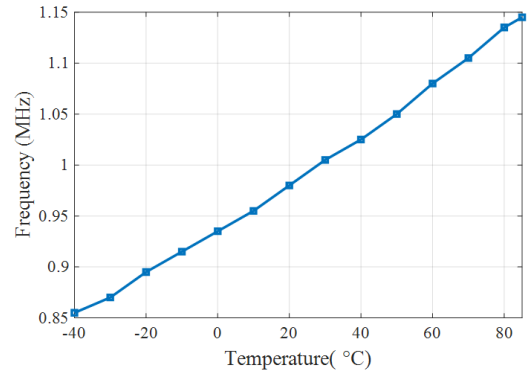


**Figure 5.** Frequency variation of a typical uncompensated subthreshold RO

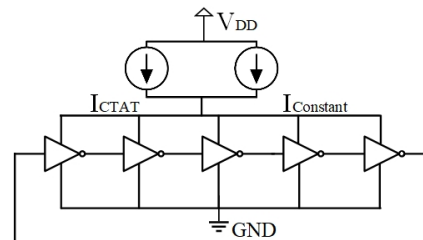


**Figure 6.** Concept of the proposed compensation technique

simulated in a standard 0.18 $\mu$ m RF CMOS technology. The first CTAT current generator is based on the thermal behaviour of the PN junction potential in a lateral BJT and the other is based on the threshold voltage of a MOS device. The circuits used for CTAT and constant current sources in this work are explained as follows.

### 2. 3. 1. 1. Generating CTAT current using Base-Emitter voltage of a BJT

As we know, the base emitter voltage ( $V_{BE}$ ) of a bipolar junction transistor (BJT) is inversely proportional to the temperature. The first order approximation of temperature dependency of the base emitter voltage is expressed as Equation (6):

$$V_{BE}(T) = V_{BE}(T_r) \frac{T}{T_r} + V_{g0} \left( 1 - \frac{T}{T_r} \right) \quad (6)$$

where the  $V_{g0}$  is the bandgap voltage of silicon at 0 K, T and  $T_r$  are the designed and reference temperatures in Kelvin respectively. Since  $\partial V_{BE} / \partial T \approx -1.5$  mV/K at room temperature,  $V_{BE}$  is a traditional solution for CTAT current generation [26]. Figure 7 illustrates the suggested structure which employs a diode-connected BJT to generate the required CTAT current [27] in this circuit. The operational amplifier in a negative feedback loop guarantees identical potentials for nodes A and B such that the current of resistor  $R_1$  will be  $V_{EB1} / R_1$ . Consequently, the output CTAT current is obtained through the current mirror transistors  $M_2$  and  $M_3$  as stated in Equation (7).

$$I_{CTAT} = \frac{V_{EB1}}{R_1} \quad (7)$$

### 2. 3. 1. 2. CTAT Current Generator Using Threshold Voltage of a MOSFET

The absolute value of the threshold voltage of a MOS devices decreases with an increase in temperature and has an almost linear relation with the temperature in the range of 200 K to 400 K [28]. As a first order approximation, the temperature dependency of the threshold voltage is expressed by Equation (8):

$$V_{TH}(T) = V_{TH}(T_0) + \alpha_{V_{TH}}(T - T_0) \quad (8)$$

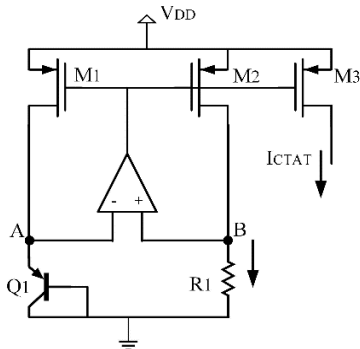


Figure 6. CTAT current generator using  $V_{EB}$

in which  $V_{TH}(T_0)$  is the threshold voltage at temperature  $T_0$ , and  $\alpha_{V_{TH}}$  is a negative temperature coefficient in a standard CMOS technology [25, 26]. Hence, absolute threshold voltage has a negative slope and can be utilized for generating a CTAT current. The circuit that used as a CTAT current source is shown in Figure 8. This circuit extracts  $V_{TH}$  and generates a CTAT current that is directly proportional to the threshold voltage of a PMOS transistor [29].

In Figure 8,  $M_3$  and  $M_4$  play the role of threshold voltage extractor. Supposing identical  $|V_{THp}|$  for all PMOS transistors, one can write:

$$V_{SD1} = V_{SG1} - V_{SD2} \quad (9)$$

In this circuit,  $M_3$  operates in the saturation region and  $M_2$  operates in the linear region permanently. So  $V_{SD2}$  can be expressed as follows:

$$V_{SD2} = \sqrt{2I} \left( \sqrt{\frac{1}{K_3} + \frac{3}{K_2}} - \sqrt{\frac{1}{K_3}} \right) \quad (10)$$

in which  $K_i = \mu_p C_{ox} (w/l)_i$ . Assuming  $K_2 = K_3 = K_1/3$ , the drain source voltage of  $M_3$  is given below:

$$V_{SD1} = |V_{THp}| + \sqrt{\frac{6I}{3K_3}} - \sqrt{\frac{2I}{K_3} + \frac{6I}{K_3}} + \sqrt{\frac{2I}{K_3}} \approx |V_{THp}| \quad (11)$$

The operational amplifier puts the voltage  $V_{SD1}$  across a resistor with low TC to provide required  $I_{CTAT}$  that is given by Equation (12).

$$I_{CTAT} = \frac{|V_{THp}|}{R} \quad (12)$$

### 2. 3. 2. Constant current source ( $I_{Constant}$ )

To implement the required constant current in Figure 6 (i.e.  $I_{Constant}$ ), a PTAT and a CTAT current are combined in such a way that a temperature independent current is generated by the circuit in Figure 9 [27]. Supposing identical aspect ratios for  $M_{1-4}$  and emitter area ratio  $A_{E1}/A_{E2}$  equals to  $n$  for  $Q_1$  and  $Q_2$ , and writing KVL for

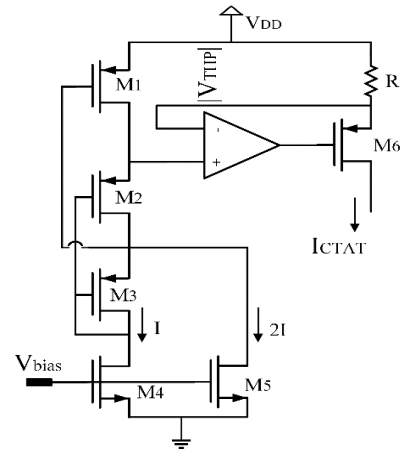


Figure 8. CTAT current generator using  $|V_{THp}|$

the loop including  $Q_1$  and  $Q_2$  and  $R_1$ , the current  $I_{PTAT}$  is obtained as Equation (13).

$$I_{PTAT} = \frac{\Delta V_{BE}}{R_1} = \frac{V_T}{R_1} \ln(n) \quad (13)$$

The CTAT current  $I_{CTAT}$  is also given by Equation (14):

$$I_{CTAT} = \frac{V_{BE3}}{R_2} \quad (14)$$

The sum of PTAT and CTAT currents is mirrored in  $M_4$  and  $I_{ref}$  is obtained as follows:

$$I_{ref} = I_{PTAT} + I_{CTAT} = \frac{V_T}{R_1} \ln(n) + \frac{V_{BE3}}{R_2} \quad (15)$$

In order to find appropriate  $R_1$  and  $R_2$  for the thermal compensation of  $I_{ref}$ , one should solve the derivative of the reference current with respect to the temperature in Equation (16).

$$\frac{\partial I_{ref}}{\partial T} = \frac{k}{qR_1} \ln(n) + \frac{\partial V_{BE3}}{\partial T} \frac{1}{R_2} = 0 \quad (16)$$

### 2. 4. Proposed Compensated RO: Transistor Level

Using CTAT current generators discussed in sections 2.3.1.1 and 2.3.1.2, and the constant current generator in Figure 9, two prototypes of the proposed compensated RO are shown in Figures 10 and 11. According to Figure 10, the CTAT current source in Figure 7 is applied to a conventional ring oscillator to compensate PTAT behaviour of the oscillation frequency of the RO in subthreshold region. In this circuit, the constant current source, which is in parallel to the CTAT current source, provides the major part of the required current for supplying the oscillator.

As shown in Figure 11, the second prototype of the proposed technique is realized by using the CTAT generator depicted in Figure 8. In this circuit, like previous prototype, the constant current generator has also the duty of supplying most of the total power required by RO.

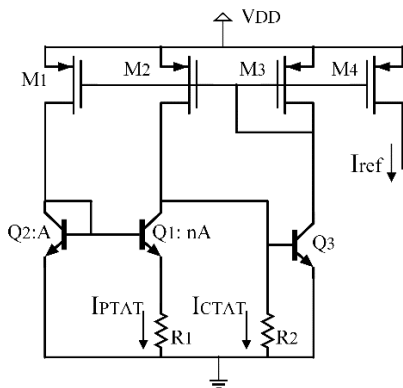


Figure 9. Constant current generator

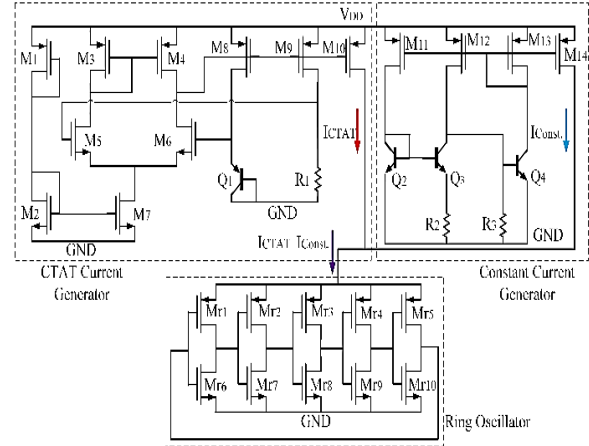


Figure 10. First circuit implementation of the proposed compensation technique

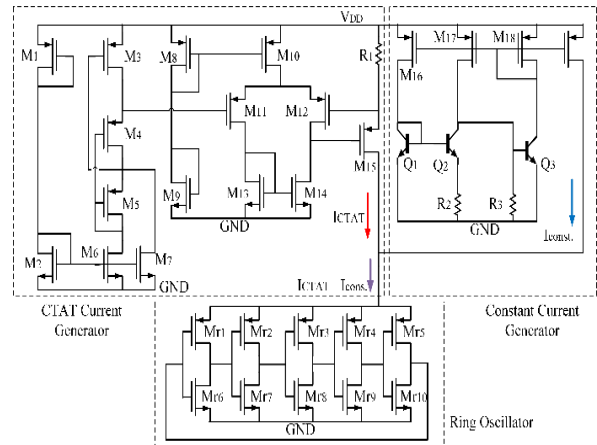


Figure 11. Second circuit implementation of the proposed compensated ring oscillator

### 3. SIMULATION RESULTS

To verify the performance of the proposed technique, both circuits depicted in Figures 10 and 11 are designed and simulated in an available commercial 0.18 $\mu\text{m}$  RF CMOS process. Tables 1 and 2 represent the circuit parameter values of the designed circuits of Figures 10 and 11, respectively. It is worth noting that the aspect ratio of NMOS ( $M_{r1}$ - $M_{r5}$ ) and PMOS ( $M_{r6}$ - $M_{r10}$ ) transistors for the RO core are chosen 23 $\mu\text{m}/1\mu\text{m}$  and 69 $\mu\text{m}/1\mu\text{m}$ , respectively.

Both circuits are designed for 1MHz oscillation frequency with a 1.8-V power supply and total current consumption of 800 nA. In this case study the constant current source with 700 nA has the major contribution to the total power consumption, though the CTAT current source generates only 100 nA to compensate the frequency deviation. The simulated total supply current, i.e.  $I_{CTAT} + I_{Const}$ , of the first and second prototypes is

depicted in Figure 12. The slope of the total current in both cases is negative and almost equal to  $-2.2 \text{ nA}/^\circ\text{C}$ .

The output waveforms of the compensated ring oscillators for different temperature values are illustrated in Figure 13. While the amplitude of output waveforms of the ROs varies by temperature, the oscillation frequency is nearly constant for both prototypes.

**TABLE 1.** Circuit parameter values for the first proposed compensated RO

Device	Size	Device	Size
M <sub>1</sub>	0.23/4.3 $\mu\text{m}$	M <sub>11</sub>	0.28/8 $\mu\text{m}$
M <sub>2</sub>	0.22/0.75 $\mu\text{m}$	M <sub>12</sub>	0.28/8 $\mu\text{m}$
M <sub>3</sub> & M <sub>4</sub>	3.6/4 $\mu\text{m}$	M <sub>13</sub>	0.28/8 $\mu\text{m}$
M <sub>5</sub> & M <sub>6</sub>	4.4/8 $\mu\text{m}$	M <sub>14</sub>	0.22/14 $\mu\text{m}$
M <sub>7</sub>	0.6/0.35 $\mu\text{m}$	R <sub>1</sub>	5.5 M $\Omega$
M <sub>8</sub>	0.22/10 $\mu\text{m}$	R <sub>2</sub>	104 k $\Omega$
M <sub>9</sub>	0.22/10 $\mu\text{m}$	R <sub>3</sub>	3.2 M $\Omega$
M <sub>10</sub>	0.22/16 $\mu\text{m}$		

**TABLE 2.** Circuit parameter values for the second proposed compensated RO

Device	Size	Device	Size
M <sub>1</sub>	0.22/0.44 $\mu\text{m}$	M <sub>11</sub> & M <sub>12</sub>	18.9/8 $\mu\text{m}$
M <sub>2</sub>	0.42/0.2 $\mu\text{m}$	M <sub>13</sub> & M <sub>14</sub>	1.54/20 $\mu\text{m}$
M <sub>3</sub>	0.6/0.18 $\mu\text{m}$	M <sub>15</sub>	0.32/4 $\mu\text{m}$
M <sub>4</sub>	0.22/0.2 $\mu\text{m}$	M <sub>16</sub>	0.28/8 $\mu\text{m}$
M <sub>5</sub>	0.22/0.2 $\mu\text{m}$	M <sub>17</sub>	0.28/8 $\mu\text{m}$
M <sub>6</sub>	0.42/0.85 $\mu\text{m}$	M <sub>18</sub>	0.28/8 $\mu\text{m}$
M <sub>7</sub>	0.23/1.6 $\mu\text{m}$	M <sub>19</sub>	0.22/13.8 $\mu\text{m}$
M <sub>8</sub>	0.26/18 $\mu\text{m}$	R <sub>1</sub>	6.6 M $\Omega$
M <sub>9</sub>	0.26/10 $\mu\text{m}$	R <sub>2</sub>	104 k $\Omega$
M <sub>10</sub>	1.05/0.18 $\mu\text{m}$	R <sub>3</sub>	3.2 M $\Omega$

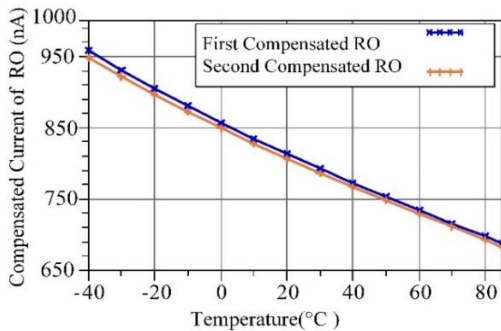


**Figure 12.** Total supply current  $I_{CTAT} + I_{Const}$

For more precise investigation of the frequency variation with temperature, Harmonic Balance (HB) analysis is performed for the proposed compensated and uncompensated ROs and their oscillation frequencies are depicted in Figure 14 for  $-40^\circ\text{C}$  to  $85^\circ\text{C}$  temperature range. Simulation results show that the temperature coefficient of the oscillation frequency for the first compensated RO is  $80.4 \text{ ppm}/^\circ\text{C}$ , while the total power consumption (including bias circuitry) is only  $14.5 \mu\text{W}$ . The temperature coefficient of the oscillation frequency for the second prototype is  $80.4 \text{ ppm}/^\circ\text{C}$  as well and the total power consumption (including bias circuitry) is  $34.1 \mu\text{W}$ . It is worth noting that the temperature coefficient of the uncompensated RO in Figure 14 is as high as  $2400 \text{ ppm}/^\circ\text{C}$ . Hence, the comparison of the temperature coefficients between compensated and uncompensated ROs in Figure 14 explicitly reveals the efficacy of the proposed technique for compensation of the subthreshold ROs.

The sensitivity of the oscillation frequency to the supply fluctuation is also shown in Figure 15. As seen in this figure the proposed circuits have less than 10% frequency variation, though the uncompensated RO has more than 100% frequency variation.

In order to examine the behavior of the compensation method against process variations, the simulated oscillation frequency versus temperature for different process corners is depicted in Figure 16. According to Figure 16, both prototypes of the compensated RO are robust against process variations.

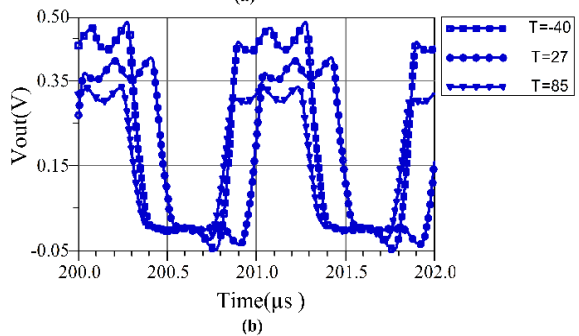
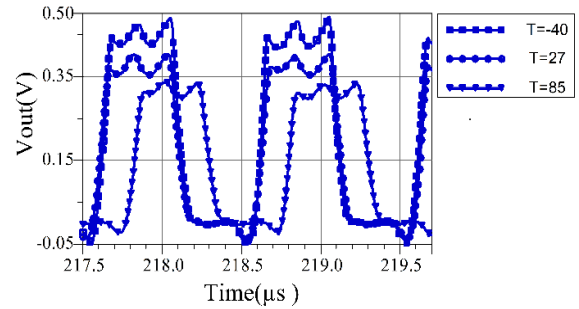


**Figure 13.** Output waveforms of the (a) first and (b) second compensated ring oscillator at different temperatures

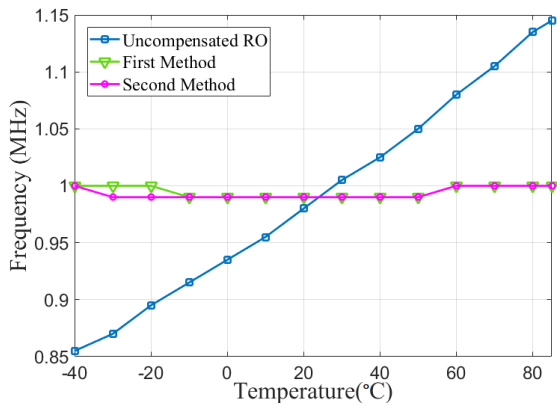


**Figure 14.** Simulated frequency versus temperature for subthreshold compensated and uncompensated ring oscillators

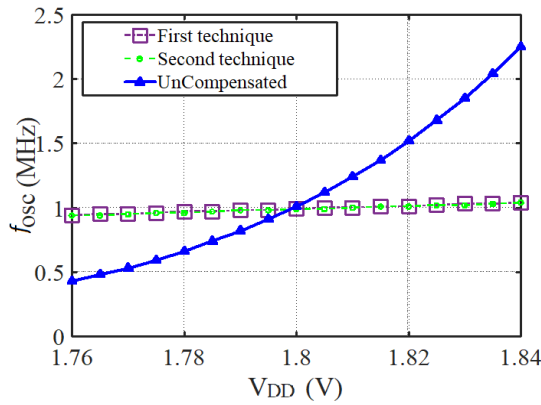


**Figure 15.** Frequency variation versus supply voltage fluctuation of the oscillators

To estimate the total active area, the layouts of both proposed circuits in Cadence are shown in Figure 17. The total die area of the first and second compensated ROs are  $296\mu\text{m}\times 293\mu\text{m}$  and  $287\mu\text{m}\times 292\mu\text{m}$ , respectively.

The performance of the proposed compensated ROs and some previous state of the art works are summarized in Table 3. Since, the different works may be designed at different frequencies with different power consumptions, the following figure of merit (FOM) is used to compare the overall performance of the circuits: The FOM is defined as  $(TC \times P_{\text{total}}) / f_{\text{osc}}$  in which  $P_{\text{Total}}$  is the total power consumption in  $\mu\text{W}$ ,  $f_{\text{osc}}$  is the oscillation frequency in MHz and TC is the temperature coefficient of the compensated oscillator in ppm/°C. Apparently the FOM of the proposed compensated ring oscillator is among the best FOMs in Table 3. That is, using an appropriate compensation technique and operating in subthreshold, an excellent frequency stability has been achieved with a very low power consumption; that results in an excellent FOM in Table 3. The proposed compensated RO provides a low TC clock signal without need for any

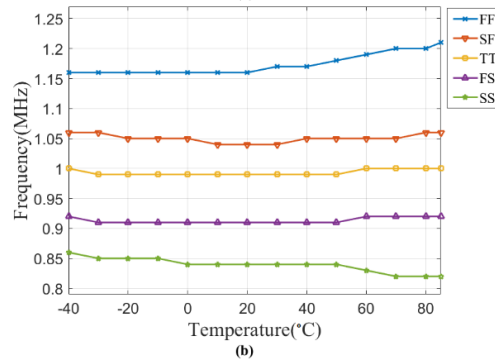
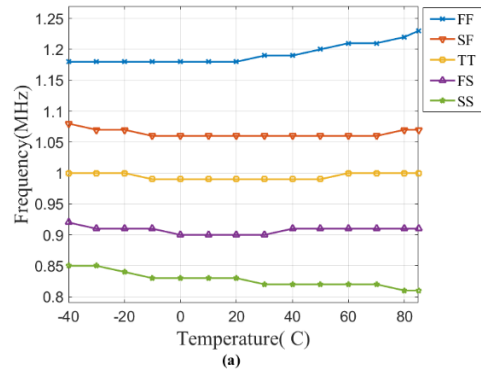
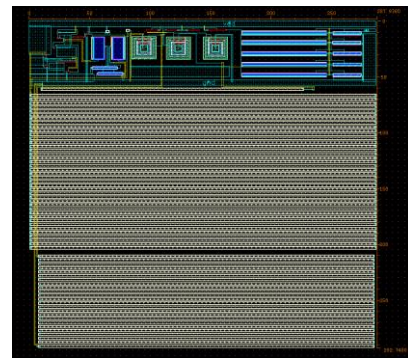
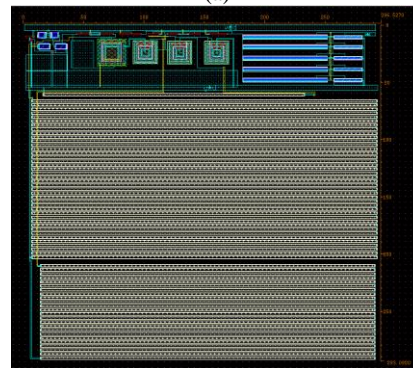


**Figure 16.** Oscillation frequency at different process corners for (a) first and (b) second compensated circuits. (FF is fast NMOS and fast PMOS, SF is slow NMOS and fast PMOS, FS is fast NMOS and slow PMOS, and SS is slow NMOS and slow PMOS corner)



(a)



(b)

**Figure 17.** The layout of (a) the first and (b) second compensated ROs

**TABLE 3.** Performance summary of the proposed and previously reported works

Reference	[8]	[29]	[30]	[7]	[31]	[6]	1 <sup>st</sup> Proposed RO	2 <sup>nd</sup> Proposed RO
Year	2019	2016	2014	2013	2009	2009		
Process (nm)	180	180	130	130	130	350	180	180
V <sub>DD</sub> (V)	1.2	3	1	2.5	1.5	3	1.8	1.8
f (MHz)	13.4	1.9	1.2	1	3.2	30	1	1
P (μW)	157.8	390	5.8	428	38.4	180	14.5	34.1
Δf/f <sub>c</sub> %	N/A	1.16	±1.8	N/A	N/A	N/A	1.005	1.005
TC (ppm/°C)	193.15	92.8	296	108	125	90	80.4	80.4
Temp. (°C)	[-20–100]	[-40 – 85]	[-40 – 80]	[-20 – 200]	[-20 – 60]	[-20 – 100]	[-40 – 85]	[-40 – 85]
Area (mm <sup>2</sup> )	0.12	0.22	0.016	0.007	0.15	0.08	0.087	0.084
FOM	2274	19048	1420	46224	1500	540	1165	2741

precise resistor, capacitor or off-chip component, and needs no special feature like trimming that makes it compatible with cost-efficient standard CMOS technology. It is worth mentioning that the most of the prior researches are devoted to compensation of RC relaxation oscillators or above-threshold ring oscillators, though here the compensation of the subthreshold RO has been targeted.

### 3. CONCLUSION

A low power thermally compensated CMOS ring oscillator is developed in which the RO core operates in subthreshold region. Since the oscillation frequency of a ring oscillator in subthreshold is proportional to the absolute value of the temperature, the proposed technique suggests combining a CTAT and a constant current source for powering up the RO. In the proposed technique, the constant current source provides the major part of biasing current and the CTAT current source has the duty of frequency compensation. To verify the performance of the technique, two different implementations of the circuit are designed and simulated in a standard 0.18μm RF-CMOS process. In one prototype of the circuit, required CTAT current is developed by utilizing the CTAT nature of the threshold voltage, though the other circuit exploits a diode-connected BJT. Simulation results showed that the TC of an uncompensated RO was dramatically reduced from 2400ppm/°C to 80.4ppm/°C while the total power consumptions of the first and second configurations were 34.1μW and 14.5μW respectively. Sensitivity analysis for the circuits regarding to the process variations and V<sub>DD</sub> fluctuations showed the robust behavior of the compensated ROs.

The main novelty of the proposed compensated RO is use of the ring oscillator in subthreshold for achieving

low power dissipation, and use of two new low power circuits for biasing and compensation. Since the thermal behavior of the RO in subthreshold is different from that of in above threshold region, therefore the required compensation technique in this paper is completely different from previous works.

### 4. REFERENCES

1. Wang, T.-M., Ker, M.-D. and Liao, H.-T., "Design of mixed-voltage-tolerant crystal oscillator circuit in low-voltage CMOS technology", *IEEE Transactions on Circuits and Systems I: Regular Papers*, Vol. 56, No. 5, (2009), 966-974. doi: 10.1109/TCSI.2009.2016172
2. Zong, Y., Dai, X., Gao, Z., Binns, R. and Busawon, K., "Simulation and evaluation of pulse-coupled oscillators in wireless sensor networks", *Systems Science & Control Engineering*, Vol. 6, No. 1, (2018), 337-349. <https://doi.org/10.1080/21642583.2018.1496043>
3. Farzeen, S., Ren, G. and Chen, C., "An ultra-low power ring oscillator for passive UHF RFID transponders", 53rd IEEE International Midwest Symposium on Circuits and Systems, (2010), 558-561. doi: 10.1109/MWSCAS.2010.5548887
4. Sundaresan, K., Allen, P.E. and Ayazi, F., "Process and temperature compensation in a 7-MHz CMOS clock oscillator", *IEEE Journal of Solid-State Circuits*, Vol. 41, No. 2, (2006), 433-442. doi: 10.1109/JSSC.2005.863149
5. Lahiri, A. and Tiwari, A., "A 140μA 34ppm/°C 30 MHz clock oscillator in 28nm CMOS bulk process", International Conference on VLSI Design (VLSID), (2013), 173-178. doi: 10.1109/VLSID.2013.184
6. Ueno, K., Asai, T. and Amemiya, Y., "A 30-MHz, 90-ppm/°C fully-integrated clock reference generator with frequency-locked loop", *ESSCIRC*, (2009), 392-395. doi: 10.1109/ESSCIRC.2009.5325940
7. Sadeghi, N., Sharif-Bakhtiar, A. and Mirabbasi, S., "A 0.007mm<sup>2</sup> 108ppm/°C 1-MHz relaxation oscillator for high-temperature applications up to 180 °C in 0.13μm CMOS", *IEEE Transactions on Circuits and Systems I: Regular Papers*, Vol. 60, No. 7, (2013), 1692-1701. doi: 10.1109/TCSI.2012.2226500
8. Chang, Y.-A. and Liu, S.-I., "A 13.4-MHz relaxation oscillator with temperature compensation", *IEEE Transactions on Very*

- Large-scale Integration (VLSI) Systems*, Vol. 27, No. 7, (2019). doi: 10.1109/TVLSI.2019.2908204
9. Tang, J. and Tang, F., "Temperature and process independent ring-oscillator using compact compensation technic", IEEE International Conference on Anti-Counterfeiting Security and Identification in Communication (ASID), (2010), 49-52. doi: 10.1109/ICASID.2010.5551842
  10. Katebi, M., Nasri, A., Toofan, S. and Zolfkhani, H., "A temperature compensation voltage-controlled oscillator using a complementary to absolute temperature voltage reference", *International Journal of Engineering, Transactions B: Applications*, Vol. 32, No. 5, (2019), 710-719. doi: 10.5829/ije.2019.32.05b.13
  11. Liu, Q., Chai, Ch., "A 1.8 GHz temperature drift compensated LC-VCO for RFID transceiver", *Analog Integrated Circuits and Signal Processing*, Vol. 105, (2020), 7-12. <https://doi.org/10.1007/s10470-020-01694-x>
  12. Rodrigues, G., Brito, D., Busse, H., Fernandes, J., Silva, J. and Rabuske, T., "A Temperature-Compensated 57 PPM/°C 10MHz, 2.4μW Stacked Ring Oscillator", IEEE International Symposium on Circuits and Systems (ISCAS), Korea, 2021. doi: 10.1109/ISCAS51556.2021.9401370
  13. Park, K.S., Khashaba, A., Abdelrahman, A., Li, Y., Wang, T., Xia, R., Pal, N. and Hanumolu, P.K., "A second-order temperature compensated 1μW/MHz 100MHz RC oscillator with ±140ppm inaccuracy from -40°C to 95°C", IEEE Custom Integrated Circuits Conference (CICC), USA, 2021. doi: 10.1109/CICC51472.2021.9431420
  14. Yan, L., Harpe, P., Osawa, M., Harada, Y., Tamiya, K., Van Hoof, C. and Yazicioglu, R.F., "24.4 A 680nA fully integrated implantable ECG-acquisition IC with analog feature extraction", IEEE Solid-State Circuits Conference Digest of Technical Papers (ISSCC), (2014), 418-419. doi: 10.1109/ISSCC.2014.6757495
  15. Yazicioglu, R.F., Kim, S., Torfs, T., Merken, P. and Van Hoof, C., "A 30μw analog signal processor ASIC for biomedical signal monitoring", IEEE Solid-State Circuits Conference Digest of Technical Papers (ISSCC), (2010), 124-125. doi: 10.1109/ISSCC.2010.5434026
  16. Chiang, Y.-H. and Liu, S.-I., "A submicrowatt 1.1-MHz CMOS relaxation oscillator with temperature compensation", *IEEE Transactions on Circuits and Systems II: Express Briefs*, Vol. 60, No. 12, (2013), 837-841. doi: 10.1109/TCSII.2013.2281920
  17. Wang, Y., Chan, P.K. and Li, K.H., "A compact CMOS ring oscillator with temperature and supply compensation for sensor applications", IEEE Computer Society Annual Symposium on VLSI (ISVLSI), (2014), 267-272. doi: 10.1109/ISVLSI.2014.15
  18. Filanovsky, I. and Allam, A., "Mutual compensation of mobility and threshold voltage temperature effects with applications in CMOS circuits", *IEEE Transactions on Circuits and Systems I: Fundamental Theory and Applications*, Vol. 48, No. 7, (2001), 876-884. doi: 10.1109/81.933328
  19. Huang, K. and Wentzloff, D., "A 1.2-MHz 5.8μW temperature-compensated relaxation oscillator in 130-nm CMOS", IEEE Transactions on Circuits and Systems II: Express Briefs, Vol. 61, No. 5, (2014), 334-338. doi: 10.1109/TCSII.2014.2312634
  20. Taur, Y. and Ning, T.H., *Fundamentals of modern VLSI devices*, Cambridge university press, (2013).
  21. Calhoun, B., Chandrakasan, A. and Wang, A., *Sub-threshold design for ultra-low-power systems*. 2006, Springer New York.
  22. Tajalli, A. and Leblebici, Y., *Extreme low-power mixed signal IC design: Subthreshold source-coupled circuits*, Springer Science & Business Media, (2010).
  23. Ueno, K., Hirose, T., Asai, T. and Amemiya, Y., "A 300 nW, 15ppm/°C, 20ppm/°C CMOS voltage reference circuit consisting of subthreshold MOSFETs", *IEEE Journal of Solid-state Circuits*, Vol. 44, No. 7, (2009), 2047-2054. doi: 10.1109/JSSC.2009.2021922
  24. Mandal, M. and Sarkar, B.C., "Ring oscillators: Characteristics and applications", *Indian Journal of Pure and Applied Physics* Vol. 48, (2010), 136-145.
  25. Najafizadeh, L., "Voltage references using mutual compensation of mobility and threshold voltage temperature effects", Ph.D. thesis, Alberta, (2004).
  26. Razavi, B., "Design of analog CMOS integrated circuits", Tsinghua University Press Co., Ltd., (2005).
  27. Palumbo, G., "Voltage references: From diodes to precision high-order bandgap circuits [book review]", *IEEE Circuits and Devices Magazine*, Vol. 18, No. 5, (2002), 45-45.
  28. Prijić, Z., Dimitrijević, S. and Stojadinović, N., "Analysis of temperature dependence of CMOS transistors threshold voltage", *Microelectronics Reliability*, Vol. 31, No. 1, (1991), 33-37. [https://doi.org/10.1016/0026-2714\(91\)90342-5](https://doi.org/10.1016/0026-2714(91)90342-5)
  29. Filanovsky, I., "Input-free  $V_{TP}$  and  $-V_{TN}$  extractor circuits realized on the same chip", *Analog Integrated Circuits and Signal Processing*, Vol. 19, No. 2, (1999), 151-157. <https://doi.org/10.1023/A:1008353815230>
  30. Zhang, S., Li, A., Han, Y., Jie, L., Han, X. and Cheung, R.C., "Temperature compensation technique for ring oscillators with tail current", *Electronics Letters*, Vol. 52, No. 13, (2016), 1108-1110. <https://doi.org/10.1049/el.2016.1039>
  31. Choe, K., Bernal, O.D., Nuttman, D. and Je, M., "A precision relaxation oscillator with a self-clocked offset-cancellation scheme for implantable biomedical SoCs", IEEE Solid-State Circuits Conference-Digest of Technical Papers, (2009), 402-403. doi: 10.1109/ISSCC.2009.4977478

## Persian Abstract

## چکیده

مصرف توان کم، اندازه کوچک سطح مورد استفاده و ساخت در فرآیند CMOS از الزامات حیاتی در طراحی نوسان سازهای حلقوی است که در افزاره ها و دستگاه‌های قابل کاشت زیستی و پوشیدنی استفاده می‌شود. اما فرکانس نوسان سازهای حلقوی به شدت به دما وابسته است. در این مطالعه یک نوسان ساز حلقوی جبران سازی شده نسبت به دما با توان مصرفی کم پیشنهاد شده است. ترانزیستورهای نوسان ساز حلقوی پیشنهادی برای دستیابی به عملکرد با مصرف توان کم و ولتاژ پایین در ناحیه زیرآستانه بایاس شده‌اند. از آنجایی که فرکانس نوسان یک نوسانگر حلقوی معمولی در ناحیه زیرآستانه با افزایش دما افزایش می‌یابد، در تکنیک پیشنهادی، از دو منبع جریان برای تغذیه نوسان ساز حلقوی استفاده می‌شود: یک مرجع جریان مستقل از دما (جریان با افزایش دما ثابت است) و یک مرجع جریان مکمل CTAT که با افزایش دما جریان آن کاهش می‌یابد. در مدار پیشنهادی، جریان CTAT بخش کوچکی از کل جریان مورد نیاز نوسان ساز را تشکیل می‌دهد و وظیفه آن فقط جبران میزان انحراف فرکانس نوسان نسبت به دما است. دو نمونه اولیه از نوسان ساز حلقوی زیرآستانه برای فرکانس هدف ۱ مگاهرتز با استفاده از فناوری 0.18 RF CMOS میکرومتر طراحی و شبیه سازی شد. ضریب حرارتی (TC) نوسان ساز حلقوی جبران سازی نشده در محدوده دمایی  $+85^{\circ}\text{C}$  تا  $-40^{\circ}\text{C}$  برابر با  $2400\text{ ppm}/^{\circ}\text{C}$  می‌باشد، در حالیکه به کارگیری روش پیشنهادی ضریب حرارتی نوسانگر حلقوی را به  $80/4\text{ ppm}/^{\circ}\text{C}$  با مصرف کل توان به اندازه  $5/14$  میکرووات کاهش داد.



## Outlier Detection in Test Samples using Standard Deviation and Unsupervised Training Set Selection

N. Mohseni<sup>a</sup>, H. Nematzadeh<sup>\*b</sup>, E. Akbarib<sup>b</sup>, H. Motameni<sup>b</sup>

<sup>a</sup> Department of Computer Engineering, Babol Branch, Islamic Azad University, Babol, Iran

<sup>b</sup> Department of Computer Engineering, Sari Branch, Islamic Azad University, Sari, Iran

### PAPER INFO

#### Paper history:

Received 09 June 2022

Received in revised form 27 September 2022

Accepted 28 September 2022

#### Keywords:

Outlier Detection

Training Set Selection

K-means

K-Nearest Neighbor

Standard Deviation

### ABSTRACT

Outlier detection is a technique to identify and remove significantly different data from the more correct and consistent data in a data set. Outlier data can have negative impact on classification and clustering performance; that should be identified and removed to improve the classification efficiency. Regardless of whether a classifying technique classifies an outlier correctly, the very notion of identifying a data as outlier is of great significance. In this paper, a new approach is proposed for outlier data detection within a test data set along with unsupervised training set selection. The selected training set is used for two-step classification. After unsupervised clustering the training set, the closest cluster to a test sample is selected using the Euclidean distance measure. Then, the outlier in the test sample is identified with the concepts of standard deviation and mean value. The results showed by evaluating the distance of each sample of the test set with the new selected data set. the accuracy of the classifiers is enhanced after detection and elimination of outlier data.

doi: 10.5829/ije.2023.36.01a.14

## 1. INTRODUCTION

The availability of large training data sets makes training set selection a significant task [1]. Extraction of a reduced and most pertinent training set is a data mining challenge for researchers. After training data selection, a learning session is performed by classifiers. Generally, classification should lead to a more accurate prediction and occasionally a reduced execution time [2-5]. TSS is also a common tool in image processing and image recognition where large data sets may be available for classification [6, 7]. Outlier data with unacceptable distance with other consistently dispersed data may at times exist. The efficient identification and eliminations of these data types will enhance the classification outcome [8]. Statistical methods such as linear regression model [9] and Principle Component Analysis (PCA) [10] have traditionally been used for outlier detection. As no single outlier detection approach can be regarded as the most efficient, several other methods have been proposed in the literature [5, 11-18]. In this paper, it is attempted to detect outlier data within the test data set together with

training data set selection task. The common trend in the literature is to detect outliers from within training data sets. However, outlier data may also exist among test data. Therefore, this research is dedicated to outlier detection in test data sets. As reviewed, no previous research has focused on outlier detection in the test data while embarking on training set selection. Contribution of this paper are as follows:

- Clustering the training set with the unsupervised method.
- Dynamic training set selection using KNN for each test sample.
- Outlier detection using standard deviation and mean average.

The related works with more details on training set selection and outlier detection techniques are reviewed next.

## 2. RELATED WORK

Regarding training set selection, a pareto-based method is proposed by Acampora et al. [19] where a multi-

\*Corresponding Author Institutional Email:

[hossein.nematzadeh@iau.ac.ir](mailto:hossein.nematzadeh@iau.ac.ir) (H. Nematzadeh)

objective function is optimized which aims to maximize accuracy and reduction rate. Due to scalability problems associated with support vector machine (SVM), this data mining technique becomes extremely complex with high execution time and memory usage. The mentioned approach reduces the training set in the preprocessing step through the selection of the most pertinent samples. Thus, regardless of the sample size the execution time and storage requirement remain the same. This method was demonstrated to enhance accuracy and reduction rate as applied to Shell Extraction algorithm [2].

Verbiest et al. [1] investigated through wrapper techniques which was applied to TSS, further improvements were made to SVM accuracy. The training set was converted into subsets which were evaluated by the mentioned SVM-based wrapper algorithms. According to the literature, five distinct TSS methods have been presented. Among these methods, the generational genetic algorithm (GGA) has delivered the best performance. As the paper concluded, using evolutionary techniques positively affects SVM accuracy though at the cost of longer execution times resulted from frequent iterations. Also, it is demonstrated that wrapper TSS exhibits better performance on experimental data sets as compared to filter TSS.

Mohammed et al. [4] have applied swarm intelligence techniques to carry out TSS. The procedure includes three steps where first, data sampling is performed to reduce input data scale which is then used to train classifiers with bagging and distance-based feature sampling algorithms. Finally, through a diverse set of meta-heuristic methods, such as grey-wolf optimization (GWO), Whale optimization algorithm (WOA) and moth-flame optimization (MFO), effective weight assignments are made to the classifiers. This method, which employs Matthews Correlation Coefficient (MCC), perfectly suits binary as well as multi-class data sets. Also, WOA delivered the poorest performance in prediction accuracy for large data sets. Despite relatively short weight assignment time through parameter modifications, the method suffers from relatively long overall execution time. Thus, the method's application is limited to offline training tasks. Hence, it is concluded that meta-heuristic methods will lead to time-consuming solutions. In the following, a review of outlier detection techniques proposed so far is presented.

Mapping functions of differential geometry were used by Lejeune et al. [13] in a shape-based detection of outliers within multivariate functional data. This method demonstrates acceptable efficiency as compared to functional-depth-based methods as outliers can be difficult to detect from multivariate functional data due to complicated relations between parameters. The mentioned research, however, performs successfully through extraction of synthetic data sets using interpretable functional curve shape characteristics.

An ensemble outlier detection method was proposed by Wang and Mao [15]; they applied to an adaptive K-Nearest Neighbor. Having higher capabilities with respect to the traditional K-Nearest Neighbor, the adaptive method uses support vector data and explores those areas with constant class probabilities with respect to the test pattern. Through the use of posterior probabilities of classifiers, this method performs in a more efficient way than the traditional methods like majority voting and selects a more suitable data set for test patterns.

Another outlier detection approach was introduced by Tang and He [14] based on relative density-based scores as an index for outlying degree. In order to estimate distribution density at the proximity of an object, the Kernel Density Estimation (KDE) was employed. Also, in addition to the conventional K-Nearest Neighbor, reverse and shared nearest neighbors were examined for efficient detection. The proposed methods were tested on diverse large and small real-life data sets including medical data. The efficiency of these methods was verified by techniques such as Receiver Operator Characteristics (ROC) and Area Under Curve (AUC).

Outlier detection through clustering approach was proposed by Christy et al. [12] with two different algorithms, namely distance-based and cluster-based, which utilized outlier scoring to detect and remove outliers of a healthcare data set. Clustering was based on similarity in only the critical properties of the data. As the results of implementation on three data sets from R package (Esoph, Diabetes, and KosteckiDillon) revealed, the cluster-based approach [20] is more competent than the other detection method. Furthermore, the results indicate that the F-score and likelihood values do not change with random data object removals.

A new method called Information Entropy-Pruning Multi-dimensional Outlier Detection (IPMOD) was introduced by Yang et al. [11] in which a combination of information entropy and a new index weight measurement were applied to multi-dimensional data helping to specify the effect of various attributes on data prediction. Consequently, a sliding window approach and subsequent distance measurements were used to determine if the data was outlier. They also lowered the proposed method complexity through pruning techniques. The provided results were indicative of the efficiency of the algorithm both in terms of accuracy and fastness of the outlier detection method as implemented on different real-life data sets such as medical databases.

An unsupervised ensemble approach, namely Boosting based autoencoder ensemble (BAE) was proposed by Hamed et al. [16] which, through creating a chain of autoencoders, guarantees robust and enhanced results. Autoencoder elements are constantly trained through weighted data sampling which also attempts to eliminate outlier data while training or diversifying the

ensemble. The mentioned work includes several tests that unanimously demonstrate superior performance of the proposed approach against conventional algorithms.

Further, a mean-shift outlier detection scheme was introduced by Yang et al. [17] which, through data modification, removes possible bias caused by the existence of outlier data. Every object in this method is substituted by its k-nearest neighbors. This guarantees the removal of outlier effect and the clustering is performed in a more efficient way. The outliers can be detected through measuring the shifted distance. This approach is demonstrated to work well for any given number of outlier data within real-life or synthetic data sets. Furthermore, Beulah and Vamsi Krishna [21] presented a density-based outlier detection for unsupervised training. In this approach, adaptive Natural Value (NV) determination is achieved through Natural Neighbor (NaN) concept while location density for an object is predicted through weighted kernel density estimation (WKDE) technique. Also, k nearest neighbors (KNN) and reverse nearest neighbors (RNN) are utilized which contribute to the modeling flexibility for different data patterns. For the sake of smoothness, Gaussian kernel function is employed and the notion of adaptive kernel width is applied to make clear distinction between correct and outlier data. Through comprehensive test cases with both real and synthetic data, the proficiency of the method in outlier detection is demonstrated.

Biglari et al. [22] followed a semi-novel approach using "Ensemble of Unsupervised Incremental Learning" method for building models that by analyzing data, can find the behavior or state change in equipment or machinery over time. This paper focuses on the behavior of data mining of machines in process/manufacturing industries. Generally, such data are continuous numerical. In addition, time series data are captured by various industrial sensors. The proposed algorithm must run in two phases, offline and online with hierarchical clustering.

A novel hybrid feature selection technique was proposed by Fränti and Sieranoja [23], which can reduce the number of features drastically with an acceptable loss of prediction accuracy. The proposed approach operates in multiple stages, starting by removing irrelevant features with a low discrimination power, and then eliminating the ones with low variation range. Afterward, among each set of features with high cross-correlation, a single feature that is strongly correlated with the output is kept. Finally, a Genetic Algorithm with a customized cost function is provided to select a small subset of the remainder of features.

### 3. BACKGROUND

Most of the reviewed research works have focused on K-means clustering and K-Nearest Neighbors (KNN)

algorithms and the results have been analyzed through SVM and Random Forest methods. In this section, the main pros and cons of K-means and KNN algorithms are studied.

#### 3.1. K-means Clustering Algorithm

The main variations of clustering technique are the partitional and hierarchical clustering algorithms. Meanwhile, each of these methods can be divided into distance-based and density-based categories. Distance-based methods are usually based on Euclidean or city block distance analyses. A data space is considered dense if it forms a dense data region. The partitional clustering is first initiated by a human as opposed to the hierarchical clustering technique [24, 25]. K-means clustering is categorized as a distance-based technique. Through this approach, a set of X samples Equation (1) is classified into k groups with  $k \leq n$  as determined by the user [26, 27].

Then the algorithm selects k samples from the set X in a random fashion and puts them as the centers of a vector  $M^0$ , as modeled by Equation (2). If a sample  $x_l$  has the minimum distance from  $m_i^r$  as in Equation (3), it is said to belong to cluster  $C_i^r$ . The use of a distance measure (*dist*) is arbitrary in K-Means approach. However, in Equation (3) the Euclidean distance is employed as it has performed well in the previous works.

$$X = (x_1, x_2, \dots, x_n) \quad (1)$$

$$M^r = m_1^r, m_2^r, \dots, m_k^r \quad (2)$$

$$x_l \in C_i^r : \text{dist}(x_l, m_i^r) \leq \{\text{dist}(x_l, m_j^r)\}_{j=1, j \neq i}^k \quad (3)$$

$$1 \leq i \leq k, \quad x_l \in X$$

The following relation is also used to calculate Euclidean distance between two d-dimensional samples of  $x_i = (f_1^i, f_2^i, \dots, f_d^i)$  and  $x_j = (f_1^j, f_2^j, \dots, f_d^j)$  as [19]:

$$ED = (\sum_{l=1}^d (f_l^i - f_l^j)^2)^{1/2} \quad (4)$$

Also, new centroids are determined through updating  $M^r$  at each iteration as in Equation (5). If the members of  $C_i^r$  and  $C_i^{r+1}$  stay unchanged in successive iterations, then it can be said that K-means procedure can stop.

$$m_i^{r+1} = \frac{1}{|C_i^r|} \sum_{x_j \in C_i^r} x_j \quad 1 \leq i \leq k \quad (5)$$

#### 3.2. K-Nearest Neighbors Regression

The K-nearest neighbor (KNN) as a regression classification technique is used to specify nearest neighbor for a given sample based on some of the most common sample measurements. For a data set D with k clusters and similar member labels (p), KNN can be obtained for test sample  $TS_h$  within a test set (TS). For this purpose, the distance of the sample test  $TS_h$ , denoted as  $d_{ji}$  between

cluster members  $x_{ji}$  is calculated using Equation (6). Then,  $d_{ji}$  is sorted in ascending order to form  $ds_{ji}$  as Equation (7) and the average of K members from  $ds_{ji}$  is calculated as  $ave_i$  to yield the best K as modeled in Equation (8). The outlier detection within  $TS_h$  is based on the cluster with the least  $ave$  value, as determined by Equation (9).

$$d_{ji} = dist(TS_h, x_{ji}) \quad h = 1, 2, \dots, |TS|$$

$$j = 1, 2, \dots, |C_i| \quad i = 1.2. \dots .p$$

$$ds_{ji} = sort(d_{ji})$$

$$ave_i = \frac{1}{K} \sum_{j=1}^K ds_{ji}$$

$$p = \min(ave)$$

Despite being regarded as a classification technique, KNN was used here as a means for distance determination. The efficiency of the proposed methods can be assessed through SVM [1-3, 28-30] and Random Forest (RF) [31] as applied to two-labeled and multi-labeled data sets, respectively. In this paper, SVM is based on linear kernel function considering box constraint of 2. Also, RF technique comprises several single decision trees bringing more accurate results compared to a single decision tree.

#### 4. PROPOSED METHOD

In this section the Euclidean distance criterion applied in our proposed method is described.

for two vectors A and B, the distance measure is as Equation (10):

$$dist(A, B) = \sqrt{\sum_{i=1}^n |A_i - B_i|^2} \cdot n = \text{vector size}$$

The overall scheme of the proposed method is given below. As shown, the whole data set is divided into two groups of training and test sets. First, using k-means method, the training data are classified into k clusters where k is the square of the training set length. Then, for each sample within test set  $ts_i$ , the closest cluster is determined using Euclidean distance and KNN regression algorithm. The data of the selected cluster are then selected and stored as the new sets of training set selection. Definitely, the more similar the determined cluster to the selected test sample  $ts_i$ , the more similar the selected test sample is to the training set samples of TSS. If the determined cluster only contains one sample, which is a rare case that may happen for synthetic data, the next most similar cluster is merged with the initial one and a new training set is developed for a more accurate and more rational calculation. Then, the standard deviation  $\sigma$  and mean value  $\mu$  of the selected training

set is calculated. To identify any outlier data, the standard deviation and mean value of the new training set is calculated. For a mean value of the new training set  $\mu$  with standard deviation  $\sigma$ , a distance larger than  $\mu + 2\sigma$  or smaller than  $\mu - 2\sigma$  between the new training set and the test sample will indicate that the test sample can be an outlier data, as shown in Figure 1 [32]. In this case, test sample outlier is detected and the classification operation is not performed. Otherwise, the test sample is regular and the finalized label  $L_i$  is identified using classifiers leading to improved classification outcome.

The overall scheme of Figure 2 can be formulated as follows:

Given a data set D as Table 1, each sample can be denoted by Equation (11). Each characteristic vector  $F_j$  is represented by Equation (12).

$$\bar{x}_i = (f_{i1} \cdot f_{i2} \cdot \dots \cdot f_{in}) \quad i = 1.2. \dots .n$$

$$\bar{F}_j = (f_{1j} \cdot f_{2j} \cdot \dots \cdot f_{nj})^t$$

if  $L = \{L_1, L_2, \dots, L_k\}$  is a set of labels, the samples belonging to each label are represented as Equation (13).

$$y^{lp} = \{x_1^{lp} \cdot x_2^{lp} \cdot \dots \cdot x_n^{lp}\} = \{x_j^{lp}\}_{j=1}^n$$

where  $\cup_{p=1}^k y_0^{lp} = \sum_{p=1}^k n_p = n \cdot p = 1.2. \dots .k$

For a total sample number of X within data set D, it is clustered into k clusters regardless of its labels using k-means classifier where k is the square of the total number of samples n. Each cluster is titled  $C_r$ :

$$C_r = Kmeans(X, k) \quad r = 1.2. \dots .k$$

where  $C = \{c_1, c_2, \dots, c_k\}$

Then, the cluster  $C_r$  with the least Euclidean distance from  $TS_i$  is selected as the new training set as Equation (15):

$$TSS = \min\{C_r\}_{r=1}^k$$

In the proposed unsupervised algorithm, the samples are clustered irrespective of their labels. Then, the mean distance of the cluster members  $C_r$  from a test sample in  $TS_i$  are calculated using algorithm 1.

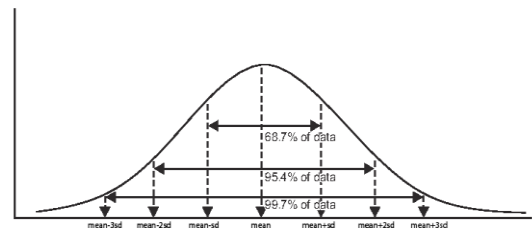
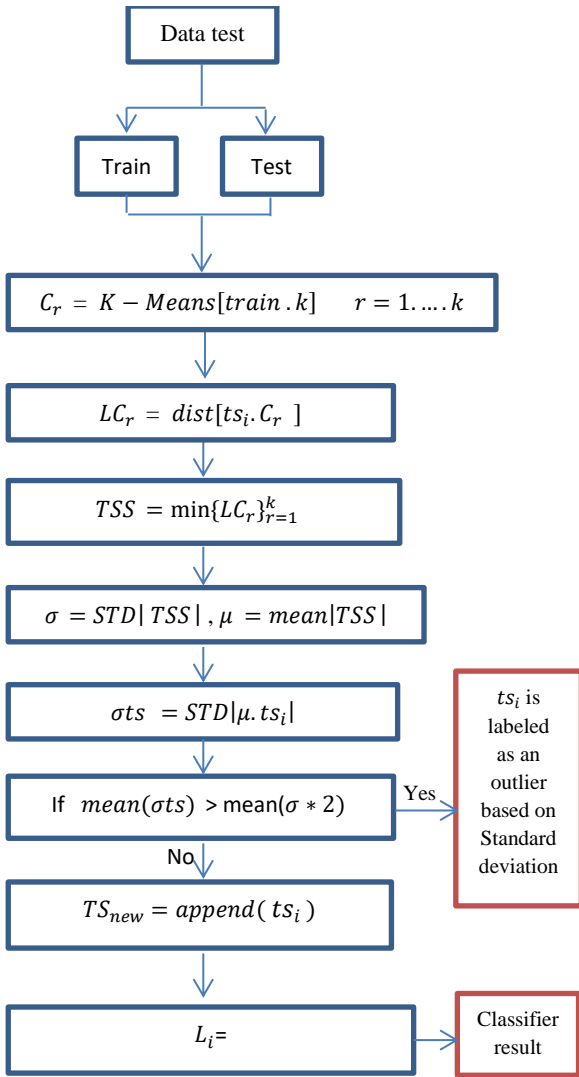


Figure 1. Normal distribution with mean and standard deviation



**Figure 2.** Overall procedure for the proposed outlier data detection method

**TABLE 1.** A sample data set

	$F_1$	$F_2$	$F_3$	...	$F_m$	LABEL
$x_1$	$f_1^1$	$f_1^2$	$f_1^3$	...	$f_1^m$	1
$x_2$	$f_2^1$	$f_2^2$	$f_2^3$	...	$f_2^m$	2
$x_3$	$f_3^1$	$f_3^2$	$f_3^3$	...	$f_3^m$	3
$\vdots$	$\vdots$	$\vdots$	$\vdots$	$\ddots$	$\vdots$	$\vdots$
$x_n$	$f_n^1$	$f_n^2$	$f_n^3$	...	$f_n^m$	$l$

Finally, the new training set TSS with the least mean distance is dynamically determined for a test sample  $TS_i$ . In the next step, it should be determined if the test sample  $TS_i$  is an outlier or not. For this purpose, first the standard

deviation  $\sigma$  and then the mean value of the test set TSS are calculated. Afterwards, the distance between the test sample and the mean value of the new training set TSS is obtained. If the distance exceeds  $\mu + 2\sigma$  or is below  $\mu - 2\sigma$ , the test sample is identified as an outlier data. This is illustrated in algorithm 2.

It is expected that through implementing Algorithm 4-2, outlier data will be removed and the classification accuracy will improve along with other measurement indices.

## 5. EXPERIMENTAL RESULT

We begin this section by introducing two- and multi-label data sets for the qualitative evaluation of the proposed method. Then the 5-fold validation function and the

**Algorithm 1.** finding  $\min\{C_r\}_{r=1}^k$

**Input:**  $C_r = \{x_1, x_2, \dots, x_k\}, ts_h$

**Output:** TSS

```

FOR i = 1 to k
    d[i] ← Ave dist[ $ts_h, x_i$ ]
END
Min = ∞
FOR i=1 to k
    IF d[i] < Min THEN
        index = i
        Min = d[index]
    END IF
END FOR
mc ← d[index]
TSS =  $C_{mc}$ 
    
```

**Algorithm 2.** Outlier data detection

**Input:**

1.  $Train = (x_1, x_2, \dots, x_n)$
2.  $Ts = (t_1, t_2, \dots, t_m)$
3.  $k = \sqrt{n}$  .  $k$  is the number of cluster

**Output:**

label of test  $Ts$  as an outlier and classification

```

FOR i ← 1 to m
    TSS =  $\min\{C_r\}_{r=1}^k \cdot Ts$ 
     $\sigma$  = Standard Deviation(TSS)
     $\mu$  = mean(TSS)
     $\sigma Ts$  = Standard Deviation( $\mu \cdot Ts$ )
    IF mean( $\sigma Ts$ ) > mean( $2 * \sigma$ ) THEN
         $Ts$  is labeled as an outlier
    ELSE
        NewTs ←  $Ts$ 
    END IF
END FOR
 $L_{pnew}$  ← Classifier (Train, NewTs)
 $L_{pold}$  ← Classifier (Train, Ts)
Compare( $L_{pnew}, L_{pold}$ )
    
```

required hardware and software are given in section 5.2. The measurement criteria are presented in section 5.3. Finally, the results and discussions along with a comparison between the proposed method and other advanced algorithms are presented in section 5.4.

**5. 1. Data Sets** In this research, 12 data sets are used to evaluate the proposed method. Table 2 stated the number of samples, dimension (or characteristic) size and the class (or label) size of each data set. For evaluation of the proposed method, as described in section 4, eight credible data sets of Table 5 (rows 1 to 9) adopted from UCI reference are used. Also, three artificial data sets corresponding to rows 10 to 12 of Table 2 are used.

## 5. 2. Experimental Setup and Measurement Criteria

In order to assess the efficiency of the proposed method, support vector machine (SVM) clustering is used for double-class data and Random Forest (RF) clustering is applied for multi-class data clustering. In this research, SVM is based on a linear core function with box limit 2. RF consists of several decision trees which usually performs better than a group of individual trees.

As mentioned, a 5-fold approach is adopted to evaluate the proposed technique such that the data set is divided into test and training sets. 20 percent of the data volume is randomly selected as the test data while the remaining 80 percent is used as the training set. Also, the final results are based on the means values obtained through several iterations.

The algorithm is run in MATLAB 2018 on a personal computer with Intel Core i5, 3.2 Hz along with 6GB RAM and hard drive capacity of 240GB SSD on 64bit Windows 10 operating system.

A major criterion in the algorithm evaluation is the classification accuracy. As mentioned, a certain classifier

**TABLE 2.** Data Sets

No	Data set	Sample size	Dimension size	Class size
1	Bcwisconsin	569	30	2
2	wisconsin	312	3	2
3	Australian	690	15	2
4	german	1000	25	2
5	heart	270	14	2
6	Ecoli	336	8	8
7	PV	210	19	7
8	Yeast	1484	9	10
9	CTG	2126	22	10
10	R15	600	3	15
11	Spr	312	3	3
12	pathbas	300	3	3

may not have the same accuracy for all classification tasks. Therefore, different methods are used for increasing the classifier accuracy. In this research, we use the training set selection (TSS) method.

In order to determine the accuracy of the algorithms for double-class data, the following parameters should be determined:

True Positive (TP), True Negative (TN), False Positive (FP), False Negative (FN).

Given the above parameters, some indices like precision, recall and F-Measure can be calculated.

**Accuracy:** based on the above parameters, the classifier's accuracy for two-class data is determined by:

$$\text{Accuracy}_{\text{two-labeled}} = \frac{TP+TN}{TP+TN+FP+FN} \quad (16)$$

In multi-class or multi-label data, the accuracy is the ratio of correctly-labeled data  $p_i$  to the total number of initially labeled data  $I_i$  as formulated in Equation (17).

$$\text{Accuracy}_{\text{multi-labeled}} = \frac{1}{|TS|} \sum_{i=1}^{|TS|} \text{Match}(p_i, I_i) \quad (17)$$

**Precision:** precision is defined as the ratio of data correctly classified into a certain class to the whole number of data put correctly or incorrectly into the same class, as calculated below:

$$\text{Precision} = \frac{TP}{TP+FP} \quad (18)$$

Recall: is the ratio of data correctly classified into a certain class to the number of data put inside the same class, as calculated by:

$$\text{Recall} = \frac{TP}{TP+FN} \quad (19)$$

**F-measure:** using the obtained Recall and Precision factors, the weighted index F-measure can be calculated. F-measure is a suitable parameter to evaluate the classification method and is also a weighted average of the precision and recall quantities. Ideally, F-measure is 1 for a well-performed classification algorithm while it becomes zero for the worst classification. This is calculated as:

$$F - \text{measure} = 2 \times \frac{\text{Precision} \times \text{Recall}}{\text{Precision} + \text{Recall}} \quad (20)$$

**Normalized Mutual Information (NMI):** This parameter gives the difference between the predicted labels and the true test data labels. In fact, this is a measure of the conformance of the labels between the two partitions.

For multi-class data sets having more than two labels, NMI is obtained as in Equation (21) where  $\mathbf{h}_a = \{c_1^a, c_2^a, \dots, c_{k_a}^a\}$  and  $\mathbf{h}_b = \{c_1^b, c_2^b, \dots, c_{k_b}^b\}$  are two clusters from data set D with n samples and  $k_a$  and  $k_b$  clusters.  $n_{ij}$  is the cross-section of cluster  $c_i$  in the cluster set  $\mathbf{h}_a$  with cluster  $c_j$  in the cluster set  $\mathbf{h}_b$ . Also,  $n_{ia}$  is the

number of objects in cluster  $c_i$  of the cluster set  $h_a$  while  $n_{bj}$  is the number of objects in cluster  $c_j$  of the cluster set  $h_b$ .

$$NMI(h_a, h_b) = \frac{-2 \sum_{i=1}^{k_a} \sum_{j=1}^{k_b} n_{ij} \log\left(\frac{n \times n_{ij}}{n_{ia} \times n_{bj}}\right)}{\sum_{i=1}^{k_a} n_{ia} \log\left(\frac{n_{ia}}{n}\right) + \sum_{j=1}^{k_b} n_{bj} \log\left(\frac{n_{bj}}{n}\right)} \quad (21)$$

### 5. 3. Results of the Proposed Method

The proposed method is applied on 12 sets of two-class and multi-class data as given in Table.2 Some of the data sets such as spr, r15 and pathbas are synthetic data sets. The data distribution within these sets are shown in Figure 3 where the data of the same labels are color-separated from others. K-fold averaging with  $k=5$  is used to obtain

the results. Also, the SVM classifier with linear core function and the RF classifier are used for two-class data and multi-class data, respectively. For two-class data sets, the number of outliers as well as the accuracy, precision, recall and f-measure parameters are obtained while for multi-class data, the accuracy and NMI indices are calculated to evaluate the proposed method.

Table 3 shows the accuracy, precision, recall and F-score parameters for two-class data sets while Table 4 gives the accuracy and NMI values for multi-class data sets prior to using the proposed approach.

Tables 5 and 6 show the same parameters after the application of the proposed method. The final rows give the number of detected outlier data. The accuracy does not necessarily increase with the increased outliers detected. This is because the classifiers may correctly determine the label of data whereas the data may later be identified as outlier. It is important to note that the

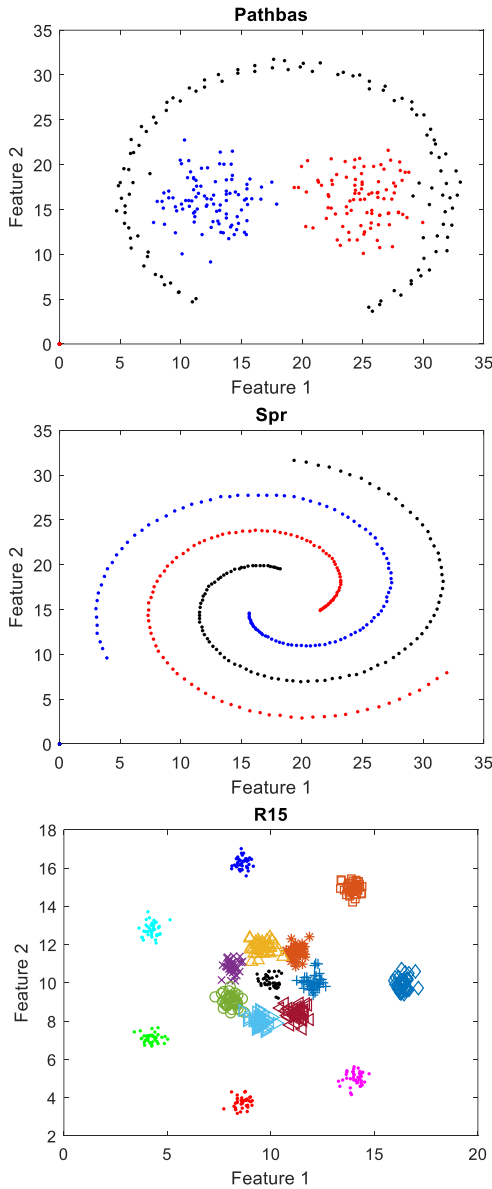


Figure 3. Artificial two-class data sets

TABLE 3. Evaluation parameters before application of the proposed method on the two-class data sets

Data sets	Accuracy	Precision	Recall	F-score
Bcwisconsin	0.95	0.97	0.95	0.96
Wisconsin	0.69	0.83	0.79	0.79
Australian	0.79	0.80	0.75	0.77
German	0.76	0.90	0.81	0.84
Heart	0.83	0.88	0.83	0.85

TABLE 4. Evaluation parameters before application of the proposed method on the multi-class data sets

Data sets	Accuracy	NMI
Yeast	0.61	0.40
CTG	0.91	0.82
Ecoli	0.84	0.74
PV	0.91	0.89
pathbas	0.99	0.95
R15	0.99	0.99
Spr	0.99	0.96

TABLE 5. Evaluation parameters after application of the proposed method on the two-class data sets

Data sets	MV Acc	MV Precision	MV Recall	MV Fscore	Outliers detected
Bcwisconsin	<b>0.96</b>	<b>0.98</b>	<b>0.96</b>	<b>0.97</b>	7
Wisconsin	0.69	0.83	0.79	0.79	0
Australian	0.79	<b>0.81</b>	0.75	<b>0.78</b>	8
German	0.76	0.90	0.81	0.84	1
Heart	<b>0.84</b>	<b>0.89</b>	<b>0.84</b>	<b>0.86</b>	2

**TABLE 6.** Evaluation parameters after application of the proposed method on the multi-class data sets

Data sets	MV Acc	MV NMI	Outliers detected
Yeast	<b>0.62</b>	0.40	<b>2</b>
CTG	0.91	0.82	<b>2</b>
Ecoli	<b>0.87</b>	<b>0.77</b>	<b>2</b>
Pv	<b>0.92</b>	<b>0.90</b>	<b>3</b>
Pathbas	0.99	0.95	0
R15	0.99	0.99	0
Spr	0.99	0.96	0

number of the identified outliers in tables 5 and 6 is the sum of the outliers in 5-fold execution. The bold parameters indicate an improvement compared to before application of the proposed method.

As indicated by the results of Tables 5 and 6, removing the outliers from the test samples and classification using the new test samples improves the final accuracy. Therefore, it can be said that outlier detection and removal has been effective on the results of the proposed method leading to improved measurement indices. The last column in Table 5 gives the number of detected outlier data. As seen, no outliers were detected using the proposed approach for Wisconsin data set while in BCwisconsin and Heart data sets, the accuracy has been improved through outlier detection and elimination.

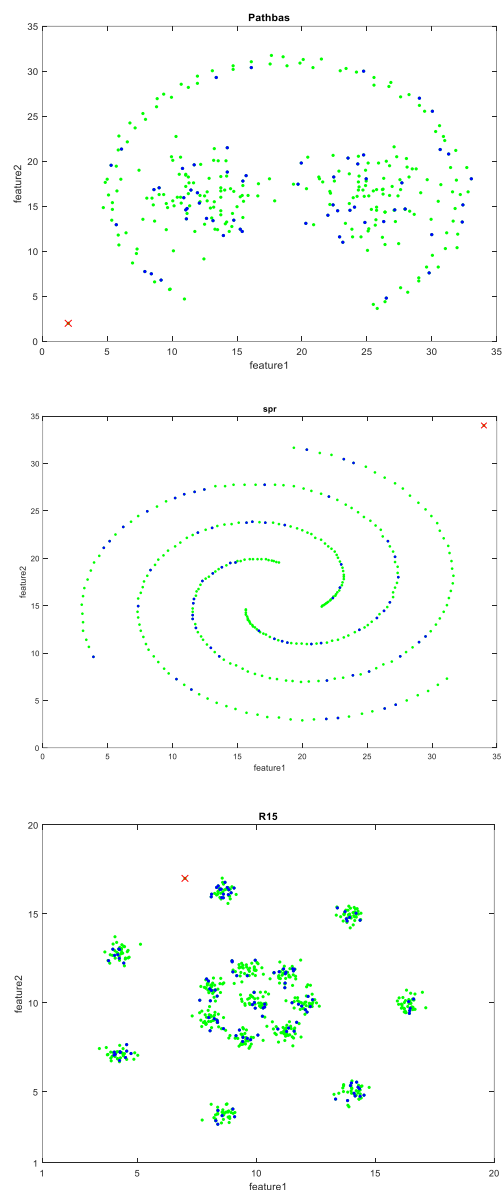
Similarly, Table 6 gives the accuracy and NMI measurement for multi-class data sets after the application of the proposed method. Again, the last column is the number of outlier data in 5-fold execution. The bold values indicate improvement with respect to before implementing the proposed method.

Again, the results indicate that outlier detection and removal positively affects the outcome of the proposed approach leading to improved measurement indices. As shown in Table.6 , no outlier was detected in data sets spr, r15 and pathbas which can be justified by the kin of distribution shown in Figure 3 . As seen, the accuracy has been improved after outlier detection and removal from data sets *E. coli*, yeast and pv while the accuracy for CTG data set has remained the same despite the detection of two outlier data.

Furthermore, the experiment results and outlier data in Table 2 indicate that three data sets, namely, spr, r15 and pathbas do not contain any outliers. Nonetheless, to make sure of the accuracy of the proposed method, some outlier data were added to these data sets to observe if the proposed technique is able to detect these outliers. As the results indicate, the proposed method was able to detect all outliers from the three data sets. These outlier data are

shown with mark x and in red color in Figure 4. The training sets are colored green and the regular test data are shown as blue dots.

The execution time given in Table 7 is the time-summation of k-means classification, determining the closest cluster, classification model and the classification of the test samples. The results of Table 7 indicate that even by including the k-means clustering time, the average execution time of the proposed approach, for all databases except german and Austration, is considerably better than ODT-SUTSS<sup>1</sup> that of the method proposed by Mohseni et al. [5].

**Figure 4.** Training, test and outlier data distribution

<sup>1</sup> Outlier Detection Test - SUPervised Training Set Selection

**TABLE 7.** Comparison of the execution times

Methods Data sets	Propose Method	Jacard Measure	Cosine Measure	Dice Measure	ODT-SUTSS method
Bcwisconsin	<b>2973</b>	608	2969	1024	4601
Wisconsin	<b>563</b>	207	480	287	974
Australian	5183	98	1671	385	<b>2154</b>
German	8903	67	2586	397	<b>3049</b>
Heart	<b>629</b>	410	629	539	1577
Yeast	<b>1208</b>	909	1163	1120	3192
CTG	<b>1903</b>	1625	1891	1874	5390
Ecoli	<b>195</b>	107	123	117	347
PV	<b>75</b>	41	65	54	160
Pathbas	<b>99</b>	88	97	94	278
R15	<b>240</b>	178	230	213	621
Spr	<b>108</b>	95	103	99	297

For a more accurate comparison, the execution time of the proposed method is calculated for each of jacard, cosine and dice criteria introduced in ODT-SUTSS method and is then compared against the total time and majority voting approach presented by Mohseni et al. [5].

For the ODT-SUTSS method proposed, three different criteria are used to select new training set for each sample of the test set. Then, using the majority voting technique, the outlier detection and predictions are performed. Therefore, the overall execution time given in the last column of Table 7 is higher. Given the results of execution times, the proposed method is faster than ODT-SUTSS method by Mohseni et al. [5] for a majority of cases.

In the following, the accuracy values in the proposed method is compared with ODT-SUTSS method, which is shown in Table 8. As indicated by the results of Table 8, accuracy values in the proposed method for most datasets is equal to ODT-SUTSS and for Yeast dataset the value has increased significantly.

Additionally, the accuracies of German and PV datasets are very close to ODT-SUTSS and are less than other datasets. *E coli* had the lowest accuracy. It should be noted that the accuracy values presented in Table 8 for ODT-SUTSS are the best values obtained for different alphas.

All in all, the interpretations in Table 8 confirms the proposed method achieved an acceptable degree of accuracy.

**TABLE 8.** Comparison of the accuracy

Methods Data set	Propose method	OTD-SUTSS
Bcwisconsin	<b>0.96</b>	0.96

wisconsin	0.69	0.79
Australian	0.79	0.84
german	0.76	0.78
heart	<b>0.84</b>	0.84
Ecoli	0.62	0.86
PV	0.91	0.93
Yeast	<b>0.87</b>	0.63
CTG	<b>0.92</b>	0.92
R15	<b>0.99</b>	0.99
Spr	<b>0.99</b>	0.99
pathbas	<b>0.99</b>	0.99

## 6. CONCLUSIONS

In this paper, a new solution for outlier data detection in test samples and training data selection is proposed. As proposed, the outlier data can be detected and removed through the concepts of standard deviation prior to the classification. 12 different two-class and multi-class data sets were used to evaluate the efficiency of the proposed technique. As proposed, the data within training set are initially divided into several clusters and then, using distance criterion, the closest cluster to the test sample is identified. The data within the selected cluster are then used as the new training set. The standard deviation of the test sample with respect to the new training set is obtained and in case of falling outside the set limits, it is identified as an outlier data. As indicated by the results, the accuracy of classifiers is increased through efficient outlier detection while the execution time is reduced in majority of cases. The proposed method follows an unsupervised training procedure.

## 7. REFERENCES

- Verbiest, N., Derrac, J., Cornelis, C., García, S. and Herrera, F., "Evolutionary wrapper approaches for training set selection as preprocessing mechanism for support vector machines: Experimental evaluation and support vector analysis", *Applied Soft Computing*, Vol. 38, (2016), 10-22. <https://doi.org/10.1016/j.asoc.2015.09.006>
- Liu, C., Wang, W., Wang, M., Lv, F. and Konan, M., "An efficient instance selection algorithm to reconstruct training set for support vector machine", *Knowledge-Based Systems*, Vol. 116, (2017), 58-73. <https://doi.org/10.1016/j.knosys.2016.10.031>
- Zechner, M. and Granitzer, M., "A competitive learning approach to instance selection for support vector machines", in International Conference on Knowledge Science, Engineering and Management, Springer., (2009), 146-157.
- Mohammed, A.M., Onieva, E. and Woźniak, M., "Training set selection and swarm intelligence for enhanced integration in multiple classifier systems", *Applied Soft Computing*, Vol. 95, (2020), 106568. <https://doi.org/10.1016/j.asoc.2020.106568>
- Mohseni, N., Nematzadeh, H. and Akbari, E., "Outlier detection in test samples and supervised training set selection", *International Journal of Nonlinear Analysis and Applications*, Vol. 12, No. 1, (2021), 701-712. <https://dx.doi.org/10.22075/ijnaa.2021.4878>
- Ren, Z., Wu, B., Zhang, X. and Sun, Q., "Image set classification using candidate sets selection and improved reverse training", *Neurocomputing*, Vol. 341, (2019), 60-69. <https://doi.org/10.1016/j.neucom.2019.03.010>
- Santiago-Ramirez, E., Gonzalez-Fraga, J.A., Gutierrez, E. and Alvarez-Xochihua, O., "Optimization-based methodology for training set selection to synthesize composite correlation filters for face recognition", *Signal Processing: Image Communication*, Vol. 43, (2016), 54-67. <https://doi.org/10.1016/j.image.2016.02.002>
- Smiti, A., "A critical overview of outlier detection methods", *Computer Science Review*, Vol. 38, (2020), 100306. <https://doi.org/10.1016/j.cosrev.2020.100306>
- Rath, S., Tripathy, A. and Tripathy, A.R., "Prediction of new active cases of coronavirus disease (covid-19) pandemic using multiple linear regression model", *Diabetes & Metabolic Syndrome: Clinical Research & Reviews*, Vol. 14, No. 5, (2020), 1467-1474. <https://doi.org/10.1016/j.dsx.2020.07.045>
- Chen, T., Martin, E. and Montague, G., "Robust probabilistic pca with missing data and contribution analysis for outlier detection", *Computational Statistics & Data Analysis*, Vol. 53, No. 10, (2009), 3706-3716. <https://doi.org/10.1016/j.csda.2009.03.014>
- Yang, Y., Fan, C., Chen, L. and Xiong, H., "Ipmod: An efficient outlier detection model for high-dimensional medical data streams", *Expert Systems with Applications*, Vol. 191, (2022), 116212. <https://doi.org/10.1016/j.eswa.2021.116212>
- Christy, A., Gandhi, G.M. and Vaithyasubramanian, S., "Cluster based outlier detection algorithm for healthcare data", *Procedia Computer Science*, Vol. 50, (2015), 209-215. <https://doi.org/10.1016/j.procs.2015.04.058>
- Lejeune, C., Mothe, J., Soubki, A. and Teste, O., "Shape-based outlier detection in multivariate functional data", *Knowledge-Based Systems*, Vol. 198, (2020), 105960. <https://doi.org/10.1016/j.knosys.2020.105960>
- Tang, B. and He, H., "A local density-based approach for outlier detection", *Neurocomputing*, Vol. 241, (2017), 171-180. <https://doi.org/10.1016/j.neucom.2017.02.039>
- Wang, B. and Mao, Z., "A dynamic ensemble outlier detection model based on an adaptive k-nearest neighbor rule", *Information Fusion*, Vol. 63, (2020), 30-40. <https://doi.org/10.1016/j.inffus.2020.05.001>
- Karlapalem, K., Cheng, H., Ramakrishnan, N., Agrawal, R., Reddy, P.K., Srivastava, J. and Chakraborty, T., "Advances in knowledge discovery and data mining: 25th pacific-asia conference, pakdd 2021, virtual event, may 11-14, 2021, proceedings, part i, Springer Nature, Vol. 12712, (2021).
- Yang, J., Rahardja, S. and Fränti, P., "Mean-shift outlier detection and filtering", *Pattern Recognition*, Vol. 115, (2021), 107874. <https://doi.org/10.1016/j.patcog.2021.107874>
- Wahid, A. and Annavarapu, C.S.R., "Nanod: A natural neighbour-based outlier detection algorithm", *Neural Computing and Applications*, Vol. 33, No. 6, (2021), 2107-2123. <https://doi.org/10.1007/s00521-020-05068-2>
- Acampora, G., Herrera, F., Tortora, G. and Vitiello, A., "A multi-objective evolutionary approach to training set selection for support vector machine", *Knowledge-Based Systems*, Vol. 147, (2018), 94-108. <https://doi.org/10.1016/j.knosys.2018.02.022>
- Esfandian, N. and Hosseinpour, K., "A clustering-based approach for features extraction in spectro-temporal domain using artificial neural network", *International Journal of Engineering, Transactons B: Applications*, Vol. 34, No. 2, (2021), 452-457. doi: 10.5829/ije.2021.34.02b.17.
- Beulah, D. and Vamsi Krishna Raj, P., "The ensemble of unsupervised incremental learning algorithm for time series data", *International Journal of Engineering, Transactons B: Applications*, Vol. 35, No. 2, (2022), 319-326. doi: 10.5829/ije.2022.35.02b.07.
- Biglari, M., Mirzaei, F. and Hassanpour, H., "Feature selection for small sample sets with high dimensional data using heuristic hybrid approach", *International Journal of Engineering, Transactons B: Applications*, Vol. 33, No. 2, (2020), 213-220. doi: 10.5829/ije.2020.33.02b.05.
- Fränti, P. and Sieranoja, S., "How much can k-means be improved by using better initialization and repeats?", *Pattern Recognition*, Vol. 93, (2019), 95-112. <https://doi.org/10.1016/j.patcog.2019.04.014>
- Luchi, D., Rodrigues, A.L. and Varejão, F.M., "Sampling approaches for applying dbscan to large datasets", *Pattern Recognition Letters*, Vol. 117, (2019), 90-96. <https://doi.org/10.1016/j.patrec.2018.12.010>
- Akbari, E., Dahlan, H.M., Ibrahim, R. and Alizadeh, H., "Hierarchical cluster ensemble selection", *Engineering Applications of Artificial Intelligence*, Vol. 39, (2015), 146-156. <https://doi.org/10.1016/j.engappai.2014.12.005>
- Singh, D., Gosain, A. and Saha, A., "Weighted k-nearest neighbor based data complexity metrics for imbalanced datasets", *Statistical Analysis and Data Mining: The ASA Data Science Journal*, Vol. 13, No. 4, (2020), 394-404. <https://doi.org/10.1002/sam.11463>
- Chen, J., Zhang, C., Xue, X. and Liu, C.-L., "Fast instance selection for speeding up support vector machines", *Knowledge-Based Systems*, Vol. 45, (2013), 1-7. <https://doi.org/10.1016/j.knosys.2013.01.031>
- Nematzadeh, Z., Ibrahim, R. and Selamat, A., "Improving class noise detection and classification performance: A new two-filter cndc model", *Applied Soft Computing*, Vol. 94, (2020), 106428. <https://doi.org/10.1016/j.asoc.2020.106428>
- Speiser, J.L., Miller, M.E., Tooze, J. and Ip, E., "A comparison of random forest variable selection methods for classification prediction modeling", *Expert Systems with Applications*, Vol. 134, (2019), 93-101. <https://doi.org/10.1016/j.eswa.2019.05.028>
- Zhou, Q., Zhou, H. and Li, T., "Cost-sensitive feature selection using random forest: Selecting low-cost subsets of informative

- features", *Knowledge-Based Systems*, Vol. 95, (2016), 1-11. <https://doi.org/10.1016/j.knosys.2015.11.010>
31. Nematzadeh, Z., Ibrahim, R., Selamat, A. and Nazerian, V., "The synergistic combination of fuzzy c-means and ensemble filtering for class noise detection", *Engineering Computations*, (2020). <https://doi.org/10.1108/EC-05-2019-0242>
32. Lee, D.K., In, J. and Lee, S., "Standard deviation and standard error of the mean", *Korean Journal of Anesthesiology*, Vol. 68, No. 3, (2015), 220-223. <https://doi.org/10.4097%2Fkjae.2015.68.3.220>

---

### Persian Abstract

---

#### چکیده

تشخیص دورافتاده تکنیکی برای شناسایی و حذف داده های بسیار متفاوت از داده های صحیح تر و سازگارتر در یک مجموعه داده است. داده های پرت می تواند تأثیر منفی بر عملکرد طبقه بندی و خوشه بندی داشته باشد. که باید شناسایی و حذف شوند تا کارایی طبقه بندی بهبود یابد. صرف نظر از اینکه یک تکنیک طبقه بندی، یک داده پرت را به درستی طبقه بندی می کند یا خیر، خود مفهوم شناسایی داده ها به عنوان پرت از اهمیت زیادی برخوردار است. در این مقاله، یک رویکرد جدید برای تشخیص داده های پرت در مجموعه داده های آزمایشی همراه با انتخاب مجموعه آموزشی بدون نظارت پیشنهاد شده است. مجموعه آموزشی انتخاب شده برای طبقه بندی دو مرحله ای استفاده می شود. پس از خوشه بندی بدون نظارت مجموعه آموزشی، نزدیک ترین خوشه به نمونه آزمایشی با استفاده از اندازه گیری فاصله اقلیدسی انتخاب می شود. سپس، نقطه پرت در نمونه آزمایشی با مفاهیم انحراف معیار و مقدار میانگین شناسایی می شود. نتایج با ارزیابی فاصله هر نمونه از مجموعه آزمون با مجموعه داده انتخابی جدید نشان داده شد. دقت طبقه بندی کننده ها پس از شناسایی و حذف داده های پرت افزایش می یابد.

---



## Multi-criteria– Recommendations using Autoencoder and Deep Neural Networks with Weight Optimization using Firefly Algorithm

G. Spoorthy\*, S. G. Sanjeevi

Department of CSE, NIT Warangal, Warangal, India

### PAPER INFO

#### Paper history:

Received 12 July 2022

Received in revised form 06 October 2022

Accepted 15 October 2022

#### Keywords:

Multi-Criteria Recommendation Systems

Autoencoder

Firefly Algorithm

Deep Neural Networks

Deep Learning

### ABSTRACT

Demand for personalized recommendation systems elevated recently by e-commerce, news portals etc., to grab the customer interest on the sites. Collaborative filtering proves to be powerful technique but it always suffers from data sparsity, cold-start and robustness issues. These issues have been tackled by some approaches resulting in higher accuracy. Few of them take user profiles, item attributes and rating time as the side information along with ratings to give interpretative personalized recommendations. These type of approaches tries to find which factors mainly impacted the user to rate an item. Another approach extends the single-criteria ratings of collaborative filtering to multi-criteria ratings. Our approach exploits non-linear interpretative recommendations by exploring Multi-criteria ratings by combination of Autoencoders with dropout layer and firefly algorithm optimized weights for deep neural networks. Our approach solves data sparsity, scalability issues and fetch accurate recommendations. Experimental evaluations have been done using Yahoo! Movie and MovieLens datasets. Our approach outperforms in robustness and accuracy with respect to previous research works.

doi: 10.5829/ije.2023.36.01a.15

### NOMENCLATURE

RS	Recommendation System	AaRS	Attribute aware Recommendation System
MC	Multi-Criteria	AE	Autoencoder
SC	Single Criteria	DNN	Deep Neural Networks
FA	Firefly Algorithm	U, I, W	Users, Items, Weights
MCAE-	Multi-Criteria based Recommendations using Autoencoder and Deep		
FADNN	Neural Networks with Firefly Algorithms for Weight Optimization		

## 1. INTRODUCTION

Over the past decade, recommendation systems (RS) have got the popularity around many applications. Applications such as e-commerce, news portals, Instagram actively use the RS tools to drag interest of the and so on customers. RS foresee the unknown user interests by past user preferences, product relevance to recommend products that the user may be interested in near future. The popularity of RS is mainly due to dealing the vast data (number of products in catalogue) and producing highly relevant recommendations which help the customers. The main objective of RS is to fetch interesting items/products to the users/customers from the vast list of products that user maybe interested in near

future. It is not surprising RS helps the users to great extent in making decisions and decreases the search time by reducing the search space of a lakh to few tens. RS are also used in software development to learn resources [1]. RS models can be built using content-based filtering (CBF) [2], collaborative filtering (CF) [3-5] and Hybrid (combination) strategies [6]. CF is further divided into user-based CF [3], item-based CF [4] and trust aware CF [7]. The pitfall of traditional RS are data sparsity and cold start issues [8]. Data Sparsity issue is caused due to limited ratings provided by the user and the vast variety of items in catalogue. Cold-start issue is caused due to new users who do not have past history and due to newly uploaded items which does not have a rating yet. To surpass the data sparsity pitfalls, latent vectors are used

\*Corresponding Author Institutional Email: [gspoorthy6@gmail.com](mailto:gspoorthy6@gmail.com)  
(G. Spoorthy)

which lead to the linear models such as PCA [9], Matrix factorization [10]. They are important techniques used with RS. Later on non-linear models such as AutoRec [11], Variational Autoencoder [12] became prominent. To surpass Cold-start pitfalls attribute-aware RS [13] using the user profiles, product attributes came into existence.

Recent years of research saw major setback with the RS using single rating based observations of user preferences. Single rating cannot be the major part of recommendation as it possesses abstract information regarding the basis by which the rating has been given. Such cases lead to inaccurate recommendations. For example, in movie recommendations the rating can be given by a user may be due to his/her interest in a particular genre, or cast, or age of the user. Predominantly based on distinct product attributes and user profiles a user chooses a product. Extending information of users and items can improve prediction accuracy leading to robust recommendations. These Systems are known as Attribute-aware Recommender systems (AaRS). As for the previous research [14], these AaRS can be classified into four types namely: (i) Discriminate Matrix factorization (ii) Generative Matrix factorization (iii) Factorization Machines and (iv) Heterogeneous graphs. The variation of these categories comes from user, product and attributes interactions. Discriminate matrix factorization models take the attributes as the prior input knowledge to latent representation of users/ items as output. Generative matrix factorization models take attribute distributions and rating distributions to learn. Factorization Machines consider the attributes as user identity representation and build latent representations for predicting ratings. Heterogeneous graphs, as the name suggests represents attributes, users and items as heterogeneous graphs and link prediction is viewed as recommendation. Several topics on AaRS [14] are produced by extending matrix factorization, kernel based models, probabilistic models, and models of deep neural networks. Enhancing AaRS can be done using multi-criteria systems (MCs). These systems try to build the user preferences with respect to two or more criteria ratings to attain robust recommendations. For example, movieLens data [15] have cast attribute ratings from the IMDB *url* attribute by which the recommender system can be trained using actor rating, director rating, etc., These MCs try to include the items quality factor for recommender model. MCs gain popularity because of the quality of recommendations and the robustness of the model. Multi-matrix factorization (MMF) [16] calculates the attribute ratings by computing inner product of user latent vectors and attribute latent vectors using MMF. Later on both user preference ratings and attributes overall performance are integrated to generate recommendations. The performance of the above model

depends on the weights chosen for integrating task. MovieANN [17] clusters users and also clusters movies using k-means and x-means respectively. In recommendation phase user and movie clusters are mapped to the target user. A multi layered neural network is used to decide whether to recommend the movie or not. The performance depends on parameters and with linearity of matrix factorization. To surpass this limitation we are using non-linear transformations to enrich beauty of matrix factorization expressiveness. Our model uses a deep neural network and meta-heuristic approach to perform non-linear transformations.

Meta-heuristic algorithms include nature inspired algorithms (such as PSO, FA), evolutionary algorithms (such as GA) tend to get high-level near optimal solutions based on the behaviour of agents (such as particles, firefly and chromosomes). It is said that in literature [18] compared with back propagation (with feed forward network) PSO gives better non-linear function to train neural networks. Meta-heuristic approach gives an optimal solution to many problems and improves the model accuracy. PSO [19], GA [20], FA [21], Projectiles optimization [22], combination of PSO and back-propagation [23] and combination of GA and PSO [24] have been applied in literature to train neural networks.

The deep learning (DL) plays a prominent role in the emerging research domains. DL extracts features that gives more meaning to the data. Neural networks [25] with the non-linear transformations efficiently find the non-linear interactions between users and items. For MCs deep neural networks gives higher quality recommendations. Our models primarily address the following: non-linear transformations for user-item interactions to overcome scalability issue. Quality and robustness of the recommendations are attained by shifting single criteria ratings to MCs. To attain the optimization of weights in the DNN we use Firefly Algorithm. The paper flow goes as follows: Preliminaries are discussed in the section 2. Proposed methodology MCAE-FADNN is described in section 3. Experimental Evaluation is shown in section 4 and finally conclusions described in section 5.

## 2. PRELIMINARIES

Fundamental concepts of MCs, DNN and Firefly algorithm and its importance in dealing with the issues caused by data sparsity, robustness and quality of the RS are discussed below:

**2.1. Problem Definition** Collaborative filtering-based RS attained popularity by computing nearest neighbours of the users who share similar preferences based on the “ratings” given by users for overall product (based on single rating). Technically written as function

of  $U \times I \rightarrow R$  where ‘U’, ‘I’, ‘R’ are set of users, items and ratings respectively. From this data we find patterns that represent the preferences of the users. Single criteria (SC) frameworks try to approximate the utility function.

$$\arg \max_{i \in \text{item}} f(u, i) \forall u \in U, \forall i \in I \tag{1}$$

The model selects ‘k’ items that maximizes Equation (1). But internally, entire model depends on a sparse matrix for the recommendations. For example, in movieLens dataset the utility function is based on the overall rating given by user on a movie i.e., SC. Such ratings may not reflect the user opinion on the movie: like user may like the cast but not the movie (or) user may have liked the movie but not the cast (or) the movie may not be having good visuals etc. To increase the quality of the recommendations and to maximize utility function MC based approaches are being currently used.

**2. 2. Multi-criteria based Recommendations**

MC based Recommendations surpass the limitations of SC by extending utility function from over all item rating score to including all the criteria ratings which effect the opinion of user. Technically written as:

$$f(u, i) = r_1 \times r_2 \times \dots \times r_c \tag{2}$$

where  $r_1, r_2, \dots, r_c$  are the ratings of the item from 1 to c w.r.t ‘c’ criteria.

Users rate the items on different criteria. For instance, movie RS can extend their preferences based on four different criteria namely genres, actors, directors and plot. A user may like the genre and plot but strongly dislikes actors and director has rated the overall rating as 4. The ratings for the users preferences according to the above four criteria are (5, 2, 1, 5). That user preference ratings may be partly or entirely different from other users. Two of the other users might have given the overall rating as 4 but their user preferences for the above four criteria could be for example (4, 3, 1, 5) and (2, 1, 2, 5) respectively. The 3 users maybe classified as similar by SC since it considers only overall ratings. Hence, MCs are preferred over SCs. Table 1 summarized user-item multi-criteria matrix. With the extension of SCs to MCs we need to change our models which can adopt all the rating criteria into the model. Model based approaches

**TABLE 1.** Representation of MCs for user(U), Item(I)

	$i_1$	$i_2$	$i_3$	$i_4$	$i_5$
$u_1$	$4_{(5,2,1,5)}$	$3_{(4,1,2,2)}$			$1_{(2,1,2,2)}$
$u_2$			$5_{(5,NA,4,4)}$		$3_{(2,3,2,3)}$
$u_3$	$4_{(4,3,1,5)}$	$5_{(3,5,4,3)}$			$2_{(4,2,1,1)}$
$u_4$	$1_{(1,2,1,1)}$		$3_{(1,4,1,3)}$	$5_{(5,5,NA,2)}$	
$u_5$	$4_{(2,1,2,NA)}$	$2_{(1,3,3,1)}$			

often learn from the training model and build the prediction model to predict the unknown ratings.

Machine learning models like probabilistic models, SVR, kernel backdrop models are shown to have good prediction accuracy. All these model based techniques have similar aggregate function: the conjunction of all the MC ratings to get overall rating prediction.

**2. 3. Autoencoders**

The objective of Auto-encoder is to attain a ‘d’ dimensional representation (where  $d \ll m$ ) of a matrix  $n \times m \forall \min(\text{Error}(x, \text{decode}(\text{encode}(x)))$ ). In this paper, we learn non-linear latent vectors for users criteria using auto-encoders. For each auto-encoder we give ratings and criteria matrix. The non-linear latent vectors formed from criteria matrix are termed as criteria latent vectors or attribute latent vectors as termed in literature [16]. While performing the task we place the dropout layers (removing the connections temporarily) so that the preference of each criteria gets more elevated. The mathematical formulae for this phase is given below:

Encoder: It encodes high dimensional matrix  $X = \{x_1, x_2, \dots, x_m\}$  to fewer dimensional matrix called hidden representation  $h = \{h_1, h_2, \dots, h_d\}$  by a function ‘f(x)’ having activation function ‘ $a_e$ ’ at encoder

$$h = a_e(W_x + b) \tag{3}$$

In-order to penalize least important data and avoid getting into over-fitting issues we use the dropout layer. The dropout layer temporarily drops the penalized neuron links so that activation function can’t be applied on them.

Decoder: It decodes the hidden representation  $h = \{h_1, h_2, \dots, h_k\}$  back to reconstructed matrix of  $x: x' = \{x'_1, x'_2, \dots, x'_n\}$  by a function  $g(h)$  having activation function  $a_d$  at decoder

$$x' = a_d(W'_h + b') \tag{4}$$

After reconstructing the network error is calculated as follows:

$$\text{Error}(E) = \sum_{x_0 \in X} \|x_0 - g(f(x_0))\|_2^2 + \lambda(\|W_1\|_2^2 + \|W_1\|_2^2) \tag{5}$$

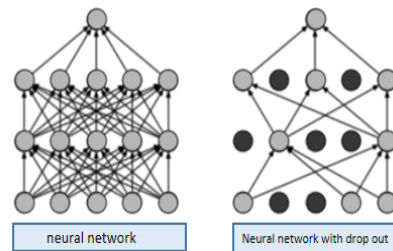


**Figure 1.** Autoencoder and Autoencoder with dropout layer

## 2. 4. Deep Neural Networks for multi criteria based recommendation

Deep learning (DL) possess a vast range of applications namely image processing, natural language processing and computer vision domains. In Recommendation systems data sparsity issues are cleared using DL models. Along with data sparsity issues DL methods try to capture non-linear interactions between users and items. Neural networks surpass limitations of matrix factorization and enhance the approximations. With the explicit SC feed back, AutoRec [11] attains non-linear user item interactions using auto encoder architecture. Auto encoder learns to reprint the input to output to give low-dimensional representations. AutoRec focuses on reconstructing the output layer in such a way that the network fills the missing entries giving more scope to the increase in prediction accuracy. Deep factorization machines [26] learn pairwise-linear interactions between users and items by using multilayer perceptron and deep network models gives high end non-linear interactions. MovieANN [17] combines content based filtering and collaborative filtering models by mapping user and items clusters formed in the initial phase and fed into multilayer perceptron to attain recommendations. DNN based recommendations using MC ratings with stacked encoders are done [27]. In this approach, link between the overall ratings and individual criteria are attained by rigorous adjustment of loss function by changing the weights of hidden layers and the output layer. Later on in DHARS [26] combination of neural collaborative filtering and stacked denising auto encoder enhance the RS accuracy. Comparison of SC based RS and MC based RS is done with an artificial neural network framework [25] proves the MC Based RS outperforms SC based RS.

**2. 5. Firefly Algorithm** Firefly algorithm (FA) proposed by Yang [28], is a meta-heuristic which is nonlinear and stochastic in nature. The entire FA depends on two key points: light intensity and degree of attractiveness between fireflies.

$$I_i = I_0 e^{-\gamma r_{ij}} \quad (6)$$

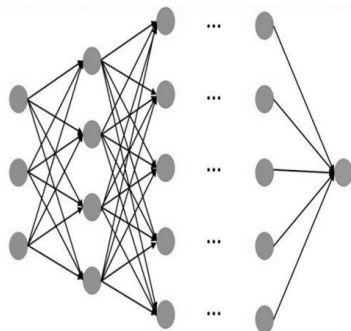


Figure 2. Deep Neural Network

where  $I(i)$  is the light intensity at 'i',  $I(0)$  is the light intensity at  $r(ij)=0$ .

$$\beta_{ij} = \beta_0 e^{-\gamma r_{ij}} \quad (7)$$

where  $\beta(ij)$  is the attraction between 'i' and 'j',  $\beta(0)$  is the initial attraction at  $r(ij)=0$ .

$$x_i = x_i + \beta_{ij}(x_j - x_i) + \alpha \varepsilon_{ij} \quad (8)$$

A meta-heuristic algorithm should deal two components namely exploration and exploitation. The exploration component is also known as intensification. This aspect is achieved by the randomness of the FA. Fine tuning of the randomness will make the FA best with respect to local and global search. The exploitation component is also known as diversification. This aspect is achieved by the knowing the local information. The exploitation increases the convergence speed whereas exploration decreases the convergence speed.

## 3. MCAE-FADNN

This section deals with the proposed algorithm: Multi criteria based recommendations using Autoencoder and deep neural network with weight initialization by Firefly algorithm (MCAE-FADNN). Our model is divided into 3 phases where in the phase 1 deals with predicting missing criteria ratings using AutoEncoder (AE), phase 2 deals with predicting overall ratings for the missing criteria in the training set and phase 3 predicts the recommendations for test set and evaluates the performance of the method.

### 3. 1. Firefly Algorithm for Weight Optimization

Step 1: The initial population and initialize cluster centers are randomly generated.

Step 2: Repeat 3 to 16 from pseudo code.

Step 3: Pick smallest distance of weights from center as weights of MCAE-FADNN.

Firefly algorithm (FA) for weight optimization is given below:

TABLE 2. FA for weight optimization

<p>Initialization:  Maximum iteration <math>T=200</math>, <math>t=1</math>  <math>N_{pop}</math>, <math>m</math>, <math>n</math> are number of population, dimensions and clusters respectively.  <math>\alpha = 0.5</math>  The initial population are randomly generated.  <math>W = \begin{bmatrix} W_1 \\ \vdots \\ W_{N_{pop}} \end{bmatrix}</math>, where  <math>W_i = [w_1, w_2, \dots, w_n], \forall i = 1, 2, \dots, N_{pop}</math>,  <math>C_j = [c_1, c_2, \dots, c_m] \forall j = 1, 2, \dots, n</math>  And <math>w_i = w_i + \text{rand}(0) \times (w_u - w_l)</math></p>
-------------------------------------------------------------------------------------------------------------------------------------------------------------------------------------------------------------------------------------------------------------------------------------------------------------------------------------------------------------------------------------------------------------------------------------------------------------------------------------------------------------------------------------------------------------------------------------------------------------------------

$W_i$  is the solution,  $C_j$  is the  $j^{\text{th}}$  cluster of  $i^{\text{th}}$  solution,  $w_i$  is the position of  $w$  at  $i$ .

**Objective Function**  

$$fitness: d_{w_i, c_j} = \sum_{k=1}^n (w_{ik} - c_{jk})^2$$

1. Initialize each firefly as a cluster  
 $C = \{c_i\} \forall i = 1, 2, \dots, m$
2. Calculate distance between clusters
3. Randomly select  $k$  fireflies
4. Find the initial light intensities using Equation (6)
5. Light intensity at  $I_i$  at  $w_i$  is determined by  $f(x)$
6. While( $t < T$ )
  7. For  $i=1$  to  $m$
  8. For  $j=1$  to  $m$
  9. if ( $I_i < I_j$ )
  10. Move firefly  $i$  to  $j$  using Equation (7)
  11. End if
  12. End For
  13. End For
  14. Update the light intensity  $f(w)$  using Equation (8)
  15.  $t=t+1$
  16. End While
  17. Pick smallest distance of weights from center as weights of MCAE-FADNN  

$$\sum_{w_i \in W} \min_{i,j} (dist(W_i, c_j))$$

**3. 2. Multi-criteria Ratings**

The related work shows the importance of multi- criteria ratings. This section deals with how the criteria ratings are exploited to build fine connections between user preference w.r.t all the criteria. To attain the MC ratings we will append user (U), item (I) and rating (R) matrix to U, I, R, C1,C2,...Ck, where C1,C2,...Ck are ‘k’ different criteria. We explore user interest as shown in Table 1 and consider the matrix is represented as  $R_{k \times n \times m}$ . The entire model works in three phases. The three phases are described below:

**Phase 1:** It starts with taking every criteria as input. In order to increase the credibility of the system and reduce the effect of missing values they are replaced by ‘0’. Then we build the fewer representation of the training data using autoencoder (AE). Dropout layer is appended to AE to get a generalized model which does not suffer from over-fitting. The autoencoder in the decoder layer reconstructs missing values on which we predict the criteria based rankings in training phase.

**Phase 2:** Once the criteria based ranking values of missing values are calculated we normalize them. For deep neural network weights are learnt using firefly algorithm. The above step is to reduce the effect of random weights on the system. Firefly algorithm enables optimized weights of the DNN. Using optimal weights and the normalized rating values as input DNN predicts the overall ratings for missing values.

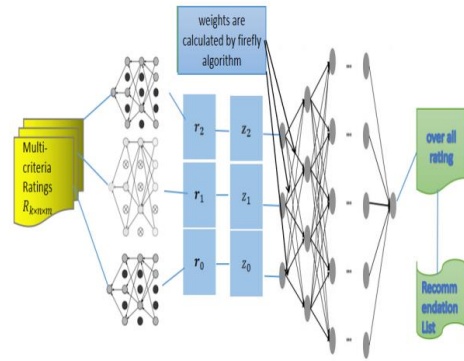


**Figure 3.** MCAE-FADNN

**Phase 3:** In this phase, the prediction task is done for the test set without using dropout layer. Once the overall ratings are calculated the recommendations are made.

**TABLE 3.** MCAE-FADNN (pseudo code)

**Input:**  $R_{k \times n \times m}$   
**Parameter initialization:**  
 Number of epochs:200  
 Number of hidden layers: ‘h’  
 Number of neurons in each hidden layer: ‘l’  
 Learning rate:0.001  
 Dropout:0.1  
 Loss Function : MSE  
**Output:**  $Pred_{n \times m}$   
**Phase1:** Autoencoder AE  
 1: Decompose  $R_{k \times n \times m}$  into ‘k’  $R_{n \times m}$  matrices  
 2: For Each ‘k’  $R_{n \times m}$  criteria based matrix C do  
 3: Update the C matrix with 0 for all missing values (ex: [7 NAN 4 2 1] -> [7 0 4 2 1])  
 4: Split dataset to create training and test datasets (80% and 20%)  
 // constructing fewer representation by building an autoencoder AE  
 5: For each Epoch do  
 6: For each user U in training set R is given as input to AE  
 7: Encode the preferences of users in C by Equation (3). Dropout the neurons with least importance.  
 8: Decode the resultant in 7 by Equation (4)  
 9: Find reconstruction error by Equation (5)  
 10: Update weights and biases of AE  
 11: End For  
 12: End For  
 13: Now the trained network of AE is AE’  
 14: Predict the criteria based ranking for missing values in C using AE’ ( $\{r_0, r_1, \dots, r_k\}$ )  
 15: End For  
**Phase 2:** Train a DNN to predict overall rating  
 16: for each user in U do  
 17: Normalize the ratings input obtained in 15 using mean ( $\mu$ ) and standard deviation( $\sigma$ ) in the below formula  

$$z_i = \frac{r_i - \mu_i}{\sigma_i}$$

```

18: The output of normalization of input vector is
     $Z = [z_0, z_1, \dots, z_k]^T$ 
// Dense ReLU is used as activation function for Z
19: Calculate initial weights using firefly Algorithm
20: For each user u in U do
21:   For each z in Z do
22:     Compute  $\text{ReLU}(z) = \max(z, 0)$ 
23:     For each hidden 'l' layers in L do
24:        $h_l = \text{ReLU}(W_l h_{l-1} + b_l)$ 
25:     End For
26:   Predict overall rating using:
     $r_{ui} = \text{ReLU}(W_L h_{L-1} + b_L)$ 
Phase 3: Recommendation phase
28: for each user u in U and item i in I in test set
29:   Calculate criteria ratings  $[r_0, r_1, \dots, r_k]^T$ 
30:   Normalize  $[r_0, r_1, \dots, r_k]^T$  to  $[z_0, z_1, \dots, z_k]^T$ 
31:   Compute overall rating  $r_{ui}$ 
32:   Recommend items using the ratings  $r_{ui}$ 
33: End For
34: Analyse the Recommendations

```

#### 4. EXPERIMENTAL EVALUATION

We compare our model with AEMC [29], MovieANN [17], Multi-criteria recommendations using stacked encoder [27]. These models are denoted by their respective reference numbers [17, 27, 29] in the graphs shown below in section 4.2.

##### 4.1. Dataset Description

In this paper, for evaluating our model we have used 2 datasets namely: Yahoo!Movie(YM), MovieLens 1M. Yahoo! Movie MC Dataset contains 1716 users, 965 movies and 34800 MC ratings with 4 criteria. A movie is rated by the user in four categories: Actors, Directors, story and visuals. Along with the four criteria ratings, user gives the overall rating for the movie. Overall we have 34800 ratings. As a pre-processing step we transformed the ratings of each criteria from  $A^+, A, A^-, \dots, C^-$  ranging from 1 to 5. For MovieLens 1M dataset, multi-criteria ratings are extracted from IMDB and they are mapped to our MovieLens dataset. A movie is rated by the user in four categories: Actors, Directors, genre and plot. LDA [21] is used if any criteria vaguely structured to make it fit for our model. The parameters shown at the beginning of the Table 3 are used with the MCAE-FADNN algorithm. For criteria ratings, we have set Adam optimizer with learning rate 0.001 and dropout as 0.001. The dropout can happen at any stage of the autoencoder layers. Weights of the DNN are learned by using firefly algorithm.

##### 4.2. Classification of Research Issues

Many recommendation models focus on certain research issues. The research issues maybe scalability, sparsity, cold-start and accuracy. One can consider only one aspect or all aspects. In our model, we focused on dealing sparsity, scalability and accuracy aspects.

Autoencoder with dropout layer is used due to the larger weights of the neural network becoming more complex, making the model vulnerable to over fitting. Dropout layers with autoencoders temporarily drop certain amount of nodes (dropped nodes are temporarily out of reach). This in turn helps the model compute fast and it serves as a regularization model. Autoencoders with drop out layer makes our model deal with the sparse data. If single criteria ratings suffer from sparsity issues there is a possibility for multi-criteria ratings to also suffer from sparsity issues. This part of our model is specifically included for dealing with sparsity issues.

Another issue we handled is scalability issue. Recommendation systems require large amount of data to train the model. Usually clustering methods are used to solve the scalability issues. Recently for deep neural networks the scalability is the prominent issue to deal with when the accuracy of the recommendation model is at stake. To deal with this issue we have used the normalization technique. The normalization is done for each of the criteria ratings given by the user using step 17 in the pseudo code.

The main objective of the multi-criteria based recommendations is to recommend the more relevant recommendations which are based on the overall ratings given by the user. The overall ratings depend on multiple attributes/criteria of an item. The overall ratings are calculated with respect to the preferences of the user. The preferences of different users may be different. Based on the user preferences the weights for the attributes should vary. To capture the user preference we change weights to optimize objective function  $d_{w,c_j}$  shown in Firefly algorithm pseudo code. The weight optimization searches optimal weights which reflect the user preferences. This leads to more prominent and effective solution of recommendations as every aspect of user behaviour have been captured. In the previous research works [30, 31] have used Genetic algorithm (GA) and Particle swarm optimization (PSO) for multi criteria based recommendations. The above models failed to address sparsity and scalability issues. We have addressed them in our model. We have used firefly algorithm for weight optimization. The reason for us to use firefly algorithm is computational cost for firefly algorithm is much less compared to GA and PSO. This has been proved by Yang et al. [32]. He et al. [33] proved that FA is the efficient algorithm as FA deals with both exploration and exploitation components of meta heuristic approaches. PSO doesn't have randomization element making it vulnerable in exploration aspect. The average time complexity of GA, PSO and FA are  $O(n^{3/2} \log n)$ ,  $O(nm)$  and  $O(n \log n)$  respectively, where 'n' is population size, 't' is number of iterations and 'm' is complexity of cost function. The above factors make our model more efficient and accurate.

**4. 3. Evaluation** We compare M.A.E, RMSE, Precision, recall and F2 obtained using MCAE-FADNN with related previous research works AEMC [29], MovieANN [17] and stacked AE [27]. The formulae for calculating M.A.E, RMSE, Precision and recall are shown below.

$$MAE = \frac{\sum_{u,i}^N |r(u,i) - P(u,i)|}{N} \tag{9}$$

where  $r(u,i)$  and  $P(u,i)$  are actual rating and predicted ratings and ‘N’ is number of items.

$$RMSE = \sqrt{\frac{1}{N} \sum_{u,i}^N (P(u,i) - r(u,i))^2} \tag{10}$$

where  $r(u,i)$  and  $P(u,i)$  are actual rating and predicted ratings and ‘N’ is number of items.

$$Precision = \frac{TP}{TP+FP} \tag{11}$$

where TP is True Positives, FP is the False Positives

$$Recall = \frac{TP}{TP+FN} \tag{12}$$

where TP is True Positives, FN is False Negatives

$$MAP = \frac{\sum_{n=1}^K Precision(n) \times Relevant(n)}{MIN\{K, \{Relevant Movies\}\}} \tag{13}$$

For ‘K’ recommendations, Precision(n) is precision and Relevant(n) returns 1 if the item is relevant else 0.

$$F2 = \frac{5 \times Precision \times Recall}{4 \times Precision + Recall} \tag{14}$$

MCAE-FADNN shows that by using AE with dropout layer makes our model deal successfully with over-fitting problem. MCAE-FADNN makes the DNN learn optimized weights. MCAE-FADNN is similar to the approach of AEMC [29] except that it differs by using DNN for aggregation. MCAE-FADNN is similar to MovieANN [17] and stacked AE [27] except that MCAE-FADNN uses weight optimization by Firefly Algorithm (FA) where as MovieANN [17] and stacked AE [27] perform weight optimization using back-propagation learning algorithm. Performance of our model is shown in comparison to [17, 27, 29] using MAE, RMSE, Precision, Recall, MAP and F2.

We varied number of epochs to find how the model is working (Table 4).

**TABLE 4.** MAE and RMSE variations w.r.t epochs

	#Epochs	MAE	RMSE
Yahoo! Movie	50	0.6635	0.7757
Yahoo! Movie	100	0.6303	0.7324
Yahoo! Movie	200	0.6261	0.7094
MovieLense	50	0.6935	0.7757

MovieLense	100	0.6603	0.7424
MovieLense	200	0.6461	0.7294

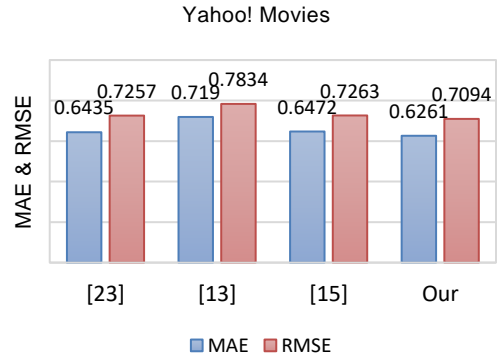


**Figure 3.** Comparison of performance of MCAE-FADNN w.r.t. related research works [17, 27, 29] for Yahoo! Movie dataset

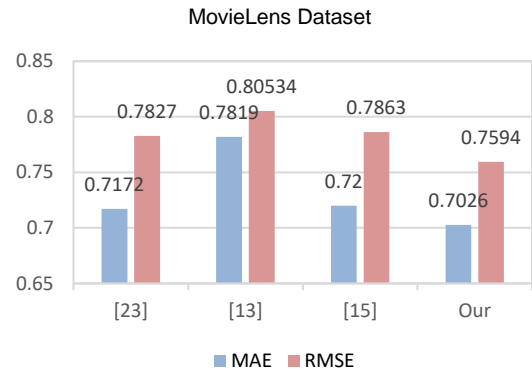


**Figure 4.** Comparison of performance of MCAE-FADNN w.r.t. previous research works [17, 27, 29] for MovieLens dataset

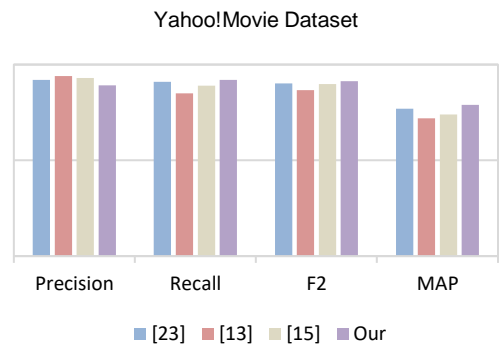


**Figure 5.** MCAE-FADNN performance w.r.t. Precision, Recall, F2 and MAP compared with previous research works [17, 27, 29] for Yahoo! Movies dataset

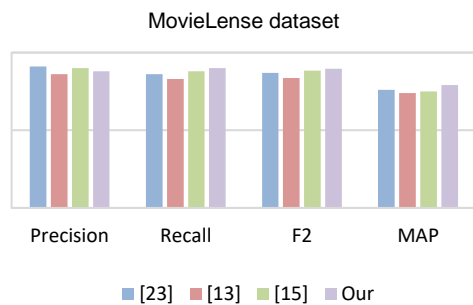


**Figure 6.** MCAE-FADNN performance w.r.t. Precision, Recall, F2 and MAP compared to compared with previous research works [17, 27, 29] for MovieLense dataset

## 5. CONCLUSIONS

Focus in the research of multi-criteria based recommendation systems revolves around the accuracy of the recommendations. In this paper, we focus on dealing with data sparsity, scalability and accuracy issues for recommendation systems. We propose MCAE-FADNN which works in three phases: (i) predicts criteria wise ratings using Autoencoder with dropout layer, (ii) builds non-linear interaction between users and items using DNN with optimized weights attained using firefly algorithm. The phase 1 deals with data sparsity issues. In phase 2 we normalized the predicted ratings in phase 1 to deal with the scalability issues. Along with that in phase 2 using weight optimization technique we increased our model accuracy. These models are multi-criteria based recommendation systems using GA and PSO as prime concepts which dealt with accuracy aspect. Our model outperforms with respect to accuracy, efficiency and computational cost by choosing Firefly technique. Finally, we compared MCAE-FADNN with AEMC, Stacked AE and MovieANN with respect to measures of MAE, RMSE, Precision, Recall, F2 and MAP and showed that using MCAE-FADNN gave better results compared to previous research works AEMC, Stacked AE and MovieANN. We would like to suggest improving the accuracy of the algorithm by dealing the cold-start issues for future scope.

## 6. REFERENCES

1. Tayefeh Mahmoudi, M., Badie, K., Moosaei, M. and Sourji, A., "A compositional adaptation-based approach for recommending learning resources in software development", *International Journal of Engineering, Transactions A: Basics*, Vol. 35, No. 7, (2022), 1317-1329. <https://doi.org/10.5829/ije.2022.35.07a.11>
2. Lops, P., Gemmis, M.d. and Semeraro, G., "Content-based recommender systems: State of the art and trends", *Recommender Systems Handbook*, (2011), 73-105. [https://doi.org/10.1007/978-0-387-85820-3\\_3](https://doi.org/10.1007/978-0-387-85820-3_3)
3. Hofmann, T. and Puzicha, J., "Latent class models for collaborative filtering", in *IJCAI*. Vol. 99, (1999).
4. Linden, G., Smith, B. and York, J., "Amazon. Com recommendations: Item-to-item collaborative filtering", *IEEE Internet Computing*, Vol. 7, No. 1, (2003), 76-80. <https://doi.org/10.1109/MIC.2003.1167344>
5. Ferreira, D., Silva, S., Abelha, A. and Machado, J., "Recommendation system using autoencoders", *Applied Sciences*, Vol. 10, No. 16, (2020), 5510. <https://doi.org/10.3390/app10165510>
6. Konstan, J.A., Riedl, J., Borchers, A. and Herlocker, J.L., "Recommender systems: A groupLens perspective", in *Recommender Systems: Papers from the 1998 Workshop (AAAI Technical Report WS-98-08)*, AAAI Press Menlo Park., (1998), 60-64.
7. Barzegar Nozari, R., Koochi, H. and Mahmodi, E., "A novel trust computation method based on user ratings to improve the recommendation", *International Journal of Engineering, Transactions C: Aspects*, Vol. 33, No. 3, (2020), 377-386. <https://doi.org/10.5829/ije.2020.33.03c.02>
8. Adomavicius, G. and Tuzhilin, A., "Toward the next generation of recommender systems: A survey of the state-of-the-art and possible extensions", *IEEE Transactions on Knowledge and Data Engineering*, Vol. 17, No. 6, (2005), 734-749. <https://doi.org/10.1109/TKDE.2005.99>
9. Vozalis, M.G. and Margaritis, K.G., "A recommender system using principal component analysis", in *Published in 11th panhellenic conference in informatics*, Citeseer. (2007), 271-283.
10. Koren, Y., Bell, R. and Volinsky, C., "Matrix factorization techniques for recommender systems", *Computer*, Vol. 42, No. 8, (2009), 30-37. <https://doi.org/10.1109/MC.2009.263>
11. Sedhain, S., Menon, A.K., Sanner, S. and Xie, L., "Autorec: Autoencoders meet collaborative filtering", in *Proceedings of the 24th international conference on World Wide Web*. (2015), 111-112.
12. Liang, D., Krishnan, R.G., Hoffman, M.D. and Jebara, T., "Variational autoencoders for collaborative filtering", in *Proceedings of the 2018 world wide web conference.*, (2018), 689-698.
13. Vlachos, M., Vassiliadis, V.G., Heckel, R. and Labbi, A., "Toward interpretable predictive models in b2b recommender systems", *IBM Journal of Research and Development*, Vol. 60, No. 5/6, (2016), <https://doi.org/10.1147/JRD.2016.2602097>
14. Chen, W.-H., Hsu, C.-C., Lai, Y.-A., Liu, V., Yeh, M.-Y. and Lin, S.-D., "Attribute-aware recommender system based on collaborative filtering: Survey and classification", *Frontiers in big Data*, Vol. 2, (2020), 49. <https://doi.org/10.3389/fdata.2019.00049>
15. Harper, F.M. and Konstan, J.A., "The movielens datasets: History and context", *Acm Transactions on Interactive Intelligent Systems (tüis)*, Vol. 5, No. 4, (2015), 1-19. <https://doi.org/10.1145/2827872>
16. Su, Y., Erfani, S.M. and Zhang, R., "Mmf: Attribute interpretable collaborative filtering", in *2019 International Joint Conference on Neural Networks (IJCNN)*, IEEE., (2019), 1-8.
17. Yücebaşı, S.C., "Movieann: A hybrid approach to movie recommender systems using multi layer artificial neural networks", *Çanakkale Onsekiz Mart Üniversitesi Fen Bilimleri Enstitüsü Dergisi*, Vol. 5, No. 2, (2019), 214-232. <https://doi.org/10.1007/s00521-022-07012-y>
18. Tallapally, D., Sreepada, R.S., Patra, B.K. and Babu, K.S., "User preference learning in multi-criteria recommendations using stacked auto encoders", in *Proceedings of the 12th ACM conference on recommender systems.*, (2018), 475-479.

19. Ujjin, S. and Bentley, P.J., "Particle swarm optimization recommender system", in Proceedings of the 2003 IEEE Swarm Intelligence Symposium. SIS'03 (Cat. No. 03EX706), IEEE. (2003), 124-131.
20. Kim, K.-j. and Ahn, H., "A recommender system using ga k-means clustering in an online shopping market", *Expert Systems with Applications*, Vol. 34, No. 2, (2008), 1200-1209. <https://doi.org/10.1016/j.eswa.2006.12.025>
21. Spoorthy, G., "Hybrid cluster based collaborative filtering using firefly and agglomerative hierarchical clustering", *International Journal of Computer and Information Technology (2279-0764)*, Vol. 10, No. 6, (2021). <https://doi.org/10.24203/ijcit.v10i6.170>
22. Kahrizi, M. and Kabudian, S., "Projectiles optimization: A novel metaheuristic algorithm for global optimization", *International Journal of Engineering, Transactions A: Basics*, Vol. 33, No. 10, (2020), 1924-1938. <https://doi.org/10.5829/ije.2020.33.10a.11>
23. Zhang, J.-R., Zhang, J., Lok, T.-M. and Lyu, M.R., "A hybrid particle swarm optimization-back-propagation algorithm for feedforward neural network training", *Applied Mathematics and Computation*, Vol. 185, No. 2, (2007), 1026-1037. <https://doi.org/10.1016/j.amc.2006.07.025>
24. Juang, C.-F., "A hybrid of genetic algorithm and particle swarm optimization for recurrent network design", *IEEE Transactions on Systems, Man, and Cybernetics, Part B (Cybernetics)*, Vol. 34, No. 2, (2004), 997-1006. <https://doi.org/10.1109/TSMCB.2003.818557>
25. Hassan, M. and Hamada, M., "A neural networks approach for improving the accuracy of multi-criteria recommender systems", *Applied Sciences*, Vol. 7, No. 9, (2017), 868. <https://doi.org/10.3390/APP7090868>
26. Kiran, R., Kumar, P. and Bhasker, B., "Dnnrec: A novel deep learning based hybrid recommender system", *Expert Systems with Applications*, Vol. 144, (2020), 113054. <https://doi.org/10.1016/j.eswa.2019.113054>
27. Gudise, V.G. and Venayagamoorthy, G.K., "Comparison of particle swarm optimization and backpropagation as training algorithms for neural networks", in Proceedings of the 2003 IEEE Swarm Intelligence Symposium. SIS'03 (Cat. No. 03EX706), IEEE., (2003), 110-117.
28. Yang, X.-S., "Firefly algorithms for multimodal optimization", in International symposium on stochastic algorithms, Springer., (2009), 169-178.
29. Shambour, Q., "A deep learning based algorithm for multi-criteria recommender systems", *Knowledge-Based Systems*, Vol. 211, (2021), 106545. <https://doi.org/10.1016/j.knosys.2020.106545>
30. Gupta, S. and Kant, V., "An aggregation approach to multi-criteria recommender system using genetic programming", *Evolving Systems*, Vol. 11, No. 1, (2020), 29-44. <https://doi.org/10.1007/s12530-019-09296-3>
31. Choudhary, P., Kant, V. and Dwivedi, P., "A particle swarm optimization approach to multi criteria recommender system utilizing effective similarity measures", in Proceedings of the 9th International Conference on Machine Learning and Computing. (2017), 81-85.
32. Yang, X.-S. and He, X., "Firefly algorithm: Recent advances and applications", arXiv preprint arXiv:1308.3898, (2013). <https://doi.org/10.1504/IJSI.2013.055801>
33. He, X., Liao, L., Zhang, H., Nie, L., Hu, X. and Chua, T.-S., "Neural collaborative filtering", in Proceedings of the 26th international conference on world wide web. (2017), 173-182.

---

### Persian Abstract

---

#### چکیده

تقاضا برای سیستم های توصیه شخصی اخیراً توسط تجارت الکترونیک، پورتال های خبری و غیره افزایش یافته است تا علاقه مشتری را در سایت ها جلب کند. ثابت شده است که فیلتر مشارکتی یک تکنیک قدرتمند است، اما همیشه از مشکلات پراکندگی داده، شروع سرد و استحکام رنج می برد. این مسائل با برخی رویکردها حل شده است که منجر به دقت بالاتر می شود. تعداد کمی از آنها نمایه های کاربر، ویژگی های آیتم ها و زمان رتبه بندی را به عنوان اطلاعات جانبی همراه با رتبه بندی ها برای ارائه توصیه های شخصی تفسیری می گیرند. این نوع رویکردها تلاش می کنند تا مشخص کنند چه عواملی عمدتاً بر کاربر برای رتبه بندی یک آیتم تأثیر گذاشته است. رویکرد دیگر، رتبه بندی های تک معیاری فیلترینگ مشارکتی را به رتبه بندی های چند معیاره گسترش می دهد. رویکرد ما از توصیه های تفسیری غیرخطی با بررسی رتبه بندی های چند معیاره با ترکیبی از رمزگذارهای خودکار با وزن های بهینه شده لایه حذفی و الگوریتم کرم شب تاب برای شبکه های عصبی عمیق استفاده می کند. رویکرد ما پراکندگی داده ها، مشکلات مقیاس پذیری و دریافت توصیه های دقیق را حل می کند. ارزیابی های تجربی با استفاده از Yahoo! مجموعه داده های Movie و MovieLens رویکرد ما در استحکام و دقت نسبت به کارهای تحقیقاتی قبلی بهتر عمل می کند.

---



## Application of Finite Element Method for Simulation of Rock Mass Caving Processes in Block Caving Method

B. Alipenhani, H. Bakhshandeh Amnieh\*, A. Majdi

School of Mining Engineering, College of Engineering, University of Tehran, Tehran, Iran

### PAPER INFO

#### Paper history:

Received 18 August 2022

Received in revised form 19 September 2022

Accepted 22 October 2022

#### Keywords:

Block Caving

Numerical Modelling

Cavability

Caving Height

### ABSTRACT

Determining the caving height in the block caving method requires considering a suitable caving criterion discussed in this study. The comparison between different caving criteria and choosing appropriate caving criteria for use in rock mass cavability study is the main idea of this study, which has not been investigated in previous studies. In this paper, through FEM (Finite Element Method) software, the height of the caving area in different undercutting stages was calculated using the criteria of displacement and shear and tensile failure. The results revealed that when using shear and tensile failure, the height of the caving was almost four times higher than the displacement criterion. The height of the caving reaches 249.15 m in this case. However, it is 59 and 107 m considering the allowable displacement and strain criteria, respectively. According to empirical methods, the caving propagated to the highest block height. Thus, the shear and tensile failure criteria predict the caving height better than the displacement criteria.

doi: 10.5829/IJE.2023.36.01a.16

### NOMENCLATURE

MRMR	Mining Rock Mass Rating	GSI	Geological strength index	$S_1$	Maximum principal stress
CPF	Caving Propagation Factor	$\epsilon_{all}$	Allowed strain	$S_3$	Minimum principal stress
FEM	Finite Element Method	$\epsilon_u$	Critical strain	$m_b$	Hoek Brown Constant
$\sigma_c$ , UCS,	Uniaxial Compressive Strength	$U_{max}$	Maximum Displacement	s	
LTCC	Longwall Top Coal Caving	RES	rock engineering system	SRM	Syntetic Rock Mass

## 1. INTRODUCTION

In open pit mines, the ore is extracted from different blocks and benches [1]. There is a possibility of high production. Block caving is the best method to exploit deep mass deposits, competing with open-pit mining [2]. There is some large deposit that extends from the surface to deep underground. Such deposits should be extracted by combining open pit and underground mining methods [3]. In these cases, Block caving is an appropriate option [2].

In the large-scale caving method, it is essential to cave the ore and rock columns [4]. In addition to empirical methods, numerical modelling is used to determine the rock mass cavability. Numerical methods are extensively used in solving stress-deformation boundary value problems related to mining geomechanics. Analytical

methods cannot solve these problems. The problems occur when it is impossible to describe the boundary conditions, such as problem geometry with simple mathematical functions, partial differential equations being nonlinear, the problem space being heterogeneous, or the equations comprising the corresponding rock mass being nonlinear. Such conditions are primarily present in caving analyzes associated with nonlinear definitions and rock mass behaviour [4].

According to Brown [4], reviewing caving mines, numerical modelling provides a more accurate mathematical and fundamental understanding of caving initiation and propagation than empirical (or analytical) methods.

Rock masses are assumed to have continuous behaviour in continuum numerical models since rock mass behaviour is not controlled kinematically by

\*Corresponding Author Institutional Email: [hbakhshandeh@ut.ac.ir](mailto:hbakhshandeh@ut.ac.ir)  
(H. Bakhshandeh Amnieh)

discontinuities. The rock mass characteristics are defined as equivalent, i.e., a combination of intact rock and joints. Also, the response of materials is assumed to be described by the theories of elasticity and plasticity, which are expressed as flexible deformation and plastic yield [5].

In general, the methods used for assessing the rock mass cavability and propagation of caving are divided into three categories: analytical, empirical, and numerical. Tables 1 and 2 show the history of the performed studies in this field.

In past research, different caving criteria were not considered, as shown in Tables 1 and 2. Another issue that has not been investigated in past studies is the height of caving according to different criteria. These two issues are discussed in this paper.

The finite element method is common in solving the problems of tunnels and underground spaces [6, 7]. This paper uses this method to analyze the caving behaviour of the rock mass in the block caving method.

It is essential to choose the rock mass caving criterion to investigate its cavability in the block caving method. The main idea of this paper is to determine the appropriate criteria for rock mass caving. To date, no study has been presented that compares different criteria of displacement, shear and tensile failure, and strain in the rock mass caving in the block caving method. In the present paper, the caving behaviour of the rock mass was evaluated using displacement criteria, shear and tensile failure and strain. On the real scale, numerical modelling on stepwise propagation of undercutting, deformation, induced stresses, and height of caving was calculated and compared.

## 2. RESEARCH METHODOLOGY

The rock mass parameters inserted in the software are critical to achieve a reliable output in modelling with FEM. In a numerical model, the physical and mechanical properties of the rock mass are obtained from the detailed design report of the Iron cap mine [8]. Iron Cap deposit, part of the KSM property located in the Coast Mountains of northwestern British Columbia. The location, dimensions, and dip of the mineralized material at Iron Cap indicated that it was suitable for block caving.

The rock mass characteristics have been obtained using Rock Data software based on the characteristics of intact rock and discontinuities and fractures (including faults and cracks). Therefore, the effect of the geological strength index (GSI) was indirectly investigated. In other words, by entering the value of the geological strength index in the Rock Data software, the output of this software, which is the characteristics of the rock mass, has been used as the input of the FEM software.

The cavability assessments made using Laubscher's and Mathews' methods indicate that the size (diameter) of the footprint required to initiate and propagate caving is approximately 100 m [8]. For better representation, the properties of the rock mass entered in the modelling are presented in Table 3. In this table, UCS shows the uniaxial compressive strength of intact rock, and GSI shows the geological strength index. The undercutting operation is modelled in a 2D finite element environment. Then, the height of the caving is measured considering the two criteria of displacement and shear and tensile failure. Also, Sakurai's critical strain criterion [9] was investigated. The amount of allowed strain was calculated according to the relations provided by Sakurai [10], representing the allowed strain at each step of undercutting and displacement followed by excavation (Equations (1) and (2)). Finally, a suitable criterion is proposed to estimate the caving height in the block caving method.

$$\varepsilon_{all} = \frac{\sigma_c}{E}, \quad (1)$$

$$\varepsilon_u = \frac{U_{max}}{Span} \quad (2)$$

In order to validate the modelling results, Laubscher and Flores' models were used. These two methods are explained below.

**2. 1. Laubscher Caving Chart** In 1990, Laubscher developed the most commonly used method to estimate cavability based on a combination of data from large mines in South Africa. Laubscher's caving chart illustrates the three possible modes as follows [11]:

- No caving (stable);
- Transition status: It is a situation in which caving begins, but its propagation is low.
- Caving: It is a condition in which continuous caving occurs.

Using this chart and determining the mining rock mass rating (MRMR) and the hydraulic radius of the deposit footprint, the status of the rock mass can be determined (Figure 1).

**2. 2. Flores's Coefficient** Flores and Karzulovic [15] proposed a propagation coefficient (CPF) for caving to determine whether the caving is probable, transition, or spontaneous, which is very similar to the transition and stable areas of Laubscher. CPF was defined as the ratio between the difference of the principal stresses in the caving area and the maximum difference of the stresses that the rock mass can withstand (Equation (3)).

$$CPF = \frac{S_1 - S_3}{S_{1Max} - S_3} = \frac{S_1 - S_3}{\sigma_c (m_b \frac{S_2 + S_3}{\sigma_{ci}})^a} \quad (3)$$

**TABLE 1.** History of continuous numerical modelling used for rock mass caving assessment.

References	Purpose and application	Disadvantage
Palama and Agarwal [12]	Numerical modelling of caving progress at the El Teniente mine	The assumption of the environment's elasticity in modelling could not explain the mechanism of stress caving. They are not considering different criteria for caving.
Barla et al. [13]	2D finite element simulation at the Grace Mine in Pennsylvania, USA	This model revealed the limitations of the elastic modelling performed by Palama and Agarwal. They are not considering different criteria for caving.
Rech and Loring [14]	Reproduction of caving conditions at the Henderson mine in Colorado, USA	Lack of modelling the caving propagation and not calculating the height of caving
Singh et al. [15]	Study of caving at the Rajpura Dariba mine using FLAC software	The assumption of elasticity of the environment in modelling They are not considering different criteria for caving.
Lorig [16]	Caving simulation in axial-symmetric models considering cylindrical undercut and lithostatic stress	The difference between the shape of caving in the numerical model and real cases They are not considering different criteria for caving.
Trueman et al. [17]	Determining the amount of stresses in production and undercut production tunnels in some block and panel caving mines as well as the required support system	Lack of modelling of the caving process
Brown [4]	Investigation of the effects of depth, stress, large-scale discontinuities, rock mass strength, and groundwater on the cavability by determining the caving propagation factor (CPF)	The assumption of vertical caving propagation and homogeneous rock mass properties can be considered as the limitations of the practicality of this method (CPF method). They are not considering different criteria for caving.
Yasitli and Unver [18]	Evaluation of the abutment pressure around the face and the type of the material flow into the stope	They aimed to investigate the stress concentration surrounding the undercut face and the type of material flow into the stope.
Pierce et al. [19]	3D Simulation of caving behavior at the Northparkes mine	They are not considering different criteria for caving. They are not calculating the height of the caving.
Beck et al. [20]	Evaluation of the caving propagation behavior in nickel and diamond deposits using Abaqus	They are not considering different criteria for caving. They are not calculating the height of the caving.
Gauri Shankar et al. [21]	Investigation of the effects of mining depth, extraction height, horizontal stresses, immediate roof thickness, immediate roof strength, main roof thickness, and main roof strength on the caving behavior	They are not considering different criteria for caving. They are not calculating the height of the caving.
Woo et al. [22]	Evaluation of subsidence at the Palabora mine using FLAC3D	Lack of modelling of the caving process They are not calculating the height of the caving.
Sainsbury [5]	Studying the caving propagation and subsidence	They are not considering different criteria for caving and using displacement alone. They are not calculating the height of the caving.
Potvin et al. [23]	Centrifuge modelling of caving mechanism using 3DEC and FLAC3D	They are not considering different criteria for caving. Small-scale modelling of caving differs significantly from real-scale results.
Öge et al. [24]	Prediction of cavability in the Top Coal method using the empirical and numerical methods	They are assuming displacement criteria for caving alone. They are not calculating the height of the caving.
Xia et al. [25]	Investigation of the mechanism of ground pressure damage caused by poor undercutting using FLAC3D	They are not calculating the height of the caving. They are not considering different criteria for caving. Lack of modelling of the caving process
Xia et al. [26]	Investigation of the mechanism of ground pressure damage process on the extraction opening during deposit extraction by FLAC3D	They are not calculating the height of the caving. They are not considering different criteria for caving.

**TABLE 2.** History of analytical, Distinct element numerical modelling, physical and other methods used for rock mass caving assessment

Model type	References	Purpose and application	Disadvantage
Analytical	Somehneshein et al.) [27]	Determination of the optimal block size in the block caving method by the analytical method	They are not considering different criteria for caving and using shear strength alone. They are not calculating the height of the caving.
	Gao et al. [28]	Modelling of progressive caving of layers on top of coal mining panel by the long wall method using UDEC	They are not considering different criteria for caving and using displacement alone. They are not calculating the height of the caving.
	Rafiee et al. [11]	Investigating the effect of 7 different parameters on cavability using the SRM technique	They are not calculating the height of the caving. They are not considering different criteria for caving and using displacement alone.
	Song et al. [29]	Numerical modelling based on 3D particles for process simulation (LTCC)	Modelling the discharge process in the LTCC method and not modelling the process of creating an undercut and caving initiations and propagation
Numerical Modelling	Mohammadi et al. [30]	Evaluating the cavability of the immediate roof and estimating the caving span in the long wall method	They are not calculating the height of the caving. They are not considering different criteria for caving and using displacement alone.
	Wang et al. [31]	Investigating the effect of top coal block size on the caving mechanism	They are not calculating the height of the caving. They are not considering different criteria for caving
	Alipenhani et al. [32]	Determination of caving hydraulic radius of rock mass in the block caving method using numerical modelling and multivariate regression	They are not considering different criteria for caving and using displacement alone.
	Alipenhani et al. [33]	Cavability Assessment of Rock Mass in Block Caving Mining Method based on Numerical Simulation and Response Surface Methodology	They are not considering different criteria for caving and using displacement alone.
Physical modelling	Jacobsz and Kearsley [34]	In a centrifuge experiment, the results of placing a weak mass of artificial rock under high and low horizontal stress conditions were examined.	Lack of modelling of the caving process
	Bai et al. [35]	In this study, experiments were performed on two large-scale physical models including sand, gravel, gypsum, and mica to investigate the cavability of top coal with hard rock bands based on two real cases.	They are not calculating the height of the caving. They are not considering different criteria for caving.
	Khosravi et al. [36]	Investigation of caving mechanism in the block caving method using physical modelling	They are not calculating the height of the caving. They are not considering different criteria for caving Small-scale modelling of caving that differs greatly from real-scale results
	Alipenhani et al. [37]	Physical model simulation of block caving in jointed rock mass	Lack of modelling of the caving process in continuum mode
Fuzzy rock engineering system	Rafiee et al. [10]	Investigation of the effective factors on cavability using fuzzy system	They are not calculating the height of the caving. They are not considering different criteria for caving
RES	Rafiee et al. [38]	Investigation of the factors affecting cavability using rock engineering system (RES)	They are not calculating the height of the caving. They are not considering different criteria for caving
Probabilistic	Mohammadi et al. [30]	Presenting a probabilistic model for estimating the minimum caving span in the long wall method	They are not calculating the height of the caving. They are not considering different criteria for caving

**TABLE 3.** Input material parameters are used in numerical modelling [40].

Parameter	UCS (intact rock)	GSI	mi	D	Hoek Brown Criterion			Mohr-Coulomb		Rock Mass Parameters		
					mb	s	a	C	$\varphi$	$\sigma_t$	$\sigma_{cm}$	$E_m$
Unit	MPa	-	-	-	-	-	-	MPa	°	MPa	MPa	GPa
Value	102	65	20	1	2.49	0.0049	0.501	5.18	35.42	0.2	21.9	14.22

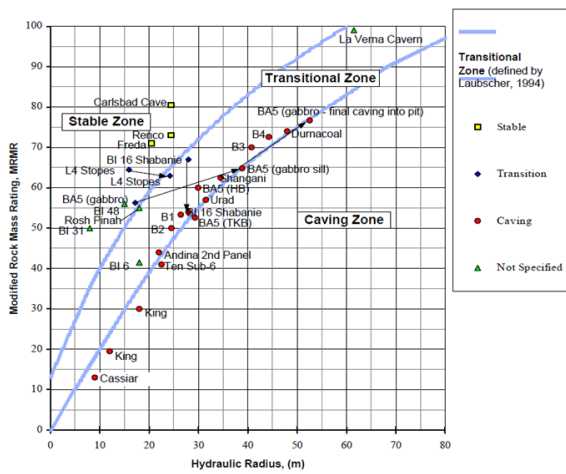


Figure 1. Laubscher caving chart [2]

where  $S_1$  (maximum principal stress) and  $S_3$  (minimum principal stress) are known from the results of the numerical models,  $\sigma_c$  is the uniaxial compressive strength of the intact rock, and  $m_b$ ,  $s$  and  $a$  are material constants that depend on the value of  $m_i$  and the geological strength index of the rock mass, GSI.

The schematic flowchart of the methodology is depicted in Figure 2.

### 3. NUMERICAL MODELLING

**3.1. Development of the Numerical Model** Two-dimensional modelling facilitates entering more details considering the computer capacity available in the model. The model geometry and geomechanical properties used in the modelling were selected based on Iron cap mine data. Based on the typical values mentioned in the international caving study, the width and height of the

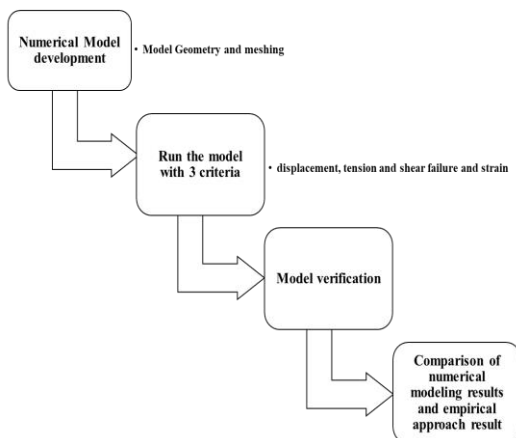


Figure 2. Schematic flowchart of the methodology

undercutting were 100 and 8 m, respectively [6]. The boundary dimensions were 500 m in the horizontal direction (from the edge of the section) and 500 m in the vertical direction. A mesh sensitivity study was conducted on the dimensions (Figure 3). The mesh density was 1500 based on a sensitivity analysis. Figure 4 represents the results of vertical displacement in the center of the undercutting roof for different dimensions of the model boundary distance. The results are considered for the case where the undercut is fully excavated (100 m). Based on the height of the ore block (400 m) in the Iron cap mine and the possibility of displaying the height of the caving area, the whole ore column was modelled. Eight-node elements with four integration points were used to increase the accuracy of the modelling results. Numerical modelling was performed in a continuous environment. Figure 5 represents the model geometry. As seen, the undercutting is excavated in ten steps. The modelling consists of eleven steps, the first of which is to balance the model and the next steps are sequential digging the undercutting.

The shape of the yield zone, the amount of displacement, and the stress changes were measured at different stages of undercutting propagation. After constructing the numerical model and applying the boundary conditions, the model was implemented until equilibrium was reached. Then, the undercutting operation was conducted from the left in steps of 10 m (Figure 5). In caving mines, the undercut excavation steps are usually 10 meters. Accordingly, in the numerical model, the excavation step in each stage is 10 meters. To release the stress and permit the ore to collapse properly, the time steps about 30 minutes were undertaken (in each step). At each stage, displacement and stress values were recorded. In the initial stage, boundary conditions were applied, and the Mohr-Coulomb failure criterion was considered for the materials.

In the numerical model, Mohr-Coulomb behavioural model was used. The model was first balanced with elastic behaviour based on the modelling process. Then, the behavioural model of the rock mass was changed to Mohr-Coulomb, and a undercut was created. The sides of the model were limited in the horizontal direction, and the lower part of the model was limited in the horizontal and vertical directions.

### 4. RESULTS ANALYSIS AND DISCUSSION

Figures 5 and 6 represent the displacement and failure changes at different undercutting stages described in the following lines.

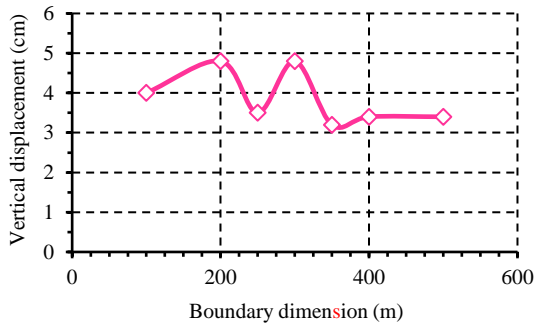


Figure 3. The effect of different boundary distances on modelling results

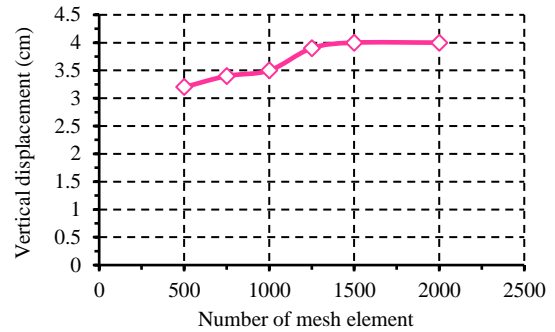


Figure 4. The displacement of the undercutting roof in different dimensions of the element

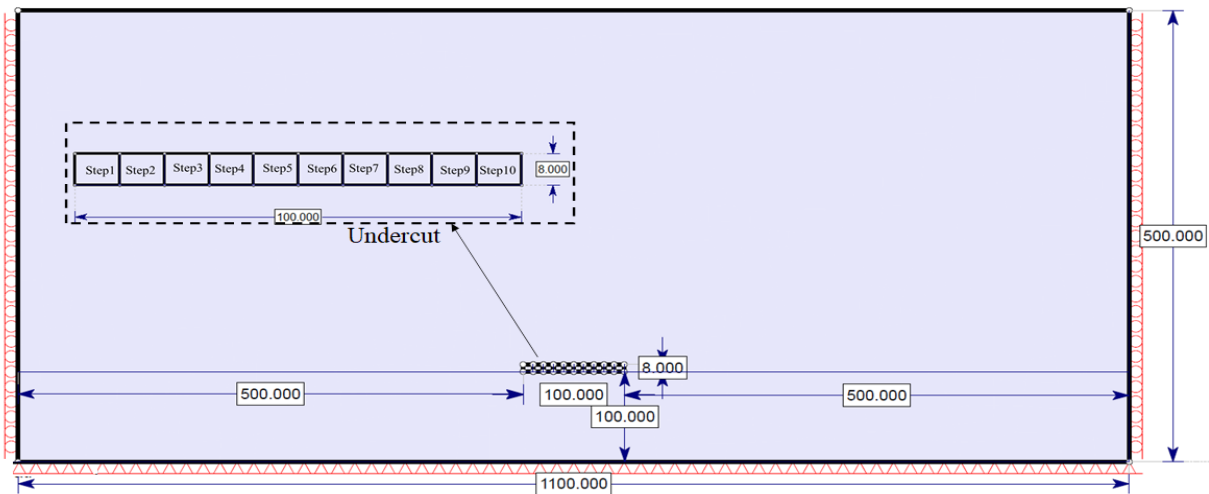


Figure 5. Model geometry and boundary condition

**4. 1. Displacement Changes Around the Undercut**

As it is known, by undercutting operations, the rock mass above the undercutting loses its support and undergoes deformation and failure. In stage 1, where undercutting progresses 10 m, a very small deformation of a few millimetres is observed in the rock mass (Figure 6). Therefore, no failure or caving occurs, and the rock mass remains unchanged at this stage. However, by progressing the undercutting, the maximum amount of stress was created, thus increasing the displacements. According to Sainsbury [5], a displacement of 1 m indicates the caving. Accordingly, in the seventh stage (undercutting width of 70 m), caving initiates. Accordingly, the height of the caved area is 3.44 m. Figure 7 represents the maximum displacement at each stage. As seen, when the undercutting progresses, the amount of displacements increases. The slope of these changes highly increased from the span of 60 m onwards. Up to the 70-meter span, the amount of displacement is less than 1 meter, which indicates that the caving has not been initiated.

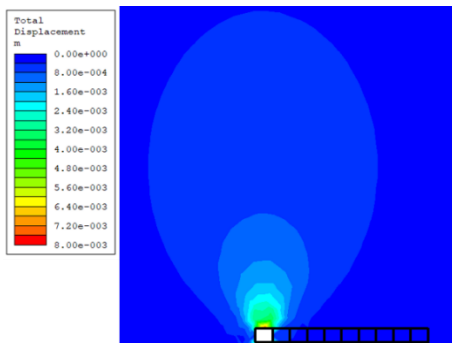
As a result of undercutting, stresses are redistributed

around the undercut. The stress concentration increases on both sides of the undercut. As the undercutting progresses, the de-stressed zone height and stress concentration increase. When the value of this stress concentration reaches a certain level, the materials of the undercut’s roof begin to fail and move (Figures 6 and 7).

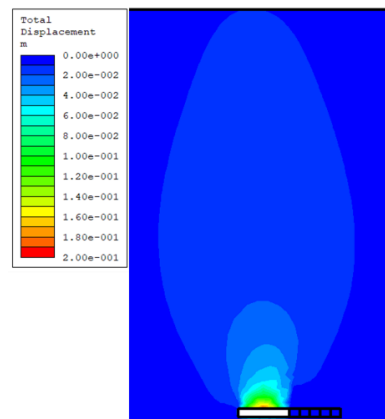
As shown in Figure 6, the caving area is an ellipsoid with a vertical extension. This area is the motion ellipsoid, and the regions with less displacement are called active ellipsoids.

Figure 8 represents the changes in the caved area's height at different undercutting stages. In the 70-meter span where caving occurred, the caving height is limited. As the span increases, the caving height increases up to 60 meters (in a 100-meter span).

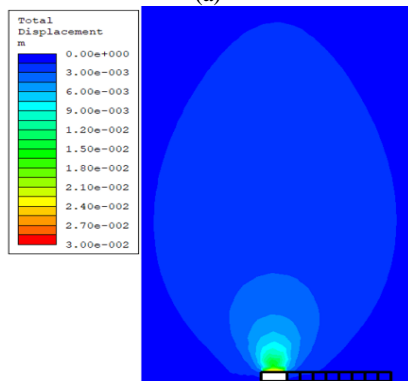
The ratio of the caving height to the span width increases with the increase in the width of the span. This ratio reaches 0.6 at the maximum span (100m), indicating insufficient span width. However, in a mining operation, the span width of 100 meters is enough to cave the entire ore column. This indicates the inappropriateness of displacement criteria for caving.



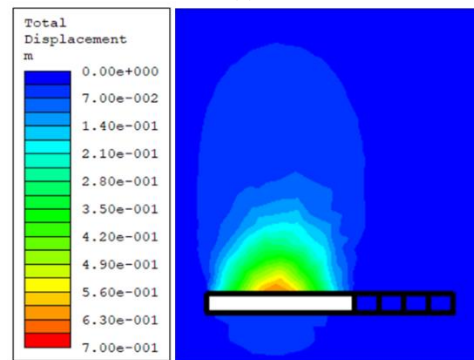
(a)



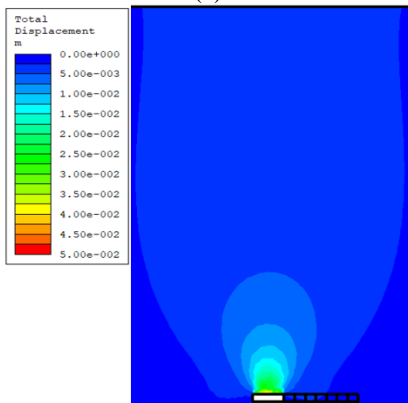
(e)



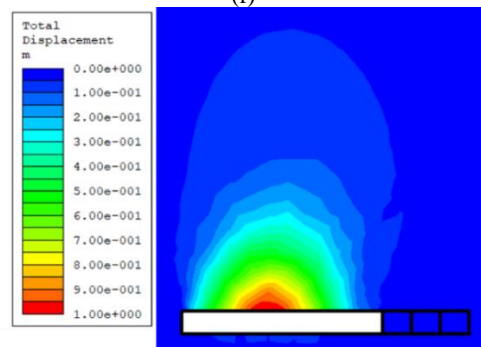
(b)



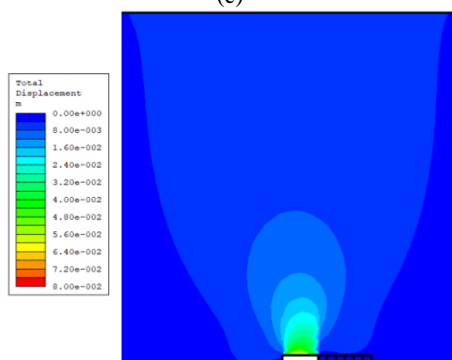
(f)



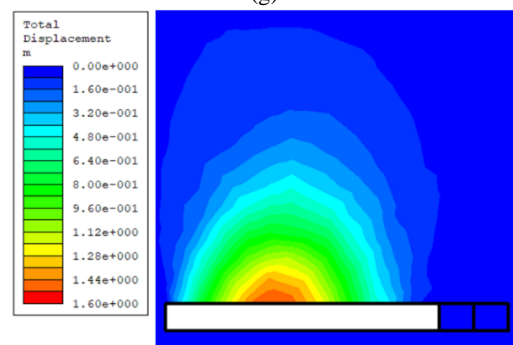
(c)



(g)



(d)



(h)

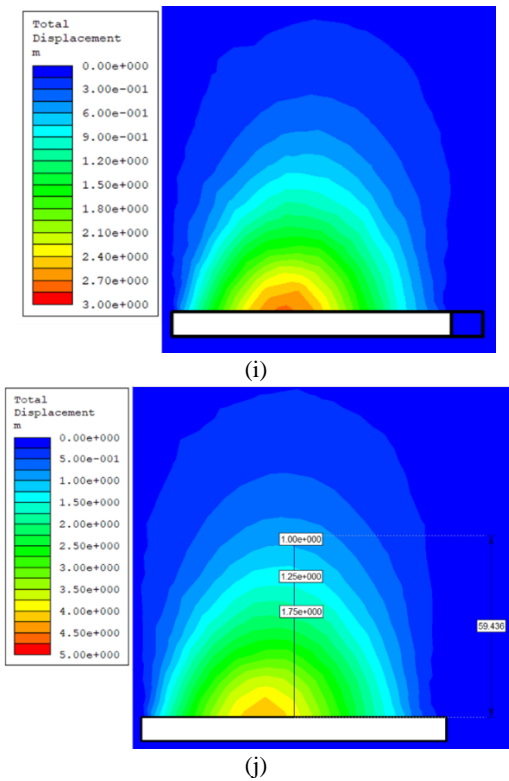


**Figure 6.** Contours of vertical displacement in different sequence :a) stage 1 (span = 10m) b) stage 2 (span = 20m), c) stage 3 (span = 30m), d) stage 4 (span = 40m), e) stage 5 (span = 50m), f) stage 6 (span = 60m). g) stage 7 (span = 70m), h) stage 8 (span = 80m), i) stage 9 (span = 90m), j) stage 10 (span = 100m)

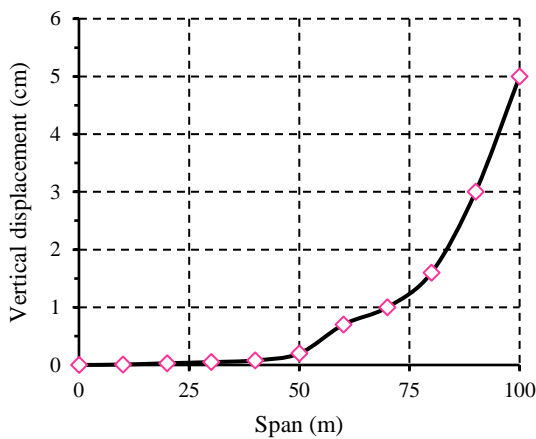


**Figure 7.** Vertical displacement in undercutting stages

**4. 2. Changes in Areas with Failure Around Undercutting**

As stated in section 4.1, in the case using the 1-meter displacement as the caving criterion, the caving initiate from the 70-meter span. However, in

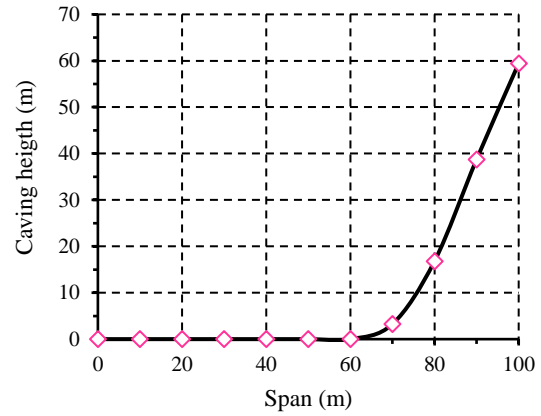


**Figure 8.** Caving height in undercutting stages

the case of using the shear and tensile failure criterion, in the second stage (undercut span of 20 m), some elements experienced tensile, and shear failure and the caving initiate (Figure 9). At this stage, the height of the caved area is 9.51 m. Thus, a shear failure was created. Furthermore, the shape of the caved area is different in the two cases. Likewise, as the undercutting progresses 30 m, the yielded areas increase and widen, thus propagating the caving.

The numerical modelling results confirm that a conceptual model of a self-sustained propagating cave was developed by Duplancic and Brady [38], as shown in Figure 10.

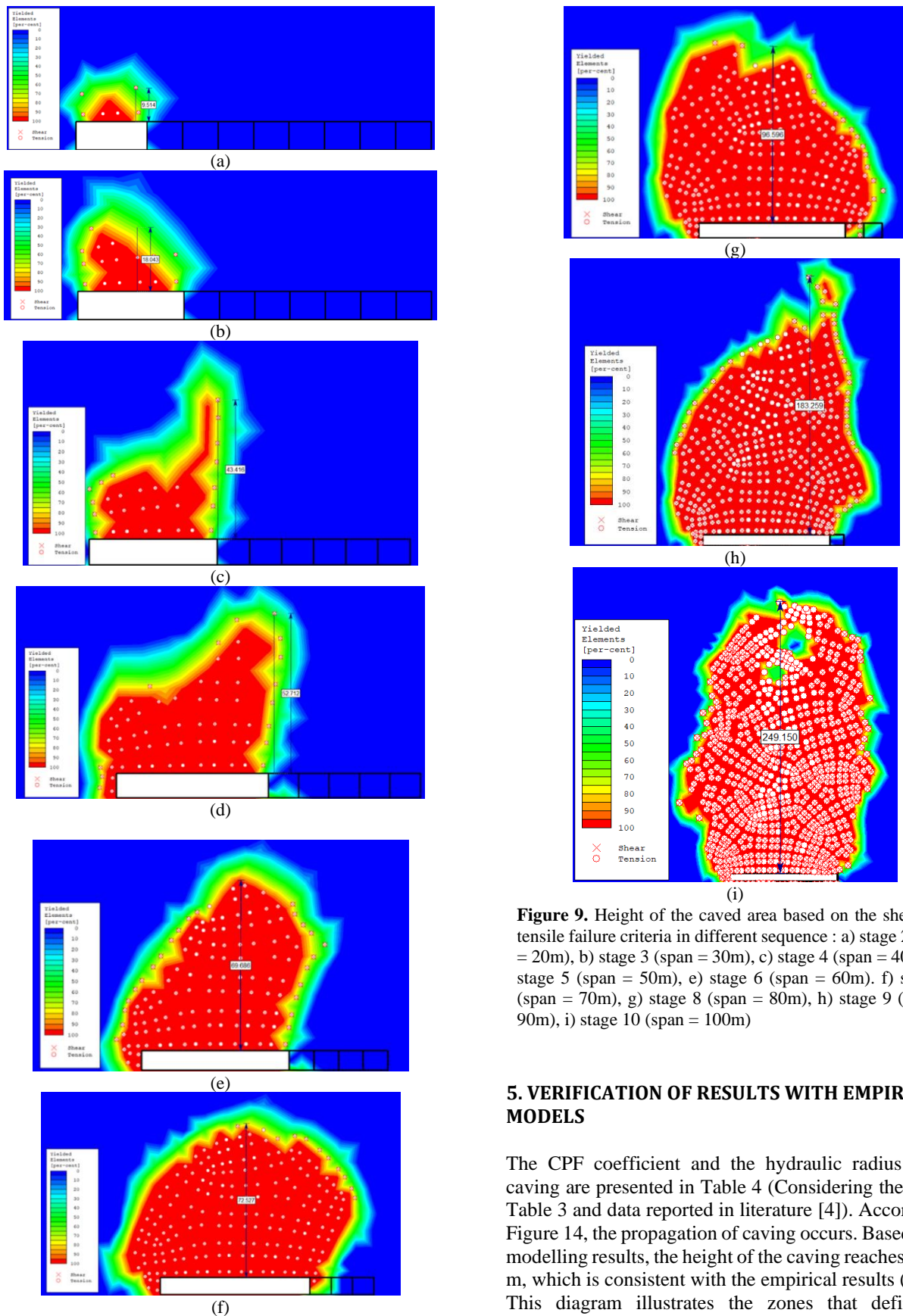
The intact zone at the upper side of the caving zone in the numerical model is the elastic region in Dupancic conceptual model.

Figure 11 shows the results of measuring the height of the caving area based on the shear failure criterion. Figure 12 also shows a diagram based on the results obtained from both criteria and the plastic strain criterion.

As evident in Figure 12, the ratio of the height of the caving zone to the span in the case of considering the criterion of tensile shear failure is higher than in the other two cases (twice as much on average).

The strain contour corresponding to the 100-meter span is shown in Figure 13. As it is known, the caving height obtained from this criterion is higher than the displacement criterion and lower than the tensile failure criterion. It can be said that the strain criterion is more suitable than the displacement criterion to determine the height of the caving.

According to the results, the height of the caving area in the shear and tensile failure criterion is much higher than the displacement criterion. The height of the caving obtained from the strain criterion is within the values obtained from the other two methods.



**Figure 9.** Height of the caved area based on the shear and tensile failure criteria in different sequence : a) stage 2 (span = 20m), b) stage 3 (span = 30m), c) stage 4 (span = 40m), d) stage 5 (span = 50m), e) stage 6 (span = 60m). f) stage 7 (span = 70m), g) stage 8 (span = 80m), h) stage 9 (span = 90m), i) stage 10 (span = 100m)

### 5. VERIFICATION OF RESULTS WITH EMPIRICAL MODELS

The CPF coefficient and the hydraulic radius of the caving are presented in Table 4 (Considering the data in Table 3 and data reported in literature [4]). According to Figure 14, the propagation of caving occurs. Based on the modelling results, the height of the caving reaches 249.15 m, which is consistent with the empirical results (220m). This diagram illustrates the zones that define the

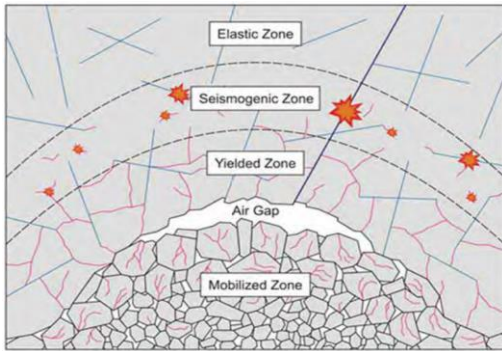


**Figure 10.** Conceptual diagram showing the main behavioural regions of a propagating cave based on underground observations and instrumentation [5]

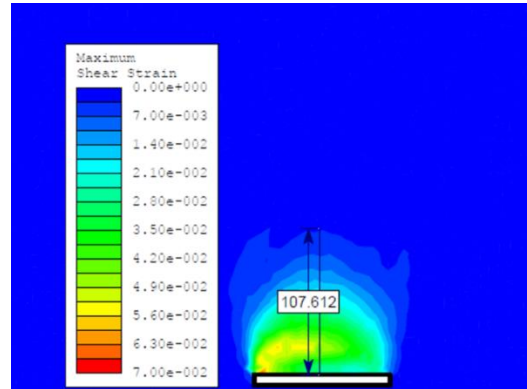


**Figure 13.** The strain contour around undercut (span = 100 m)

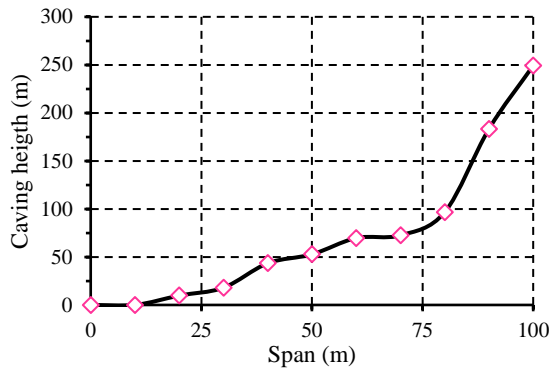


**Figure 11.** Height of the caved area in different undercutting stages based on the shear and tensile failure criteria

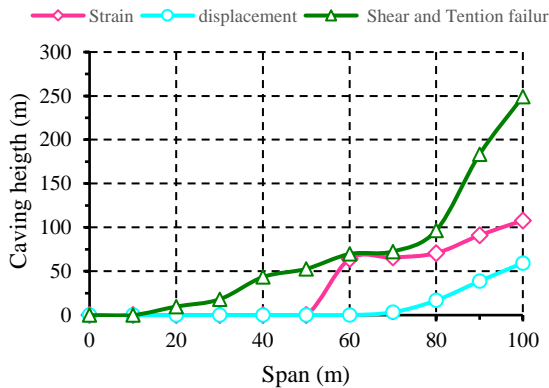


**Figure 12.** The changes in the height of the caved area in different undercutting stages based on different criteria

likelihood of caving propagation in terms of the Caving Propagation Factor. The h/B ratio can be calculated by calculating the CPF.

Moreover, according to the Laubscher diagram, a hydraulic radius of 25 m (100 by 100 m) is enough to start and propagate the caving, which is close to the modelling results.

**TABLE 4.** Determination of caving hydraulic radius based MRRM and presented equation

Factor	Calculated values	rate
Rock block rate	$RBS = 0.8 \times IRS = 0.8 \times 102 = 81.6$	10
joint spacing	2.8m	22
RQD	93%	14
Joint condition	Large scale: Moist, straight, small scale: Moist, rough undulating, No alteration and no filling, $C = 0$ and $\varphi = 30$ ( $40 \times 0.7 \times 0.75 = 27$ )	21
Orientation adjustment	3 joints, 2 inclined (60 degree)	0.8
Water adjustment	An environment without water is considered.	1
Blasting adjustment	None	1
Weathering adjustment	None	1
induced stresses adjustment	Depth of 600 meters	0.9
Sum of rates	82	
MRRM	$67 \times 0.8 \times 0.9 = 48.24$	48
Caving hydraulic radius from Laubscher chart	25 m	
Span (B)	100 m	
CPF	1.13	
h/B	2.2	
H (m)	$2.2 \times 100 = 220$	

RBS = Rock block strength, IRs = Intuit rock strength

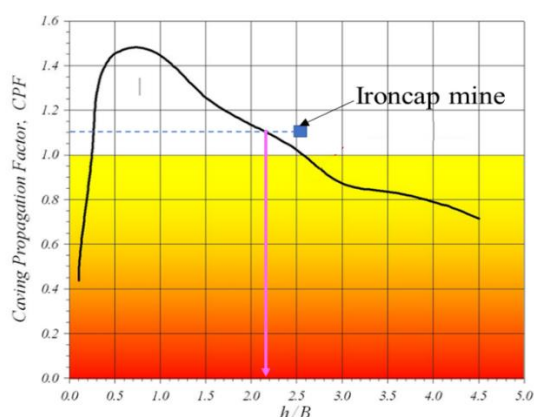


**Figure 14.** The propagation status of Iron cap mine caving using CPF

## 6. CONCLUSION

Block caving has a high production capacity and can be compared with the open pit method regarding operational costs and production rate.

For realistic numerical modelling of the caving mechanism in the block caving method, stresses in the cave back, the displacements, tensile and shear failure, and strain, two-dimensional numerical modelling has been used in FEM software. In addition, the input parameters of the numerical model were obtained from the design report of Iron Cap Deposits.

The caving of the rock mass using displacement criteria, shear, tensile failure, and strain initiated at the span width of 70 meters, 20 meters, and 60 meters, respectively. However, the caving propagations in these spans do not propagate to the top level of the ore block. In order to continue the caving up to the height of the ore block, the span was increased to 100 meters. In this span, the shear and tensile failure criteria have closer results to the actual case than the other two criteria. According to the modelling results, the maximum height of the caving area is obtained using the shear and tensile failure criteria. The height of the caving reaches 249.15 m in this case. However, it is 59 and 107 m considering the allowable displacement and strain criteria, respectively. The predicted caving height using the tensile failure criterion is closer to the empirical results. Moreover, the shape of the caving zone is closer to the shape of the cave back observed in caving mines when using shear and tensile failure criteria.

Using the data of the Iron Cap mine, the value of MRMR 48 is obtained, which is obtained by placing it in the Laubscher chart and using the caving propagation factor. The value of the caving height is 220 meters.

The obtained results largely confirm the general results of previous studies, which shows the reliability of this modelling and its results.

## 5. REFERENCES

- Rahmanpour, M. and Osanloo, M., "Resilient decision making in open pit short-term production planning in presence of geologic uncertainty", *International Journal of Engineering, Transactions A: Basics*, Vol. 29, No. 7, (2016), 1022-1028. doi: 10.5829/idosi.ije.2016.29.07a.18.
- Laubscher, D.H., "Cave mining handbook", *De Beers, Johannesburg*, Vol., No., (2003), 138.
- Soltani Khaboushan, A. and Osanloo, M., "An uncertainty-based transition from open pit to underground mining", *International Journal of Engineering, Transactions A: Basics*, Vol. 32, No. 8, (2019), 1218-1224. doi: 10.5829/ije.2019.32.08b.19.
- Brown, E.T., "Block caving geomechanics", (2002).
- Sainsbury, B., "A model for cave propagation and subsidence assessment in jointed rock masses", University of South Wales, (2012).
- Hematian, J., "Appropriate loading techniques in finite element analysis of underground structures", *International Journal of Engineering, Transactions A: Basics*, Vol. 11, No. 1, (1998), 43-52.
- Ali, D., Abbas, H. and Abdullah, T., "Numerical analysis of stress distribution during tunneling in clay stone rock", *International Journal of Engineering, Transactions A: Basics*, Vol. 33, No. 8, (2020), 1472-1478. doi: 10.5829/IJE.2020.33.08B.05.
- Smolik, J., *Pre-feasibility block cave mine design - iron cap deposit*. 2012: Vancouver: Seabridge Gold Inc.
- Sakurai, S., "Lessons learned from field measurements in tunnelling", *Tunnelling and underground space technology*, Vol. 12, No. 4, (1997), 453-460. doi: 10.1016/S0886-7798(98)00004-2.
- Rafiee, R., Ataei, M., KhalooKakaie, R., Jalali, S.E. and Sereshki, F., "A fuzzy rock engineering system to assess rock mass cavability in block caving mines", *Neural Computing and Applications*, Vol. 27, No. 7, (2016), 2083-2094. doi: 10.22059/IJMG.2022.339663.594953
- Rafiee, R., Ataei, M., KhalooKakaie, R., Jalali, S., Sereshki, F. and Noroozi, M., "Numerical modeling of influence parameters in cavability of rock mass in block caving mines", *International Journal of Rock Mechanics and Mining Sciences*, Vol. 105, (2018), 22-27. <https://doi.org/10.1016/j.ijrmmms.2018.03.001>
- Palma, R. and Agarwal, R., *A study of the cavability of primary ore at the el teniente mine*. 1973, Technical Report from Colombia University, New York.(niepublikowane).
- Barla, G., Boshkov, S. and Pariseau, W., "Numerical modeling of block caving at the grace mine", *Geomechanics Applications in Underground Hardrock Mining, Turyn, Wlochy*, (1980), 241-256.
- Rech, W. and Lorig, L., "Predictive numerical stress analysis of panel caving at the henderson mine", *Proc. of MASSMIN*, Vol. 92, (1992), 55-62.
- Singh, U., Stephansson, O. and Herdocia, A., "Simulation of progressive failure in hanging-wall and footwall for mining with sub-level caving", *Transactions of the Institution of Mining and Metallurgy Section A-Mining Industry*, Vol. 102, (1993), A188-A194.
- Lorig, L., "The role of numerical modelling in assessing caveability", Itasca Consulting Group Inc., Report to the International Caving Study, ICG00-099-3-16, (2000).
- Trueman, R., Pierce, M. and Wattimena, R., "Quantifying stresses and support requirements in the undercut and production level drifts of block and panel caving mines", *International Journal of Rock Mechanics and Mining Sciences*, Vol. 39, No. 5, (2002), 617-632. [https://doi.org/10.1016/S1365-1609\(02\)00060-6](https://doi.org/10.1016/S1365-1609(02)00060-6)

18. Yasitli, N. and Unver, B., "3d numerical modeling of longwall mining with top-coal caving", *International Journal of Rock Mechanics and Mining Sciences*, Vol. 42, No. 2, (2005), 219-235.
19. Pierce, M., Young, P., Reyes-Montes, J. and Pettitt, W., *Six monthly technical report, caving mechanics, sub-project no. 4.2: Research and methodology improvement and sub-project 4.3, case study application. Itasca consulting group, inc., report to mass mining technology project, 2004-2007*. 2006, ICG06-2292-1-Tasks 2-3-14, March.
20. Beck, D., Reusch, F. and Arndt, S., "Estimating the probability of mining-induced seismic events using mine-scale, inelastic numerical models", in *Deep Mining 2007: Proceedings of the Fourth International Seminar on Deep and High Stress Mining*, Australian Centre for Geomechanics., (2007), 31-41.
21. Singh, G.S.P. and Singh, U.K., "Numerical modeling study of the effect of some critical parameters on caving behavior of strata and support performance in a longwall working", *Rock Mechanics and Rock Engineering*, Vol. 43, No. 4, (2010), 475-489. <https://doi.org/10.1007/s00603-009-0061-1>
22. Woo, K.-S., Eberhardt, E., Rabus, B., Stead, D. and Vyazmensky, A., "Integration of field characterisation, mine production and insar monitoring data to constrain and calibrate 3-d numerical modelling of block caving-induced subsidence", *International Journal of Rock Mechanics and Mining Sciences*, Vol. 53, (2012), 166-178. <https://doi.org/10.1016/j.ijrmms.2012.05.008>
23. Cumming-Potvin, D., Wesseloo, J., Pierce, M., Garza-Cruz, T., Bouzeran, L., Jacobsz, S. and Kearsley, E., "Numerical simulations of a centrifuge model of caving", in *Caving 2018: Proceedings of the Fourth International Symposium on Block and Sublevel Caving*, Australian Centre for Geomechanics., (2018), 191-206.
24. Öge, İ.F., "Prediction of top coal cavability character of a deep coal mine by empirical and numerical methods", *Journal of Mining Science*, Vol. 54, No. 5, (2018), 793-803. <https://doi.org/10.1134/S1062739118054903>
25. Xia, Z., Tan, Z., Pei, Q. and Wang, J., "Ground pressure damage evolution mechanism of extraction level excavations induced by poor undercutting in block caving method", *Geotechnical and Geological Engineering*, Vol. 37, No. 5, (2019), 4461-4472. <https://doi.org/10.1007/s10706-020-01264-y>
26. Xia, Z., Tan, Z. and Miao, Y., "Damage evolution mechanism of extraction structure during mining gently dipped orebody by block caving method", *Geotechnical and Geological Engineering*, Vol. 38, No. 4, (2020), 3891-3902. <https://doi.org/10.1007/s10706-020-01264-y>
27. Somehreshin, J., Oraee-Mirzamani, B. and Oraee, K., "Analytical model determining the optimal block size in the block caving mining method", *Indian Geotechnical Journal*, Vol. 45, No. 2, (2015), 156-168. <https://doi.org/10.1007/s40098-014-0119-1>
28. Gao, F., Stead, D. and Coggan, J., "Evaluation of coal longwall caving characteristics using an innovative udec trigon approach", *Computers and Geotechnics*, Vol. 55, No., (2014), 448-460.
29. Song, Z. and Konietzky, H., "A particle-based numerical investigation on longwall top coal caving mining", *Arabian Journal of Geosciences*, Vol. 12, No. 18, (2019), 1-18. <https://doi.org/10.1007/s12517-019-4743-z>
30. Mohammadi, S., Ataei, M., Kakaie, R., Mirzaghobanali, A. and Aziz, N., "A probabilistic model to determine main caving span by evaluating cavability of immediate roof strata in longwall mining", *Geotechnical and Geological Engineering*, Vol. 39, No. 3, (2021), 2221-2237. <https://doi.org/10.1007/s10706-020-01620-y>
31. Wang, J., Wei, W., Zhang, J., Mishra, B. and Li, A., "Numerical investigation on the caving mechanism with different standard deviations of top coal block size in ltcc", *International Journal of Mining Science and Technology*, Vol. 30, No. 5, (2020), 583-591. <https://doi.org/10.1016/j.ijmst.2020.06.001>
32. Alipenhani, B., Majdi, A. and Bakhshandeh Amnieh, H., "Determination of caving hydraulic radius of rock mass in block caving method using numerical modeling and multivariate regression", *Journal of Mining and Environment*, Vol. 13, No. 1, (2022), 217-233. doi: 10.22044/jme.2022.11589.2149.
33. Alipenhani, B., Majdi, A. and Bakhshandeh Amnieh, H., "Cavability assessment of rock mass in block caving mining method based on numerical simulation and response surface methodology", *Journal of Mining and Environment*, Vol. 2, (2022), 579-606. <https://doi.org/10.22044/jme.2022.11858.2176>
34. Jacobsz, S., Kearsley, E., Cumming-Potvin, D. and Wesseloo, J., *Modelling cave mining in the geotechnical centrifuge*, in *Physical modelling in geotechnics*. 2018, CRC Press.809-814.
35. Bai, Q., Tu, S. and Wang, F., "Characterizing the top coal cavability with hard stone band (s): Insights from laboratory physical modeling", *Rock Mechanics and Rock Engineering*, Vol. 52, No. 5, (2019), 1505-1521. <https://doi.org/10.1007/s00603-018-1578-y>
36. Heydarnoori, V., Khosravi, M.H. and Bahaaddini, M., "Physical modelling of caving propagation process and damage profile ahead of the cave-back", *Journal of Mining and Environment*, Vol. 11, No. 4, (2020), 1047-1058. doi: 10.22044/jme.2020.9845.1908.
37. Alipenhani, B., Bakhshandeh Amnieh, H. and Majdi, A., "Physical model simulation of block caving in jointed rock mass", *International Journal of Mining and Geo-Engineering*, (2022). doi: 10.22059/IJMG.2022.339663.594953.
38. Rafiee, R., Ataei, M., Khalokakaie, R., Jalali, S.M.E. and Sereshki, F., "Determination and assessment of parameters influencing rock mass cavability in block caving mines using the probabilistic rock engineering system", *Rock Mechanics and Rock Engineering*, Vol. 48, No. 3, (2015), 1207-1220. <https://doi.org/10.1007/s00603-014-0614-9>

---

**Persian Abstract**

---

**چکیده**

تعیین ارتفاع تخریب در روش تخریب بلوکی مستلزم در نظر گرفتن معیار مناسب به عنوان معیار تخریب است که در این تحقیق به آن پرداخته شده است. مقایسه معیارهای مختلف تخریب و انتخاب معیار تخریب مناسب برای استفاده در مطالعه قابلیت تخریب توده سنگ ایده اصلی این تحقیق است که در مطالعات قبلی مورد بررسی قرار نگرفته است. در این مقاله با استفاده از نرم افزار اجزاء محدود ارتفاع ناحیه تخریب در مراحل مختلف زیربرش با استفاده از معیارهای جابه‌جایی و شکست برشی و کششی محاسبه شد. نتایج نشان داد که هنگام استفاده از معیار شکست برشی و کششی، ارتفاع تخریب تقریباً ۴ برابر بیشتر از معیار جابه‌جایی است. ارتفاع تخریب در این مورد به ۲۴۹.۱۵ متر می‌رسد. اما این مقدار بر اساس معیارهای جابه‌جایی و کرنش مجاز به ترتیب ۵۹ و ۱۰۷ متر است. طبق روش‌های تجربی، تخریب تا بالاترین ارتفاع بلوک ماده معدنی گسترش می‌یابد. بنابراین، معیار شکست برشی و کششی، ارتفاع تخریب را بهتر از معیار جابه‌جایی پیش‌بینی می‌کند.

---



## Energy Harvesting from Vibrating Cantilever Structure of Different Base Materials using Piezoelectric Material: Theoretical and Experimental Approach

A. Krishna, S. Palanivelu\*

Vehicle Dynamics Laboratory, Department of Automotive Engineering, School of Mechanical Engineering, Vellore Institute of Technology, Vellore, India

### PAPER INFO

#### Paper history:

Received 14 June 2022

Received in revised form 27 October 2022

Accepted 03 November 2022

#### Keywords:

Piezoelectric Material

Frequency Spectrum Analysis

Energy Harvesting

### ABSTRACT

Energy conversion from one form to the other forms the basis for many inventions. Non utilized energy of mechanical vibration has attracted many researchers to focus on energy harvesting from vibrating structures. Piezoelectric material when attached to a vibrating structure converts mechanical energy into electrical energy. Today, harvesting energy ranges from micro level to macro level and has obtained its importance in wide range of real time application such as from low powered electronic devices to solar, wind and hydroelectric energy systems, respectively. The current work presents a detailed theoretical and experimental study on a cantilever type beam structure embedded with piezoelectric material on different base materials to understand micro level energy harvesting. Euler Bernoulli beam theory based mathematical model is excited with an impulse load at the free end for a broader frequency spectrum analysis. Finally, the proposed energy harvesters, cantilever specimens of three different base materials are ranked based on their maximum voltage and maximum instantaneous power outputs experimentally for the given impulse excitation. Out of three base materials considered steel and copper-based energy harvesters generated a maximum voltage output of 0.16mV and 0.13mV, respectively which corresponds to a maximum instantaneous power output of approximately 1.96nW and 1.69nW, respectively. Aluminum-based energy harvester performed the least among the three contributing to 0.81nW.

doi: 10.5829/ije.2023.36.01a.17

### NOMENCLATURE

$\omega$	Angular natural frequency		
$A(x)$	Area	$h_b$	Height of the base layer
$YI$	Bending modulus	$h_p$	Height of the piezoelectric layer
$\varepsilon_1$	Axial strain	$L$	Length
$\sigma_1$	Bending stress	$R_L$	Load resistance
$B$	Breadth	$m$	Mass
$i(t)$	Current	$r$	Mode number
$\rho$	Density	$M(x, t)$	Moment function
$W(x, t)$	Displacement function	$\varepsilon_{33}^s$	Permittivity at constant strain
$T_r(t)$	Displacement function with 't' variable alone	$\varepsilon_{33}^T$	Permittivity at constant stress
$\varphi_r(x)$	Displacement function with the 'x' variable alone	$d_{31}$	Piezoelectric moduli
$x$	Distance	$V(x, t)$	Shear force function
$h_{pc}$	Distance between the neutral axis of layers	$C_s$	Strain rate damping coefficient
$q(t)$	Electric charge	$C_a$	Viscous air damping coefficient
$D$	Electric displacement vector	$t$	Time
$E$	Electric field	$v(t)$	Voltage
$f(x, t)$	Force function	$Y_b$	Young's modulus of the base material
$P_y$	Impulse Load	$Y_p$	Young's modulus of piezoelectric material

\*Corresponding Author Institutional Email: [psakthivel@vit.ac.in](mailto:psakthivel@vit.ac.in)  
(S. Palanivelu)

Please cite this article as: A. Krishna, S. Palanivelu, Energy Harvesting from Vibrating Cantilever Structure of Different Base Materials using Piezoelectric Material: Theoretical and Experimental Approach, *International Journal of Engineering, Transactions A: Basics*, Vol. 36, No. 01, (2023), 152-162

## 1. INTRODUCTION

Piezoelectric, magnetostrictive, electromagnetic and electrostatic are the most researched energy harvesting technologies from environmental vibration in recent years due to their appreciable advantages such as fewer constraints in utilization, accessibility and availability in abundance in nature. Among these methods, piezoelectric energy transduction procedure is highly reliable and popular for the following reasons; Bulky bias magnets and pickup coils, makes the Magnetostrictive transduction method highly nonlinear and complicated. Chae et al. [1] proposed a linear energy harvester based on the electromagnetic principle used in a combination of a sliding permanent magnetic array and a ferrofluid as a lubricant. Deng and Dapino [2] have published a review article on magnetostrictive vibration energy harvesters and their advantage over electrochemical batteries which requires frequent recharging. Due to the simplicity in implementation and high-reliability piezoelectric energy transduction devices are of great interest in recent years [3]. Lafarge et al. [3] presented their idea of harvesting energy using piezoelectric cantilever beams on a vehicle suspension with a validated simulation with prototype testing in the laboratory.

Today, we could witness there are many application areas, to mention a few, healthcare and lifestyle industries and automotive industries use extensively the application of wireless sensor networks such as electrocardiogram (ECG) patch, autonomous health monitoring systems, heart rate measurement sensors, tire pressure tracking system, assist technologies like antilock brake system (ABS) and traction control system (TCS), respectively. It requires uninterrupted power supply to sensors for their optimal performance. Vullers et al. [4] published their work on energy harvesting methods for such autonomous wireless sensor networks. Application of piezoelectric transducers bonded with the structure can be used for its health monitoring. One such application of piezoelectric transducers is reported in the article published by Delebarre et al. [5] for aeronautical composite structures in their production line. Another novelty in using piezoelectric materials in the automotive tire application is the direct conversion of energy obtained due to strain into electrical energy and the work carried out by Van Den Ende et al. [6] is an evidence for the same. Piezoelectric transducers can be accounted for harvesting energy from pneumatic tires due to the deflection it produces during loading. Khameneifar and Arzanpour [7] used stacked piezoelectric material inside the pneumatic tire structure to harvest energy from its vibration. The work carried out by Chan [8] emphasizes the application of piezoelectric energy harvesting method from bus vibration in the low frequency range up to 14

Hz to the tune of 90  $\mu$ W.

Geometrical aspects are very important for energy harvester. The work of Wu et al. [9] on an asymmetric type M-shaped cantilever with three proof masses at the end, a longitudinal zigzag structure proposed by Zhou et al. [10] enhances energy harvesting from low frequency vibration. A power peak of 330 $\mu$ W was observed at a resonant frequency of 16 Hz was reported by Zhao et al. [11] with an elastic thin beam of spiral shape model. Muthlif and Nordin [12] studied the effect of varying the dimensions of the piezoelectric cantilever beam from the voltage generation. Erturk et al. [13] reported a model consists of electromechanical elements with an L-shaped structure of a vertical and a horizontal thin beam, with lumped masses so that the conventional cantilever beams have almost similar resonant frequencies. A power of 0.65mW was produced at a frequency of 1.71 kHz over the resistance 5.6k $\Omega$  at 80 N force by a 25mm diameter piezoelectric membrane was reported by Ericka et al. [14] from an unimorph membrane. Tadi Beni et al. [15, 16] investigated with the help of nonlinear formulation of isotropic piezoelectric Euler-Bernoulli nano-beam formed the basis for low energy harvesting at nanolevel. Fakharian [17], designed a planar monopole antenna, a lowprofile structure with a fractal geometry based thin radiation patch material, that can operate at 10-dB impedance bandwidth from 0.92 to 2.58 GHz.

A state of the art review papers published by Wei and Jing [18], Dixit et al. [19] and Mahidur et al. [20] on various energy harvesting techniques and their wide range of viable applications is very interesting to read and comprehend our understanding of the topic well. Roundy and Wright [21] developed a power generating MEMS device with a thin-film piezoelectric material that offered a high power density. The cantilever model is fitted with a bimorph structure having proof mass added to its end to reduce its resonant frequency. It was found that a model of 170 $\times$ 260  $\mu$ m size generated 1  $\mu$ W of uninterrupted electrical power. Erturk and Inman [22] concluded based on their analytical study, a design that would generate a power of up to 250  $\mu$ W/cm<sup>3</sup> upon an excitation frequency of 120 Hz at 2.5 m/s<sup>2</sup>. Jia et al. [23] proposed a piezoelectric material based bimorph structure with more degrees of freedom model that improved energy harvester bandwidth from 6 Hz to 24 Hz. Shams Nateri and Azizollah Ganji [24] studied the effect of piezoelectric material properties on MEMS based hydrophone.

This paper presents micro level energy harvesting from a cantilever beam with three different base material when they are embedded with piezoelectric material through a detailed analytical formulation based on Euler Bernoulli beam theory with complementary finite element modal analysis and appropriate experimental study.

**2. MATHEMATICAL MODELING**

**2. 1. Euler Bernoulli Beam**

An unimorph cantilever shaped piezoelectric energy harvester is illustrated in Figure 1. Simialr formaulaton can be observed from the paper published by Muthlif and Nordin [12] and Shah-Mohammadi et al. [25] to model a cantilever beam for energy harvesting study. A perfect bond is assumed to exist between the non-active and the active layers of the unimorph beam. The breadth of the beam is  $b$  in the Y-Z plane. The model is assumed to have a uniform cross-section and remains normal to the axis of deformation after deformation.

Also, strain rate (internal) and air (external) around the structure constitute the damping mechanism to account damping properties of the model. An impulse excitation  $P_y$  is given at the free end of the beam at time  $t=0$  s as shown in Figure 1. The electromechanically coupled equation obtained for the beam responses is solved using the separation of variables. The decoupled solution for the electrical and mechanical responses is determined using MATLAB.

In this section, the basic governing equation is formulated for an Euler Bernoulli Beam from the basic force balance and moment balance equations. A small section of elemental length ' $dx$ ' as revealed in Figure 2 taken at a distance ' $x$ ' from the fixed end. Figure 3 shows the free body diagram of the element, to represent the shear force and bending moment acting on the element that is taken for developing the mathematical differential equations and later integrated to the entire length with cross section shown in Figure 4 to obtain the general equation for the transverse displacement of the composite beam.

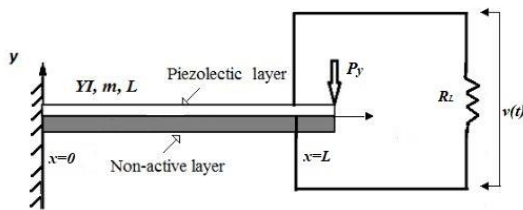


**Figure 1.** Piezoelectric energy harvester cantilever model

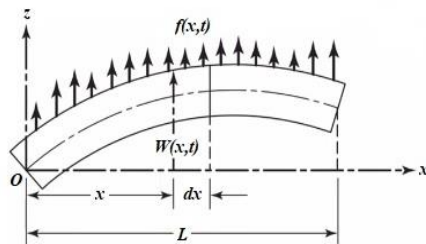


**Figure 2.** Euler Bernoulli Beam

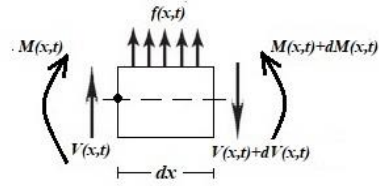


**Figure 3.** Cut section of Euler Bernoulli Beam

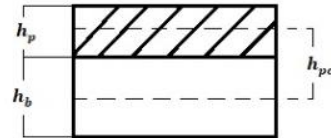


**Figure 4.** Cross-sectional view of the cantilever beam

Force equation:

$$\rho[A(x)]dx \frac{\partial^2 w(x,t)}{\partial t^2} = V - (V + dV) + f(x, t)dx \tag{1}$$

Moment equation:

$$(M + dM) - M - ((V + dV)dx) + f(x, t)dx \frac{dx}{2} = 0 \tag{2}$$

$$dV = \frac{\partial V}{\partial x} dx \tag{3}$$

$$dM = \frac{\partial M}{\partial x} dx \tag{4}$$

Substituting Equation (3) into Equation (1) leads to,

$$\rho A(x)dx \frac{\partial^2 W(x,t)}{\partial t^2} = -\frac{\partial V}{\partial x} dx + f(x, t)dx \tag{5}$$

Substituting Equations (3) and (4) in Equation (2) leads to:

$$\frac{\partial M}{\partial x} dx - Vdx - \frac{\partial V}{\partial x} dx^2 + f(x, t) \frac{dx^2}{2} = 0 \tag{6}$$

The term  $dx^2$  can be approximated to 0 (negligible value), therefore:

$$V = \frac{\partial M(x,t)}{\partial x} \tag{7}$$

Substituting Equation (7) into Equation (5):

$$\rho A \frac{\partial^2 W(x,t)}{\partial t^2} = -\frac{\partial^2 M(x,t)}{\partial x^2} + f(x, t) \tag{8}$$

According to Euler-Bernoulli beam theory:

$$M(x, t) = YI(x) \frac{\partial^2 W(x,t)}{\partial x^2} \tag{9}$$

Substituing Equation (9) into Equation (8) and thus Equation (8) can be rewritten as:

$$\rho A(x) \frac{\partial^2 W(x,t)}{\partial t^2} = -\frac{\partial^2}{\partial x^2} \left( YI(x) \frac{\partial^2 W(x,t)}{\partial x^2} \right) + f(x, t) \tag{10}$$

For a uniform beam, the geometric or material properties do not change along the x-direction. Thus:

$$\rho A \frac{\partial^2 W(x,t)}{\partial t^2} + YI \frac{\partial^4 W(x,t)}{\partial x^4} = f(x, t) \quad (11)$$

Equation (11) is the general equation for the transverse displacement of the beam.

## 2. 2. Mechanical Equation of Motion with Electrical Coupling

Incorporating the two types of damping mechanisms, one the viscous damping for air and the other is Kelvin-Voigt damping for strain rate to account bending from both spring and the dashpot, into the general Equation (11). This model is widely used to account creep phenomenon due to viscoelastic nature of the material in Euler-Bernouli beam and more about this constitute model can be observed from literature [26, 27]. Thus, according to the effect of base excitation, the general equation of motion can be written as follows:

$$\frac{\partial^2 M(x,t)}{\partial x^2} + C_s I \frac{\partial^2 W(x,t)}{\partial x^2 \partial t} + C_a \frac{\partial W(x,t)}{\partial t} + m \frac{\partial^2 W(x,t)}{\partial t^2} = f(x, t) \quad (12)$$

The stress-strain relationship of the beam and the piezoelectric (PZT) layer is given by Equation (13),

$$\sigma_1^b = Y_b \varepsilon_1^b \quad (13)$$

$$\sigma_1^p = Y_p (\varepsilon_1^p - d_{31} E_3) \quad (14)$$

Subscripts 1, 3 in Equation (14) refer to  $x$  and  $y$  directions respectively, and denote axial strain and polarization directions. The first moment of stress distribution across the cross-section is integrated to get internal moment.

$$M(x, t) = - \int_{-(h_b/2)}^{(h_b/2)} \sigma_1^b y dy - \int_{(h_b/2)}^{(h_b/2)+h_p} \sigma_1^p y dy \quad (15)$$

Since the cantilever beam comprises of both base material and PZT material, the terms  $m$ , and  $YI$  should be expressed for the composite beam.

$$m = B(\rho_b h_b + \rho_p h_p) \quad (16)$$

$$YI = B \left[ Y_b \left( \frac{h_b^3}{12} \right) + \frac{Y_p}{3} \left( \left( \frac{h_p}{2} + h_p \right)^3 - \left( \frac{h_b^3}{8} \right) \right) \right] \quad (17)$$

The strain due to bending is obtained in terms of the radius of curvature.

$$\varepsilon_1 = -y \frac{\partial^2 W(x,t)}{\partial x^2} \quad (18)$$

Using Equations (13), (14) and (18), the internal moment equation can be modified to:

$$M(x, t) = YI \frac{\partial^2 W(x,t)}{\partial x^2} + \vartheta v(t) \quad (19)$$

where,

$$\vartheta = - \frac{Y_p B d_{31}}{2} (h_p + h_b) \quad (20)$$

If the active piezoelectric layer does not cover the entire length of the beam but to a distance ' $x$ ' where  $x < L$ , then the coupling term  $\vartheta$  needs to be multiplied by the Heaviside function.

Equation (19) can be re-written as:

$$M(x, t) = YI \frac{\partial^2 W(x,t)}{\partial x^2} + \vartheta v(t) [H(x) - H(x - L)] \quad (21)$$

With Equation (21), we can rewrite Equation (11) as:

$$YI \frac{\partial^4 W(x,t)}{\partial x^4} + C_s I \frac{\partial^5 W(x,t)}{\partial x^4 \partial t} + C_a \frac{\partial W(x,t)}{\partial t} + m \frac{\partial^2 W(x,t)}{\partial t^2} + \vartheta v(t) \left[ \frac{d\delta(x)}{dx} - \frac{d\delta(x-L)}{dx} \right] = -P_y \delta(x - L) \delta(t) \quad (22)$$

where,  $(-P_y \delta(x - L) \delta(t))$  is an impulse excitation given at the free end of the beam at  $t=0$  s. Equation (22) is the mechanical governing Equation of motion with electric coupling shown in Figure 5.  $C_p$  represents the capacitance of the piezoelectric material, and  $R_L$  denotes the internal loss and the circuit is used for converting the mechanical stress into current.

## 2. 3. General Solution

Equation (22) is solved considering position and time dependency parts of displacement using principle of separation of variables and the solution is given by Equation (23):

$$W(x, t) = \sum_{r=1}^{\infty} \varphi_r(x) T_r(t) \quad (23)$$

where,  $\varphi_r(x)$  refer to mass normalized eigen functions and  $T_r(t)$  refer to the modal coordinates of the beam considered for its  $r^{\text{th}}$  mode. For proportionately damped system the eigenfunction denoted by  $\varphi_r(x)$  is the same as the eigenfunction for an undamped beam undergoing free vibration.

$$\varphi_r(x) = \sin \left( \frac{\beta_r x}{L} \right) - \sinh \left( \frac{\beta_r x}{L} \right) + \lambda_r \left[ \cos \left( \frac{\beta_r x}{L} \right) - \cosh \left( \frac{\beta_r x}{L} \right) \right] \quad (24)$$

$\beta_r$  represents a range of frequency numbers of its dimensionless form and obtained by solving the characteristic Equation given by Equation (25):

$$1 + \cos \beta_r \cosh \beta_r = 0 \quad (25)$$

and:

$$\lambda_r = \frac{-\cos \beta_r - \cosh \beta_r}{-\sin \beta_r + \sinh \beta_r} \quad (26)$$

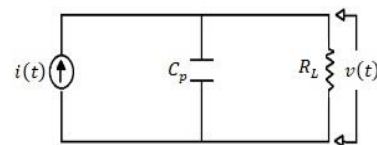


Figure 5. Simple Electrical circuit for the energy harvester

The roots of Equation (25) are obtained by using a MATLAB function 'fzero'. The first 4 values of  $\beta_r$  are  $\beta_1 = \pm 1.875$ ;  $\beta_2 = \pm 4.694$ ;  $\beta_3 = \pm 7.8547$ ; and  $\beta_4 = \pm 10.9955$ ; hence,  $\beta_r \approx (2r - 1)\frac{\pi}{2}$  with all  $r \geq 3$

The mass normalized eigenfunction  $\varphi_r(x)$  must satisfy the orthogonality condition given by Equation (27):

$$\int_{x=0}^L m \varphi_s \varphi_r dx = \delta_{rs} \quad (27)$$

The undamped natural frequency  $\omega_r$  is expressed as:

$$\omega_r = \beta_r^2 \sqrt{\frac{YI}{\rho A}} \quad (28)$$

Equation (22) is multiplied by  $\varphi_s$  and integrated between 0 to L to get the coupled electromechanical differential equation to solve for the modal response and is given by Equation (29):

$$\frac{\partial^2 T(t)}{\partial t^2} + 2\xi_r \omega_r \frac{\partial T(t)}{\partial t} + \omega_r^2 T(t) + \chi_r v(t) = F_r(t) \quad (29)$$

where:

$$2\xi_r = \left( \frac{C_s I \omega_r}{2YI} + \frac{C_d}{2m\omega_r} \right) \quad (30)$$

$$\chi_r = \vartheta \left( \frac{d\varphi_r(x)}{dx} \right)_{x=L} \quad (31)$$

The mechanical damping as mentioned earlier the strain rate and viscous air-damping are given by  $2\xi_r$ . Equation (29) is solved using Duhamel's integral and is given by Equation (32):

$$T(t) = \frac{1}{\omega_{d_r}} \int_{\tau=0}^t [F_r(\tau) - \chi_r v(\tau)] e^{-\xi_r \omega_r (t-\tau)} \sin(\omega_{d_r} (t-\tau)) d\tau \quad (32)$$

where,  $\omega_{d_r} = \omega_r \sqrt{1 - \xi_r^2}$  is the damped natural frequency of the  $r^{\text{th}}$  mode.

**2. 4. Electrical Circuit Equation** The electrical circuit equation with mechanical coupling term is obtained by considering the following piezoelectric constitutive relation:

$$D_3 = d_{31} \sigma_1 + \varepsilon_{33}^T E_3 \quad (33)$$

Equation (33) is modified to express axial stress  $\sigma_1$  in terms of bending strain ( $\varepsilon_1$ ) and Young's modulus of piezoelectric material ( $Y_p$ ). Since  $\varepsilon_{33}^T = \varepsilon_{33}^S + d_{31}^2 Y_p$ , we replace permittivity at constant stress ( $\varepsilon_{33}^T$ ) with permittivity at constant strain ( $\varepsilon_{33}^S$ ). Also  $E(t) = -\frac{v(t)}{h_p}$ .

Therefore Equation (33) becomes:

$$D_3(x, t) = -d_{31} Y_p h_{pc} \frac{\partial^2 W(x, t)}{\partial x^2} - \varepsilon_{33}^S \frac{v(t)}{h_p} \quad (34)$$

where,  $h_{pc}$  is the distance from the neutral axis to the center of the piezoelectric layer of the beam considered. The electric charge  $q(t)$  generated can be obtained by integrating the electric displacement over the electrode area:

$$q(t) = \int D \cdot \hat{n} dA = - \int_{x=0}^L \left( d_{31} Y_p h_{pc} B \frac{\partial^2 W(x, t)}{\partial x^2} + \varepsilon_{33}^S B \frac{v(t)}{h_p} \right) dx \quad (35)$$

$$i(t) = \frac{dq(t)}{dt} = - \int_{x=0}^L \left( d_{31} Y_p h_{pc} B \frac{\partial^3 W(x, t)}{\partial x^2 \partial t} + \frac{\varepsilon_{33}^S B L}{h_p} \frac{dv(t)}{dt} \right) dx \quad (36)$$

$$v(t) = R_L i(t) = -R_L \left\{ \int_{x=0}^L \left( d_{31} Y_p h_{pc} B \frac{\partial^3 W(x, t)}{\partial x^2 \partial t} + \frac{\varepsilon_{33}^S B L}{h_p} \frac{dv(t)}{dt} \right) dx \right\} \quad (37)$$

Thus, the electric circuit equation can be written as:

$$\frac{\varepsilon_{33}^S B L}{h_p} \frac{dv(t)}{dt} + \frac{v(t)}{R_L} = - \int_{x=0}^L \left( d_{31} Y_p h_{pc} B \frac{\partial^3 W(x, t)}{\partial x^2 \partial t} \right) dx \quad (38)$$

Equation (39) is obtained from the circuit is shown in Figure 5 applying Kirchhoff's law.

$$C_p \frac{dv(t)}{dt} + \frac{v(t)}{\tau_c} = \sum_{r=1}^{\infty} \varphi_r \frac{dT_r(t)}{dt} \quad (39)$$

where,

$$\varphi_r = \frac{d_{31} Y_p h_{pc} h_p}{\varepsilon_{33}^S B L} \left( \frac{d\varphi_r(x)}{dx} \right)_{x=L} \quad (40)$$

$$\tau_c = \frac{R_L \varepsilon_{33}^S B L}{h_p} \quad (41)$$

Leibniz rule is used to carry out differentiation operation under an integral sign. Substituting  $\frac{dT}{dt}$  in the above equation leads to:

$$\frac{dv(t)}{dt} = \frac{d}{dt} \int_{\tau=0}^t [F_r(\tau) + \chi_r v(\tau)] e^{-\xi_r \omega_r (t-\tau)} \sin(\omega_{d_r} (t-\tau)) d\tau + \int_{\tau=0}^t [F_r(\tau) + \chi_r v(\tau)] e^{-\xi_r \omega_r (t-\tau)} (-\xi_r \omega_r \sin(\omega_{d_r} (t-\tau)) + \omega_{d_r} \cos(\omega_{d_r} (t-\tau))) d\tau \quad (42)$$

Therefore,

$$\frac{dv(t)}{dt} + \frac{v(t)}{\tau_c} = \sum_{r=1}^{\infty} \varphi_r \int_{\tau=0}^t [F_r(\tau) + \chi_r v(\tau)] e^{-\xi_r \omega_r (t-\tau)} (-\xi_r \omega_r \sin(\omega_{d_r} (t-\tau)) + \omega_{d_r} \cos(\omega_{d_r} (t-\tau))) d\tau \quad (43)$$

Equation (43) is solved using Laplace transforms and thus a decoupled solution for the voltage function  $v(t)$  is obtained. The right hand side of the equation is expressed by a convolution of two terms  $t$  and  $\tau$ , where in Laplace transform it can be defined as the product of Laplace transform of each term individually. A stepwise procedure is explained to apply Laplace transform and the final expression for voltage is shown below,

$$sV(s) + \frac{1}{\tau_c} V(s) = \sum_{r=1}^{\infty} \{ \varphi_r L[-P_y \delta(t)] + \chi_r v(t) L[e^{\xi_r \omega_r (t-\tau)} \sin \omega_d (t-\tau)] + \chi_r v(t) L[\omega_d \cos \omega_d (t-\tau)] \} \quad (44)$$

$$sV(s) + \frac{1}{\tau_c} V(s) = \sum_{r=1}^{\infty} \varphi_r [-P_y \varphi_{x=L} + \chi_r V(s)] \left( \frac{-\xi_r \omega_r \omega_d}{(s + \xi_r \omega_r)^2 + \omega_d^2} + \left( \frac{\omega_d (s + \xi_r \omega_r)}{(s + \xi_r \omega_r)^2 + \omega_d^2} \right) \right) \quad (45)$$

which implies,

$$V(s) = \frac{(-P_y \varphi_{x=L} \varphi_r \omega_d \tau_c \chi_r) s}{\tau_c s^3 + (2\xi_r \omega_r + 1) s^2 + (\tau_c \omega_r^2 + 2\xi_r \omega_r + \chi_r \varphi_r \omega_d \tau_c) s + \omega_r^2} \quad (46)$$

The values of  $\omega_r$ ,  $\omega_d$ ,  $\tau_c$ ,  $\chi_r$  can be obtained from the formulas expressed above. The first four modes were taken for analyzing the solution. The damping ratios considered are given in brackets (0.010, 0.013, 0.033, 0.064, 0.106) were experimentally calculated for the same dimensions reported in the literature [17]. Equation (46) becomes:

$$V(s) = (-P_y \varphi_{x=L} \varphi_r \omega_d \tau_c) \left( \frac{s}{(s-a)(s-b)(s-c)} \right) \quad (47)$$

Inverse Laplace transform applied on Equation (47) gives a closed form decoupled expression for voltage that is generated within the considered piezoelectric layer for impulse excitation given at the tip.

$$v(t) = (-P_y \varphi_{x=L} \varphi_r \omega_d \tau_c) (Ae^{at} + Be^{bt} + Ce^{ct}) \quad (48)$$

Where:

$$A = \frac{a}{(a-b)(a-c)}, B = \frac{b}{(a-b)(b-c)}, C = \frac{c}{(a-c)(b-c)} \quad (49)$$

Substituting  $v(t)$  in Equation (32) a decoupled solution is obtained for the modal response of the considered unimorph cantilever beam and upon integrating the expression from  $\tau = 0$  to  $t$ , the solution obtained can be written as:

$$\begin{aligned} T(t) = & -P_y \varphi_{x=L} e^{-\xi_r \omega_r t} \sin(\omega_d t) + \\ & \chi_r P_y \varphi_{x=L} \varphi_r \omega_d \tau_c \left[ \left( \frac{A}{(a+\xi_r \omega_r)^2 + \omega_d^2} (e^{at} + e^{-\xi_r \omega_r t} ((a + \xi_r \omega_r) \sin(\omega_d t) - \omega_d \cos(\omega_d t))) \right) + \left( \frac{B}{(b+\xi_r \omega_r)^2 + \omega_d^2} (e^{bt} + e^{-\xi_r \omega_r t} ((b + \xi_r \omega_r) \sin(\omega_d t) - \omega_d \cos(\omega_d t))) \right) + \left( \frac{C}{(c+\xi_r \omega_r)^2 + \omega_d^2} (e^{ct} + e^{-\xi_r \omega_r t} ((c + \xi_r \omega_r) \sin(\omega_d t) - \omega_d \cos(\omega_d t))) \right) \right] \end{aligned} \quad (50)$$

Therefore,  $W(x, t) = \sum_{r=1}^{\infty} \varphi_r(x) T_r(t)$  can be written as:

$$\begin{aligned} W(x, t) = & \sum_{r=1}^{\infty} \left\{ \sin - \sinh \left( \frac{\beta_r}{L} x \right) + \lambda_r \left[ \cos \left( \frac{\beta_r}{L} x \right) - \cosh \left( \frac{\beta_r}{L} x \right) \right] \right\} \left\{ -P_y \varphi_{x=L} e^{-\xi_r \omega_r t} \sin(\omega_d t) + \chi_r P_y \varphi_{x=L} \varphi_r \omega_d \tau_c \left[ \left( \frac{A}{(a+\xi_r \omega_r)^2 + \omega_d^2} (e^{at} + e^{-\xi_r \omega_r t} ((a + \xi_r \omega_r) \sin(\omega_d t) - \omega_d \cos(\omega_d t))) \right) + \left( \frac{B}{(b+\xi_r \omega_r)^2 + \omega_d^2} (e^{bt} + e^{-\xi_r \omega_r t} ((b + \xi_r \omega_r) \sin(\omega_d t) - \omega_d \cos(\omega_d t))) \right) + \left( \frac{C}{(c+\xi_r \omega_r)^2 + \omega_d^2} (e^{ct} + e^{-\xi_r \omega_r t} ((c + \xi_r \omega_r) \sin(\omega_d t) - \omega_d \cos(\omega_d t))) \right) \right] \right\} \end{aligned} \quad (51)$$

### 3. FINITE ELEMENT SIMULATION

A finite element cantilever shaped piezoelectric energy harvester with and without tip mass is modeled in ABAQUS for finite element modal analysis of the compound structure to understand its mechanical

behavior and to determine the fundamental natural frequency.

### 3. 1. Model Geometry and Material Definition

TABLE 1. Properties of the base material

Properties of material	Aluminum	Copper	Steel	Unit
Density	2800	8700	8000	kg/m <sup>3</sup>
Young's Modulus	70×10 <sup>9</sup>	110×10 <sup>9</sup>	215×10 <sup>9</sup>	N/m <sup>2</sup>
Poisson's Ratio	0.3	0.3	0.3	-

TABLE 2. Properties of Piezoelectric material

Parameters	PZT-5H	Unit
Density	7500	kg/m <sup>3</sup>
Uniaxial Modulus (E1)	60.61×10 <sup>9</sup>	N/m <sup>2</sup>
Uniaxial Modulus (E2)	60.61×10 <sup>9</sup>	N/m <sup>2</sup>
Uniaxial Modulus (E3)	48.31×10 <sup>9</sup>	N/m <sup>2</sup>
Poisson's Ratio (Nu12)	0.289	-
Poisson's Ratio (Nu13)	0.49	-
Poisson's Ratio (Nu23)	0.49	-
Shear Modulus (G12)	23.5×10 <sup>9</sup>	N/m <sup>2</sup>
Shear Modulus (G13)	23.0×10 <sup>9</sup>	N/m <sup>2</sup>
Shear Modulus (G23)	23.0×10 <sup>9</sup>	N/m <sup>2</sup>

The piezoelectric energy harvester is modeled as a cantilever beam of 100 mm length and 20 mm breadth. The thickness of the base material is 0.5 mm whereas that of the piezoelectric material is 0.4 mm. Three different base materials are used namely aluminum, copper and steel. Also, tip mass of 10 grams is attached to the free end of the cantilever beam to study its effect on the eigen frequencies. The properties of the base material, as well as the piezoelectric patch are shown in Tables 1 and 2, respectively.

### 3. 2. Assembly and Meshing

Meshing of the energy harvester model is done with 8 elements along with the thickness and mesh size of 0.001 along the width and length of the beam. SC8R element type which is a general purpose in-plane 8-noded quadrilateral continuum shell element, is selected for base material. PZT material has meshed with an approximate global size of 0.001. C3D8E element type which is an 8-node linear piezoelectric brick is assigned to the PZT patch. PZT patch and the base material are connected using tie constraints with node to surface discretization method.

The PZT patch is set to be the master surface while the base material is the slave surface.

**3. 3. Boundary Condition and Loading** All translational and rotational degrees of freedom are fixed at one end of the energy harvester. The modal analysis technique is carried out to determine the modal parameters of the cantilever shaped energy harvester. The effect of tip mass was well understood by adding a mass of 10 grams at the free end of the cantilever. The tip mass showed a progressive improvement in the overall design of the cantilever by lowering the eigen frequencies of the structure.

**4. EXPERIMENTAL ANALYSIS**

Figure 6 shows the experimental setup arranged to realize the proposed energy harvester. Energy harvester samples with three different base materials are used in this experiment. Samples are made with 3 PZT materials connected in series which are fixed on the respective base materials. The samples are clamped with a fixed base for support. An impulse load is applied using an impact hammer to understand the mechanical and electrical behavior of the system. An ICP type 100 mV/g sensitivity tri-axial accelerometer is attached to the cantilever obtains the vibration response of the structure. A clean, noise-free frequency response low cost PZT ceramic material of high dielectric constant value with high charge sensitivity is used. BNC cables are used to connect the accelerometer sensor as well as the PZT leads to the Dynamic Signal Analyzer (DSA). Impact hammer, PZT beam, and the accelerometer are connected to three different channels on the DSA which enables us to extract the required transfer function. Each sample is investigated for an average of 5 trials for accuracy. The spectral frequency range was limited to 100 Hz because the first mode lies within this range and it is at this initial mode that the energy harvester will be able to generate maximum output as all the other modes may result in the

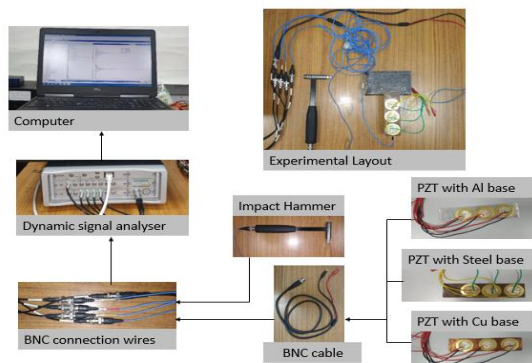


Figure 6. Experimental setup and the energy harvester

partial charge canceling due to opposite directional stress regions [23].

**5. RESULTS AND DISCUSSIONS**

**5. 1. Mathematical Modeling Results** Equation (24) is solved in MATLAB and is used to predict the mechanical behavior of the energy harvester corresponding to each mode as depicted in Figure 7. The derived Equations (48) and (51) represent the voltage and mechanical response respectively of the energy harvester under impulse loading. The equations are solved using MATLAB and the responses are studied for three different base materials such as aluminium, copper, and steel.

The time response of tip displacement and its frequency spectrum for aluminum base material are shown in Figures 8(a) and 8(b). A peak response at the time of impact decreases exponentially to zero value in a very short time interval. The frequency spectrum energy voltage function has its maximum amplitude at the first natural frequency of 52 Hz approximately and it is at this frequency that the harvester can produce maximum voltage amplitude of about 0.09 mV which is equivalent to an instantaneous power output of around  $0.81 \times 10^{-9} \text{W}$  across a  $10 \Omega$  load resistance.

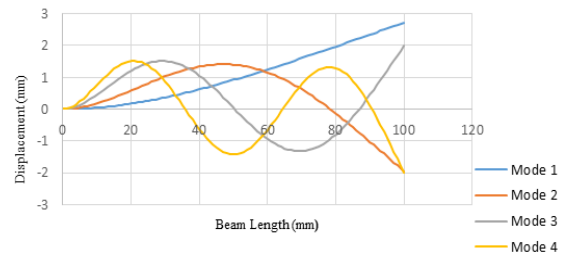
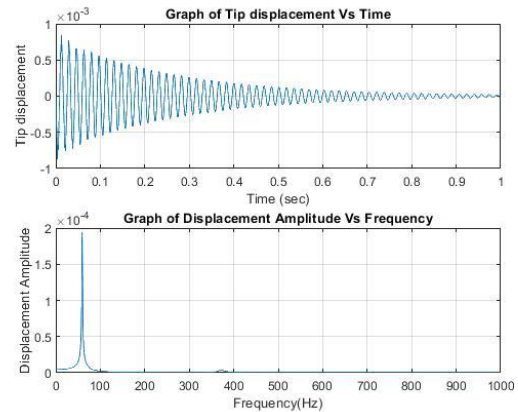
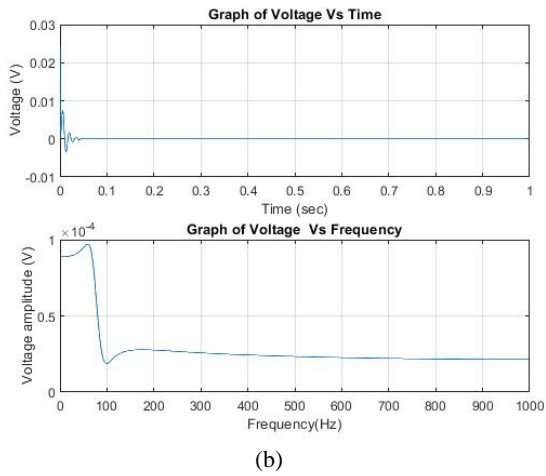


Figure 7. Mode shapes of the proposed rectangular cantilever beam



(a)



**Figure 8.** (a) Graph of tip displacement as function of time and its corresponding frequency spectrum, (b) Graph of voltage response as a function of time and its corresponding frequency spectrum for Aluminium

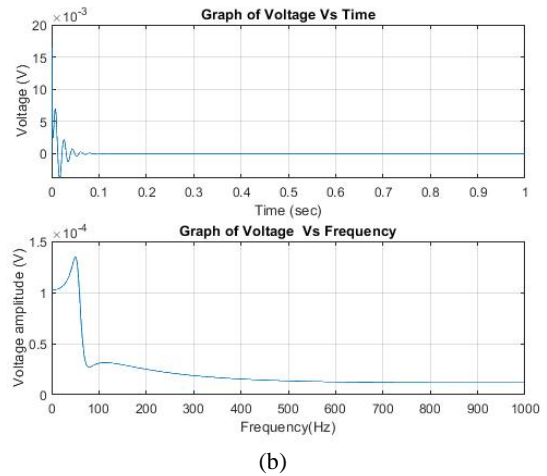


**Figure 9.** (a) Graph of tip displacement as function of time and its corresponding frequency spectrum, (b) Graph of voltage response as a function of time and its corresponding frequency spectrum for Copper

A similar trend in tip displacement and voltage generated can be seen in copper and steel-based harvesters. Figures 9(a) and 9(b) and Figures 10(a) and 10(b) show the variation of tip displacement and voltage as time varies and its frequency spectrum for copper and steel respectively.

The copper-based energy harvester was capable of generating an output voltage of 0.13 mV while that of steel showed the highest voltage reading of approximately 0.14 mV. Steel-based energy harvester showed a slightly better energy harvesting capability among the three base elements. The average instantaneous power output of copper and steel across a load resistance of  $10\Omega$  comes out to be around  $1.69 \times 10^{-9}$  W and  $1.96 \times 10^{-9}$  W, respectively. Even though a small peak is seen in the frequency range of 200 Hz to 300 Hz where the second natural frequency of the harvester lie,

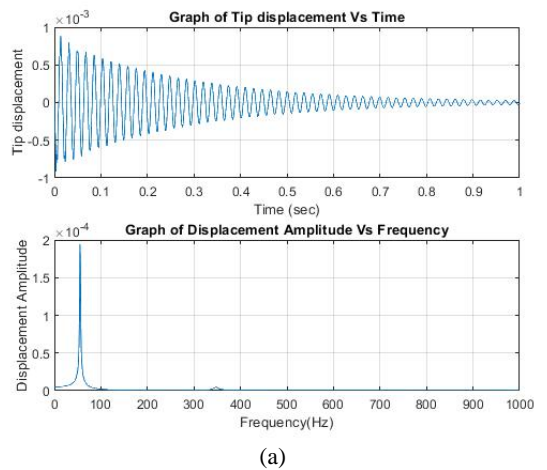


**Figure 10.** (a) Graph of tip displacement as function of time and its corresponding frequency spectrum, (b) Graph of voltage response as a function of time and its corresponding frequency spectrum for Steel

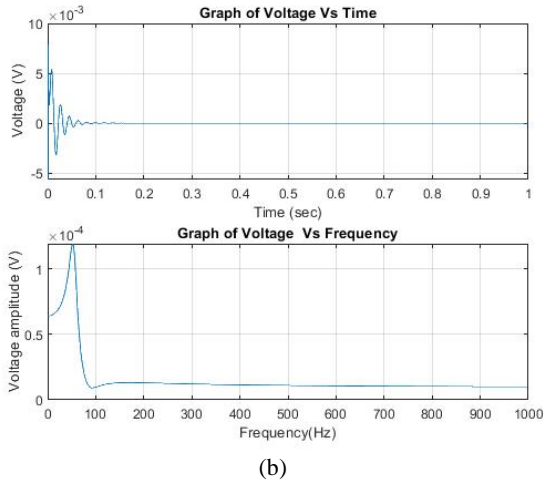
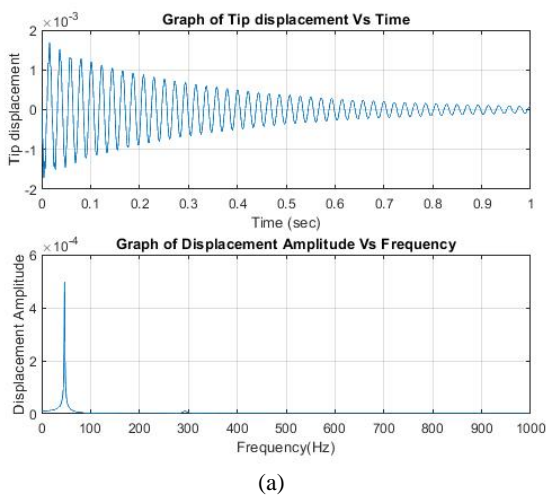


**Figure 10.** (a) Graph of tip displacement as function of time and its corresponding frequency spectrum, (b) Graph of voltage response as a function of time and its corresponding frequency spectrum for Steel

it is not taken into consideration as the energy harvested at the first natural frequency has the highest magnitude. A similar observation can be ascribed from literature [7].

**5. 2. Modal Analysis Results** Figures 11 and 12 depict the first four mode shapes of the proposed cantilever shaped energy harvester without tip mass and with tip mass (10 g), respectively. Furthermore, the addition of tip mass drastically lowers the natural frequency of the cantilever beam as mentioned in Table 3. However, the whole study is restricted to the first natural frequency because only this region yields maximum voltage output [23]. Hence it is proposed to examine the frequency response function obtained for the impulse excitation where accelerometer mass act as the tip mass.

**5. 3. Experimental Results** Figure 13 deals with the electrical and mechanical responses of the three samples to time. An exponential decay can be observed over both the responses for not more than one second. These trends are validated with similar observations from mathematical modeling depicted in the previous section.

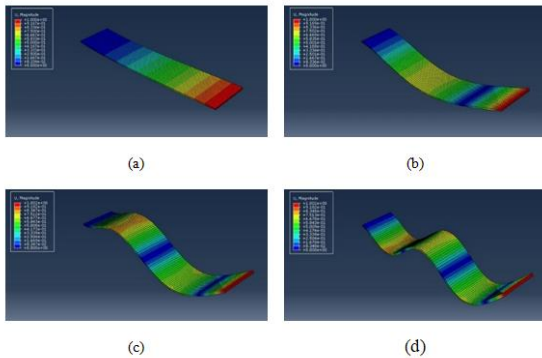


**Figure 11.** Different mode shapes of simple cantilever shaped energy harvester without tip mass: (a) 1<sup>st</sup> Mode, (b) 2<sup>nd</sup> Mode, (c) 3<sup>rd</sup> Mode, (d) 4<sup>th</sup> Mode

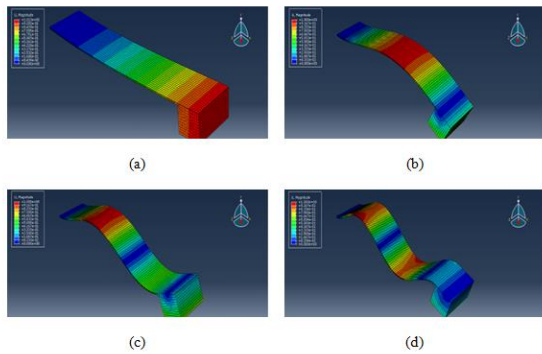


**Figure 12.** Different mode shapes of simple cantilever shaped energy harvester with tip mass: (a) 1<sup>st</sup> Mode, (b) 2<sup>nd</sup> Mode, (c) 3<sup>rd</sup> Mode, (d) 4<sup>th</sup> Mode

**TABLE 3.** Reduction in natural frequencies due to the addition of tip mass

Mode number	Natural Frequency (Hz)					
	Copper		Steel		Aluminum	
	0 gm	10 gm	0 gm	10 gm	0 gm	10 gm
1	41.014	16.48	49.863	16.078	44.642	30.343
2	257.08	237.06	312.5	126.07	279.85	278
3	410.28	257.09	477.95	175.33	477.19	310.39
4	721.03	644.81	876.2	483.68	784.78	801.37

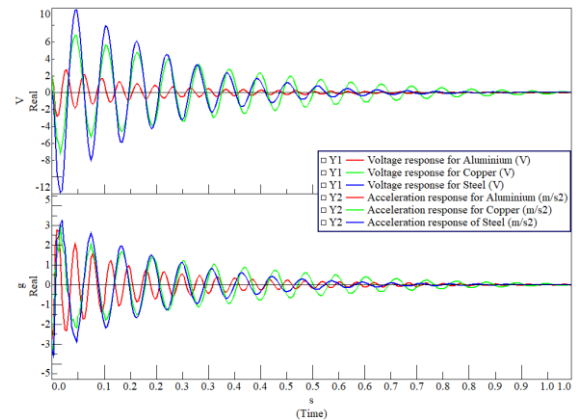


**Figure 13.** Voltage and acceleration response for three samples as a function of time

The corresponding frequency spectra are depicted in Figure 14 where the frequency of interest is restricted to 100 Hz because maximum energy harvesting is occurring at a first natural frequency according to literature [21].

The result indicates that steel and copper-based energy harvesters were capable of generating an instantaneous voltage output of 0.13mV and 0.11mV, respectively while aluminum-based energy harvester was

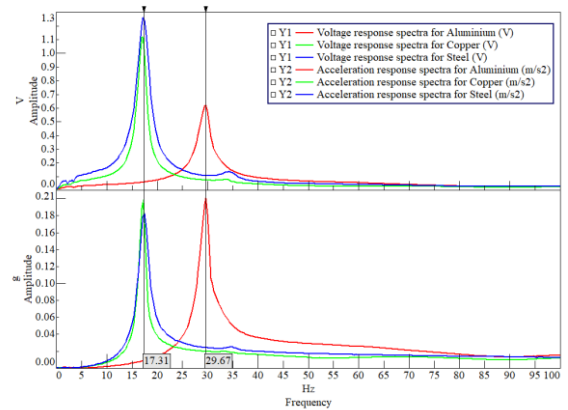


**Figure 14.** Voltage and acceleration response for three samples as a function of frequency

capable of generating a mere 0.06mV at its first natural frequency. Importantly, the effect of tip mass is captured during the experiment and it almost closer to the numerical results frequencies given in Table 3 for different base material with tip mass.

## 6. CONCLUSION

This paper distinctively investigates the energy harvesting capability for a given impulse loading condition that characterizes our test specimen's energy transfer characteristics. The finite element modal analysis results showed a detrimental reduction in the natural frequency of the cantilever structure upon the addition of a tip mass. The first natural frequency of Copper and Steel reduced to 16.48 Hz and 16.078 Hz, respectively; while that of Aluminum dropped down to 30.343 Hz with the addition of 10gm tip mass. Experimental work carried out exposes the wide range of possibilities as well as simplicity in using piezoelectric material in vibration energy harvesting. Among the three base materials mentioned in this work, steel and copper-based energy harvesters were capable of generating a maximum voltage output of 0.16mV and 0.13mV, respectively which corresponds to a maximum instantaneous power output of approximately 1.96nW and 1.69nW, respectively. However, aluminum-based energy harvester performed the least among the three contributing to a mere 0.81nW.

## 7. ACKNOWLEDGMENT

Authors convey their sincere thanks to Vehicle Dynamics Laboratory, Department of Automotive Engineering, Vellore Institute of Technology, Vellore for the test facility provided to carry out the necessary experiments for the current paper.

## 8. REFERENCES

- Chae, S.H., Ju, S., Choi, Y., Chi, Y.-E. and Ji, C.-H., "Electromagnetic linear vibration energy harvester using sliding permanent magnet array and ferrofluid as a lubricant", *Micromachines*, Vol. 8, No. 10, (2017), 288. <https://doi.org/10.3390/mi8100288>
- Deng, Z. and Dapino, M.J., "Review of magnetostrictive vibration energy harvesters", *Smart Materials and Structures*, Vol. 26, No. 10, (2017), 103001.
- Lafarge, B., Grondel, S., Delebarre, C. and Cattan, E., "A validated simulation of energy harvesting with piezoelectric cantilever beams on a vehicle suspension using bond graph approach", *Mechatronics*, Vol. 53, (2018), 202-214. <https://doi.org/10.1016/j.mechatronics.2018.06.004>
- Vullers, R.J., Van Schaijk, R., Visser, H.J., Penders, J. and Van Hoof, C., "Energy harvesting for autonomous wireless sensor networks", *IEEE Solid-State Circuits Magazine*, Vol. 2, No. 2, (2010), 29-38. doi: 10.1109/MSSC.2010.936667.
- Delebarre, C., Grondel, S. and Rivart, F., "Autonomous piezoelectric structural health monitoring system for on-production line use", *Advances in Applied Ceramics*, Vol. 114, No. 4, (2015), 205-210. <https://doi.org/10.1179/1743676114Y.0000000220>
- Van den Ende, D., Van de Wiel, H., Groen, W. and Van der Zwaag, S., "Direct strain energy harvesting in automobile tires using piezoelectric pzt-polymer composites", *Smart Materials and Structures*, Vol. 21, No. 1, (2011), 015011.
- Khameneifar, F. and Arzanpour, S., "Energy harvesting from pneumatic tires using piezoelectric transducers", in *Smart Materials, Adaptive Structures and Intelligent Systems*. Vol. 43314, (2008), 331-337.
- Chan, M., "Low-grade waste vibration energy recovery from hong kong franchised buses", *International Journal of Green Energy*, Vol. 11, No. 4, (2014), 431-437. <https://doi.org/10.1080/15435075.2013.777913>
- Wu, M., Ou, Y., Mao, H., Li, Z., Liu, R., Ming, A. and Ou, W., "Multi-resonant wideband energy harvester based on a folded asymmetric m-shaped cantilever", *Aip Advances*, Vol. 5, No. 7, (2015), 077149. <https://doi.org/10.1063/1.4927466>
- Zhou, S., Chen, W., Malakooti, M.H., Cao, J. and Inman, D.J., "Design and modeling of a flexible longitudinal zigzag structure for enhanced vibration energy harvesting", *Journal of Intelligent Material Systems and Structures*, Vol. 28, No. 3, (2017), 367-380. doi: <https://doi.org/10.1177/1045389X16645862>
- Zhao, N., Yang, J., Yu, Q., Zhao, J., Liu, J., Wen, Y. and Li, P., "Three-dimensional piezoelectric vibration energy harvester using spiral-shaped beam with triple operating frequencies", *Review of Scientific Instruments*, Vol. 87, No. 1, (2016), 015003. <https://doi.org/10.1063/1.4940417>
- Muthalif, A.G. and Nordin, N.D., "Optimal piezoelectric beam shape for single and broadband vibration energy harvesting: Modeling, simulation and experimental results", *Mechanical Systems and Signal Processing*, Vol. 54, (2015), 417-426. <https://doi.org/10.1016/j.ymssp.2014.07.014>
- Erturk, A., Renno, J.M. and Inman, D.J., "Modeling of piezoelectric energy harvesting from an l-shaped beam-mass structure with an application to uavs", *Journal of Intelligent Material Systems and Structures*, Vol. 20, No. 5, (2009), 529-544. <https://doi.org/10.1177/1045389X08098096>
- Ericka, M., Vasic, D., Costa, F., Poulin, G. and Tliba, S., "Energy harvesting from vibration using a piezoelectric membrane", in *Journal de Physique IV (Proceedings)*, EDP sciences. Vol. 128, (2005), 187-193.
- Y., T.B., A., J. and H., R., "Size effect on free transverse vibration of cracked nano-beams using couple stress theory", *International Journal of Engineering, Transactions B: Applications*, Vol. 28, No. 2, (2015), 296-304. doi: 10.5829/idosi.ije.2015.28.02b.17.
- Beni, Z.T., Ravandi, S.A.H. and Beni, Y.T., "Size effect on free transverse vibration of cracked nano-beams using couple stress theory", *International Journal of Engineering, Transactions C: Aspects*, Vol. 28, No. 2, (2015), 296-304. doi: 10.5829/ije.2018.31.09c.15.
- Fakharian, M., "A wideband fractal planar monopole antenna with a thin slot on radiating stub for radio frequency energy harvesting applications", *International Journal of Engineering, Transactions B: Applications*, Vol. 33, No. 11, (2020), 2181-2187. doi: 10.5829/ije.2020.33.11b.08.
- Wei, C. and Jing, X., "A comprehensive review on vibration energy harvesting: Modelling and realization", *Renewable and Sustainable Energy Reviews*, Vol. 74, (2017), 1-18. <https://doi.org/10.1016/j.rser.2017.01.073>

19. Dixit, N.K., K. J. Rangra and Y. C. Sharma, "Review study on piezoelectric energy harvesters and their applications", *International Journal of Computer Science Engineering*, Vol. 6, No. 9, (2018), 607-616. <https://doi.org/10.1016/j.joule.2018.03.011>
20. Sarker, M.R., Julai, S., Sabri, M.F.M., Said, S.M., Islam, M.M. and Tahir, M., "Review of piezoelectric energy harvesting system and application of optimization techniques to enhance the performance of the harvesting system", *Sensors and Actuators A: Physical*, Vol. 300, (2019), 111634. <https://doi.org/10.1016/j.sna.2019.111634>
21. Roundy, S. and Wright, P.K., "A piezoelectric vibration based generator for wireless electronics", *Smart Materials and Structures*, Vol. 13, No. 5, (2004), 1131.
22. Erturk, A. and Inman, D.J., "On mechanical modeling of cantilevered piezoelectric vibration energy harvesters", *Journal of Intelligent Material Systems and Structures*, Vol. 19, No. 11, (2008), 1311-1325. <https://doi.org/10.1177/1045389X07085639>
23. Jia, Y., Wei, X., Xu, L., Wang, C., Lian, P., Xue, S., Al-Saadi, A. and Shi, Y., "Multiphysics vibration fe model of piezoelectric macro fibre composite on carbon fibre composite structures", *Composites Part B: Engineering*, Vol. 161, (2019), 376-385. <https://doi.org/10.1016/j.compositesb.2018.12.081>
24. Shams Nateri, M. and Azizollah Ganji, B., "The effect of material properties on sensitivity of the microelectromechanical systems piezoelectric hydrophone", *International Journal of Engineering, Transactions C: Aspects*, Vol. 30, No. 12, (2017), 1848-1855. doi: 10.5829/ije.2017.30.12c.05.
25. Rezazadeh, G., Khanchehgardan, A., Shah-Mohammadi-Azar, A. and Shabani, R., "Mechanical response of a piezoelectrically sandwiched nano-beam based on the non-local theory", *International Journal of Engineering, Transactions C: Aspects*, Vol. 26, No. 12, (2013), 1515-1524. doi: 10.5829/idosi.ije.2013.26.12c.12.
26. Raposo, C., Bastos, W. and Avila, J., "A transmission problem for euler-bernoulli beam with kelvin-voigt damping", *Applied Mathematics and Information Sciences*, Vol. 5, No. 1, (2011), 17-28.
27. Hosseini Hashemi, S. and Bakhshi Khaniki, H., "Free vibration analysis of nonuniform microbeams based on modified couple stress theory: An analytical solution", *International Journal of Engineering, Transactions B: Applications*, Vol. 30, No. 2, (2017), 311-320. doi: 10.5829/idosi.ije.2017.30.02b.19.

---

### Persian Abstract

#### چکیده

تبدیل انرژی از یک شکل به شکل دیگر اساس بسیاری از اختراعات را تشکیل می دهد. انرژی استفاده نشده ارتعاش مکانیکی بسیاری از محققان را به تمرکز بر برداشت انرژی از سازه های ارتعاشی جذب کرده است. مواد پیزوالکتریک هنگامی که به یک ساختار ارتعاشی متصل می شوند، انرژی مکانیکی را به انرژی الکتریکی تبدیل می کنند. امروزه برداشت انرژی از سطح خرد تا سطح کلان متغیر است و اهمیت خود را در گستره وسیعی از کاربردهای بلادرنگ مانند از دستگاه های الکترونیکی کم توان گرفته تا سیستم های انرژی خورشیدی، بادی و برق آبی به دست آورده است. کار فعلی یک مطالعه تئوری و تجربی دقیق بر روی یک ساختار تیر از نوع کنسول تعبیه شده با مواد پیزوالکتریک بر روی مواد پایه مختلف برای درک میزان برداشت انرژی در سطح میکرو ارائه می کند. مدل ریاضی مبتنی بر تئوری پرتو اویلر برنولی با یک بار ضربه ای در انتهای آزاد برای تجزیه و تحلیل طیف فرکانس گسترده تر برانگیخته می شود. در نهایت، برداشت کننده های انرژی پیشنهادی، نمونه های کنسولی از سه ماده پایه مختلف بر اساس حداکثر ولتاژ و حداکثر خروجی توان لحظه ای آنها به صورت تجربی برای تحریک ضربه ای داده شده رتبه بندی می شوند. از سه ماده پایه در نظر گرفته شده، برداشت کننده های انرژی مبتنی بر فولاد و مس، حداکثر ولتاژ خروجی به ترتیب  $0.16 \text{ mV}$  و  $0.13 \text{ mV}$  تولید کردند که به ترتیب مربوط به حداکثر توان خروجی لحظه ای تقریباً  $1.96 \text{ nW}$  و  $1.69 \text{ nW}$  است. برداشت کننده انرژی مبتنی بر آلومینیوم در بین سه دستگاهی که در تولید  $0.81$  نانوات مشارکت داشتند، کمترین عملکرد را داشت.

---



## Recent Trends in Stabilization of Expansive Soil using Calcined Clay

V. Janani, P. T. Ravichandran\*

Department of Civil Engineering, College of Engineering and Technology, SRM Institute of Science and Technology, Kattankulathur, Chennai, Tamil Nadu, India

### PAPER INFO

#### Paper history:

Received 29 August 2022  
Received in revised form 30 October 2022  
Accepted 03 November 2022

#### Keywords:

Soil Stabilization  
Expansive Soil  
Calcined Clay  
Unconfined Compressive Test  
X-Ray Diffraction Analysis  
Scanning Electron Microscope

### ABSTRACT

Expansive soils have the tendency to more swelling, shrinking and compressibility by variation in soil-water interaction affecting the alteration in the bearing capacity of soil. There are several methods used to stabilize the soils and promote sustainable development in the construction industry. In this, soil stabilization is prime and efficient techniques to improve the strength by altering the physical characteristics of the soil. In addition, admixtures improved the chemical characteristics of soil and also attained stability by improving the bonding between the soil structures. Soil stabilization has been experimented by many researchers and successfully used in several field applications especially using cement, lime, ashes, chemicals etc. An alternative to these options mentioned is using natural cementitious material such as calcined clay as an admixture. This work focuses on the effect, the development of the strength properties of treated soils with varying percentages of calcined clay as 2%, 4%, 6%, 8% and 10% under varying curing times. The enhanced strength behaviours of the expansive soil were determined by performing the unconfined compression test and also the microstructural studies like SEM and XRD for the selected samples. The results indicate that the maximum strength was attained on 8% admixture treated soil. Thus calcined clay acts as a natural cost-effective and eco-friendly stabilizer in place of replacement of cement to stabilize expansive soil which develops the strength characteristics of the expansive soil and also reduces environmental pollution.

doi: 10.5829/ije.2023.36.01a.18

## 1. INTRODUCTION

Soil is one of the essential materials needed to decide the execution of construction. Rapid urbanization leads to the requirement of different forms of infrastructural development all over the world. Site feasibility plays major role in the selection of project; generally, prefer the soil with good bearing capacity [1]. Due to scarcity of land, it is impossible to obtain a construction field that meets the design requirements without ground modification in most geotechnical projects [2]. Under this circumstance it is necessary to give more importance to the subsurface which withstands the construction. Challenges arises to utilize the weak and problematic soil and converting them into the good soil by any suitable technology required to improve the behaviour of the soil which means for enhancing the properties of its original

nature [3]. Expansive soil is one of the most problematic soil due to its volume change behaviour when interacting with the water and also due to the presence of montmorillonite clay minerals which is expansive in nature [4] and its spread covers around 12% of landmass. Ground improvement technique is the essential Techniques consist of several methods that vary based on the soil type and other factors which have been widely used to increase the load carrying capacity of the soil. One of the effective methods of enhancing the strength characteristics by addition of material along with the natural soil is called the stabilization method [5-7]. It plays an important part in the development of characteristics in a short period. Soil can be stabilized by means of physical, chemical and biological [8-11] methods to increase the weight bearing capabilities and performance of in-situ subsoil. The commonly used

\*Corresponding Author Institutional Email: [ravichap@srmist.edu.in](mailto:ravichap@srmist.edu.in)  
(P. T. Ravichandran)

stabilization techniques are cement stabilization, lime stabilization, stabilization with flyash, bitumen stabilization etc. [12-15].

Many researchers involved in the field of soil stabilization using admixtures suggested this is one of the most widespread ground improvement techniques. The stabilized soil can be used in wide engineering applications in the field of earth structures, pavement, hydraulic structures etc. Several studies were done by adding soil with admixtures in any form, either powder or liquid to enhance the strength characteristics of the soil. Traditional admixtures like lime [16], cement [17] and its byproducts have stabilized the problematic nature of expansive soil and helped to improve the strength characteristics of soil but that leads to the depletion of natural resources. So upcoming research are done by adding industrial by-products such as GGBS [18, 19], flyash [15, 20, 21], phosphogypsum [22], Dolochar [23] etc and agriculture waste such as groundnut shell ash [24-26], bagasse ash [27, 28], etc. This admixture improves the strength, drainage, and permeability characteristics of the soil. However, this will be economical compared to other kinds of stabilization but long term usage of these wastes leads to the contamination of ground and groundwater. Hence it is necessary to adopt natural pozzolanic material which should provide a sustainable environment.

Calcined clay is one of the effective supplementary Cementitious materials for cement [29]. During the collection of literature, it was found that there are no traces of attempts made to stabilize the soil using calcined clay. In this research, experiments were conducted to examine the influence of the calcined clay on the strength behaviour of the expansive soil. This paper presents the influence of calcined clay (CC) on the engineering characteristics of expansive soils and their inherent ecological potential. A series of Unconfined Compression Test and Microstructural studies were performed on soil and soil treated with 2%, 4%, 6%, 8% and 10% percentages of Calcined clay. The laboratory test results of untreated and treated soils were compared and showed the increment in the strength properties of soil.

## 2. MATERIALS AND METHODOLOGY

In this study, the soil sample was collected from the site in Tharamani (Chennai, Tamil Nadu, India) at a depth of 1.2m from ground level. The series of test were carried out on the naturally dried and pulverized soil to find out the physical properties and Expansive nature of the soil as per the Bureau of Indian Standards (BIS). As per the IS: 2720 (Part 3) – 1987 the specific gravity of the soil is 2.5, and the particle size distribution showed that more than 50 % passes through 75 microns, the range of 4%

sand, 9% silt and 87% clay. The consistency limits as per IS: 2720 (Part 5) – 1985 of the soil were 65% liquid limit and 22% plastic limit and 6% shrinkage limit, showing the soil is highly plastic which comes under the category of high compressible clay (CH) as per the IS: 1498 (Part 20) – 1970 specification and ASTM D2487 [30]. The free swell index value of the soil is 210% showing a very high expansiveness as per the IS: 2720 (Part 40) – 1977. The above test results showed that the virgin soil is highly expansive and more compressible. Hence, it requires soil stabilization in order to enhance the soil behaviour. The additive used for this soil treatment is calcined clay which possesses high pozzolanic natural material and is eco-friendly. The properties of the virgin soil are given in Table 1.

The unconfined compression test and its sample preparation for untreated and treated soil were carried out as per the IS: 2720 (Part 10) – 1973 code specification. The specimens were prepared in the standard dimension of size 38mm × 76mm with the slenderness ratio 2 as per the IS: 2720 (Part 7) – 1980 specification and mixed at the optimum moisture content (OMC) obtained from the standard proctor compaction test. After preparation, the sample was weighed and sealed with the polyethene wrap under the maintained temperature of 25° -30°C [34] and kept on moist saw dust and gunny bags to prevent moisture loss.

Figures 1 and 2 show the prepared UCC sample wrapped and kept in bed for the curing process. The same procedure is followed for the treated sample of different proportions of calcined clay and kept for 1, 3, 7, 14, 28, and 60 days curing by covering it with the gunny bags. The untreated and treated samples were tested at the strain rate of 1.2 mm/min as per the IS2729-Part 10.



Figure 1. UCC samples in polyethene wrapper



Figure 2. UCC samples under curing process

TABLE 1. Properties of the virgin soil

Specific Gravity, G	Particle Size Distribution (%)			Atterberg Limits (%)			Standard Proctor Test		Free swell Index (%)	UCS, (kPa)
	Sand, S	Silt, M	Clay, C	Liquid limit, WL	Plastic limit, WP	Shrinkage limit, WS	MDD (g/cc)	OMC (%)		
2.65	4	9	87	65	22	6	1.64	18.9	210	138

3. RESULTS and DISCUSSION

In this, the test results of the unconfined compression test and microstructural studies of the untreated soil then the soil treated with 2%, 4%, 6%, 8% and 10% Calcined Clay (CC) were discussed and also analysed its changes in the strength characteristics of the soil.

**3.1. Unconfined Compression Test** The test was conducted on the untreated and treated soil samples at the different curing periods and the typical stress-strain characteristics curve for the untreated and treated soil with 2, 4, 6, 8 and 10 % of Calcined clay under curing of 14 days are given in Figure 3. The results show the increment in the unconfined compression strength value by increasing the percentage of calcined clay from 138kPa to 355kPa up to 8% calcined treated soil furthermore addition of 2% of calcined clay reduces the UCS value. It was observed that the rate of increment is more with an increase in the percentage of calcined clay. Many researchers reported that the reduction in the strength of soil once the stabilizer content has exceeded the optimum point [31-33]. This behaviour is similar for all other curing time periods of 1, 3, 7, 14, 28 and 60 days of the calcined clay treated soil. The more quantity of calcined clay provides more interaction between the soil and admixture and thus increasing the strength of the treated soil. The reduction in the compressive strength of soil once the stabilizer/binder content has exceeded a certain level has been reported by various researchers [34].

Figures 4 and 5 show the stress-strain relationship graph for the soil treated with 6% and 8% calcined clay under 1, 3, 7, 14, 28 and 60 days curing periods. The unconfined compression strength increases with an increase in curing period. Also, it was observed that the UCS value increased due to the influence of the curing period, but the percentage of increment is higher in the early days of curing compared with the later. The stress-strain behaviour is ductile in the early days of curing but the pattern changed to brittle at the later stage.

Figure 6 shows the UCC soil sample and their mode of failure pattern. This pattern is similarly maintained for all other percentages of the calcined clay. The variation is due to the pozzolanic materials is present in the calcined clay react with the soil minerals and alter the

behaviour from ductile to brittleness compared with the virgin soil.

The unconfined compression strength value increases the strength upto 8% with the addition of calcined clay with soil due to more amounts cementitious components present in calcined clay reacting with the soil minerals. The effect of the admixture and curing period of the soil treated with varying percentages of calcined clay is given in Figures 7 and 8. The results show that the UCS value got rapidly increased in the order of 101-202 kPa with an

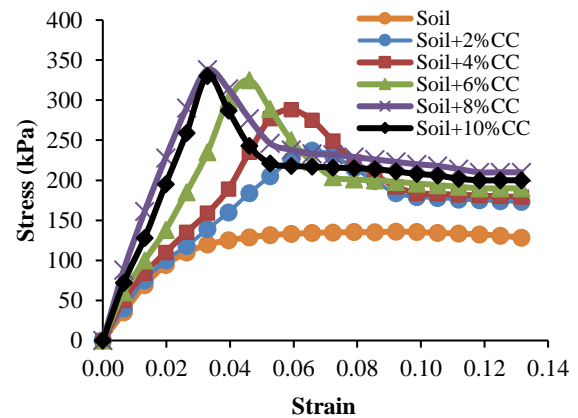


Figure 3. Stress strain Characteristics curve of the Untreated and 2%, 4%, 6%, 8% and 10% Calcined clay treated for 14 days curing period

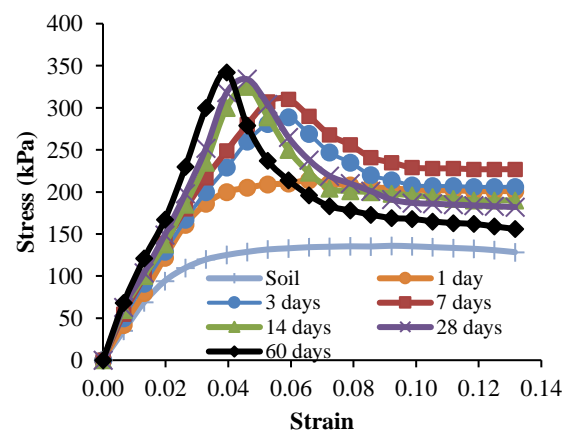
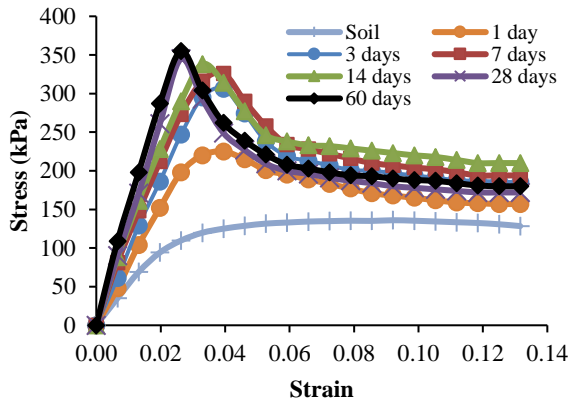
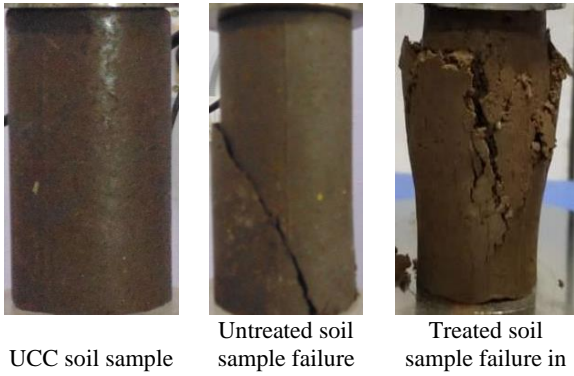


Figure 4. Stress strain characteristics graph for 6% Calcined clay treated soil under different curing period

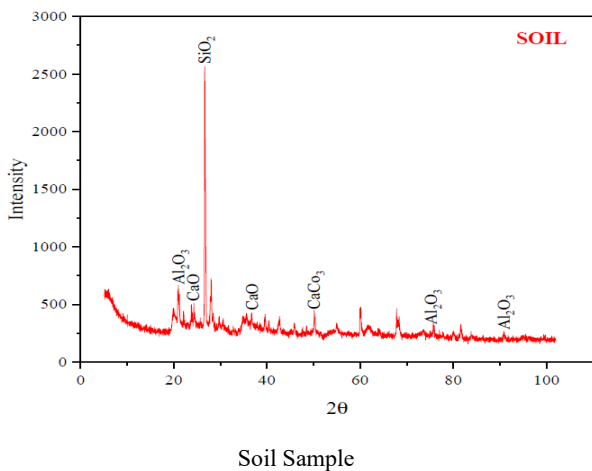


**Figure 5.** Stress strain characteristics graph for 8% Calcined clay treated soil under different curing period

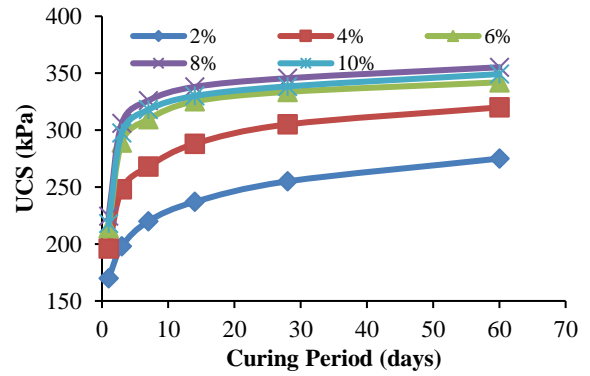


**Figure 6.** UCC soil sample with failure mode

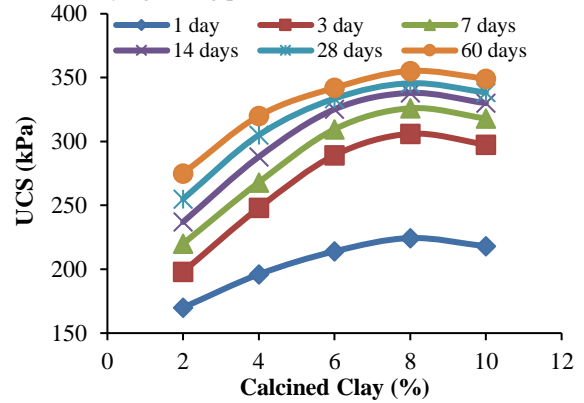
increase in the percentage of calcined clay of 2 to 8% at the age of 14 days curing period. However, an increase in calcined clay declined with increasing in curing period of 60 days was 17-39kPa. It was observed that the



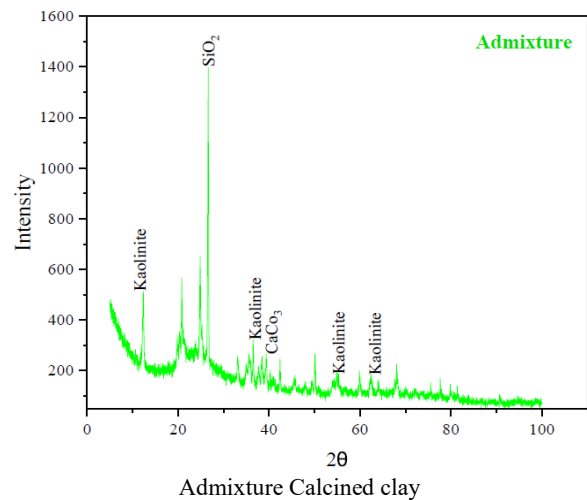
percentage increment in strength is more in the early days of curing due to the occurrence of high reactive siliceous and alumina content compared to that of the later days due to the slowdown of the reaction of additives.



**Figure 7.** Effect of admixture on the Calcined clay treated soil for varying curing period



**Figure 8.** Effect of curing period on the soil treated with varying percentage of Calcined clay



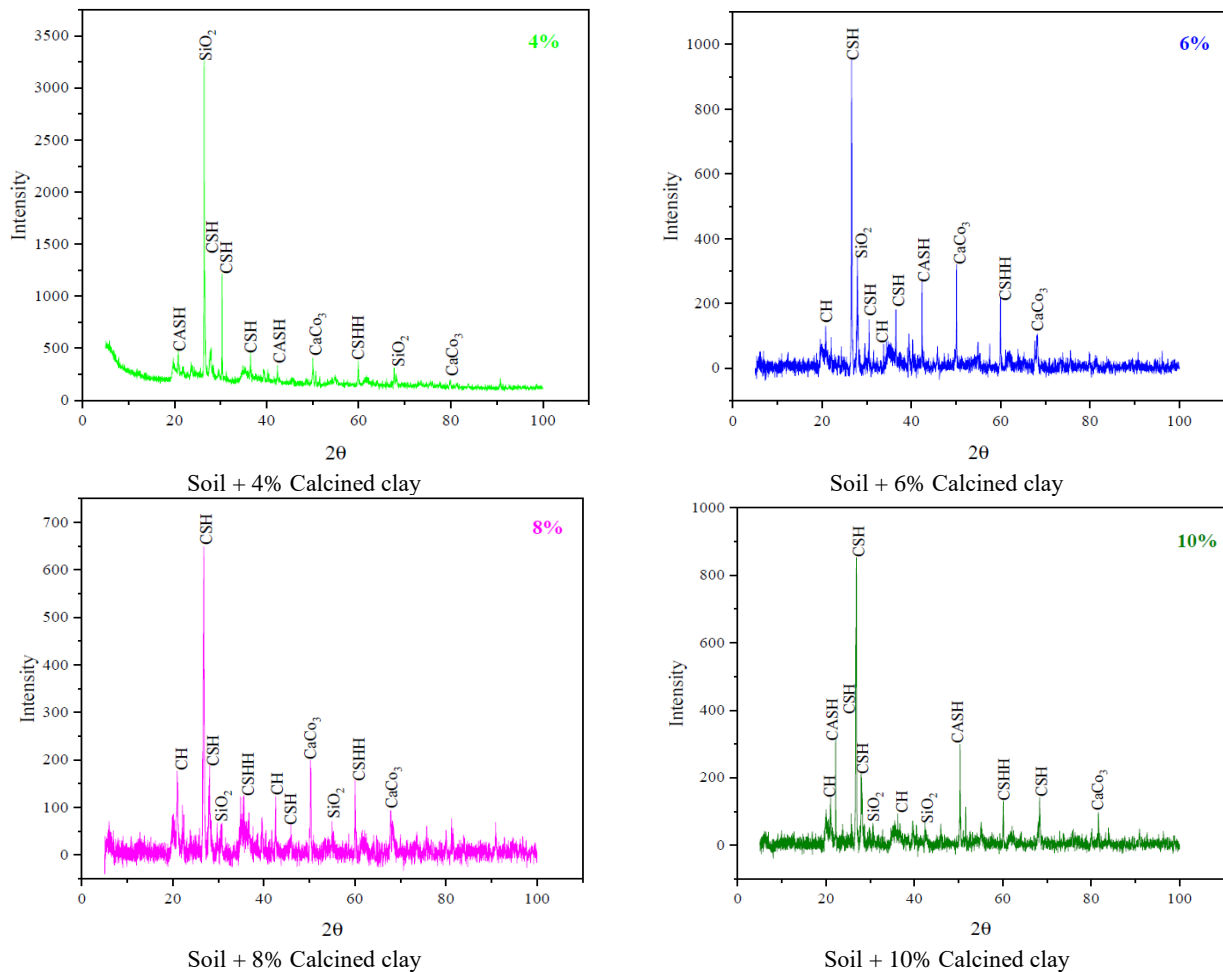


**Figure 9.** XRD patterns of virgin soil, calcined clay and soil added with different percentage of calcined clay (4%, 6%, 8% and 10%) for 14 days curing period

### 3. 2. Microstructural Studies

The XRD analysis and SEM studies were conducted for the expansive soil, calcined clay and soil treated with varying percentage of calcined clay at 14 days curing to observe the reason for the change in the soil to know the mineralogical composition of the materials of untreated and treated soil.

#### 3. 2. 1. X- Ray Diffraction Analysis

The geological properties of the soils are largely depend on the phases/minerals present in the soil rather than the chemical composition, type of minerals present or structure. The identification of the minerals is largely predicting the swelling and expansive behavior of the soil. The XRD pattern of the expansive soil used in this study is evident that the expansive soil consists of the clay mineral like montmorillonite and non-clay mineral of quartz ( $\text{SiO}_2$ ). The expansive soil is also identified with the mixed layer minerals such as illite–smectite and illite-montmorillonite. The peaks at the  $2\theta$  value of 26.6, 20.8, 50.1, 55.3, 59.9, 64, 67.7 and 68 are attributed

to the presence of quartz mineral. The mixed layered phases identified in the present soil attribute to the swelling potential of soil with increasing liquid limit value. XRD pattern of the calcined clay shows the amorphous halo in the range of  $18-28^\circ 2\theta$  represents the reorganized aluminosilicates of the kaolin as a result of the amorphisation during the calcination. The inserted image clearly shows the amorphous hump clearly. In addition to this, the crystalline phases of quartz,  $\text{CaCO}_3$ , kaolinite ( $\text{Al}_2\text{Si}_2\text{O}_5(\text{OH})_4$ ) etc are also present. Some of the remaining kaolinite peaks represent the incomplete decomposition of kaolinite after the calcination.

The absence of montmorillonite minerals and the formation of illite phases indicates the complete decomposition of the montmorillonite mineral before calcination. XRD Analysis X-ray diffraction analyses were conducted on samples of the four various percentages of 4, 6, 8, and 10 % at curing period of 14 days to study the phase nature of the materials and identified the main reacting compounds like CH, CASH,  $\text{CaCO}_3$ , C-S-H and  $\text{SiO}_2$ .

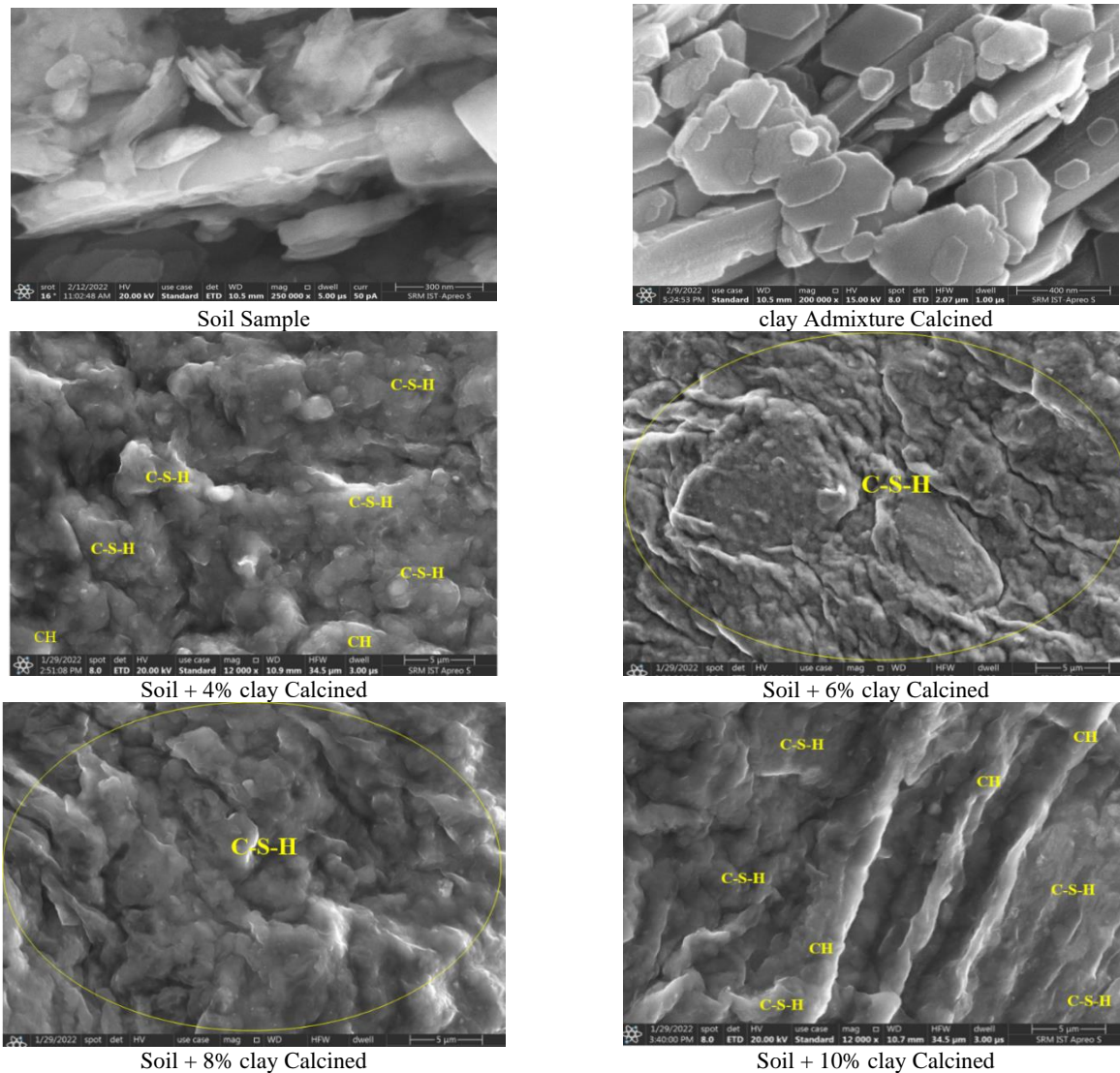


**Figure 10.** SEM images of virgin soil, calcined clay and soil added with different percentage of calcined clay (4, 6, 8 and 10%) for 14 days curing period.

The XRD pattern of the soil, calcined clay and soil stabilized with 4, 6, 8 and 10% calcined clay treated soil at 14 days curing period are presented in Figure 9. The weight percent is calculated based on the dry weight of the soil sample. The mineralogical composition of the treated soil represents that the calcined clay treated sample showed significant phase changes when simply mixing soil and calcined clay. That may be due to the fact that the calcined clay requires alkaline/acid condition to dissolve the reactive silica and alumina to form the aluminosilicate hydrate type gel. The calcined clay treated soil reveals the formation of a new mineral of calcium silicate hydrate (CSH) in the diffraction peak angle  $2\theta$  value of  $29^\circ$ . Also, additional calcite peaks ( $\text{CaCO}_3$ ) at the diffraction angle of  $38^\circ$  formed due to cementitious

reactions [35]. These hydration products are formed due to the pozzolanic reaction of the compounds in the soil and calcined clay.

**3. 2. 2. Scanning Electron Microscope** The soil samples were analyzed for morphology changes with the addition of admixtures using a high-resolution field emission electron microscope FEI's Quanta 200 FEG FESEM with elemental mapping and EDAX. SEM imaging essentially provides a visual characterization of the sample surface, making meaningful inferences from the image is harder. SEM Analysis to get the evolution images for the samples on the treated soil of four different percentages, such as 4, 6, 8 and 10% at 14 days curing period. SEM was carried out and illustrated. Since very

fine particles are used for taking images after the magnification and sizes may be adjusted by the operator without being aware of it and without knowing the significance of the images, it can be noted that some factors that affect the soil moisture system starting from the sample preparation up to the images taken by the operators. It was discovered that a minor adjustment and move results in two distinct images, one of which depicts appropriately moistened soils and the other, from the same sample, depicting improperly moistened soil; hence it can be stated that the SEM images are taken from the sample. Their corresponding inferences should be considered with respect to that particular image and not extrapolated to other regions.

SEM showed the microstructures of calcined clay, supporting the earlier assertion. Figure 10 shows the soil, admixture and 4, 6, 8, 10 % of treated soil under 14 days of curing and the dispersion of calcined clay is highlighted above. It indicates that the particles are randomly dispersed and incorporated within clay and hydration-product matrix. The interface between the calcined clay and stabilized clay matrix is also shown in the figures, illustrating that calcined clay particles are not required to participate in the hydration and pozzolanic interactions between hydrated products and clay minerals. It should be highlighted that sand and silt particles are only included in a clay matrix that has been stabilized when hydration process products, like CSH, adhere to the clay surface and bind sand particles to create a stabilizing paste. As previously indicated, the clay/silt particles should only interact in a safe and solid way.

#### 4. CONCLUSION

From the test results the following observation on the strength and microstructural behaviour of the untreated and 2, 4, 6, 8 and 10% of Calcined clay treated soil under 1, 3, 7, 14, 28 and 60 days of curing were obtained

From the study of the unconfined compression test, it was examined that the UCS values increased from 138 to 355 kPa at 8% optimum calcined clay for 60 days of curing. An increase in the strength of UCS value is due to the development of cementitious compounds in the treated soil. The incremental strength is directly proportional to an increase in the proportion of admixture and curing phase up to optimum content.

The mineralogical studies show the formation of calcium hydroxide and CSH gel formation is more on the later days of curing compared to the earlier. Also, it shows the chemical reaction between the compounds present in the admixture and soil that forms the Cementitious bonding of the treated soil.

Thus, calcined clay acts as a natural pozzolanic material for the replacement of cement that improves the

strength characteristics of the expansive soil in the ground improvement techniques and also reduces environmental pollution.

#### 5. REFERENCES

1. Wang, F., Wang, H., Jin, F. and Al-Tabbaa, A., "The performance of blended conventional and novel binders in the in-situ stabilisation/solidification of a contaminated site soil", *Journal of Hazardous Materials*, Vol. 285, (2015), 46-52. doi: <https://doi.org/10.1016/j.jhazmat.2014.11.002>
2. Ayadat, T., Hanna, A.M. and Hamitouche, A., "Soil improvement by internally reinforced stone columns", *Proceedings of the Institution of Civil Engineers-Ground Improvement*, Vol. 161, No. 2, (2008), 55-63. <https://doi.org/10.1680/jgrim.2022.175.3.165>
3. Phanikumar, B., Rao, A. and Suresh, K., "Compressive load response of expansive clay beds reinforced with granular pile-anchors-in-situ", *Ground Improvement*, Vol. 161, No. 3, (2008), 121-129. doi: 10.1139/t03-075.
4. Prusinski, J.R. and Bhattacharja, S., "Effectiveness of portland cement and lime in stabilizing clay soils", *Transportation Research Record*, Vol. 1652, No. 1, (1999), 215-227. <https://doi.org/10.3141/1652-28>
5. Wild, S. and Tasong, W., "Influence of ground granulated blastfurnace slag on the sulphate resistance of lime-stabilized kaolinite", *Magazine of Concrete Research*, Vol. 51, No. 4, (1999), 247-254. <https://doi.org/10.1680/mac.1999.51.4.247>
6. Yang, H.-P. and Zheng, J.-L., "The new engineering treatment techniques of expansive soils subgrade for guangxi nanning-youyi guan expressway, in Unsaturated soils 2006. 2006.439-450.
7. Hunter, D., "Lime-induced heave in sulfate-bearing clay soils", *Journal of Geotechnical Engineering*, Vol. 114, No. 2, (1988), 150-167. [https://doi.org/10.1061/\(ASCE\)0733-9410\(1988\)114:2\(150\)](https://doi.org/10.1061/(ASCE)0733-9410(1988)114:2(150))
8. Lee, L.M., Ng, W.S., Tan, C.K. and Hii, S.L., "Bio-mediated soil improvement under various concentrations of cementation reagent", in Applied mechanics and materials, Trans Tech Publ. Vol. 204, (2012), 326-329.
9. Tasong, W.A., Wild, S. and Tilley, R.J., "Mechanisms by which ground granulated blastfurnace slag prevents sulphate attack of lime-stabilised kaolinite", *Cement and Concrete Research*, Vol. 29, No. 7, (1999), 975-982. [https://doi.org/10.1016/S0008-8846\(99\)00007-1](https://doi.org/10.1016/S0008-8846(99)00007-1)
10. Javdanian, H., "The effect of geopolymerization on the unconfined compressive strength of stabilized fine-grained soils", *International Journal of Engineering, Transactions B: Applications*, Vol. 30, No. 11, (2017), 1673-1680. doi: 10.5829/ije.2017.30.11b.07.
11. Rahmnejad, M. and Toufigh, V., "Influence of curing time and water content on unconfined compressive strength of sand stabilized using epoxy resin", *International Journal of Engineering, Transactions B: Applications*, Vol. 31, No. 8, (2018), 1187-1195. doi: 10.5829/ije.2018.31.08b.05.
12. Oza, J. and Gundaliya, P., "Study of black cotton soil characteristics with cement waste dust and lime", *Procedia Engineering*, Vol. 51, (2013), 110-118. <https://doi.org/10.1016/j.proeng.2013.01.017>
13. Miller, G.A. and Azad, S., "Influence of soil type on stabilization with cement kiln dust", *Construction and Building Materials*, Vol. 14, No. 2, (2000), 89-97. [https://doi.org/10.1016/S0950-0618\(00\)00007-6](https://doi.org/10.1016/S0950-0618(00)00007-6)

14. Wild, S., Kinuthia, J., Jones, G. and Higgins, D., "Suppression of swelling associated with ettringite formation in lime stabilized sulphate bearing clay soils by partial substitution of lime with ground granulated blastfurnace slag (GGBS)", *Engineering Geology*, Vol. 51, No. 4, (1999), 257-277. [https://doi.org/10.1016/S0013-7952\(98\)00069-6](https://doi.org/10.1016/S0013-7952(98)00069-6)
15. Takhelmayum, G., Savitha, A. and Krishna, G., "Laboratory study on soil stabilization using fly ash mixtures", *International Journal of Engineering Science and Innovative Technology (IJESIT)*, Vol. 2, No. 1, (2013), 477-482. doi.
16. Bell, F., "Lime stabilization of clay minerals and soils", *Engineering Geology*, Vol. 42, No. 4, (1996), 223-237. [https://doi.org/10.1016/0013-7952\(96\)00028-2](https://doi.org/10.1016/0013-7952(96)00028-2)
17. Rajasekaran, G., "Sulphate attack and ettringite formation in the lime and cement stabilized marine clays", *Ocean Engineering*, Vol. 32, No. 8-9, (2005), 1133-1159. doi. <https://doi.org/10.1016/j.oceaneng.2004.08.012>
18. Priyanga, G., Krishnan, K.D. and Ravichandran, P., "Characteristics of rubberized soil with ground granulated blast-furnace slag as binder material", *Materials Today: Proceedings*, Vol. 5, No. 2, (2018), 8655-8661. <https://doi.org/10.1016/j.matpr.2017.12.290>
19. Manimaran, A., Santhosh, S. and Ravichandran, P., "Characteristics study on sub grade soil blended with ground granulated blast furnace slag", *Rasayan Journal of Chemistry*, Vol. 11, No. 1, (2018), 401-404. doi: 10.7324/RJC.2018.1112044.
20. Indiramma, P., Sudharani, C. and Needhidasan, S., "Utilization of fly ash and lime to stabilize the expansive soil and to sustain pollution free environment—an experimental study", *Materials Today: Proceedings*, Vol. 22, (2020), 694-700. <https://doi.org/10.1016/j.matpr.2019.09.147>
21. Dahale, P., Nagarnaik, P. and Gajbhiye, A., "Engineering behavior of remolded expansive soil with lime and flyash", *Materials Today: Proceedings*, Vol. 4, No. 9, (2017), 10581-10585. <https://doi.org/10.1016/j.matpr.2017.06.423>
22. Krishnan, K.D., Ravichandran, P., Janani, V., Annadurai, R. and Gunturi, M., "Effect of phosphogypsum and fly ash stabilisation on the strength and microstructure of clay", *Indian Concrete Journal*, Vol. 89, No. 7, (2015), 81-86.
23. Janani, V. and Pandey, S., "Study on soil strength improvement using dolochar as sustainable material", *Journal of Green Engineering*, Vol. 10, (2020), 2420-2431.
24. Manimaran, A., Seenu, S. and Ravichandran, P., "Stimulation behaviour study on clay treated with ground granulated blast slag and groundnutshell ash", *International Journal of Engineering, Transactions B: Applications*, Vol. 32, No. 5, (2019), 673-678. doi: 10.5829/ije.2019.32.05b.08.
25. Sujatha, E.R., Dharini, K. and Bharathi, V., "Influence of groundnut shell ash on strength and durability properties of clay", *Geomechanics and Geoengineering*, Vol. 11, No. 1, (2016), 20-27. <https://doi.org/10.1080/17486025.2015.1006265>
26. Divya, S., Anusuya, K., Priya, P., Sobana, V. and Manjula, K., "Stabilization of black cotton soil using groundnut shell ash", *International Journal of Scientific Development and Research*, Vol. 6, No. 3, (2021). <https://doi.org/10.21741/9781644901618-6>
27. Chittaranjan, M., Vijay, M. and Keerthi, D., "Agricultural wastes as soil stabilizers", *International Journal of Earth Sciences and Engineering*, Vol. 4, No. 06, (2011), 50-51.
28. Imran, M. and Khan, A.A., "Characterization of agricultural waste sugarcane bagasse ash at 1100 c with various hours", *Materials Today: Proceedings*, Vol. 5, No. 2, (2018), 3346-3352. doi. <https://doi.org/10.1016/j.matpr.2017.11.577>
29. Jamsawang, P., Poorahong, H., Yoobanpot, N., Songpiriyakij, S. and Jongpradist, P., "Improvement of soft clay with cement and bagasse ash waste", *Construction and Building Materials*, Vol. 154, (2017), 61-71. <https://doi.org/10.1016/j.conbuildmat.2017.07.188>
30. Soil, A.C.D.-o. and Rock, "Standard practice for classification of soils for engineering purposes (unified soil classification system) 1, ASTM international, (2017).
31. Marandi, S.M., Ghasemi, M. and Shahiri, J., "Effects of partial substitution of styrene-butadiene-styrene with granulated blast-furnace slag on the strength properties of porous asphalt", *International Journal of Engineering, Transactions A: Basics*, Vol. 30, No. 1, (2017), 40-47. doi: 10.5829/idosi.ije.2017.30.01a.06.
32. Zha, F., Liu, S., Du, Y. and Cui, K., "Behavior of expansive soils stabilized with fly ash", *Natural Hazards*, Vol. 47, No. 3, (2008), 509-523. doi: 10.1007/s11069-008-9236-4.
33. Basha, E., Hashim, R., Mahmud, H. and Muntohar, A., "Stabilization of residual soil with rice husk ash and cement", *Construction and Building Materials*, Vol. 19, No. 6, (2005), 448-453. doi. <https://doi.org/10.1016/j.conbuildmat.2004.08.001>
34. Sharma, A.K. and Sivapullaiah, P., "Ground granulated blast furnace slag amended fly ash as an expansive soil stabilizer", *Soils and Foundations*, Vol. 56, No. 2, (2016), 205-212. <https://doi.org/10.1016/j.sandf.2016.02.004>
35. Yong, R.N. and Ouhadi, V.R., "Experimental study on instability of bases on natural and lime/cement-stabilized clayey soils", *Applied Clay Science*, Vol. 35, No. 3-4, (2007), 238-249. <https://doi.org/10.1016/j.clay.2006.08.009>

---

### Persian Abstract

#### چکیده

خاک‌های گسترده تمایل به تورم، انقباض و تراکم‌پذیری بیشتر با تغییر در برهمکنش خاک و آب دارند که بر تغییر ظرفیت باربری خاک تأثیر می‌گذارد. روش‌های مختلفی برای تثبیت خاک و ترویج توسعه پایدار در صنعت ساختمان استفاده می‌شود. در این زمینه، تثبیت خاک، تکنیک اصلی و کارآمد برای بهبود استحکام با تغییر خصوصیات فیزیکی خاک است. علاوه بر این، افزودنی‌ها ویژگی‌های شیمیایی خاک را بهبود بخشیدند و همچنین با بهبود پیوند بین ساختارهای خاک، به پایداری رسیدند. تثبیت خاک توسط بسیاری از محققین آزمایش شده است و با موفقیت در چندین کاربرد میدانی به ویژه با استفاده از سیمان، آهک، خاکستر، مواد شیمیایی و غیره استفاده شده است. این کار بر روی تأثیر، توسعه ویژگی‌های مقاومتی خاک‌های تیمار شده با درصد‌های مختلف خاک رس کلسینه شده به صورت ۲، ۴، ۶، ۸ و ۱۰ درصد در زمان‌های مختلف پخت تمرکز دارد. رفتارهای مقاومتی افزایش یافته خاک منبسط با انجام آزمایش فشار نامحدود و همچنین مطالعات ریزساختاری مانند SEM و XRD برای نمونه‌های انتخاب شده تعیین شد. نتایج نشان می‌دهد که حداکثر مقاومت در خاک تیمار شده با مخلوط ۸ درصد به دست آمد. بنابراین خاک رس کلسینه شده به عنوان یک تثبیت کننده طبیعی مقرون به صرفه و سازگار با محیط زیست به جای جایگزینی سیمان برای تثبیت خاک گسترده عمل می‌کند که ویژگی‌های مقاومتی خاک گسترده را توسعه می‌دهد و همچنین آلودگی محیطی را کاهش می‌دهد.

---



## Chemical Reaction-Diffusion Model Around a Vessel for Studying Temperature and Concentration of Three Chemical Species by Finite Element Method

P. Pasha<sup>a</sup>, F. Taghinia<sup>b</sup>, F. Nadalinia Chari<sup>b</sup>, B. Jalili<sup>c</sup>, P. Jalili<sup>c</sup>, D. Domiri Ganji<sup>b</sup>

<sup>a</sup> Department of Mechanical Engineering Mazandaran University of Science and Technology, Babol, Iran

<sup>b</sup> Department of Mechanical Engineering Noshirvani University of Technology, Babol, Iran

<sup>c</sup> Engineering, Faculty of Engineering, North Tehran Branch, Islamic Azad University, Tehran, Iran

### PAPER INFO

#### Paper history:

Received 06 September 2022

Received in revised form 11 October 2022

Accepted 12 October 2022

#### Keywords:

Finite Element Method

Chemical Reaction

Diffusion

Arrhenius Equations

### ABSTRACT

In this paper, the temperature and concentration of species around a vessel using the reaction and diffusion relations were investigated. The reactions between 3 chemical species, and the relationship between temperature changes and the rate of chemical reactions were studied. The novelty of this paper is the use of different coefficients of material with diffusion constants and also considering the concentration and temperature of materials involved in the reaction with non-heat sources and with heat source modes. So that showed the concentration and heat transfer rate of substances involved in the chemical reactions in the form of two-dimensional and three-dimensional diagrams about their distance from the borders of the vessel. The finite element method is utilized for calculated differential equations. According to the results obtained, when the temperature of the reactants increased more heat is released; the concentration also changed a lot, and its amount increased. However, in products such as substance (c), it has an inverse relationship with reactants (a) and (b) in such a way that as the concentration and temperature of the reactants increased, these values decreased in the product. On average, concentration changes in the distance from the center to the surroundings the maximum heat source mode was about 76% less than the average heat source mode and about 14% less than the non-heat source mode.

doi: 10.5829/ije.2023.36.01a.19

### NOMENCLATURE

$K_t$	diffusivities	$H_2$	Activation energy/k for C
$K_a$	diffusivities	$a_0, b_0, c_0$	Initial distribution
$K_b$	diffusivities	T	Temperature
$K_1$	Reaction coef for A+B	Q	Heta transfer
$H_1$	Activation energy/k for A+B	A, B, C	Chemical component
$K_2$	Reaction coef for C	C	Concentration

## 1. INTRODUCTION

Reaction-diffusion frameworks are scientific models which compare to a few physical marvels. The foremost common is the alteration in space and time of the concentration of one or more chemical substances: neighborhood chemical responses in which the substances are changed into each other, and dissemination which causes the substances to spread out over a surface in space. Reaction-diffusion frameworks

are connected in chemistry. In any case, the framework can portray dynamic forms of non-chemical nature. Cases are found in science, geography, material science (neutron dissemination hypothesis), and biology. Waqas [1] studied the recreation of changed nanofluid demonstrated within the stagnation locale of cross liquid by the expanding-contracting barrel. Farooq et al. [2] investigated the transport of half-breed sort nanomaterial in the peristaltic movement of thick liquid considering nonlinear radiation, entropy optimization, and slip

\*Corresponding Author Email: [pasha.pooya@yahoo.com](mailto:pasha.pooya@yahoo.com) (P. Pasha)

impacts. This article examines entropy optimization in cross-breed nanomaterial streams through turning peristaltic channel dividers. Waqas [3] examined the scientific and computational system for warm exchange investigation of a ferromagnetic non-Newtonian fluid subjected to heterogeneous and homogeneous responses. Waqas [4] considered the chemical response effect in double-diffusive non-Newtonian fluid highlighting variable liquid thermo-solute traits. This thinks about focuses on a two-dimensional rate sort Maxwell fabric stream designed by a vertical moving surface. Warm source/sink and variable conductivity properties are included in vitality expression. Waqas et al. [5] investigated the nonlinear scientific examination of thermally radiative stratified nano liquid, including the perspectives of the attractive field, Robin conditions, and warm radiation. Waqas [6] studied the Dissemination of stratification-based chemically responsive Jeffrey fluid, including blended convection. The rate of heat-mass exchange is taken note higher when stratification factors are expanded because an increase in stratification factors yields lower solute and warm areas. Waqas et al. [7] researched the expository assessment of Oldroyd-B nano liquid beneath thermo-solute Robin conditions and stratifications. Waqas et al. [8] examined the Gyrotactic bioconvection stratified stream of magnetized micropolar nano liquid arranged by stretchable emanating surface with Joule warming and thick dissemination. Guedri et al. [9] considered the warm angles of attractively driven micro-rotational nanofluid designed by exponential emanating sheet. To accomplish such points, nanoparticle-based dispersed fluids may be utilized as working fluids instead of standard fluids to reinforce sun-powered vitality acknowledgment. Waqas et al. [10] investigated the transport of chemically receptive thixotropic nanofluid stream by convectively warmed permeable surface. Ebermann et al. [11] researched the expository and numerical approach to decide compelling dissemination coefficients for composite weight vessels. Shadman et al. [12] studied the combined septum and chamfer balances on threatened extending surface beneath the impact of nanofluid and the attractive parameters for revolving seals in computer equipment. In this paper, the variety of temperature and speed within the x-direction and the precise speed of the nanofluids stream through triangular and rectangular, and chamfer fins were examined within the presence of a uniform, attractive field. Fathollahi et al. [13] reviewed the application of numerical and computational strategies to explore the changes within the liquid parameters of the liquid passing over blades of distinctive shapes with the limited component strategy. Abdollahzadeh et al. [14] reviewed the studying the half-breed of radiation and attractive parameters on Maxwell fluid with  $\text{TiO}_2$  nanotube impact of distinctive edges. Pasha and Domiri-Ganji [15] examining the crossover examination of micropolar

ethylene-glycol nanofluid on extending surface mounted triangular, rectangular, and chamfer blades by FEM technique and optimization with RSM strategy. Darezereshki et al. [16] studied the chemical handle of synthesizing zinc oxide (ZnO) with nanorod and circular morphologies. The response temperature of all steps amid the blend of ZnO nano powders moved to a higher temperature as the pH of the beginning arrangement expanded from 6 to 11. Due to the effortlessness, the display strategy can be proposed as a helpful way to deliver unadulterated ZnO nanoparticles utilizing  $\text{ZnSO}_4$  and  $\text{ZnCl}_2$  arrangements without utilizing any harmful and natural chemicals. Wang et al. [17] investigated the numerical examination of the heat-fluid characteristic interior high-speed precise contact ball bearing greased up with oil. Madani et al. [18] researched the A sequence-based solvency indicator made with widened press excitation leftover systems.

Kunkel et al. [19] investigated the Modeling coronavirus spike protein flow: suggestions for immunogenicity and safe elude. Hosseini et al. [20] reviewed the creation of an Al/Mg bimetallic thin-walled ultrafine-grained tube by extreme plastic distortion diary of materials building and execution. Alrwashdeh et al. [21] investigated the effect of turbocharger compression ratio on performance of the spark-ignition internal combustion engine. The present study is the use of a series of chemically coupled fluid equations that, by using the relationships between them and changes in a series of chemical parameters in software called FlexPDE, were able to study the concentration of reactants and products and also with changes in heat transfer to the center examined the shape of the vessel, the temperature in different areas of the vessel, and showed the heat flux at the boundaries. Also, the relationships between concentration and temperature and the relationship between reaction rate and these factors were investigated. The purpose and necessity of this research are that while getting acquainted with the effect of chemical reactions on concentration and temperature and the relationship between them, were able to visualize these chemical agents with a finite mathematical-fluid method and method and by changing the physical parameters of materials. Reagents, reactions, and heat transfer changes can reach the highest efficiency. Using the finite element method, obtained two-dimensional and three-dimensional diagrams and contours that depicted the changes in concentration and temperature of the products and the reactant and showed that they also showed significant changes in the opposite direction. The novelty of this paper is the use of different coefficients of material diffusion constants and also considering the concentration and temperature of materials involved in reacting with non-heat sources and with heat source modes. So that showed the concentration and heat transfer rate of substances

involved in chemical reactions in the form of two-dimensional and three-dimensional diagrams to their distance from the borders of the vessel. The main challenge in this article is to investigate the changes in the concentrations of substances involved in chemical reactions around the plate, which are calculated in two cases without internal heat energy or internal heat production. Among the achievements of this article, it can be mentioned that during this article, using the FEM calculation method, the concentrations, and temperatures of the reactant and product materials were analyzed, and the result was obtained that a heat source around the plate, heat transfer and concentration distribution is improved. In general, in the present study, the inner plate's surface meshing was done with the finite element method. The meshing and the number of elements were obtained. In the second part, the preliminary results of the present study were compared with a similar article, and in the third part, with diagrams. Moreover, two-dimensional and three-dimensional contours have been used to investigate the temperature and concentration of reactants and products as shown in Figure 1.

**1. 1. Problem Definition** In this paper, using the reaction and diffusion relations, the reaction between 3 chemical species, and the relationship between temperature changes and the rate of chemical reaction, investigate the temperature and concentration of species around a vessel (according to Figure 2). As described three chemical components, A, B, and C, which react and diffuse, and a temperature, which is affected by the reactions.

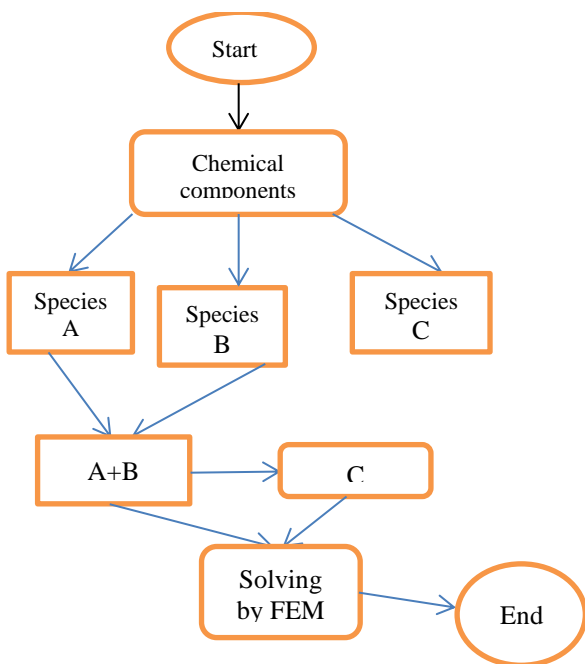


Figure 1. Flowchart of the problem

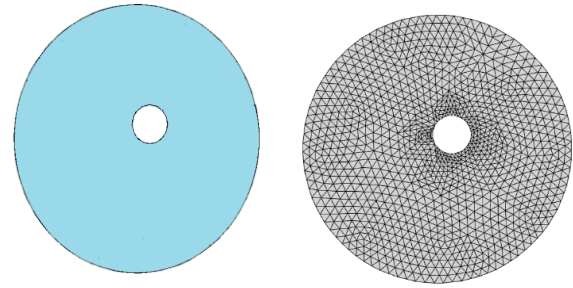


Figure 2. Geometry and mesh of the problem

Assumptions:

- I) A combines with B to form C, liberating heat.
- II) C decomposes to A and B, absorbing heat. The decomposition rate is temperature dependent.
- III) A, B, C and Temperature diffuse with differing diffusion constants.

The boundary of the vessel is held cold, and heat is applied to a circular exclusion patch near the center, intended to model an immersion heater. What is an immersion heater? The simple answer is that it may be a device that gives hot water to your house and is fueled by electricity. The immersion water heater is partitioned from your central warming boiler or radiators, which means that even if your central warming fails, you should still be able to have warm water in your house. A, B, and C cannot diffuse out of the boundary. This example shows the application of FlexPDE to the solution of reaction-diffusion problems. The complete equations, including the Arrhenius terms that describe the system, are [11]:

$$\text{div} \left( K_t \cdot \frac{\partial T}{\partial x} \vec{i} + \frac{\partial T}{\partial y} \vec{j} + \frac{\partial T}{\partial z} \vec{k} \right) + Q + K_1 \cdot e^{-H_1/(T+273)} \cdot (0.0025) \cdot A \cdot B - K_2 \cdot e^{-H_2/(T+273)} \cdot (0.0025) \cdot C \cdot (T+273) = 0 \quad (1)$$

$$\text{div} \left( K_a \cdot \frac{\partial A}{\partial x} \vec{i} + \frac{\partial A}{\partial y} \vec{j} + \frac{\partial A}{\partial z} \vec{k} \right) - K_1 \cdot e^{-H_1/(T+273)} \cdot A \cdot B + K_2 \cdot e^{-H_2/(T+273)} \cdot C \cdot (T+273) = 0 \quad (2)$$

$$\text{div} \left( K_b \cdot \frac{\partial B}{\partial x} \vec{i} + \frac{\partial B}{\partial y} \vec{j} + \frac{\partial B}{\partial z} \vec{k} \right) - K_1 \cdot e^{-H_1/(T+273)} \cdot A \cdot B + K_2 \cdot e^{-H_2/(T+273)} \cdot C \cdot (T+273) = 0 \quad (3)$$

$$\text{div} \left( K_c \cdot \frac{\partial C}{\partial x} \vec{i} + \frac{\partial C}{\partial y} \vec{j} + \frac{\partial C}{\partial z} \vec{k} \right) + K_1 \cdot e^{-H_1/(T+273)} \cdot A \cdot B - K_2 \cdot e^{-H_2/(T+273)} \cdot C \cdot (T+273) = 0 \quad (4)$$

where  $K_t$ ,  $K_a$ ,  $K_b$ , and  $K_c$  are the diffusion constants,  $E_{AB}$  is the heat liberated when A and B combine, and  $Q$  is any internal heat source. A, B, and C are the chemical components, T is the temperature parameter, and  $H_1$  and  $H_2$  are the activation energy parameter for A+B and C species.  $K_1$  is the reaction coefficient for A+B, and  $K_2$  is the reaction coefficient for C.

The boundary layer is [11]: in the  $(0,-1) \rightarrow \text{Temp}=0$ ,

$$a^{\wedge}=0, b^{\wedge}=0, c^{\wedge}=0 \quad (5)$$

In the  $(-0.2, 0) \rightarrow \text{Temp}=100,$

$$a'=0, b'=0, c'=0 \tag{6}$$

Notice that the system is non-linear, as it contains terms involving A.B and C.Temp.

There are infinite solutions to these equations, differing only in the total species count. Since species are conserved, the initial conditions uniquely determine the final solution. However, this fact is not embodied in the steady-state equations. The only way to impose this condition on the steady-state system is through an integral constraint equation, which describes the conservation of the total species number.

### 3. METHODOLOGY

**3. 1. Finite Element Method (FEM)** A finite element method (abbreviated as FEM) is a numerical method to obtain a surmised solution to a course of problems administered by elliptic partial differential equations. These problems are called boundary value problems, comprising a partial differential equation. (FEM) is an amazingly valuable device within the field of gracious building for numerically approximating physical structures as complex as standard expository arrangements. The advantages of using this method are high adaptability, great accuracy, time-dependent simulation, and better visualization of the boundaries of the studied shape. Similar results can be achieved with other mathematical methods, such as VIM, but they do not have the application of this method. The finite element method can be a fundamental numerical technique. One of the common sense applications for this strategy is the FlexPDE scheme, which realizes the nonlinear fragmentary differential equations and the modulus differential equations. FlexPDE yield is added to a "problem-solving environment" in which the overall strengthening of the valences is working, which is necessary to determine the movable differentiation equation systems.

**3. 2. Validation for Methods** In this section, for validation, compared our work by Ebermann et al. [11] in Table 1. The amount of computational error in our work is very low compared to Ebermann work. The maximum number of errors happened in  $x=0.5$  and minimum number of errors happened in  $x=1$ .

### 4. RESULTS AND DISCUSSION

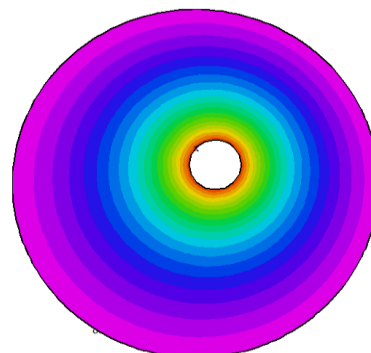
The set of shapes above (Figure 3) shows the temperature changes of reactive particles around the vessel in different heat and heat reaction modes. As mentioned before, around the inner circular vessel and its center, due

to the addition of the heat flow of the boundary layer with high thermal thickness, the thermal flux is maximum in its boundary layer points. As far from the center of the vessel, the crushing vessel is largely spread around, and the temperature of the reaction of the species decreases, and more heat is released, resulting in a small thermal boundary layer. Figures 3(a) and 3(b) show that do not have heat production in the center of the vessel, but due to the import of heat following shapes C-3 and D-3, there is much heat around the inner vessel and hot vortex behind the vessel (a) vessel is formed. In general, with the increase in the heat given to the reactive species (a) and (b), more energy from these species spreads into the environment, a larger boundary layer is formed, and the heat transfer level becomes larger, resulting in increased efficiency and heat flux. The temperature gradient (difference between two arbitrary particles on the plane) of material a has lower values with increasing heat transfer to the center than in the case without a heat source.

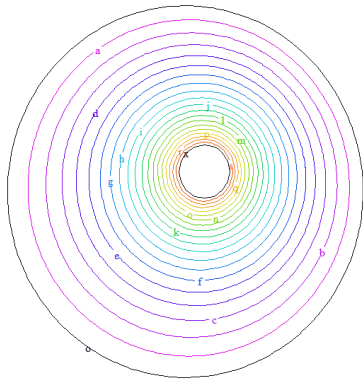
First, describe the relationship between the concentration of reactants and temperature and the thermal diffusion coefficient (according to Figure 4). In general, higher-concentration molecules move to a lower-concentration region, which means that the heat diffusion flux is related

**TABLE 1.** Comparison of temperature for present work and Ebermann’s work [11] at  $K_t=0.05, H_1=10, K_1=1$

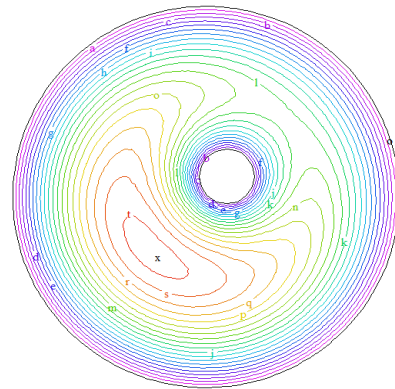
		$x = -1.5$	$x = -1$	$x = 0$	$x = 0.5$	$x = 0.75$	$x = 1$
<b>Temp</b>	Present work	0	26	48	68.9	80	10
	Ebermann et al. [11]	0	25.8	49	66.9	80	10
<b>Concentration</b>	Present work	7.79	7.88	7	8.04	8.34	8
	Ebermann et al. [11]	7.79	7.88	7	8.03	8.34	8



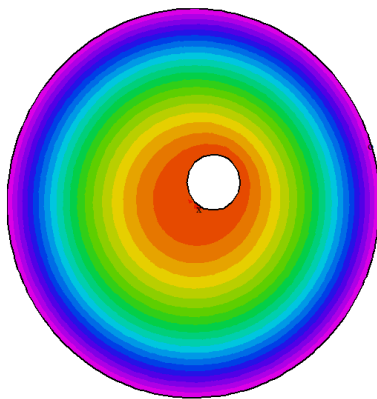
(a) Temperature profile around the vessel for heat source=0



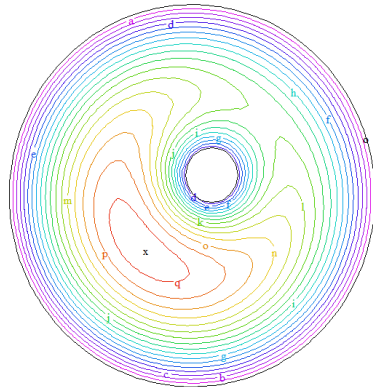
(b) Stream line of temperature profile around the vessel for heat source=0



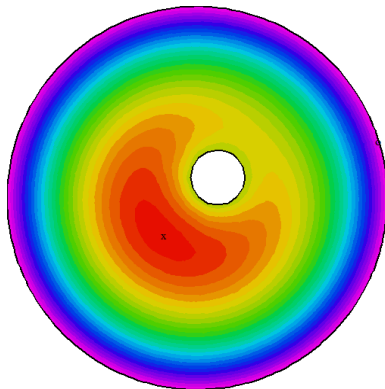
(f) Stream line of Temperature profile for heat source=4  
**Figure 3.** Temperature alterations around the vessel for different values of heat source



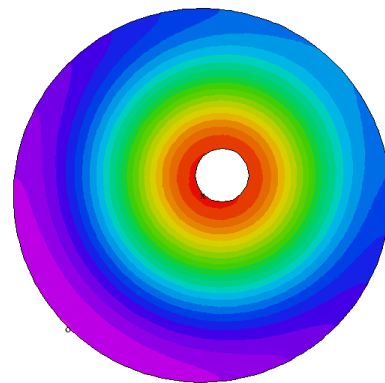
(c) Temperature profile around the vessel for heat source=2



(d) Stream line of Temperature profile for heat source=2

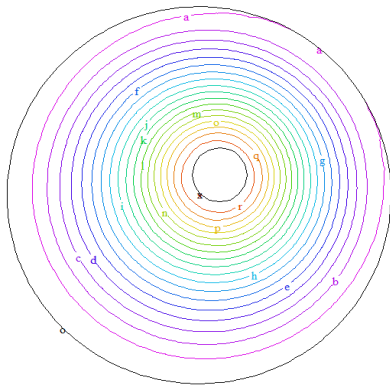


(e) Temperature profile around the vessel for heat source=4

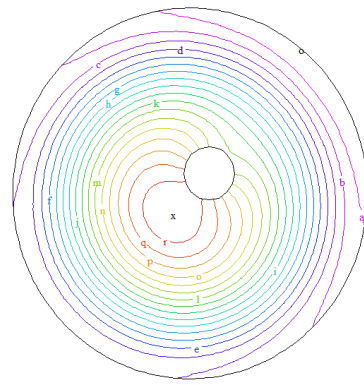


(a) Concentration profile around the vessel for heat source=0

to the concentration gradient. Let us now examine the relationship between the concentration of reactants and temperature. Since the rate of collision of species with each other increases with increasing temperature, concluded that the rate of the chemical reaction is directly related to temperature. Also, the reaction rate increases with increasing reactant concentration and decreases with decreasing concentration. According to Figure 4, reactant concentration (component a) is directly related to temperature and heat transfer, so it increases with increasing temperature concentration and decreases with decreasing temperature. In the case of no heat source, the material concentration is evenly distributed around the inner vessel. Since it is directly related to temperature, the amount of concentration is greater around the circular boundary. As it moves away from the center, this value decreases. By adding a heat source and giving extra heat to the center, reciprocating currents are created with multiple amplitudes. The higher this amount of inlet heat, the larger the reciprocating currents behind the inner vessel. We conclude that the weak flow behind the body increases, and the pressure decreases with increasing heat.

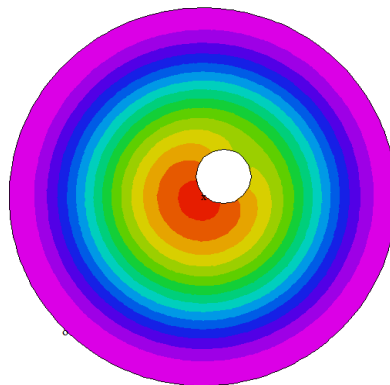


(b) Stream line of concentration profile around the vessel for heat source=0



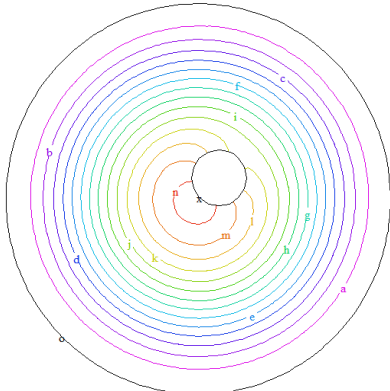
(f) Stream line of concentration profile around the vessel for heat source=4

**Figure 4.** Concentration alterations around the vessel for different values of heat source for component (a)

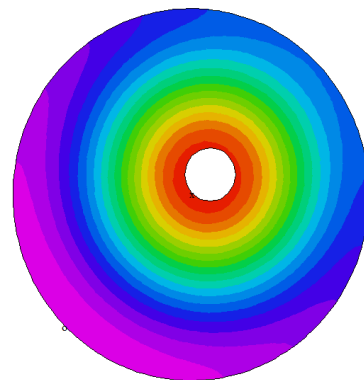


(c) Concentration profile around the vessel for heat source=2

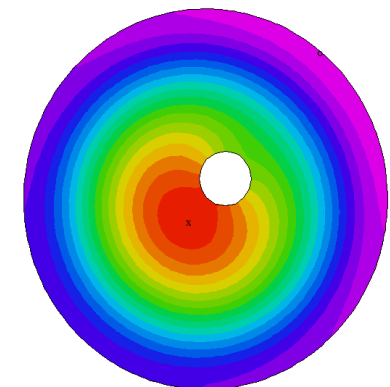
Figure 5 shows the changes in the concentration of reactant (b) around the plate and that the species is scattered around with a high diffusion coefficient. The higher the heat given to the center of the plate, the higher the specie diffusion coefficient and the better the reaction rate for the formation of substance (c).



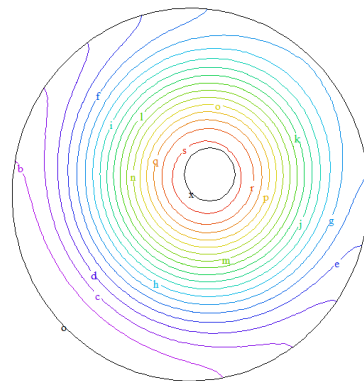
(d) Stream line of concentration profile around the vessel for heat source=2



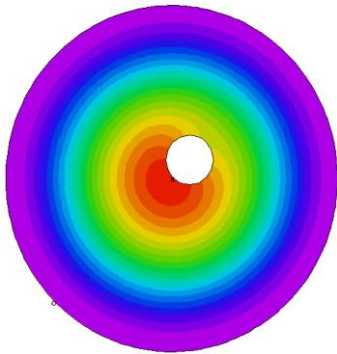
(a) Concentration profile around the vessel for heat source=0 for component (b)



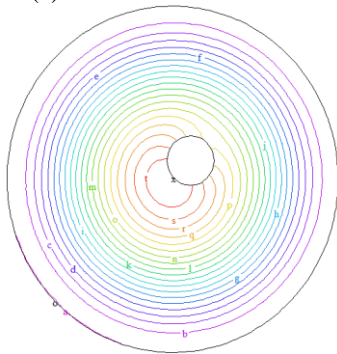
(e) Concentration profile around the vessel for heat source=4



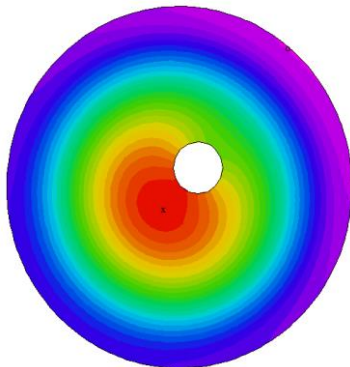
(b) Stream line of concentration profile around the vessel for heat source=0 for component (b)



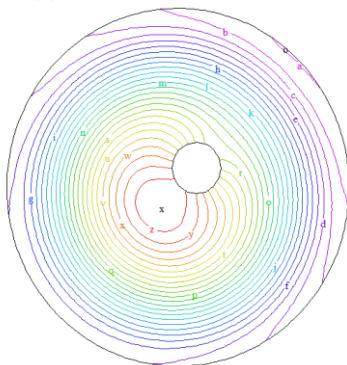
(c) Concentration profile around the vessel for heat source=2 for component (b)



(d) Stream line of concentration profile around the vessel for heat source=2 for component (b)

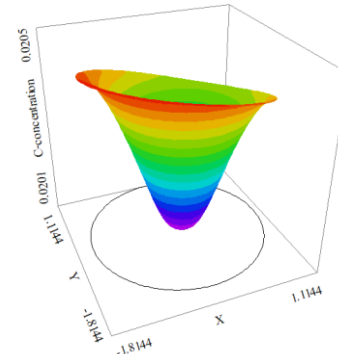


(e) Concentration profile around the vessel for heat source=2 for component (b)

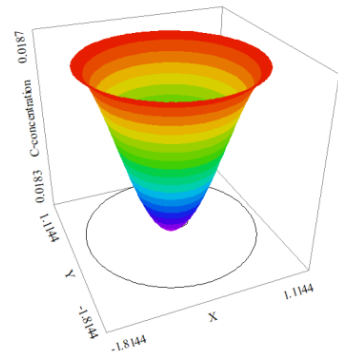


(f) Stream line of concentration profile around the vessel for heat source=2 for component (b)

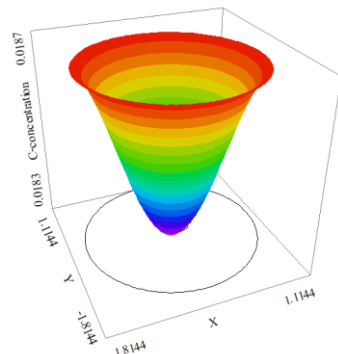
**Figure 5.** Concentration alterations around the vessel for different values of heat source for component (b)



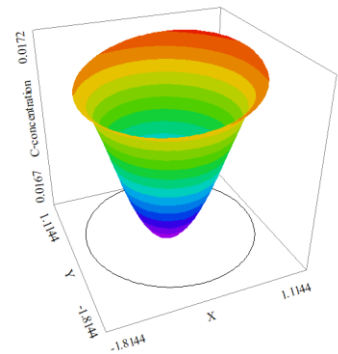
(a) 3D concentration profile for component (c) near the vessel by heat source=0



(b) 3D concentration profile for component (c) near the vessel by heat source=2 .



(b) 3D concentration profile for component (c) near the vessel by heat source=2

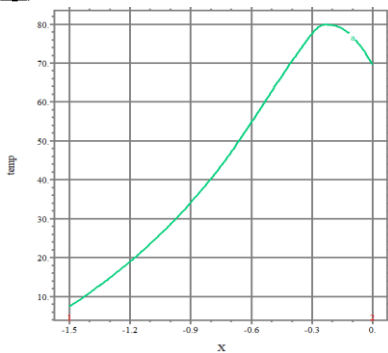
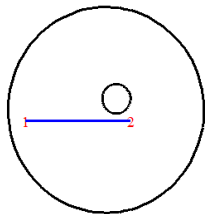


(c) 3D concentration profile for component (c) near the vessel by heat source=4

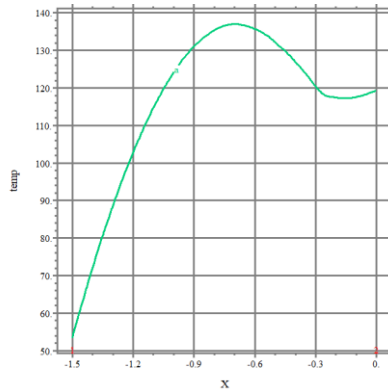
**Figure 6.** Three-dimensional images concentration alterations around the vessel for component (c)

The above figures (Figure 6) show in 3D the concentration of exothermal c around the vessel. In contrast to the previous states of species (a) and (b), where heat is dissipated from the center around, in this case, the heat around the center is greater. This is because substance (c) releases heat during a reaction and breaks it down into species a and b. Due to the addition of a heat source, the higher the heat and temperature around substance (c), the smaller the thermal boundary layer around the inner vessel and the larger around the outer vessel, and the greater the concentration around the boundary layer, the thicker it becomes. As the concentration increases, the viscosity increases, and the speed slows down.

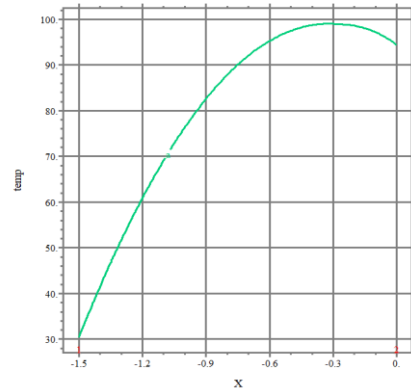
The diagrams in Figure 7 show the temperature composition changes of the materials involved in the chemical reaction at different heat sources at regular intervals. Given these changes on a graph and the



(a) Two dimensional graph of temperature changes in terms of distance from the center of the vessel to outside the environment for heat source=0



(b) Two dimensional graph of temperature changes in terms of distance from the center of the vessel to outside the environment for Heat source=4



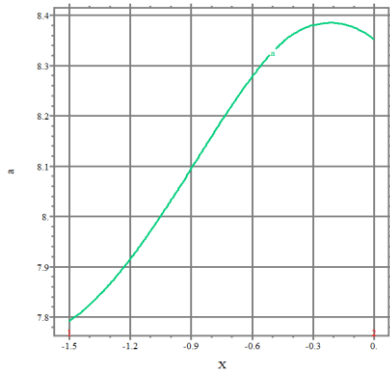
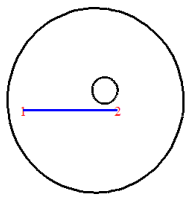
(c) Two dimensional graph of temperature changes in terms of distance from the center of the vessel to outside the environment for Heat source =2

**Figure 7.** Temperature changes of reacting materials at certain intervals with different heat sources

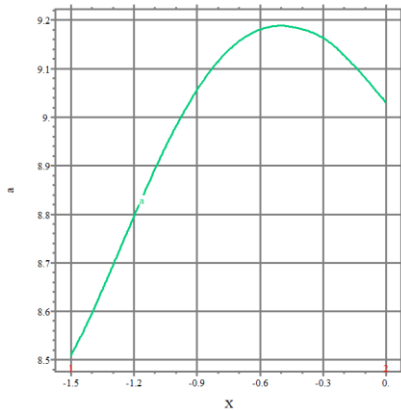
numerical representation of each distance, interpret the results with a very low error rate. In the case without a heat source and low diffusion coefficient, according to Figure 7(a), with increasing distance from  $x = -1.5$  to  $x = 0$ , the graph ascends, and the temperature increases to reach the peak. At  $x = -0.2$ , have the maximum temperature, which is the thermal peak. The temperature at this point is 80 degrees. Now, by adding a heat source in Figures 7(b) and 7(c), these graphical changes are created with larger amplitude, and a more extensive thermal boundary layer is formed around the central vessel. On average, temperature changes and heat transfer in the distance from the center to the surroundings in the maximum heat source mode is about 65% more than the average heat source mode and about 44% more than the non-heat source mode.

Figure 8 shows the diagrams of changes in the diffused concentration of reactant around the skeletal boundaries of the vessel with different heat sources. According to Figure 8(a), the closer get to the center of the vessel shape, the higher the concentration of the reaction material, increasing viscosity. This description applies to other diagrams as well and applies to them as well. Adding a heat source to the center around the vessel shape increases the concentration of the reactants, thus increasing the heat released from them. The lower the heat transfer to the center, the less heat is released and the lower the concentration. The maximum value of concentration occurs at  $x = -0.6$  in the heat source=4. On average, concentration changes in the distance from the center to the surroundings in the maximum heat source mode is about 57% more than the average heat source mode and about 28% more than the non-heat source mode.

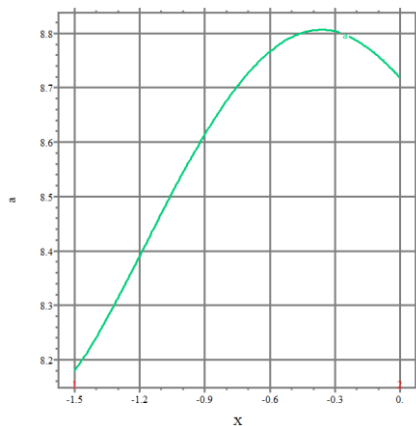
Table 2 shows the diagrams of changes in the diffused concentration of reactant around the skeletal boundaries of the vessel with different heat sources. According to



(a) Two dimensional graph of concentration component (a) changes in terms of distance from the center of the vessel to outside the environment for heat source=0



(b) Two dimensional graph concentration component (a) in terms of distance from the center of the vessel to outside the environment for source=4



(c) Two dimensional graph of concentration component (a) in terms of distance from the center of the vessel to outside the environment for Heat source =2

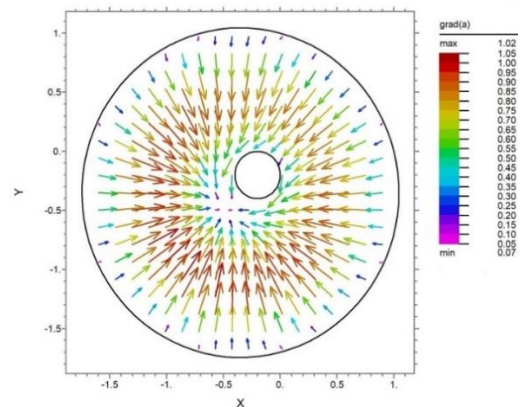
**Figure 8.** Concentration changes of reacting materials at certain intervals with different heat sources

**TABLE 2.** Numerical comparison of concentration between different heat sources for component ( c )

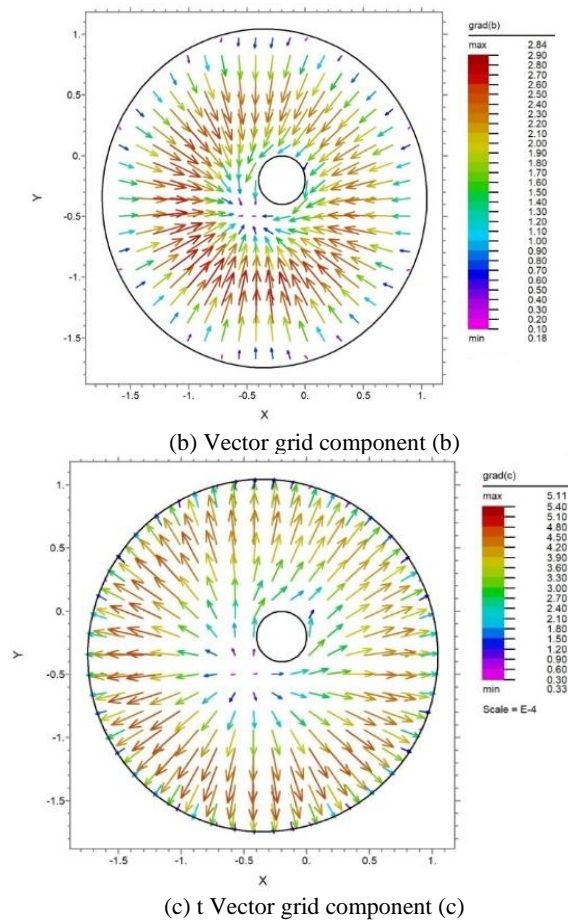
x	Heat source=0	Heat source=2	Heat source=4
-1.5	2.04	1.87	1.71
-1.4	2.02	1.82	1.65
-1.3	2.01	1.71	1.58
-1	1.88	1.44	1.22
-0.6	1.56	0.89	1
-0.2	1.09	0.76	0.83
0	1	0.54	0.60

Table 2, the maximum amount of concentration exists at  $x=-1.5$  for heat source=0 and the minimum concentration exists at  $x=0$  for heat source=4 by  $C=0.60$ . According to the numbers obtained in the table above, concluded that as the intensity of heat transfer to the center of the vessel increases, the concentration of reactant material (c) decreases, and the lower the temperature, the higher the concentration. On average, concentration changes in the distance from the center to the surroundings in the maximum heat source mode is about 76% less than the average heat source mode and about 14% less than the non-heat source mode. By releasing heat, substance c decomposes into materials (a) and (b) and emits some heat. This indicates that as the diffusion coefficient of the decomposed material increases, the concentration of the material decreases, and the reaction rate increases.

As seen in the above images (Figure 9), the movement vector of the material particles involved in the chemical reactions around the vessel and the temperature gradient lines of the reacting and produced particles have been drawn. The temperature vector lines for reacting particles (a) and (b) around the inner vessel have low values; because heat is released and their size is small. However, passing through the internal boundary layer makes this vector larger than the initial state. Particle (c)



(a) Vector grid component (a)



**Figure 9.** Simulation of motion vector of chemical reaction particles for temperature parameter

absorbs heat because it decays. This article's thermal lines around the outer vessel's boundaries have larger sizes than the lines near the boundaries of the inner vessel.

#### 4. CONCLUSION

In this paper, investigated the temperature and concentration of species around a vessel using the reaction and diffusion relations and the reaction between 3 chemical species, and the relationship between temperature changes and the rate of a chemical reaction. The novelty of this paper is the use of different coefficients of material diffusion constants and also considering the concentration and temperature of materials involved in reacting with non-heat sources and with heat source modes so that based on heat sources with different degrees of temperature and showed the concentration of reactant and product in the form of graphs and contours by FEM method. The finite Element Method is utilized for calculated differential equations.

- According to the results obtained, when the temperature of the reactants increases and more heat is released, the concentration also changes a lot, and its amount increases, but in products such as substance c, it has an inverse relationship with reactants a and b in such a way that As the concentration and temperature of the reactants increase, these values decrease in the product.
- Temperature changes and heat transfer in the distance from the center to the surroundings in the maximum heat source mode is about 65% more than the average heat source mode and about 44% more than the non-heat source mode.
- On average, concentration changes in the distance from the center to the surroundings in the maximum heat source mode is about 57% more than the average heat source mode and about 28% more than the non-heat source mode.

#### 5. REFERENCES

1. Waqas, M., "Simulation of revised nanofluid model in the stagnation region of cross fluid by expanding-contracting cylinder", *International Journal of Numerical Methods for Heat & Fluid Flow*, (2019). doi: 10.1108/HFF-12-2018-0797.
2. Farooq, S., Khan, M.I., Waqas, M., Hayat, T. and Alsaedi, A., "Transport of hybrid type nanomaterials in peristaltic activity of viscous fluid considering nonlinear radiation, entropy optimization and slip effects", *Computer Methods and Programs in Biomedicine*, Vol. 184, (2020), 105086. doi: 10.1016/j.cmpb.2019.105086.
3. Waqas, M., "A mathematical and computational framework for heat transfer analysis of ferromagnetic non-newtonian liquid subjected to heterogeneous and homogeneous reactions", *Journal of Magnetism and Magnetic Materials*, Vol. 493, (2020), 165646. doi: 10.1016/j.jmmm.2019.165646.
4. Waqas, M., "Chemical reaction impact in dual diffusive non-newtonian liquid featuring variable fluid thermo-solutal attributes", *Chemical Physics Letters*, (2022), 139661. doi: 10.1016/j.cplett.2022.139661.
5. Waqas, M., Nisar, U., Shehzad, S., Irfan, M. and Khan, W., "A non-linear mathematical analysis of thermally radiative stratified nanoliquid featuring the aspects of magnetic field, robin conditions and thermal radiation", *International Communications in Heat and Mass Transfer*, Vol. 125, (2021), 105199. doi: 10.1016/j.icheatmasstransfer.2021.105199.
6. Waqas, M., "Diffusion of stratification based chemically reactive jeffrey liquid featuring mixed convection", *Surfaces and Interfaces*, Vol. 23, (2021), 100783. doi: 10.1016/j.surfin.2020.100783.
7. Waqas, M., Hayat, T., Alsaedi, A. and Khan, W.A., "Analytical evaluation of oldroyd-b nanoliquid under thermo-solutal robin conditions and stratifications", *Computer Methods and Programs in Biomedicine*, Vol. 196, (2020), 105474. doi: 10.1016/j.cmpb.2020.105474.
8. Waqas, M., Sadiq, M.A. and Bahaidarah, H.M., "Gyrotactic bioconvection stratified flow of magnetized micropolar nanoliquid configured by stretchable radiating surface with joule heating and viscous dissipation", *International Communications in Heat and Mass Transfer*, Vol. 138, (2022), 106229. doi: 10.1016/j.icheatmasstransfer.2022.106229.

9. Guedri, K., Khan, W., Alshehri, N.A., Mamat, M., Jameel, M., Xu, Y.-J., Waqas, M. and Galal, A.M., "Thermal aspects of magnetically driven micro-rotational nanofluid configured by exponential radiating surface", *Case Studies in Thermal Engineering*, Vol. 39, (2022), 102322. doi: 10.1016/j.csite.2022.102322.
10. Waqas, M., Alzahrani, F. and Khan, M.I., "Transport of chemically reactive thixotropic nanofluid flow by convectively heated porous surface", *Chemical Physics Letters*, Vol. 803, (2022), 139742. doi: 10.1016/j.cplett.2022.139742.
11. Ebermann, M., Bogenfeld, R., Kreikemeier, J. and Glüge, R., "Analytical and numerical approach to determine effective diffusion coefficients for composite pressure vessels", *Composite Structures*, Vol. 291, (2022), 115616. doi: 10.1016/j.compstruct.2022.115616.
12. Shadman, P., Parhizi, Z., Fathollahi, R., Zarinfar, M., Anisimova, E.Y. and Pasha, P., "Combined septum and chamfer fins on threated stretching surface under the influence of nanofluid and the magnetic parameters for rotary seals in computer hardware", *Alexandria Engineering Journal*, Vol. 62, (2023), 489-507. doi: 10.1016/j.aej.2022.07.044.
13. Fathollahi, R., Hesarakhi, S., Bostani, A., Shahriyari, E., Shafiee, H., Pasha, P., Chari, F.N. and Ganji, D.D., "Applying numerical and computational methods to investigate the changes in the fluid parameters of the fluid passing over fins of different shapes with the finite element method", *International Journal of Thermofluids*, Vol. 15, (2022), 100187. doi: 10.1016/j.ijft.2022.100187.
14. Abdollahzadeh, M.J., Fathollahi, R., Pasha, P., Mahmoudi, M., Samimi Behbahan, A. and Domiri Ganji, D., "Surveying the hybrid of radiation and magnetic parameters on maxwell liquid with TiO<sub>2</sub> nanotube influence of different blades", *Heat Transfer*, Vol. 51, No. 6, (2022), 4858-4881. doi: 10.1002/hjt.22526.
15. Pasha, P. and Domiri-Ganji, D., "Hybrid analysis of micropolar ethylene-glycol nanofluid on stretching surface mounted triangular, rectangular and chamfer fins by fem strategy and optimization with RSM method", *International Journal of Engineering, Transactions B: Applications*, Vol. 35, No. 5, (2022), 845-854. doi: 10.5829/IJE.2022.35.05B.01.
16. Darezereshki, E., Behrad Vakylabad, A. and Yousefi, M., "Chemical process of synthesizing zinc oxide (ZnO) with nanorod and spherical morphologies", *International Journal of Engineering, Transactions B: Applications*, Vol. 34, No. 8, (2021), 1888-1897. doi: 10.5829/ije.2021.34.08b.10.
17. Wang, B., Wang, Z., Sun, C. and Wu, Y., "Numerical investigation of the heat-fluid characteristic inside high-speed angular contact ball bearing lubricated with grease", *International Journal of Engineering, Transactions B: Applications*, Vol. 34, No. 5, (2021), 1313-1320. doi: 10.5829/ije.2021.34.05b.26.
18. Madani, M., Lin, K. and Tarakanova, A., "Dsressol: A sequence-based solubility predictor created with dilated squeeze excitation residual networks", *International Journal of Molecular Sciences*, Vol. 22, No. 24, (2021), 13555. doi: 10.3390/ijms222413555.
19. Kunkel, G., Madani, M., White, S.J., Verardi, P.H. and Tarakanova, A., "Modeling coronavirus spike protein dynamics: Implications for immunogenicity and immune escape", *Biophysical Journal*, Vol. 120, No. 24, (2021), 5592-5618. doi: 10.1101/2021.08.19.456973.
20. Hosseini, S., Roostaei, M., Mosavi Mashhadi, M. and Faraji, G., "Fabrication of al/mg bimetallic thin-walled ultrafine-grained tube by severe plastic deformation", *Journal of Materials Engineering and Performance*, Vol. 31, No. 5, (2022), 4098-4107. doi: 10.1007/s11665-021-06514-5.
21. Alrwashdeh, S.S., Ala'a, M. and Murtadha, T.K., "Effect of turbocharger compression ratio on performance of the spark-ignition internal combustion engine", *Emerging Science Journal*, Vol. 6, No. 3, (2022), 482-492. doi: 10.28991/ESJ-2022-06-03-04

---

### Persian Abstract

#### چکیده

در این مقاله دما و غلظت گونه‌ها در اطراف یک ظرف با استفاده از روابط واکنش و انتشار، واکنش بین ۳ گونه شیمیایی و رابطه بین تغییرات دما و سرعت یک واکنش شیمیایی بررسی شده است. نکته جدید این مقاله استفاده از ضرایب مختلف ثابت های انتشار مواد و همچنین در نظر گرفتن غلظت و دمای مواد درگیر در واکنش با منابع غیرحرارتی و با حالت های منبع گرمایی است به طوری که غلظت و سرعت انتقال حرارت مواد درگیر را نشان می دهد. واکنش های شیمیایی به شکل نمودارهای دو بعدی و سه بعدی در مورد فاصله آنها از مرزهای ظرف. با توجه به نتایج به دست آمده، زمانی که دمای واکنش دهنده‌ها افزایش می یابد و گرمای بیشتری آزاد می شود، غلظت نیز تغییر زیادی کرده و مقدار آن افزایش می یابد. اما در محصولاتی مانند ماده (ج) با واکنش دهنده های (الف) و (ب) رابطه معکوس دارد به گونه ای که با افزایش غلظت و دمای واکنش دهنده ها، این مقادیر در محصول کاهش می یابد. به طور متوسط، تغییرات غلظت در فاصله از مرکز تا محیط اطراف در حالت منبع حرارت حداکثر حدود ۷۶ درصد کمتر از حالت متوسط منبع گرما و حدود ۱۴ درصد کمتر از حالت منبع حرارت غیر گرما است.

---



# Hybrid Beamforming for Dual Functioning Multi-input Multi-output Radar using Dimension Reduced-baseband Piecewise Successive Approximation

V. Kadam<sup>\*a</sup>, A. Deshmukh<sup>b</sup>, S. Bhosale<sup>a</sup>

<sup>a</sup>Electrical Engineering Department, Veermata Jijabai Technological Institute, Mumbai, India

<sup>b</sup>Electronics and Telecommunication engg. Department, Sinhgad College of Engineering, Pune, India

## PAPER INFO

### Paper history:

Received 05 October 2022

Received in revised form 23 October 2022

Accepted 05 November 2022

### Keywords:

Dual Functioning Radar Communication

Hybrid Beamforming

Multi-input Multi-output Radar

Spectrum Sharing

## ABSTRACT

A reliable and effective hybrid beamforming design for dual functioning multi-input multi-output (MIMO) radar is a challenging research problem because of the concerns related to limited user capacity, interference, and lack of performance trade-off. Due to the shortage of available spectrum, radar frequency spectrum sharing has become vital in emerging 5G communication systems. This will reduce spectrum congestion, therefore receiving significant attention. The existing hybrid beamforming methods reduce the radio frequency (RF) chains but improving user capacity is still a major concern. Future dual radar-communication designs are having challenges in enhancing the user capacity with minimum RF chains, interference mitigation, and hardware cost reduction. This work proposes a novel approach to a hybrid beamforming mechanism for dual-functioning MIMO radar. This mechanism uses the dimension-reduced baseband piecewise successive approximation integrated with a digital precoder. At the analog precoder, the piecewise successive iterative approximation approach is applied to perform the analog beamforming. The novel hybrid beamforming with lens antenna array integration improves the user capacity and reduces power requirement, interference, and expenses. The simulation results showed improved performances compared to existing state-of-the-art methods in terms of bit error rate, spectral efficiency, energy efficiency, and response time.

doi: 10.5829/ije.2023.36.01a.20

## NOMENCLATURE

MIMO	Multi-input multi-output	DR-BPSA	Dimension reduced baseband piecewise successive approximation
$I_{(i,k)}$	Input Signal	MUI	Mutual user interference
$D_{(i,k)}$	Digital precoding output	PSIA	Piecewise successive iterative approximation
$D_{(i,k)}^{RF}$	Transmitting signal	$\sigma$	Noise vector component
$A_{(i,j)}$	Transmitted Signal	$\gamma_i$	The signal-to-interference-plus-noise ratio for ith user
$S_i^r$	Radar probing signal	$H$	Communication channel
$S_i^c$	Communication signal	$U^H$	Transformation matrix $n \times m$
$P_t$	Total power	$\eta_{SE}$	Spectral efficiency
$F_{RF}$	The analog precoding weight matrix	$\eta_{EE}$	Energy efficiency
$F_{BB}$	The digital precoding weight matrix	$R$	Achievable sum rate
$l(\hat{\theta}_1)$	Lens antenna array steering vector	$P_{RF}$	Power consumed by RF chain
$K$	Set of the received signal	$P_{SW}$	Power consumed by switch
$N_{RF}$	Total number of transmit antennas	$P_{BB}$	Power consumed by baseband station

## 1. INTRODUCTION

The recent progress of wireless communication standards in commercial industry applications needs high-speed

communication mechanisms like millimeter-wave (mm-wave) for MIMO systems [1]. The emerging mm-wave interfaces, running from 30-300 GHz, provide a chance to reach such loaded capacity requirements for future

\*Corresponding Author Institutional Email:  
[vskadam\\_p18@ee.vjti.ac.in](mailto:vskadam_p18@ee.vjti.ac.in) (V. Kadam)

Please cite this article as: V. Kadam, A. Deshmukh, S. Bhosale, Hybrid Beamforming for Dual Functioning Multi-input Multi-output Radar using Dimension Reduced-baseband Piecewise Successive Approximation, *International Journal of Engineering, Transactions A: Basics*, Vol. 36, No. 01, (2023), 182-190

wireless communications. But the available communication frequency spectrum cannot meet the excess requirement of uplink and downlink frequency [2]. Notwithstanding the large transmission data transfer capacities of orders of magnitude, shorter wavelengths at mm-wave permit and aerials in an indistinguishable physical location were obtained [3]. Spectral congestion problems demand the radar frequency band share to fulfill the requirements. The feasibility of sharing the hardware platform between radar functioning and communication system is the highest among the available options [4]. Currently, L-band, S-band, C-band, and mm-wave band are existing cases that share the frequency spectrum. These elements are linked to the massive MIMO, leading to an increase in multiplexing and beamforming. It found that mm-wave and massive MIMO could accomplish the order-of-magnitude increment in the system limit. However, designing the mm-wave massive MIMO is challenging due to high transceiver complexity and energy depletion [5]. The dual-functioning radar communication system design shares the common hardware to reduce weight on shipborne or airborne platforms, making it hardware efficient, cost-efficient, and power-efficient. But at the same time, every antenna in the MIMO configuration requires one dedicated radio frequency (RF) chain. In this case, using an extensive number of antennas in the mm-wave MIMO system leads to an equally vast product of RF chains. This case applies to the dual-functioning MIMO system also. Furthermore, it was observed that the RF chain elements drain around 70% of the overall transceiver energy requirement [6]. As an outcome, the cost and consumption of energy caused by a high number of RF chains in the mm-wave MIMO system turn uneconomic in reality.

Traditional baseband digital beamformers in MIMO systems demand that every antenna should have a devoted RF chain containing a digital to analog converter, up-converter, power amplifier, and signal mixer [7]. Thus, energy consumption and expense restrain the implementation of a fully-digital architecture. To overcome such challenges, beamforming practices have been forced to rely on fewer RF chains. Although analog beamforming is implemented for enhancing spatial resolution in the MIMO radars, it is limited in the application of the communication domain since all processing has been done in the RF domain [8]. By utilizing the high gain, the analog beamforming is used in distinctive wireless personal area networks (WPAN) and wireless fidelity (Wi-Fi) to get a high data rate. But the performance of the before-mentioned methods is achieved with an inadequate increment in system complexity of the joint radar-communication systems compared to independent designs [9]. If only an analog structure is used at the transmitter since only one RF chain is equipped for supporting one data in a cycle, the

size, cost, and spectrum efficiency are the points to compromise. In such cases, hybrid (analog+digital) beamforming architecture has fetched attention, achieving a reliable trade-off of analog and digital precoding through phase shifters and baseband weights optimization.

A significant amount of research has been initiated to design hybrid beamforming systems using fully connected structures [10]. But considering mm-wave communications, antennas like uniform area array (UPA) and uniform linear array (ULA) have not been practical for a fully connected structure as they require many power amplifiers and phase shifters. The radar-specific design will add more complexity to it. It leads to excessive energy consumption, poor spectral efficiency, and high computational costs [11]. The sub-connected structure performs better than the fully-connected structure, reducing power consumption and hardware complexity with less performance degradation. Still, the current solutions are ineffective for dual-functioning massive MIMO radar systems. Figure 1 illustrates a dual-functioning MIMO radar system, including analog and digital precoding at the transmitter level. The signal processing structure of the receiver is the same as that of the transmitter design. The hybrid beamforming techniques are successful in minimizing the required number of RF chains and aim to improve massive MIMO performance by incorporating parameters such as spectral efficiency (SE) and energy efficiency (EE) [12]. However, for future dual-functioning radar communication systems, the main requirement is user capacity improvement, along with SE, EE, and computational efficiency (CE).

To address these issues, a novel mechanism of hybrid beamforming with lens antenna arrays for the dual-functioning MIMO radar is proposed [13]. The use of lens antennas not only reduces the RF chains but also reduces the interferences while improving the user capacity [14]. Furthermore, narrow beams can be preserved using a lens antenna array with fewer RF

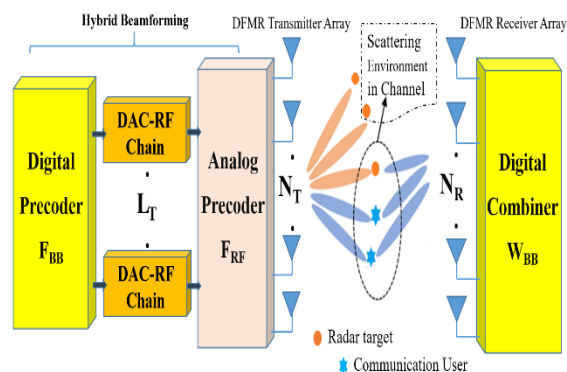


**Figure 1.** Hybrid beamforming system architecture for DF-MIMO radar

chains, resulting in a significant reduction in the power required per beam and intra-beam interferences [15, 16].

The remainder of the paper consists of sections such as related literature in section 2, proposed methodology in section 3, simulation results in section 4, and conclusion in section 5.

### 1. 1. Literature Related Work

The hybrid (analog-digital) beamforming approach was proposed by Khalid [17] for the massive MIMO communication systems in the sparse mm-wave channels. They designed a hybrid regularized channel diagonalization approach that combines analog RF precoding with linear digital precoding to observe the performance. Zhang et al. [18] have optimized hybrid beamforming for the massive MIMO relay system by defining the objective function of maximizing the sum rate of the massive MIMO system. The piecewise successive approximation technique was then applied to reduce the information loss. The hybrid beamforming techniques were proposed by Du et al. [19] for the multi-user massive MIMO-OFDM systems. They offered an alternating maximization system in that analogy beamforming had optimized using the Riemannian manifold.

The non-orthogonal multiple access (NOMA) had adopted by Lee et al. [20] for the efficient hybrid beamforming in massive MIMO systems. The NOMA was applied by selecting two users with the higher channel correlation, and then RF beamforming and digital beamforming were applied to both users. The power allocation was used to achieve intra-pair user fairness. The transmission of the mm-wave system was examined by Ozbek et al. [21] via the linear beamforming methods for physical layer systems. They designed secure multi-user mm-wave massive MIMO systems using hybrid beamforming at the legitimate users, eavesdroppers, and base stations. The massive MIMO system was exploited by Zhai et al. [22] with hybrid beamforming to improve the computational efficiency of over-the-air computation at minimum cost. They have designed the scenario of scalable multi-antenna devices sending data simultaneously to the access point. The access point had integrated with massive antennas. The downlink mm-wave massive MIMO system was investigated by Zhan and Dong [23] with a novel interference cancellation approach on hybrid beamforming. They have designed different successive interference cancellation techniques to address the intra-user and inter-user interference in dual communication systems. Gao et al. [24] have proposed novel wideband two-hybrid beamforming techniques according to true-time-delay lines and virtual sub-array lines to discard the beam squint effect. The transmit beamforming focused by Vlachos and Thompson [25] with the novel approach of low-end elements to improve the EE with reduced impacts on SE. They designed a novel analogy precoder

where the RF chains were deactivated according to the optimization algorithm rather than reduction.

The framework for approximating the optimal fully-digital beamformer with a suitable hybrid one has been proposed by Fortunati et al. [26] for efficient hybrid beamforming. But dedicated RF chains to each antenna including power amplifiers, digital to analog, and up-converters consume excess power, and the cost of a complete hardware setup is unbearable. To overcome these issues, the RF chains are reduced using fully analog or hybrid configuration, but this increases the system complexity. Ioushua and Eldar [27] designed the alternating minimization of approximation gap (Alt-MaG) framework using the hybrid beamforming for the massive MIMO systems. But the infinite resolution of phase shifters and network switches makes its hardware implementation impractical. Then, Zhang et al. [28] made an attempt to maximize the entire mm-wave communication system's sum rate. They designed piecewise successive iterative approximation (PSIA) for analog precoder to perform analog beamformer and combiner but failed to handle the system complexity. The piecewise successive approximation (PSA) method was used in the digital precoder stage to prevent data loss. Another novel hybrid beamforming model had designed by Zhang et al. [29] for a multi-user mm-wave massive MIMO communication system with the objective function of sum-rate maximization. They adopted a two-stage design technique for joint transmitter and receiver design in sub-connected configuration to avoid system complexity due to fully connected configuration. The analog beamformer and combiner were designed using the piecewise dual joint iterative approximation (PDJIA) technique. The baseband piecewise successive approximation (BPSA) was designed for digital beamforming to satisfy the criterion of information loss prevention. But this compromises the computational efficiency. Thus there is a need for an efficient hybrid beamforming design that will achieve the best trade-off between achievable sum rate and energy efficiency.”

### 1. 2. Contribution

The work presented in this paper has background of hybrid beamforming using piecewise successive iterative approximation (PSIA) and baseband piecewise successive approximation (BPSA) techniques as described by Zhang et al. [28, 29]. In addition to this, reduction in dimensions of sparse beamspace channel of the MIMO system using lens antenna array is proposed as a novelty. This not only reduces the required number of RF chains but also increases the energy efficiency required in most of the RF systems. The contribution is listed as follows:

- To address the lower spectrum efficiency performance of existing hybrid beamforming methods, the dimension reduction of beamspace channel matrices and lens antenna technology are

investigated to improve SE performance through successive approximation interference cancellation.

- To reduce the required number of RF chains, the novel hybrid beamforming design incorporates the dimension reduction-baseband piecewise successive approximation (DR-BPSA) beamforming technique at baseband precoding and the optimal piecewise successive iterative approximation (PSIA) technique at analog precoding. This novel hybrid beamforming design ensures reduced RF chains with higher energy efficiency without loss of information.

The performance of the designed DR-BPSA hybrid beamforming approach is compared with the existing methods by simulations. This ensures the effectiveness of the proposed design as it can achieve a higher spectrum and energy efficiency against the variable number of users.

## 2. PROPOSED METHODOLOGY

Here, a dual functioning MIMO radar system is considered, which transmits communication signal and radar probing signal simultaneously to the downlink mm-wave users and target, respectively. It uses the lens antenna array to minimize the RF chains and improve the user capacity of the mm-wave massive MIMO communication function. The number of RF chains and base stations to the number of users concerns constraints, as mentioned by Zhang et al. [29].

**2.1. System Model** Figure 2 shows the proposed hybrid beamforming design blocks. In this design, the input  $I_{(i,k)}$  is passed to the digital precoder block, where we applied the Dimensional Reduced-BPSA approach to satisfy the objective of avoiding information loss. The BPSA approach of the digital precoding is adapted from literature [26] with modification in channel matrix dimensions to reduce the number of required RF chains that produced  $D_{(i,k)}$ . After that, DAC is applied on  $D_{(i,k)}$  to convert the digital signals to analog signals before allocating the RF channels. In analog beamforming, the transmitted signals  $(D_{(i,k)}RF)$  are mapped by performing the analog beamformer and combiner using the PSIA approach. Here the PSIA technique is adopted from literature [25] to maximize the sum rate performance. The output vector  $A_{(i,j)}$  is further transformed for antenna array allocation using power allocations.

The lens antenna arrays transform the spatial domain channel into a beam space channel matrix. The lens antenna array signals are mathematically represented to realize the spatial discrete Fourier transformation FT using transform matrix  $U$  of size  $n \times n$ . The input signal  $S_i$  is given by:

$$S_i = FT [ U S_i^r + (I-U) S_i^c ] \quad (1)$$

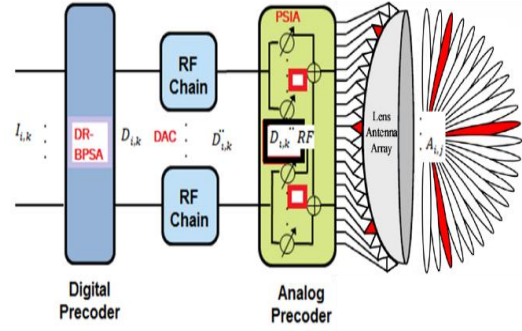


**Figure 2.** Proposed hybrid beamforming design block-diagram for DF-MIMO radar

where,  $S_i^r$  and  $S_i^c$  represent the radar and communication signals, respectively. In the hybrid beamforming model, the transmitted signal  $A_{(i,j)}$  with maximum allotted power constraint  $P_i$  is given by:

$$A_{(i,j)} = W_{RF} W_{BB} P S_i \quad (2)$$

$W_{RF}$  and  $W_{BB}$  are the analog and baseband (digital) beam weight matrix, respectively.  $P$  is a power allocation matrix with  $\|P\|^2 = P_t$ . Without loss of generality, the flat Rayleigh fading environment is considered as transmission channel  $H$ . The transform matrix  $U$  contains the  $n$  directional array steering vectors for channel matrix  $H$ , represented as:

$$U = [l(\hat{\theta}_1) \ l(\hat{\theta}_2) \ \dots \ l(\hat{\theta}_n)]^H \quad (3)$$

The lens antenna array steering vector  $l(\hat{\theta}_1)$  is represented as:

$$l(\hat{\theta}) = \frac{1}{\sqrt{n}} [e^{-j\pi\theta z}] \quad (4)$$

where,  $\hat{\theta}_j = \frac{1}{n} (j - \frac{n+1}{2})$ ,  $j = 1, 2, \dots, n$  and  $z \in q \frac{n-1}{2}$ ,  $q=0, 1, 2, \dots, n-1$  represents the predefined spatial direction. Then, the received signal vector  $Y$  using the lens antenna arrays is expressed as:

$$Y = W_{RF} H^H U^H D P K + \sigma \quad (5)$$

where  $H^H$  is the  $n \times m$  channel matrix,  $U^H$  is the transformation matrix of size  $n \times m$ ,  $D = f(W_{BB})$  represents the BPSA precoding matrix,  $P$  represents the power allocation matrix for all users, and  $K$  represents the set of received signals for each user as  $K=[k_1, k_2, \dots, k_m]$ . The  $\sigma \sim CN(0, \sigma_0 I_N)$  represents the noise vector. The mutual user interference (MUI) at the receiver is estimated as  $(HX-S_i)$ , which is a key measure of performance and closely related to the achievable sum rate. Thus, the achievable sum rate  $R$  is inversely proportional to mutual user interference [30], and it is given as:

$$R = \sum_{i=0}^K \log_2 (1+\gamma_i) \quad (6)$$

where,  $\gamma_i$  is the signal-to-interference-plus-noise ratio of the  $i^{th}$  user.

**2. 2. Proposed DR-BPSA Approach** Now, according to Equation (5), the terms for each  $i^{th}$  user is further elaborated as:

$$\left. \begin{aligned} H_{i,j} &= HU_i \\ D_{i,k} &= D_i \end{aligned} \right\} \quad (7)$$

where  $HU_i$  represents the beam space channel vector using lens antenna arrays and  $D_i$  represents BPSA digital precoding vector for the  $i^{th}$  user.

DR-BPSA approach uses the beamspace MIMO system to convert the traditional spatial channel to beamspace channel. For this purpose, it uses a lens antenna array to capture channel sparsity with the intention of reducing the required number of RF chains. Since the scattering in mm-wave communications is not rich, the number of effective propagation paths is limited and less than the total number of RF chains at the transmitter. This occupies only a small number of dominant beams. As a result, the mm-wave beamspace channel is sparse. Thus a small number of dominant beams is selected to significantly reduce the dimension of the MIMO system and the number of required RF chains without obvious performance loss. This selection is made by choosing the strongest element amongst the non-zero elements in the sparse channel vector. Then the influence of the selected channel component is ignored from the total beamspace channel estimation. Beam selection is depending upon the total number of users. As the one beam attend only one supporting user at the same frequency. The total number of user should be equal to the available number of RF chains. This is considered as fundamental limit if the beamspace MIMO system. The received signal vector from Equation (5) is represented using the DR approach as:

$$Y = W_{RF} H_{DR}^H U_{DR}^H D_{DR} P K + \sigma \quad (8)$$

where,  $H_{DR} = H_{DR}^H U_{DR}^H$  is the Dimension-Reduced beamspace channel matrix with the selected number of beams with their index set of size  $r \times m$ .  $D_{DR}$  is the BPSA precoding vector according to dimensionality reduced beam space channel vector. The original size  $n \times m$  is reduced to  $r \times m$  after applying the DR technique where  $r < n$ . As the number of dimensions is reduced in  $D_{DR}$  It reduces the required number of RF channels, directly affecting cost and energy efficiency. The elements in Equation (6) are then revised after applying Dimension Reduction (DR) as:

$$\left. \begin{aligned} H_{i,j} &= HU_{DR}^i \\ D_{i,k} &= D_{DR}^i \end{aligned} \right\} \quad (9)$$

Therefore, the above novel design of modified BPSA scheme at digital precoder ensures energy efficiency with

improved user capacity and without data loss. Then, the below steps are performed for each  $D_{i,k}$  with its corresponding  $H_{i,j}$  to update the hybrid beamforming weights using successive approximations [29] to get optimized weights for beamformers in the mm-wave massive MIMO communication system. The design steps and flowchart of the proposed hybrid beamforming are illustrated in Figure 3.

**2. 3. Flowchart of the Proposed Methodology**

The functionality of PSIA has already proven effective with the hybrid beamforming approach [27]. But it suffered from the challenges of performance trade-offs considering the parameters EE, SE, and CE. The proposed novel hybrid beamforming design with the lens antenna arrays technique overcomes these challenges.

**Algorithm for Proposed Hybrid Beamforming Design**

---

**Input:**  $S_i, W_{RF}, W_{BB}$ ;  
**For**  $k=1$  to  $K$ , **do**  
 Obtain  $\tilde{D}_{i,k} = DAC(D_{i,k})$ ;  
 Calculate  $H^H$  by  $W_{RF} H W_{BB}$ ;  
 Apply DR-BPSA to update  $H^H$  and  $D_{i,k}$  ;  
 Obtain  $HU_{DR}^i$  and  $D_{DR}^i$ ;  
 Allocate RF channel for each  $D_{i,k}^i$  to get  $D_{i,k}^{i,RF}$ ;  
 Normalize  $W_{BB}$  by  $W_{BB}(i) = \frac{W_{BB}(i)}{\|W_{RF} W_{BB}(i)\|}$ ,  $i=1, \dots, n$   
 Apply PSIA analog beamforming on  $D_{i,k}^{i,RF}$ ;  
 Get the analog beamformer  $D_{i,k}^{i,RF}$ ;  
**End for**  
**Output:**  $A_{i,j}, H_{i,j}$

---

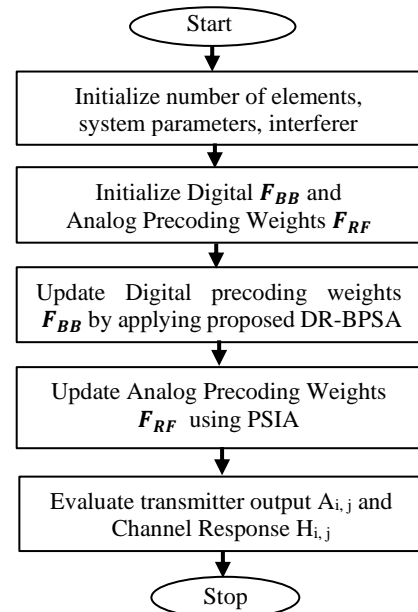


**Figure 3.** Flowchart for the proposed hybrid beamforming

After the lens array allocation to form the beam space channel matrix and hybrid precoding, the power allocation with lens antenna arrays must be adequate to improve the EE, SE, and CE by mitigating interference.

### 3. SIMULATION RESULTS AND DISCUSSION

This section presents the experimental results simulated on the MATLAB platform and a comparative analysis of the proposed model. The performances are measured in terms of SE, EE, BER, and CE in terms of response time.

**i. Spectrum Efficiency:** It is the optimized use of spectrum or bandwidth so that the maximum amount of data can be transmitted with the fewest transmission errors. Spectrum efficiency  $\eta_{SE}$  is defined as the achievable sum rate, and it is calculated as:

$$\text{Spectrum Efficiency } (\eta_{SE}) = \sum_{j=0}^n \sum_{i=1}^{|S_n|} R_{i,j} \quad (10)$$

where  $n$  is the total number of transmit antennas (256 in this work),  $S_n$  is the set of users served by the  $n^{\text{th}}$  beam. The  $R_{i,j}$  is represents the achievable rate of  $i^{\text{th}}$  user at  $j^{\text{th}}$  beam.

**ii. Energy Efficiency:** It is defined as the ratio between the achievable sum rate  $R_{\text{sum}}$  and the total power consumption. The EE is represented as  $\eta_{EE}$  and computed by:

$$\eta_{EE} = \frac{R_{\text{sum}}}{P_{\text{P}} + N_{\text{RF}} P_{\text{RF}} + N_{\text{RF}} P_{\text{SW}} + P_{\text{BB}}} \text{ (bps/Hz/W)} \quad (11)$$

For BER and CE parameters, the standard formulas are adopted. The BER has been computed among the transmitted and received signals to estimate the errors. For CE, the resource utilization criteria is estimated in terms of the processing speed of each technique. The CE counts the total processing time required to perform the mm-wave MU-MIMO communications in seconds. Complexity of the system is also possible to address using total processing time.

As per the simulation parameters mentioned in Table 1, the mm-Wave MIMO with a varying number of users is designed to check the scalability of the proposed model. The number of users ( $m$ ) varies from 10 to 50 with constant transmit power and the total number of beams. Figures 4 to 6 demonstrates the outcome of SE, EE, and BER rates using different hybrid beamforming techniques and the conventional baseline (FD-MIMO) method [26].

**TABLE 1.** Simulation parameters for user density scenario

Parameter	SNR	$n$	$P_t$	$P_{RF}$	$P_{SW}$	$P_{BB}$	$m$
User Density Scenario	10 dB	256	32 mW	300 mW	5 mW	200 mW	10:5:50

The SE performance shown in Figure 4 reveals that with the increase in the number of users, the spectral performance gained due to the increasing number of transmitting signals in the mm-wave multi-user MU-MIMO communication system. Among all these methods, the conventional baseline FD-MIMO technique shows a much higher SE rate than all other hybrid beamforming techniques. The FD-MIMO technique delivered the higher SE due to the dedicated RF allocation to each beam in the communication system. But, this has led to significant energy consumption (Figure 5) and an expensive approach (Figure 6). FD-MIMO techniques need many RF chains, limiting the user capacity. The outcomes of EE and BER revealed the limitations of the FD-MIMO technique. The mm-wave massive DF MIMO radar is introduced to overcome these challenges using a hybrid beamforming approach. Therefore, the analysis of all hybrid beamforming methods is presented in this section.

From Figure 4 (SE), Figure 5 (EE), and Figure 6 (BER), it is observed that the proposed DR-BPSA method delivered better performances compared to recent hybrid beamforming techniques. Among four hybrid beamforming methods, the Alt-Mag method [26] shows the worst performance for SE, EE, and BER due to its tedious approach to performing the analog and digital precoding tasks via the alteration minimization for approximation gap. The other two techniques, PSIA [28] and PDJIA [29], failed to achieve the trade-off among SE, EE, and BER rates. PSIA method achieved a better EE than the PDJIA technique but was unable to improve the SE and BER performances compared to the PDJIA method and vice versa. In the proposed DR-BPSA method, these limitations are overcome using a novel hybrid beamforming technique that utilizes the benefits of BPSA (digital precoder) and PSIA (analog precoder) with the mechanism of dimension reduction. Table 2 further demonstrates each method's outcome values of

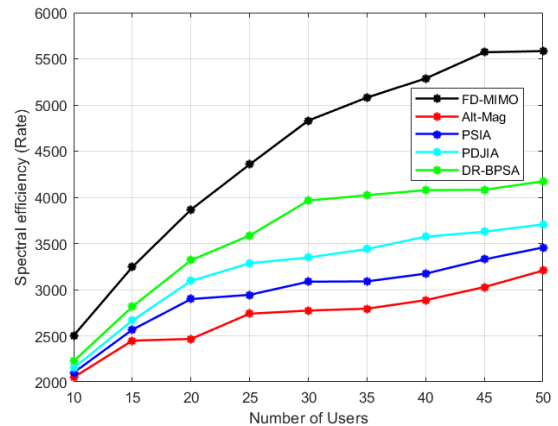


**Figure 4.** Spectral efficiency analysis for user density scenario

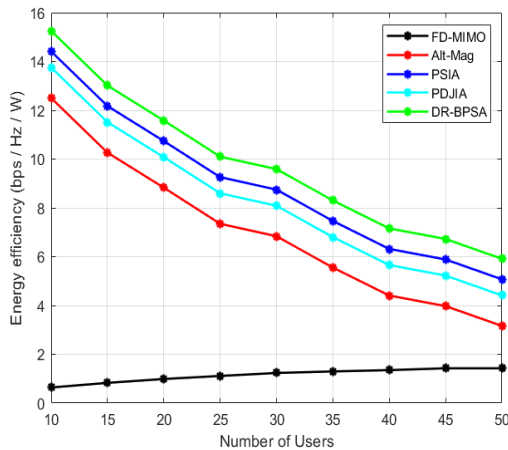


**Figure 5.** Energy efficiency analysis for user density scenario

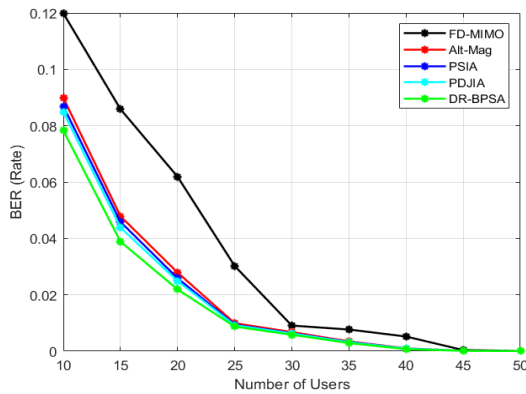


**Figure 6.** BER analysis for user density scenario

**TABLE 2.** Performance analysis for user density scenario

Methods	Energy Efficiency (bps/Hz/W)	Spectral Efficiency (bps/Hz)	Bit Error Rate	Cost-Efficiency (Seconds)
FD-MIMO [26]	1.1744	$4.5983 \times 10^{03}$	0.0356	1.92
Alt-Mag [27]	7.2719	$2.7854 \times 10^{03}$	0.0208	1.79
PSIA [28]	9.1819	$3.0354 \times 10^{03}$	0.0199	1.67
PDJIA [29]	8.5219	$3.2854 \times 10^{03}$	0.0193	1.76
DR-BPSA	10.0219	$3.6604 \times 10^{03}$	0.0175	1.58

SE, EE, and BER rates. From these outcomes, it is claimed that the proposed DR-BPSA technique successfully addressed the limitations of existing methods concerning the performance trade-off. The novel approach of hybrid beamforming with its integration with lens antenna arrays method reduces the required number of RF channels with maximum system throughput and higher user capacity support.

#### 4. CONCLUSION

This paper proposes the novel hybrid beamforming approach called Dimension Reduced Baseband Piecewise Successive Approximation in Hybrid Beamforming for the dual functioning MIMO radar system with a core focus on hybrid beamforming improving the performances in terms of spectral efficiency, energy efficiency, bit error rate, and cost-efficiency. The proposed hybrid beamforming technique overcomes the challenges of existing hybrid beamforming solutions, such as lack of performance trade-off and limited user capacity. This hybrid beamforming technique is integrated with the lens antenna array system to improve the user capacity with minimum resource utilization and computational efforts without data loss. The DR-assisted digital beamformer produced the reduction of RF channels with energy efficiency. The analog beamformer further performed the ZF-based analog precoding through PSIA operations to mitigate the inter-beam interferences. The experimental results showed the proposed design achieved an acceptable trade-off among all the parameters compared to the state-of-art techniques. The energy efficiency performance improved by 18 %, spectral efficiency performance improved by 19 %, and Bit Error Rate reduced by 17.5 %. The response time of the proposed method reduces effectively, so it is beneficial in terms of cost-efficiency. Applying the swarm intelligence or optimization algorithms for analog and digital beamformers will be an exciting extension of this work.

#### 5. REFERENCES

- Paul, B., Chiriyath, A.R. and Bliss, D.W., "Survey of rf communications and sensing convergence research", *IEEE Access*, Vol. 5, (2016), 252-270. doi: 10.1109/ACCESS.2016.2639038.
- Johnston, J., Venturino, L., Grossi, E., Lops, M. and Wang, X., "Mimo ofdm dual-function radar-communication under error rate and beampattern constraints", *IEEE Journal on Selected Areas in Communications*, Vol. 40, No. 6, (2022), 1951-1964. doi: 10.1109/JSAC.2022.3156651.
- Tamaddondar, M. and Noori, N., "Hybrid massive mimo channel model based on edge detection of interacting objects and cluster concept", *International Journal of Engineering, Transactions B: Applications*, Vol. 35, No. 2, (2022), 471-480. doi: 10.5829/ije.2022.35.02b.23.
- Martone, A. and Amin, M., "A view on radar and communication systems coexistence and dual functionality in the era of spectrum sensing", *Digital Signal Processing*, Vol. 119, (2021), 103135. https://doi.org/10.1016/j.dsp.2021.103135
- Liu, F., Masouros, C., Petropulu, A.P., Griffiths, H. and Hanzo, L., "Joint radar and communication design: Applications, state-of-the-art, and the road ahead", *IEEE Transactions on Communications*, Vol. 68, No. 6, (2020), 3834-3862. doi: 10.1109/TCOMM.2020.2973976.
- Gregorio, F., González, G., Schmidt, C. and Cousseau, J., Massive mimo systems, in *Signal processing techniques for*

- power efficient wireless communication systems. 2020, Springer.193-216.
7. Ali, E., Ismail, M., Nordin, R. and Abdulah, N.F., "Beamforming techniques for massive mimo systems in 5g: Overview, classification, and trends for future research", *Frontiers of Information Technology & Electronic Engineering*, Vol. 18, No. 6, (2017), 753-772. doi: <https://doi.org/10.1631/FITEE.1601817>
  8. Londhe, G.D. and Hendre, V.S., "Review on beamforming techniques for millimeter wave massive mimo", in Proceedings of the International e-Conference on Intelligent Systems and Signal Processing, Springer., (2022), 291-303.
  9. Ying, F., Ahmed, F. and Li, R., "A multiband multiple-input multiple-output antenna system for long term evolution and wireless local area networks handsets", *International Journal of Engineering*, Vol. 29, No. 8, (2016), 1087-1093. doi: [10.5829/idosi.ije.2016.29.08b.08](https://doi.org/10.5829/idosi.ije.2016.29.08b.08).
  10. Liu, F. and Masouros, C., "Hybrid beamforming with sub-arrayed mimo radar: Enabling joint sensing and communication at mmwave band", in ICASSP 2019-2019 IEEE International Conference on Acoustics, Speech and Signal Processing (ICASSP), IEEE., (2019), 7770-7774.
  11. Dilli, R., "Performance analysis of multi user massive mimo hybrid beamforming systems at millimeter wave frequency bands", *Wireless Networks*, Vol. 27, No. 3, (2021), 1925-1939. <https://doi.org/10.1007/s11276-021-02546-w>
  12. Payami, S., Ghorraishi, M., Dianati, M. and Sellathurai, M., "Hybrid beamforming with a reduced number of phase shifters for massive mimo systems", *IEEE Transactions on Vehicular Technology*, Vol. 67, No. 6, (2018), 4843-4851. doi: [10.1109/TVT.2018.2807921](https://doi.org/10.1109/TVT.2018.2807921).
  13. Jiang, Z.-M., Zhang, P., Rihan, M., Huang, L. and Zhang, J., "Maximum likelihood approach to doa estimation using lens antenna array", *EURASIP Journal on Wireless Communications and Networking*, Vol. 2019, No. 1, (2019), 1-7. <https://doi.org/10.1186/s13638-019-1549-3>
  14. Faridani, M. and Ghalamkari, B., "Four-element lens array antenna for advanced point-to-(multi) point high-bandwidth wireless communication", *Journal of Computational Electronics*, Vol. 17, No. 3, (2018), 1082-1089. <https://doi.org/10.1007/s10825-018-1204-y>
  15. Ansarudin, F., Abd Rahman, T., Yamada, Y., Rahman, N.H.A. and Kamardin, K., "Multi beam dielectric lens antenna for 5g base station", *Sensors*, Vol. 20, No. 20, (2020), 5849. <https://doi.org/10.3390/s20205849>
  16. dos Santos, R.A., Lobão da Silva Fré, G., da Silva, L.G., Paiva, M.C.d. and Spadoti, D.H., "Ultra-wideband dielectric lens antennas for beamsteering systems", *International Journal of Antennas and Propagation*, Vol. 2019, (2019). doi: <https://doi.org/10.1155/2019/6732758>
  17. Khalid, F., "Hybrid beamforming for millimeter wave massive multiuser mimo systems using regularized channel diagonalization", *IEEE Wireless Communications Letters*, Vol. 8, No. 3, (2018), 705-708. doi: [10.1109/LWC.2018.2886882](https://doi.org/10.1109/LWC.2018.2886882).
  18. Zhang, Y., Du, J., Chen, Y., Han, M. and Li, X., "Optimal hybrid beamforming design for millimeter-wave massive multi-user mimo relay systems", *IEEE Access*, Vol. 7, (2019), 157212-157225. doi: [10.1109/ACCESS.2019.2949786](https://doi.org/10.1109/ACCESS.2019.2949786).
  19. Du, J., Xu, W., Zhao, C. and Vandendorpe, L., "Weighted spectral efficiency optimization for hybrid beamforming in multiuser massive mimo-ofdm systems", *IEEE Transactions on Vehicular Technology*, Vol. 68, No. 10, (2019), 9698-9712. doi: [10.1109/LWC.2018.2886882](https://doi.org/10.1109/LWC.2018.2886882).
  20. Lee, Y.-R., Lee, W.-S., Jung, J.-S., Park, C.-Y., You, Y.-H. and Song, H.-K., "Hybrid beamforming with reduced rf chain based on pzf and pd-noma in mmwave massive mimo systems", *IEEE Access*, Vol. 9, (2021), 60695-60703. doi: [10.1109/ACCESS.2021.3073502](https://doi.org/10.1109/ACCESS.2021.3073502).
  21. Özbek, B., Erdoğan, O., Busari, S.A. and Gonzalez, J., "Hybrid beamforming strategies for secure multicell multiuser mmwave mimo communications", *Physical Communication*, Vol. 46, (2021), 101319. <https://doi.org/10.1016/j.phycom.2021.101319>
  22. Zhai, X., Chen, X., Xu, J. and Ng, D.W.K., "Hybrid beamforming for massive mimo over-the-air computation", *IEEE Transactions on Communications*, Vol. 69, No. 4, (2021), 2737-2751. doi: [10.1109/TCOMM.2021.3051397](https://doi.org/10.1109/TCOMM.2021.3051397).
  23. Zhan, J. and Dong, X., "Interference cancellation aided hybrid beamforming for mmwave multi-user massive mimo systems", *IEEE Transactions on Vehicular Technology*, Vol. 70, No. 3, (2021), 2322-2336. doi: [10.1109/TVT.2021.3057547](https://doi.org/10.1109/TVT.2021.3057547).
  24. Gao, F., Wang, B., Xing, C., An, J. and Li, G.Y., "Wideband beamforming for hybrid massive mimo terahertz communications", *IEEE Journal on Selected Areas in Communications*, Vol. 39, No. 6, (2021), 1725-1740. doi: [10.1109/JSAC.2021.3071822](https://doi.org/10.1109/JSAC.2021.3071822).
  25. Vlachos, E. and Thompson, J., "Energy-efficiency maximization of hybrid massive mimo precoding with random-resolution dacs via rf selection", *IEEE Transactions on Wireless Communications*, Vol. 20, No. 2, (2020), 1093-1104. doi: [10.1109/TWC.2020.3030772](https://doi.org/10.1109/TWC.2020.3030772).
  26. Fortunati, S., Sanguinetti, L., Gini, F., Greco, M.S. and Himed, B., "Massive mimo radar for target detection", *IEEE Transactions on Signal Processing*, Vol. 68, (2020), 859-871. doi: [10.1109/TSP.2020.2967181](https://doi.org/10.1109/TSP.2020.2967181).
  27. Ioushua, S.S. and Eldar, Y.C., "A family of hybrid analog-digital beamforming methods for massive mimo systems", *IEEE Transactions on Signal Processing*, Vol. 67, No. 12, (2019), 3243-3257. doi: [10.1109/TSP.2019.2911255](https://doi.org/10.1109/TSP.2019.2911255).
  28. Zhang, Y., Du, J., Chen, Y., Li, X., Rabie, K.M. and Kharel, R., "Near-optimal design for hybrid beamforming in mmwave massive multi-user mimo systems", *IEEE Access*, Vol. 8, (2020), 129153-129168. doi: [10.1109/ACCESS.2020.3009238](https://doi.org/10.1109/ACCESS.2020.3009238).
  29. Zhang, Y., Du, J., Chen, Y., Li, X., Rabie, K.M. and Kharel, R., "Dual-iterative hybrid beamforming design for millimeter-wave massive multi-user mimo systems with sub-connected structure", *IEEE Transactions on Vehicular Technology*, Vol. 69, No. 11, (2020), 13482-13496. doi: [10.1109/TVT.2020.3029080](https://doi.org/10.1109/TVT.2020.3029080).
  30. Liu, F., Zhou, L., Masouros, C., Li, A., Luo, W. and Petropulu, A., "Toward dual-functional radar-communication systems: Optimal waveform design", *IEEE Transactions on Signal Processing*, Vol. 66, No. 16, (2018), 4264-4279. doi: [10.1109/TSP.2018.2847648](https://doi.org/10.1109/TSP.2018.2847648).

---

**Persian Abstract**

---

**چکیده**

یک طراحی پرتوهای هیبریدی قابل اعتماد و موثر برای رادار چند ورودی چند خروجی دو کاره (MIMO) یک مشکل تحقیقاتی چالش برانگیز است زیرا نگرانی‌های مربوط به محدودیت ظرفیت کاربر، تداخل، و عدم تبادل عملکرد وجود دارد. به دلیل کمبود طیف در دسترس، اشتراک گذاری طیف فرکانس رادار در سیستم های ارتباطی نوظهور 5G حیاتی شده است. این امر ازدحام طیف را کاهش می دهد، بنابراین نکات قابل توجهی را به خود جلب می کند. روش های هیبریدی شکل دهی پرتوهای موجود، زنجیره های فرکانس رادیویی (RF) را کاهش می دهند، اما بهبود ظرفیت کاربر همچنان یک نگرانی اصلی است. طرح های ارتباطی دوگانه راداری آینده با چالش هایی در افزایش ظرفیت کاربر با حداقل زنجیره های RF، کاهش تداخل و کاهش هزینه ساخت افزار مواجه هستند. این کار یک رویکرد جدید به یک مکانیسم ترکیبی شکل دهی پرتو برای رادار MIMO با عملکرد دوگانه پیشنهاد می کند. این مکانیسم از تقریب متوالی تکه ای باند کاهش یافته استفاده می کند که با یک پیش کدگذار دیجیتال ادغام شده است. در پیش کدگذار آنالوگ، رویکرد تقریب تکراری تکه تکه برای انجام شکل دهی پرتو آنالوگ اعمال می شود. شکل دهی پرتو هیبریدی جدید با ادغام آرایه آنتن لنز ظرفیت کاربر را بهبود می بخشد و نیاز به برق، تداخل و هزینه ها را کاهش می دهد. نتایج شبیه سازی عملکرد بهتری را در مقایسه با روش های پیشرفته موجود از نظر نرخ خطای بیت، بازده طیفی، بازده انرژی و زمان پاسخ نشان داد.

---

## AIMS AND SCOPE

The objective of the International Journal of Engineering is to provide a forum for communication of information among the world's scientific and technological community and Iranian scientists and engineers. This journal intends to be of interest and utility to researchers and practitioners in the academic, industrial and governmental sectors. All original research contributions of significant value focused on basics, applications and aspects areas of engineering discipline are welcome.

This journal is published in three quarterly transactions: Transactions A (Basics) deal with the engineering fundamentals, Transactions B (Applications) are concerned with the application of the engineering knowledge in the daily life of the human being and Transactions C (Aspects) - starting from January 2012 - emphasize on the main engineering aspects whose elaboration can yield knowledge and expertise that can equally serve all branches of engineering discipline.

This journal will publish authoritative papers on theoretical and experimental researches and advanced applications embodying the results of extensive field, plant, laboratory or theoretical investigation or new interpretations of existing problems. It may also feature - when appropriate - research notes, technical notes, state-of-the-art survey type papers, short communications, letters to the editor, meeting schedules and conference announcements. The language of publication is English. Each paper should contain an abstract both in English and in Persian. However, for the authors who are not familiar with Persian, the publisher will prepare the latter. The abstracts should not exceed 250 words.

All manuscripts will be peer-reviewed by qualified reviewers. The material should be presented clearly and concisely:

- *Full papers* must be based on completed original works of significant novelty. The papers are not strictly limited in length. However, lengthy contributions may be delayed due to limited space. It is advised to keep papers limited to 7500 words.
- *Research notes* are considered as short items that include theoretical or experimental results of immediate current interest.
- *Technical notes* are also considered as short items of enough technical acceptability with more rapid publication appeal. The length of a research or technical note is recommended not to exceed 2500 words or 4 journal pages (including figures and tables).

*Review papers* are only considered from highly qualified well-known authors generally assigned by the editorial board or editor in chief. Short communications and letters to the editor should contain a text of about 1000 words and whatever figures and tables that may be required to support the text. They include discussion of full papers and short items and should contribute to the original article by providing confirmation or additional interpretation. Discussion of papers will be referred to author(s) for reply and will concurrently be published with reply of author(s).

## INSTRUCTIONS FOR AUTHORS

Submission of a manuscript represents that it has neither been published nor submitted for publication elsewhere and is result of research carried out by author(s). Presentation in a conference and appearance in a symposium proceeding is not considered prior publication.

Authors are required to include a list describing all the symbols and abbreviations in the paper. Use of the international system of measurement units is mandatory.

- On-line submission of manuscripts results in faster publication process and is recommended. Instructions are given in the IJE web sites: [www.ije.ir](http://www.ije.ir)-[www.ijeir.info](http://www.ijeir.info)
- Hardcopy submissions must include MS Word and jpg files.
- Manuscripts should be typewritten on one side of A4 paper, double-spaced, with adequate margins.
- References should be numbered in brackets and appear in sequence through the text. List of references should be given at the end of the paper.
- Figure captions are to be indicated under the illustrations. They should sufficiently explain the figures.
- Illustrations should appear in their appropriate places in the text.
- Tables and diagrams should be submitted in a form suitable for reproduction.
- Photographs should be of high quality saved as jpg files.
- Tables, Illustrations, Figures and Diagrams will be normally printed in single column width (8cm). Exceptionally large ones may be printed across two columns (17cm).

## PAGE CHARGES AND REPRINTS

The papers are strictly limited in length, maximum 8 journal pages (including figures and tables). For the additional to 8 journal pages, there will be page charges. It is advised to keep papers limited to 3500 words.

### **Page Charges for Papers More Than 8 Pages (Including Abstract)**

For International Author ***	\$55 / per page
For Local Author	100,000 Toman / per page

## AUTHOR CHECKLIST

- Author(s), bio-data including affiliation(s) and mail and e-mail addresses).
- Manuscript including abstracts, key words, illustrations, tables, figures with figure captions and list of references.
- MS Word files of the paper.



THOMSON REUTERS

WEB OF SCIENCE



Scopus®



CAS®

A DIVISION OF THE AMERICAN CHEMICAL SOCIETY



 Crossref



Scientific Indexing Services

Google  
Scholar